PONTIFICIA UNIVERSIDAD CATOLICA DE CHILE
ESCUELA DE INGENIERIA

BEHAVIOR OF RECTANGULAR REINFORCED CONCRETE COLUMNS CONFINED WITH CFRP JACKETS AND ANCHORS

JOSÉ LUIS JIMÉNEZ ULLOA

Thesis submitted to the Office of Research and Graduate Studies in partial fulfillment of the requirements for the Degree of Master of Science in Engineering

Advisor:
HERNÁN SANTA MARÍA OYANEDEL

Santiago de Chile, (November, 2017)

© MMXVII, José Luis Jiménez Ulloa

PONTIFICIA UNIVERSIDAD CATOLICA DE CHILE
ESCUELA DE INGENIERIA

BEHAVIOR OF RECTANGULAR REINFORCED CONCRETE COLUMNS CONFINED WITH CFRP JACKETS AND ANCHORS

JOSÉ LUIS JIMÉNEZ ULLOA

Members of the Committee:

HERNÁN SANTA MARÍA OYANEDEL

JOSE LUIS ALMAZAN CAMPILLAY

JORGE CARVALLO WALBAUM

JORGE VERA ANDREO

Thesis submitted to the Office of Research and Graduate Studies in partial fulfillment of the requirements for the Degree of Master of Science in Engineering

Santiago de Chile, (November, 2017)

© MMXVII, José Luis Jiménez Ulloa

To my family, for being a source of constant encouragement and unconditional love

ACKNOWLEDGEMENTS

During the development I received help from many people for which I am very grateful. I would like to thank specially professor Hernan Santa Maria for his support, advice and the freedom he provided to choose the path of the present investigation.

This thesis would not have been possible without the help, support and guidance of many friends including Raul Alvarez, Jaime Arriagada, Matias Urrejola, Pablo Alcaino, Camilo Guzman, Willy Rios, Alvaro Tapia, Jairo Rojas and many other friends I have met during my stay at the university. I would also like to thank the members of the committee, José Luis Almazán, Jorge Carvallo and Jorge Vera for reviewing the present thesis.

Finally, I want to thank to all my family, my father Teodoro, my mother Daysi and my sister Jazmin for their unconditional support. They have been constant source of encouragement and love.

Thanks to all!

TABLE OF CONTENTS

Page

ACKNOWLEDGEMENTS ii

LIST OF TABLES vii

LIST OF FIGURES x

ABSTRACT xxi

RESUMEN xxii

1. INTRODUCTION 1
    1.1 Motivation 1
        1.1.1 Seismic design and detailing of wall boundary elements 3
        1.1.2 Brittle failure of wall boundary elements in Chile 15
    1.2 Objectives 27
    1.3 Hypothesis 28
    1.4 Methodology 29
    1.5 Conclusions 32

2. FRP CONFINEMENT MODELS 33
    2.1 Overview 33
    2.2 Design – oriented models for circular FRP – confined columns 35
    2.3 Design – oriented models for rectangular FRP – confined columns 38
        2.3.1 Model M. Hosotani, K. Kawashima and J.-I. Hoshikuma (1998) 43
        2.3.2 Model C. P. Pantelides, Z. Yan and L. D. Reaveley (2004) 45
        2.3.3 Model M. N. Youssef, M. Q. Feng and A. S. Mosallam (2007) 48
        2.3.4 Model G. Wu, Z. S. Wu and Z. T. Lu (2007) 50
        2.3.5 Model J. G. Teng, T. Jiang, L. Lam and Luo (2009) 55
        2.3.6 Model C. Pellegrino and C. Modena (2010) 57
        2.3.7 Model Z. Wang, D. Wang, S. Smith and D. Lu (2012) 60
        2.3.8 Model Y.-Y. Wei and Y.-F. Wu (2012) 63
        2.3.9 Model N. F. Hany, E. G. Hantouche and M. H. Harajli (2015) 64
    2.4 Design – oriented models for FRP jackets and anchors 66

2.4.1 Model T. C. Triantafillou et al (2015) 68
2.4.2 Model N. F. Hany, E. G. Hantouche and M. H. Harajli (2016) 69
2.5 Summary 73

3. EXPERIMENTAL PROGRAM 74
3.1 Overview 74
3.2 Materials 77
3.2.1 Concrete 77
3.2.2 Steel reinforcement 78
3.2.3 CFRP reinforcement 79
3.3 Design of the specimens 83
3.3.1 Design of the steel reinforcement 83
3.3.2 Design of the CFRP transverse reinforcement 93
3.4 Fabrication 95
3.4.1 Timber formwork 95
3.4.2 Steel reinforcing cages 97
3.4.3 Placing of concrete 98
3.4.4 Manual surface preparation 101
3.4.5 CFRP installation 103
3.5 Instrumentation 113
3.5.1 Strain gages 113
3.5.2 Image data correlation 116
3.5.3 Linear variable differential transformers (LVDT) 118
3.6 Loading arrangement 119
3.7 Test procedure 121
3.8 Summary 121

4. EXPERIMENTAL RESULTS 123
4.1 Overview 123
4.2 Failure mode of specimens 127
4.2.1 Specimens 000-10a and 000-10b 127
4.2.2 Specimens 000-15a and 000-15b 131
4.2.3 Specimen 225-10 134
4.2.4 Specimen 225-15 136
4.2.5 Specimen 235-10 138

4.2.6 Specimen 235-15 140
4.2.7 Specimen 325-10 142
4.2.7 Specimen 325-15 144
4.2.8 Specimen 335-10 146
4.2.9 Specimen 335-15 148
4.3 Specimens axial behavior 150
4.4 Strain gage measurements 156
4.5 Digital image correlation 164
4.6 Other measurements 173
4.7 Summary 174

5. FINITE ELEMENT MODELS 176
5.1 Overview 176
5.2 Description of models 176
5.3 Materials 181
5.3.1 Concrete 181
5.3.2 Steel reinforcement 186
5.3.3 CFRP reinforcement 189
5.4 Loading method 193
5.5 Group 1 models results 194
5.5.1 Specimens axial behavior 194
5.5.2 Concrete stress distribution 200
5.5.3 Steel stress distribution 212
5.5.4 CFRP ultimate stress 215
5.5.5 Widening of specimens 220
5.6 Group 2 models results 226
5.6.1 Specimens axial behavior 226
5.6.2 CFRP ultimate stress 228
5.6.3 Widening of specimens 233
5.7 Summary 235

6. DESIGN ORIENTED MODEL 239
6.1 Overview 239
6.2 Assumptions of proposed procedure 242
6.3 Prediction of increments in the axial parameters 246

6.4 Summary 264

7. CONCLUSIONS 267
7.1 Experimental models 267
7.2 Finite element models 270
7.3 Design-oriented models 272
7.4 Future research 274

REFERENCES 277

APPENDIX A: MEASURED AND ESTIMATED CONCRETE PROPERTIES 286

APPENDIX B: STRAIN RATE OF LOADING IN CFRP-CONFINED TESTS 293

APPENDIX C: CONCRETE PRINCIPAL STRESSES AND STEEL AXIAL STRESS IN ANSYS MODELS OF TESTED SPECIMENS 298
C.1 Specimen 225-10 300
C.2 Specimen 225-15 301
C.3 Specimen 235-10 302
C.4 Specimen 235-15 303
C.5 Specimen 325-10 304
C.6 Specimen 325-15 305
C.7 Specimen 335-10 306
C.8 Specimen 335-15 307

APPENDIX D: AXIAL STRESS-STRAIN CURVES OF tested specimens using design oriented models 308
D.1 225-10 310
D.2 225-15 312
D.3 235-10 314
D.4 235-15 316
D.5 325-10 318
D.6 325-15 320
D.7 335-10 322
D.8 335-15 324
D.9 Matlab design-oriented closed models 326

LIST OF TABLES

Page

Table 2.1: FRP-confinement model (Hosotani, Kawashima, & Hoshikuma, 1998)..... 44

Table 2.2: FRP-confinement model (Pantelides & Yan, 2007) 46

Table 2.3: FRP-confinement model (Youssef, Feng, & Mosallam, 2007) 49

Table 2.4: FRP-confinement model (Wu, Wu, & Lu, 2007) 52

Table 2.5: FRP-confinement model (Teng, Jiang, Lam, & Luo, 2009)..... 56

Table 2.6: FRP-confinement model (Pellegrino & Modena, 2010)..... 58

Table 2.7: FRP-confinement model (Wang, Wang, Smith, & Lu, 2012b) 61

Table 2.8: FRP-confinement model (Wei & Wu, 2012)..... 63

Table 2.9: FRP-confinement model (Hany, Hantouche, & Harajli, 2015) 65

Table 2.10: FRP-confinement model (Triantafillou, et al., 2016) 68

Table 2.11: FRP-confinement model (Hany, Hantouche, & Harajli, 2016) 70

Table 3.1: List of specimens tested in the present investigation..... 77

Table 3.2: Steel reinforcement A 630-420 H properties (NCh 204, 2006)..... 79

Table 3.3: CSS-UCF10 Dry fiber properties..... 80

Table 3.4: CSS-ES Epoxy matrix properties 82

Table 3.5: CSS-UCF10 Cured composite properties 82

Table 3.6: Verification of overall buckling of the specimens..... 93

Table 4.1: Summary of specimen parameters 124

Table 4.2: Summary of specimen results related to the axial stress-strain curve 125

Table 5.1: Summary CFRP failure hoop stresses according to ANSYS models. 217

Table 6.1: Predictions for the parameter εcmax according to experimental and theoretical models 248

Table 6.2: Predictions for the parameter fcmax according to experimental and theoretical models 248

Table 6.3: Predictions for the parameter Ec according to experimental and theoretical models 248

Table 6.4: Predictions for the parameter εcult according to experimental and theoretical models 249

Table 6.5: Predictions for the parameter fcult according to experimental and theoretical models 249

Table 6.6: Predictions for the parameter ED according to experimental and theoretical models 249

Table 6.7: Predictions for the increments in the ratio εcmax/εcomax according to experimental and theoretical models..... 251

Table 6.8: Predictions for the increments in the ratio fcmax/fcomax according to experimental and theoretical models..... 251

Table 6.9: Predictions for the increments in the ratio Ec/Eco according to experimental and theoretical models 251

Table 6.10: Predictions for the increments in the ratio εcult/εcoult according to experimental and theoretical models..... 252

Table 6.11: Predictions for the increments in the ratio fcult/fcoult according to experimental and theoretical models..... 252

Table 6.12: Predictions for the increments in the ratio ED/EDo according to experimental and theoretical models..... 252

Table 6.13: Ratio of theoretical to experimental predictions of increment ratio εcmax/ εcomax..... 254

Table 6.14: Ratio of theoretical to experimental predictions of increment ratio fcmax/ fcomax 254

Table 6.15: Ratio of theoretical to experimental predictions of increment ratio Ec/Eco... 254

Table 6.16: Ratio of theoretical to experimental predictions of increment ratio εcult/εcoult 254

Table 6.17: Ratio of theoretical to experimental predictions of increment ratio fcult/fcoult 255

Table 6.18: Ratio of theoretical to experimental predictions of increment ratio ED/EDo . 255

Table A.1: Tested concrete properties 581 days after the 28th day of aging..... 287

Table A.2: Tested concrete properties 581 days after the 28th day of aging..... 289

Table A.3: Estimated concrete properties at the day of testing..... 292

LIST OF FIGURES

Page

Figure 1.1: Common sections of structural walls (Paulay & Priestley, 1992) 4

Figure 1.2: Common height discontinuities of structural walls 4

Figure 1.3: Boundary extensions design by: (a) Method I, (b) Method II. (ACI Committee 318, 2014; Moehle, Ghodsi, Hooper, Fields, & Gedhada, 2011) 8

Figure 1.4: Reinforcement requirements for: (a) Special boundary elements, (b) Ordinary boundary elements (ACI Committee 318, 2014; Moehle, Ghodsi, Hooper, Fields, & Gedhada, 2011) 9

Figure 1.5: Walls designed to the same solicitations under U.S. and Chilean requirements from the 1980s (Moehle & Wallace, 1989) 11

Figure 1.6: Verification of boundary elements requirement and transverse reinforcement (DS 60, 2010; Music & Ponce, 2014) 14

Figure 1.7: (a) Typical floor plan of a Canal Beagle building. (b) Elevation central wall, axis 2. (c) Elevation typical wall, axes A, B, C, D and E. (d) Wall boundary element failure (complete lack of boundary detailing, concrete crushing and bar buckling) (Lüders & Cruz, 1986) 17

Figure 1.8: (a) Floor plan of Acapulco building. (b) Elevation axis J - J'. (c) Wall boundary element failure (complete lack of boundary detailing, concrete crushing and bar buckling) (Wood, Wight, & Moehle, 1987) 19

Figure 1.9: Predominant damage in shear walls: Concrete crushing, buckling and fracture of vertical bars and opening of transverse bars. (Carpenter, et al., 2011) 22

Figure 1.10: Damage pattern behavior for coupled walls without lintels or coupling beams (Westenenk, et al., 2013) 24

Figure 1.11: Schematic explanation of the observed damage pattern behavior of flag-shaped walls (Westenenk, et al., 2013) 24

Figure 1.12: Subsections of specimens 225-15 and 325-15 treated as independent columns 28

Figure 1.13: Methodology scheme 30

Figure 2.1: Typical FRP and mild-steel stress-strain curves (Teng, Chen, Smith, & Lam, 2002) 35

Figure 2.2: Stress – strain model for FRP – confined concrete (Lam & Teng, 2003a) adopted by the current American code (ACI Committee 440, 2008).....36

Figure 2.3: Stress – strain model for FRP – confined concrete (Lam & Teng, 2003a) adopted by the current American code (ACI Committee 440, 2008).....37

Figure 2.4: Design – oriented model for steel confined concrete (Mander, Priestley, & Park, 1988a).....38

Figure 2.5: Typical stress-strain model for FRP confinement with softening behavior.....39

Figure 2.6: Examples of FRP – confinement with CFRP jackets and anchors: (a) (Hany, Hantouche, & Harajli, 2016), (b) (Triantafillou, et al., 2016).....67

Figure 3.1: Example of alphanumeric code for column naming (specimen 10-335).....76

Figure 3.2: Layout of CFRP reinforcement. CFRP anchors are intercalated between CFRP wraps 76

Figure 3.3: Conceptual definition of unidirectional CFRP composite material (Liu, Zwingmann, & Schlaich, 2015) 80

Figure 3.4: Carbon fiber compared to human hair (Liu, Zwingmann, & Schlaich, 2015) ..81

Figure 3.5: Installation of an epoxy matrix (viscous liquid state) to a wrap of unidirectional carbon fibers.....81

Figure 3.6: Elevation view of steel reinforcement distribution. (dimensions in cm.).....84

Figure 3.7: Transverse steel reinforcement as seen from above. (dimensions in cm) 85

Figure 3.8: Experimental results of steel bar buckling (Monti & Nuti, 1992).....87

Figure 3.9: Distribution of vertical steel reinforcement for columns with a thickness of: (a) 15 cm (b) 10 cm 90

Figure 3.10: Lateral instability of wall boundary previously yielded in tension (Parra & Moehle, 2014). 92

Figure 3.11: Lateral instability of wall boundary previously yielded in tension (Parra & Moehle, 2014). 92

Figure 3.12: Location, diameter and edge radius of precast holes.....94

Figure 3.13: Timber boxes as formwork.....96

Figure 3.14: Turned wood rods to precast holes for CFRP anchors 97

Figure 3.15: Fabrication of steel reinforcing cages....98

Figure 3.16: Placing of concrete....99

Figure 3.17: (a) Concrete with an 18-cm slump, used for all specimens. (b) Four concrete cylinders used to test the 28-day compression strength. (c) Storage of specimens inside laboratory until testing....100

Figure 3.18: Specimen with rounded corners and pre-cast holes edges....101

Figure 3.19: (a, b, c) Process of rounding corners. (d, e, f) Process of rounding pre-cast hole edges....102

Figure 3.20: CFRP roll as received from manufacturer....103

Figure 3.21: Dimensions of strips cut from the CFRP roll (units in cm)....104

Figure 3.22: Cutting holes in CFRP wraps to let CFRP anchors pass through....105

Figure 3.23: Fabrication of CFRP anchors....106

Figure 3.24: Fabrication of CFRP anchors (continuation)....107

Figure 3.25: Preparation of epoxy resin....108

Figure 3.26: Installation of CFRP wraps and CFRP anchors....110

Figure 3.27: Installation of CFRP wraps and CFRP anchors (continuation)....111

Figure 3.28: Installation of CFRP wraps and CFRP anchors (continuation)....112

Figure 3.29: Location of strain gages on the CFRP wrap....113

Figure 3.30: Installation of strain gages over CFRP wrap....114

Figure 3.31: Installation of strain gages over CFRP wrap (continuation)....115

Figure 3.32: Installation of strain gages over CFRP wrap (continuation)....116

Figure 3.33: Specimen being tested. Strain gages and LVDTs installed. Sides painted white with black dots for image data correlation to capture the complete deformation field. (a) Large side view (Side A). (b) Small side view (Side B)....117

Figure 3.34: Location of vertical and horizontal LVDTs (units in cm)....118

Figure 3.35: (a, b) Testing machine component. (c, d) Top and bottom rectification of specimens....120

Figure 4.1: Failure mode of specimen 000-10a 129

Figure 4.2: Failure mode of specimen 000-10b 130

Figure 4.3: Failure mode of specimen 000-15a 132

Figure 4.4: Failure mode of specimen 000-15b 133

Figure 4.5: Failure mode of specimen 225-10 135

Figure 4.6: Failure mode of specimen 225-15 137

Figure 4.7: Failure mode of specimen 235-10 139

Figure 4.8: Failure mode of specimen 235-15 141

Figure 4.9: Failure mode of specimen 325-10 143

Figure 4.10: Failure mode of specimen 325-15 145

Figure 4.11: Failure mode of specimen 335-10 147

Figure 4.12: Failure mode of specimen 335-15 149

Figure 4.13: Mechanism to capture an average vertical compression displacement 150

Figure 4.14: Experimental axial total load vs average displacement for control specimens 151

Figure 4.15: Experimental axial total load vs average displacement for specimens with 2 layers of CFRP wrapping (15 cm in thickness) 152

Figure 4.16: Experimental axial total load vs average displacement for specimens with 3 layers of CFRP wrapping (15 cm in thickness) 152

Figure 4.17: Experimental axial total load vs average displacement for specimens with 2 layers of CFRP wrapping (10 cm in thickness) 153

Figure 4.18: Experimental axial total load vs average displacement for specimens with 3 layers of CFRP wrapping (10 cm in thickness) 153

Figure 4.19: Experimental axial concrete stress vs average axial strain for control specimens 154

Figure 4.20: Experimental axial concrete stress vs average axial strain for specimens with 2 layers of CFRP wrapping (15 cm in thickness) 154

Figure 4.21: Experimental axial concrete stress vs average axial strain for specimens with 3 layers of CFRP wrapping (15 cm in thickness) 155

Figure 4.22: Experimental axial concrete stress vs average axial strain for specimens with 2 layers of CFRP wrapping (10 cm in thickness) 155

Figure 4.23: Experimental axial concrete stress vs average axial strain for specimens with 3 layers of CFRP wrapping (10 cm in thickness) 156

Figure 4.24: CFRP strain vs axial load. Specimen: 225-10. Strain gage location: corner.157

Figure 4.25: CFRP strain vs axial load. Specimen: 225-15. Strain gage location: corner.157

Figure 4.26: CFRP strain vs axial load. Specimen: 235-10. Strain gage location: corner.158

Figure 4.27: CFRP strain vs axial load. Specimen: 235-15. Strain gage location: corner.158

Figure 4.28: CFRP strain vs axial load. Specimen: 325-10. Strain gage location: (a) corner, (b) middle 159

Figure 4.29: CFRP strain vs axial load. Specimen: 325-15. Strain gage location: (a) corner, (b) middle 160

Figure 4.30: CFRP strain vs axial load. Specimen: 335-10. Strain gage location: (a) corner, (b) middle 161

Figure 4.31: CFRP strain vs axial load. Specimen: 335-15. Strain gage location: (a) corner, (b) middle 162

Figure 4.32: Strains immediately before failure captured by DIC. Specimen 225-10.....165

Figure 4.33: Strains immediately before failure captured by DIC. Specimen 225-15.....166

Figure 4.34: Strains immediately before failure captured by DIC. Specimen 235-10.....167

Figure 4.35: Strains immediately before failure captured by DIC. Specimen 235-15.....168

Figure 4.36: Strains immediately before failure captured by DIC. Specimen 325-10.....169

Figure 4.37: Strains immediately before failure captured by DIC. Specimen 325-15.....170

Figure 4.38: Strains immediately before failure captured by DIC. Specimen 335-10.....171

Figure 4.39: Strains immediately before failure captured by DIC. Specimen 335-15.....172

Figure 5.1: Transverse cross-section of group 1 models. Due to symmetry, only 1/4 of each column is modeled with internal borders blocked from horizontal displacement. 179

Figure 5.2: Transverse cross-section of group 2 models. Due to symmetry, only 1/2 of each subsection is modeled with internal borders blocked from horizontal displacement. 181

Figure 5.3: Geometry of ANSYS element SOLID65 (ref) 182

Figure 5.4: Geometry of concrete hexahedral elements. Specimen 000-15 184

Figure 5.5: Geometry of concrete tetrahedral elements. Specimen 225-10.....185

Figure 5.6: Geometry of ANSYS element BEAM188.....188

Figure 5.7: Geometry of transverse reinforcement 189

Figure 5.8: Geometry of ANSYS SHEEL41 element.....190

Figure 5.9: Geometry of CFRP elements, front view. Specimen 225-10 191

Figure 5.10: CFRP elements back view. Specimen 225-10.....192

Figure 5.11: Comparison of axial behavior of experimental and ANSYS models without CFRP confinement and a 15-cm thickness 196

Figure 5.12: Comparison of axial behavior of experimental and ANSYS models without CFRP confinement and a 10-cm thickness 196

Figure 5.13: Comparison of axial behavior of experimental and ANSYS models of specimens 225-15 and 235-15.....198

Figure 5.14: Comparison of axial behavior of experimental and ANSYS models of specimens 325-15 and 335-15.....198

Figure 5.15: Comparison of axial behavior of experimental and ANSYS models of specimens 225-10 and 235-10.....199

Figure 5.16: Comparison of axial behavior of experimental and ANSYS models of specimens 325-10 and 335-10.....199

Figure 5.17: Direction of concrete principal stresses with respect of global coordinates. Y: axial direction, X and Z: horizontal directions.....201

Figure 5.18: Total deformation of a column without predrilled holes, without rounded corners and without CFRP reinforcement. Scale amplified 31 times. Units: mm 202

Figure 5.19: Principal stress orientation and minimum principal stresses. Specimen O1-000-10-A 203

Figure 5.20: Middle and maximum principal stresses. Specimen O1-000-10-A.....204

Figure 5.21: Total deformation of a column with predrilled holes, with rounded corners and without CFRP reinforcement. Scale amplified 31 times. Units: mm.....205

Figure 5.22: Principal stress orientation and minimum principal stresses. Specimen O1-000-10-C.....206

Figure 5.23: Middle and maximum principal stresses. Specimen O1-000-10-C.....207

Figure 5.24: Total deformation of a column with predrilled holes, with rounded corners and with CFRP reinforcement. Scale amplified 18 times. Units: mm.....208

Figure 5.25: Principal stress orientation and minimum principal stresses. Specimen O1-325-10.....209

Figure 5.26: CFRP elements back view. Specimen 225-10.....210

Figure 5.27: Middle and maximum principal stresses 7th step. Specimen O1-325-10 211

Figure 5.28: Middle and maximum principal stresses 12th step. Specimen O1-325-10 212

Figure 5.29: Steel stirrup axial stresses at final step (7th step). Specimen O1-000-10-A ..213

Figure 5.30: Steel stirrup axial stresses at final step (7th step). Specimen O1-000-10-C...214

Figure 5.31: Steel stirrup axial stresses at 7th step. Specimen O1-325-10.....214

Figure 5.32: Steel stirrup axial stresses at final step (12th step). Specimen O1-325-10.....215

Figure 5.33: CFRP elements back view. Specimen 225-10.....216

Figure 5.34: CFRP wraps maximum principal stresses. Specimens 225-10 and 225-15 ..218

Figure 5.35: CFRP wraps maximum principal stresses. Specimens 235-10 and 235-15 ..219

Figure 5.36: CFRP wraps maximum principal stresses. Specimens 325-10 and 325-15 ..219

Figure 5.37: CFRP wraps maximum principal stresses. Specimens 335-10 and 335-15 ..220

Figure 5.38: CFRP elements back view. Specimen 225-10.....221

Figure 5.39: Experimental and ANSYS widening curves of Specimen 225-10.....222

Figure 5.40: Experimental and ANSYS widening curves of Specimen 225-15.....222

Figure 5.41: Experimental and ANSYS widening curves of Specimen 235-10.....223

Figure 5.42: Experimental and ANSYS widening curves of Specimen 235-15.....223

Figure 5.43: Experimental and ANSYS widening curves of Specimen 325-10 224

Figure 5.44: Experimental and ANSYS widening curves of Specimen 325-15 224

Figure 5.45: Experimental and ANSYS widening curves of Specimen 335-10 225

Figure 5.46: Experimental and ANSYS widening curves of Specimen 335-15 225

Figure 5.47: Comparison of axial behavior between Group 1 and 2 (15-cm thickness) ...227

Figure 5.48: Comparison of axial behavior between Group 1 and 2 (10-cm thickness) ...227

Figure 5.49: CFRP Maximum principal stresses. Specimen 225-10, subsection VI: (a) Group 1 model (b) Group 2 model.....229

Figure 5.50: CFRP Maximum principal stresses. Specimen 225-10, subsection V: (a) Group 1 model (b) Group 2 model.....229

Figure 5.51: CFRP Maximum principal stresses. Specimen 235-10, subsection VI: (a) Group 1 model (b) Group 2 model.....230

Figure 5.52: CFRP Maximum principal stresses. Specimen 235-10, subsection IV: (a) Group 1 model (b) Group 2 model.....230

Figure 5.53: CFRP Maximum principal stresses. Specimen 225-15, subsection III: (a) Group 1 model (b) Group 2 model.....231

Figure 5.54: CFRP Maximum principal stresses. Specimen 225-15, subsection II: (a) Group 1 model (b) Group 2 model.....231

Figure 5.55: CFRP Maximum principal stresses. Specimen 235-15, subsection III: (a) Group 1 model (b) Group 2 model.....232

Figure 5.56: CFRP Maximum principal stresses. Specimen 235-15, subsection I: (a) Group 1 model (b) Group 2 model.....232

Figure 5.57: Widening curves comparison between Group 1 and 2 models (Spec. 225-10) 233

Figure 5.58: Widening curves comparison between Group 1 and 2 models (Spec. 225-15) 234

Figure 5.59: Widening curves comparison between Group 1 and 2 models (Spec. 235-10) 234

Figure 5.60: Widening curves comparison between Group 1 and 2 models (Spec. 235-15) 235

Figure 6.1: Investigation methodology scheme 241

Figure 6.2: Sub columns of specimens 225-15 and 325-15 treated as independent columns 242

Figure 6.3: Sub columns of specimens 235-15 and 335-15 treated as independent columns 243

Figure 6.4: Sub columns of specimens 225-10 and 325-10 treated as independent columns 243

Figure 6.5: Sub columns of specimens 235-10 and 335-10 treated as independent columns 244

Figure 6.6: Theoretical increment compared with experimental increments for ec_{max}. 256

Figure 6.7: Theoretical increment compared with experimental increments for fc_{max}. 257

Figure 6.8: Theoretical increment compared with experimental increments for E_c. 258

Figure 6.9: Theoretical increment compared with experimental increments for ec_{ult}.....259

Figure 6.10: Theoretical increment compared with experimental increments for fc_{ult}. 260

Figure 6.11: Theoretical increment compared with experimental increments for E_D.....261

Figure A.1: Concrete cylinders tested after 28 days of aging. 286

Figure B.1: Vertical LVDTs readings until change of displacement rate. Specimen 225-10 294

Figure B.2: Vertical LVDTs readings until change of displacement rate. Specimen 225-15 294

Figure B.3: Vertical LVDTs readings until change of displacement rate. Specimen 235-10 295

Figure B.4: Vertical LVDTs readings until change of displacement rate. Specimen 235-15 295

Figure B.5: Vertical LVDTs readings until change of displacement rate. Specimen 325-10 296

Figure B.6: Vertical LVDTs readings until change of displacement rate. Specimen 325-15 296

Figure B.7: Vertical LVDTs readings until change of displacement rate. Specimen 335-10 297

Figure B.8: Vertical LVDTs readings until change of displacement rate. Specimen 335-15 297

Figure C.1: Concrete (a) minimum, (b) middle and (c) maximum stress. Specimen 225-10 300

Figure C.2: Steel stress at an axial strain of: (a) 0.003 (b) 0.006. Specimen 225-10.....300

Figure C.3: Concrete (a) minimum, (b) middle and (c) maximum stress. Specimen 225-15 301

Figure C.4: Steel stress at an axial strain of: (a) 0.003 (b) 0.006. Specimen 225-15.....301

Figure C.5: Concrete (a) minimum, (b) middle and (c) maximum stress. Specimen 235-10 302

Figure C.6: Steel stress at an axial strain of: (a) 0.003 (b) 0.006. Specimen 235-10.....302

Figure C.7: Concrete (a) minimum, (b) middle and (c) maximum stress. Specimen 235-15 303

Figure C.8: Steel stress at an axial strain of: (a) 0.003 (b) 0.006. Specimen 235-15.....303

Figure C.9: Concrete (a) minimum, (b) middle and (c) maximum stress. Specimen 325-10 304

Figure C.10: Steel stress at an axial strain of: (a) 0.003 (b) 0.006. Specimen 325-10.....304

Figure C.11: Concrete (a) minimum, (b) middle and (c) maximum stress. Specimen 325-15 305

Figure C.12: Steel stress at an axial strain of: (a) 0.003 (b) 0.006. Specimen 325-15.....305

Figure C.13: Concrete (a) minimum, (b) middle and (c) maximum stress. Specimen 335-10 306

Figure C.14: Steel stress at an axial strain of: (a) 0.003 (b) 0.006. Specimen 335-10.....306

Figure C.15: Concrete (a) minimum, (b) middle and (c) maximum stress. Specimen 335-15 307

Figure C.16: Steel stress at an axial strain of: (a) 0.003 (b) 0.006. Specimen 335-15.....307

Figure D.1: Specimen 225-10 axial stress-strain curve prediction with design-oriented models according to the proposed methodology....310

Figure D.2: Specimen 225-10 axial stress-strain curve prediction with design-oriented models according to the proposed methodology (continuation)....311

Figure D.3: Specimen 225-15 axial stress-strain curve prediction with design-oriented models according to the proposed methodology....312

Figure D.4: Specimen 225-15 axial stress-strain curve prediction with design-oriented models according to the proposed methodology (continuation)....313

Figure D.5: Specimen 235-10 axial stress-strain curve prediction with design-oriented models according to the proposed methodology....314

Figure D.6: Specimen 235-10 axial stress-strain curve prediction with design-oriented models according to the proposed methodology (continuation)....315

Figure D.7: Specimen 235-15 axial stress-strain curve prediction with design-oriented models according to the proposed methodology....316

Figure D.8: Specimen 235-15 axial stress-strain curve prediction with design-oriented models according to the proposed methodology (continuation)....317

Figure D.9: Specimen 325-10 axial stress-strain curve prediction with design-oriented models according to the proposed methodology....318

Figure D.10: Specimen 325-10 axial stress-strain curve prediction with design-oriented models according to the proposed methodology (continuation)....319

Figure D.11: Specimen 325-15 axial stress-strain curve prediction with design-oriented models according to the proposed methodology....320

Figure D.12: Specimen 325-15 axial stress-strain curve prediction with design-oriented models according to the proposed methodology (continuation)....321

Figure D.13: Specimen 335-10 axial stress-strain curve prediction with design-oriented models according to the proposed methodology....322

Figure D.14: Specimen 335-10 axial stress-strain curve prediction with design-oriented models according to the proposed methodology (continuation)....323

Figure D.15: Specimen 335-15 axial stress-strain curve prediction with design-oriented models according to the proposed methodology....324

Figure D.16: Specimen 335-15 axial stress-strain curve prediction with design-oriented models according to the proposed methodology (continuation)....325

ABSTRACT

This investigation studies the behavior of rectangular reinforced concrete columns confined with carbon fiber reinforced polymer (CFRP) wraps and anchors. These walls like columns represent shear wall boundary elements retrofitted with CFRP confinement.

A new retrofit technique is proposed by wrapping the wall-like columns with full CFRP jacketing and the inclusion of fan-shaped CFRP anchors sandwiched between CFRP wraps. CFRP reinforcement generates passive confinement by arching action (similar to steel stirrups and ties confinement) and amplify the area of the effectively confined concrete core.

A design modeling procedure is proposed (closed-form equations that depend only on geometric characteristics and nominal material properties). This procedure is based on steel confinement modeling techniques, results from nonlinear finite element models and existing models for columns confined with CFRP wraps but no CFRP anchors.

Results show that the proposed retrofit technique can increase the compression ductility in concrete columns. Tests show increments in the ultimate deformation of specimens maintaining high levels of compression stress. Also, it is observed that CFRP confinement prevents vertical bars buckling and opening of transverse stirrups, while maintaining the integrity of the specimens until the end of the tests.

The proposed modelling procedure predicts, with a good level of accuracy, the increments in parameters that characterize the axial stress-strain curve due to the use of the proposed CFRP confining system.

Keywords: CFRP confinement, rectangular columns, reinforced concrete, CFRP anchors

RESUMEN

La presente investigación estudia el comportamiento de columnas rectangulares de hormigón armado confinadas con envolturas y anclajes de polímero reforzado con fibra de carbono (CFRP). Estas columnas representan elementos de borde de muros de corte confinados con CFRP.

Se propone una nueva técnica de rehabilitación, envolviendo las columnas con camisas de CFRP y la inclusión de anclajes de CFRP en forma de abanico intercalados entre las camisas de CFRP. El refuerzo CFRP genera un confinamiento pasivo mediante acción de arco (similar a la generada por estribos de acero) y amplifica el área del núcleo de hormigón efectivamente confinado.

Se propone un procedimiento de modelación de diseño (ecuaciones cerradas que solo dependen de características geométricas y propiedades de material nominales). Este procedimiento se basa en: técnicas de modelos de diseño de confinamiento con trabas y estribos, resultados obtenidos de modelos de elementos finitos no lineales y modelos existentes para columnas confinadas con CFRP pero sin anclajes de CFRP.

Los resultados muestran que la técnica de rehabilitación propuesta logra aumentar la ductilidad a compresión de las columnas de hormigón armado. Los ensayos muestran incrementos en la deformación última de los especímenes manteniendo niveles altos de tensión de compresión. También se observa que el confinamiento de CFRP evita el pandeo de barras verticales y apertura de estribos horizontales, al mismo tiempo que mantiene la integridad de la probeta hasta el final del ensayo.

La metodología de modelamiento propuesta predice, con buen grado de exactitud, los incrementos en parámetros que caracterizan la curva tensión – deformación axial debidos al uso del sistema de confinamiento CFRP propuesto.

Palabras Claves: Confinamiento de CFRP, columnas rectangulares, hormigón armado, anclajes de CFRP

1. INTRODUCTION

1.1 Motivation

Fiber reinforced polymers (FRP) have been present in many areas of investigation, such as the aerospace industry, since the 1920s. The use of these materials in civil engineering applications was only possible after the development of cheaper manufacture processes (Eckold, 1994). Retrofit of reinforced concrete (RC) structures with FRP composites has been subject to extensive research since the 1980s (Teng, Chen, Smith, & Lam, 2002). The current research seeks to improve the understanding of FRP – confinement in reinforced concrete elements.

According to the current seismic design philosophy, uncoupled concrete slender structural walls can withstand strong ground motions mainly if a ductile flexural yielding is achieved at the base of the wall. Key factors to achieve this behavior are: (a) keep global compressive stress low, (b) keep global shear stress low, (c) avoid splice failures and (d) design a confined, stable flexural compression zone (Moehle, Ghodsi, Hooper, Fields, & Gedhada, 2011). Typically, uncoupled structural walls meet the fourth key factor by strengthening their boundary elements with closely spaced transverse reinforcement enclosing concentrated vertical boundary bars at the wall edges. Required transverse reinforcement provisions at wall boundaries are based on column provisions (ACI Committee 318, 2014; ACI Committee 105, 1933).

The February 27th, 2010 Offshore Maule earthquake of moment magnitude M_w = 8,8 impacted the most densely populated region of Chile, including the cities of Viña del Mar, Santiago and Concepción, causing an estimated 30 billion U.S. dollars damage to residential

buildings, industry, lifelines and other infrastructure (Jünemann, de la Llera, Hube, Cifuentes, & Kausel, 2015). Overall, the performance of most tall buildings was satisfactory and damage was not widespread; however, the few buildings that were damaged presented brittle behavior characterized by crushing of concrete under flexural-compressive action, buckling and fracture of vertical reinforcement and opening of horizontal reinforcement (Naeim, et al., 2011; Carpenter, et al., 2011; Rojas, et al., 2011). These damages may not be explained by a specific parameter; however, most researchers agree inadequate wall confinement contributed to the brittle damage observed in structural walls (Hube, Marihuén, de la Llera, & Stojadinovic, 2014; Alarcon, Hube, & de la Llera, 2014; Westenenk, et al., 2013; Massone, et al., 2012; Jünemann, Hube, de la Llera, & Kausel, 2012; Wallace, et al., 2012).

Ductility is perhaps the most influential property of structures located in regions with high seismic activity. Moderate to great earthquakes impose on buildings deformations that could easily exceed elastic behavior. Therefore, resisting systems must be designed to respond in the inelastic domain while sustaining a high portion of their initial strength to minimize severe damage and avoid collapse (Paulay & Priestley, 1992). FRP – confinement retrofit could prove to be a powerful technique to achieve the desired ductility in damaged structural walls or walls susceptible to brittle behavior.

At a basic level, FRP-confinement is a well understood mechanism: as concrete is subject to axial compression it expands laterally producing a passive confining pressure from the FRP jacket system, which translates into an increase of ductility and load carrying capacity. FRP – confinement becomes more significant at high levels of axial strain due to concrete dilatation after cracking.

The main motivation of the current research is to explore the application of FRP – confinement to boundary elements of slender structural walls by studying the behavior of FRP – confined rectangular reinforced concrete columns with high aspect ratio.

1.1.1 Seismic design and detailing of wall boundary elements

RC structural walls (known as shear walls or special structural walls) are an efficient lateral-force-resisting system, being able to provide nearly optimum means of achieving an aimed ductility, strength and stiffness (Paulay & Priestley, 1992). They counteract the impact of lateral loads originated mainly from earthquakes and wind. These structures are widespread in many earthquake-prone countries such as Canada, Chile, New Zealand, Turkey, USA and many others (Moroni, 2011). Individual structural walls may have different types of sections (Figure 1.1) and discontinuities along their height (Figure 1.2).

Boundary elements are a portion along a wall edge or opening that is strengthened by longitudinal and transverse reinforcement (Moehle, Ghodsi, Hooper, Fields, & Gedhada, 2011). They are critical members to achieve ductile behavior because they provide stability against lateral wall-buckling, enable effective confinement, strengthen the edges of walls to resist stress reversals and prevent reinforcement buckling (Wight & MacGregor, 2012). Well confined boundary elements will not experience axial strength reduction after spalling, will present higher deformation capacity and strength, and will distribute inelasticity along a higher height. Important recommendations for boundary elements can be found in many design codes such as ASCE 7-10, IBC-12 and UBC-97; however, the ACI code provides with the most comprehensive approach for detailing.

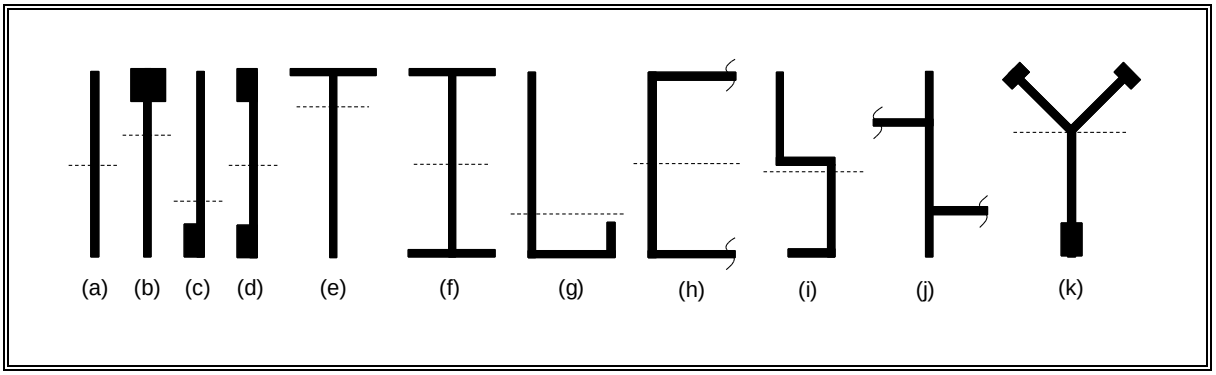

Figure 1.1: Common sections of structural walls (Paulay & Priestley, 1992)

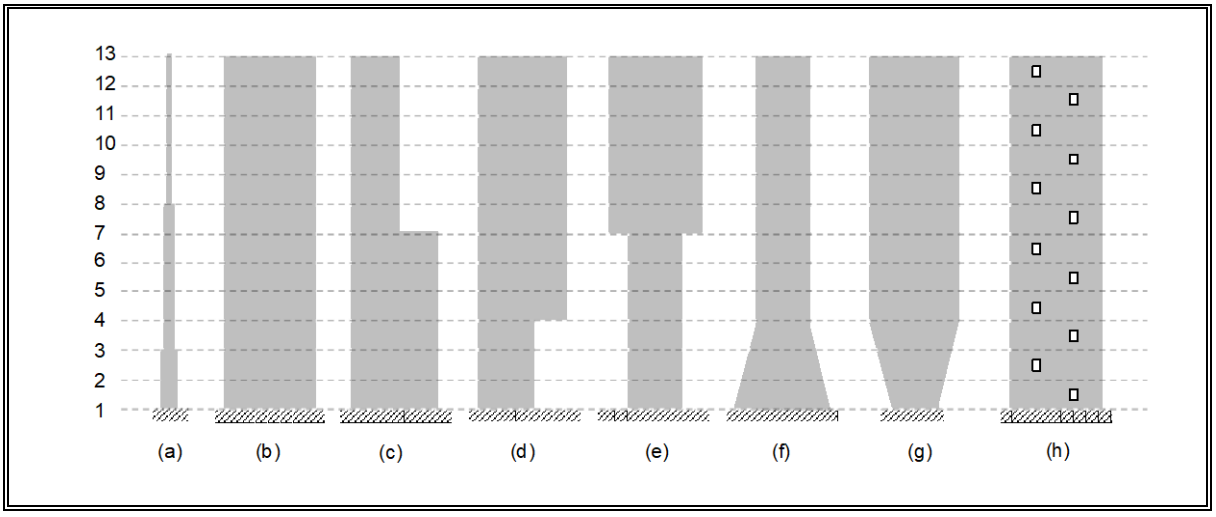

Figure 1.2: Common height discontinuities of structural walls

1.1.1.1 Boundary elements according to ACI Code

Boundary elements are classified in two categories (Moehle, Ghodsi, Hooper, Fields, & Gedhada, 2011): special boundary elements (SBE) and ordinary boundary elements (OBE). OBE is a term not used in ACI 318 but helpful to clarify detailing. Structural walls should always have boundary elements, what needs to be defined is whether they require special boundary elements or ordinary boundary elements.

In general terms, special boundary elements are required when the combined seismic and gravity load generates high compressive stresses ($> 0.2f_c'$).

Special boundary elements are not required when compressive stresses are low; however, buckling of boundary longitudinal reinforcement is still a thread due to cyclic load reversals even under low compressive stresses. Therefore, ordinary boundary elements are needed when moderate amounts of boundary longitudinal reinforcement exist$\left(A_{s,be}/A_{g,be} > 400/f_y\right)$.

$A_{s,be}$ = total area of longitudinal reinforcement at wall boundary.

$A_{g,be}$ = gross area of wall boundary containing longitudinal reinforcement.

ACI Code guidelines for the design of boundary elements are continuously upgraded based on the experience of the latest earthquakes and experimental tests. Although ACI 318 - 14 and previous versions have important differences, the basic idea for the detailing of boundary elements in these codes remains.

ACI Code gives: two methods to determine whether special or ordinary boundary elements are needed. The first method is design for walls that are effectively continuous from the base to top and have a single critical section at the base of the wall, and is mainly based on a displacement-based approach summarized in Equation 1. The second method applies to all walls that do not comply with the characteristics of the first method and basically states that SBE are needed if the maximum calculated compressive stress at the extreme fiber (corresponding to load combinations including earthquake effects) exceeds $0.2f_c'$.

$$c \geq \frac{l_w}{600\left(1.5\frac{\delta_u}{h_w}\right)} \tag{1.1}$$

$\delta_u/h_w \geq 0.005$

$h_w =$ height of the entire wall, or segment of the wall considered.

$l_w =$ horizontal length of the entire wall in the direction of the shear force.

$\delta_u =$ design displacement, defined as the total lateral displacement deflection of the top of the building for the design-basis earthquake.

$c =$ largest neutral axis depth to extreme compression fiber calculated for the factored axial force and nominal moment strength consistent with the direction of the design displacement δ_u.

1.1.1.2 Required detailing of boundary elements

Figures 1.3 and 1.4 briefly summarizes detailing specifications for SBE and OBE according to the ACI code (sections 18.10.6.4 and 18.10.6.5 respectively) (ACI Committee 318, 2014).

If SBE are required, transverse reinforcement provisions in the current American code (ACI Committee 318, 2014) are defined by greater of equations (1.2) and (1.3) for rectilinear hoops and equations (1.4) and (1.5) for spiral or circular hoops.

$$\frac{A_{sh}}{sb_c} = 0.3\left(\frac{A_g}{A_{ch}} - 1\right)\frac{f_c'}{f_{yt}} \tag{1.2}$$

$$\frac{A_{sh}}{sb_c} = 0.09\frac{f_c'}{f_{yt}} \tag{1.3}$$

$$\rho_s = 0.45\left(\frac{A_g}{A_{ch}} - 1\right)\frac{f_c'}{f_{yt}} \tag{1.4}$$

$$\rho_s = 0.12\frac{f_c'}{f_{yt}} \tag{1.5}$$

Where,

A_g = gross area of the wall section that is to be confined according to method I or II.

A_{ch} = area of concrete core within A_g, measured outside of peripheral hoop legs.

A_{sh} = total cross-sectional area of transverse reinforcement, including crossties, within spacing s and perpendicular to dimension b_c.

s = center-to-center spacing of transverse reinforcement.

b_c = cross-sectional dimension of member core measured to the outside edges of the transverse reinforcement composing area A_{sh}.

ρ_s = ratio of volume of spiral reinforcement to total volume of core confined by the spiral, measured out-to-out of spirals.

Although these expressions are used for boundary elements of structural walls subject lateral loads, they are based on experimental and analytical research of reinforced concrete ties columns subject to pure axial load (ACI Committee 105, 1933). The ACI Committee 105 carefully chose these equations based on the following guidelines:

- Design formulas reflect the results of tests
- The formulas adhere to fundamental principles established by tests or theory.
- Formulas are not entirely empirical
- They do not infer different factors of safety for the concrete and the steel which is brought about through an attempt to control time yield.

Equations (1.2) y (1.4) are based on the fundamental principle that the transverse reinforcement shall be of such amount and quality that the load – carrying capacity of the transverse reinforcement shall be greater than that of the concrete shell outside the core (ACI Committee 105, 1933). Equations (1.3) and (1.5) do not provide adequate transverse

reinforcement for thin walls because they were design for larger columns with gross cross – sectional area A_g less than approximately 1.25 times the core area.

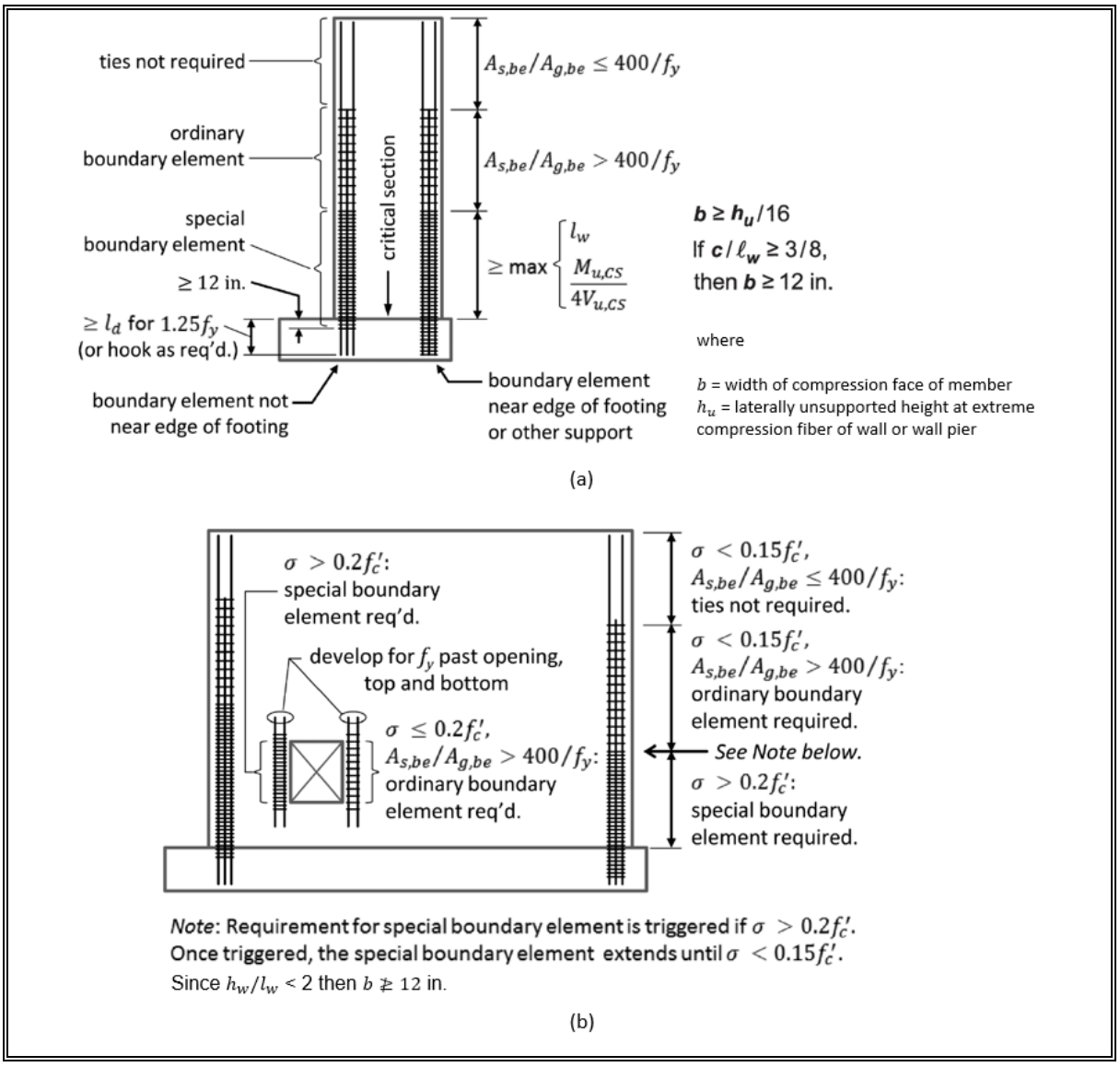

Figure 1.3: Boundary extensions design by: (a) Method I, (b) Method II. (ACI Committee 318, 2014; Moehle, Ghodsi, Hooper, Fields, & Gedhada, 2011)

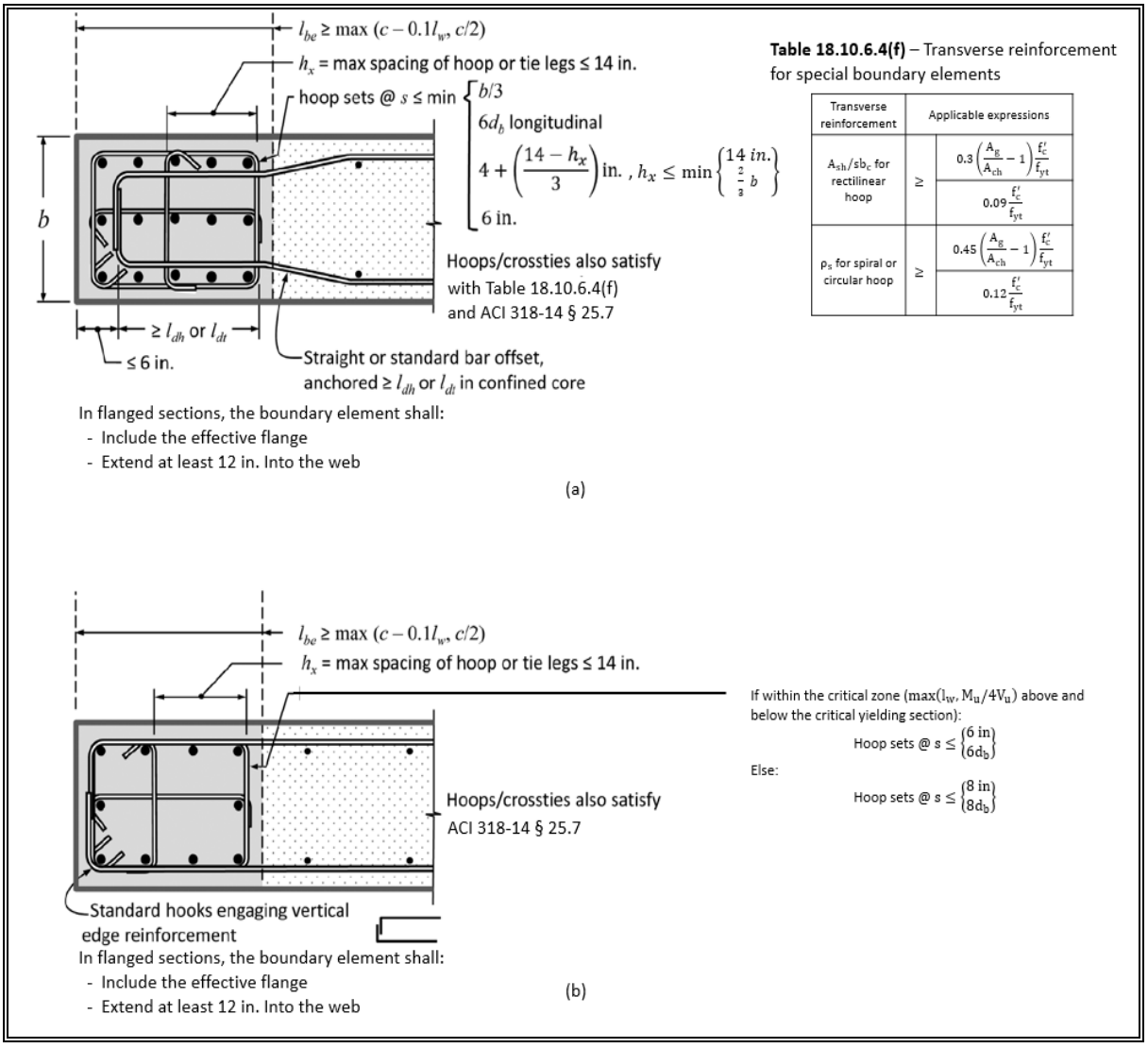

Figure 1.4: Reinforcement requirements for: (a) Special boundary elements, (b) Ordinary boundary elements (ACI Committee 318, 2014; Moehle, Ghodsi, Hooper, Fields, & Gedhada, 2011)

Since SBE provisions are based on tied column provisions subject to pure axial load, the present research assumes that retrofit of boundary elements in structural walls with FRP confinement also can be based on FRP confined columns subject to pure axial load.

Detailing requirements for seismic provisions in Chile are usually adopted from international codes but with a series of exceptions specified on national guidelines. These exceptions will be presented in the next subsection.

1.1.1.3 Boundary elements according to Chilean Code

Seismic code provisions in Chile are issued by the Instituto Nacional de Normalización (INN). The INN is a member of the International Organization for Standardization and the Comisión Panamericana de Normas Tecnicas.

Code provisions in Chile evolved in accordance with the observed behavior of structures during important earthquakes. For example, Chile developed in the early 1900's constructions with both frame and wall philosophies; however, after the earthquakes of 1930's construction of frame buildings declined due to observed failures (Riddell, Wood, & de la Llera, 1987). To this date structural wall buildings remain the most common lateral force resisting system in Chile. Detailing of boundary elements in Chile was heavily influenced by the observed behavior of structures during the 1985 and 2010 earthquakes.

1.1.1.3.1 1985 Algarrobo, Chile earthquake

At the time of the 1985 Algarrobo earthquake, the official Chilean guidelines on detailing of reinforced concrete structures were based on the 1952 and 1959 versions of the German DIN 1045, a code that did not contain seismic provisions to produce ductile structures (NCh 429, 1957; NCh 430, 1961). For this reason, RC wall buildings at the time lacked ductile detailing requirements for boundary elements (Riddell, Wood, & de la Llera, 1987; Wood, Wight, & Moehle, 1987).

During the 1985 earthquake, Viña del Mar buildings had a very good performance mainly due to the relatively large amount of wall area (typically 6% of the floor area) (Riddell, Wood, & de la Llera, 1987). Thanks to this characteristic, Chilean buildings were stiff and redundant enough to resist high lateral loads with low amounts of reinforcement (Wood, Wight, & Moehle, 1987). This good performance served as a basis for future code provisions, in particular, for the elimination of special boundary element requirements. A design example following codes from the 1980's is shown in Figure 1.5, where two walls were designed for the same axial load, shear and moment using U.S. and Chilean provisions.

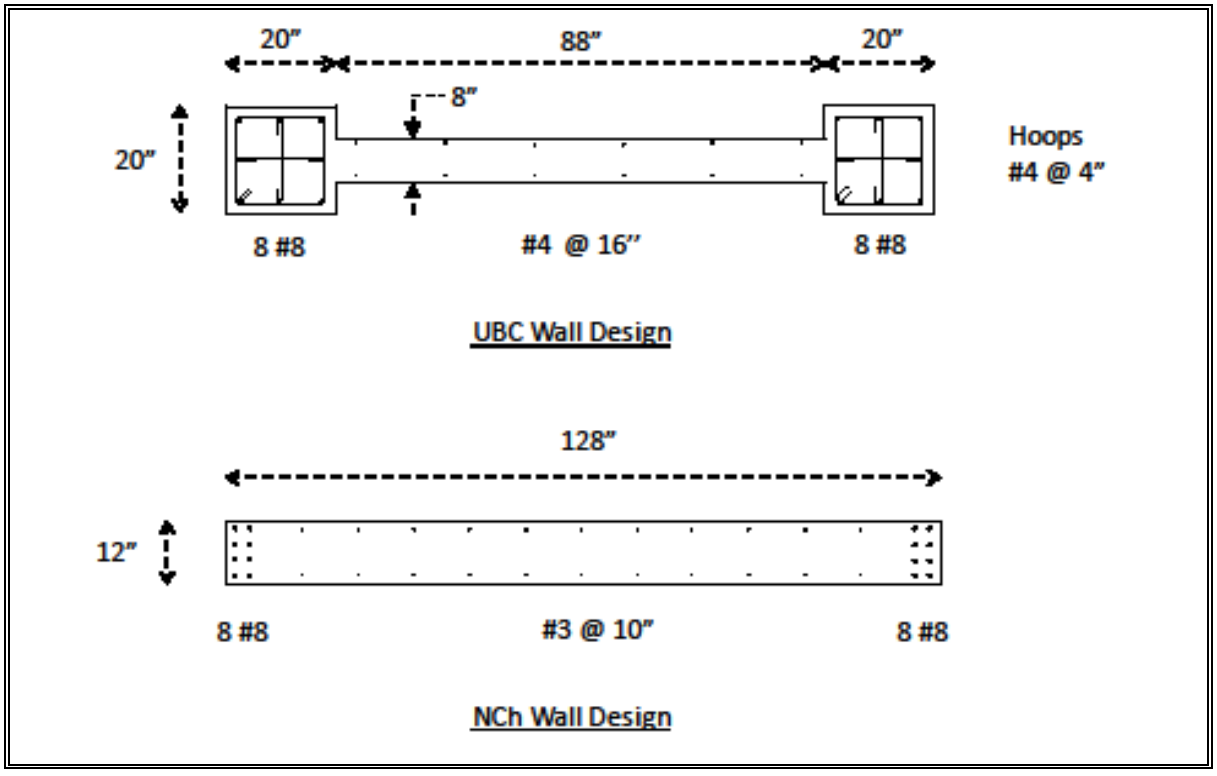

Figure 1.5: Walls designed to the same solicitations under U.S. and Chilean requirements from the 1980s (Moehle & Wallace, 1989)

It is important to note, that despite the satisfactory behavior of most buildings during the 1985 earthquake, the few exceptions that suffered severe damage warned for the need of ductile requirements for future earthquakes. The Acapulco building and the Canal Beagle housing complex had RC shear walls with significant stressed chords and required confined boundary members (Wyllie, et al., 1986). The specific observed damage of these structures is described in Section 1.1.2.

It was concluded that for the particular earthquake of 1985 ductile requirements were not necessary; however, not all issues of earthquake engineering practice can be settled by a single earthquake and the need more substantial detailing, for different earthquakes and for special wall configurations, required further study (Moehle & Wallace, 1989).

1.1.1.3.2 2010 Maule, Chile earthquake

At the time of the 2010 Maule earthquake, the official Chilean code on earthquake resistant design of buildings was based on their satisfactory behavior during the 1985 Algarrobo earthquake (NCh 433, 1996; Rojas, Lew, & Naeim, 2010). Detailing requirements were based on American guidelines (ACI Committee 318, 1995), but boundary element detailing was not necessary to meet according to the transitory Annex B of NCh 433 (1996). Although this exception was based on the “satisfactory behavior” of walls during the 1985 earthquake, the lack of boundary elements was one of the factors that influenced brittle damage of buildings during the 2010 Maule earthquake. One year prior to the 2010 Maule earthquake, the official Chilean code removed the transitory Annex B in NCh 433 (1996, Mod. 2009) making boundary element detailing mandatory.

After the 2010 Maule earthquake, several modifications were introduced to the RC design code in Chile, the new guidelines are based on a later American guideline (ACI

Committee 318, 2008) with a series of modifications specified by a presidential supreme decree (DS 60, 2010). A brief description detailing boundary elements according to the new Chilean provisions is shown in Figure 1.6. It is important to note that the latest to date Chilean provisions on does not consider the latest American provisions, specifically, it defines the need for SBE with a previous version of equation (1.1).

Code provision for the detailing of boundary elements are constantly been updated, new recommendations are provided and past ones are improved. Experience obtained from past earthquakes is key to generate more precise and correct recommendations. The next section explores past earthquakes that helped improve current codes, describing observed brittle behavior of buildings and recent experimental studies that aim to understand the causes of such behavior.

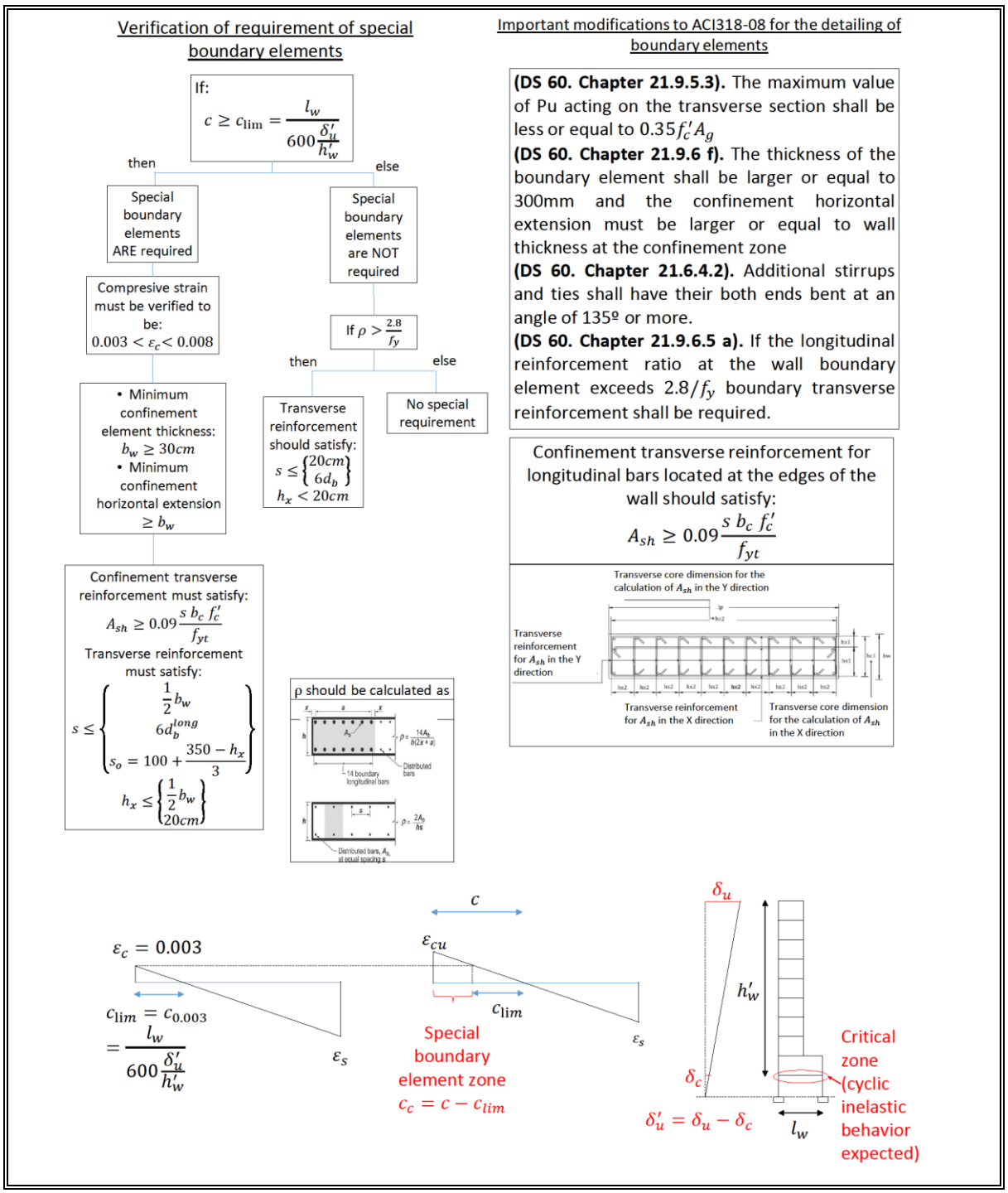

Figure 1.6: Verification of boundary elements requirement and transverse reinforcement

(DS 60, 2010; Music & Ponce, 2014)

1.1.2 Brittle failure of wall boundary elements in Chile

The Chilean earthquakes of 1985 and 2010 were the base for several modifications of building codes at their time. In this section, observed damage of wall boundary elements during those earthquakes will be explored.

1.1.2.1 1985 Algarrobo, Chile earthquake

The March 3rd Offshore Algarrobo earthquake with a magnitude M_s = 7:8 impacted central Chile and coastal cities, and caused an estimated 2 billion U.S. dollars damage to dwellings, port facilities, lifelines, and bridges (Riddell, Wood, & de la Llera, 1987). The epicenter was located approximately 80 km southwest of Viña del Mar at a local depth of 33 km (Wood, Wight, & Moehle, 1987).

At the time, the city of Viña del Mar had an inventory of 400 RC buildings ranging in height from 5 to 23 stories, from this inventory only 9% (36/400) buildings suffered major damage and from the severely damaged buildings 28 were located at the Canal Beagle housing complex (Riddell, Wood, & de la Llera, 1987). This high concentration of damaged buildings was the result of a particular ground motion amplification condition (U.S. Geological Survey, 1986).

Although the low percentage of damaged buildings indicates a very good global performance, the lack of confined boundary elements was a critical factor for the damage suffered by buildings in the Canal Beagle and the Acapulco building (Wyllie, et al., 1986).

1.1.2.1.1 Canal Beagle Housing Complex

Canal Beagle was composed of 84 buildings, with 4 to 5 stories, constructed in two stages from 1973 to 1978. Structures belonging to each stage are equal to each other and were constructed simultaneously, discarding problems related to construction singularities (Lüders & Cruz, 1986).

The lateral – force – resisting system for all the buildings consisted of RC walls oriented in two perpendicular directions. The first direction, as can be seen in axis 2 of Figure 1.7a, had only one continuous resisting wall from base to top. The second direction, as can be seen in axes A, B, C, D and E of Figure 1.7a, had a series of walls connected by coupling beams.

Characteristics of observed failures among all buildings were remarkably alike with a slight variation their magnitude. Wall damage concentrated in the first two floors and included spalling, crushing of concrete and rupture and buckling of longitudinal reinforcement (Figure 1.7d). It was concluded that although the Canal Beagle structures were subjected to an earthquake 40% larger than the design basis earthquake, they were far from collapse (Lüders & Cruz, 1986). Finally, the authors recommended that confinement reinforcement should be carefully detailed in order to reach ductile behavior and make the most concrete strength and suggested that construction companies should hire reviewers with knowledge of minimum confinement detailing.

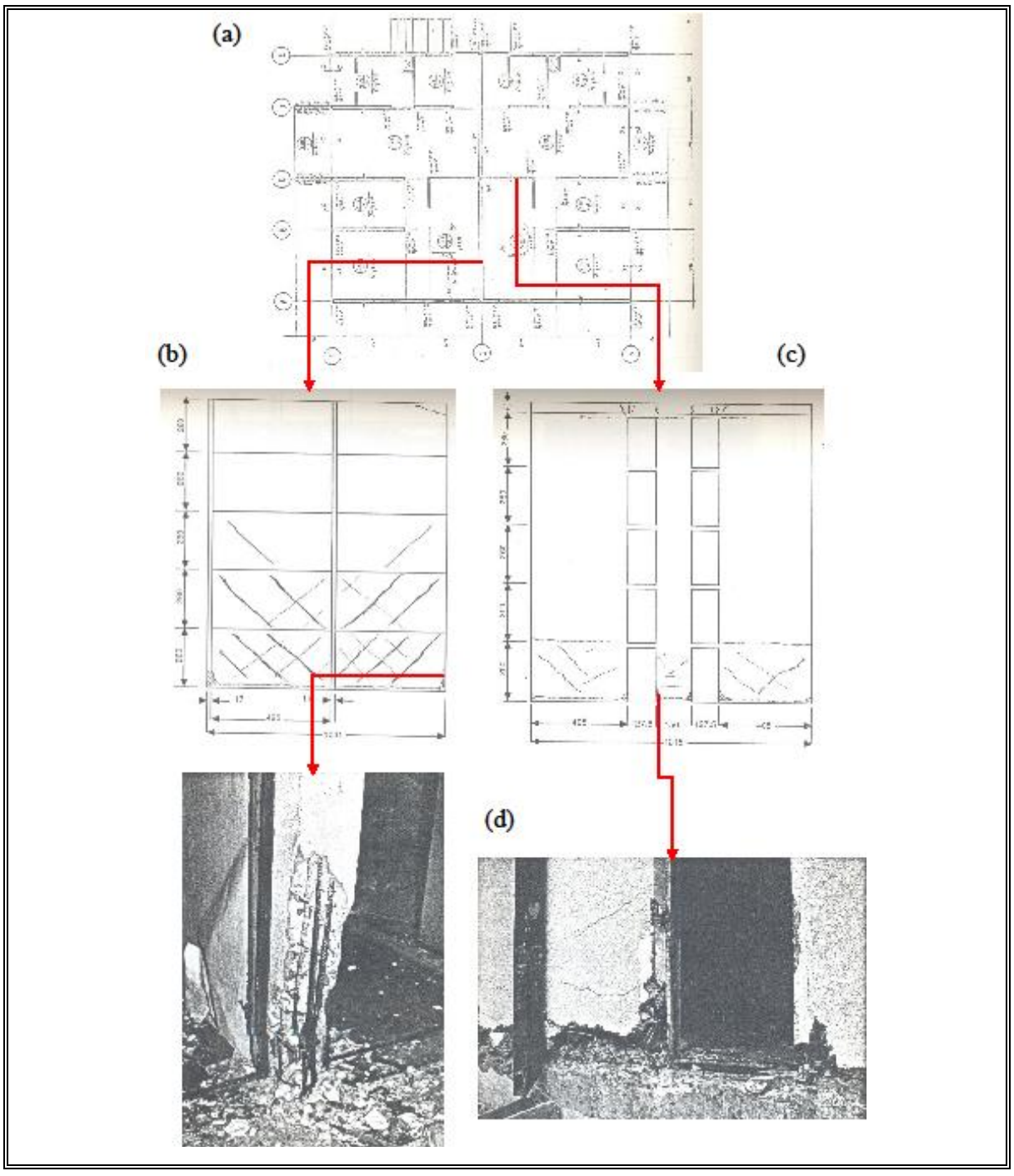

Figure 1.7: (a) Typical floor plan of a Canal Beagle building. (b) Elevation central wall, axis 2. (c) Elevation typical wall, axes A, B, C, D and E. (d) Wall boundary element failure (complete lack of boundary detailing, concrete crushing and bar buckling) (Lüders & Cruz, 1986)

1.1.2.1.2 Acapulco Building

The Acapulco building was constructed in 1962 and is the oldest high rise structure in Viña del Mar (Wood, Wight, & Moehle, 1987). As can be seen in Figure 1.8a, the building is almost symmetrical about axis Y and transverse shear walls are oriented at 60° with respect to the central walls, forming a herringbone pattern (Figure 1.8b).

During the earthquakes of 1965 and 1971, the building suffered light damage and nonstructural repairs were made. During the major 1985 earthquake, severe damage occurred at wall boundaries. Plain bars were used for reinforcement inside walls and twisted bars were used at boundaries, however, concrete crushing and buckling of boundary reinforcement were observed (Figure 1.8c). The total repair cost of the building was approximately 180,000,000 pesos which was about one-third of the commercial value of the building.

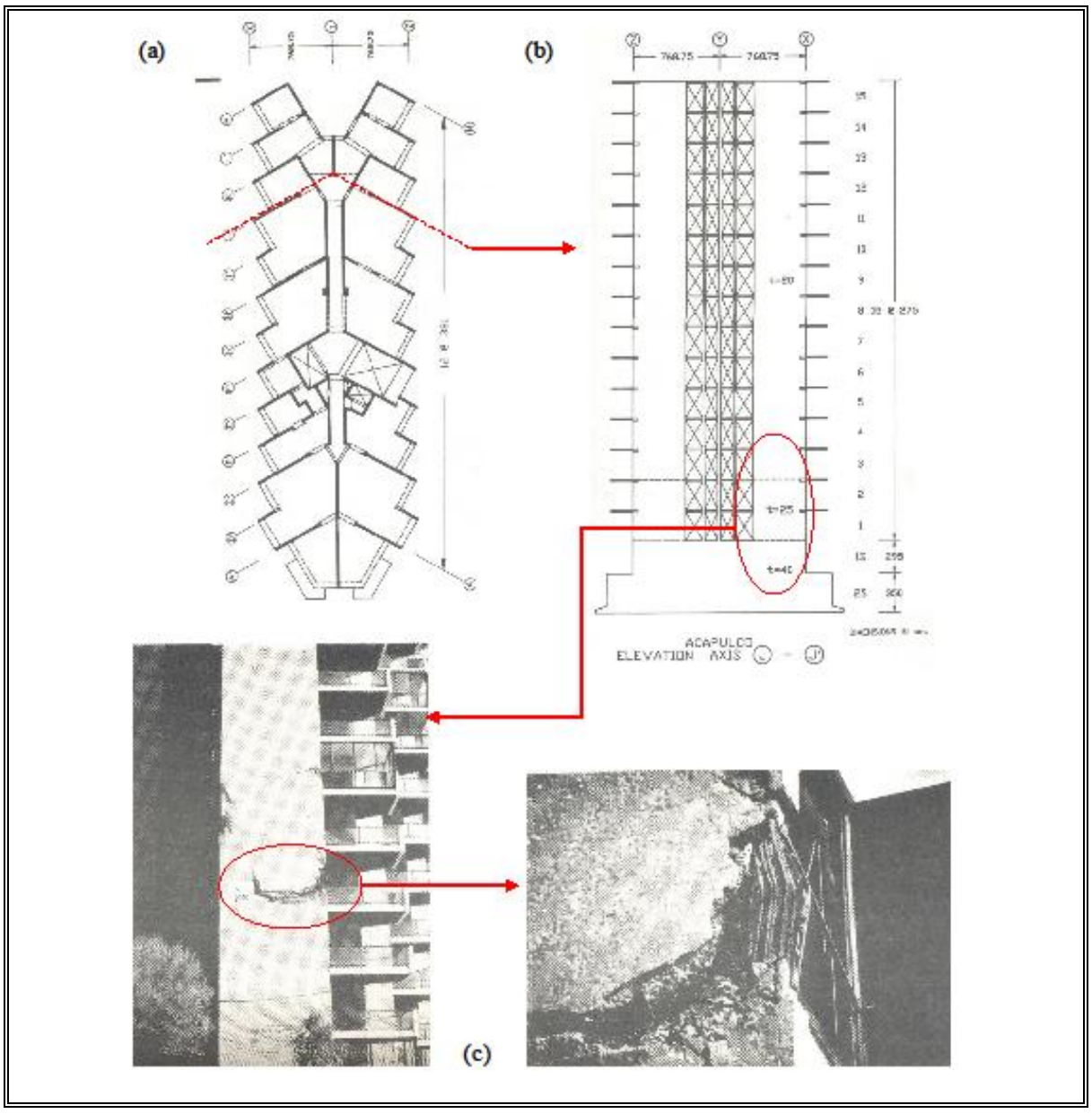

Figure 1.8: (a) Floor plan of Acapulco building. (b) Elevation axis J - J'. (c) Wall boundary element failure (complete lack of boundary detailing, concrete crushing and bar buckling) (Wood, Wight, & Moehle, 1987)

1.1.2.2 2010 Maule, Chile earthquake

The February 27th Offshore Maule earthquake of moment magnitude M_w = 8.8, impacted the most densely populated region of Chile, including the cities of Viña del Mar, Santiago and Concepción, causing an estimated 30 billion U.S. dollars damage to residential buildings, industry, lifelines and other infrastructure (Jünemann, de la Llera, Hube, Cifuentes, & Kausel, 2015).

A building survey showed that damage was generally concentrated in buildings constructed after year 2000 (Jünemann, Hube, de la Llera, & Kausel, 2012). Between 1985 (year of the Algarrobo, Chile earthquake) and 2009, a total of 1939 construction permits were issued for reinforced concrete buildings with nine or more floors (Comité Inmobiliario, Cámara Chilena de la Construcción (CChC), 2002). Only 2% (40/1939) of the newer building stock of south-central Chile suffered severe damage and just one of these buildings collapsed (Wallace, et al., 2012).

After the 2010 Maule earthquake, 6 buildings were issued with a demolition order and 20 other buildings were declared inhabitable in Santiago; Viña del Mar presented 2 partially collapsed buildings and 6 buildings were declared inhabitable; Concepción suffered the collapse of 1 building and severe damage to 10 other buildings (Comisión Provisoria Terremoto, 2010).

The Los Angeles Tall Buildings Structural Design (LATBSDC) reconnaissance team made several observations on the performance of tall buildings in Santiago (Naeim, et al., 2011), Viña del Mar (Carpenter, y otros, 2011) and Concepción (Rojas, y otros, 2011). The LATBSDC performance reports present an overview of the damage characteristics of individual buildings located in the three cities. Overall, the performance of the majority of

tall buildings was satisfactory and damage was not widespread, however, the buildings that were damaged presented very similar characteristics:

- Crushing of concrete due to heavy compression at the end of the wall, buckling and fracture of steel bars in boundary element and opening of transverse reinforcement were the principal types of damage experienced in tall buildings (Figure 1.9). Also, the long duration of the earthquake generated cyclic fatigue during the strong shaking.
- Vertical reinforcing was generally centered in the wall thickness and in some cases the vertical bars were closer to one face, generating eccentric loadings.
- The cover of thin walls is relatively a large percentage of the gross area. Once spalling occurs, the remaining core area is so small that a dramatic decrease on strength and stiffness is generated.
- Detailing for confinement was not observed in the majority of shear walls. Lack of cross ties, lack of 135 and lack of seismic hooks was observed in almost all shear walls. In most cases, walls were too thin to detail for confinement. This is most likely attributed to section B.2.2 of the old Chilean code (NCh 433, 1996) because it allowed an exception to ACI 318-95 for the requirement of boundary elements.

Figure 1.9: Predominant damage in shear walls: Concrete crushing, buckling and fracture of vertical bars and opening of transverse bars. (Carpenter, et al., 2011)

- The principal type of damage is located at or near the ground level due to compression and tension effects in walls.
- Prevalent vertical discontinuities in the structural system were found at the ground floor mainly at transition areas such as residential units above the lobby and parking areas below the lobby. Flag-shaped walls (Figure 1.2d) were frequently found in lower stories for vehicular circulation. This type of wall caused stress concentrations, due to axial-flexural interaction, in the top corner which lead to a brittle “unzipping” type of failure (Figure 1.11). They were designed on the assumption that the floor slab would be capable of distributing shear from the more flexible flag-shaped wall to adjacent walls; this assumption proved to be not warranted (Westenenk, et al., 2013).

- Lintels and coupling beams were reduced or even eliminated after the 1985 Algarrobo earthquake, losing a good source for energy dissipation. This generated a variable pattern behavior, as shown in Figure 1.10, where damage propagated from the edges of the wall, due to axial-flexural interaction, toward the center of the wall causing shear damage.

The low percentage of severely damage tall RC buildings made the overall behavior to be considered acceptable. However, damage was brittle and characterized by crushing of concrete under flexural-compressive action, buckling and fracture of vertical reinforcement and opening of horizontal reinforcement. Most researchers agree that although these damages may not be explained by a specific parameter, inadequate wall confinement contributed to the brittle damage observed in structural walls (Jünemann, de la Llera, Hube, Cifuentes, & Kausel, 2015).

A requisite to ductile behavior of reinforced concrete elements in compression is that, after spalling, the confined core axial strength is larger than the strength of the unconfined gross cross-section. Shear walls of damaged buildings during the Maule earthquake tend to have small thickness: 69% of the inventory present values lower than 21cm (Jünemann, de la Llera, Hube, Cifuentes, & Kausel, 2015). This small thickness leaves littles area of concrete to be confined after spalling, reducing significantly the post-spalling strength even with large volumetric ratio of confinement reinforcement. For this reason there is reasonable doubt whether boundary elements confined with classic methods (transverse reinforcement) could have performed better and in a ductile manner (Westenenk, et al., 2013).

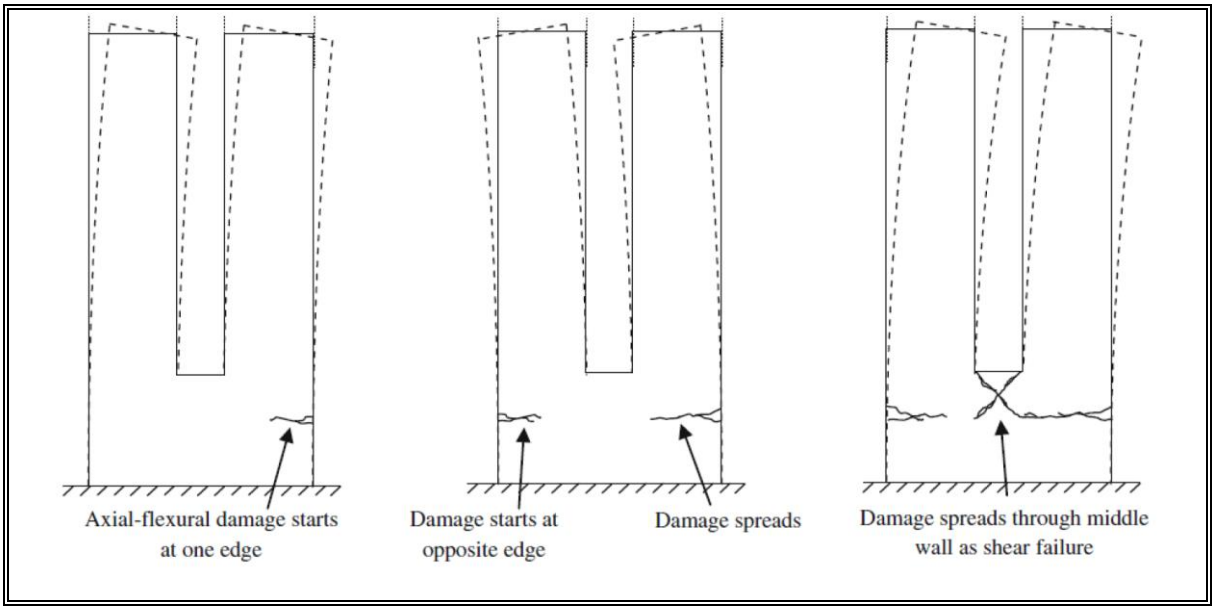

Figure 1.10: Damage pattern behavior for coupled walls without lintels or coupling beams (Westenenk, et al., 2013)

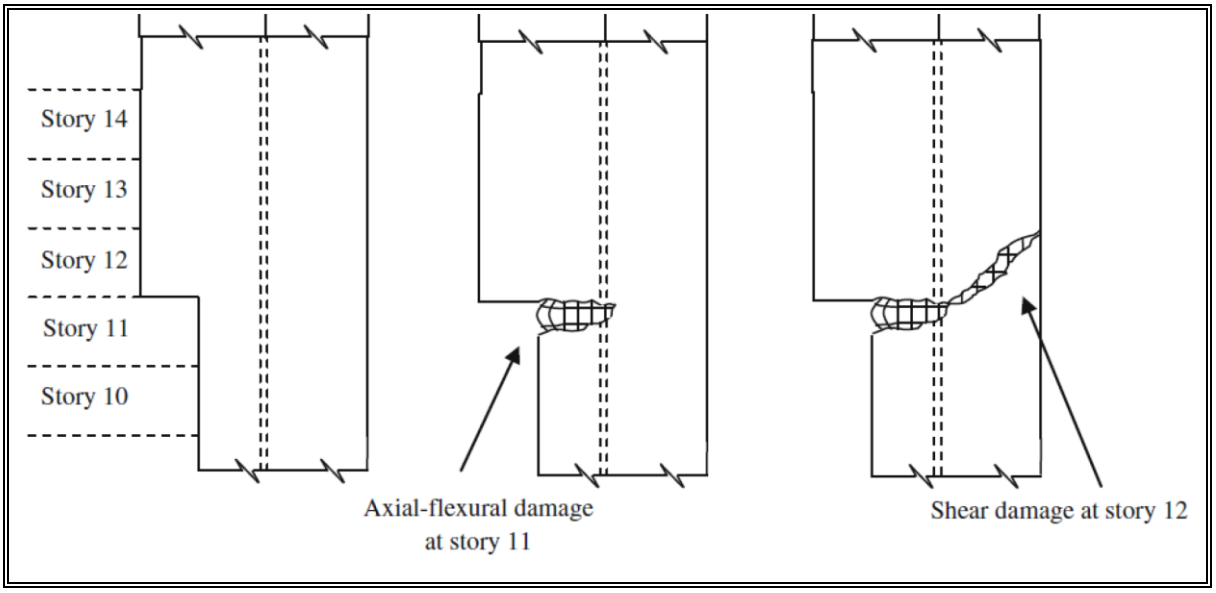

Figure 1.11: Schematic explanation of the observed damage pattern behavior of flag-shaped walls (Westenenk, et al., 2013)

Seven thin boundary element wall-like columns with detailing according to the American guidelines (ACI Committee 318, 2011) were subject to a uniaxial displacement controlled compression test (Arteta & Moehle, 2010). Results from the tests suggested that ductile behavior of thin boundary elements cannot be obtained with ACI 318 – 11 provisions. Although increasing volumetric ratio of confinement reinforcement and decreasing its horizontal spacing improved behavior, a ductile response could not be achieved. Behavior remained brittle because of buckling of longitudinal bars and reduced post-spalling axial capacity of the confined core. These results point out the importance of preventing buckling of vertical reinforcement and reducing spalling of concrete cover. These tasks can prove difficult to achieve for already constructed thin walls of the newer stock of buildings in Chile with ratios of s/d_b reaching values as high as 16.7 (Alarcon, Hube, Jünemann, & de la Llera, 2015).

An experimental program tested slender RC walls with unconfined walls in order to reproduce the observed damage during the 2010 Maule earthquake. In one investigation, six ½ - scaled slender walls were subject to a conventional quasi-static cyclic incremental lateral displacement and to a constant axial load $\left(0.15f_c'A_g\right)$, design with characteristic detailing of five damaged buildings and a M/Vl_w ratio of 2.5 (Hube, Marihuén, de la Llera, & Stojadinovic, 2014). Another investigation tested three additional specimens to study the effect of the axial load variation $\left(0.15f_c'A_g, 0.25f_c'A_g, 0.35f_c'A_g\right)$ (Alarcon, Hube, & de la Llera, 2014). From these two studies, the most relevant results for boundary elements are:

- The use of closed stirrups and cross-ties with reduced spacing $(s/d_b = 4.5)$ can have a significant impact increasing ductility displacement (30% increase), increasing energy dissipation and decreasing strength degradation (from 6% to 2%). Vertical

reinforcement did not buckle in at least one specimen. This observation agrees with experimental results of other investigation (Kuang & Ho, 2009).

- The average measured plastic hinge of thin walls was $2.63t_w$. A similar value for the plastic hinge height, $2.5t_w$, was proposed by an investigation (Takahashi, et al., 2013). This observation suggests Method I of determining whether special boundary elements are required is un-conservative for thin walls.
- The current axial load ratio (ALR) of 0.35 adopted in the current Chilean code and also section 1921.6.6.4(3) of the Uniform Building Code of 1997 is not adequate for slender walls with non-seismic boundary detailing. Failure of the specimen with ALR of 0.35 was observed to be brittle and extremely sudden, concrete crushing occurred immediately after spalling of the concrete cover. For slender walls, limiting the ALR to less than 0:35 does not guaranty flexural tension reinforcement yields before the flexural compression zone reaches the compressive capacity.

The brittle behavior observed in some buildings during the earthquakes of 1985 and 2010, especially at boundary elements of shear walls, is evidence for the need of ductility retrofit of Chilean constructions. Concrete confinement retrofit could prove to be a powerful technique to provide the desired ductility. The next section explores a literature review of the mechanical behavior of confined concrete with special attention towards FRP – confined concrete.

1.2 Objectives

The main objective of the present research is to develop an experimental model for the axial stress – strain relation of rectangular reinforced concrete columns confined with CFRP jackets and CFRP anchors. The main purpose of the stress-strain model is to predict increases in the axial parameters of shear wall boundary elements after they are retrofitted with CFRP jackets and CFRP anchors.

To achieve this objective, five specific objectives are followed:

- The construction and testing of columns confined with CFRP jackets and CFRP anchor are constructed and tested under monotonic loading.
- The review of existing design-oriented models for rectangular columns confined with CFRP jackets without CFRP anchors
- The adaption of these models to predict the stress-strain curve parameters of columns confined with CFRP jackets and CFRP anchor.
- The development of finite element models to capture the internal behavior of stresses in the different materials (concrete, CFRP, steel bars) which cannot be easily captured in experimental testing.
- The verification of the predictions of the stress-strain curve parameters from the adapted design-oriented model with the actual measured stresses and strains in the experimental tests.

1.3 Hypothesis

The principal hypothesis for the development of the present research is that a design-oriented model can be developed for high aspect ratio rectangular concrete columns confined with CFRP jackets and CFRP anchors by adapting existing design-oriented models for CFRP – confined rectangular concrete columns without CFRP anchors. The proposed methodology involves dividing the transverse cross-section of the column in sub sections between anchors, and treat this sub columns as independent columns with the internal border blocked from any horizontal displacement (Figure 1.12).

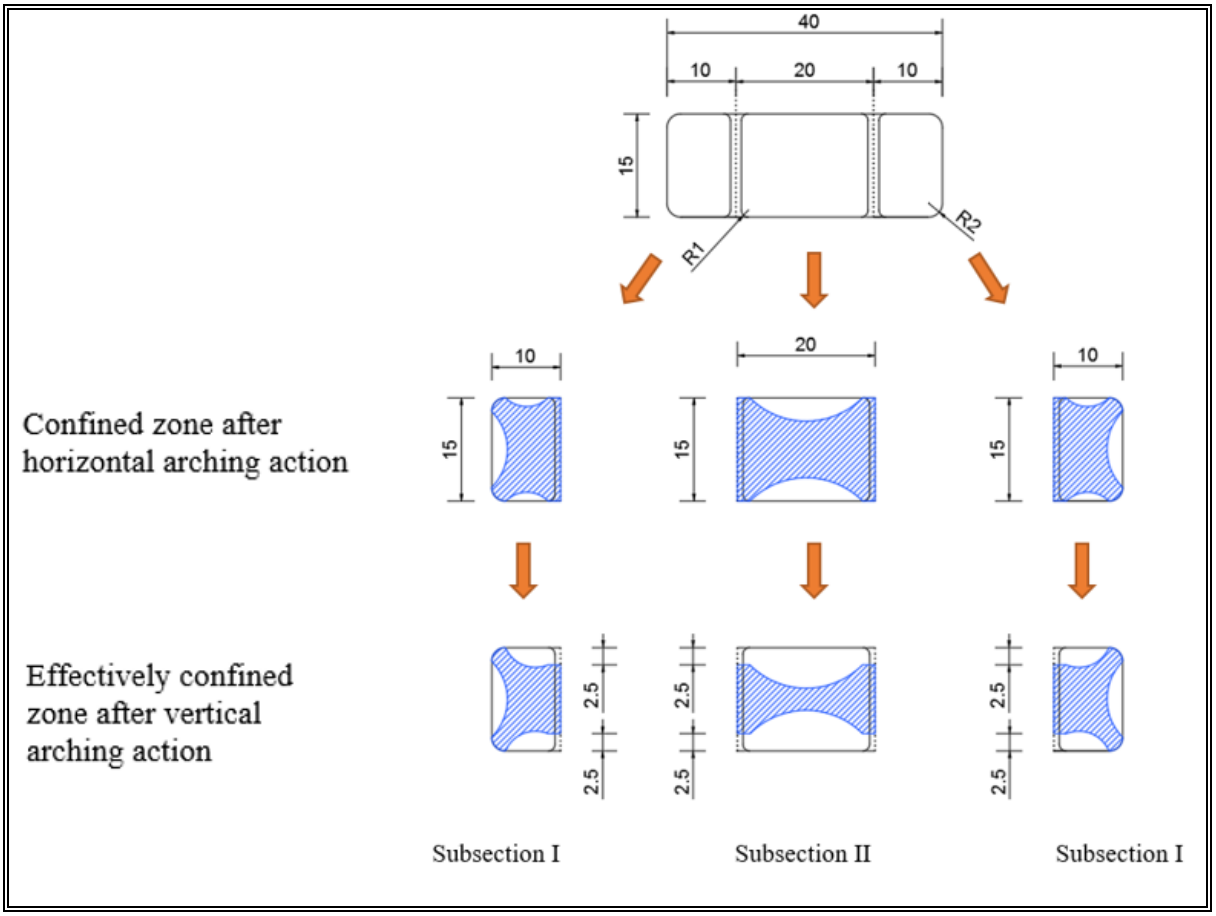

Figure 1.12: Subsections of specimens 225-15 and 325-15 treated as independent columns

1.4 Methodology

A brief explanation of the methodology followed in this study is presented in Figure 1.13. The study focuses on the determination of parameters that determine the concrete axial stress-strain behavior: maximum stress (f_c^{max}), strain at maximum stress (ε_c^{max}), modulus of elasticity (E_c), ultimate stress (f_c^{ult}), ultimate strain (ε_c^{ult}) and descending slope (E_D).

The experimental tests are considered the closest approximation to real behavior of shear wall boundary elements. The axial parameters for concrete with and without CFRP confinement are obtained from confined specimens and control specimens, respectively. From the experimental data, the experimental variation of each axial parameter is studied by dividing each confined specimen parameter with the respective control specimen parameter.

With the proposed model, the axial parameters are theoretically obtained. The theoretically model uses existing design models, nominal and geometrical properties, as well as results from the FEM models. The predicted parameters are compared with the nominal unconfined concrete properties, since most of the existing design models are calibrated with nominal unconfined concrete properties. The theoretical variation of each axial parameter is calculated by diving each parameter predicted with the proposed model by the respective nominal unconfined concrete parameters.

Finally, the predicted increments from the experimental tests and the theoretical modal are compared. Each axial parameter is analyzed individually and the existing design models that predict increments more accurately are selected for each axial parameter.

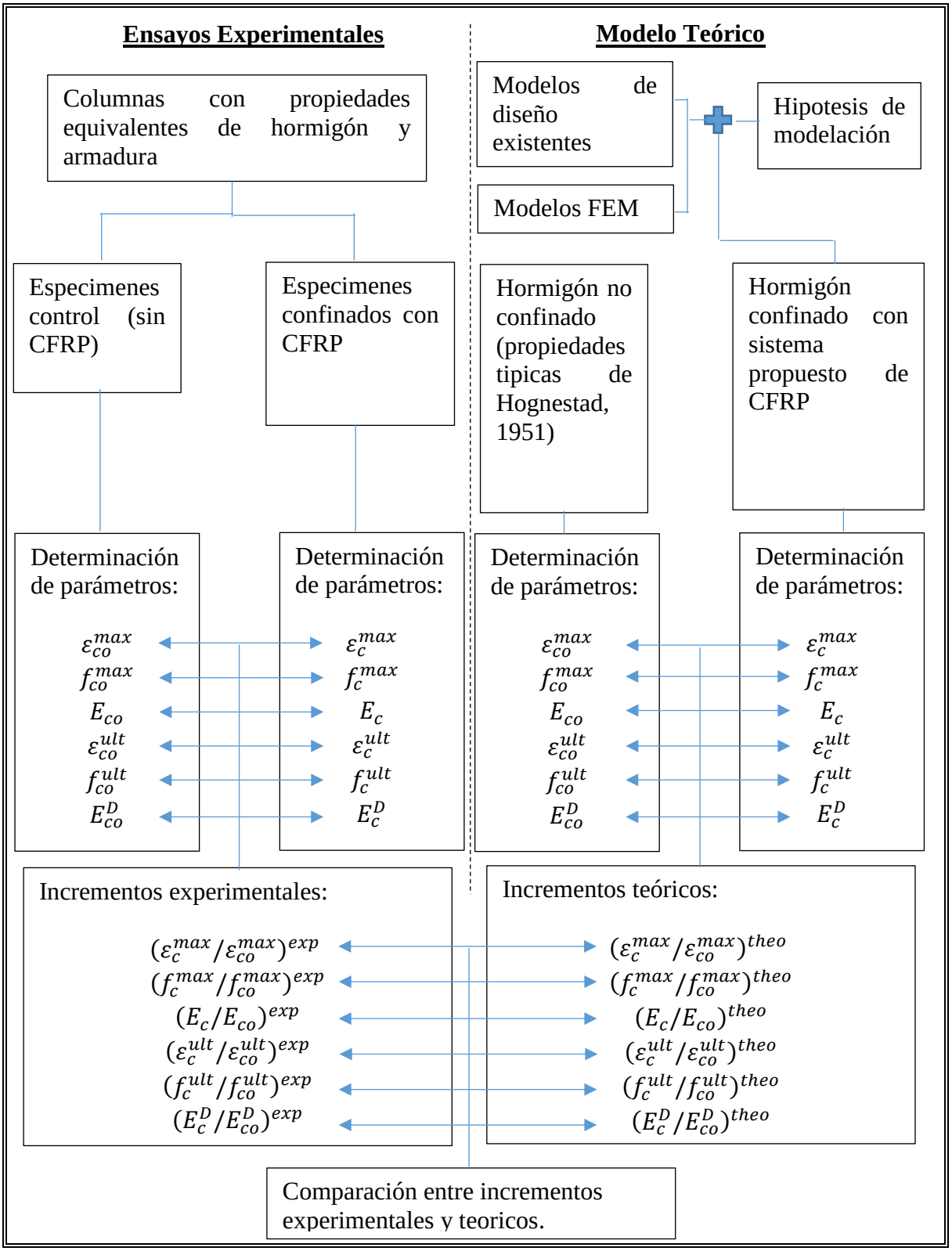

Figure 1.13: Methodology scheme

The methodology is divided in according to the content of each of the main chapters of the present thesis.

- Chapter 1: motivation, objectives, hypothesis, methodology and principal conclusions.
- Chapter 2: review of existing design-oriented models for concrete columns confined with CFRP jackets and without CFRP anchors. Additionally, design-oriented models specifically calibrated for columns confined with CFRP jackets and anchors are found.
- Chapter 3 and Chapter 4: construction and testing of eight rectangular reinforced concrete columns confined with CFRP jackets and CFRP. A wet – layup process is followed for the installation of the CFRP. Anchors are located between CFRP jackets in a sandwiched disposition to avoid premature bonding failure. A forced controlled testing machine is used.
- Chapter 5: development of nonlinear finite element models for each tested column. The programs Solid Works and Ansys are used to construct the finite element models. The results of these models are compared with the experimental measurements and some of the results are used for the design-oriented model.
- Chapter 6: comparison of the predicted increments in the axial stress-strain curve parameters (maximum stress, strain for the maximum stress, ultimate stress, ultimate strain, modulus of elasticity, slope of descending branch) with the actual experimentally measured increments.
- Chapter 7: conclusion of the present study and recommendations for further research.

1.5 Conclusions

The principal conclusions reached on this investigation are:

- Concrete confined with CFRP jackets and CFRP anchors can hold its maximum stress against large axial deformations.
- The CFRP jackets and CFRP anchors system could delay buckling of vertical bars and opening of stirrups.
- The axial ultimate strain (ε_c^{ult}) of concrete confined with CFRP jackets and CFRP anchors showed important increments, reaching values as high as 2.83 times the unconfined value.
- The design oriented procedure based on the subdivision of the column cross-section in independent sub columns demonstrated to generate increment predictions as accurate as models specifically calibrated for rectangular columns confined with CFRP wraps and anchors.
- Finite element models are very useful to obtain parameters not easily captured with experimental tests such as concrete elements stress state and CFRP rupture stress.
- Research on the present topic is still at an early stage, few models are available in the literature with only tens of experimental tests. Much research is need in studying: a more efficient and practical application procedure of CFRP confinement with the inclusion of CFRP anchors, a greater variety of rectangular columns with different aspect ratios and different transverse steel reinforcement, and the development of FEM models that can more accurately predict the behavior of confined concrete elements due to the CFRP system.

2. FRP CONFINEMENT MODELS

In this chapter, a review of existing design-oriented models is presented. All design oriented models reviewed in this chapter are later used for the proposed design methodology.

2.1 Overview

FRP can provide a passive type of confinement to concrete. That means that as concrete is subject to axial compression it expands laterally producing a passive confining pressure from the FRP jacket system. Although it is generally accepted that confined concrete has significantly more strength and ductility than unconfined concrete, the relationship between the axial strain and axial stress of FRP – confined concrete is not fully understood due to the many parameters involved.

These parameters can be classified by their influence on: dilatation of concrete (e.g. modulus of elasticity of cement paste and aggregates, compression and traction strength of concrete, buckling strength of the longitudinal reinforcement, spread of micro cracking and others), lateral pressure transmitted by the confining material (e. g. modulus of elasticity and strength of the confining and bonding material, geometry of the member and others) and loading procedure (e. g. load distribution, rate of loading, stiffness degradation due to cyclic loading and others). The great number of parameters hinders a rigorous analysis (non-linear FEM models) of the mechanical behavior of confined concrete.

An intelligent alternative to FEM models are experimental stress – strain models. They simplify the analysis by assuming a response curve that depends on few parameters. These parameters are usually determined by predictive closed – form equations originated

from regression analysis based on experimental data. The applicability of these models can be expanded with the use of cross-sectional analysis by assigning the closed-form stress – strain response curve to fibers throughout the section (considering all the Euler-Bernoulli beam theory assumptions). A great number of stress-strain models have been proposed for FRP-confined concrete since the 1990s. These models can be classified in two categories (Lam & Teng, 2003a):

- Design – oriented models: closed – form stress – strain curves determined from closed – form models for critical points, such as the ultimate and transition points.
- Analysis – oriented models: incremental stress – strain curves determined from an active confinement model and equilibrium and radial displacement considerations (Spoelstra & Monti, 1999).

The present research aims to develop of a design – oriented model for rectangular reinforced concrete columns with high aspect ratio confined with CFRP jackets and CFRP anchors. Design-oriented models are widely accepted for their simplicity; however, they rely heavily on regressions of experimental data.

Some researchers have proposed models for FRP-confinement with softening behavior based on previous steel-confinement models (Samaan, Mirmiran, & Shahawy, 1998; Zhao & Xie, 2000; Saadatmanesh, Ehsani, & Li, 1994). However, these models can lead to unsafe design due to the great difference in response between FRP and steel (Mirmiran & Shahawy, Behavior Of Concrete Columns Confined By Fiber Composites, 1997). Steel presents a highly ductile response and FRP presents a highly brittle response of FRP. Steel hoops provide a maximum confinement pressure once their yielding stress is reached at relatively low axial strain values, while FRP-confinement pressure continues to

grow until FRP rupture is reached at tension values as high as 10 times the yield stress (Figure 2.1).

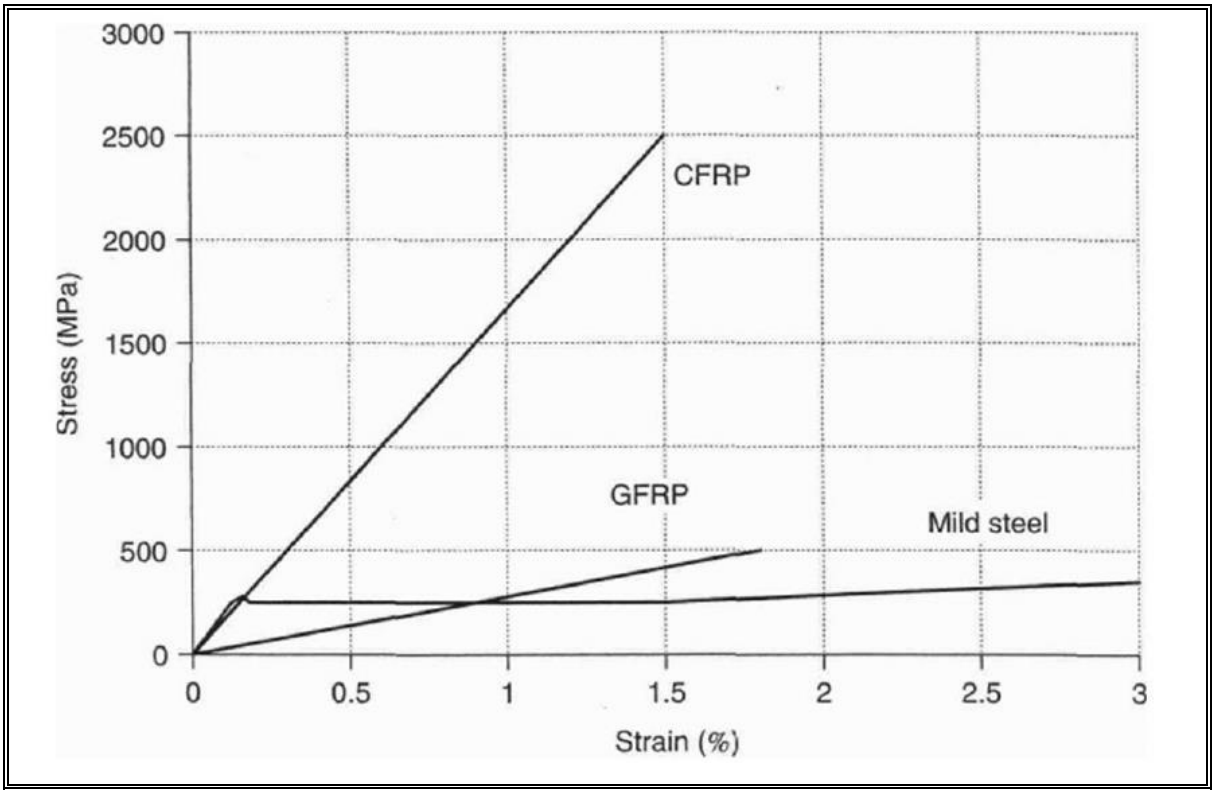

Figure 2.1: Typical FRP and mild-steel stress-strain curves (Teng, Chen, Smith, & Lam, 2002)

2.2 Design – oriented models for circular FRP – confined columns

In the case of circular columns, many models have been developed based on experimental observation. Most of them use the maximum confining pressure due to the FRP jacket (f_l), shown in equation (1.16), as the key parameter to determine the ultimate point. As an example, Figure 2.2 and equations (1.17) and (1.18) show the model adopted by the current American code (ACI Committee 440, 2008; Lam & Teng, 2003a).

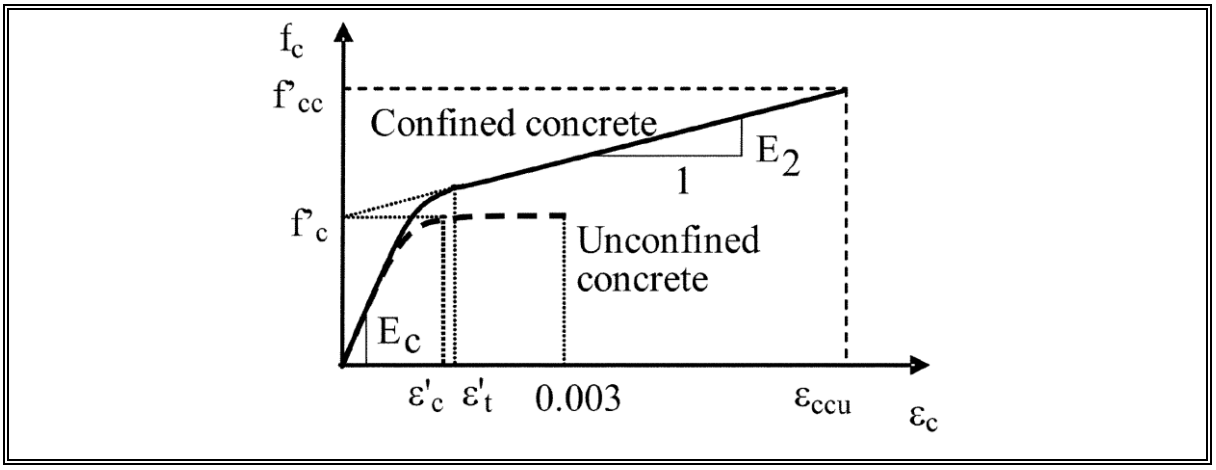

Figure 2.2: Stress – strain model for FRP – confined concrete (Lam & Teng, 2003a) adopted by the current American code (ACI Committee 440, 2008)

$$f_l = \frac{2 f_{frp} t_{frp}}{D} \tag{1.16}$$

$$f'_{cc} = f'_c + \psi_f 3.3 \kappa_a f_l \tag{1.17}$$

$$\varepsilon_{ccu} = \varepsilon'_c \left(1.50 + 12 \kappa_b \frac{f_l}{f'_c} \left(\frac{\varepsilon_{fe}}{\varepsilon'_c}\right)^{0.45}\right) \tag{1.18}$$

The calibration parameters and variables, apart from f_l, will not be explained here because it is not the focus of the current research. It is important to explain with detail the physical principle f_l is based on because that same concept is used for rectangular FRP – confined columns.

Just like in the case of circular columns confined with steel spiral or ties (Mander, Priestley, & Park, 1988a), the lateral confining pressure (f_l) may be found by considering the half body confined and assuming a uniform lateral stress on the concrete core (Figure 2.3). Considering a column with a height equal to a unit, the equilibrium of forces shown in equation (1.19) is the concept behind equation (1.16).

$$f_l D = 2 f_{frp} t_{frp} \tag{1.19}$$

It is important to point out that several models use an equivalent version to equation (1.16) by introduction the volumetric ratio of FRP (ρ_{frp}), as is shown in equations (1.20) and (1.21)

$$\rho_{frp} = \frac{\pi D}{\frac{\pi D^2}{4}} = \frac{4}{D} \tag{1.20}$$

$$f_l = \frac{1}{2} \rho_{frp} f_{frp} t_{frp} \tag{1.21}$$

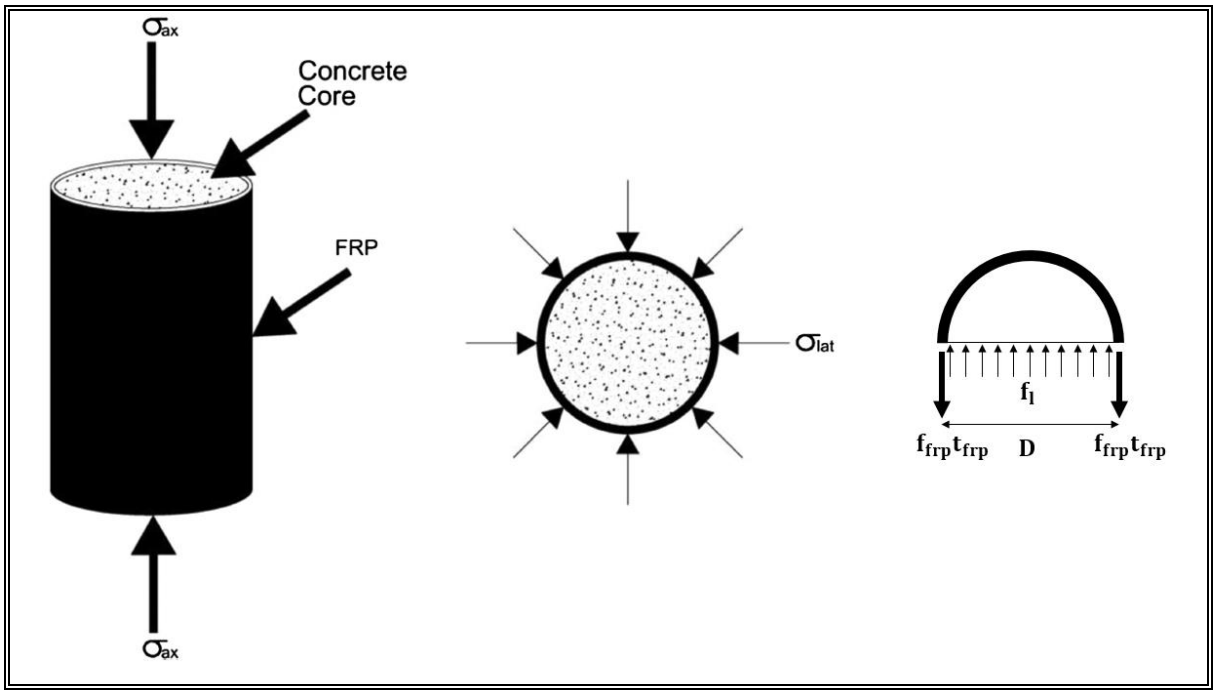

Figure 2.3: Stress – strain model for FRP – confined concrete (Lam & Teng, 2003a) adopted by the current American code (ACI Committee 440, 2008)

2.3 Design – oriented models for rectangular FRP – confined columns

For rectangular FRP – confined columns, a uniform lateral stress is also assumed and either equation (1.21) with the actual FRP volumetric ratio (ρ_{frp}) or equation (1.16) with an equivalent diameter for rectangular cross – sections, for example $D = \frac{2bh}{b+h}$ (ACI Committee 440, 2008) or $D = \sqrt{b^2 + h^2}$ (Lam & Teng, 2003a), are used.

No matter how high is the aspect ratio of a rectangular columns, most design – oriented models use a single lateral stress as the key parameter for their predictions, just like in the case of circular columns.

It is important to point out that design oriented model for rectangular columns confined with steel spirals or ties do not base their predictions on a single lateral stress. These models consider two lateral stresses, each on one direction of the rectangular cross section, and use them to determine the confined concrete strength (Figure 2.4).

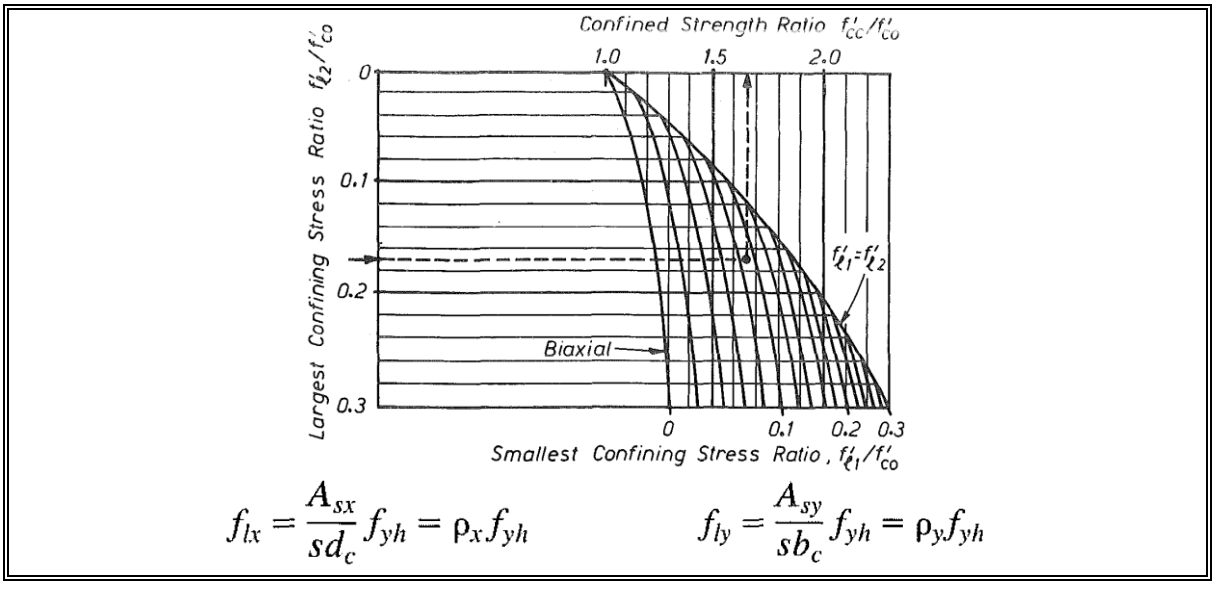

Figure 2.4: Design – oriented model for steel confined concrete (Mander, Priestley, & Park, 1988a)

The assumption of a uniform lateral stress on concrete is valid for circular cross section due to geometric symmetry, but this is not the case for rectangular cross – sections. In rectangular sections, stresses concentrate at corners and is irregular between them. Therefore, equations (1.16) and (1.21) are less appropriate for rectangular columns than for circular. The error in the assumption tends to grow as the aspect ratio (h/b) of the rectangular cross section grows.

A review of models specifically created for FRP – confinement capable of detecting softening behavior is now presented. Usually FRP design-oriented models with softening behavior present the following characteristics (Figure 2.5).

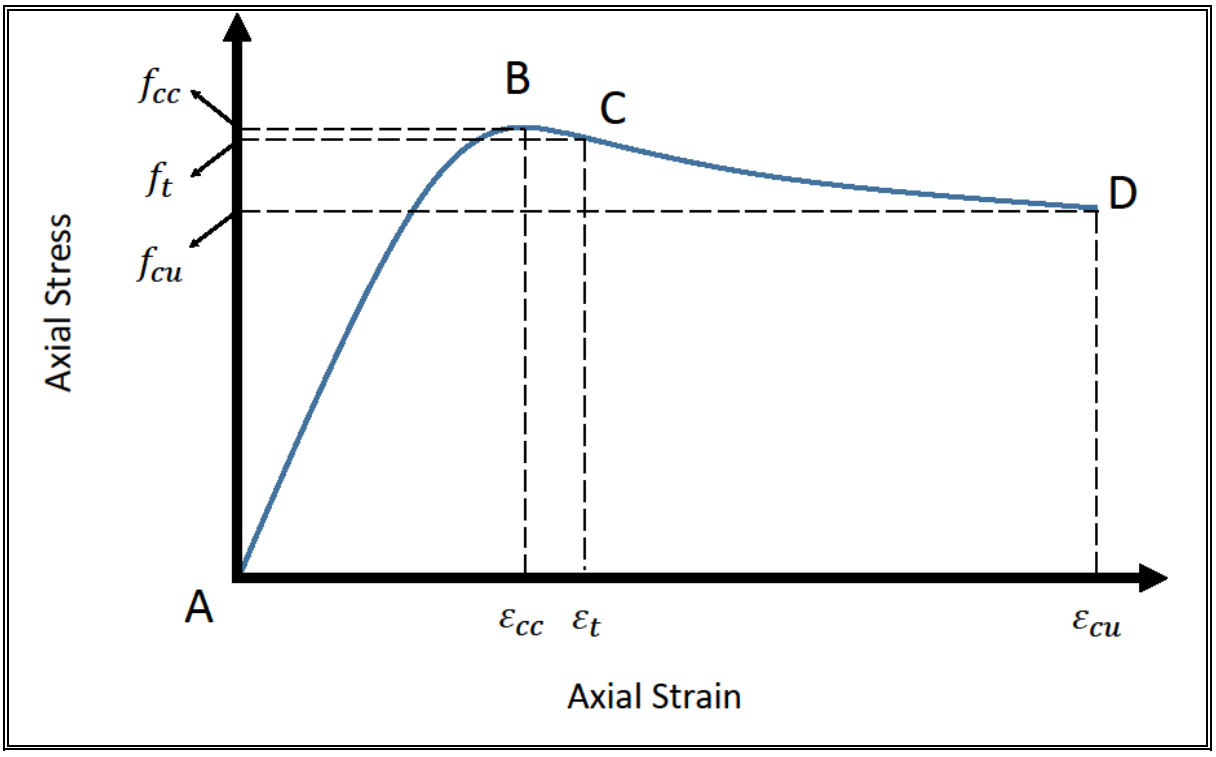

Figure 2.5: Typical stress-strain model for FRP confinement with softening behavior

- All models assume an initial zero stress-strain state (Point A).

- Some models predict the confined compressive strength point (Point B), others predict the transition point (Point C). By definition, these points are different but occur very close to each other.
    - The transition point is defined as the instant after which the confining stress provided by the FRP jacket increases or decreases proportional to the applied load (Youssef, Feng, & Mosallam, 2007). Before the transition point, the behavior is almost identical to unconfined concrete.
    - The confined compressive strength point occurs at the maximum stress state. This point is easier to identify in the experimental curve since the maximum stress can be numerically identified, but lacks the physical interpretation of the transition point.
- Most models predict an ultimate point (Point D). The ultimate point is defined as the instant when the first noticeable rupturing of the FRP sheets occurs (Wei & Wu, 2012). After the ultimate point, the curve may continue to develop but with a wobbling and unstable behavior which is very difficult to predict (Figure 2.5).
- Models assume different mathematical function between points.

To ease comparison between models, the nomenclature of the variables used on each model is changed to a standard nomenclature:

$A_{s,l}$ = total area of longitudinal steel in a column.

b = breadth of cross section, edge length in square cross-sections, diameter in circular cross-sections, shorter edge length in rectangular cross-sections.

b_{frp} = width of the FRP sheet in the case of partially wrapped prisms.

$D =$ diameter in circular cross-sections. Many models for confinement of rectangular cross-sections adapt models for confinement of circular cross-sections by calculating an equivalent diameter. Some examples are:

$D = \frac{2bh}{b+h}$ (ACI Committee 440, 2008).

$D = \sqrt{b^2 + h^2}$ (Lam & Teng, 2003a; Hany, Hantouche, & Harajli, 2015).

$D = h$ (Wu, Wu, & Lu, 2007).

$D = b$ (Wei & Wu, 2012).

$E_c =$ elastic modulus of unconfined concrete, it can be taken as $4730\sqrt{f'_{co}}$ (MPa) (ACI Committee 318, 2014).

$E_s =$ elastic modulus of steel, (200.000 MPa).

$E_{frp} =$ FRP modulus of elasticity obtained from flat coupon tensile tests.

$E_{frp,h} =$ FRP modulus of elasticity in the hoop direction.

$f_{cc} =$ maximum confined concrete stress, Point B in Figure 2.5.

$f'_{co} =$ unconfined concrete compressive strength (cylindrical samples).

$f_{cc} =$ ultimate confined concrete stress, Point D in Figure 2.5.

$f_l =$ confining pressure provided by the FRP jacket system.

$f_t =$ confined concrete transition stress, Point C in Figure 2.5.

$f_{y,h} =$ transverse steel reinforcement yield stress.

$f_{y,l} =$ longitudinal steel reinforcement yield stress.

$f_{30} =$ compressive strength of unconfined concrete grade C30. H35 in Chilean nomenclature ($f'_{co} = 30MPa$).

$h =$ larger edge in rectangular cross-sections.

$\frac{h}{b}$ = cross-section aspect ratio.

r = radius of rounded corner.

s_{frp} = separation between FRP sheets in the case of partially wrapped prisms.

t_{frp} = thickness of the FRP jacket.

ν_{frp} = ultimate Poisson's ratio of FRP-confined equivalent cylinders.

ε_{cc} = confined concrete strain corresponding to f_{cc}, Point B in Figure 2.5.

ε_{co} = unconfined concrete strain corresponding to f'_{co}. Some typical value are: $\varepsilon_{co} = 0.002$ and $\varepsilon_{co} = 0.000937\sqrt[4]{f'_{co}}$ (MPa) (Popovics, 1973).

ε_{cu} = confined concrete ultimate strain, Point D in Figure 2.5.

ε_{frp} = FRP ultimate tensile strain obtained from flat coupon tensile tests.

$\varepsilon_{frp,h}$ = actual hoop rupture strain of the FRP sheet. It can be related to ε_{frp} with the use of an efficiency factor κ_{ε}.

$\varepsilon_{frp,t}$ = FRP sheet hoop strain at the transition point Figure 2.5, a value of 0.002 was suggested by (Youssef, Feng, & Mosallam, 2007).

ε_t = confined concrete transition strain, Point C in Figure 2.5.

ε_u = unconfined concrete ultimate axial strain, commonly accepted to be $1.75\varepsilon_{co} = 0.0035$ in design codes such as BS 8110 (British Standards Institution 1997) and ENV 1992-1-1 (European Committee for Standardization 1991) or 0.0038 (Hognestad, 1951).

κ_{ε} = efficiency factor that relates $\varepsilon_{frp,h}$ to ε_{frp} as $\varepsilon_{frp,h} = \kappa_{\varepsilon}\varepsilon_{frp}$. The value of κ_{ε} varies with the type of FRP and cross-section. Average values of 0.586, 0.788, 0.851 and 0.624 are recommended for confining cylindrical specimens with CFRP, high modulus CFRP, AFRP and GFRP respectively (Lam & Teng, Design-Oriented Stress-Strain Model

For FRP - Confined Concrete, 2003a). For square and rectangular cross-sections, a recommended a value for κ_ε is 0.50 (Pantelides & Yan, 2007). For square cross-sections with b > 300mm, a recommended a value for κ_ε is 0.40 (Wang, Wang, Smith, & Lu, 2012b). For square cross-sections with 150mm < b < 300mm, a recommended a value for κ_ε is 0.60 (Wang, Wang, Smith, & Lu, 2012b). For square cross sections, a recommended value is $\kappa_\varepsilon = 0.31 + 1.42\left(\frac{r}{b}\right)$ (Pantelides, Yan, & Reaveley, 2004). For rectangular cross sections, a recommended value is $\kappa_\varepsilon = 0.25 + 0.71\left(\frac{r}{b}\right)$ (Pantelides, Yan, & Reaveley, 2004). For rectangular and circular cross sections without steel reinforcement, a recommended value is $\kappa_\varepsilon = 0.25 + 0.25\left(\frac{2r}{b}\right)$ (Pellegrino & Modena, 2010). For rectangular and circular cross sections with steel reinforcement a recommended value is $\kappa_\varepsilon = \gamma C^{-0.7} \leq 0.8$, where $C = \frac{E_s \rho_{s,l}}{E_{frp}\rho_{frp}}$ and $\gamma = 0.7$ for CFRP and $\gamma = 1.5$ for GFRP (Pellegrino & Modena, 2010).

ρ_{frp} = volumetric ratio of the FRP, (FRP jacket volume divided by concrete volume).

$\rho_{s,l}$ = longitudinal reinforcement ratio, for rectangular cross-sections $\frac{A_{s,}}{bh}$.

$\rho_{s,h}$ = transverse reinforcement volumetric ratio, volume of transverse reinforcement divided by concrete volume.

2.3.1 Model M. Hosotani, K. Kawashima and J.-I. Hoshikuma (1998)

- Experimental data base: test results from 22 specimens (11 square and 11 circular) of plain concrete tested under pure axial load. All specimens had a 600mm height and a 200mm breadth of cross-section and an unconfined strength of 30 N/mm^2.

- Transition point and Confined compressive strength point: both points are considered equal, but the transition point nomenclature is used. The original paper proposes separate equations for circular and rectangular cross-sections.
- Ultimate point: the original paper proposes separate equations for circular and rectangular sections. It only proposes equations for the ultimate strain and not for the ultimate stress, however, equations for the slope of the descending portion are proposed
- Stress-Strain curve: two portion curve, the first portion resembles the unconfined concrete path and ends with a horizontal slope. The second portion is linear and descending. It is not a soft curve since the slope at the transition point is different for both portions. It depends on four parameters $(E_g, \varepsilon_{cu}, f_t, \varepsilon_t)$.

Table 2.1: FRP-confinement model (Hosotani, Kawashima, & Hoshikuma, 1998)

Characteristic	Description
Transition point	$\frac{f_t}{f'_{co}} = 1.0 + 1.53\frac{\rho_{frp}E_{frp,h}\varepsilon_{frp,h}}{f'_{co}}$ $\varepsilon_t = 0.00330 + 0.00995\frac{\rho_{frp}E_{frp,h}\varepsilon_{frp,h}}{f'_{co}}$ Where $\rho_{frp} = \frac{4t_{frp}}{D}$
Ultimate point	$\varepsilon_{cu} = 0.00340 + 0.0802\left(\frac{\rho_{frp}E_{frp,h}\varepsilon_{frp,h}}{f'_{co}}\right)^{3/4}\left(\frac{f_{frp,h}}{E_{frp,h}}\right)^{1/2}$ $E_g = -1.198\frac{(f'_{co})^2}{\rho_{frp}E_{frp,h}\varepsilon_{frp,h}} + 0.012\sqrt{\rho_{frp}}E_{frp,h}$

Stress – strain curve	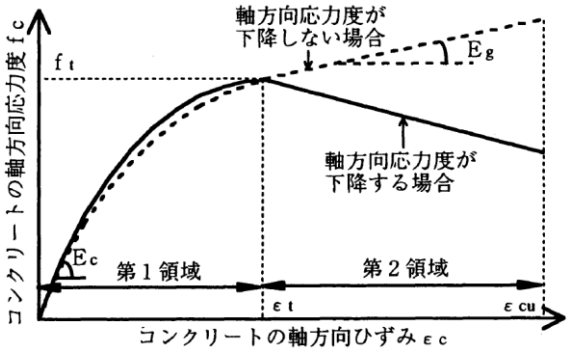
Stress – strain equations	$f_c(\varepsilon_c) = \left\{ \begin{array}{ll} E_c\varepsilon_c\left(1-\frac{1}{n}\left(\frac{\varepsilon_c}{\varepsilon_t}\right)^{n-1}\right) & 0 \le \varepsilon_c \le \varepsilon_t \\ f_t + E_g(\varepsilon_c - \varepsilon_t) & \varepsilon_t \le \varepsilon_c \le \varepsilon_{cu} \end{array} \right\}$ Where $n = \frac{E_c\varepsilon_t}{E_c\varepsilon_t - f_t}$

2.3.2 Model C. P. Pantelides, Z. Yan and L. D. Reaveley (2004)

- Experimental data base: test results from 14 plain concrete specimens without shape modification (five circular, five square, two rectangular with aspect ratio of 2:1 and two rectangular with aspect ratio 3:1) confined with CFRP and GFRP in a complete and partial distribution (strips) taken from other investigation (Yan, 2005).
- Confined compressive strength point and Transition point: for softening behavior both points are considered equal. The original paper nomenclature is changed for comparative purposes. The original paper proposed separate equations for hardening and softening behavior taken from other investigation (Yan, 2005) originally based on the plasticity approach of (William & Warnke, 1975) and the concept of elastic modulus degradation of (Pantazopoulou & Mills, 1995).
- Curve based on a bilinear four-parameter formulation (Richard & Abbott, 1975)

Table 2.2: FRP-confinement model (Pantelides & Yan, 2007)

Characteristic	Description
Transition point	$\frac{f_t}{f'_{co}} = \max\left(1, \frac{-4.322 + 4.721\sqrt{1 + 4.193\frac{f_l}{f'_{co}}} - 2\frac{f_l}{f'_{co}}}{0.0768 \ln\left(\frac{f_l}{f'_{co}}\right) + 1.122}\right)$ $\varepsilon_t = 0.004$
	For hardening behavior $\left(\frac{f_l}{f'_{co}} \geq 0.2\right)$: $\frac{f_t}{f'_{co}} = \frac{E_0 \varepsilon_t}{1 + 2\beta\varepsilon_t}$ $\varepsilon_t = 0.004$ Where $\beta = 190\left(\frac{f_l}{f'_{co}}\right)^{-0.8}$ $f_l = \frac{1}{2}\rho_{frp} k_s k_\varepsilon E_{frp} \varepsilon_{frp}$ $k_s = \begin{cases} \text{Rectangular:} & 1 - \frac{(b-2r)^2 + (h-2r)^2}{3hb} \\ \text{Square:} & 1 - \frac{2(b/r-2)^2}{3(b/r)^2} \\ \text{Circular:} & 1 \end{cases}$ $\rho_{frp} = \begin{cases} \text{Rectangular:} & 2(b+h)t_{frp}/hb \\ \text{Square:} & 4t_{frp}/b \\ \text{Circular:} & 4t_{frp}/D \end{cases}$ $E_0 = 1.15E_c = 5500\sqrt{f'_{co}}$ f'_{co} units in MPa

Ultimate point	For softening behavior $\left(\frac{f_l}{f'_{co}} < 0.2\right)$: $\frac{f_{cu}}{f'_{co}} = 0.0768 \ln\left(\frac{f_l}{f'_{co}}\right) + 1.122$ $\varepsilon_{cu} = \frac{f_{cu}(1 + 2\beta k_\varepsilon \varepsilon_{frp})}{E_0}$ For hardening behavior $\left(\frac{f_l}{f'_{co}} \geq 0.2\right)$: $\frac{f_{cu}}{f'_{co}} = -4.322 + 4.721\sqrt{1 + 4.193\frac{f_l}{f'_{co}}} - 2\frac{f_l}{f'_{co}}$ $\varepsilon_{cu} = \frac{f_{cu}(1 + 2\beta k_\varepsilon \varepsilon_{frp})}{E_0}$
Stress – strain curve	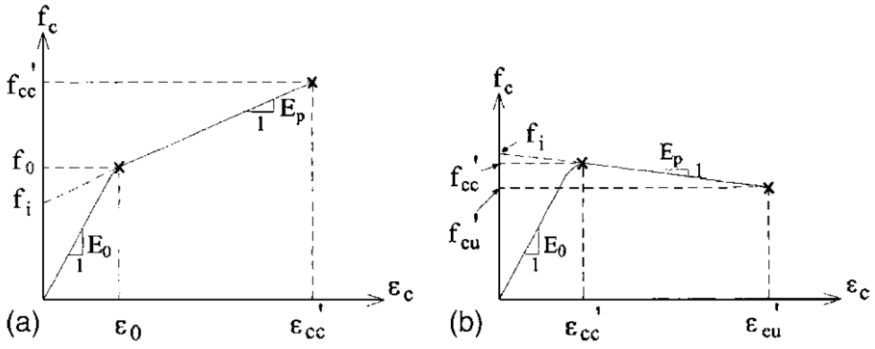
Stress – strain equations	$f_c(\varepsilon_c) = \frac{(E_0 - E_p)\varepsilon_c}{\left(1 + \left(\frac{(E_0 - E_p)\varepsilon_c}{f_i}\right)^n\right)^{1/n}} + E_p\varepsilon_c$ Where $E_p = \frac{f_{cu} - f_t}{\varepsilon_{cu} - \varepsilon_t}$ $f_i = f_{cu} - E_p\varepsilon_{cu}$ $E_{c0} = \frac{f_t}{\varepsilon_t}$ $n = 1 + \frac{1}{\frac{E_0}{E_{c0}} - 1}$

2.3.3 Model M. N. Youssef, M. Q. Feng and A. S. Mosallam (2007)

- Experimental data base: test results from a total of 81 large unreinforced specimens (27 rectangular, 27 circular and 27 square) tested under pure axial load and an additional 30, 152mm x 305mm (6in. x 12in.) concrete cylinders. Both carbon/epoxy and E-glass/epoxy jackets were used to confine the column specimens. The FRP laminates were applied directly to the pretreated surfaces of the specimens providing unidirectional lateral confinement in the hoop direction. An overlap of 152 mm (6-in.) was used to ensure the development of full composite tensile strength. Ready-mix concrete with nominal 28-day strength of 27.58 MPa (4000 psi) to 34.47 MPa (5000 psi) was used.
- Transition point and Confined compressive strength point: both points are considered equal. The original paper uses the transition point nomenclature and proposes separate equations for circular and rectangular cross-sections.
- Ultimate point: the original paper proposes separate equations for circular and rectangular cross-sections.
- Stress-Strain curve: two portion curve, the first portion resembles the unconfined concrete path and ends with a horizontal slope. The second portion is linear and descending. It is not a soft curve since the slope at the transition point is different for both portions. It depends on four parameters $(f_{cu}, \varepsilon_{cu}, f_t, \varepsilon_t)$.

Table 2.3: FRP-confinement model (Youssef, Feng, & Mosallam, 2007)

Characteristic	Description
Transition point	$\frac{f_t}{f'_{co}} = 1.0 + 1.1350\left(\frac{\rho_{frp}E_{frp,h}\varepsilon_{frp,t}}{f'_{co}}\right)^{5/4}$ $\varepsilon_t = 0.002 + 0.0775\left(\frac{\rho_{frp}E_{frp,h}\varepsilon_{frp,t}}{f'_{co}}\right)^{6/7}\left(\frac{E_{frp,h}\varepsilon_{frp,h}}{f'_{co}}\right)^{1/2}$
Ultimate point	$\frac{f_{cu}}{f'_{co}} = 0.5 + 1.225\left(\frac{f_l}{f'_{co}}\right)^{3/5}$ $\varepsilon_{cu} = 0.004325 + 0.2625\left(\frac{f_l}{f'_{co}}\right)\left(\frac{E_{frp}\varepsilon_{frp,h}}{f'_{co}}\right)^{1/2}$
	Where $f_l = k_e f_{lu}$ $f_{lu} = \frac{1}{2}\rho_{frp}E_{frp,h}\varepsilon_{frp,h}$ $\rho_{frp} = \frac{4t_{frp}}{D}$ $k_e = \frac{1 - \frac{(b-2r)^2+(h-2r)^2}{3hb} - \rho_{s,l}}{1-\rho_{s,l}}$, for rectangular cross-sections
Stress – strain curve	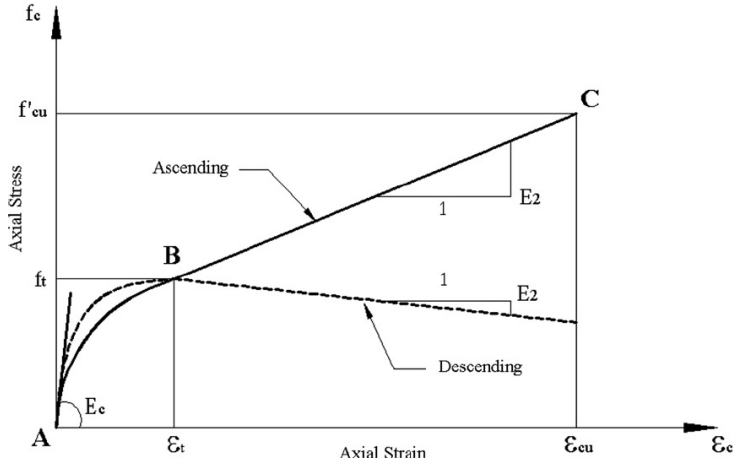

Stress – strain equations	$$E_2 = \frac{f_{cu} - f_t}{\varepsilon_{cu} - \varepsilon_t}$$ With softening behavior $E_2 < 0$: $$f_c(\varepsilon_c) = \begin{cases} E_c\varepsilon_c\left(1 - \frac{1}{n}\left(\frac{\varepsilon_c}{\varepsilon_t}\right)^{n-1}\right) & \text{if} \quad 0 \le \varepsilon_c \le \varepsilon_t \\ f_t + E_2(\varepsilon_c - \varepsilon_t) & \text{if} \quad \varepsilon_t \le \varepsilon_c \le \varepsilon_{cu} \end{cases}$$ Where $$n = \frac{E_c\varepsilon_t}{E_c\varepsilon_t - f_t}$$ With hardening behavior $E_2 \ge 0$: $$f_c(\varepsilon_c) = \begin{cases} E_c\varepsilon_c\left(1 - \frac{1}{n}\left(1 - \frac{E_2}{E_c}\right)\left(\frac{\varepsilon_c}{\varepsilon_t}\right)^{n-1}\right) & \text{if} \quad 0 \le \varepsilon_c \le \varepsilon_t \\ f_t + E_2(\varepsilon_c - \varepsilon_t) & \text{if} \quad \varepsilon_t \le \varepsilon_c \le \varepsilon_{cu} \end{cases}$$ Where $$n = \frac{(E_c - E_2)\,\varepsilon_t}{E_c\varepsilon_t - f_t}$$

2.3.4 Model G. Wu, Z. S. Wu and Z. T. Lu (2007)

- Experimental data base: Test results of more than one hundred specimens developed by various authors. Some characteristics of the specimens include: square and rectangular cross-sections, corner radii range from 5 and 50 mm, axial compressive strength of unconfined concrete range from 23.6 to 75.4 MPa, side length of prism between 100 and 500 mm, height between 150 and 1500 mm, three types of CFRP, GFRP and AFRP, tensile strength of FRP between 230 and 4433 MPa, modulus of FRP between 13.6 and 640 GPa, thickness of FRP between 0.11 and 8.0 mm and no longitudinal or no transverse reinforcements are used in all specimens.
- Transition point and Confined compressive strength point: for softening behavior both points are considered equal, for comparative purposes the transition point nomenclature is used. The original paper uses the nomenclature $(\varepsilon_{cp}, \sigma_{cp})$.

- Ultimate point: Softening response occurs when $\frac{f_l}{f'_{co}} < 0.13$.
- Stress-Strain curve: 3 stress-strain models are proposed.
    - Model I: cannot capture strain hardening, only softening. A parabolic equation is suggested for the first region before the transitional point and a curvilinear equation is suggested after the transitional point. The stress-strain curve is determined by three parameters f_t, ε_t and f_{cu}.
    - Model II considers separate models for softening and hardening behavior.
    - Model III is a two-portion curve with a parabolic first portion and a linear second portion. The stress-strain curve is determined by three parameters $f_t, \varepsilon_t, f_{cu}$ and ε_{cu}

Table 2.4: FRP-confinement model (Wu, Wu, & Lu, 2007)

Characteristic	Description
Transition point	$$\frac{f_t}{f'_{co}} = 1 + 0.0008\alpha k_1 \lambda_1$$ $$\frac{\varepsilon_t}{\varepsilon_{co}} = 1 + 0.0034\alpha k_2 \lambda_1$$ Where $$\alpha = \frac{f_{30}}{f'_{co}} = \frac{30\text{MPa}}{f'_{co}}$$ $$\lambda_1 = \frac{\rho_{frp} E_{frp}}{\sqrt{f'_{co}}} \quad (E_{frp}: \text{ unit GPa}, f'_{co}: \text{ unit MPa})$$ $$k_1 = \left\{ \begin{array}{ll} 1 & E_{frp} \leq 250 \text{ (GPa)} \\ \sqrt{E_{frp}/250} & E_{frp} > 250 \text{ (GPa)} \end{array} \right\} (E_{frp}: \text{ unit GPa})$$ $$k_2 = \left\{ \begin{array}{ll} 1 & E_{frp} \leq 250 \text{ (GPa)} \\ E_{frp}/250 & E_{frp} > 250 \text{ (GPa)} \end{array} \right\} (E_{frp}: \text{ unit GPa})$$ $$\rho_{frp} = \left\{ \begin{array}{ll} \frac{2(b+h)t_{frp}}{bh} & \text{for fully wrapped prisms.} \\ \frac{2(b+h)t_{frp}b_{frp}}{bh(b_{frp}+s_{frp})} & \text{for partially wrapped prisms.} \end{array} \right\}$$
Ultimate point	$$\frac{f_{cu}}{f'_{co}} = \left\{ \begin{array}{ll} k_3\left(0.75 + 2.5\frac{f_l}{f'_{co}}\right) & \text{if } \frac{f_l}{f'_{co}} < 0.13 \\ k_3\left(0.739 + 3.418\frac{f_l}{f'_{co}} - 1.215\left(\frac{f_l}{f'_{co}}\right)^2\right) & \text{if } \frac{f_l}{f'_{co}} \geq 0.13 \end{array} \right\}$$ $$\varepsilon_{cu} = \left\{ \begin{array}{ll} k_4\varepsilon_u\left(1.3 + 6.3\frac{f_l}{f'_{co}}\right) & \text{if } \frac{f_l}{f'_{co}} < 0.13 \\ \frac{\varepsilon_{frp}}{\nu_{frp}} & \text{if } \frac{f_l}{f'_{co}} \geq 0.13 \end{array} \right\}$$ Where $$f_l = \frac{1}{2}\rho_{frp} E_{frp} \varepsilon_{frp}$$ $$\nu_{frp} = 0.56\left(\frac{f_l}{f'_{co}}\right)^{-0.66}$$

<table>
<tr>
<td></td>
<td>

$$k_3 = \left\{ \begin{array}{ll} (2-\alpha)\frac{r}{h} + 0.5\alpha & \text{if } E_{frp} \le 250 \text{ (GPa)} \\ \left(2 - \sqrt{\frac{E_{frp}}{250}}\alpha\right)\frac{r}{h} + 0.5\sqrt{\frac{E_{frp}}{250}}\alpha & \text{if } E_{frp} > 250 \text{ (GPa)} \end{array} \right\} (E_{frp}: \text{ unit GPa})$$

if $\frac{f_l}{f'_{co}} < 0.13$

$$k_4 = \left\{ \begin{array}{ll} (2-1.6\alpha)\frac{r}{h} + 0.8\alpha & \text{if } E_{frp} \le 250 \text{ (GPa)} \\ \left(2 - 1.6\sqrt{\frac{E_{frp}}{250}}\alpha\right)\frac{r}{h} + 0.8\sqrt{\frac{E_{frp}}{250}}\alpha & \text{if } E_{frp} > 250 \text{ (GPa)} \end{array} \right\} (E_{frp}: \text{ unit GPa})$$

if $\frac{f_l}{f'_{co}} \ge 0.13$

$$k_4 = (2-1.6\alpha)\frac{r}{h} + 0.8\alpha$$

</td>
</tr>
<tr>
<td>Stress – strain curve: Model I</td>
<td>

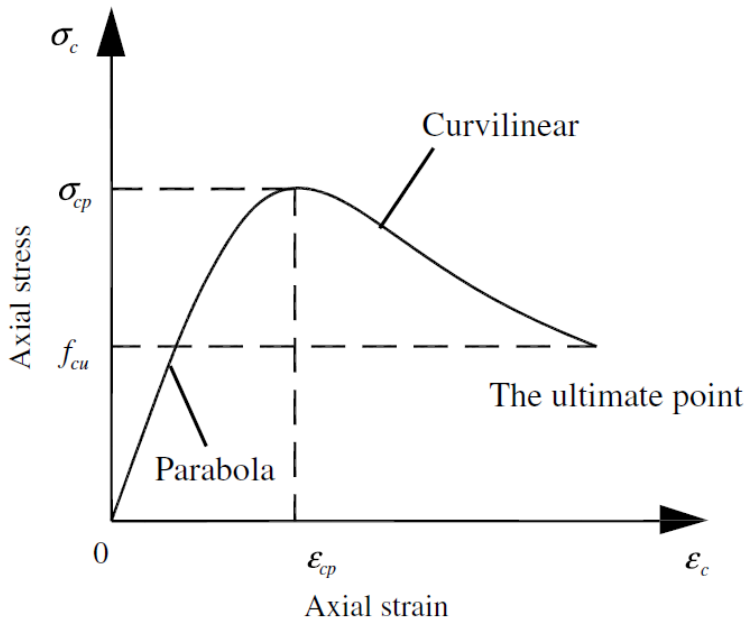

</td>
</tr>
<tr>
<td>Stress – strain equations: Model I</td>
<td>

$$f_c(\varepsilon_c) = \left\{ \begin{array}{ll} f_t\,(2x - x^2) & \text{if } x \le 1 \\ f_t x^A e^{1-x^4} & \text{if } x > 1 \end{array} \right\}$$

Where

$$x = \frac{\varepsilon_c}{\varepsilon_t}$$

$$A = -5130B^2 + 44B - 0.778$$

$$B = \frac{f_t}{10^6 \varepsilon_t} \quad f_t \text{ units in MPa}$$

</td>
</tr>
</table>

Stress – strain curve: Model II	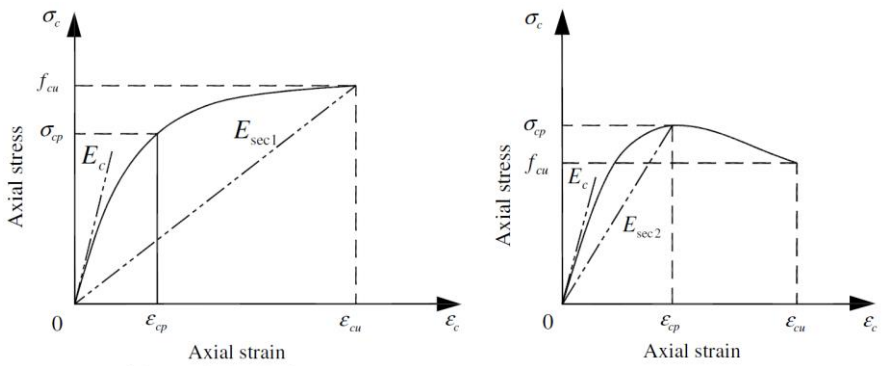 (a) With a strain-hardening response (b) With a strain-softening response
Stress – strain equations: Model II	With hardening behavior ($f_t \leq f_{cu}$): $f_c(\varepsilon_c) = \frac{f_t x_1 n_1}{n_1 - 1 + x_1^{n_1}}$ Where $x_1 = \frac{\varepsilon_c}{\varepsilon_{cu}}$ $n_1 = \frac{E_c}{E_c - E_{sec1}}$ $E_{sec1} = \frac{f_{cu}}{\varepsilon_{cu}}$
	With softening behavior ($f_t > f_{cu}$): $f_c(\varepsilon_c) = \frac{f_t x_2 n_2}{n_2 - 1 + x_2^{n_2}}$ Where $x_2 = \frac{\varepsilon_c}{\varepsilon_t}$ $n_2 = \frac{E_c}{E_c - E_{sec2}}$ $E_{sec2} = \frac{f_t}{\varepsilon_t}$

Stress – strain curve: Model III	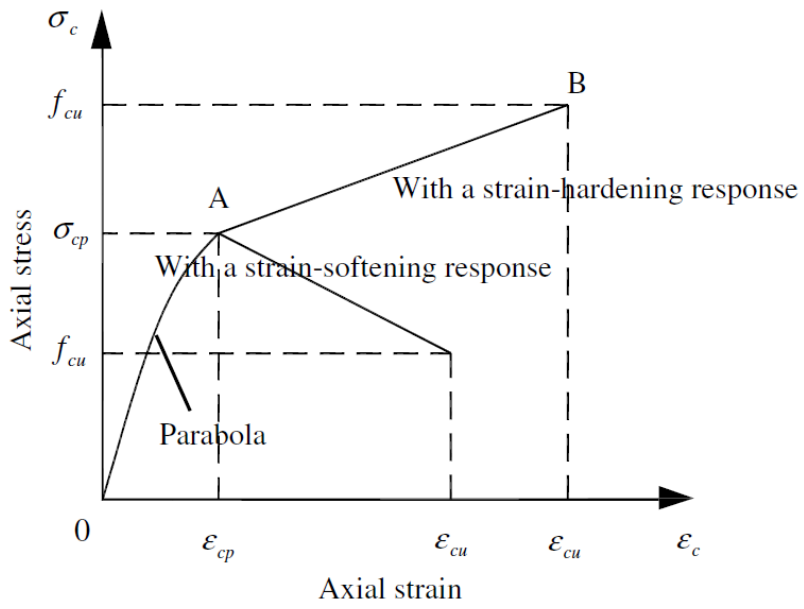
Stress – strain equations: Model III	$f_c(\varepsilon_c) = \begin{cases} f_t\,(2\varepsilon_c/\varepsilon_t - (\varepsilon_c/\varepsilon_t)^2) & \varepsilon_c \le \varepsilon_t \\ f_t + \frac{(f_{cu}-f_t)(\varepsilon_c-\varepsilon_t)}{\varepsilon_{cu}-\varepsilon_t} & \varepsilon_c > \varepsilon_t \end{cases}$

2.3.5 Model J. G. Teng, T. Jiang, L. Lam and Luo (2009)

- Experimental data base: Test results of 48 tests on plain concrete cylinders 152 mm x 305 mm confined with varying amounts of carbon FRP and glass FRP, with the unconfined concrete strength ranging from 33.1 to 47.6 MPa. Full details of these tests are available in Jiang and Teng (2007). The database covers a wide range of FRP confinement levels, the most lightly confined specimens exhibited a stress-strain curve with a descending branch. The paper proposes two versions of modifications a previous investigation (Lam & Teng, 2003a), only version II is review because this version can capture softening. This model was developed for circular columns; however, it is reviewed because it is one of the few models capable of capturing softening behavior.

- Stress-Strain curve: two portion curve with a parabolic first portion and a linear second portion. It depends on two parameters $(f_{cu}, \varepsilon_{cu}, \varepsilon_t)$, the slope at the transition point is the same for the two portions. For softening behavior, the confined compressive strength is taken equal to the unconfined compressive strength.

Table 2.5: FRP-confinement model (Teng, Jiang, Lam, & Luo, 2009)

Characteristic	Description
Confined compressive strength point	$\frac{f_{cc}}{f'_{co}} = \begin{cases} 1 + 3.5\,(\rho_K - 0.01)\,\rho_\varepsilon & \text{if} \quad \rho_K \geq 0.01 \\ 1 & \text{if} \quad \rho_K < 0.01 \end{cases}$
Transition point	$\varepsilon_t = \frac{2f'_{co}}{E_c - E_2}$ In the case of softening behavior $(\rho_K < 0.01)$ the transition point and the confined compressive strength point are the same point and reduce to: $f_t = f'_{co}$ $\varepsilon_t = \frac{2f'_{co}}{E_c}$
Ultimate point	$\frac{f_{cu}}{f'_{co}} = 1 + \left(3.2\rho_K^{0.9} - 0.06\right)\rho_\varepsilon$ $\frac{\varepsilon_{cu}}{\varepsilon_{co}} = 1.75 + 6.5\rho_K^{0.8}\rho_\varepsilon^{1.45}$ Where if $\rho_K > 0 \Rightarrow f_{cu} \geq 0.85f'_{co}$ if $\rho_K = 0 \Rightarrow f_{cu} = 0.85f'_{co}$

Stress – strain curve	$$f_c(\varepsilon_c) = \left\{ \begin{array}{ll} E_c\varepsilon_c - \frac{(E_c-E_2)^2}{4f'_{co}}\varepsilon_c^2 & \text{if} \quad 0 \le \varepsilon_c \le \varepsilon_t \\ \left\{ \begin{array}{ll} f'_{co} + E_2\varepsilon_c & \text{if } \rho_K \ge 0.01 \\ f'_{co} - \frac{f'_{co}-f_{cu}}{\varepsilon_{cu}-\varepsilon_{co}}(\varepsilon_c - \varepsilon_{co}) & \text{if } \rho_K < 0.01 \end{array} \right\} & \text{if} \quad \varepsilon_t \le \varepsilon_c \le \varepsilon_{cu} \end{array} \right\}$$ Where $$\rho_K = \frac{2E_{frp,h}t_{frp}}{(f'_{co}/\varepsilon_{co})\,D}$$ $$\rho_\varepsilon = \frac{\varepsilon_{frp,h}}{\varepsilon_{co}}$$ $$E_2 = \frac{f_{cc} - f'_{co}}{\varepsilon_{cu}}$$
Stress – strain equations	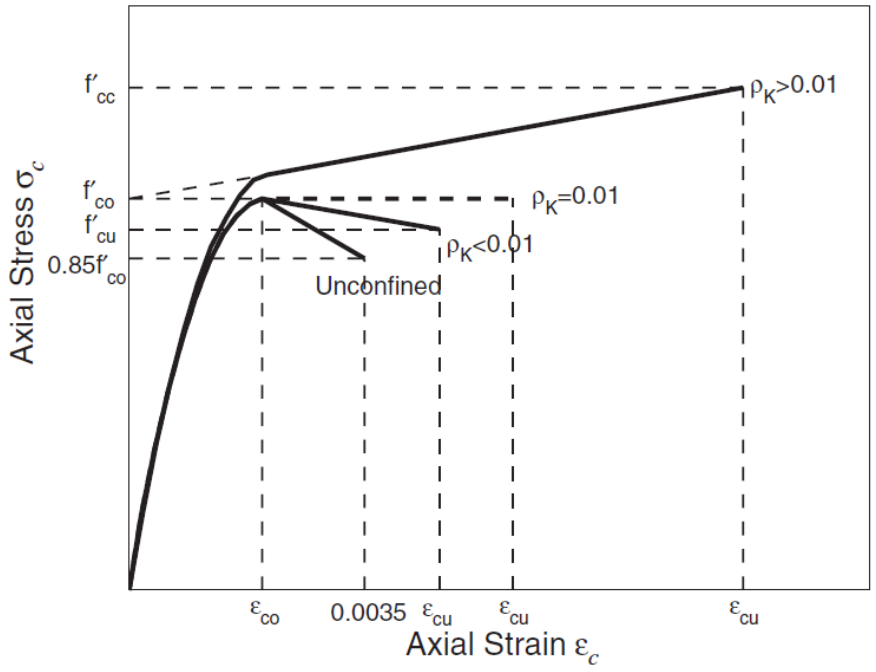

2.3.6 Model C. Pellegrino and C. Modena (2010)

- Experimental data base: A database with experimental results available in literature regarding axial compression tests of FRP confined concrete columns. This database included characteristics and experimental results of 219 FRP confined circular cross section and without steel reinforcement, 85 FRP confined circular cross section and steel

reinforcement, 135 FRP confined with rectangular cross section and 156 FRP confined without steel reinforcement and rectangular cross section and steel reinforcement.

Table 2.6: FRP-confinement model (Pellegrino & Modena, 2010)

Characteristic	Description
Confined compressive strength point	For softening behavior $(2r/b < 0.3)$: $\frac{\varepsilon_{cc}}{\varepsilon_{cu}} = 0.55 + 1.5 * (2r/b)$ $\frac{f_{cc}}{f'_{co}} = 1 + k_A k_R \frac{P_u}{f_{co}}$ For hardening behavior $(2r/b \geq 0.3)$: this equations are used to calculate the ultimate point and instead of a compressive strength point a transition point exists.
Transition point	$f_t = f'_{co}$ $\varepsilon_t = \varepsilon_{co}$
Ultimate point	$\frac{f_{cu}}{f'_{cc}} = \begin{cases} 0.55 + 1.5(2r/b) & \text{if } 2r/b < 0.3 \\ 1 & \text{if } 2r/b \geq 0.3 \end{cases}$ $\frac{\varepsilon_{cu}}{\varepsilon_{co}} = 2 + B\left(\frac{P_u}{f'_{co}}\right)$ $B = \begin{cases} 23 & \text{for circular without steel} \\ 28 & \text{for circular with steel} \\ 23 & \text{for rectangular without steel} \\ 28 & \text{for rectangular with steel} \end{cases}$

Where

$$k_A = A\left(\frac{P_u}{f'_{co}}\right)^{-\alpha}$$

$$A = \begin{cases} 3.55 & \text{for circular without steel} \\ 2.95 & \text{for circular with steel} \\ 2.25 & \text{for rectangular without steel} \\ 1.35 & \text{for rectangular with steel} \end{cases}$$

$$\alpha = \begin{cases} -0.15 & \text{for circular without steel} \\ -0.40 & \text{for circular with steel} \\ -0.25 & \text{for rectangular without steel} \\ -0.50 & \text{for rectangular with steel} \end{cases}$$

$$k_R = \begin{cases} 1 - 2.5(0.3 - 2r/b) & \text{if } 2r/b < 0.3 \\ 1 & \text{if } 2r/b \geq 0.3 \end{cases}$$

$$P_u = f_{lf} + f_{ls}A_{cc}/A_g$$

$$f_{lf} = \frac{1}{2}k_v k_h \rho_{frp} E_{frp} \varepsilon_{frp,h}$$

$$\rho_{frp} = \begin{cases} \frac{4t_{frp}}{D} & \text{Circular columns} \\ \frac{2t_{frp}(b+h)}{bh} & \text{Rectangular columns} \end{cases}$$

$$k_h = 1 - \frac{(b-2r)^2 + (h-2r)^2}{3bh}$$

$$k_v = \left(1 - \frac{s_{frp}}{2b}\right)^2$$

$$f_{ls} = \frac{1}{2}k_{es}k_v\rho_{s,h}f_{y,h}$$

k_{es}, k_v = steel confinement coefficients (Sheikh & Uzumeri, 1982)

Stress – strain curve

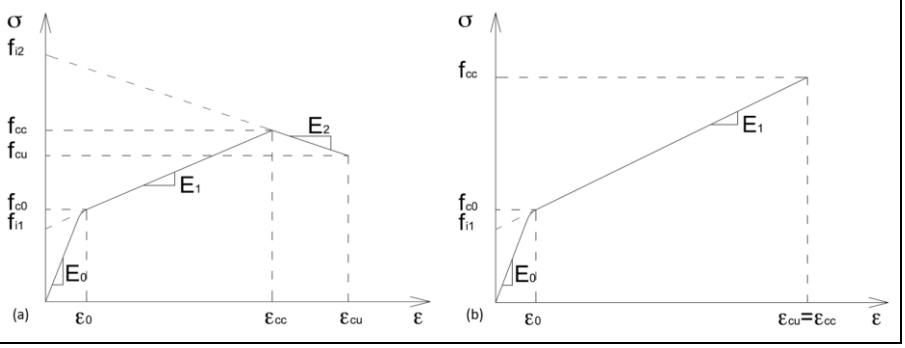

Stress – strain equations	$$f_c(\varepsilon_c) = \begin{cases} \frac{\varepsilon_c(E_c-E_1)}{\left(1+\left(\frac{\varepsilon_c(E_c-E_1)}{f_{i1}}\right)^n\right)^{1/n}} + E_1\varepsilon_c & \text{if} \quad 0 \le \varepsilon_c \le \varepsilon_t \\ E_2\varepsilon_c - f_{i2} & \text{if} \quad \varepsilon_t \le \varepsilon_c \le \varepsilon_{cu} \end{cases}$$ Where $$E_1 = \frac{f_{cc} - f'_{co}}{\varepsilon_{cc} - \varepsilon_{co}}$$ $$E_2 = \frac{f_{cu} - f'_{cc}}{\varepsilon_{cu} - \varepsilon_{cc}}$$ $$E_{co} = \frac{f'_{co}}{\varepsilon_{co}}$$ $$f_{i1} = f_{cc} - E_1\varepsilon_{cc}$$ $$f_{i2} = \frac{\varepsilon_{cu}f'_{co} - \varepsilon_{co}f'_{cu}}{\varepsilon_{co} - \varepsilon_{cu}}$$ $$n = 1 + \frac{1}{\frac{E_c}{E_{c0}} - 1}$$

2.3.7 Model Z. Wang, D. Wang, S. Smith and D. Lu (2012)

- Experimental data base: A total of 34 square unreinforced and reinforced concrete columns of varying geometric properties were fabricated and tested under different uniaxial compression patterns (Wang, Wang, Smith, & Lu, 2012a). To verify the accuracy of the various components of the new model, the tests collected from the open literature were used. More specifically, for verification of the monotonic stress-strain component of the new model, the tests of other investigations were utilized (Youssef, 2003; Rocca, 2007; Wang & Wu, 2008).
- Transition point and Confined compressive strength point: for softening behavior both points are considered equal.

Table 2.7: FRP-confinement model (Wang, Wang, Smith, & Lu, 2012b)

Characteristic	Description
Transition point	$\frac{f_t}{f'_{co}} = 1 + 0.35\lambda_f + 0.5\lambda_h + 0.85\lambda_l$ $\frac{\varepsilon_t}{\varepsilon_{co}} = 1 + 2.0\lambda_f + 2.5\lambda_h$
Ultimate point	$\frac{f_{cu}}{f'_{co}} = 0.2 + 3.47\left(\frac{f_{lf}}{f'_{co}}\right)^{0.64} + 0.59\left(\frac{f_{ls}}{f'_{co}}\right)^{0.2}$ $\frac{\varepsilon_{cu}}{\varepsilon_{co}} = 2 + 73.31\left(\frac{f_{lf}}{f'_{co}}\right)^{1.07} + 5.06\left(\frac{f_{ls}}{f'_{co}}\right)^{0.03}$ Where $\lambda_f = \frac{\kappa_a \rho_{frp} E_{frp} \varepsilon_{frp}}{f'_{co}}$ $\lambda_h = \frac{\rho_{s,h} f_{y,h}}{f'_{co}}$ $\lambda_l = \frac{\rho_{s,l} f_{y,l}}{f'_{co}}$ $\rho_{frp} = \frac{4t_{frp}}{b}$ $\kappa_a = \frac{1 - \frac{2(b-2r)^2}{3bh} - \rho_{s,l}}{1 - \rho_{s,l}}$, for square cross-sections $f_{lf} = 0.5\kappa_a \rho_{frp} E_{frp} \varepsilon_{frp,h}$ $f_{ls} = 0.5\kappa_{es}\kappa_v \rho_{s,h} f_{y,h}$ κ_{es}, κ_v = steel confinement coefficients (Sheikh & Uzumeri, 1982)

Stress – strain curve	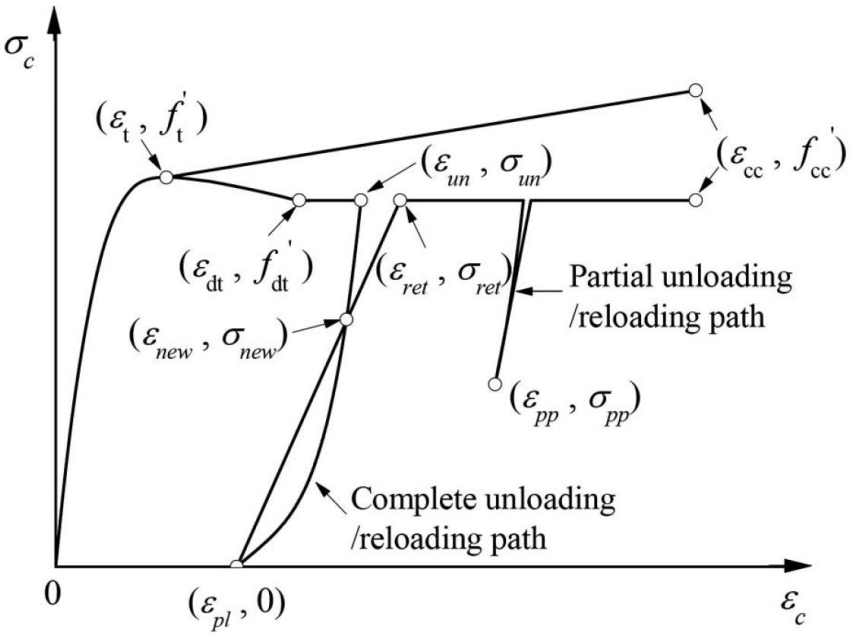
Stress – strain equations	For softening behavior $E_2 < 0$: $\frac{f_c(\varepsilon_c)}{f_t} = \begin{cases} A\left(\frac{\varepsilon_c}{\varepsilon_t}\right) + (3-2A)\left(\frac{\varepsilon_c}{\varepsilon_t}\right)^2 + (A-2)\left(\frac{\varepsilon_c}{\varepsilon_t}\right)^3 & \text{if} \quad 0 \le \varepsilon_c \le \varepsilon_t \\ \frac{\frac{\varepsilon_c}{\varepsilon_t}}{\alpha\left(\frac{\varepsilon_c}{\varepsilon_t}-1\right)^2+\frac{\varepsilon_c}{\varepsilon_t}} & \text{if} \quad \varepsilon_t \le \varepsilon_c \le \varepsilon_{dt} \\ \frac{f_{cu}}{f_t} & \text{if} \quad \varepsilon_{dt} \le \varepsilon_c \le \varepsilon_t \end{cases}$ For hardening behavior $E_2 \ge 0$: $\frac{f_c(\varepsilon_c)}{f_t} = \begin{cases} A\left(\frac{\varepsilon_c}{\varepsilon_t}\right) + (3-2A)\left(\frac{\varepsilon_c}{\varepsilon_t}\right)^2 + (A-2)\left(\frac{\varepsilon_c}{\varepsilon_t}\right)^3 & \text{if} \quad 0 \le \varepsilon_c \le \varepsilon_t \\ 1 + \frac{E_2}{E_p}\left(\frac{\varepsilon_c}{\varepsilon_t} - 1\right) & \text{if} \quad \varepsilon_t \le \varepsilon_c \le \varepsilon_{cu} \end{cases}$ Where $E_2 = \frac{f_{cu} - f_t}{\varepsilon_{cu} - \varepsilon_t}$ $E_p = \frac{f_t}{\varepsilon_t}$ $A = \frac{E_c}{E_p}$ $\alpha = 1 - \left(\frac{f_{cu}}{f_t}\right)^{1.66}$

2.3.8 Model Y.-Y. Wei and Y.-F. Wu (2012)

- Experimental data base: Test results of 432 FRP-wrapped plain concrete short columns with concrete strength between 18 and 55 MPa, including 194 circular columns, 170 square columns, and 68 rectangular columns. Of the results for these 432 columns, 100 are from the authors own tests, and the remainders are collected from the literature. A summary of the database is provided in the paper.
- Confined compressive strength point: not directly predicted by regression analysis, but can be obtained from the stress-strain curve in the first portion and is located very close to the transition point.
- Stress-Strain curve: two portion curve with a parabolic first portion and a linear second portion. It depends on three parameters $(f_{cu}, \varepsilon_{cu}, f_t)$, parameter ε_t is calculated from the condition that the slope at the transition point is the same for the two portions.

Table 2.8: FRP-confinement model (Wei & Wu, 2012)

Characteristic	Description
Transition point	$\frac{f_t}{f'_{co}} = 1 + 0.43\left(\frac{2r}{b}\right)^{0.68}\left(\frac{h}{b}\right)^{-1}\left(\frac{f_l}{f'_{co}}\right)$ $\varepsilon_t = \frac{f_t + f_{cu} + E_c\varepsilon_{cu} - \sqrt{(f_t + f_{cu} + E_c\varepsilon_{cu})^2 - 8f_tE_c\varepsilon_{cu}}}{2E_c}$
Ultimate point	$\frac{f_{cu}}{f'_{co}} = 0.5 + 2.7\left(\frac{2r}{b}\right)^{0.4}\left(\frac{f_l}{f'_{co}}\right)^{0.73}\left(\frac{h}{b}\right)^{-1}$ $\frac{\varepsilon_{cu}}{\varepsilon_{co}} = 1.75 + 12\left(\frac{f_l}{f'_{co}}\right)^{0.75}\left(\frac{f_{30}}{f'_{co}}\right)^{0.62}\left(0.36\frac{2r}{b} + 0.64\right)\left(\frac{h}{b}\right)^{-0.3}$

Stress – strain curve	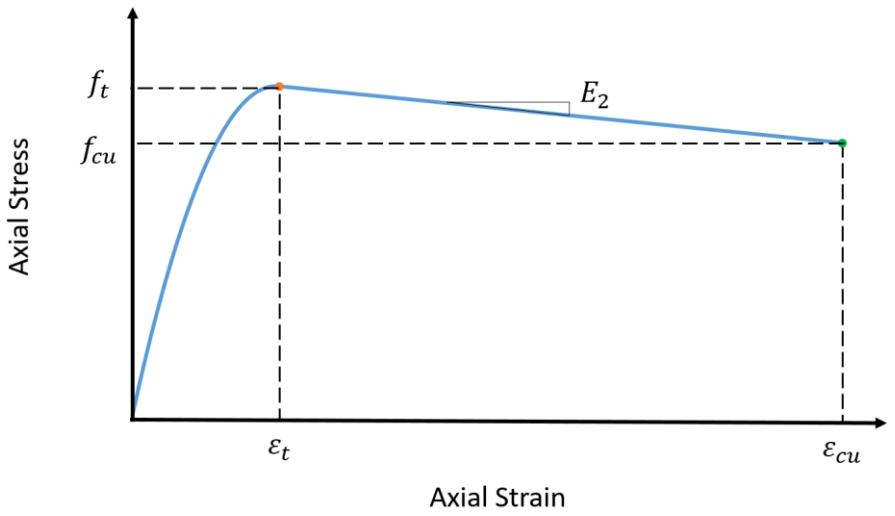
Stress – strain equations	$$f_c(\varepsilon_c) = \begin{cases} E_c\varepsilon_c + \frac{f_t - E_c\varepsilon_t}{\varepsilon_t^2}\varepsilon_c^2 & \text{if} \quad 0 \le \varepsilon_c \le \varepsilon_t \\ f_t + E_2(\varepsilon_c - \varepsilon_t) & \text{if} \quad \varepsilon_t \le \varepsilon_c \le \varepsilon_{cu} \end{cases}$$ Where $$E_2 = \frac{f_{cu} - f_t}{\varepsilon_{cu} - \varepsilon_t}$$ $$f_l = \frac{2E_{frp}\varepsilon_{frp}t_{frp}}{b}$$

2.3.9 Model N. F. Hany, E. G. Hantouche and M. H. Harajli (2015)

- Experimental data base: 18 plain concrete specimens (3 circular, 5 square, 5 rectangular with aspect ratio of 1.29 and 5 rectangular with aspect ratio of 1.54) were fabricated and tested under axial cyclic compression loading. Some specimens were confined in a full wrapping mode and other with FRP strips in a partial mode. Previous studies have shown that the envelope stress – strain obtained by cyclic loading is almost identical to the one obtained by monotonic loading (Lam & Teng, 2009; Lam, Teng, Cheung, & Xiao, 2006; Abbasnia & Holakoo, 2012). Models were calibrated with the constructed

specimens and other authors (Lam & Teng, 2003a; Lam & Teng, 2003b; Abbasnia & Ziaadiny, 2015).

- Transition point: to be able to describe hardening and softening behaviors using a unified model, an average value of $1.15f'_{co}$ is considered as the intercept of the second part, based on experimental observation.
- Stress-Strain curve: a parabolic first branch describing the first stage of the response and a linear second branch describing the second stage.

Table 2.9: FRP-confinement model (Hany, Hantouche, & Harajli, 2015)

Characteristic	Description
Transition point	$f_t = 1.15f'_{co}$ $\varepsilon_t = \frac{2.3f'_{co}}{E_c - E_2}$
Ultimate point	$\frac{f_{cu}}{f'_{co}} = 0.7 + 4.62\left(k_v\frac{A_e}{A_c}\right)\left(\frac{b}{h}\right)^{0.92}\left(\frac{f_l}{f'_{co}}\right)$ $\frac{\varepsilon_{cu}}{\varepsilon_{co}} = 3.89 + 14.76\left(k_v\frac{A_e}{A_c}\right)\left(\frac{h}{b}\right)^{0.94}\left(\frac{f_l}{f'_{co}}\right)$
Stress – strain curve	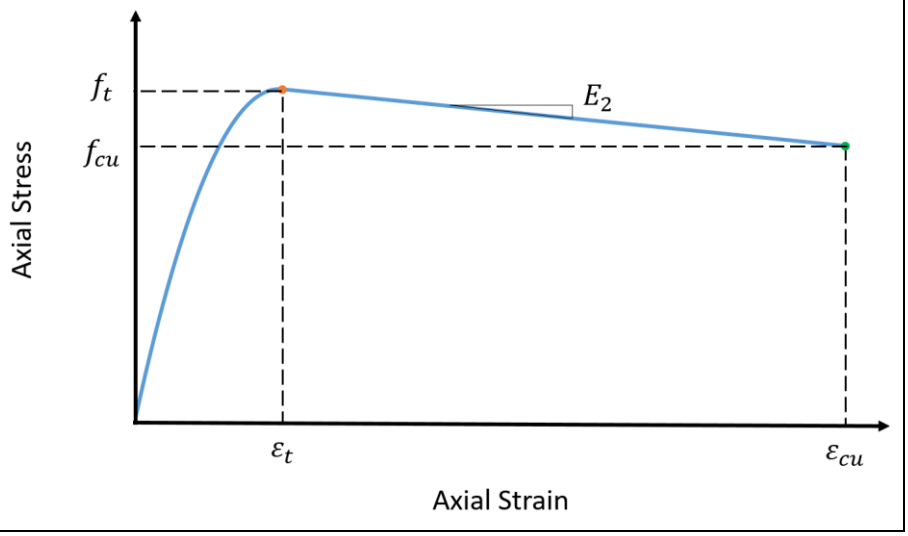

Stress – strain equations	$$f_c(\varepsilon_c) = \left\{ \begin{array}{ll} E_c\varepsilon_c + \frac{(E_c-E_2)^2}{4.6f'_{co}}\varepsilon_c^2 & \text{if} \quad 0 \le \varepsilon_c \le \varepsilon_t \\ 1.15f'_{co} + E_2(\varepsilon_c) & \text{if} \quad \varepsilon_t \le \varepsilon_c \le \varepsilon_{cu} \end{array} \right\}$$ Where $$E_2 = \frac{f_{cu} - 1.15f'_{co}}{\varepsilon_{cu}}$$ $$f_l = \frac{\rho_{frp}E_{frp}\varepsilon_{frp,h}}{2}$$ $$\frac{A_e}{A_c} = 1 - \frac{(b/h)(h-2r)^2 + (h/b)(b-2r)^2}{3A_c}$$ $$k_v = \left(1 - \frac{s_{frp}}{2b}\right)\left(1 - \frac{s_{frp}}{2h}\right)$$ for rectangular columns (Mander et al., 1988b) $$\rho_{frp} = \frac{4t_{frp}}{D}$$ $$D = \sqrt{b^2 + h^2}$$ (Lam & Teng, 2003b)

2.4 Design – oriented models for FRP jackets and anchors

Recently, the combination of FRP jackets and anchors has demonstrated to be a powerful technique to increase the strength and ductility of rectangular columns with high aspect ratio. Basically, the method consists on crossing through drilled or pre-cast holes FRP fan shaped anchors in addition to the complete FRP wrapping (Figure 2.6).

Very few researchers have studied the behavior of rectangular columns with FRP jackets and anchors, the present work has only found five published papers were dealing with this subject. Of these five investigations, one proposes a model for the complete stress – strain curve (Hany, Hantouche, & Harajli, 2016), one proposes a model to predict the compressive strength of confined concrete (f_t in the softening case) (Triantafillou, et al., 2016) and the other three papers do not propose any model but provide with an experimental test data of 5 columns (Akgun, Demir, & Ilki, 2010), 5 columns (Ilki, Peker, Karamuk, Demir, & Kumbasar, 2008) and 3 columns (Tan, 2002) confined with FRP

jackets and anchors. The publications that presented a design – oriented model will be reviewed.

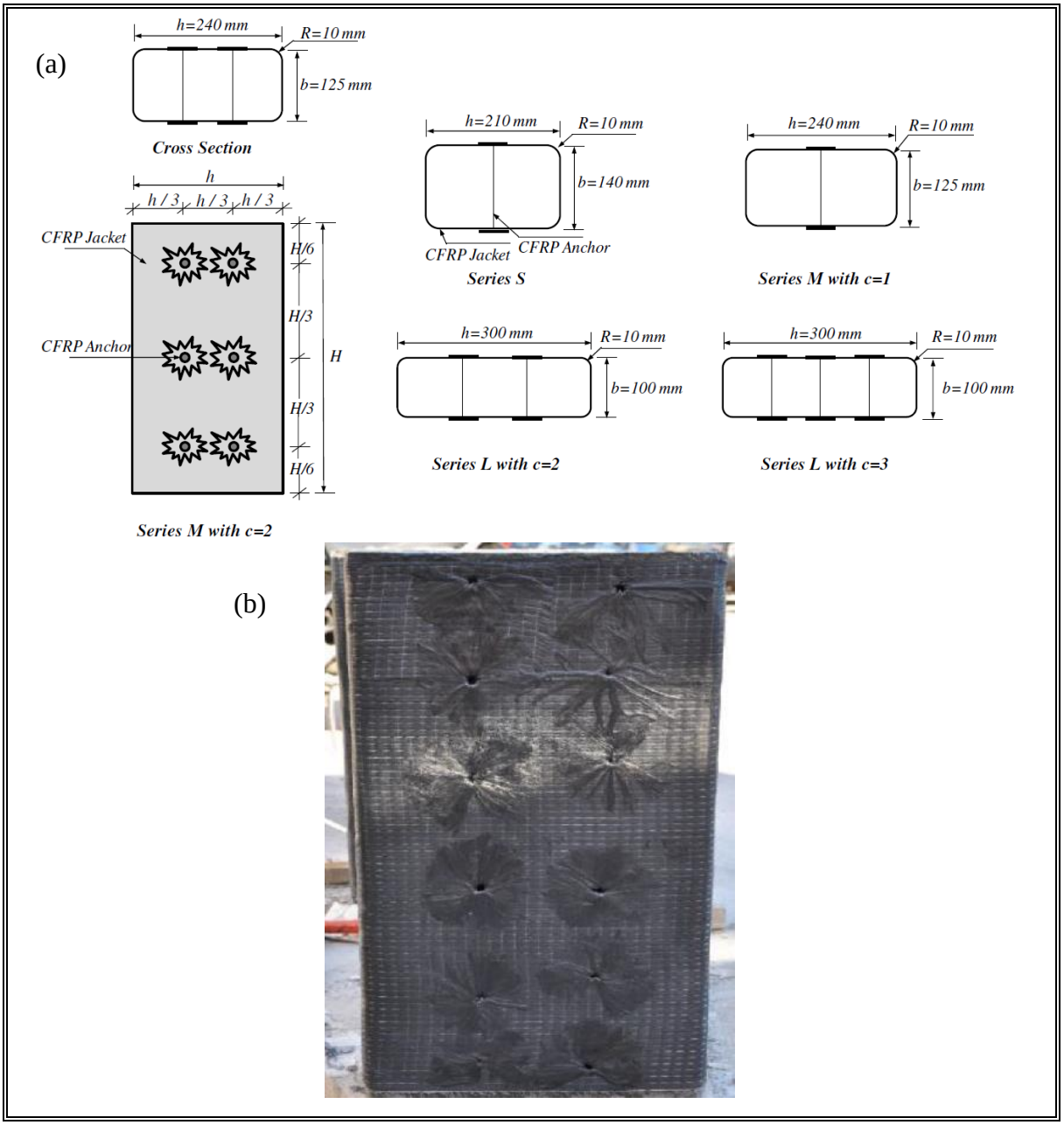

Figure 2.6: Examples of FRP – confinement with CFRP jackets and anchors: (a) (Hany, Hantouche, & Harajli, 2016), (b) (Triantafillou, et al., 2016)

2.4.1 Model T. C. Triantafillou et al (2015)

- Experimental data base: 45 rectangular reinforced concrete columns with various FRP confinement schemes. The wall-like specimens had cross sectional dimensions of 150 by 450mm and 150 by 600mm (aspect ratio 3 and 4), a height of 800 mm, a longitudinal steel ratio of 1%, transverse reinforcement of 8-mm diameter bars with a 150mm spacing and corners rounded to a 20 mm radius. The authors designed 15 different FRP confinement designs. They combined the use of complete FRP jacketing (2 or 3 layers) with FRP anchors (heavy and light) and additional U-shaped FRP hoop near the edges in order to increase the area of effectively confined concrete.
- Compressive strength: the original paper uses the nomenclature f_{cc}, however sin all the experiments had a softening behavior the nomenclature f_t is used in the current work.

Table 2.10: FRP-confinement model (Triantafillou, et al., 2016)

Characteristic	Description
Compressive strength	$\frac{f_t}{f'_{co}} = 1 + 3.3\left(\frac{b}{h}\right)^2 \alpha_f \frac{2t_{frp}}{D}\frac{f_{frp,h}}{f'_{co}}$ Where $D = \frac{2bh}{b+h}$ $f_{frp,h} = k_1 k_R f_{frp}$ $k_R = \begin{cases} \frac{r}{60}\left(2-\frac{r}{60}\right) & \text{if } r \le 60\text{mm} \\ 1 & \text{if } r \ge 60\text{mm} \end{cases}$ $k_1 =$ factor for all other effects, no expression was given $f_{frp} = E_{frp}\varepsilon_{frp}$

$$\alpha_f \approx \frac{A_e}{bh} \approx \frac{bh - A_{un}}{bh}$$
$$= 1 - \frac{(h-2R)(h-2R+1.5ns_a) + (n+1)(b-2R)^2}{3(n+1)bh}$$

$$A_{un} = 2(n+1)\frac{2}{3}\frac{(h-2R)^2}{(n+1)^2 4} + 4\frac{1}{2}\frac{(h-2R)s_a}{(n+1)4}$$
$$+ 2(n-1)\frac{(h-2R)s_a}{(n+1)4} + 2\frac{2}{3}\frac{(b-2R)^2}{4}$$
$$= \frac{(h-2R)(h-2R+1.5ns_a) + (n+1)(b-2R)^2}{3(n+1)}$$

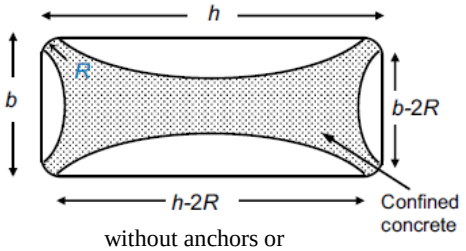

without anchors or with light anchors

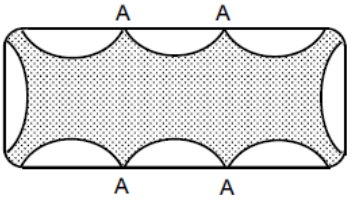

with heavy anchors, cross section at the location of anchors

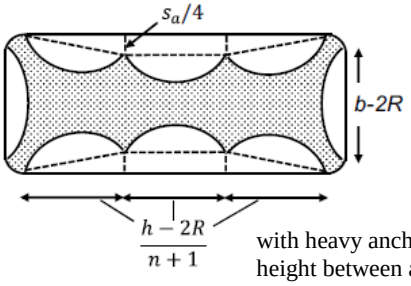

with heavy anchors, cross section at mid-height between anchors

R = corner radius

n =number of anchors at cross section

s_a =vertical spacing of anchors

2.4.2 Model N. F. Hany, E. G. Hantouche and M. H. Harajli (2016)

- Experimental data base: 27 plain concrete rectangular specimens are fabricated and tested under cyclic axial compressive loading. The specimens were classified according to their aspect ratios: 1.5 (series S), 1.92 (series M) and 3.0 (series L). Corners were

rounded to a 25mm radius. Each anchor was extended 60 mm beyond the face of the column on either side, and then spread out in a fan-shape against the hardened CFRP jacket. One additional CFRP layer over their full height was applied after the underlying layers and anchors have hardened because a pilot test without the additional layer experienced premature bond failure causing an inferior stress-strain response of this specimen.

- Transition point: an intermediate ascending branch ending at $\varepsilon_{t,2}, f_{t,2}$ was observed in some experimental tests; however, this point is not considered in the proposed model because it does not cause any significant loss of accuracy.

Table 2.11: FRP-confinement model (Hany, Hantouche, & Harajli, 2016)

Characteristic	Description
Transition point	$\frac{f'_t}{f'_{co}} = 0.88 + 0.12\left(\frac{h}{b}\right)^{0.3}\left(\frac{K_l}{f'_{co}}\right)^{0.38}$ $\frac{\varepsilon_t}{\varepsilon_{co}} = 1.06 + 0.03\left(\frac{h}{b}\right)^{0.86}\left(\frac{K_l}{f'_{co}}\right)$
Ultimate point	$\frac{f'_{cu}}{f'_{co}} = 0.7 + 4.62\left(\frac{b}{h}\right)^{0.92}\left(\frac{K_l}{f'_{co}}\right)\varepsilon_{h,rup}$ $\frac{\varepsilon_{cu}}{\varepsilon_{co}} = 3.89 + 14.76\left(\frac{h}{b}\right)^{0.94}\left(\frac{K_l}{f'_{co}}\right)\varepsilon_{h,rup}$

Stress – strain curve	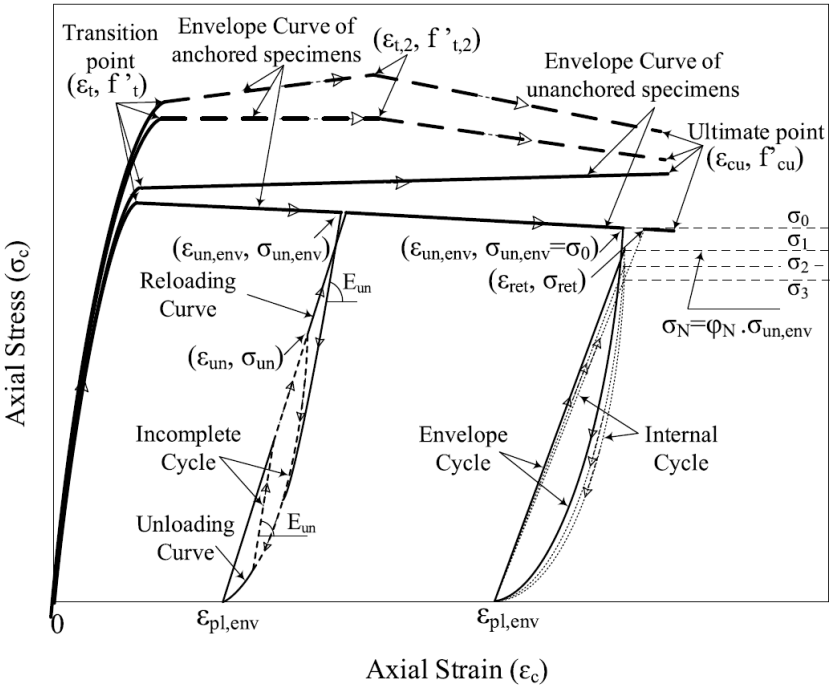
Stress – strain equations	$$\sigma_c = \frac{f_t' x r}{r - 1 + x^r}$$ where $x = \varepsilon_c/\varepsilon_t$, $r = E_c/E_c - E_{\text{sec}}$, $E_{\text{sec}} = f_t'/\varepsilon_t$ $$K_l = \left(\frac{\rho_f E_f}{2}\right)\left(\frac{A_e}{A_c}\right)$$ $$\frac{A_e}{A_c} = \frac{1}{3}\left(\frac{A_e}{A_c}\right)_1 + \frac{2}{3}\left(\frac{A_e}{A_c}\right)_2$$ $$\frac{A_e}{A_c} = 1 - \frac{(b/h)(h-2R)^2 + (h/b)(b-2R)^2}{3A_c}$$ $$k_v = \left(1 - \frac{s'}{2b}\right)\left(1 - \frac{s'}{2h}\right) \text{ for rectangular columns}$$ (Mander, Priestley, & Park, 1988a)

$$\frac{A_e}{A_c} = 1 - \frac{1}{3A_c}\left[\frac{(c+1)b}{h}\sum_{i=1}^{c+1} w_{x,i}^2 - \frac{h}{(c+1)b}(b-2R)^2\right]$$

$w_{x,i}$ = length of the base of the parabola i

internal parabola, $w_{x,i} = h/[3(c+1)]$

edge parabola $w_{x,i} = 2h/[3(c+1)] - R$

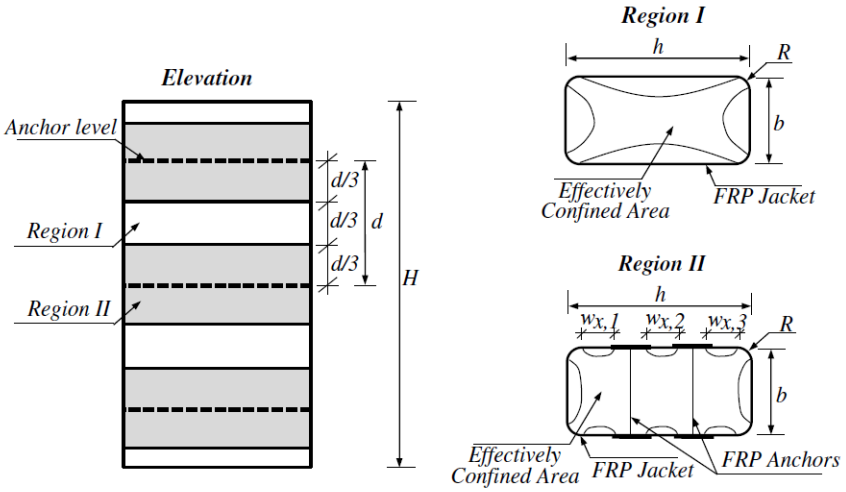

specimen elevation

specimen cross section

$$\rho_f = \rho_f' \times \frac{D'}{D} = \left(\frac{A_x}{bH} + \frac{A_y}{hH}\right) \times \frac{D'}{D}$$

$$D = \sqrt{b^2 + h^2}.$$

$$D' = 2bh/(b+h)$$

A_x and A_y = total area of FRP crossing.

2.5 Summary

In this chapter, a description of confined concrete behavior and detailed equations of existing design-oriented models are presented. All design-oriented models are capable of capturing the full axial stress-strain curve and the softening behavior of FRP-confined concrete. The existing models can be classified as:

- Models for FRP-confined concrete columns without CFRP anchors (Hany, Hantouche, & Harajli, 2015; Wei & Wu, 2012; Wang, Wang, Smith, & Lu, 2012b; Pellegrino & Modena, 2010; Teng, Jiang, Lam, & Luo, 2009; Wu, Wu, & Lu, 2007; Youssef, Feng, & Mosallam, 2007; Pantelides, Yan, & Reaveley, 2004; Hosotani, Kawashima, & Hoshikuma, 1998).
- Models for FRP-confined concrete columns with CFRP anchors (Hany, Hantouche, & Harajli, 2016; Triantafillou, et al., 2016).

3. EXPERIMENTAL PROGRAM

3.1 Overview

A total of twelve rectangular reinforced concrete columns were tested to pure axial monotonic compression to failure. The twelve specimens consisted of four control specimens with no CFRP reinforcement and eight specimens strengthened with CFRP jackets and CFRP anchors.

Figure 3.1 shows a description of a typical CFRP reinforced specimen. Specimens had a prismatic shape, with 60 cm in height and 40 cm in width. Half of the specimens had a thickness of 15 cm and half a thickness of 10 cm. While the corners of the CFRP-strengthened columns were manually rounded to a minimum 2 cm radius, the corners of the control columns were not rounded. CFRP wraps were placed 5 cm from the top and the bottom of the column). Precast holes were located inside the columns for the installation of the CFRP anchors, these holes had a diameter of 1.6 cm and round edges with a minimum 1 cm radius.

CFRP consisted of two parts: an epoxy matrix (a two-component, high-strength, high-modulus epoxy resin) and carbon fibers (unidirectional, high strength, non-corrosive carbon fabric with a 0.5 mm thickness per layer). The same materials were used for CFRP jackets and for CFRP anchors. The CFRP jacket and anchors were installed in an intercalated manner beginning and ending with a jacket layer, meaning that an anchor layer was always located between two jacket layers (Figure 3.2).

For the naming of the columns, a nomenclature found in literature is used for ease of comparison (Hany, Hantouche, & Harajli, Generalized Axial Stress-Strain Response Of Rectangular Columns Confined Using CFRP Jackets And Anchors, 2016):

T – n c r

T: thickness of the column in cm.

n: total number of CFRP jacket layers. The number of CFRP anchor layers is n-1 when $n \geq 1$, and 0 when $n = 0$. (Figure 3.2)

c: number of anchor columns.

r: number of anchor rows.

For control columns (without CFRP reinforcement) there is no need for an anchor distribution configuration, therefore, $n = 0$, $c = 0$ and $r = 0$. To further explain the use of this nomenclature an example is explained. Column “10-335”, with a thickness of 10 cm, contains: 3 layers of CFRP jackets, 2 layers of CFRP anchors, and anchors distributed in three columns and 5 rows (Figure 3.1).

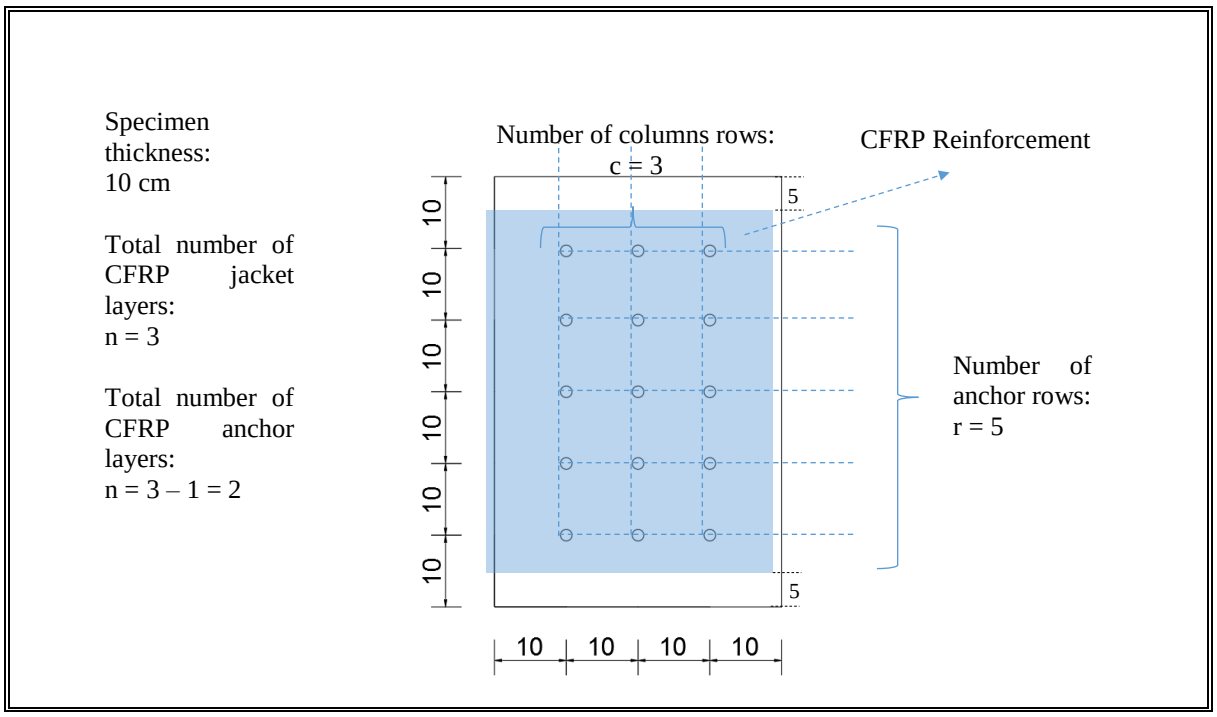

Figure 3.1: Example of alphanumeric code for column naming (specimen 10-335).

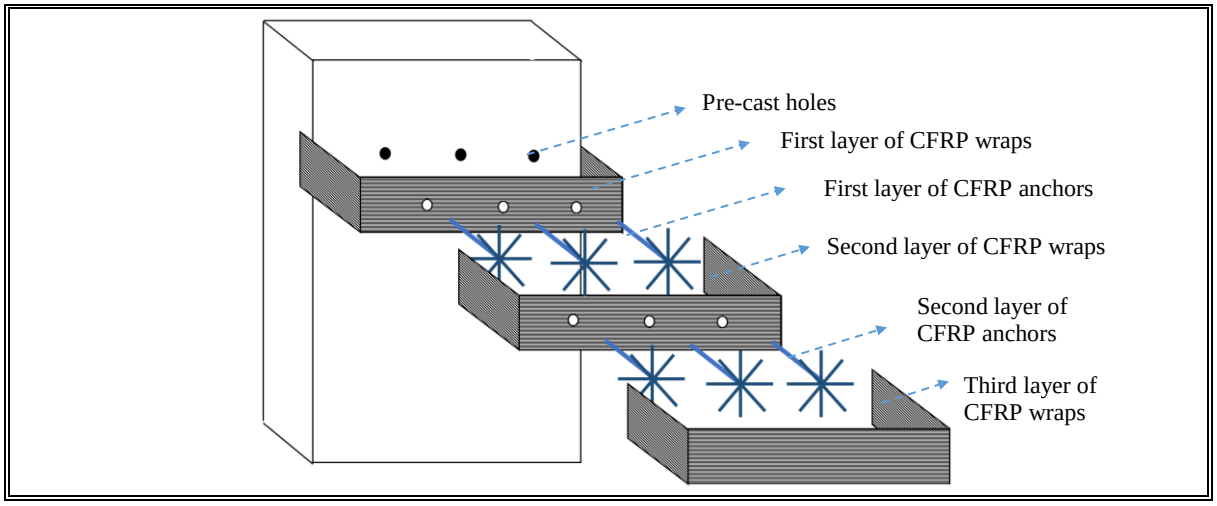

Figure 3.2: Layout of CFRP reinforcement. CFRP anchors are intercalated between CFRP wraps

Additionally, suffixes “a” and “b” are used to differentiate identical columns, for example, columns “15-000a” and “15-000b” both have a thickness of 15 cm and contain 0 layers of CFRP jackets, 0 layers of CFRP anchors. Since all specimens strengthened with CFRP are unique, suffixes “a” and “b” are only used for control columns with no CFRP reinforcement. Table 3.1 presents a complete list of the specimens tested.

Table 3.1: List of specimens tested in the present investigation

#	Thickness	Number of CFRP layers	Number of anchor columns	Number of anchor rows	Duplicate specimen
1	10	0	0	0	a
2	10	0	0	0	b
3	15	0	0	0	a
4	15	0	0	0	b
5	10	2	2	5	-
6	15	2	2	5	-
7	10	2	3	5	-
8	15	2	3	5	-
9	10	3	2	5	-
10	15	3	2	5	-
11	10	3	3	5	-
12	15	3	3	5	-

3.2 Materials

The specimens were composed of three materials: concrete, steel reinforcement (vertical and transverse) and the CFRP reinforcement.

3.2.1 Concrete

Concrete was purchased from a local ready-mix plant. The same concrete was used for all specimens and corresponded to concrete H25 according to the Chilean nomenclature (NCh 170, 1952). All specimens were constructed on the same day. The tested unconfined strength at 28 days of age ($f'_{c\,28}$) was 23.1 MPa.

Due to delays in the availability of the testing machine and CFRP materials, the specimens where tested in average at 465 days of age. Therefore, the unconfined strength of concrete at the time of testing was no longer $f'_{c\,28}$ but a higher value. The unconfined strength at the day of testing was estimated to be 37 MPa and the modulus of elasticity at the day of testing 22180 MPa. See Appendix A.

3.2.2 Steel reinforcement

Steel reinforcement was provided by a local firm. The same type of steel was used for all steel reinforcement and corresponded to steel A 630-420 H according to the Chilean nomenclature (NCh204, 2006). Minimum values of mechanical properties are specified in Table 3.2, taken from NCh204 (2006). Rupture elongation is estimated for steel bars of nominal diameters of 6, 10 and 12 mm since those were the dimensions used in the present study.

3.2.1.1 Transverse reinforcement

In all specimens, transverse reinforcement consisted of plain bars with a 6-mm nominal diameter.

3.2.1.2 Vertical reinforcement for specimens with 10 cm thickness

Vertical steel bars consisted of corrugated bars with a 10-mm nominal diameter.

3.2.1.3 Vertical reinforcement for specimens with 15 cm thickness

Vertical steel bars consisted of corrugated bars with a 12-mm nominal diameter.

Table 3.2: Steel reinforcement A 630-420 H properties (NCh 204, 2006)

Tensile yield stress f_y MPa	420 min. 580 max.
Tensile ultimate stress f_u MPa	630 min.
f_u/f_y minimum	1.25
Minimum ultimate elongation % probe $L_0 = 200\ mm$	For 6 mm diameter bars: $\frac{7000}{f_u} - 3 = 8.11\%$ For 10 mm diameter bars: $\frac{7000}{f_u} - 1 = 10.11\%$ For 12 mm diameter bars: $\frac{7000}{f_u} - 0 = 11.11\%$

3.2.3 CFRP reinforcement

Carbon fiber reinforced polymer (CFRP) reinforcement was provided by Simpson Strong-Tie. The same type of CFRP was used for all CFRP strengthened specimens.

CFRP is a composite material that consists of carbon fibers embedded in an epoxy (polymer) matrix. Carbon fibers could be distributed in many directions, but for the present study carbon fibers were oriented only in one direction (Figure 3.3). Individually, carbon fibers are very thin elements, with a diameter less than 10 μm (Figure 3.4). It is difficult to establish a thickness for composite material since it consists of numerous carbon fibers and an epoxy matrix that at installation is a viscous liquid (Figure 3.5); however, a nominal thickness of 0.5 mm per layer is reported in the manufacturer specifications when a wet-layup procedure is applied.

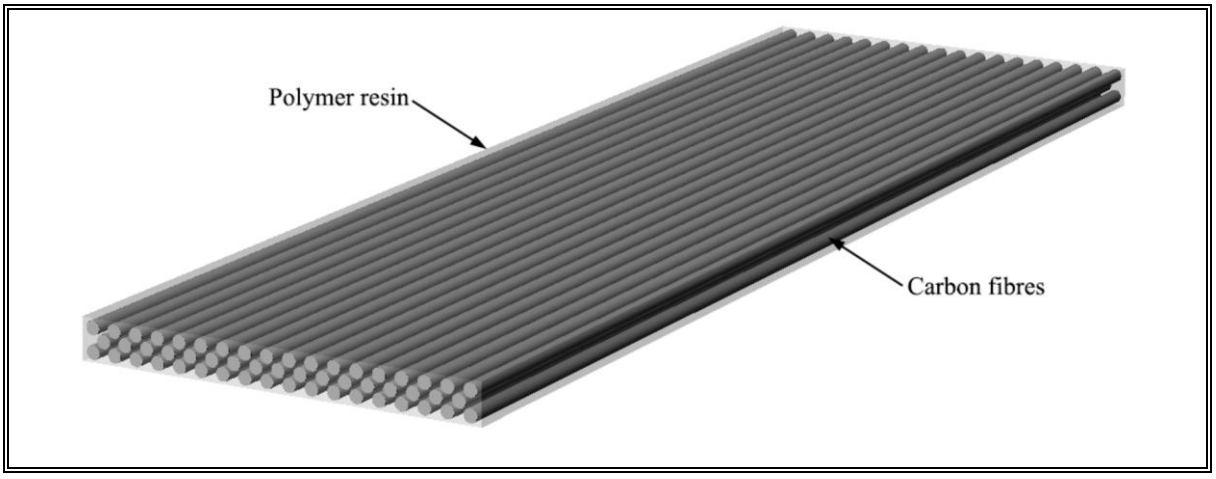

Figure 3.3: Conceptual definition of unidirectional CFRP composite material (Liu, Zwingmann, & Schlaich, 2015)

According to the manufacturer specifications, dry carbon fibers used in the present study corresponded to the type CCS-UCF10 with reported properties specified on Table 3.3.

Table 3.3: CSS-UCF10 Dry fiber properties

Tensile strength	700,000 psi (4800 MPa)
Tensile modulus	34,000 ksi (230 GPa)
Elongation at break	2.0 %
Weight	10.0 oz./yd.^{2} (340 g/m^2)
Color	Black

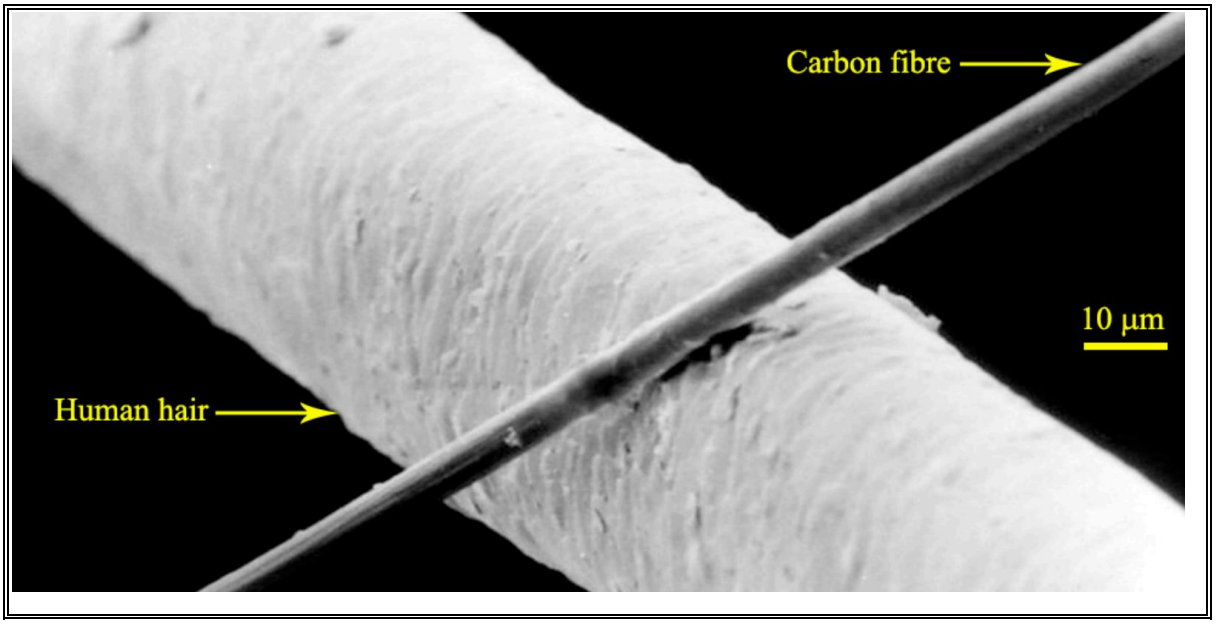

Figure 3.4: Carbon fiber compared to human hair (Liu, Zwingmann, & Schlaich, 2015)

Figure 3.5: Installation of an epoxy matrix (viscous liquid state) to a wrap of unidirectional carbon fibers.

According to the manufacturer specifications, epoxy matrix used in the present study corresponded to the type CSS-ES with reported properties specified on Table 3.4.

Table 3.4: CSS-ES Epoxy matrix properties

Property	ASTM	Cure schedule	Test value
Tensile strength	D638	7 days at 72°F (22°C) + 3 days at 140°F (60°C)	5,230 psi (36 MPa) 10,400 psi (72 MPa)
Tensile modulus	D638	7 days at 72°F (22°C) + 3 days at 140°F (60°C)	322,000 psi (2,220 MPa) 306,000 psi (2,110 MPa)
Elongation break	D638	7 days at 72°F (22°C) + 3 days at 140°F (60°C)	1.73 % 5.89 %
Flexural strength	D790	7 days at 72°F (22°C) + 3 days at 140°F (60°C)	9,150 psi (63 MPa) 18,300 psi (126 MPa)
Flexural modulus	D790	7 days at 72°F (22°C) + 3 days at 140°F (60°C)	531,000 psi (3,660 MPa) 439,000 psi (3,030 MPa)
Compressive strength	D695	7 days at 72°F (22°C) + 3 days at 140°F (60°C)	15,800 psi (109 MPa) 14,400 psi (99 MPa)
Compressive modulus	D695	7 days at 72°F (22°C) + 3 days at 140°F (60°C)	434,000 psi (2,990 MPa) 390,000 psi (2,690 MPa)
T_g	D3418	7 days at 72°F (22°C) + 3 days at 140°F (60°C)	144°F (62°C) 187°F (86°C)
Density	D792	7 days at 72°F (22°C) + 3 days at 140°F (60°C)	9.55 lbs/US gal. (1.15 kg/L) 9.55 lbs/US gal. (1.15 kg/L)

Properties of the cured composite material (carbon fibers embedded in an epoxy matrix) are presented in Table 3.5 according to the manufacturer specifications when a wet-layup procedure is applied.

Table 3.5: CSS-UCF10 Cured composite properties

Resistencia a tensión	140,000 psi (970 MPa)
Módulo de tensión	11,000 ksi (76 GPa)
Elongación de ruptura	1.3%
Espesor por lamina	0.02 in. (0.5 mm)

3.3 Design of the specimens

3.3.1 Design of the steel reinforcement

In the present investigation, design of the steel reinforcement bars involved: definition of the failure zone, distribution of transverse steel reinforcement, area of vertical steel reinforcement and height to thickness ratio.

3.3.1.1 Definition of failure zone and distribution of transverse steel reinforcement

Columns were designed to have three distinct zones in elevation: two edge zones (near the support of the columns and under the loading plate) and a central zone (Figure 3.6).

It is difficult to predict the exact location where failure will occur, but it was induced to occur in the central zone by providing the edges with more transverse reinforcement. Also, because of the larger concentration of stresses at the edge zones, it was important to provide them with larger transverse steel reinforcement to prevent premature failure.

For these reasons, edge zones were provided with closed stirrups with 135-degree hooks and cross-ties around the intersection of vertical bars with stirrups, separated 4 cm in the vertical direction (Figure 3.7a). Central zones were provided only with C-shaped reinforcement, separated 10 cm in the vertical direction (Figure 3.7b). All stirrups and ties consisted of plain bars with a 6-mm diameter.

It is important to note that transverse steel reinforcement at the edge zones was greater than the one required for special boundary elements (ACI Committee 318, 2014):

$$\min\left\{\frac{A_{sh-x}^{10\ cm\ cols}}{sb_c}, \frac{A_{sh-y}^{10\ cm\ cols}}{sd_c}\right\} = 0.00707 > \min\left\{\begin{matrix} 0.3\left(\frac{A_g}{A_{ch}} - 1\right)\frac{f_c'}{f_y} \\ 0.09\frac{f_c'}{f_y} \end{matrix}\right\} = 0.00495 \qquad (2.1)$$

$$\min\left\{\frac{A_{sh-x}^{15\ cm\ cols}}{sb_c}, \frac{A_{sh-y}^{15\ cm\ cols}}{sd_c}\right\} = 0.00707 > \min\left\{\begin{matrix} 0.3\left(\frac{A_g}{A_{ch}} - 1\right)\frac{f_c'}{f_y} \\ 0.09\frac{f_c'}{f_y} \end{matrix}\right\} = 0.00495 \qquad (2.2)$$

For the case of the central zone, transverse steel reinforcement on its own did not comply with the requirement for special boundary elements (ACI Committee 318, 2014):

$$\max\left\{\frac{A_{sh-x}^{10\ cm\ cols}}{sb_c}, \frac{A_{sh-y}^{10\ cm\ cols}}{sd_c}\right\} = 0.00141 < \min\left\{\begin{matrix} 0.3\left(\frac{A_g}{A_{ch}} - 1\right)\frac{f_c'}{f_y} \\ 0.09\frac{f_c'}{f_y} \end{matrix}\right\} = 0.00495 \qquad (2.3)$$

$$\max\left\{\frac{A_{sh-x}^{15\ cm\ cols}}{sb_c}, \frac{A_{sh-y}^{15\ cm\ cols}}{sd_c}\right\} = 0.00141 < \min\left\{\begin{matrix} 0.3\left(\frac{A_g}{A_{ch}} - 1\right)\frac{f_c'}{f_y} \\ 0.09\frac{f_c'}{f_y} \end{matrix}\right\} = 0.00495 \qquad (2.4)$$

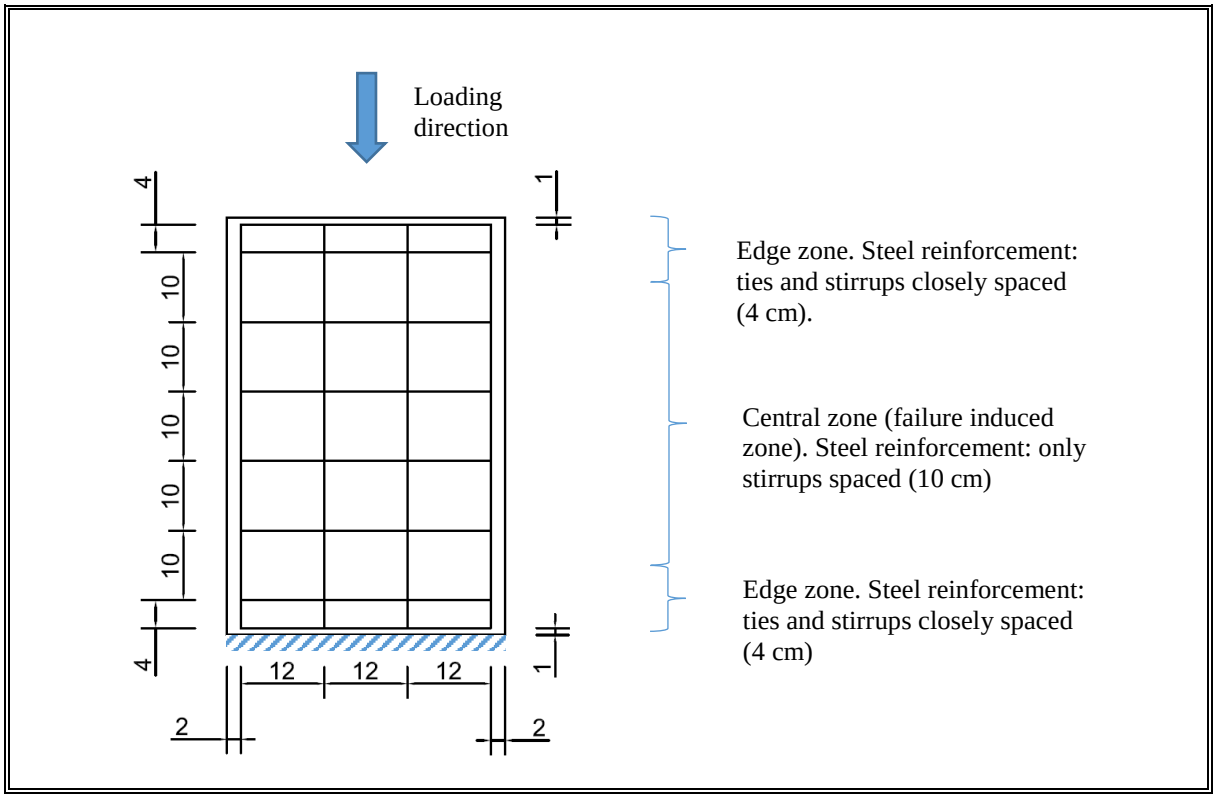

Figure 3.6: Elevation view of steel reinforcement distribution. (dimensions in cm.)

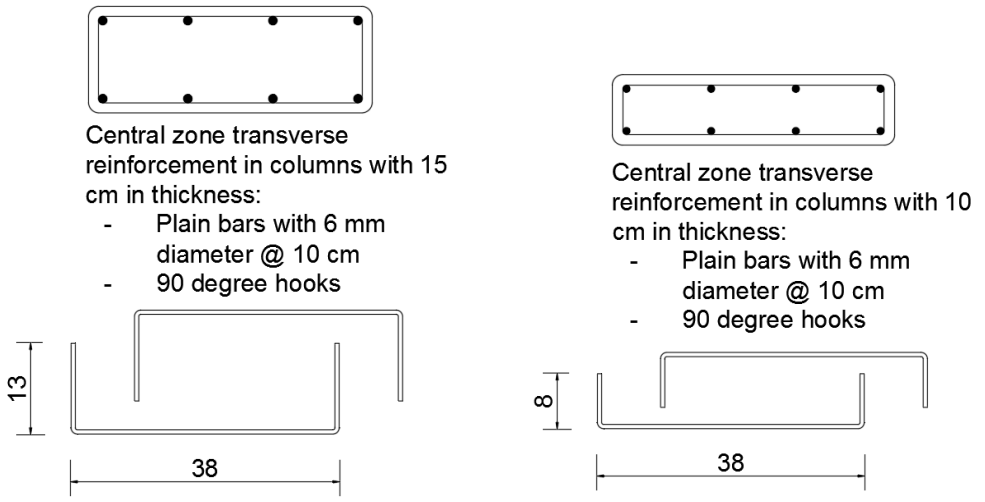

(a) Transverse steel reinforcement in central zone

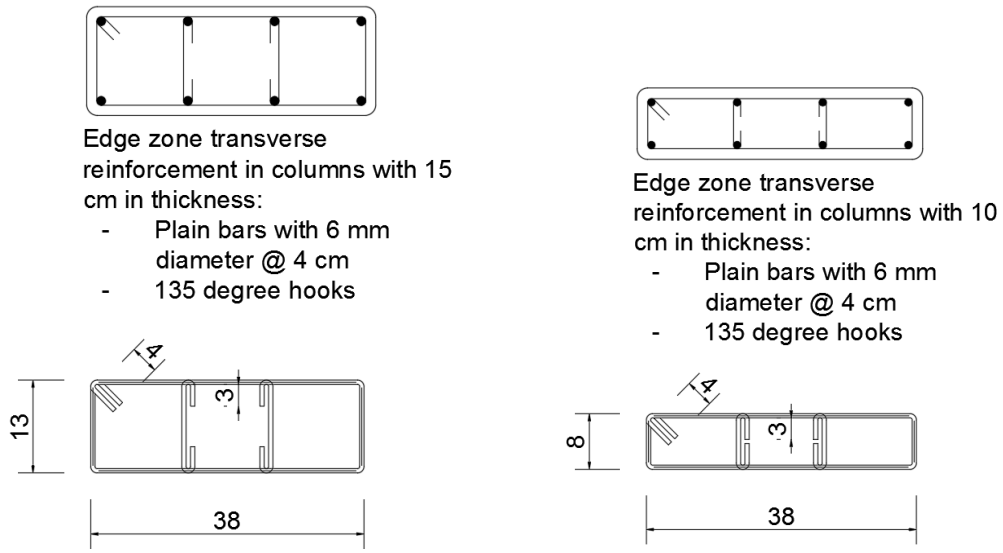

(b) Transverse steel reinforcement in edge zones

Figure 3.7: Transverse steel reinforcement as seen from above. (dimensions in cm)

3.3.1.2 Area of vertical steel reinforcement

The area of vertical steel reinforcement was determined based on three criteria: ratio of vertical steel area to gross concrete area, a desired buckling behavior for vertical steel reinforcement and the capacity of the testing machine. The final design was also verified for global buckling by checking the height to thickness ratio.

The first criteria of design, ratio of vertical steel area to gross concrete area, defined a minimum of vertical steel reinforcement. Transverse reinforcement at boundary elements of structural walls is relevant when concrete compression tension reaches values above $0.2f_c'$ and for high concentration of vertical steel reinforcement (Moehle, Ghodsi, Hooper, Fields, & Gedhada, 2011). As was explained in section 1.1.1, boundary elements in structural walls need to be provided with special detailing for transverse reinforcement when $\frac{A_{s,be}}{A_{g,be}} > \frac{400}{f_y}$ $(f_y\ in\ psi)$, where:

$A_{s,be} =$ area of vertical steel reinforcement located inside the boundary element.

$A_{g,be} =$ gross area of the boundary element zone.

All steel reinforcement bars in the present investigation correspond to A630-420-ES, which guaranties $f_y \geq 420\ MPa$. If the tested columns corresponded to boundary elements of structural walls, important transverse reinforcement would have been relevant if:

$$\frac{A_{s,be}}{A_{g,be}} > \frac{400}{f_y} = 0.00658 \qquad (2.5)$$

This ratio is taken into consideration for the definition of number and diameter of vertical bars.

The second criteria of design, a desired behavior for the buckling of vertical bars, also defined a minimum of vertical steel reinforcement. Based on the observations of (Monti & Nuti, 1992), the buckling load of steel reinforcement bars is highly correlated with the ratio of free length (L) and diameter (D), (Figure 3.8). This investigation concluded that inelastic buckling develops when the ratio L/D exceeds the critical value of 5. Clearly the specimens tested in (Monti & Nuti, 1992) were not embedded in a concrete matrix as in a real column or wall, but their results serve as a conservative design reference for cases where vertical steel reinforcement bars are required to yield in compression. Critical ratios of $s/d_b = 6$ and 8 are specified in (ACI Committee 318, 2014) for special and ordinary boundary elements, respectively, where:

$s =$ center-to-center spacing between transverse reinforcement

$d_b =$ nominal diameter of vertical bars at wall boundary elements.

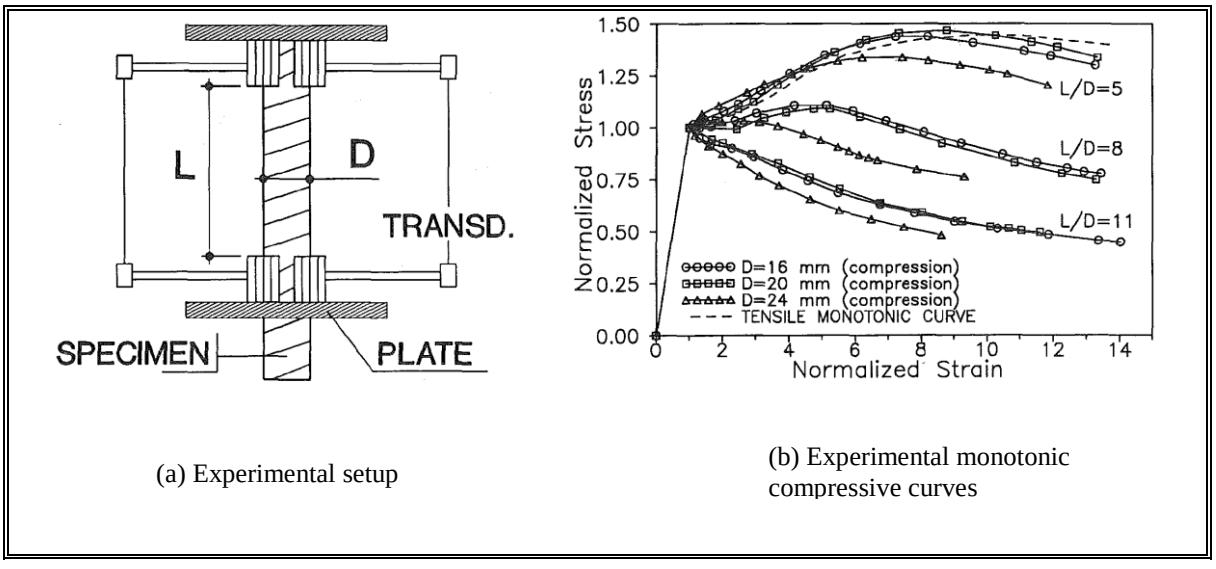

(a) Experimental setup

(b) Experimental monotonic compressive curves

Figure 3.8: Experimental results of steel bar buckling (Monti & Nuti, 1992).

The specimens in the present investigation were design so that vertical steel bars buckle elastically in columns without CFRP reinforcement and buckle inelastically in columns with CFRP reinforcement. CFRP anchors were expected to produce:

$$\frac{s}{d_b} \leq 10 \rightarrow d_b \geq 10 \ [mm] \tag{2.6}$$

Since the separation between center-to-center for stirrups in the failure zone was 10 cm, the minimum nominal diameter of vertical bars was 10 mm.

The third criteria of design, the capacity of the testing machine, defined a maximum amount of vertical steel reinforcement and transverse gross section area. Since the force controlled testing machine ADABOR available has a maximum capacity of 275 tonf (2697 kN), the strength of the columns with and without CFRP reinforcement could not be larger than said value. The most critical case corresponds to a CFRP strengthened column with steel bars yielding in compression:

$$A_{cc}f'_{cc} + A_c f'_c + A_s f_s \leq 275 \ [tonf] = 2697 \ [kN] \tag{2.7}$$

Where:

A_{cc} = area of confined concrete core

A_c = area of unconfined concrete

A_s = area of vertical steel

f'_{cc} = confined concrete stress

f'_c = unconfined concrete stress

f_s = steel stress

It is important to note that due to delays in the availability of the testing machine and CFRP materials, the specimens were tested in average 437 days after the 28 days of ageing Although the columns were originally designed considering $f'_{c\,28}$, because of the unexpected delays the compressive strength of concrete at the time of testing was higher. This caused that one of the columns (specimen 335-15) had a larger strength than the maximum capacity of the testing machine. Failure of the CFRP could not be achieved for this specimen but, as it is shown in chapter 4, it entered the nonlinear zone of the axial stress – strain curve.

Therefore, for the original design f'_c was set to be equal to $f'_{c\,28}$, the confined compressive strength was estimated to be around $1.5f'_{c\,28}$, based on previous investigations (Hany, Hantouche, & Harajli, Generalized Axial Stress-Strain Response Of Rectangular Columns Confined Using CFRP Jackets And Anchors, 2016; Triantafillou, et al., 2016). A_c was set to be equal to 0 and A_{cc} was set to be the complete gross section (CFRP transverse reinforcement wraps around the complete surface of the columns) and f_s was set to be equal to f_y. With these considerations, the amount of vertical reinforcement was

For 10 cm columns: $A_s \leq 31.23\ cm^2$ (2.8)

For 15 cm columns: $A_s \leq 14.73\ cm^2$ (2.9)

Finally, considering the three criteria ($A_{s,be}/A_{g,be}$ ratio, s/d_b ratio and the maximum capacity of the testing machine) a vertical steel reinforcement of 8 corrugated bars of 10 mm diameter was determined for columns with 10 cm thickness and 8 corrugated bars of 12 mm diameter was determined for columns with 15 cm thickness (Figure 3.9).

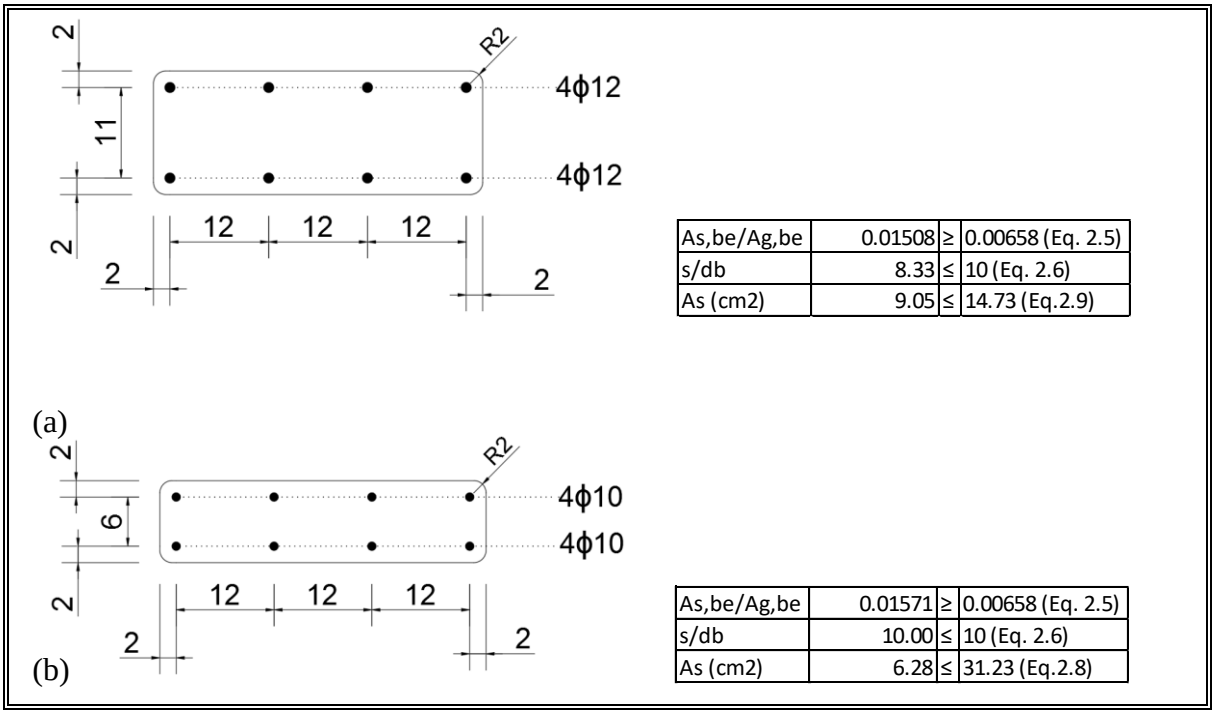

As,be/Ag,be	0.01508	≥	0.00658 (Eq. 2.5)
s/db	8.33	≤	10 (Eq. 2.6)
As (cm2)	9.05	≤	14.73 (Eq.2.9)

As,be/Ag,be	0.01571	≥	0.00658 (Eq. 2.5)
s/db	10.00	≤	10 (Eq. 2.6)
As (cm2)	6.28	≤	31.23 (Eq.2.8)

Figure 3.9: Distribution of vertical steel reinforcement for columns with a thickness of: (a) 15 cm (b) 10 cm

3.3.1.3 Verification of height to thickness ratio

It was observed that walls with high height to thickness ratio are susceptible to overall buckling. According to (Parra & Moehle, 2014), overall wall buckling will occur if:

$$\frac{b_{cr}}{kh_u} = \frac{1}{\pi}\sqrt{\frac{\epsilon_{sm}-0.005}{\kappa\xi}} \tag{2.10}$$

where,

$$\xi \leq 0.5\left(1+\frac{2m}{0.85}-\sqrt{\left(\frac{2m}{0.85}\right)^2+\frac{4m}{0.85}}\right), \delta = \xi b = \phi_{max}\left(\frac{kh_u}{\pi}\right)^2$$
$$m = \rho\frac{f_y}{f_c'}, \rho = \frac{A_s}{A_g} = \frac{A_s}{b_{cr}e}, \phi_{max} = \frac{\epsilon_{sm}-0.005}{d} \tag{2.11}$$

The parameters are explained in Figure 3.10, where a conceptual wall with two curtains of vertical steel reinforcement, is subject to a cycle of tension and compression, making the steel reinforcement yield in tension and compression.

As it is shown in Figure 3.10, the parameter ϕ_{max} represents the curvature generated due to one of the steel curtains reaching yield in compression before the other curtain. In the Parra & Moehle model, the vertical bars are assumed to yield in tension before yielding in compression as is shown in Figure 3.11.

In the present study, the columns are not subject to tension prior to compression, therefore, the parameter ϕ_{max} cannot be assumed equal to the one used by (Parra & Moehle, 2014). However, the same reasoning can be used. The columns in the present study are assumed to start with no residual stress and that one of the curtains of reinforcement reaches yielding in compression before the other. This generates a curvature equal to:

$$\phi_{max} = \frac{\varepsilon_y}{d} = \frac{0.002}{d} \tag{2.12}$$

With this change, the expression from Equation 2.10 changes to:

$$\frac{b_{cr}}{kh_u} = \frac{1}{\pi}\sqrt{\frac{0.002}{\kappa\xi}} \tag{2.13}$$

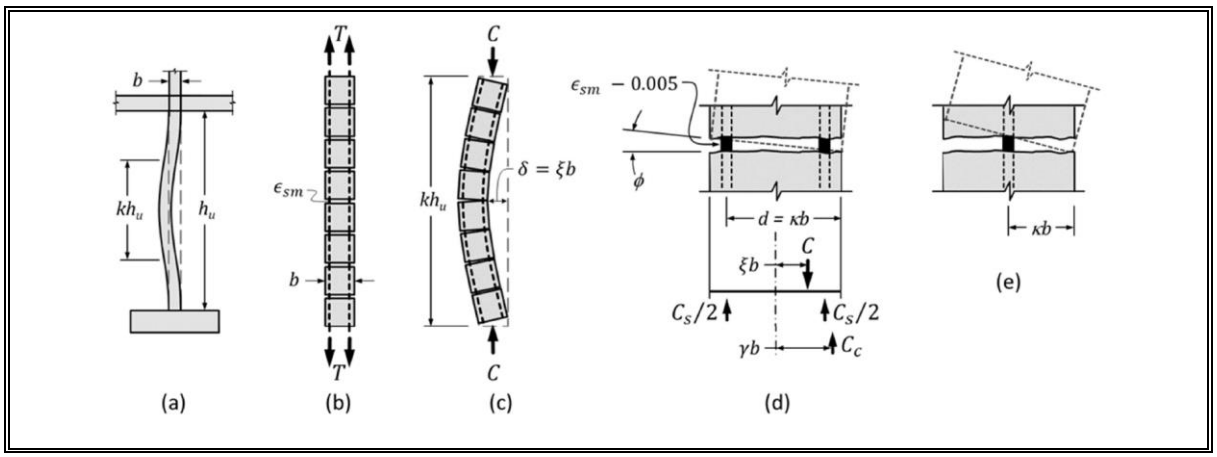

Figure 3.10: Lateral instability of wall boundary previously yielded in tension (Parra & Moehle, 2014).

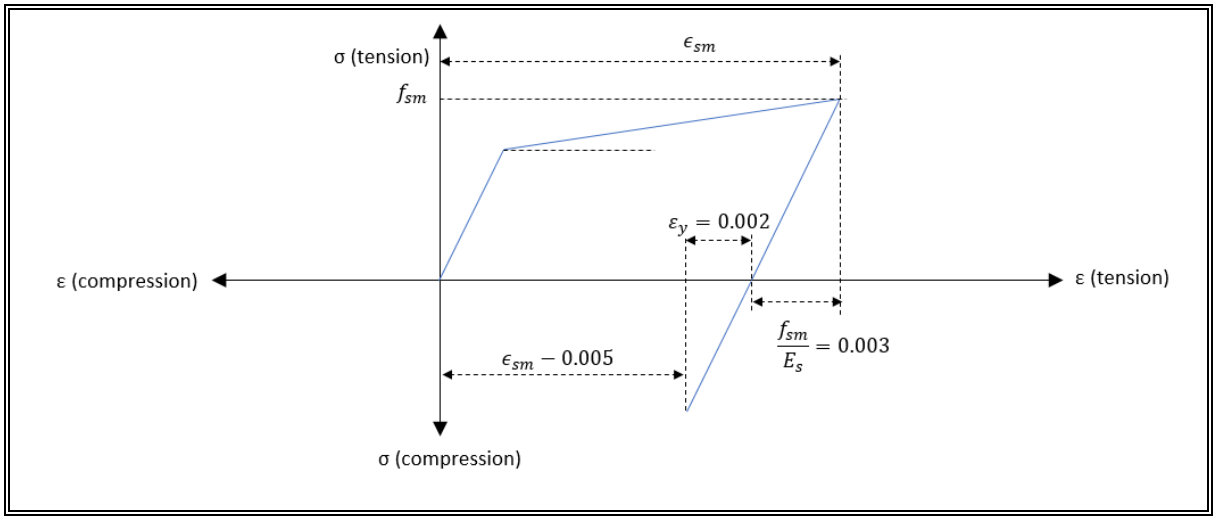

Figure 3.11: Lateral instability of wall boundary previously yielded in tension (Parra & Moehle, 2014).

With Equation 2.13, the expression of Equation 2.11 and the actual values of the specimens the critical thickness of the specimens below which the specimens would be susceptible to overall buckling are 2.23 and 2.34 cm for the specimens with thickness of 15

and 10 cm, respectively (Table 3.6). Therefore, it is concluded that none of the specimen was subject to overall buckling and, as will be explained in chapter 4, none of the specimens experienced overall buckling.

Table 3.6: Verification of overall buckling of the specimens

Specimen	15 cm in thickness	10 cm in thickness
As (cm2)	9.05	6.28
b (cm)	15	10
e (cm)	40	40
p	0.01508	0.01571
fy (MPa)	420	420
fc (MPa)	23.1	23.1
m	0.27418	0.28560
ξ	0.16941	0.16600
k	1	1
κ	0.867	0.800
h_u (cm)	60	60
b_{cr} (cm) (Eqn. 2.13)	2.23	2.34

3.3.2 Design of the CFRP transverse reinforcement

For the specimens strengthened with CFRP, three additional parameters are introduced: location, height of application and diameter of precast holes and corner radius.

3.3.2.1 Precast holes

To test different aspect ratios of the subsections inside the specimen cross transverse section, two distributions of holes were constructed: distribution 3-5 and distribution 2-5 (Figure 3.12). Distribution 3-5 consisted of 15 holes distributed regularly in 3 columns and 5 rows. Distribution 2-5 consisted of 10 holes distributed regularly in 2 columns and 5 rows.

Precast holes were separated vertically in 10 cm center-to-center to generate a ratio of $\frac{s}{d_b} \leq 10$, considering the corresponding diameters of vertical steel bars. Precast holes were carefully located so they wouldn't interfere with the steel reinforcement.

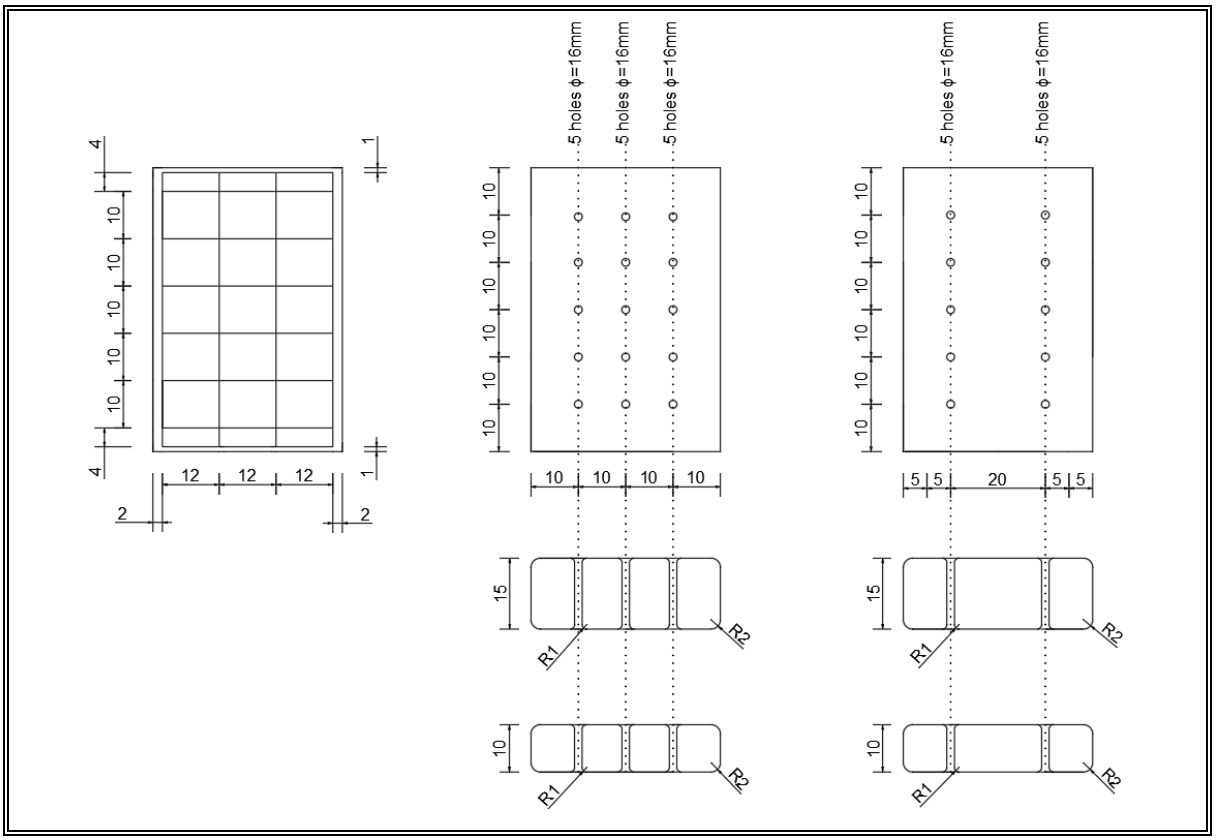

Figure 3.12: Location, diameter and edge radius of precast holes

3.3.2.2 Height of application

To avoid application of direct axial load to the CFRP confinement, CFRP wraps are applied in the central 50 cm leaving 5 cm at the top and at the bottom without CFRP confinement (Figure 3.1). As was explained in section 2.1.1.1, the top and bottom 5 cm are

provided with large confinement with the use of closely spaced hoop bars and ties to avoid failure due to concentration of stresses near the loading plates.

3.3.2.3 Corner radius

Corner rounding of rectangular sections wrapped with CFRP composite materials is necessary to avoid generating stress concentrations. Without this rounding CFRP wraps would present an early rupture, at a stress well below the CFRP capacity. There are many recommendations for a minimum radius corners should be rounded to, for example: 13 mm (ACI Committee 105, 1933), 20 mm (CNR - DT 200, 2004), 20 mm (CAN/CSA-S806, 2007), 15 to 25 mm (fib - Bulletin 35, 2006).

To avoid interference with the steel reinforcement, external corners were rounded manually to a radius of 20 mm (R1) in all specimens, and internal corners outside precast holes were manually rounded to a radius of 10 mm (R2) (Figure 3.12).

3.4 Fabrication

3.4.1 Timber formwork

All twelve specimens were fabricated using timber boxes, and were cast horizontally. These boxes were assembled from plywood boards, with 2.54 cm (1 in) in thickness, nailed together to form the shape of the tested specimens (Figure 3.13). The open side of all timber boxes had dimension of 60 x 40 cm and corresponded to the larger side of the specimens. Six timber boxes, half of all boxes, had a 15-cm depth and six had a 10-cm depth.

Timber boxes corresponding to CFRP reinforced specimens included molded wooden rods, designed to precast the holes were CFRP anchors would pass through without drilling the concrete (Figure 3.14). The wooden rods were provided by a local workshop. Edges of the wooden rods were rounded to a minimum radius of 1 cm. Timber boxes corresponding to control specimens (without CFRP reinforcement) did not include turned wooden rods.

Figure 3.13: Timber boxes as formwork

Figure 3.14: Turned wood rods to precast holes for CFRP anchors

3.4.2 Steel reinforcing cages

The reinforcing cages were assembled outside of the timber boxes (Figure 3.15a) and located inside the formwork before placing of concrete (Figure 3.15b). Steel bars were hold together with construction wire and reinforcing cages were set into position with the use of plastic rings of a 20-mm radius (black devices in Figure 3.15c and 3.15d). The disposition of the timber boxes and reinforcing cages is designed so that concrete can flow uniformly and to make the vibration process easier and more effective (Figure 3.15b).

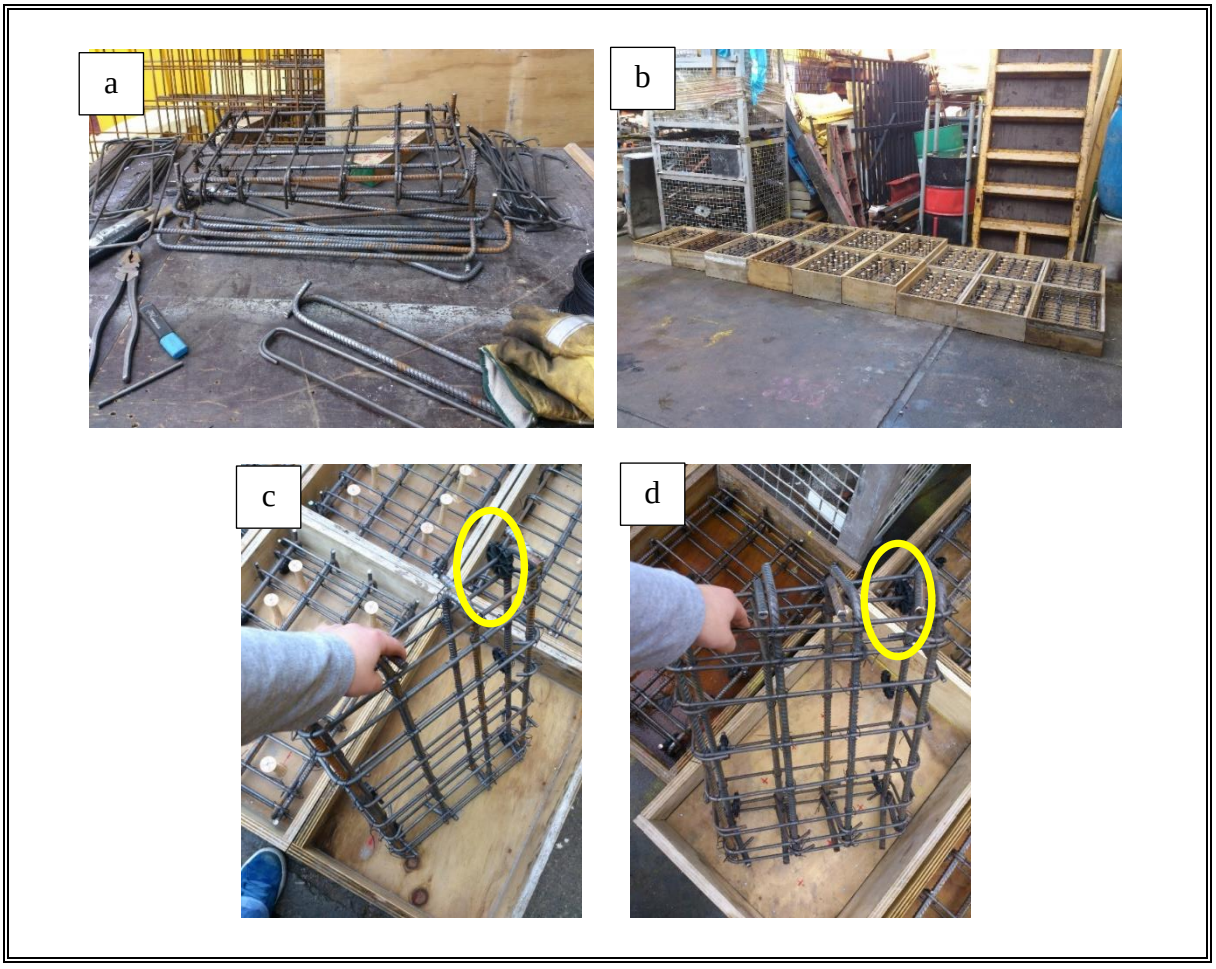

Figure 3.15: Fabrication of steel reinforcing cages

3.4.3 Placing of concrete

Concrete was poured from the ready-mix truck to a barrow (Figure 3.16a, 2.16b). Then it was poured from the barrow to the formwork with the use of shovels (Figure 3.16c).

Figure 3.16: Placing of concrete

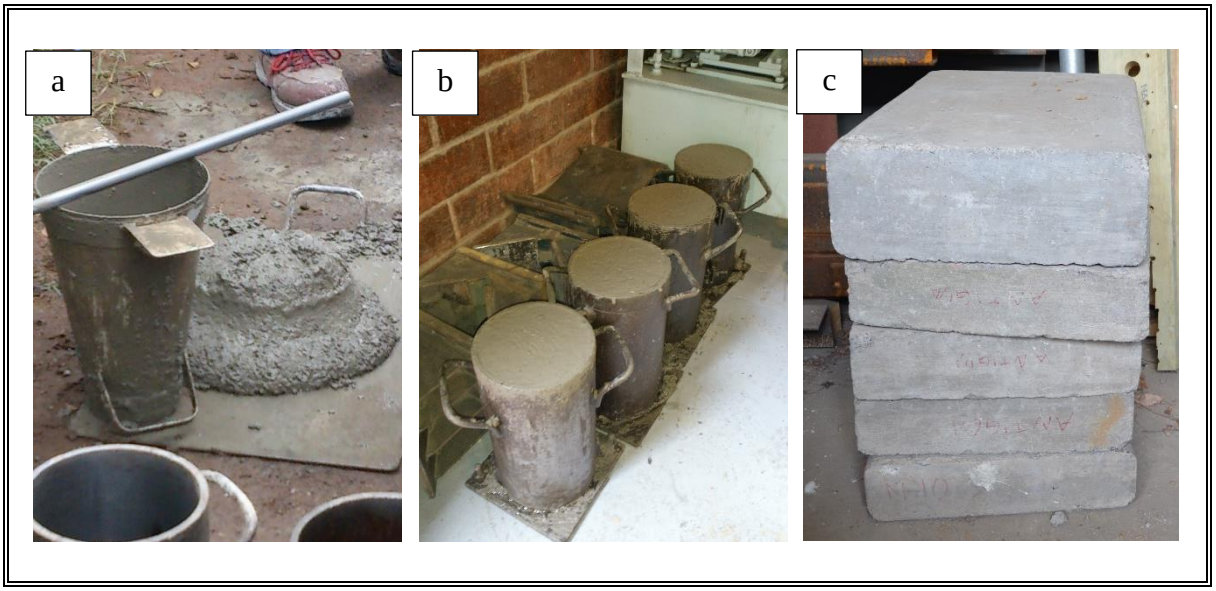

Figure 3.17: (a) Concrete with an 18-cm slump, used for all specimens. (b) Four concrete cylinders used to test the 28-day compression strength. (c) Storage of specimens inside laboratory until testing

Once in the formwork, concrete was vibrated (Figure 3.16d) and manually flushed (Figure 3.16e, 3.16f). Concrete used in all the process had 18-cm slump, measurred with an Abrams cone (Figure 3.17a). Concrete cylinders of 15 cm in diameter and 30 cm in height were fabricated to measure the unconfined strength of concrete after 28 days (Figure 3.17b).

Curing of all specimens was achieved with the same method. A plastic sheet was used to cover all the specimens to prevent excessive evaporation of surface water; also, twice a day all specimens were watered with a garden hose. Concrete cylinders were removed from their molds after two days and submerged fully inside a water tank.

After 28 days of curing, formwork of the specimens was removed by disassembling the timber boxes and perforating the wooden rods. Then specimens were stored at ambient temperature inside the laboratory (Figure 3.17c).

3.4.4 Manual surface preparation

Before installation of CFRP reinforcement, the concrete specimens were manually grinded at the corners, edges of the pre-cast holes and all sides were CFRP was installed.

Corners were rounded to a minimum radius of 20 mm (Figure 3.18.a, 3.18c). The corners and sides of the specimens were grinded with the use of a diamond tipped cup (Figure 3.19a, 3.19b and 3.19c). Sides were grinded until a uniform surface profile was achieved, surface roughness was increased to achieve intimate contact between concrete and CFRP reinforcement, but carefully grinding so no localized out of plane variations form.

Pre-cast hole edges were rounded to a minimum radius of 10-mm by manually grinding until a soft transition was formed between the pre-cast hole and the side (Figure 3.18b). The edges of the pre-cast holes were grinded with the use of aluminum oxide grinder (Figure 3.19d, 3.19e, 3.19f).

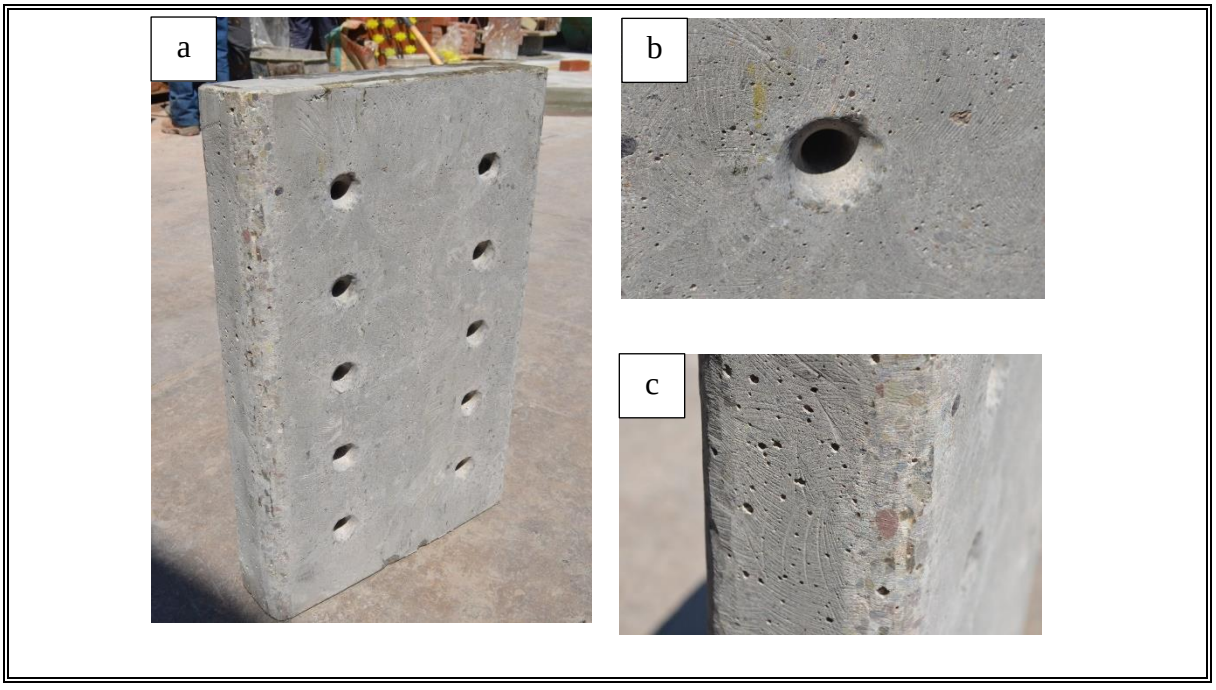

Figure 3.18: Specimen with rounded corners and pre-cast holes edges

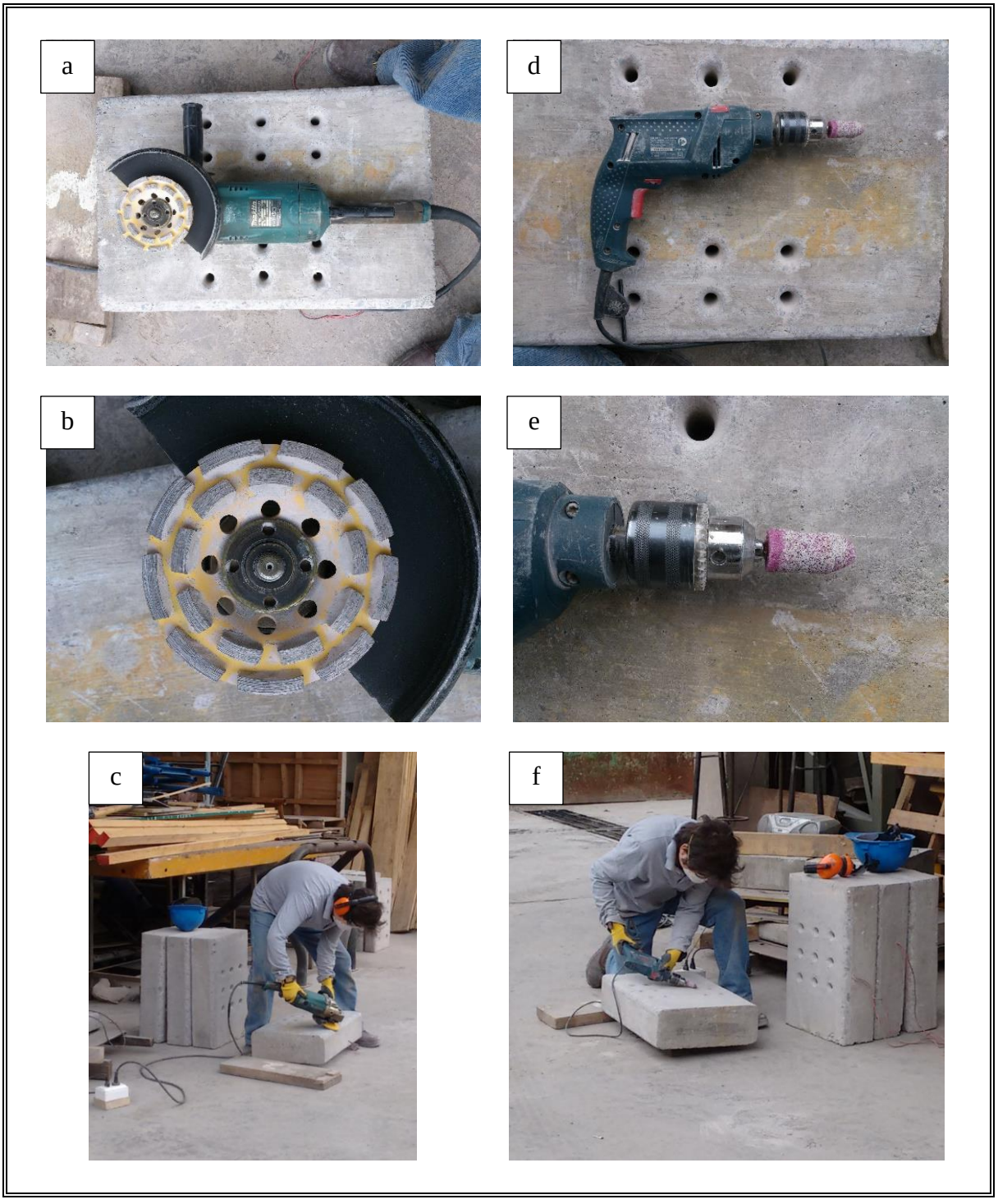

Figure 3.19: (a, b, c) Process of rounding corners. (d, e, f) Process of rounding pre-cast hole edges

3.4.5 CFRP installation

3.2.1.4 CFRP wraps fabrication

CFRP was received from Simpson Strong-Tie as a roll of 30 cm in width which was cut to construct the different components of the CFRP reinforcement (Figure 3.20). The roll was cut into large strips to fabricate the CFRP wraps and into small strips to fabricate the CFRP anchors (Figure 3.21).

Figure 3.20: CFRP roll as received from manufacturer

CFRP wraps were designed to cover the entire surface of the columns one round and overlap 10 cm. In the case of columns with a thickness of 15 cm, the length of the CFRP wraps was 120 cm (40 + 15 + 40 + 15 + 10) (Figure 3.21a). In the case of columns with a thickness of 10 cm, the length of the CFRP wraps was 110 cm (40 + 10 + 40 + 10 + 10) (Figure 3.21b). CFRP wraps of 30 and 20 cm in width were fabricated to cover a complete height of 50 cm. CFRP wraps did not cover the full height of the columns because the CFRP reinforcement was designed to increase the compression strength only by confining concrete and not by direct compression of the CFRP reinforcement.

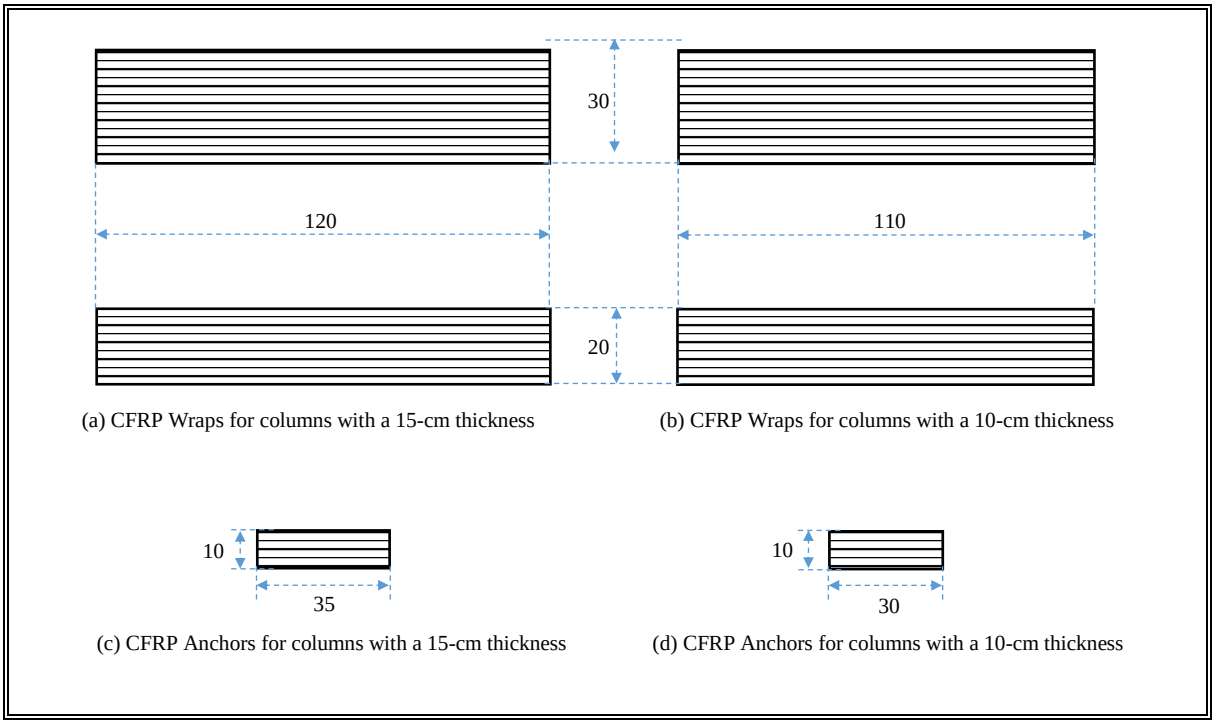

Figure 3.21: Dimensions of strips cut from the CFRP roll (units in cm)

To let CFRP anchors pass through, holes were cut in the CFRP wraps at the locations of pre-cast holes. As can be seen in Figure 3.22, only the transverse white threads were cut, leaving the longitudinal carbon fibers almost intact. During the CFRP installation, these longitudinal cuts were manually opened to let CFRP anchors pass through.

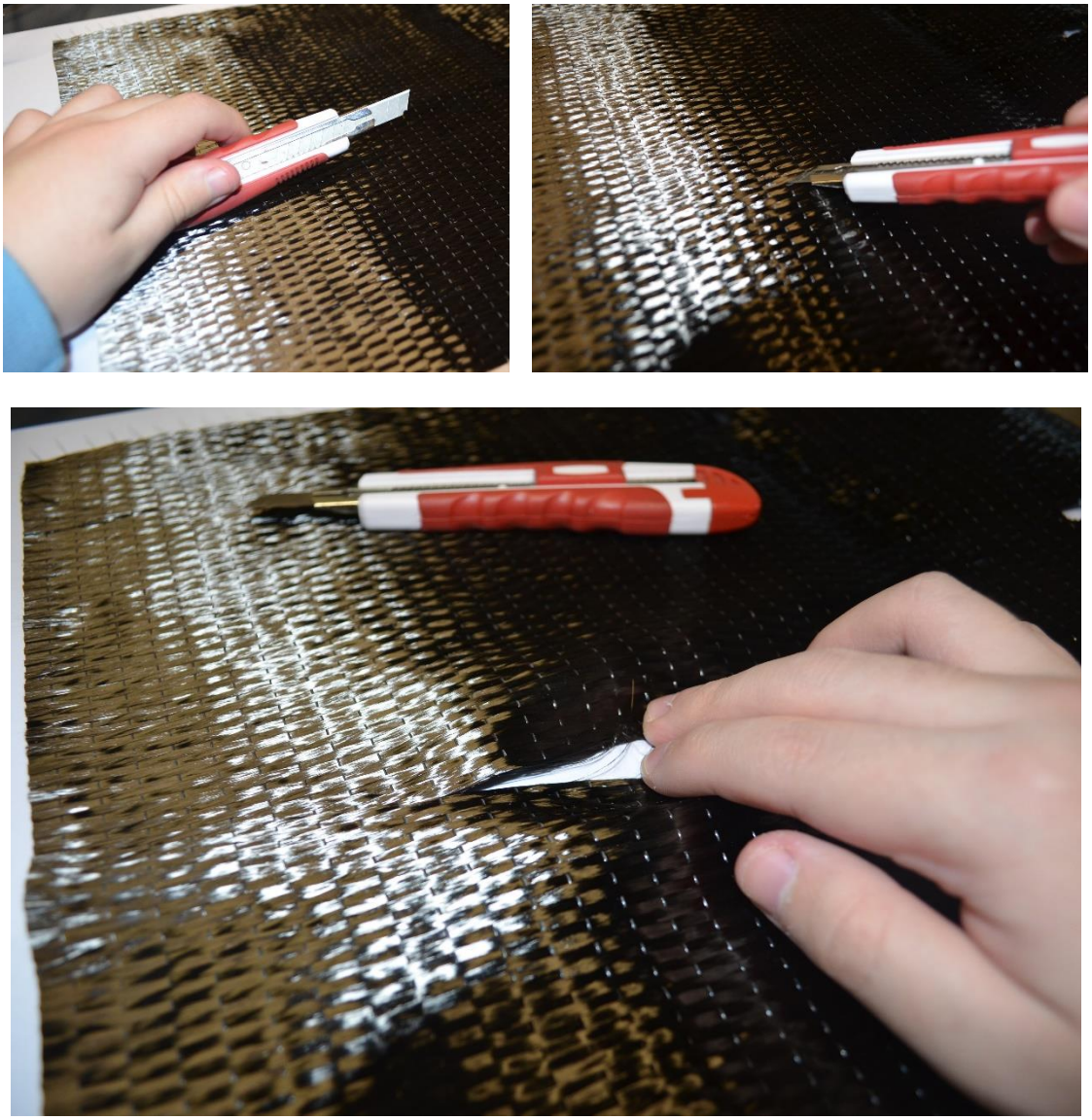

Figure 3.22: Cutting holes in CFRP wraps to let CFRP anchors pass through

3.2.1.5 CFRP anchors fabrication

CFRP anchors were fabricated from the same fabric CFRP wraps were made from. The anchors were designed to pass through the pre-cast holes inside the columns and open taking a fan shape extending 10 cm outside of the edge of the pre-cast holes. In the case of

columns with a thickness of 15 cm, the length of the CFRP anchors was 35 cm (10 + 15 + 10) (Figure 3.21c). In the case of columns with a thickness of 10 cm, the length of the CFRP anchors was 30 cm (10 + 10 + 10) (Figure 3.21d). To fabricate the largest possible quantity of anchor without wasting any carbon fiber, the anchors had a width of 10 cm.

The ends of the sheets were cut parallel to the carbon fibers to produce several thin segments of around 0.6-cm width and a 12-cm length. These small segments were design to generate a fan shaped disposition when installed (Figure 3.23).

CFRP anchor for columns with a 15-cm thickness

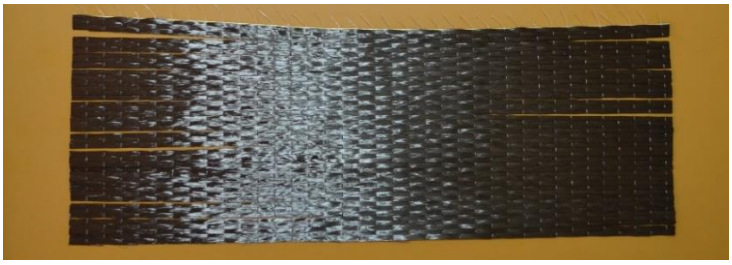

CFRP anchor for columns with a 10-cm thickness

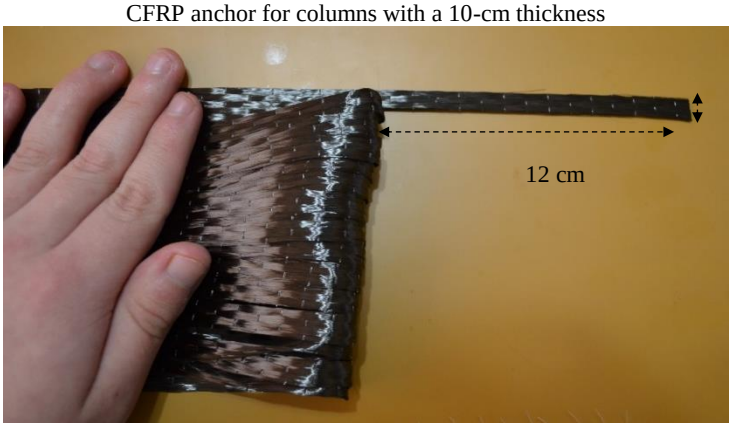

Small segment of CFRP anchor design

Figure 3.23: Fabrication of CFRP anchors

After the ends of the rectangular sheets were cut into small segments, CFRP anchors were prepared to be installed, as explained in Figure 3.24. First, a couple of wooden sticks were paste together to serve as a rigid support for the CFRP anchors (Figure 3.24a).

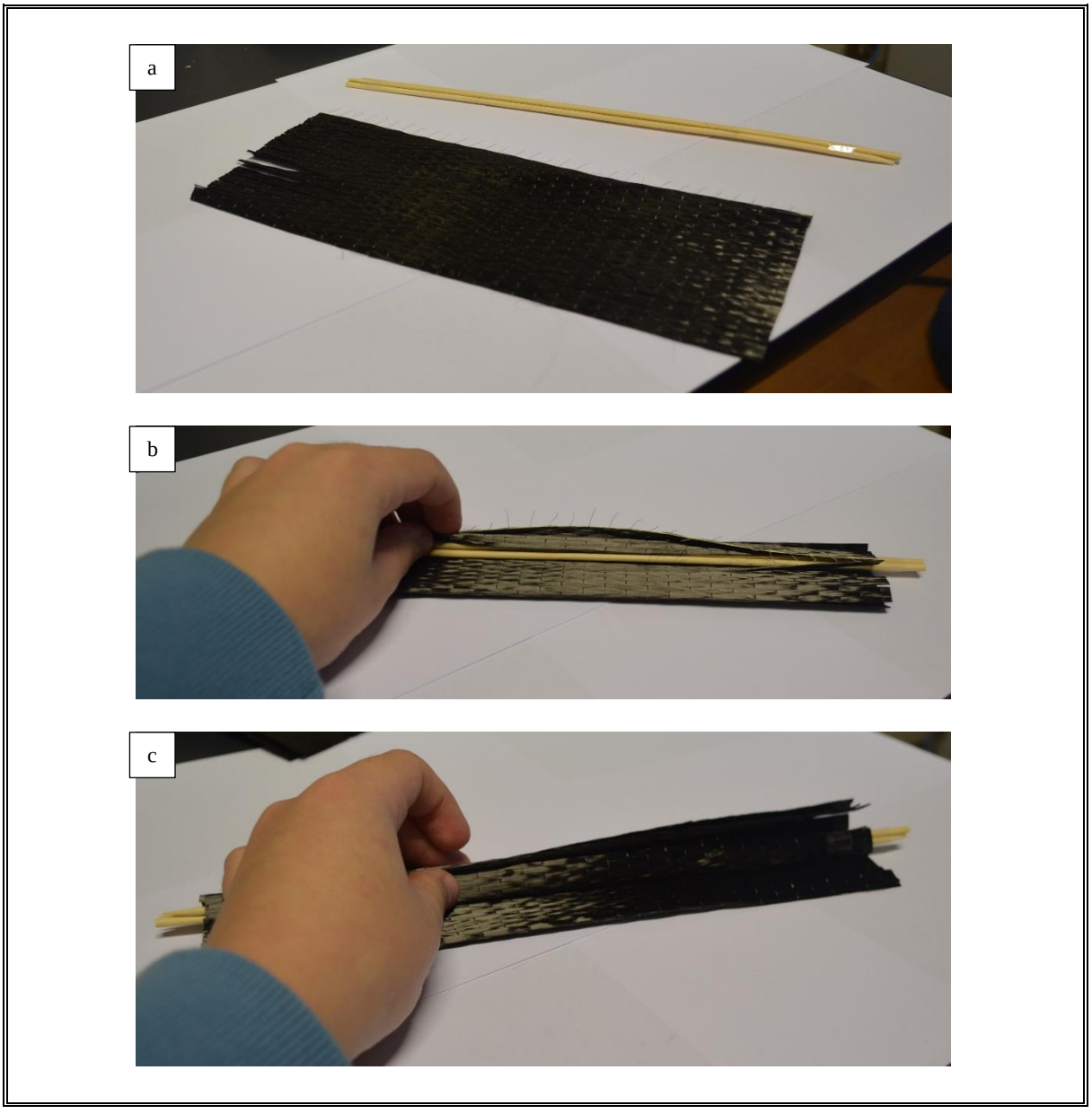

Figure 3.24: Fabrication of CFRP anchors (continuation)

In the case of CFRP anchors for specimens 15-235, 15-225, 10-235 and 10-225, only one rectangular CFRP sheet is folded around the wooden stick and secured at the edges (Figure 3.24b). In the case of CFRP anchors for specimens 15-335, 15-325, 10-335 and 10-325, two rectangular CFRP sheets are folded around the wooden stick and secured at the edges (Figure 3.24c). These is because specimens with 2 layers of CFRP wraps only need 1 layer of CFRP anchors between them and specimens with 3 layers of CFRP need 2 layers of CFRP anchors, as will be explained later.

3.2.1.6 Epoxy matrix preparation

The epoxy resin results from the chemical reaction of two components: Part A, a highly viscous and transparent material and Part B, a very fluid and honey-colored material.

Figure 3.25: Preparation of epoxy resin

The manufacturer indicated that the ratio of Part A to Part B should be 2 to 1 in volume. Considering that the density of Part A and Part B were 1.17 kg/L and 0.97 kg/L, respectively, the weight ratio of Part A to Part B was 2.41 to 1. This ratio was achieved with the use of an electronic scale (Figure 3.25a, 3.25b).

The reaction between the components is fast, after just an hour the epoxy matrix became rigid. Because of this fast reaction, the epoxy resin was fabricated only in small amounts, less than 1 L each time. After both parts were placed in the correct proportion they were mixed manually for a minimum of 5 minutes (Figure 3.25d).

3.2.1.7 Wet lay-up of CFRP wraps and anchors

The applications of the CFRP reinforcement followed the instructions given by the manufacturer. First, the surface of the column was cleaned from any dust and humidity by applying high pressurize air (Figure 3.26a). After preparing the epoxy resin as was explained before, it was applied over all the surfaces where CFRP would be in contact with concrete: on the side faces and on the surfaces inside the pre-cast holes. (Figure 3.26b). Then, the central zone of CFRP anchors were impregnated with epoxy resin to increase adherence with the concrete surface inside the pre-cast holes (Figure 3.26c). Later, all the CFRP anchors were installed inside the pre-cast holes (Figure 3.26d). Once the CFRP anchors were in place, a first CFRP wrap was impregnated with resin on both sides of the fabric (Figure 3.26e, 3.26f). The impregnated CFRP wrap was placed on the column, letting the CFRP anchors pass through the cuts on the fabrics (Figure 3.27a). Once the fabric was in place, it was pressed against the concrete with a notched spatula to reduce the number of air bubbles to the minimum possible (Figure 3.27b, 3.27c, 3.27d). After the CFRP wrap was installed, the first layer CFRP anchors was opened and impregnated with epoxy resin with

the use of a brush (Figure 3.27e, 3.27f, 3.27g). The CFRP anchors were installed at the same time from both sides of the column to increase the adherence inside the pre-cast holes by indirectly pressing against the surface by subjecting the anchors to tension (Figure 3.27h).

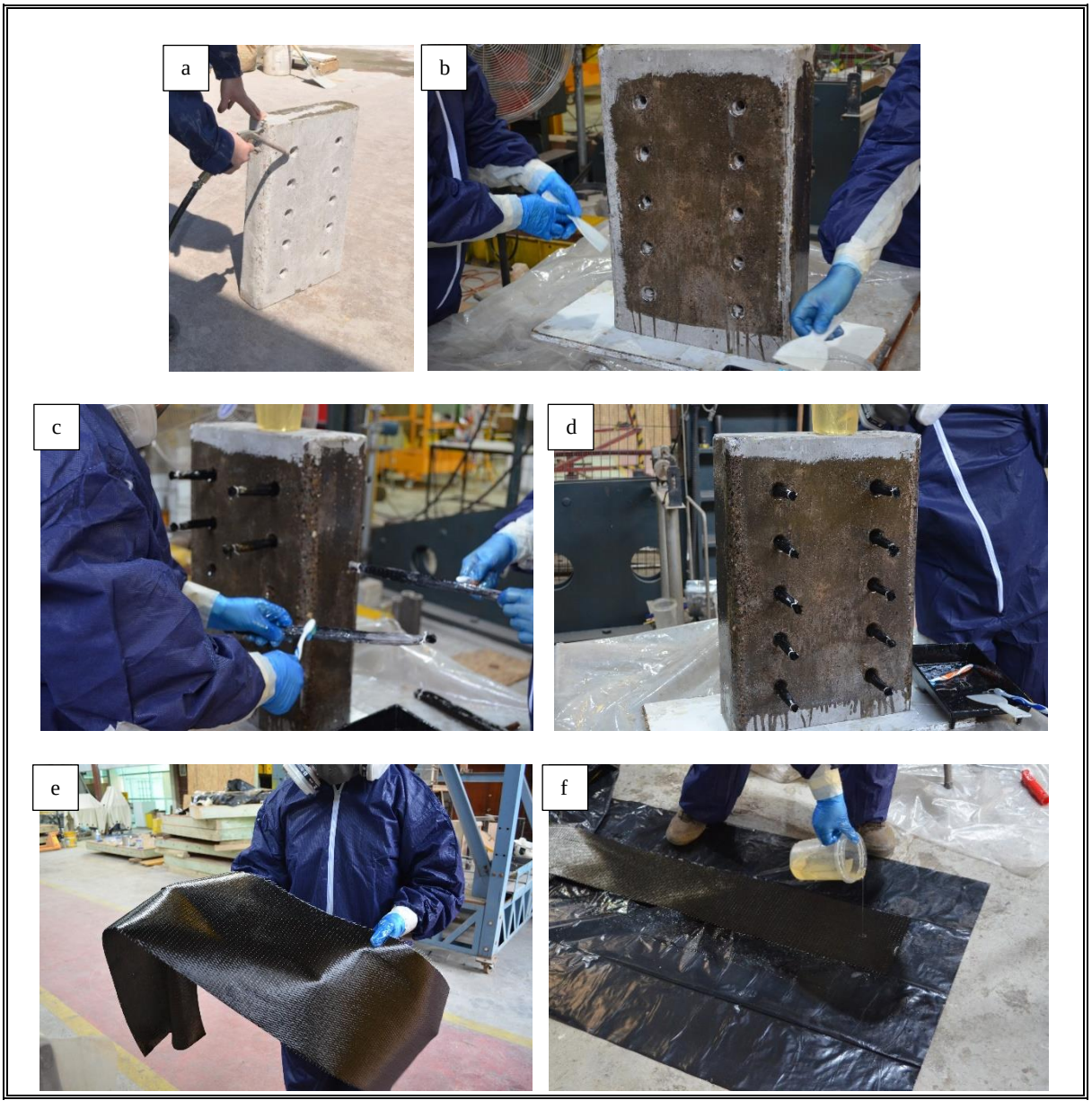

Figure 3.26: Installation of CFRP wraps and CFRP anchors

Figure 3.27: Installation of CFRP wraps and CFRP anchors (continuation)

In the case of specimens 15-225, 10-225, 15-235 and 10-235, the CFRP installation was completed with the application of a second CFRP wrap (without cuts) over the layer of CFRP anchors.

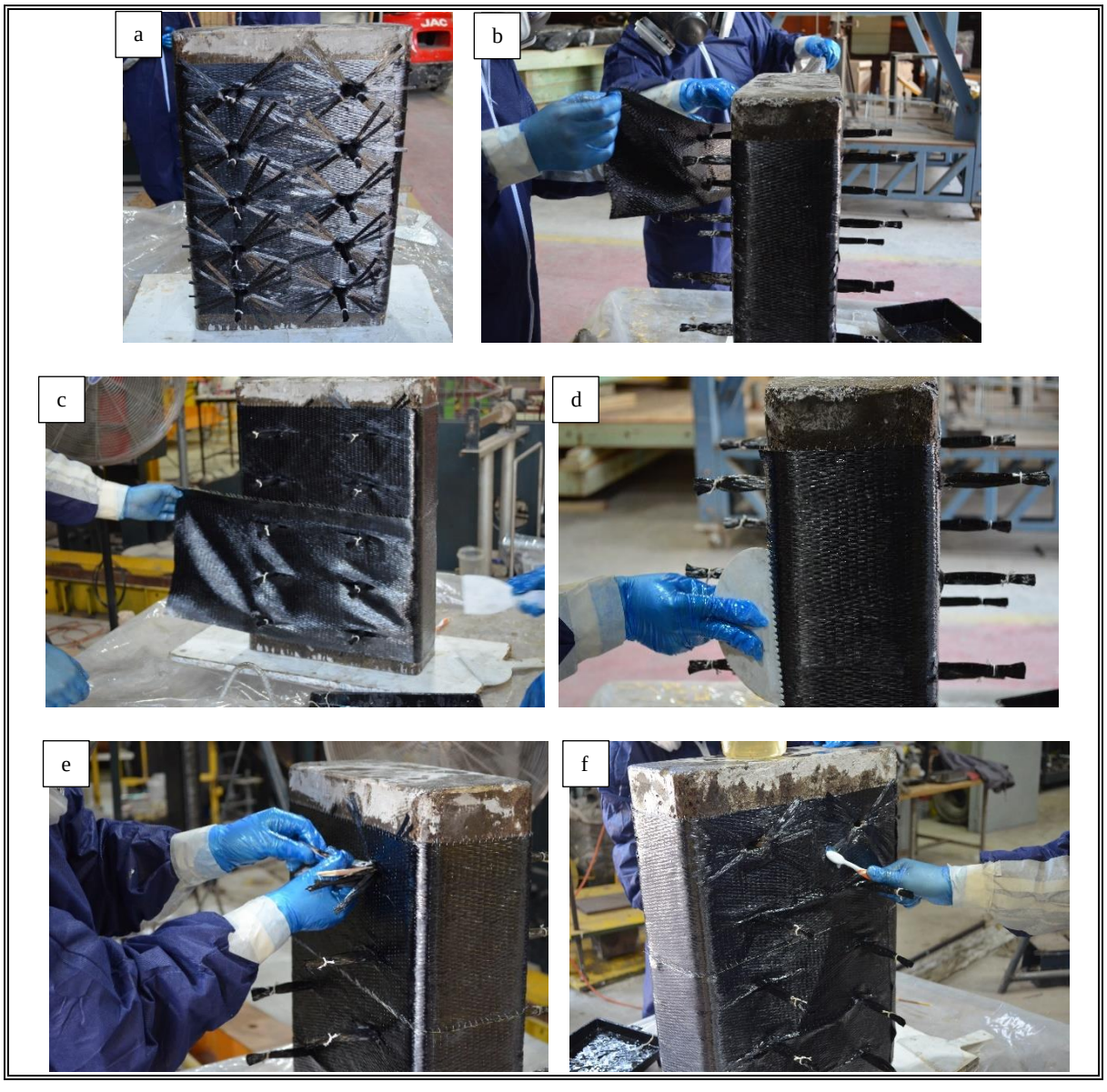

Figure 3.28: Installation of CFRP wraps and CFRP anchors (continuation)

In the case of specimens 15-325, 10-325, 15-335 and 10-335, a second CFRP wrap was applied letting the second layer of anchors pass through the cuts on the fabric (Figure

3.28a, 3.28b, 3.28c). Once the second layer of CFRP wrap was installed, just like the previous one, it was pressed against the concrete surface (Figure 3.28d). Then, the second layer of CFRP anchors was opened and impregnated with epoxy resin using a brush, just like the previous anchors layer (Figure 3.28e, 3.28f). CFRP installation was completed with the application of a third CFRP wrap (without cuts) over the second layer of CFRP anchors.

3.5 Instrumentation

3.5.1 Strain gages

A total of 12 strain gages were distributed among the columns with CFRP reinforcement (Figure 3.29). Two strain gages were placed on each of the specimens with three layers of CFRP wraps (15-325, 10-325, 15-335 and 10-335), one at the corner at mid height and one 12 cm from the edge at the same height. One strain gage was placed on each of the specimens with two layers of CFRP wraps (15-225, 10-225, 15-235 and 10-235) located at the corner of the specimen at mid height.

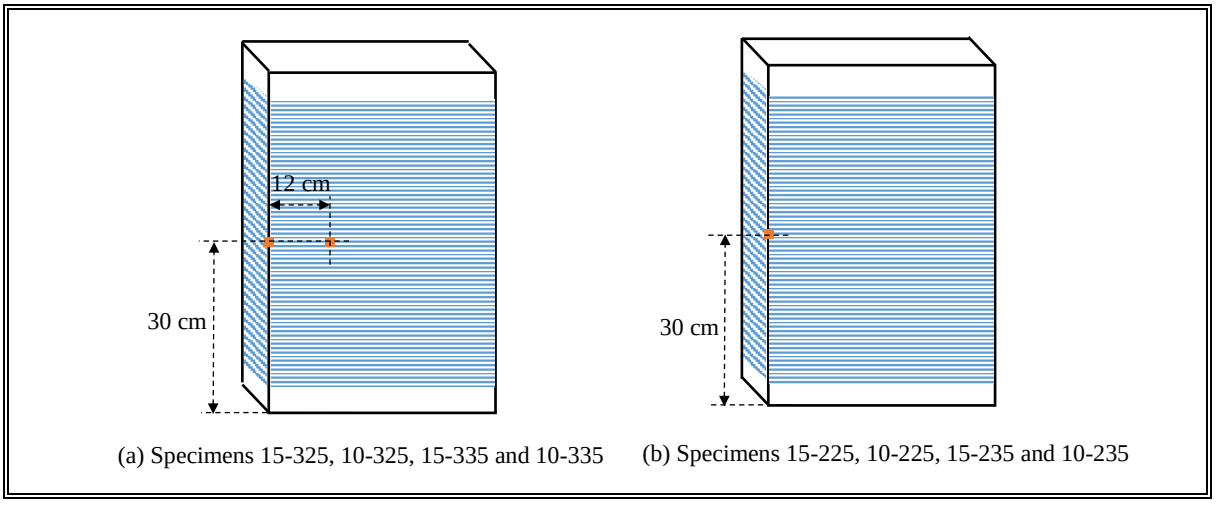

Figure 3.29: Location of strain gages on the CFRP wrap

It is important to mention that the strain gages used were specially designed to detect deformations in CFRP material, they corresponded to series BFLA-2-8 of Tokyo Sokki Kenkyujo strain gages.

The installation process of the strain gages was followed according to the manufacturer instructions (Figure 3.30). The surface where the strain gages were installed was polished with sandpaper No. 100 (Figure 3.30a, 3.30b, 3.31a). Once the surface is prepared, a two-compound glue is prepared with 1 gr of a viscous brown material mixed with 1 drop of a yellow liquid (Figure 3.31b, 3.31c). The mixed glue was immediately applied to the surface where the strain gage would be installed (Figure 3.31d). A plastic sheet, provided by the manufacturer, was applied over the mixed glue at the installation area and secure with a rubber lock (Figure 3.31e, 3.31f, 3.32a). After 30 minutes, the plastic sheet was removed leaving a smooth surface for the strain gage to be installed. A different glue was applied to the strain gage and immediately pasted to the prepared surface (Figure 3.32b, 3.32c). Finally, the installed strain gage was secured with a rubber lock (Figure 3.32d).

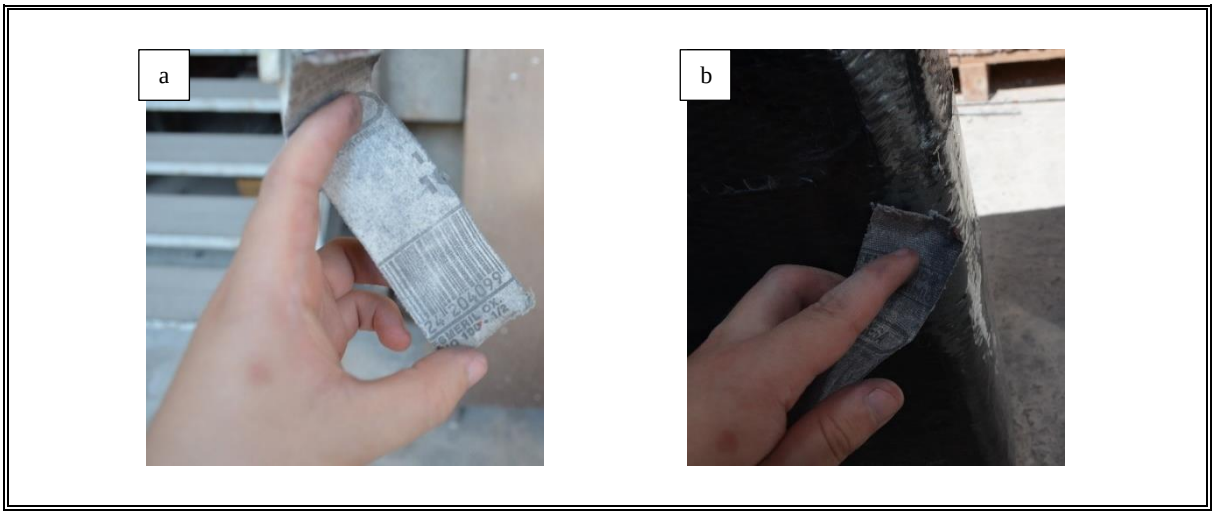

Figure 3.30: Installation of strain gages over CFRP wrap

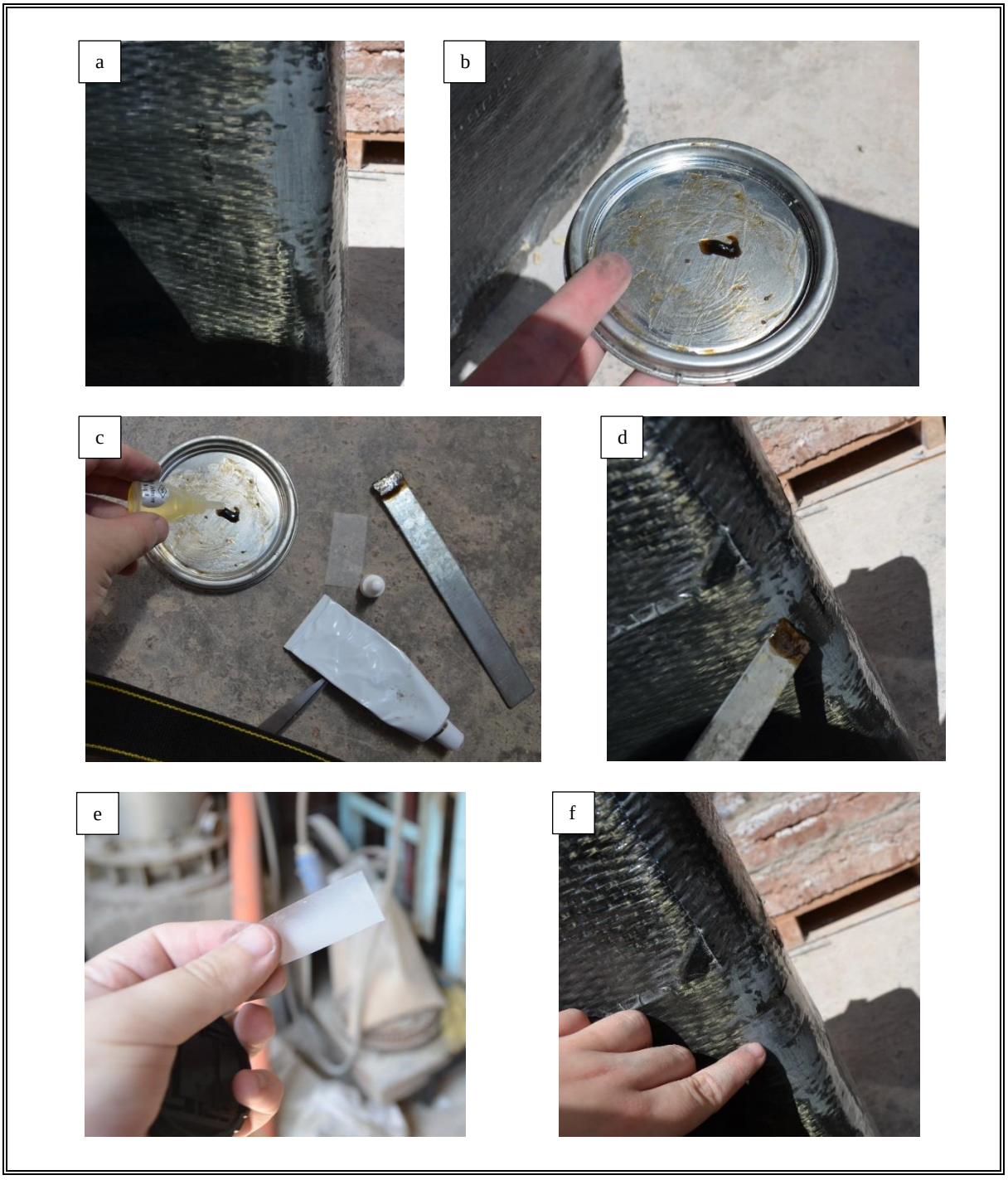

Figure 3.31: Installation of strain gages over CFRP wrap (continuation)

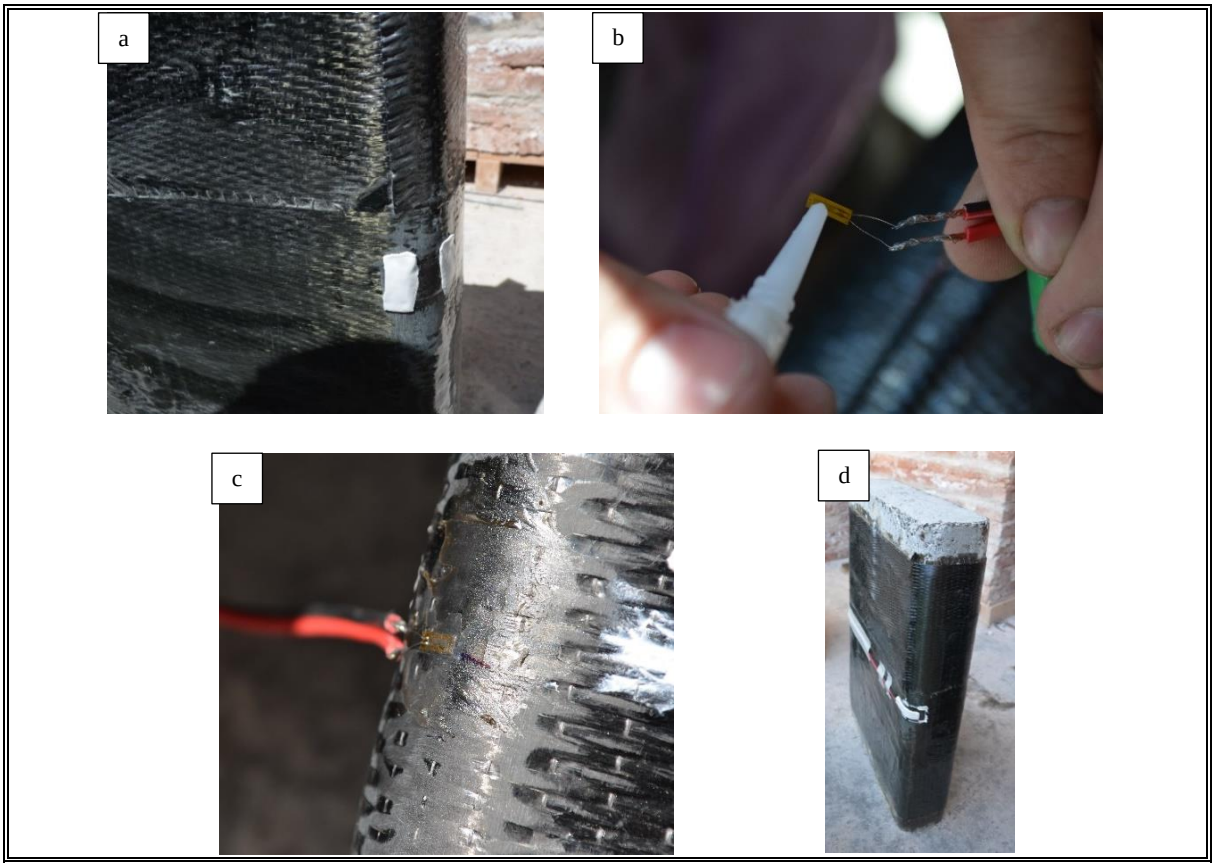

Figure 3.32: Installation of strain gages over CFRP wrap (continuation)

3.5.2 Image data correlation

Although strain gages were installed on the CFRP at the most probable zones of failure, few strain gages were installed on each specimen. To capture the complete field of deformations a technique of image data correlation is used. For this purpose, two adjacent sides of the specimens were painted white and numerous random black dots were marked throughout the two sides of the specimens (Figure 3.33). With the use of two digital cameras (Nikon d3300 and Canon EOS Rebel T3), photographs were taken of these two sides every 5 seconds while the test took place. The photographs were used to determine the

deformation field with the use of Optecal Digital Image Correlation software (Optecal, 2016).

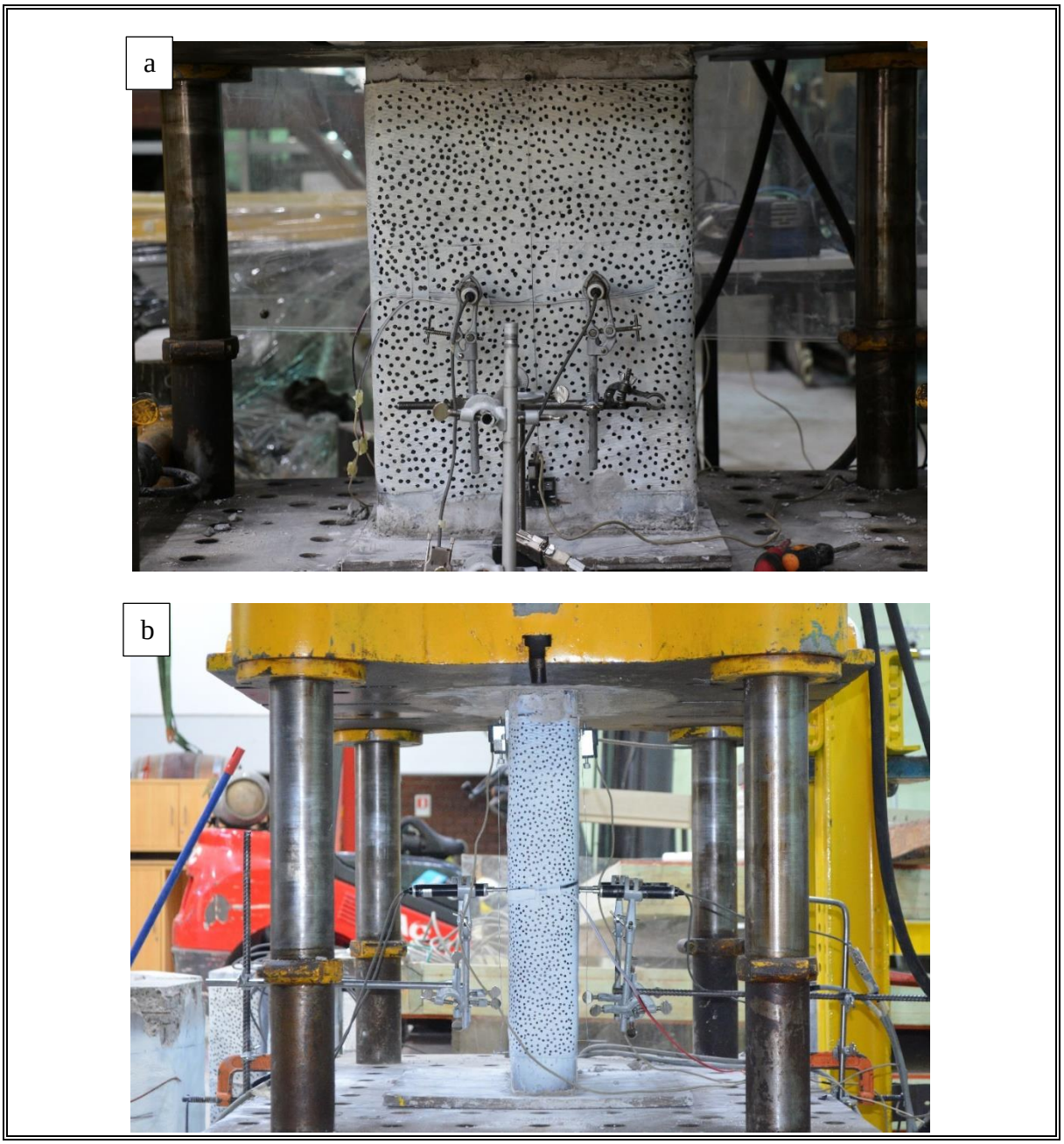

Figure 3.33: Specimen being tested. Strain gages and LVDTs installed. Sides painted white with black dots for image data correlation to capture the complete deformation field. (a) Large side view (Side A). (b) Small side view (Side B)

3.5.3 Linear variable differential transformers (LVDT)

LVDTs were installed in different positions in control specimens (without CFRP reinforcement) and CFRP reinforced columns (Figure 3.34).

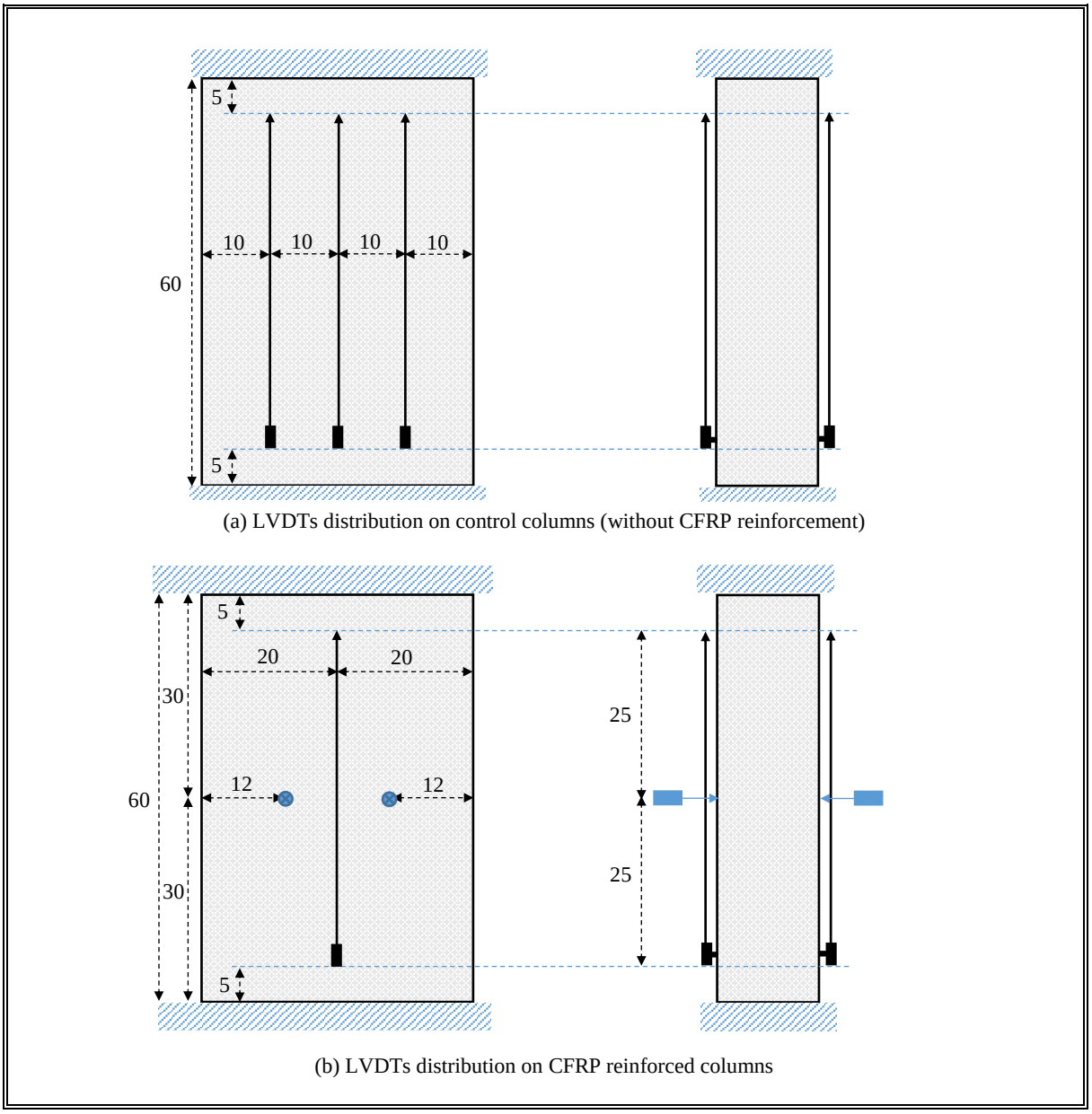

(a) LVDTs distribution on control columns (without CFRP reinforcement)

(b) LVDTs distribution on CFRP reinforced columns

Figure 3.34: Location of vertical and horizontal LVDTs (units in cm)

Vertical LVDTs with a range of 50 mm were installed to measure vertical displacement in the columns. To measure an average compression displacement of the complete height of the columns vertical LVDTs were located at the bottom of the columns. Then, a vertical thread was connected to each vertical LVDT, subject to tension and secured on at the top of the columns. Therefore, as the column was subject to compression, the tension at the thread and the vertical LDVT released and measured an average compression displacement of the complete column, this disposition can be seen in Figure 3.34.

Horizontal LVDTs were placed at mid height to measure widening of the columns, they were maintained in their position with the use of clamps (Figure 3.33).

In the case of control columns (without CFRP reinforcement), six vertical LVDTs were installed (Figure 3.34a). In the case of CFRP reinforced columns, two vertical and four horizontal LVDTs were installed (Figure 3.34b). Finally, load from the testing machine was measured with a load cell connected directly to the data acquisition system. The measurements of all LVDTs and strain gages were synchronized with the use of the software Catman (HBM, 2017).

3.6 Loading arrangement

The testing machine consisted of a force-controlled oleo hydraulic loading cell with a capacity of 275 tonf (2,697 kN), a loading cell equipment and a reaction frame (Figure 3.35a, 3.35b). Columns were placed vertically between the base of the machine and the yellow frame (Figure 3.35b). The top and bottom sides of the columns were rectified with a cement plaster mix and pressed with a very little force in the testing machine, generating a uniform surface to avoid eccentricities (Figure 3.35c, 3.35d). Since the testing machine was forced controlled, only a portion of the descending portion of the stress-strain curve could

be captured. If a displacement controlled machine was used, the increments of ductility captured could have been larger as occurred in other investigations (Triantafillou, et al., 2016; Hany, Hantouche, & Harajli, 2016). Therefore, the captured ductility increments of the present investigation can be considered conservative.

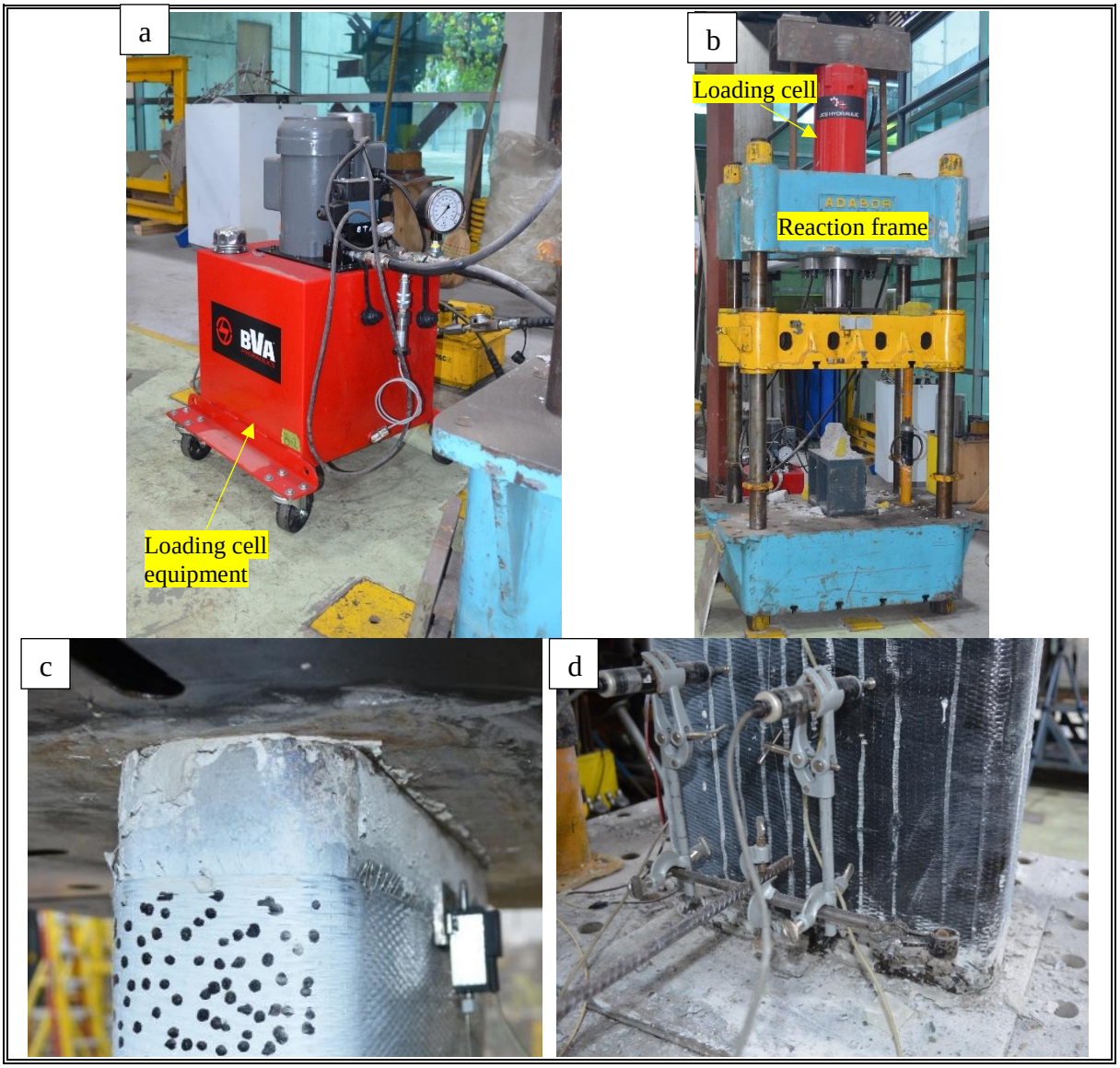

Figure 3.35: (a, b) Testing machine component. (c, d) Top and bottom rectification of specimens

3.7 Test procedure

Once the columns were set in placed and correctly instrumented, the forced controlled loading cell compressed the columns at an average rate of 0.005 mm/s until failure. Because it was a force controlled machine, not much of the descending portion of the axial strain-stress curves could be captured; however, because the frequency of the data acquisition was high, 50 Hz (capturing one data point every 0.02 seconds), the start of the descending portion was captured.

3.8 Summary

Twelve reinforced concrete columns were constructed to study the behavior of confinement with CFRP wraps and anchors. Half of the columns presented a 10-cm thickness and the other half a 15-cm thickness. From these twelve columns, eight were reinforced with CFRP confinement and four were left as control columns. Columns reinforced with CFRP were constructed with precast holes to let CFRP anchors pass. Control columns were constructed without pre-cast holes. CFRP columns presented manually rounded corners at the column external edges and at the pre-cast holes internal edges.

The objective of the specimens was to evaluate the impact of the CFRP confinement on the axial stress-strain curve parameters. The specimen without CFRP confinement were designed to experience buckling of vertical bars, transverse bar opening and concrete crushing at the center of the column. The specimens with CFRP reinforcement were design to prevent all the failure modes expected to occur in control specimens.

CFRP reinforcement was install manually with a wet lay-up procedure and consisted of wraps of 0.5mm of nominal thickness. Half the specimens presented a 2x5 CFRP anchor

disposition and half the specimens presented a 3x5 CFRP disposition. Half the specimens presented 3 layers of CFRP wraps and 2 layers of CFRP anchors and half the specimens presented 2 layers of CFRP wraps and 1 layer of CFRP anchors.

Before testing, the specimens were instrumented with vertical and horizontal LVDTs, strain gages and a painted dotted grid at the outer CFRP layer. Vertical LVDTs were used to obtain an average axial strain of the column. Horizontal LVDTs were used to capture widening of the column at a specific location. Strain gages were installed in a horizontal direction at the most probable zones of failure on the outer CFRP layer. The painted dotted grid was used to capture the field of CFRP deformations of the outer layer with the use of a digital image correlation software. A forced controlled testing machine was used.

4. EXPERIMENTAL RESULTS

4.1 Overview

The test results of twelve specimens are presented in this chapter. First the measured responses of each specimen are explained, then a comparison of these responses is discussed.

The geometric characteristics of the specimens are explained in Figure 3.1, Figure 3.2, Table 3.1, Figure 3.6, Figure 3.7, Figure 3.9, Figure 3.12, Figure 3.21, Figure 3.29 and Figure 3.34. Table 4.1 provides a summary of important detailing parameters for all specimens. Table 4.2 provides a summary of results related to the axial stress-strain curve and strain-gage readings for all specimens. Table 4.3 provides a summary of increments in result parameters due to the use of CFRP reinforcement.

In Table 4.1, ρ_s^l, ρ_s^h and ρ_{frp} stand for the volumetric ratio of longitudinal bars, hoop bars and CFRP confinement, respectively. Also, k_s^{shape} and k_{frp}^{shape} stand for the ratio of the effectively confined area to the gross section area due to hoop bars confinement and CFRP confinement, respectively, based on the arching action assumed to occur in the form of a second-degree parabola with a tangent slope of 45° (Mander, Priestley, & Park, Theoretical Stress - Strain Model For Confined Concrete, 1988a). It is important to notice that the area effectively confined by hoop bars lies inside the area effectively confined by CFRP confinement. Finally, T_x^{frp} and T_y^{frp} stand for the total cross-sectional area of the CFRP wraps and anchors through-out the specimen height. It is important to notice that all the parameters consider the specimen height as the central 50 cm, which is the zone where

CFRP confinement is applied and hoop bars generate a poor confinement as explained in section 3.1.2.

Table 4.1: Summary of specimen parameters

Specimen	Long. Bars (mm)	ρ_s^l	Hoop bars (mm)	ρ_s^h	k_s^{shape}	T_x^{frp} (mm^2)	T_y^{frp} (mm^2)	ρ_{frp}	k_{frp}^{shape}
000-10a	8 ϕ 10	0.01571	ϕ 6 @ 100	0.00136	0.00368	0	0	0	0
000-10b	8 ϕ 10	0.01571	ϕ 6 @ 100	0.00136	0.00368	0	0	0	0
000-15a	8 ϕ 12	0.01508	ϕ 6 @ 100	0.00100	0.02838	0	0	0	0
000-15b	8 ϕ 12	0.01508	ϕ 6 @ 100	0.00100	0.02838	0	0	0	0
225-10	8 ϕ 10	0.01584	ϕ 6 @ 100	0.00137	0.00371	1000	1500	0.02774	0.30332
225-15	8 ϕ 12	0.01517	ϕ 6 @ 100	0.00100	0.02854	1000	1500	0.02095	0.48939
235-10	8 ϕ 10	0.01584	ϕ 6 @ 100	0.00137	0.00371	1000	1750	0.02900	0.38909
235-15	8 ϕ 12	0.01517	ϕ 6 @ 100	0.00100	0.02854	1000	1750	0.02221	0.64139
325-10	8 ϕ 10	0.01584	ϕ 6 @ 100	0.00137	0.00371	1500	2500	0.04287	0.30332
325-15	8 ϕ 12	0.01517	ϕ 6 @ 100	0.00100	0.02854	1500	2500	0.03269	0.48939
335-10	8 ϕ 10	0.01584	ϕ 6 @ 100	0.00137	0.00371	1500	3000	0.04539	0.38909
335-15	8 ϕ 12	0.01517	ϕ 6 @ 100	0.00100	0.02854	1500	3000	0.03520	0.64139

In Table 4.2, P_{max} stands for the maximum load applied during the tests, f_c^{max} stands for the maximum estimated concrete stress, ε_c^{max} stands for the average measured axial strain corresponding to f_c^{max}, E_c stands for the average secant modulus of elasticity between points $(0,0)$ and $(\varepsilon_c^{f_c^{max}/2}, \frac{f_c^{max}}{2})$, P_{ult} stands for the last load just before the end of the test, f_c^{ult} stands for the estimated concrete stress just before the end of the test (considering an elastic perfectly plastic constitutive for the longitudinal bars), ε_c^{ult} stands for the average axial strain corresponding to f_c^{ult}, E_D stands for the average secant descending slope between points $(\varepsilon_c^{max}, f_c^{max})$ and $(\varepsilon_c^{ult}, f_c^{ult})$ and finally $\varepsilon_{frp}^{max-sg}$ and $\varepsilon_{frp}^{ult-sg}$ stand for the horizontal CFRP strains (captured by strain gages located at the corner and/or middle side of the column on the external CFRP wraps as explained in Figure 3.29) corresponding to f_c^{max} and f_c^{ult}, respectively. Since specimens 000-10a and 000-10b are identical and

000-15a and 000-15b are also identical, average results are presented in 000-10 and 000-15. Since specimen 335-15 did not reach failure, parameters P_{ult}, f_c^{ult}, ε_c^{ult} and E_D could not be obtained.

Table 4.2: Summary of specimen results related to the axial stress-strain curve

Specimen	P_{max}	f_c^{max}	ε_c^{max}	E_c	P_{ult}	f_c^{ult}	ε_c^{ult}	E_D	$\varepsilon_{frp}^{max-sg}$	$\varepsilon_{frp}^{ult-sg}$
	$tonf$	$\frac{kgf}{cm^2}$	$\frac{mm}{mm}$	$\frac{kgf}{cm^2}$	$tonf$	$\frac{kgf}{cm^2}$	$\frac{mm}{mm}$	$\frac{kgf}{cm^2}$	$\frac{mm}{mm}$	$\frac{mm}{mm}$
000-10a	147	306	0.0030	190044	143	295	0.0032	-67156	-	-
000-10b	142	304	0.0017	269342	110	212	0.0027	-89977	-	-
000-10	145	305	0.0024	229693	127	254	0.0030	-78567	-	-
000-15a	229	322	0.0027	210358	227	319	0.0028	-29524	-	-
000-15b	246	351	0.0032	188153	243	346	0.0035	-12048	-	-
000-15	238	337	0.0030	199256	235	333	0.0032	-20786	-	-
225-10	180	392	0.0032	222739	179	390	0.0033	-25698	C: 0.0004	C: 0.0004
225-15	246	353	0.0034	193278	198	272	0.0044	-89319	C: 0.0006	C: 0.0010
235-10	157	334	0.0044	142665	157	332	0.0047	-8927	C: 0.0005	C: 0.0005
235-15	254	366	0.0041	340588	246	353	0.0050	-15206	C: 0.0014	C: 0.0011
325-10	165	353	0.0070	191975	148	310	0.0085	-28031	C: 0.5062 M: 0.6370	C: 0.5384 M: 0.5486
325-15	262	380	0.0048	217056	235	334	0.0055	-75119	C: 0.0007 M: 0.0022	C: 0.0015 M: 0.0040
335-10	180	393	0.0058	221280	175	380	0.0059	-107958	C: 0.0000 M: 0.0009	C: 0.0000 M: 0.0008
335-15	275	401	0.0053	153208	-	-	-	-	C: 0.0008 M: 0.0025	C: 0.0008 M: 0.0025

In Table 4.3, $\frac{f_c^{ma}}{f_{c-000}^{max}}$, $\frac{\overline{\varepsilon_c^{max}}}{\overline{\varepsilon_{c-000}^{max}}}$, $\frac{\overline{E_c}}{\overline{E_{c-000}}}$, $\frac{f_c^{ult}}{f_{c-000}^{ult}}$ and $\frac{\overline{\varepsilon_c^{ult}}}{\overline{\varepsilon_{c-000}^{ult}}}$ stand for the increase ratio of the estimated maximum concrete stress, the average axial strain corresponding to the concrete maximum stress, the average modulus of elastic, the estimated concrete stress and average axial strain just before the end of the test with respect to the corresponding average parameters of the specimens without CFRP confinement (000-10 or 000-15). It is important to point out that the parameters of 000-10 and 000-15 are obtained from the average of parameters of 000-10a and 000-10b, 000-15a and 000-15b, respectively. Since specimen

335-15 did not reach failure, parameters $\frac{f_c^{ult}}{f_{c-000}^{ult}}$ and $\frac{\overline{\varepsilon_c^{ult}}}{\overline{\varepsilon_{c-000}^{ult}}}$ could not be obtained.

Table 4.3: Summary of increments in parameters due to CFRP confinement

Specimen	$\frac{f_c^{max}}{f_{c-000}^{max}}$	$\frac{\overline{\varepsilon_c^{max}}}{\overline{\varepsilon_{c-000}^{max}}}$	$\frac{\overline{E_c}}{\overline{E_{c-000}}}$	$\frac{f_c^{ult}}{f_{c-000}^{ult}}$	$\frac{\overline{\varepsilon_c^{ult}}}{\overline{\varepsilon_{c-000}^{ult}}}$	$\frac{\overline{E_D}}{\overline{E_{D-000}}}$
225-10	1.29	1.33	0.97	1.54	1.10	0.33
225-15	1.05	1.13	0.97	0.82	1.38	4.30
235-10	1.10	1.83	0.62	1.31	1.57	0.11
235-15	1.09	1.37	1.71	1.06	1.56	0.73
325-10	1.16	2.92	0.84	1.22	2.83	0.36
325-15	1.13	1.60	1.09	1.00	1.72	3.61
335-10	1.29	2.42	0.96	1.50	1.97	1.37
335-15	1.19	1.77	0.77	-	-	-

The axial stress-strain parameters were obtained considering:

- No concrete confinement influence from the steel stirrups according to Mander, Priestley, & Park (1988a) procedure.
- Perfectly elastic plastic behavior of steel bars and no buckling of longitudinal bars occurred before failure of the specimen: $f_s = \min(f_y, E_s\varepsilon)$.
- Nominal steel bars transverse cross section (A_s).
- Concrete load calculated as the total load minus the load carried by the vertical bars $(P_c = P_T - A_s * f_s)$. Average concrete stress obtained by dividing the concrete load by the transverse gross cross section of the column minus the nominal area of vertical steel bars $\left(f_c = \frac{P_c}{A_g - A_s}\right)$

- Individual axial strains calculated for each vertical LVDT $\left(\varepsilon_{ind} = \frac{\Delta}{h}\right)$. Average column strain, obtained as the average of individual axial strains ($\varepsilon = \overline{\varepsilon}_{ind}$).
- Since a forced control testing machine was used, the end of testing was considered as the instant before the rate of applied strain changed abruptly as is explained in Appendix B.

4.2 Failure mode of specimens

4.2.1 Specimens 000-10a and 000-10b

Specimens 000-10a and 000-10b failed explosively at a load of 147 tonf and 142 tonf, respectively. The average maximum vertical displacements before failure of the specimens, measured by vertical LVDTs, were approximately 1.58 mm and 0.98 mm, respectively. Since vertical LVDTs captured deformation inside a height of 500 mm, the corresponding average maximum vertical deformations were approximately 0.0031 and 0.0019, respectively. The columns were loaded concentrically until failure at axial compressive strain rates up to 5.99e-6/s and 1.14e-5/s. After failure, the strain rates changed abruptly because the testing machine was force controlled. For this reason, only data captured until the abrupt change in strain rate is considered.

In both specimens, failure occurred suddenly with little to no cracks on the surface prior to the explosion. During the explosions, several concrete fragments were ejected from the specimen at high speeds, LVDTs located at the surface were also ejected at high speeds. Transverse steel stirrups did not provide sufficient confinement and ductility since the specimen failed completely at the same instant that the cover outside the stirrups was lost. Failure was characterized by cover loss and vertical bar buckling.

Figure 4.1 shows the failure mode of specimen 000-10a. Buckling of steel bars was localized at the top and the bottom of the specimen (Figure 4.1a, 4.1c). Concrete cover was loss at the bottom 20 cm on the front side and at the upper 20 cm on the back side (Figure 4.1b, 4.1c). Longitudinal cracks appeared on the front side of the column (Figure 4.1c). Buckling of steel bars was influenced by the transverse steel reinforcement but not prevented (Figure 4.1d). The absence of steel ties provoked that vertical bars in the middle of the specimen buckled with an effective length much larger than the separation of stirrups (Figure 4.1d). The 90-degree shape of the transverse reinforcement provoked opening of stirrups at corners in localized failure zones (Figure 4.1a).

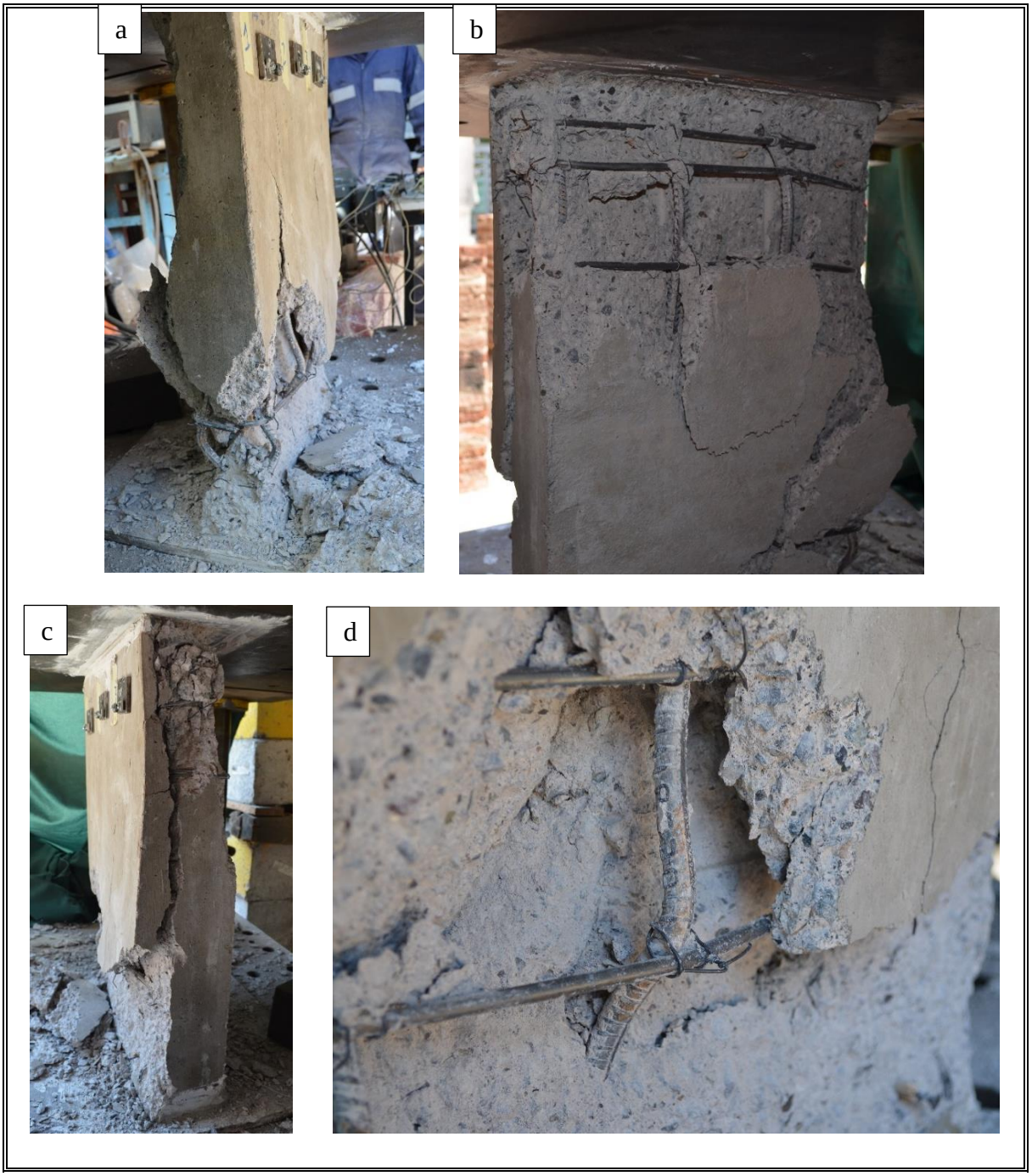

Figure 4.1: Failure mode of specimen 000-10a

Figure 4.2 shows the failure mode of specimen 000-10b. Failure was localized at the bottom of the specimen where cover was lost in all fronts (Figure 4.2a, 4.2b). Buckling of vertical bars at the middle of the specimen presented an effective longitude higher than the separation of the stirrup; however, vertical bars located at the corners experienced buckling between stirrups (Figure 4.2a, 4.2b, 4.2c).

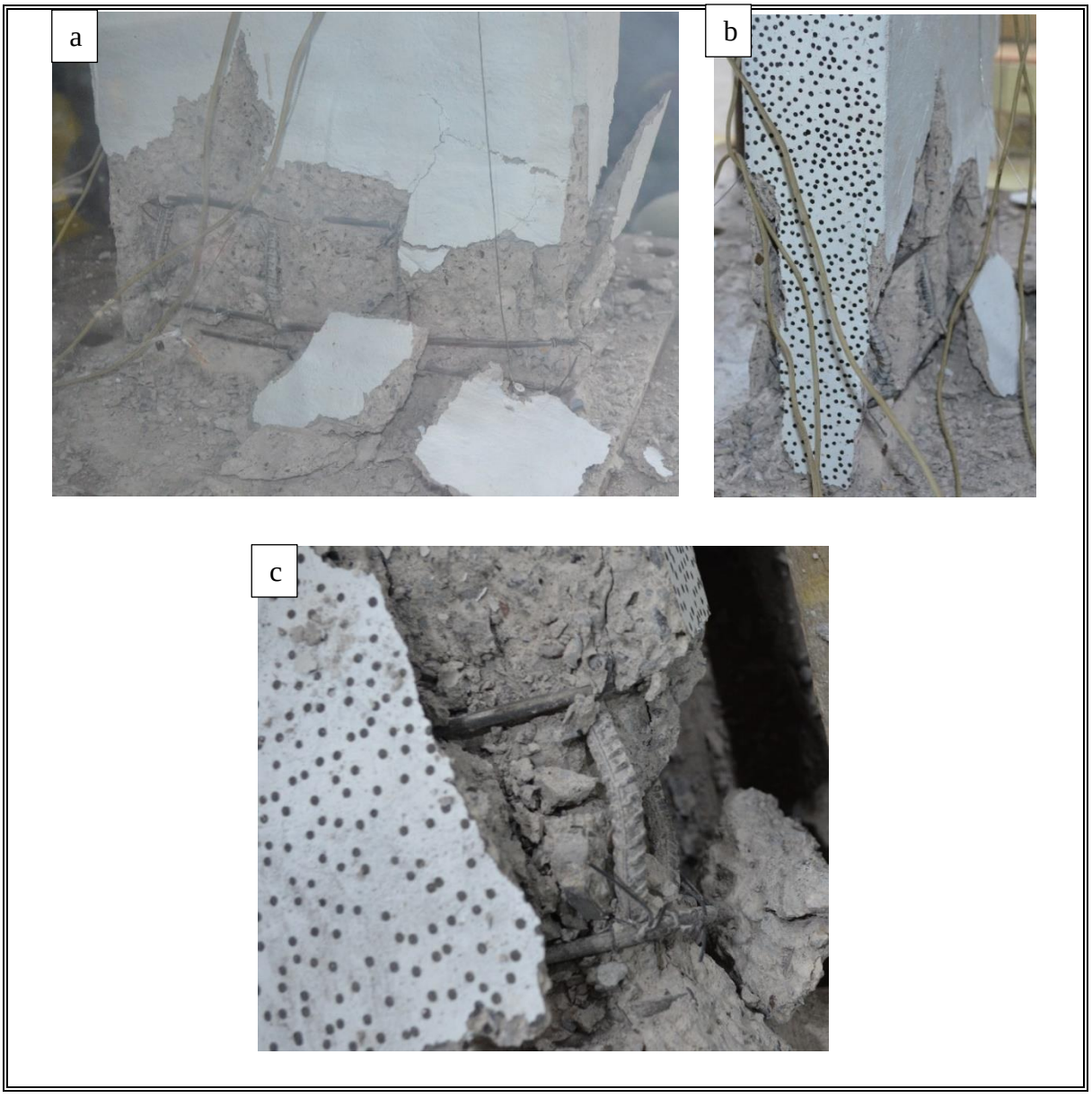

Figure 4.2: Failure mode of specimen 000-10b

4.2.2 Specimens 000-15a and 000-15b

Specimens 000-15a and 000-15b failed explosively at a load of 229 tonf and 246 tonf, respectively. The average maximum vertical displacements before failure of the specimens, measured by vertical LVDTs, were approximately 1.40 mm and 1.77 mm, respectively. Since vertical LVDTs captured deformation inside a height of 500 mm, the corresponding average maximum vertical deformations were approximately 0.0028 and 0.0035, respectively. The columns were loaded concentrically until failure with axial compressive strain rates up to 4.81e-6/s and 6.80e-6/s. After failure, the strain rates changed abruptly because the testing machine was force controlled. For this reason, only data captured until the abrupt change in strain rate is considered.

In both specimens, failure was sudden with no indication of cracks prior the explosion. During the explosions, several concrete fragments were ejected from the specimen at high speeds, LVDTs located at the surface were also ejected at high speeds. A shear band generated on both specimens, along this shear band vertical bar buckling was localized. Failure occurred just after concrete cover was lost, therefore, transverse steel reinforcement was unsuccessful in providing confinement and ductility to the columns.

Figure 4.3 shows the failure mode of specimen 000-15a. The shear band crossed fully the middle of the column at an angle of approximately 35 degrees (Figure 4.3b). All vertical bars o along the shear band buckled (Figure 4.3b, 4.3c). Vertical bars located at the middle of the column buckled with an effective length larger than the separation between stirrups (Figure 4.3b, 4.3d). Vertical bars at the corners of the column buckled with an effective length closer to the distance between stirrups (Figure 4.3c), except in corners

where transverse reinforcement opened due to 90-degree transverse reinforcement (Figure 4.3d).

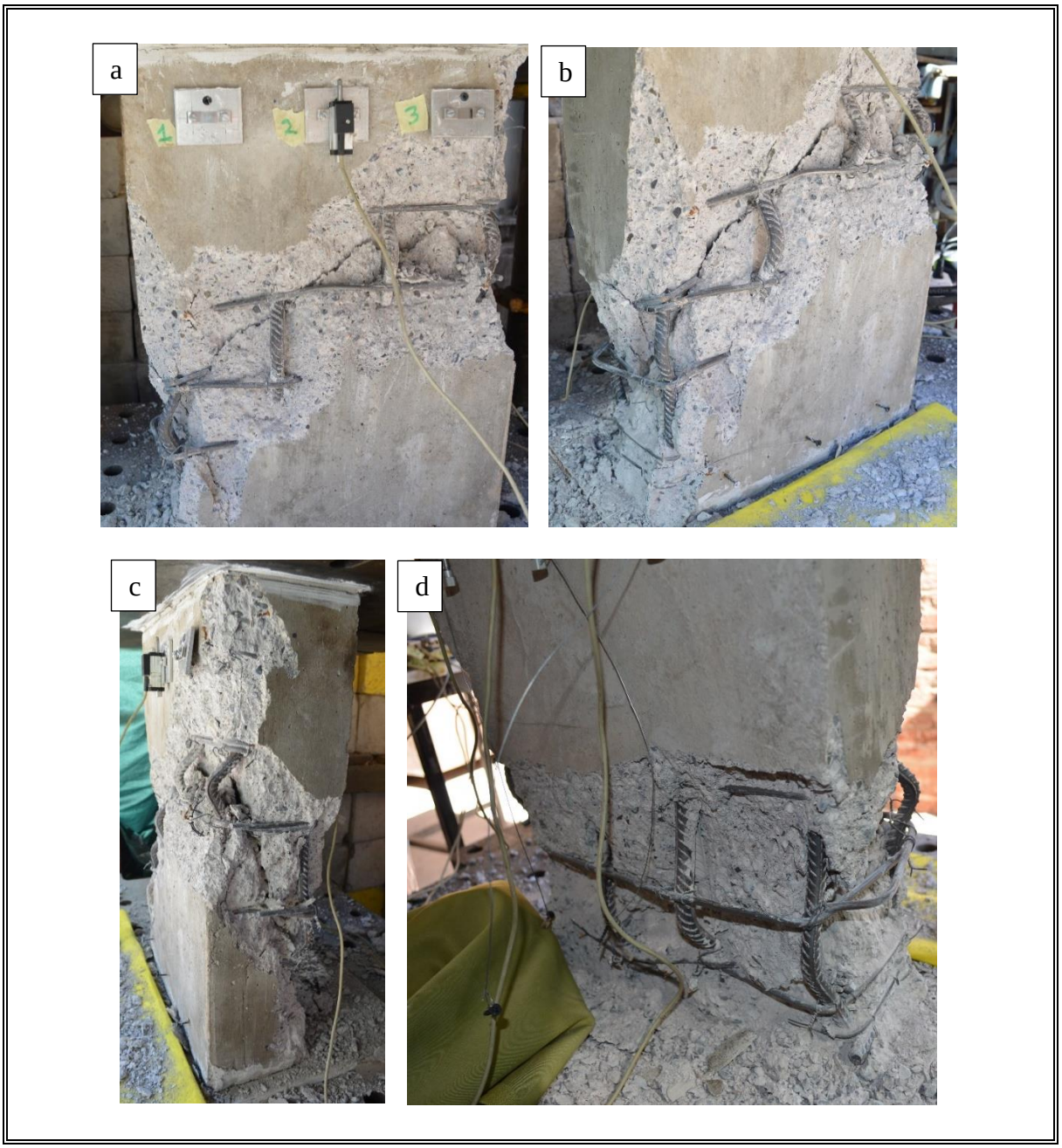

Figure 4.3: Failure mode of specimen 000-15a

Figure 4.4 shows the failure mode of specimen 000-15b. The shear band crossed half the columns at an angle of approximately 30 degrees (Figure 4.4a, 4.4c). Vertical bars at the

middle of the column buckled with an effective length larger than the separation of stirrups (Figure 4.4a). Vertical bars at the corners buckled with an effective length close to the separation between stirrups except when the stirrups opened due to the 90-degree disposition (Figure 4.4b, 4.4d)

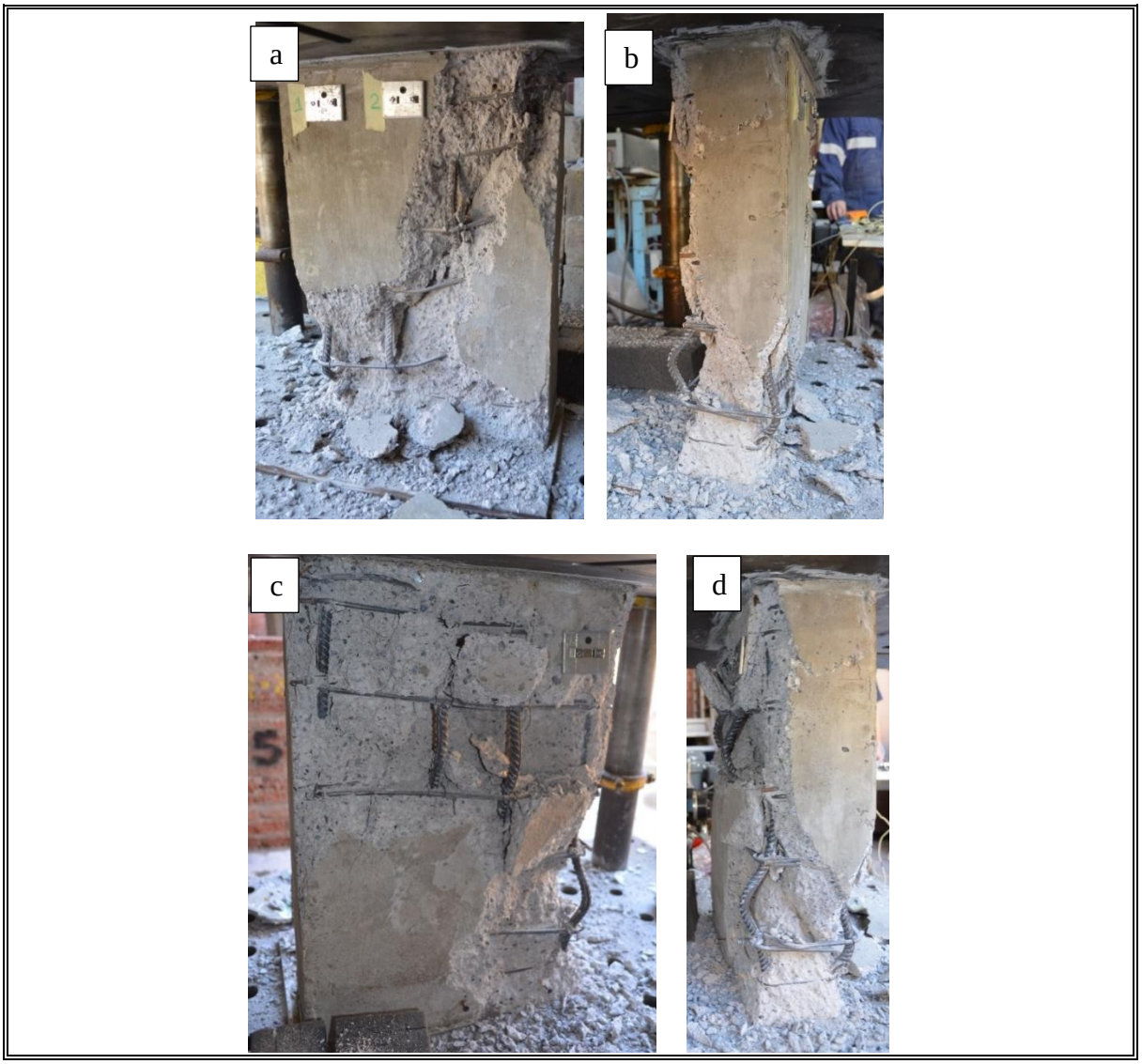

Figure 4.4: Failure mode of specimen 000-15b

4.2.3 Specimen 225-10

Specimen 225-10 failed at a load of 180 tonf. The average maximum vertical displacements before failure of the specimens, measured by vertical LVDTs, was approximately 1.59 mm. Since vertical LVDTs captured deformation inside a height of 500 mm, the corresponding average maximum vertical deformation was approximately 0.0032. The column was loaded concentrically until failure with an average axial compressive strain rate of 3.56e-5/s. After failure, the strain rates changed abruptly because the testing machine was force controlled. For this reason, only data captured until the abrupt change in strain rate is considered.

Failure was not explosive and was characterized by a progressive and localized rupture of the CFRP reinforcement at the bottom left of the specimen, the maximum load was maintained before failure. The failure zone started at the bottom corner, then propagated vertically approximately 20 cm and finally horizontally through the complete width of the column (Figure 4.5a). No other fractures of the CFRP were observed outside of the failure zone (Figure 4.5c).

After failure, crushed concrete came out of the failure zone (Figure 4.5d); however, concrete fragments were not ejected at high speeds as happened in specimens with no CFRP confinement. LVDTs located at the surface of the specimen were not ejected at high speed as was the case in specimen without CFRP confinement. Concrete outside the failure zone remained uncracked on the surface (Figure 4.5c). Since the specimen was fully wrapped with CFRP confinement, no loss of concrete cover was experienced.

Vertical steel bars located at the corner of the failure zone buckled, while vertical bars located in the middle of the column did not buckle (Figure 4.5b). CFRP confinement

prevented vertical bar buckling outside the failure zone. Buckled bars at the failure zone presented an effective length close to the height of the CFRP rupture. Two CFRP anchors located at the fracture zone were broken on the front side of the column (Figure 4.5a). Only one strain gage was installed on this specimen. This strain gage was not located at the failure zone, it was located at a corner in mid height of the specimen.

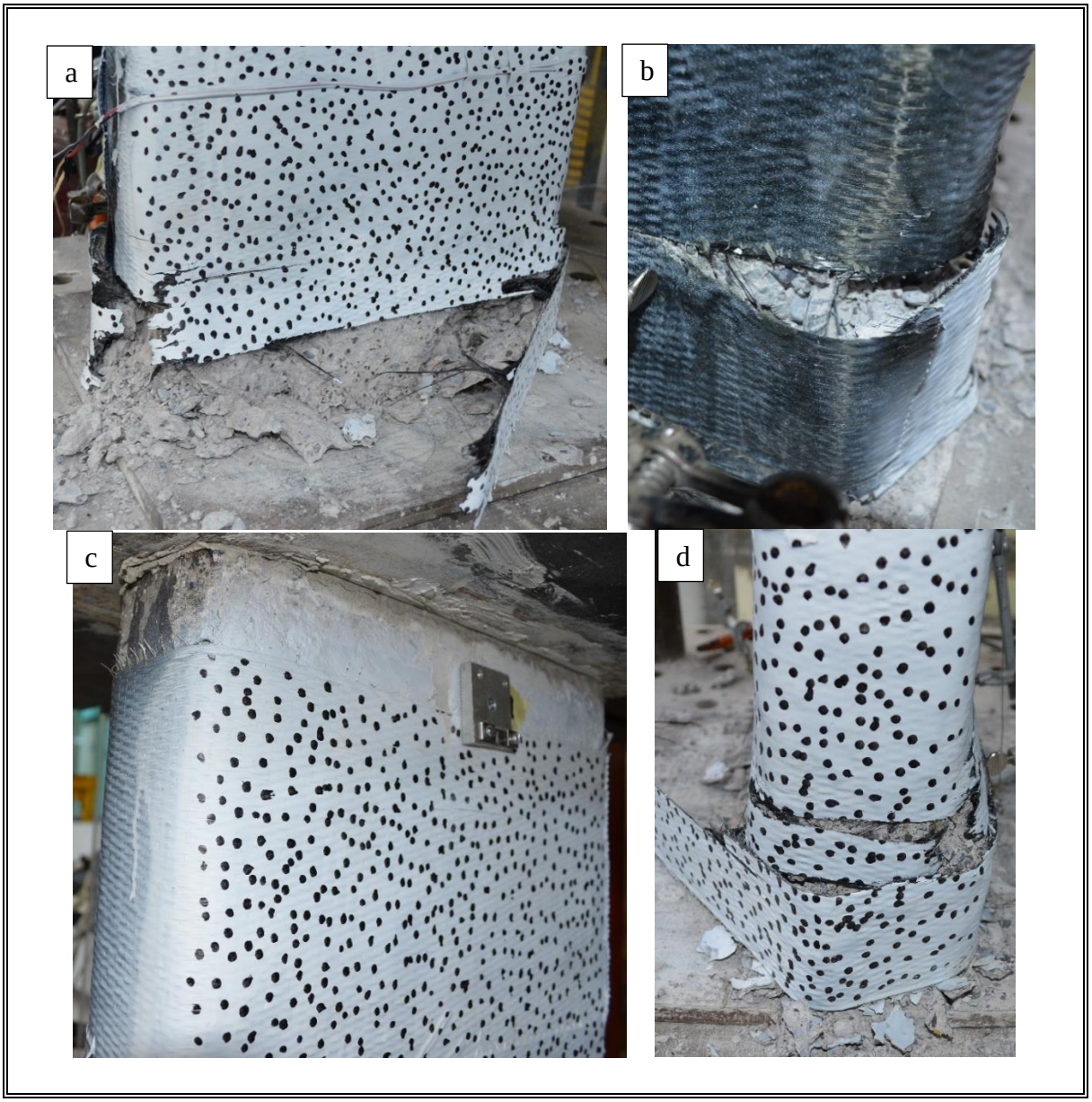

Figure 4.5: Failure mode of specimen 225-10

4.2.4 Specimen 225-15

Specimen 225-15 failed at a load of 246 tonf. The average maximum vertical displacements before failure of the specimens, measured by vertical LVDTs, was approximately 2.18 mm. Since vertical LVDTs captured deformation inside a height of 500 mm, the corresponding average maximum vertical deformation was approximately 0.0044. The column was loaded concentrically until failure with an average axial compressive strain rate of 3.41e-6/s. After failure, the strain rates changed abruptly because the testing machine was force controlled. For this reason, only data captured until the abrupt change in strain rate is considered.

Failure was not abruptly and the specimen maintained the maximum load before CFRP rupture. CFRP rupture was localized at two failure zones located at the bottom corner and mid height. Rupture of the CFRP at both failure zones occurred almost simultaneously. The bottom corner failure zone originated at the corner, then propagated in the vertical direction 10 cm approximately and horizontally in the complete width of the specimen (Figure 4.6a). Several fractures were observed in the CFRP reinforcement at the mid height failure zone, through these fractures crushed concrete was observed (Figure 4.6c, 4.6d).

Crushed concrete came out of all the failure zones. A concrete layer was attached to ruptured CFRP wraps, showing that the adherence between CFRP and surface concrete was strong (Figure 4.6d). Outside the failure zones no crushed concrete was observed (Figure 4.6a). Concrete fragments or LVDTs located at the surface of the specimen were not ejected at high speeds as happened in specimens with no CFRP confinement. Concrete outside the failure zones remained uncracked on the surface, since the specimen was fully wrapped with CFRP confinement, no loss of concrete cover was experienced (Figure 4.6a).

Vertical bars buckled only at the bottom corner failure zone. These bars buckled with an effective length close to the height of the failure zone. CFRP confinement prevented bar buckling outside of the failure zones. Opening of transverse steel reinforcement was not observed. Four CFRP anchors ruptured at the bottom corner and mid height failure zones. A strain gage was located at one corner in mid height but was not close to the failure zones.

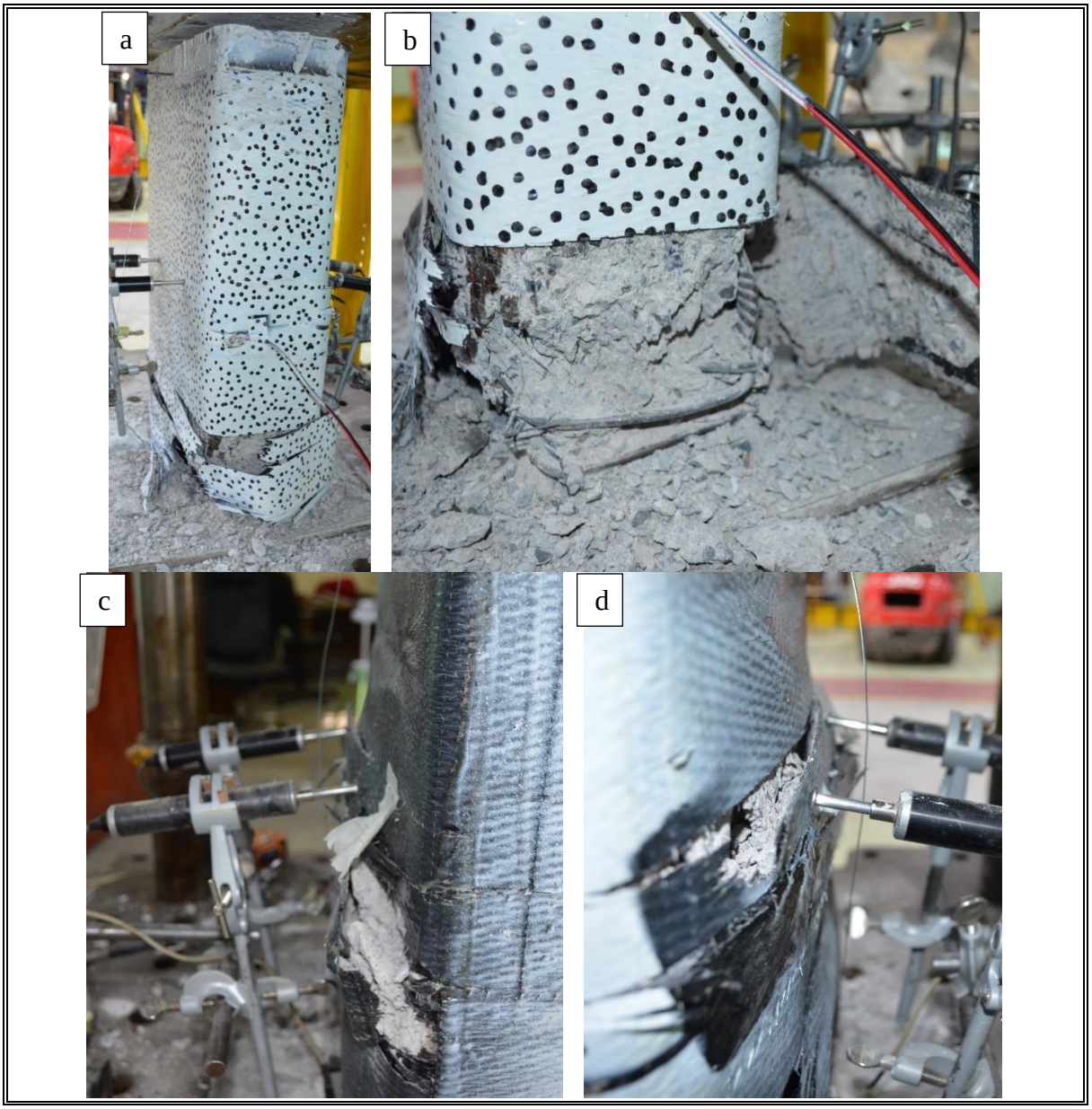

Figure 4.6: Failure mode of specimen 225-15

4.2.5 Specimen 235-10

Specimen 235-10 failed at a load of 157 tonf. The average maximum vertical displacements before failure of the specimens, measured by vertical LVDTs, was approximately 2.79 mm. Since vertical LVDTs captured deformation inside a height of 500 mm, the corresponding average maximum vertical deformation was approximately 0.0056. The column was loaded concentrically until failure with an average axial compressive strain rate of 2.05e-5/s. After failure, the strain rates changed abruptly because the testing machine was force controlled. For this reason, only data captured until the abrupt change in strain rate is considered.

Failure was not explosive and the specimen maintained values close to the maximum load before failure. CFRP rupture concentrated at the bottom of the specimen (Figure 4.7). It originated at the left corner at a height of 10 cm and then propagated horizontally in the complete width of the column (Figure 4.7a). CFRP anchor ruptured during the horizontal propagation (Figure 4.7c, 4.7d). CFRP wraps outside of the failure zone did not fracture.

No concrete cover was lost since the specimen was fully wrapped (Figure 4.7a, 4.7b). A layer of concrete cover was adhered to the fractured CFRP showing that the superficial adherence was strong. Crushed concrete came out of the failure zone (Figure 4.7c, 4.7d).

A vertical bar buckled in the failure zone at the corner of the specimen. The vertical bar buckle with an inside direction. The effective longitude of the buckle bar was close to the height of the failure zone. CFRP confinement prevented buckling of vertical bars outside of the failure zone. No steel transverse reinforcement opening was observed.

One strain gage was installed at a corner in mid height of the specimen, but not strain gage was installed near the failure zone. No concrete fragments or LVDTs on surface were ejected during the failure.

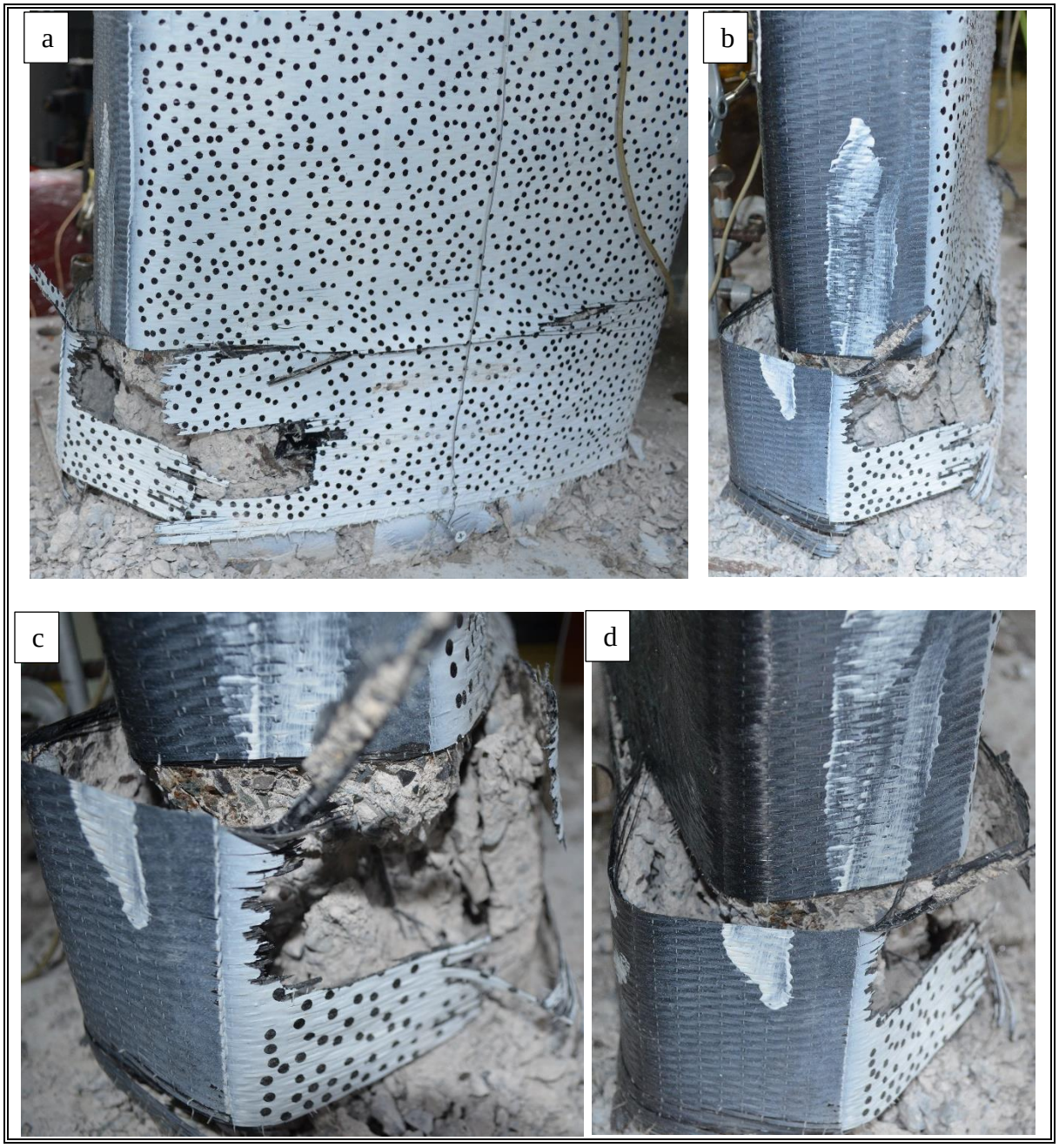

Figure 4.7: Failure mode of specimen 235-10

4.2.6 Specimen 235-15

Specimen 235-15 failed at a load of 254 tonf. The average maximum vertical displacements before failure of the specimens, measured by vertical LVDTs, was approximately 3.08 mm. Since vertical LVDTs captured deformation inside a height of 500 mm, the corresponding average maximum vertical deformation was approximately 0.0062. The column was loaded concentrically until failure with an average axial compressive strain rate of 3.31e-6/s. After failure, the strain rates changed abruptly because the testing machine was force controlled. For this reason, only data captured until the abrupt change in strain rate is considered.

Failure of the specimen was not abruptly and the specimen maintained values close to the maximum load during failure. CFRP rupture concentrated on bottom half of the column at the left and right corners. Failure on the left corner began at the bottom of the specimen, propagated vertical until mid-height of the specimen and then horizontally throughout the width of the column (Figure 4.8a, 4.8b, 4.8c). Failure on the right corner also began at the bottom, propagated vertically approximately 15 cm and horizontally around the right corner (Figure 4.8d, 4.8e).

Crushed concrete came out of the failure zones, but concrete outside the failure zones remained solid. Cover concrete was adhered to fractured CFRP showing good superficial adherence (Figure 4.8e). No concrete fragments or LVDTs were ejected at high speed as was the case with columns without CFRP confinement. Concrete cover was not lost after failure since the columns was fully wrapped in CFRP confinement.

Vertical bars located at the corners of the failure zone buckled. Bars located at corners buckled with an effective longitude close to the distance between stirrups (Figure

4.8b, 4.8e). Bars located at the middle of the column with an effective longitude higher that the distance between stirrups but only after the CFRP confinement was ruptured (Figure 4.8e). No opening of transverse steel reinforcement was observed.

CFRP anchors were fractured at the left corner failure zone (Figure 4.8e). CFRP anchors at mid height did not fractures since failure propagation followed a path where no CFRP anchors were installed (Figure 4.8a). One strain gage was installed at mid height near the right corner of the column. This strain gage was inside the failure zone.

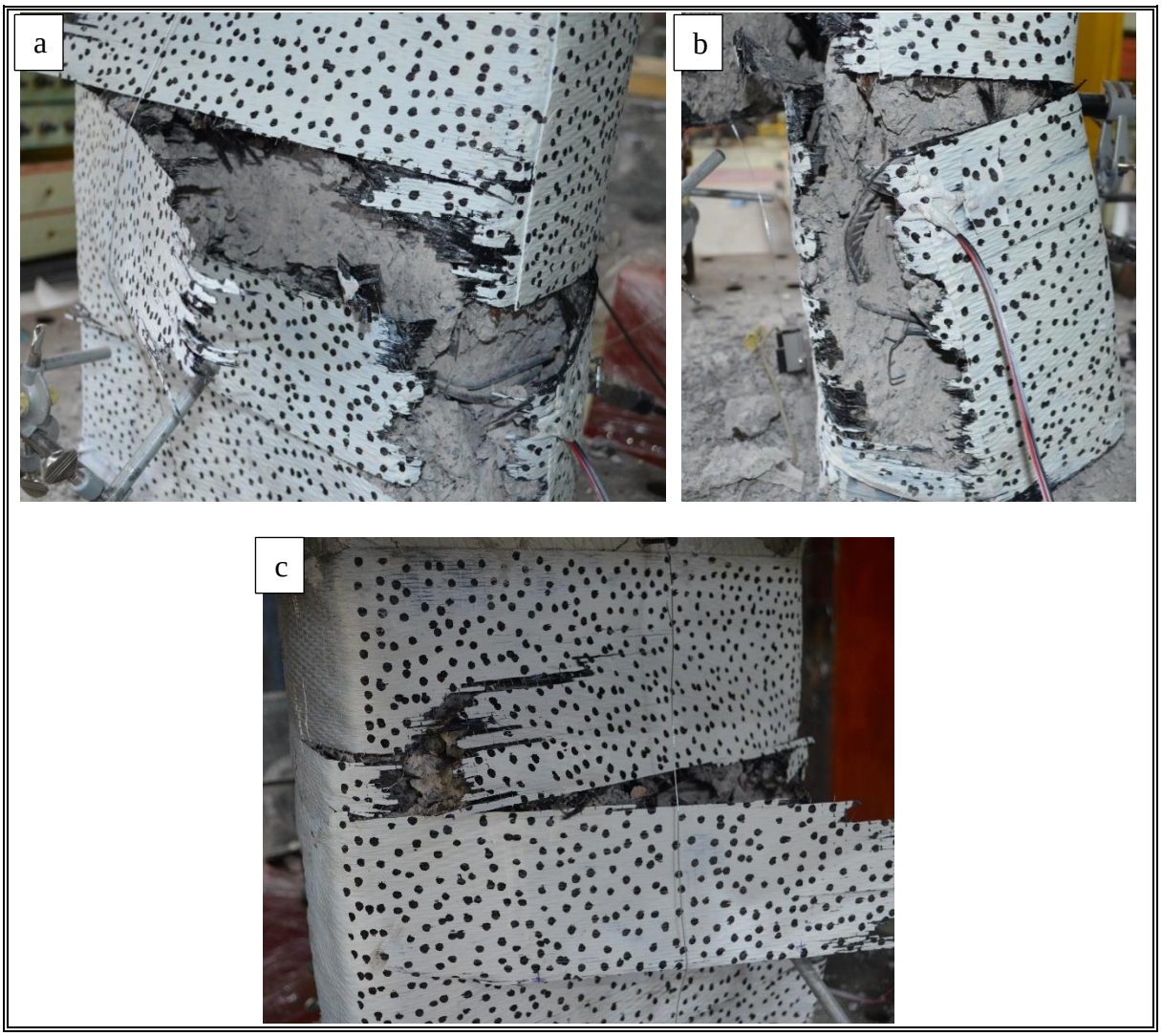

Figure 4.8: Failure mode of specimen 235-15

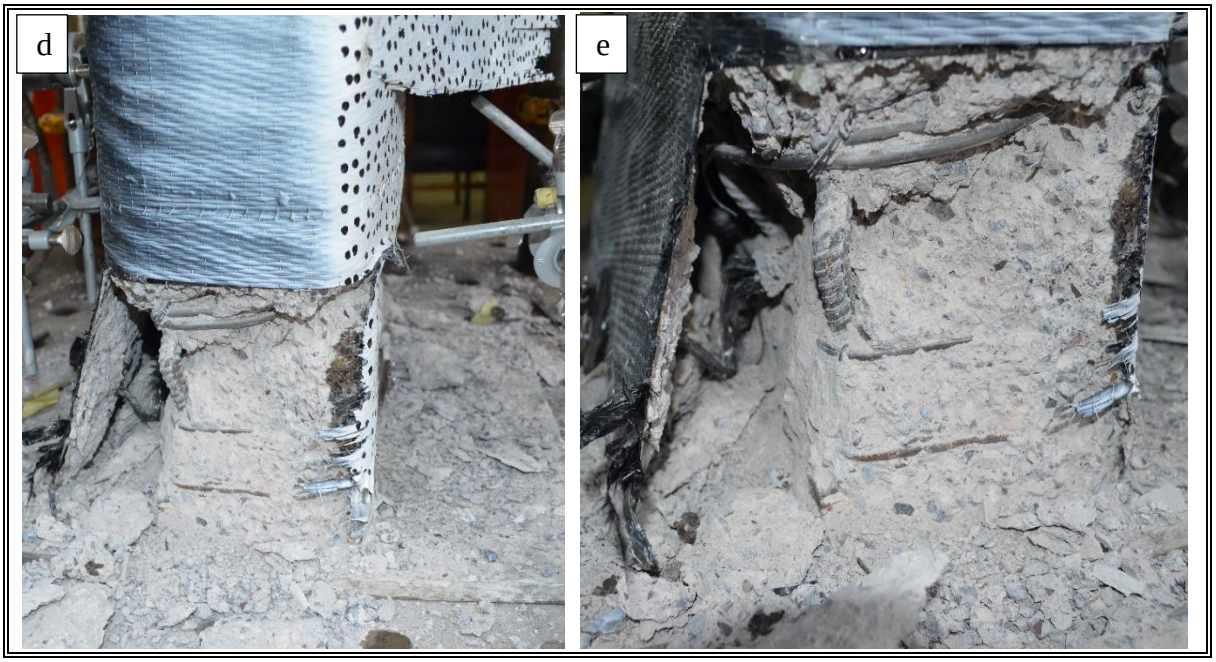

Figure 4.8: Failure mode of specimen 235-15 (continuation)

4.2.7 Specimen 325-10

Specimen 325-10 failed at a load of 165 tonf. The average maximum vertical displacements before failure of the specimens, measured by vertical LVDTs, was approximately 4.27 mm. Since vertical LVDTs captured deformation inside a height of 500 mm, the corresponding average maximum vertical deformation was approximately 0.0085. The column was loaded concentrically until failure with an average axial compressive strain rate of 3.58e-5/s. After failure, the strain rates changed abruptly because the testing machine was force controlled. For this reason, only data captured until the abrupt change in strain rate is considered.

CFRP failure was localized at the top middle portion of the column. The failure zone originated at the center of the specimen at the top CFRP fibers, then it propagated vertically 10 cm and finally horizontally in the complete width of the specimen (Figure 4.9).

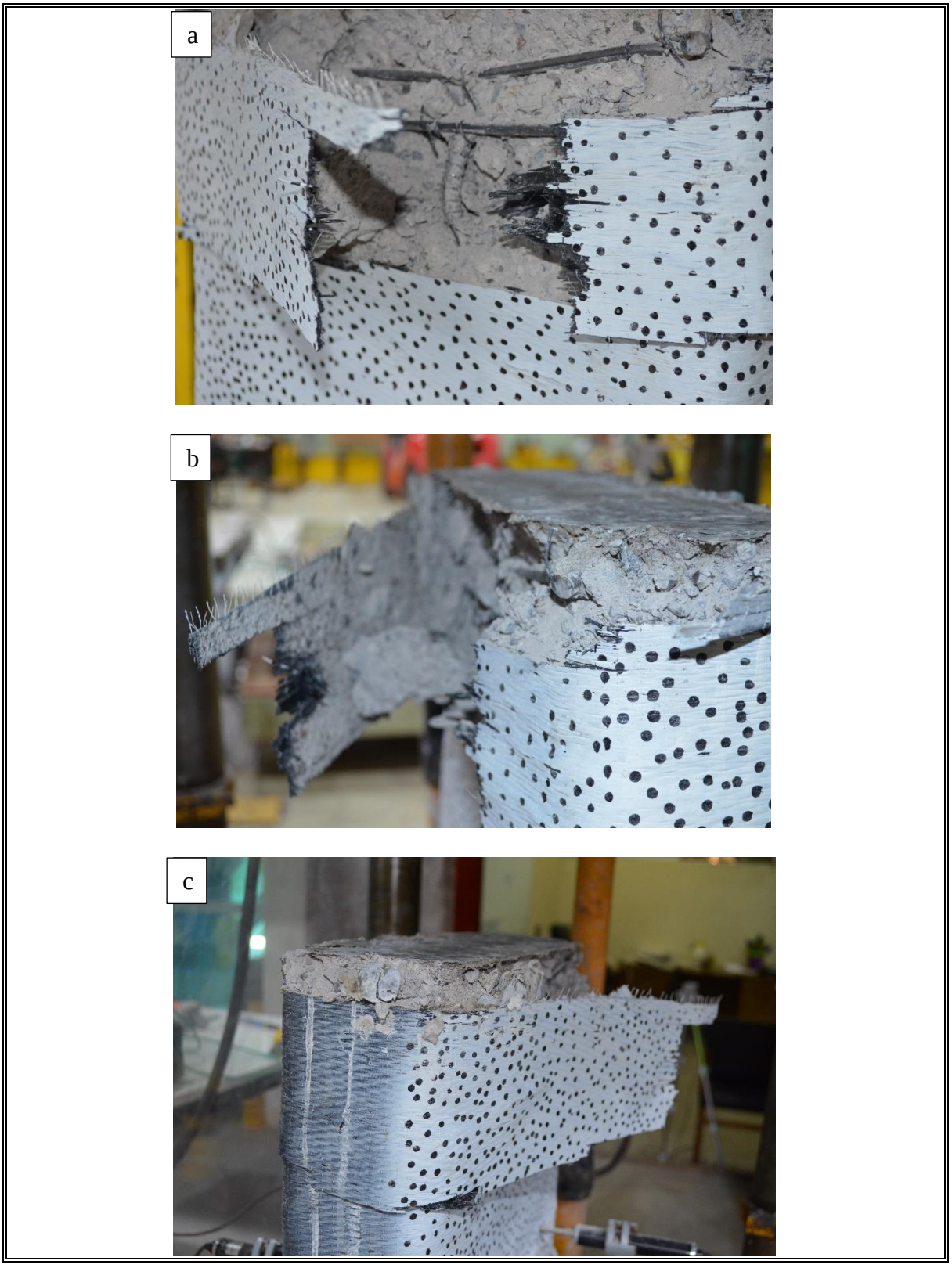

Figure 4.9: Failure mode of specimen 325-10

Two CFRP anchors ruptured as the failure zone propagated horizontally (Figure 4.9a, 3.9b). The CFRP wraps were not fractured at any of the corners of the specimen (Figure 4.9). CFRP wraps outside the failure zone did not break.

Failure was not explosive, crushed concrete came out of the failure zone (Figure 4.9a), but no fragments were ejected with high speed as in specimens without CFRP confinement. LVDTs placed on the surface of the column were no ejected as well. Concrete at the top of the specimen was not crushed (Figure 4.9a, 4.9c). Concrete cover was not lost before failure due to the column being fully wrapped.

Vertical bars located inside the failure zone at the middle of the cross section buckled with an effective longitude close to the separation between stirrups (Figure 4.9a). Vertical bars at the column corners did not buckle even the ones inside the failure zone. No opening of transverse reinforcement was observed.

Two strain gages were installed, one in at a corner mid height and other at mid height 12 cm away from the corner. None of the strain gages were located inside the failure zone but were near only 7 cm below.

4.2.7 Specimen 325-15

Specimen 325-15 failed at a load of 262 tonf. The average maximum vertical displacements before failure of the specimens, measured by vertical LVDTs, was approximately 3.77 mm. Since vertical LVDTs captured deformation inside a height of 500 mm, the corresponding average maximum vertical deformation was approximately 0.0075. The column was loaded concentrically until failure with an average axial compressive strain rate of 4.47e-6/s. After failure, the strain rates changed abruptly because the testing machine

was force controlled. For this reason, only data captured until the abrupt change in strain rate is considered.

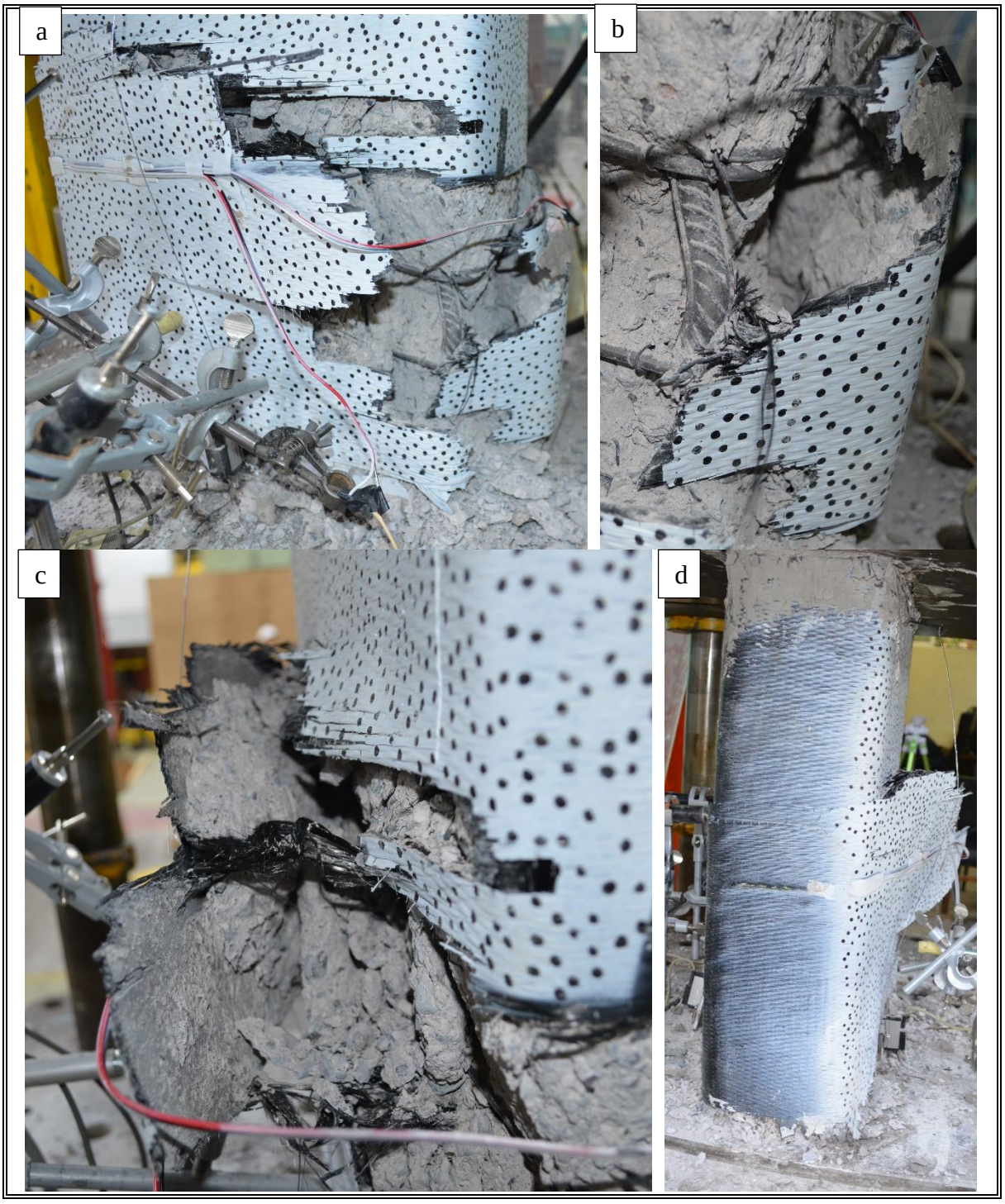

Figure 4.10: Failure mode of specimen 325-15

Failure of the specimen was not explosive and localized at the bottom half of the specimen. CFRP rupture began at the bottom right corner of the specimen, the propagated vertically until mid-height of the column and finally horizontally in the complete width (Figure 4.10a, 4.10c). Three CFRP anchors rupture along the progression of the failure zone (Figure 4.10a, 4.10c). CFRP wraps outside the failure zone were not ruptured.

Crushed concrete came out of the failure zone but no concrete fragments nor LVDTs installed on the surface were ejected as in the specimens without CFRP reinforcement. Portion of concrete cover were attached to ruptured CFRP wraps show the good quality of superficial adherence. Concrete outside of the failure zone was not damaged. Concrete cover was not lost due to the column being fully wrapped.

Vertical bars located inside the failure zone at the corner of the column buckled with an effective longitude close to the separation between stirrups (Figure 4.10a, 4.10b). Vertical bars located at the center of the cross section of the column did not buckled. Transverse reinforcement opening was not observed. Two strain gages were placed at mid-height, one on the right corner and other 12 cm away from the corner horizontally. None of the strain gages were inside the failure zone, but the second strain gage was close to the area of failure.

4.2.8 Specimen 335-10

Specimen 335-10 failed at a load of 180 tonf. The average maximum vertical displacement before failure of the specimens, measured by vertical LVDTs, was approximately 2.30 mm. Since vertical LVDTs captured deformation inside a height of 500 mm, the corresponding average maximum vertical deformation was approximately 0.0046. The column was loaded concentrically until failure with an average axial compressive strain

rate of 8.58e-6/s. After failure, the strain rates changed abruptly because the testing machine was force controlled. For this reason, only data captured until the abrupt change in strain rate is considered.

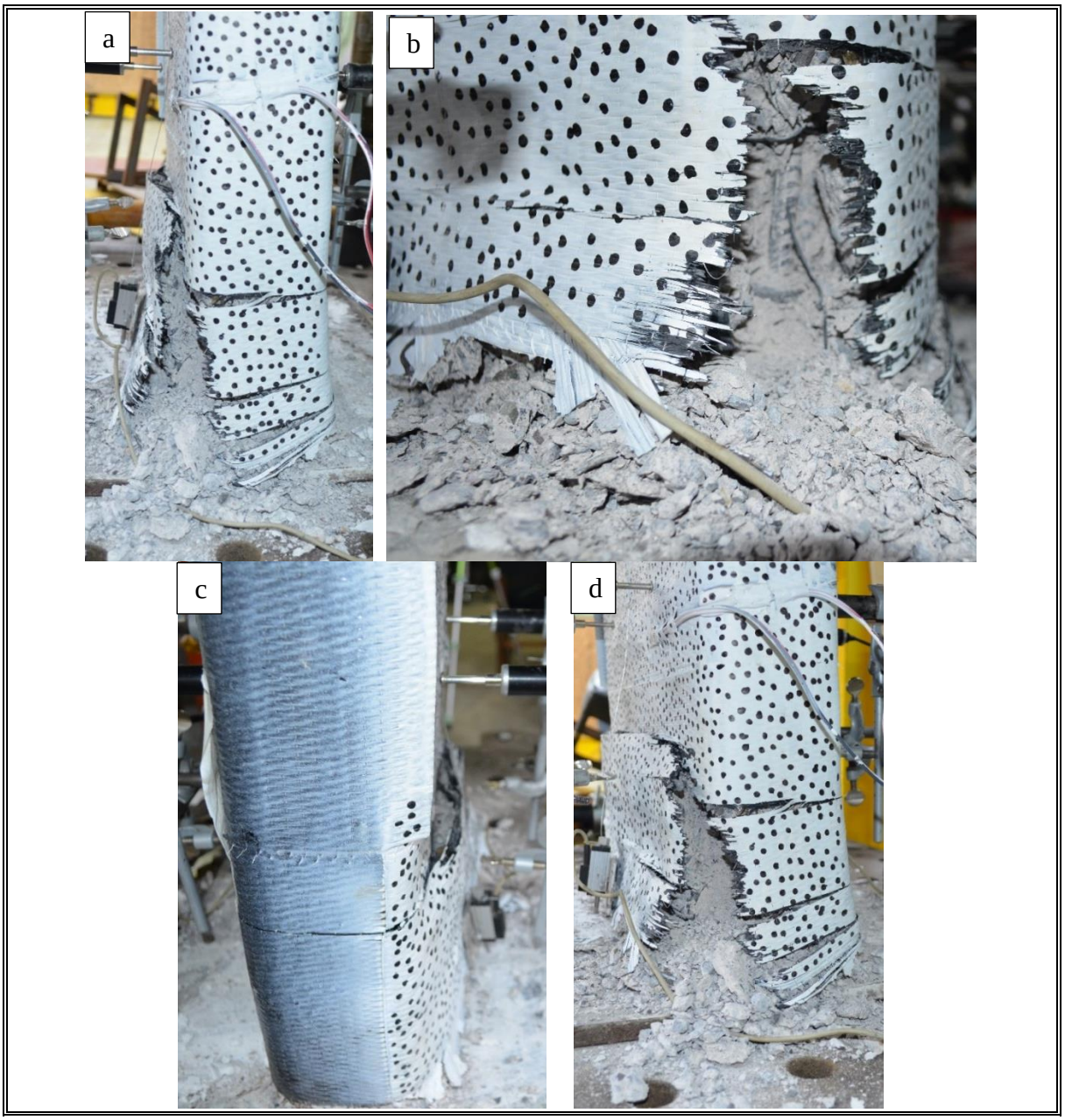

Figure 4.11: Failure mode of specimen 335-10

Failure of the specimen was not explosive and was localized at the bottom half of the column. CFRP rupture began at the bottom right corner, propagated vertically until mid-height and horizontally on the complete width of the specimen (Figure 4.11). Six CFRP anchors located at the lower half of the column were ruptured. CFRP outside the failure zone was not ruptured.

Crushed concrete came out of the failure zone. Concrete at the base of the specimen was also crushed. Concrete fragments and LVDTs placed on the surface of the column were not ejected as in columns without CFRP reinforcement. Concrete outside of the failure zone was not damaged. Cover concrete was not lost during failure due to the column being fully wrapped.

No buckling of vertical bars located at corners was observed (Figure 4.10b). Vertical bars located at the middle of the cross section inside the failure zone buckled (Figure 4.10a, 3.10d). No opening of transverse reinforcement was observed.

Two strain gages were installed at mid-height, one at a corner and the other 12 cm away horizontally from the corner. None of the strain gages were inside the failure zone.

4.2.9 Specimen 335-15

Specimen 335-15 did not fail because the maximum capacity of the testing machine was reached before rupture of the CFRP wraps, the maximum load registered was 275 tonf. The average vertical displacement at the maximum load, measured by vertical LVDTs, was approximately 2.67 mm. Since vertical LVDTs captured deformation inside a height of 500 mm, the corresponding average vertical deformation at the maximum load was approximately 0.0053. The column was loaded concentrically until the maximum capacity of the testing machine with an average axial compressive strain rate of 2.02e-6/s.

Since the column did not reach failure, no CFRP rupture, buckling of vertical bars or opening of transverse reinforcement were observed. Concrete was crushed at the bottom, but not severely enough to cause failure (Figure 4.12). No cracks were observed at any place of the CFRP jacketing.

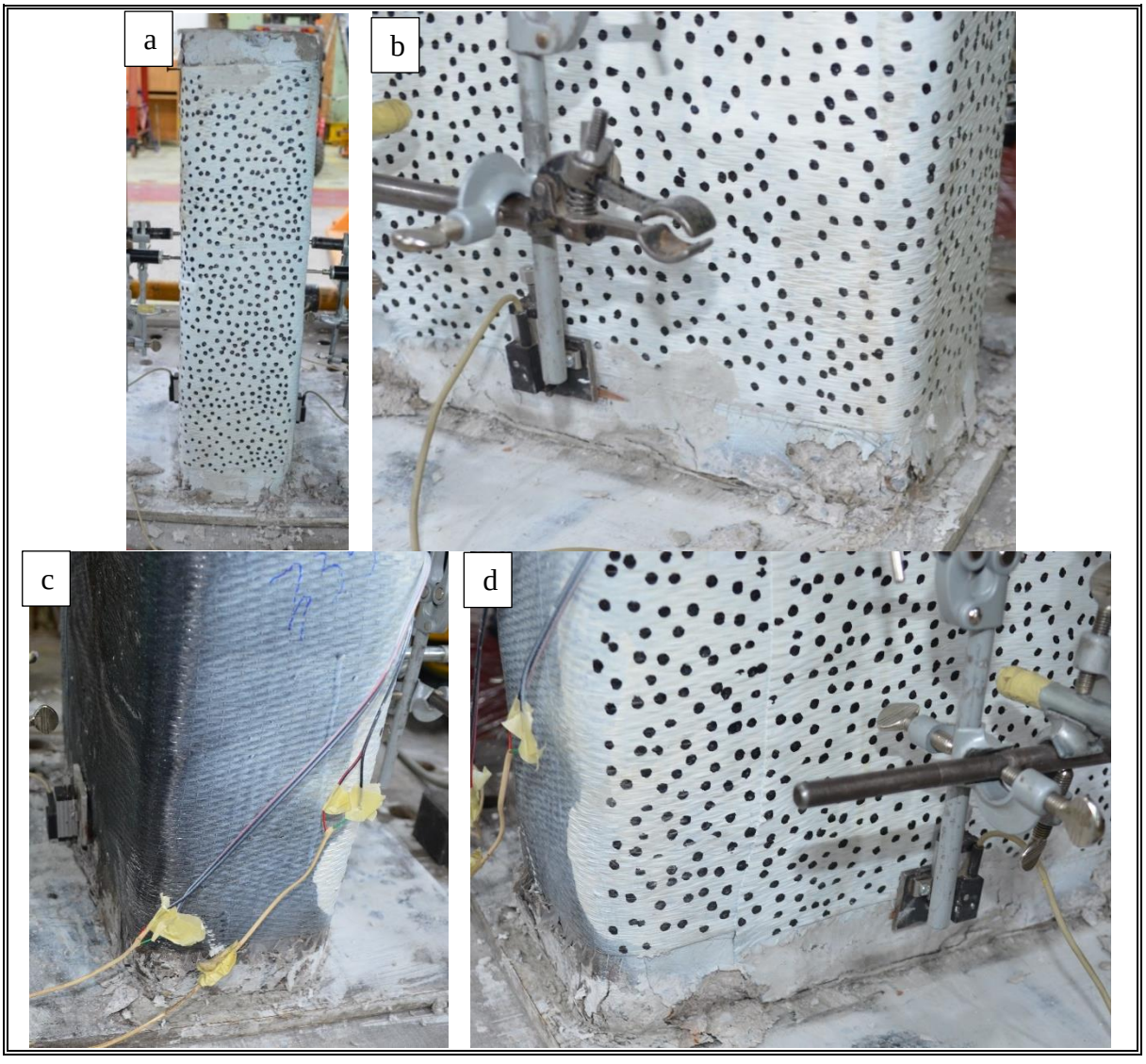

Figure 4.12: Failure mode of specimen 335-15

4.3 Specimens axial behavior

Based on the readings of vertical LVDTs and the testing machine's load cell, the axial load-displacement and stress-strain curves of the specimens are estimated. Vertical LVDTs were placed on the surface of the columns with the disposition showed in Figure 4.13. All measurements (LVDTs, load cell and strain gages where available) were synchronized and captured data at a rate of 20 Hz (20 points per second). Since the testing machine was forced controlled, captured curves presented abrupt changes at the end of the test. The captured data was considered reliable until an abrupt change in at the rate of displacement was observed. See Appendix B.

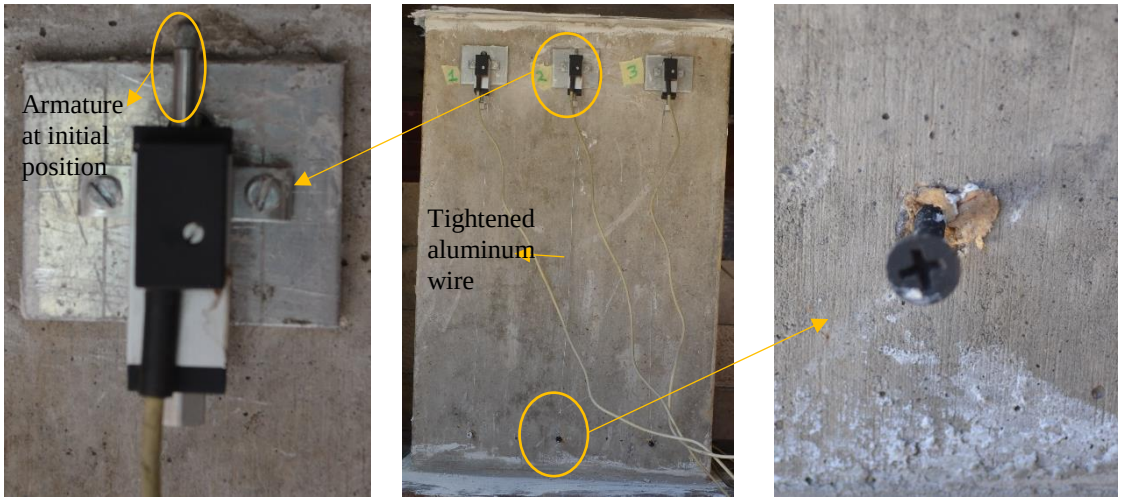

Figure 4.13: Mechanism to capture an average vertical compression displacement

Figures 4.14, 4.15, 4.16, 4.17 and 4.18 show the axial total load vs average axial compressive displacement experimentally obtained in all specimens. Figures 4.19, 4.20, 4.21, 4.22 and 4.23 show the axial compression stress of concrete vs the average axial strain

calculated from the axial load vs axial displacement readings considering the assumptions enumerated in section 3.1. A elastic-perfectly plastic behavior is assumed for the longitudinal bars since the axial strain is considered small enough to neglect hardening.

It is important to mention that since a force controlled testing machine is used, an uncontrolled rate of displacement is applied. This is critical, especially for the last stage of the test since all specimens experienced a softening type of behavior represented by a descending curve after the peak is reached. Because after the peak an uncontrolled rate of displacement is applied it is possible for the testing machine to produce failure of the specimen so fast that the testing equipment was not able to capture it. For this reason, the obtained ultimate deformations of the specimens are conservative values of the actual deformation capacity of the confined columns.

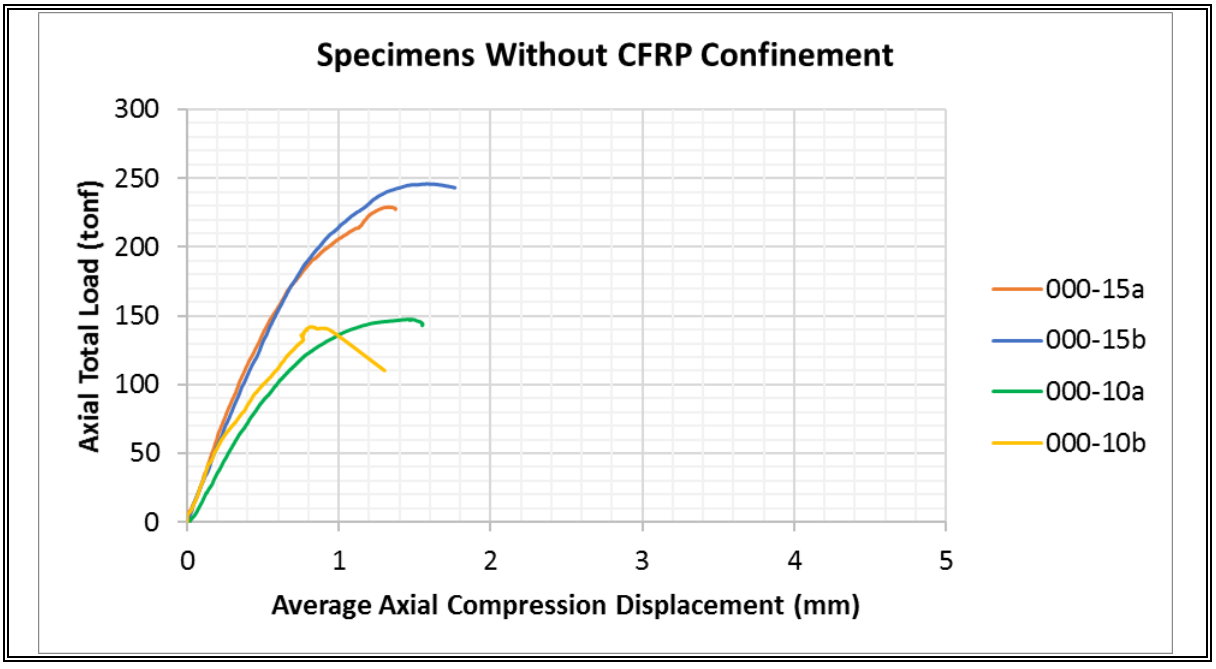

Figure 4.14: Experimental axial total load vs average displacement for control specimens

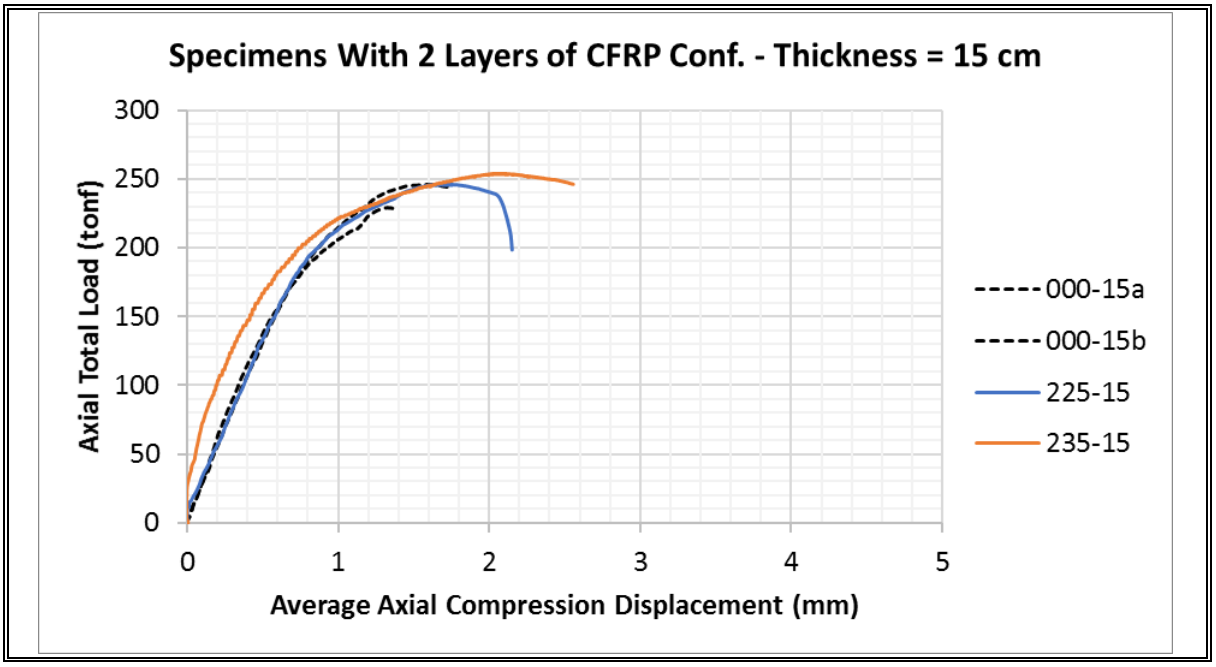

Figure 4.15: Experimental axial total load vs average displacement for specimens with 2 layers of CFRP wrapping (15 cm in thickness)

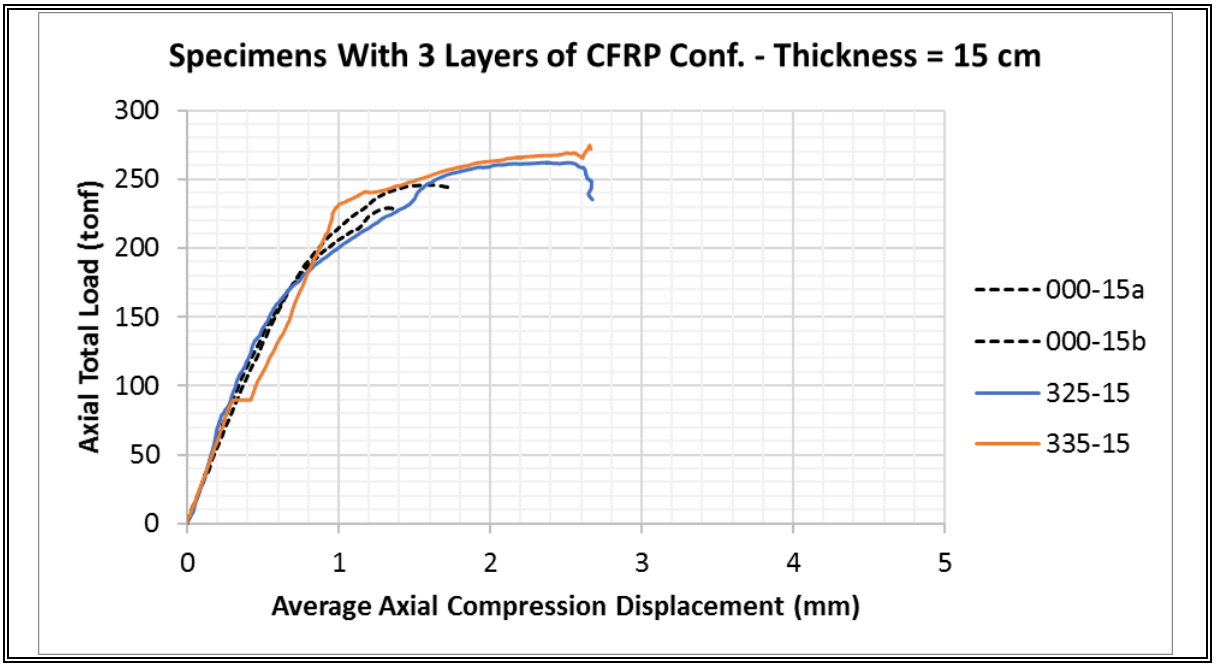

Figure 4.16: Experimental axial total load vs average displacement for specimens with 3 layers of CFRP wrapping (15 cm in thickness)

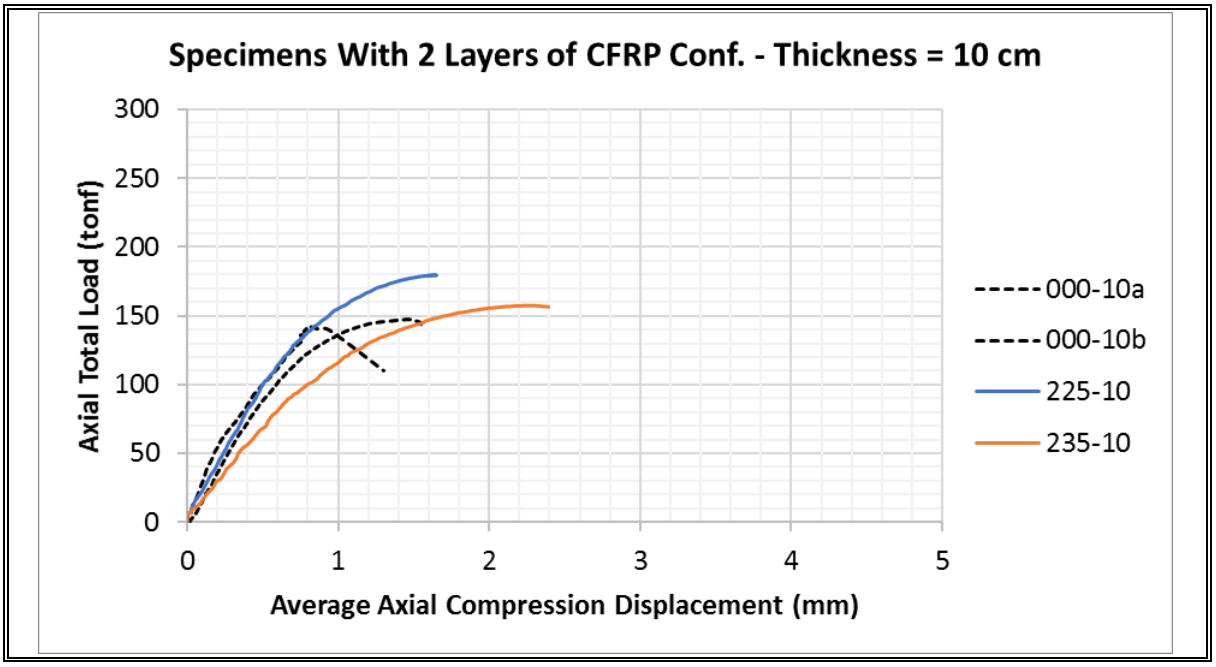

Figure 4.17: Experimental axial total load vs average displacement for specimens with 2 layers of CFRP wrapping (10 cm in thickness)

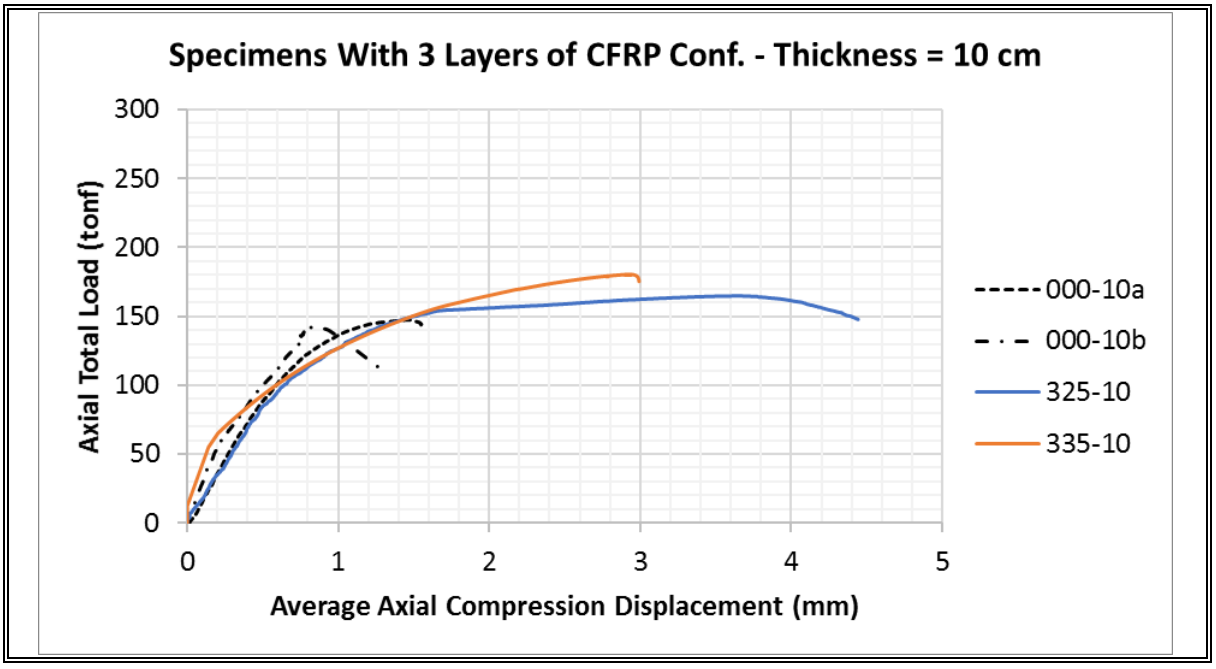

Figure 4.18: Experimental axial total load vs average displacement for specimens with 3 layers of CFRP wrapping (10 cm in thickness)

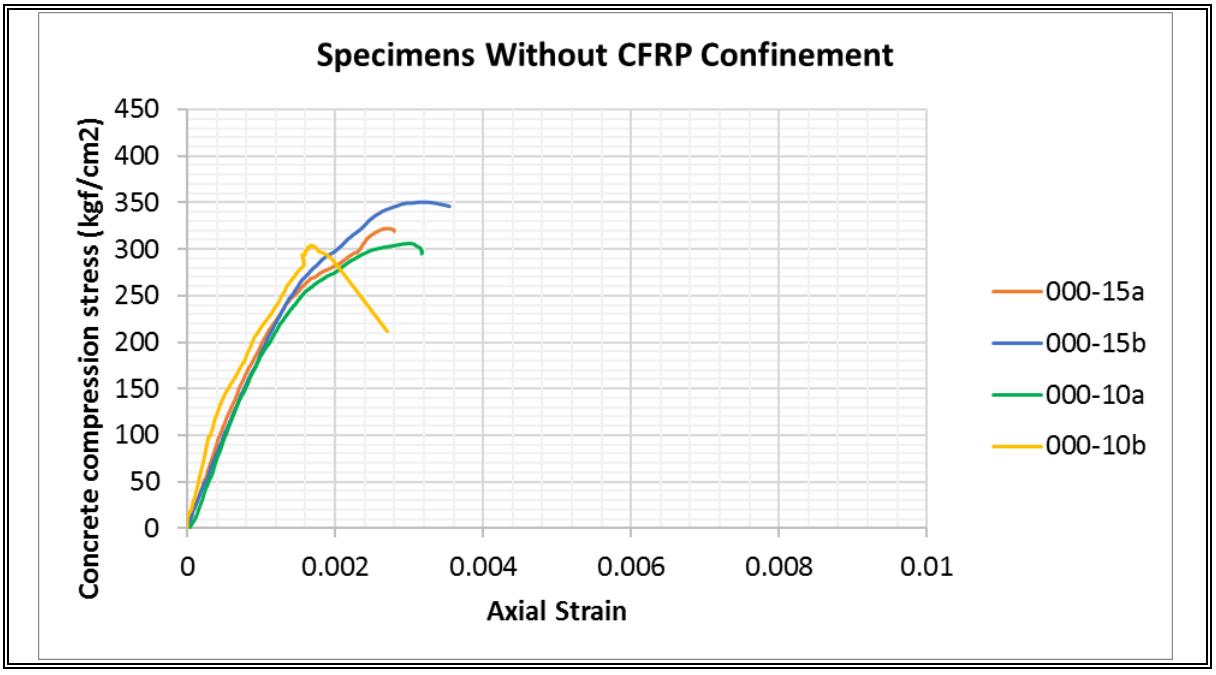

Figure 4.19: Experimental axial concrete stress vs average axial strain for control specimens

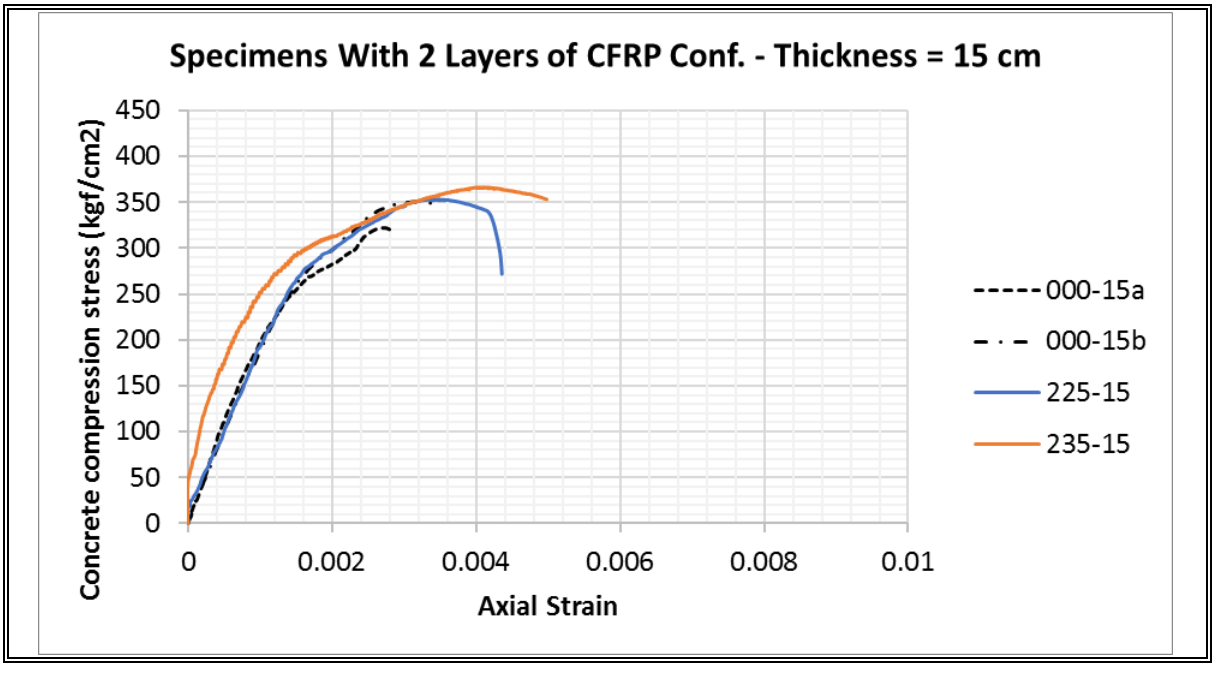

Figure 4.20: Experimental axial concrete stress vs average axial strain for specimens with 2 layers of CFRP wrapping (15 cm in thickness)

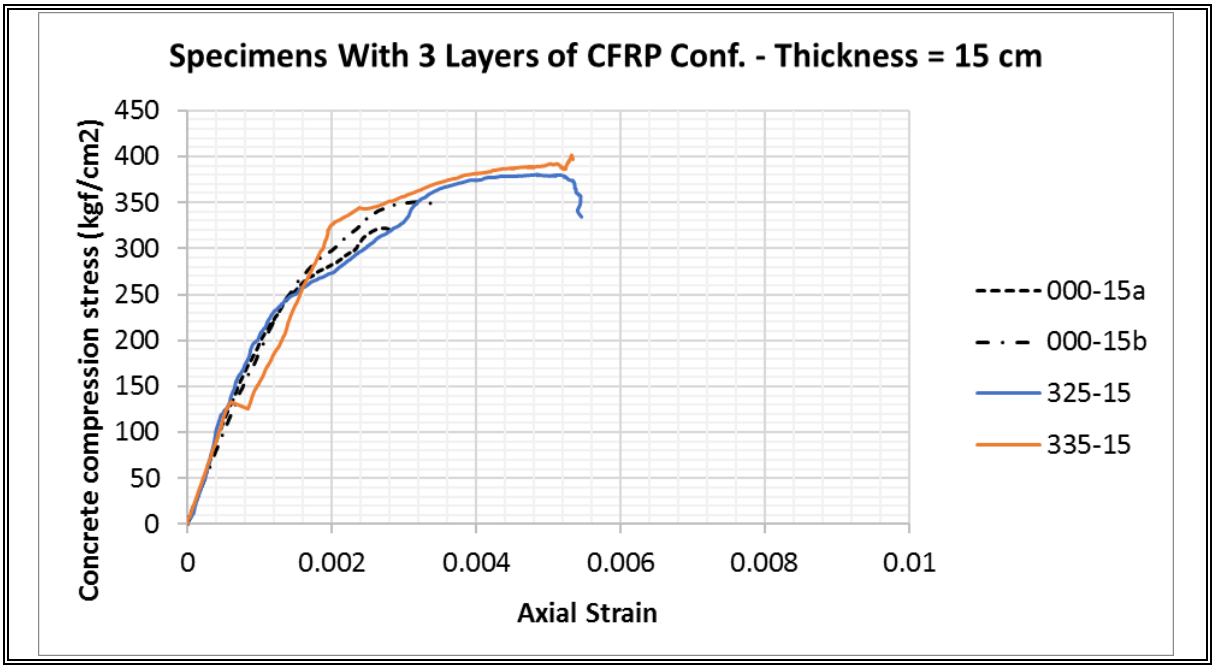

Figure 4.21: Experimental axial concrete stress vs average axial strain for specimens with 3 layers of CFRP wrapping (15 cm in thickness)

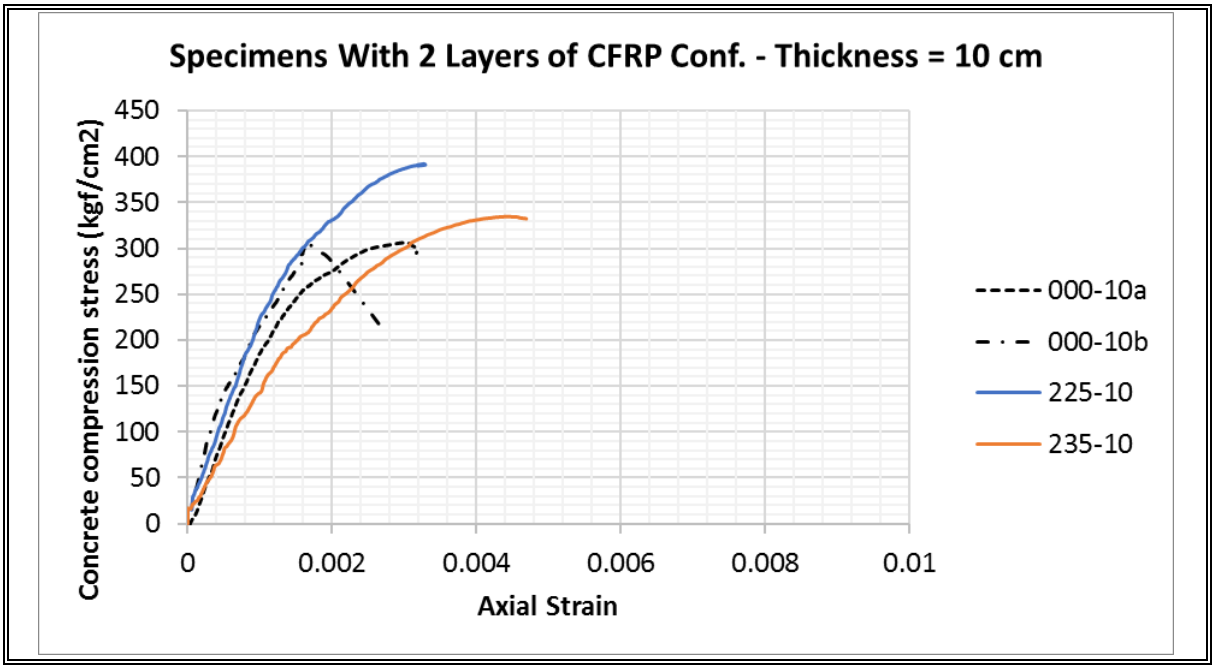

Figure 4.22: Experimental axial concrete stress vs average axial strain for specimens with 2 layers of CFRP wrapping (10 cm in thickness)

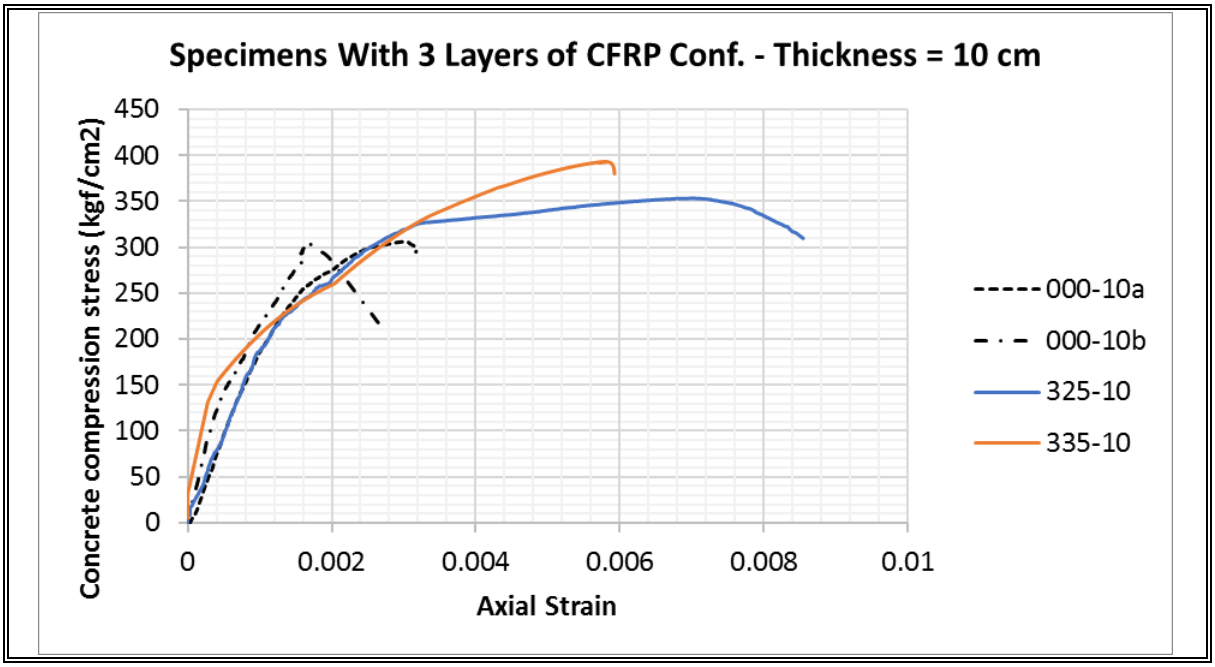

Figure 4.23: Experimental axial concrete stress vs average axial strain for specimens with 3 layers of CFRP wrapping (10 cm in thickness)

4.4 Strain gage measurements

Figures 4.24 to 4.31 show the captured CFRP horizontal strains at a corner and middle side of each column vs the total axial load applied. Specimens with 2 CFRP wraps contained one strain gage each located at the corner. Specimen with 3 CFRP wraps contained two strain gages located at the corner and middle side. The exact location of the strain gages is explained in Figure 2.29. Strain gages were installed on the outer layer of the CFRP wraps. No information was captured of inside layers or anchors with strain gages.

Since the readings of all strain gages were synchronized with the readings of axial displacement and both type of readings had the same rate of capture, the end of the curves of CFRP horizontal strains were also determined by abrupt changes in the applied rate of displacement as explained in Appendix B.

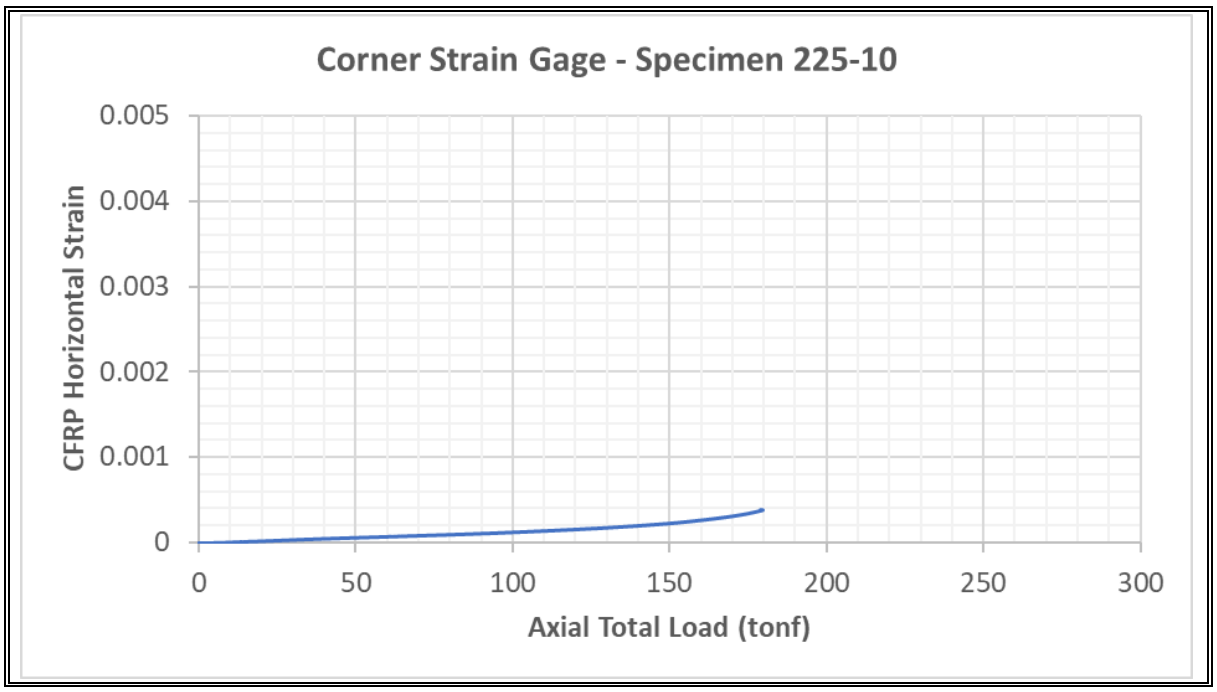

Figure 4.24: CFRP strain vs axial load. Specimen: 225-10. Strain gage location: corner

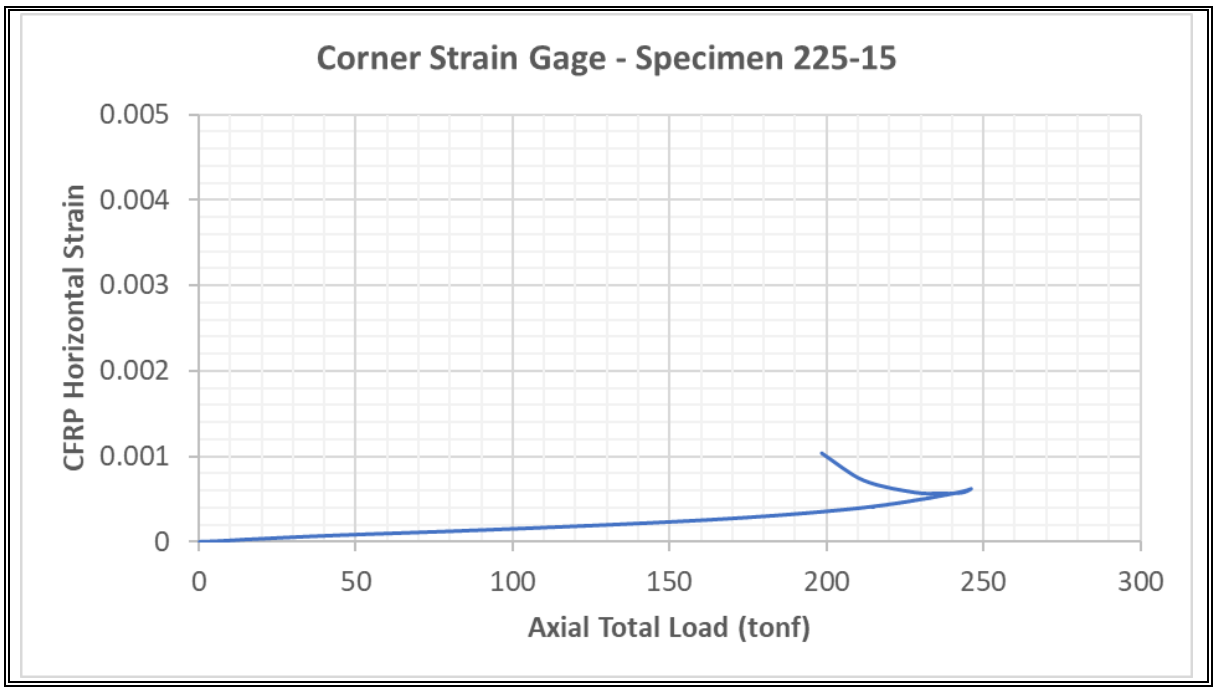

Figure 4.25: CFRP strain vs axial load. Specimen: 225-15. Strain gage location: corner

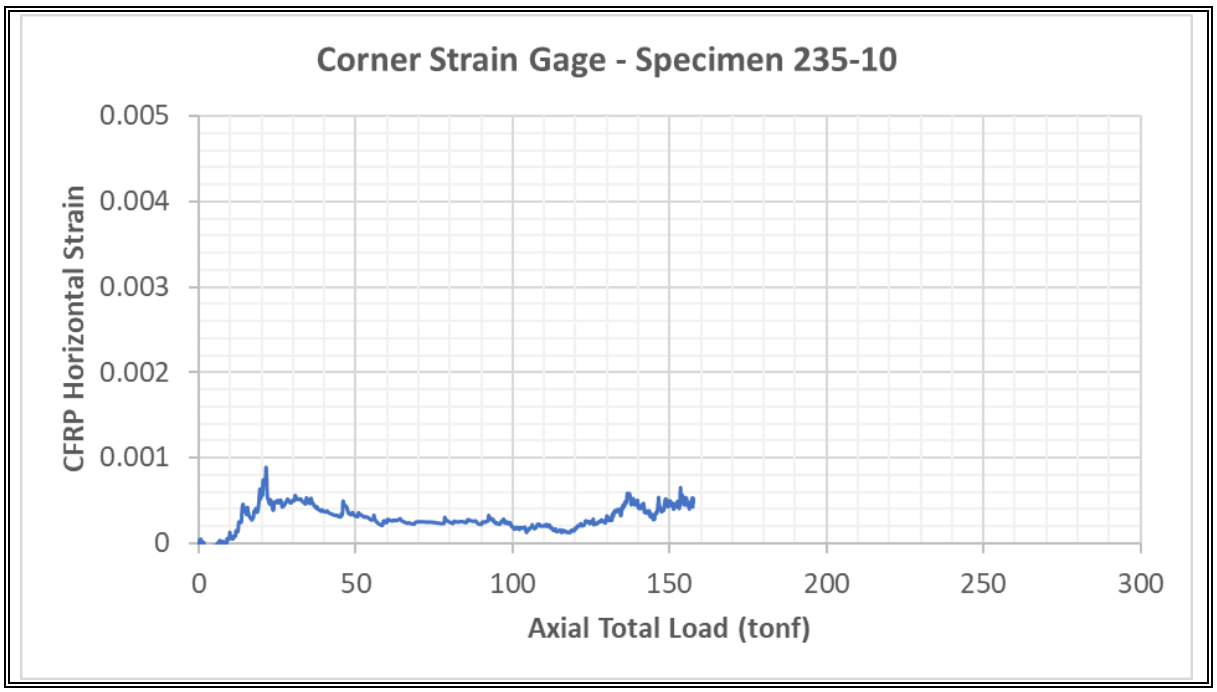

Figure 4.26: CFRP strain vs axial load. Specimen: 235-10. Strain gage location: corner

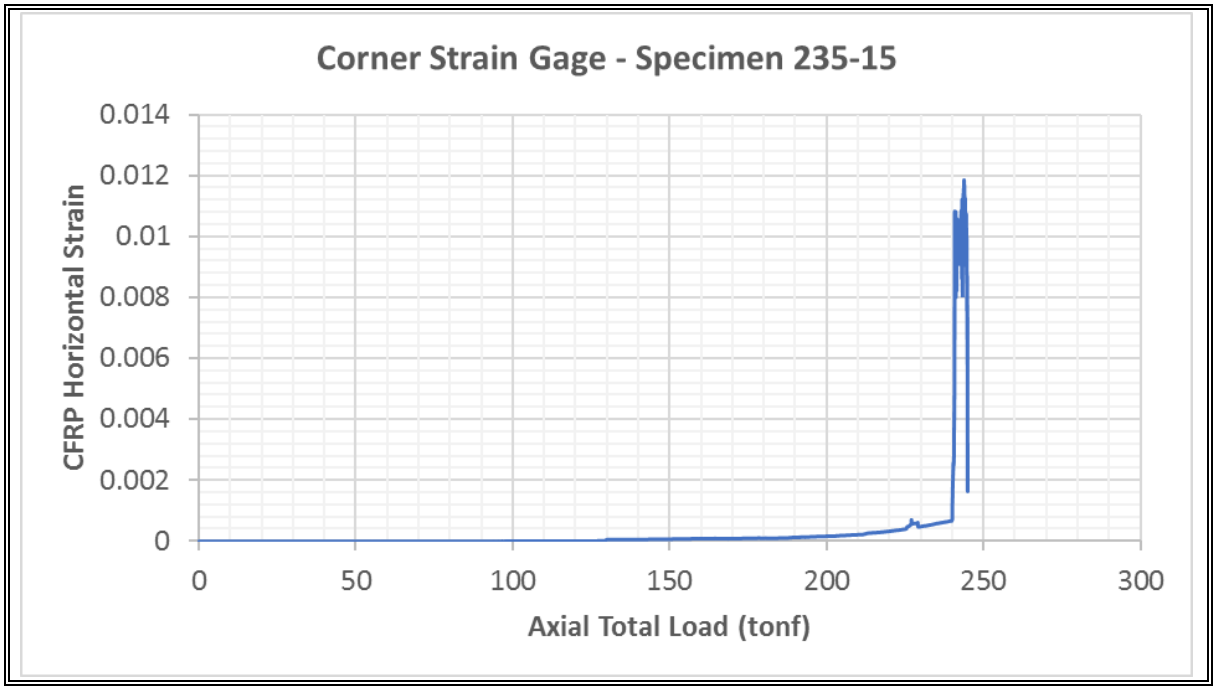

Figure 4.27: CFRP strain vs axial load. Specimen: 235-15. Strain gage location: corner

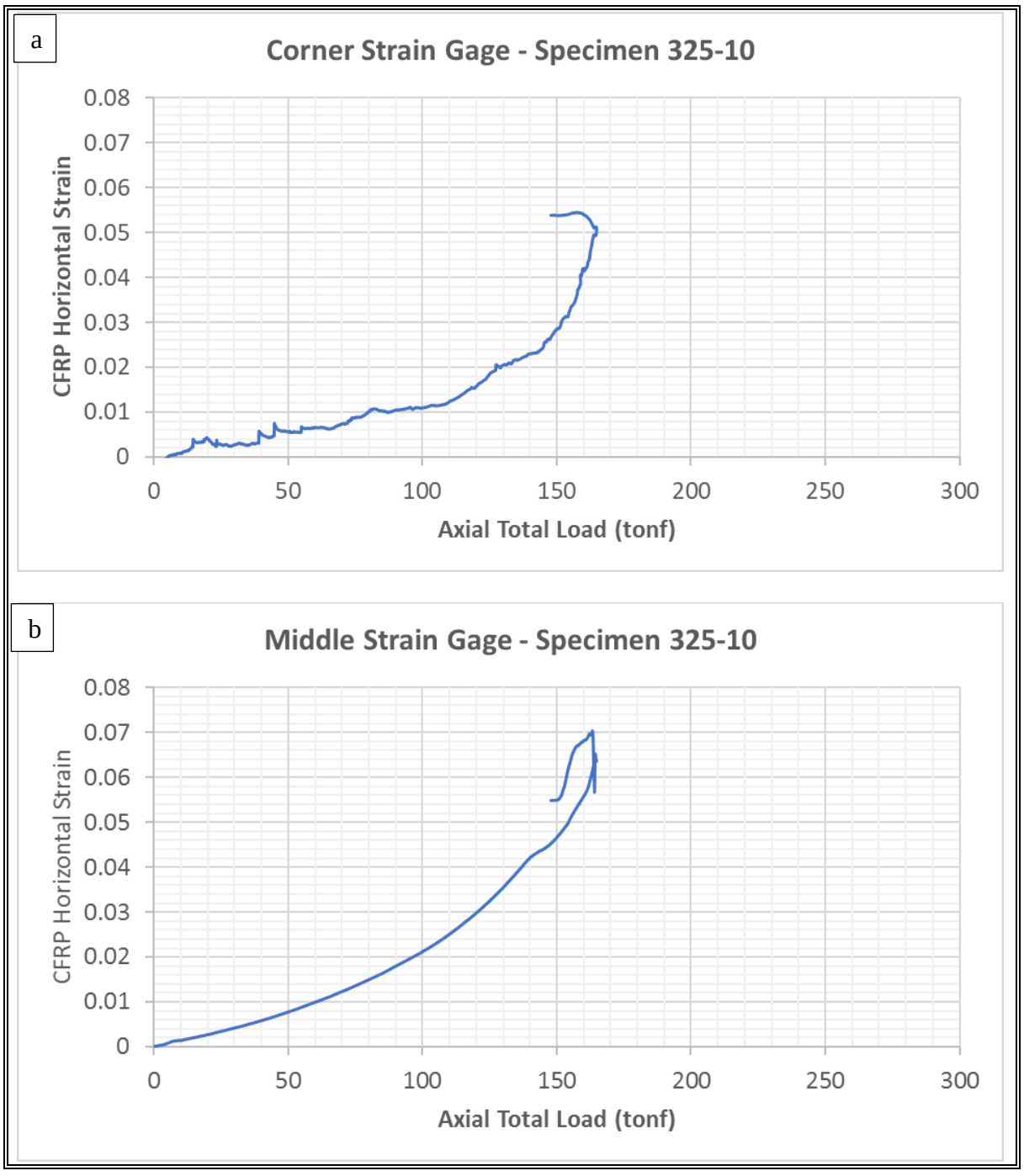

Figure 4.28: CFRP strain vs axial load. Specimen: 325-10. Strain gage location: (a) corner, (b) middle

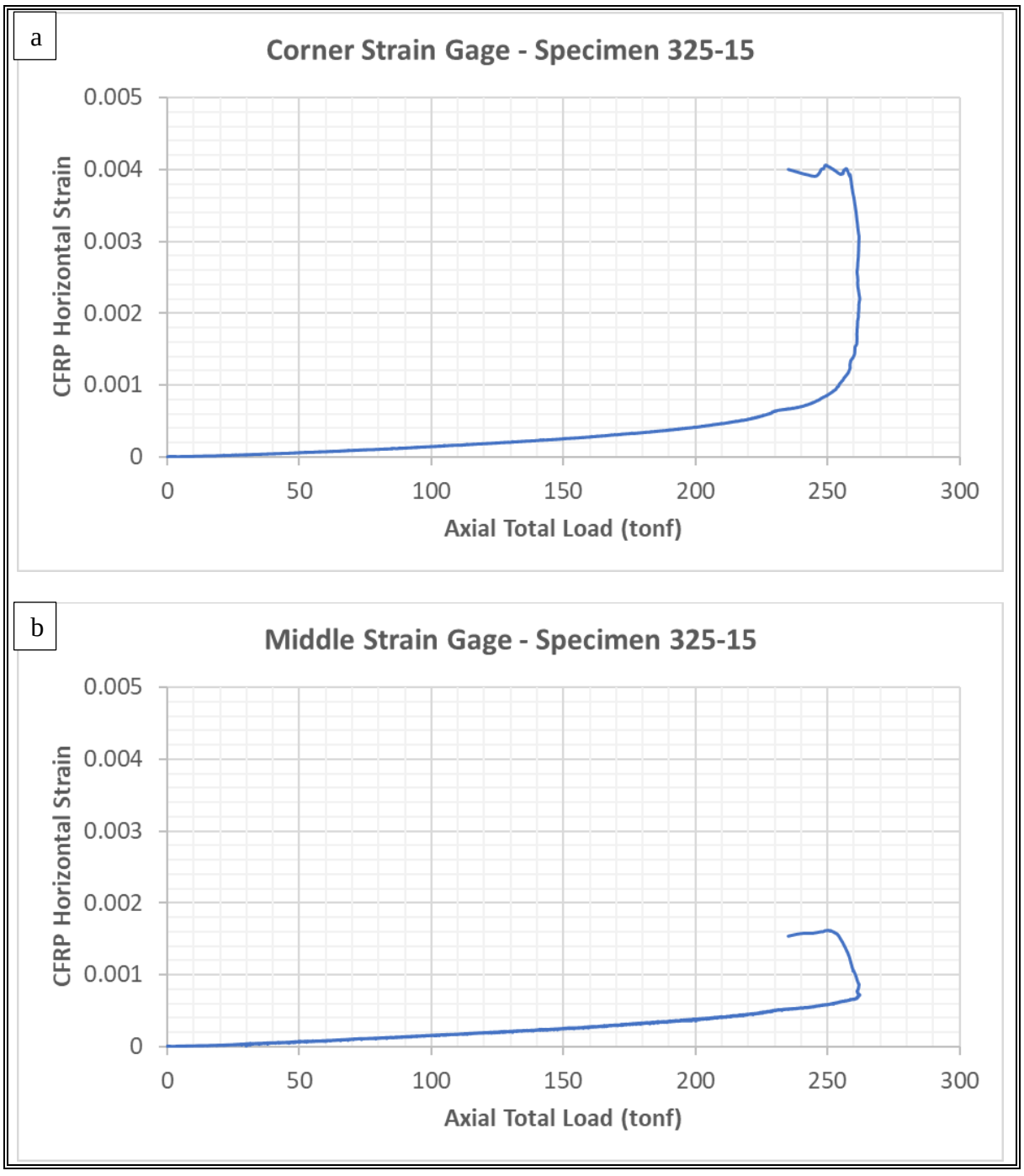

Figure 4.29: CFRP strain vs axial load. Specimen: 325-15. Strain gage location: (a) corner, (b) middle

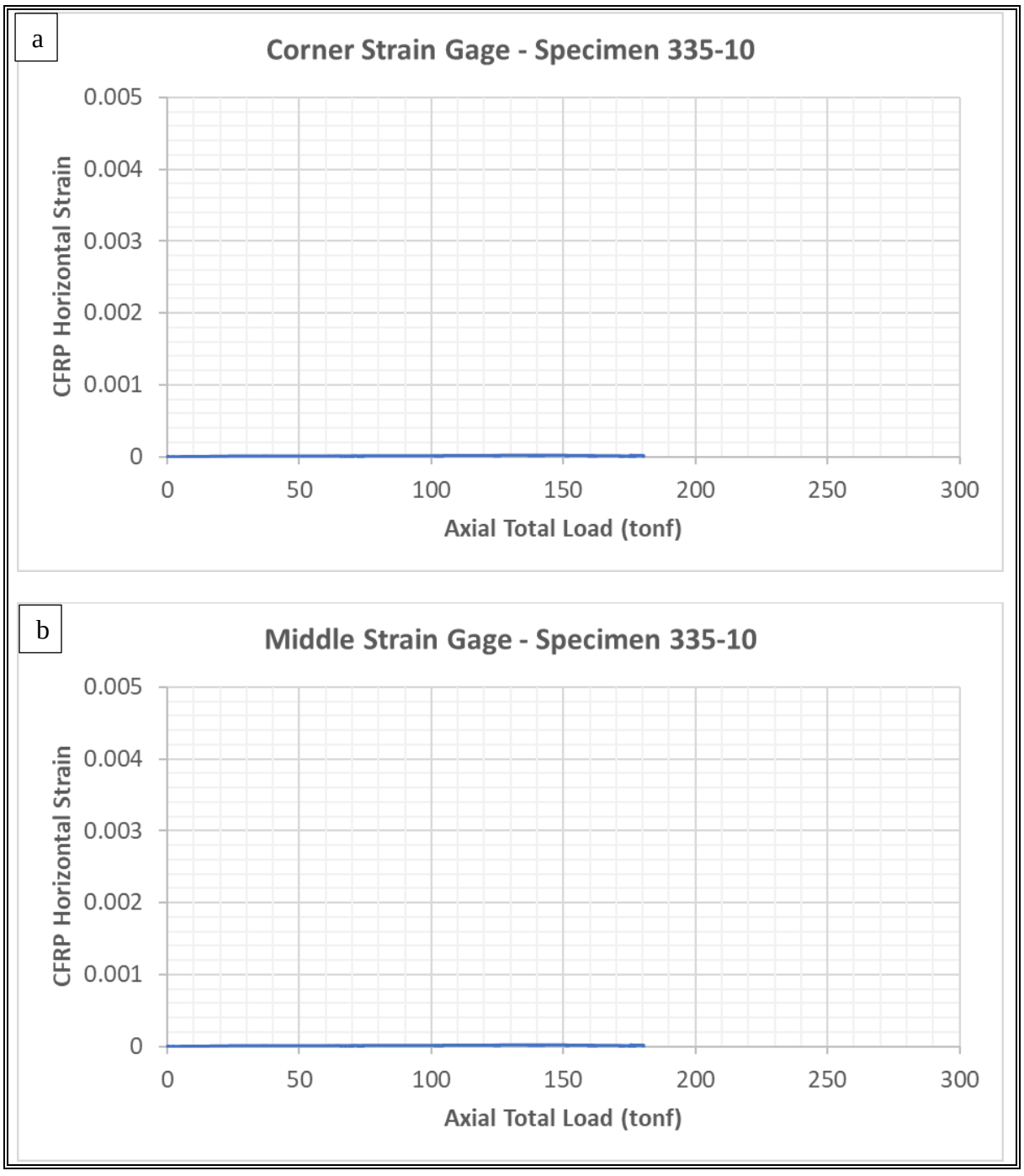

Figure 4.30: CFRP strain vs axial load. Specimen: 335-10. Strain gage location: (a) corner, (b) middle

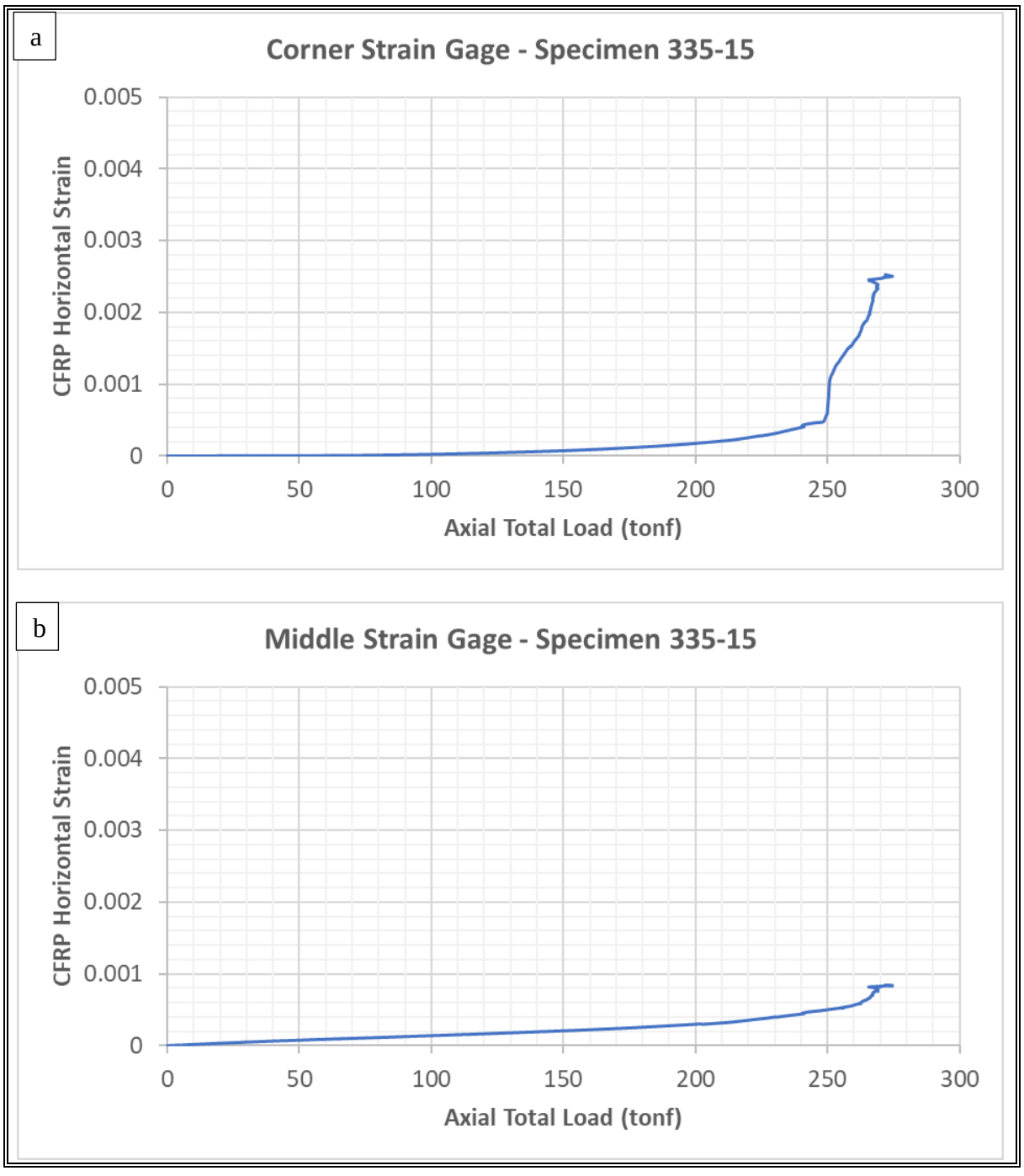

Figure 4.31: CFRP strain vs axial load. Specimen: 335-15. Strain gage location: (a) corner, (b) middle

An important characteristic shared by most strain gage readings, independent if they were located inside, near or outside the failure zone, is the shape of the load-strain curve. In most cases, the strain at low values of load was very small and increased rapidly when the load reached values near and after the peak load. This reflects that the influence of the CFRP confinement becomes more relevant at the final stages of loading. This also reflects that as soon as a localized portion of the CFRP confinement system is ruptured the load that the specimen can sustain drops abruptly.

It is important to notice that installed strain gages were usually not located inside the failure zone of the column, as is explained in section 4.2 for each specimen. Most of the strain gages captured small strains showing the heterogenous distribution of stresses. Only the strain gage of specimen 235-15 was located inside the failure zone, consequently the strains captured were high. The strain gages of specimen 325-10 were not inside the failure zone but were very close, therefore the strains captured were also high. This explains why the maximum strain gage readings of specimens 235-15 and 325-10 reached values higher than 0.01.

The strain gages of all other specimens presented small values of less than 0.005. This reflects that CFRP fibers outside the failure zone do not generate large stresses even at the last stage of loading. Although not all fibers are loaded evenly, the presence of fibers on all the concrete surface helps to maintain the integrity of the specimens. As was explained in section 4.2, unconfined specimen presented a generalized failure mode, while CFRP confined specimens presented a localized failure mode.

4.5 Digital image correlation

As was explained in section 2.5.2, with the use of the software Optecal, by painting a white layer with a grid of black dots over the CFRP reinforcement and by taking photographs at rate of 1 photograph every 5 seconds, the field of displacements of the outer CFRP wrap is captured. The strains calculated with this technique are presented in Figures 4.32 to 4.39. These graphics show the field of strains in the x direction (horizontal) and y direction (vertical) at the closest instant before failure of the specimen. All the strains showed in these figures were calculated for the last photograph took prior to failure of the column.

To clearly visualize the strain distribution, each figure is accompanied with a graphic legend that correlates the colors presented with the corresponding strains. Horizontal strains are displayed between a strain of 0 and the largest strain value captured. Vertical strains are displayed between a strain of 0 and a strain of -0.02.

The equipment installed to capture the widening of the specimens was placed over the digital image correlation grid. This was inevitable since the system to capture widening needed to be placed on both ends of the specimens. However, since the software Optecal allows to remove any portion of the photograph that is not to be analyzed, the presence of this equipment did not harm the digital image correlation process.

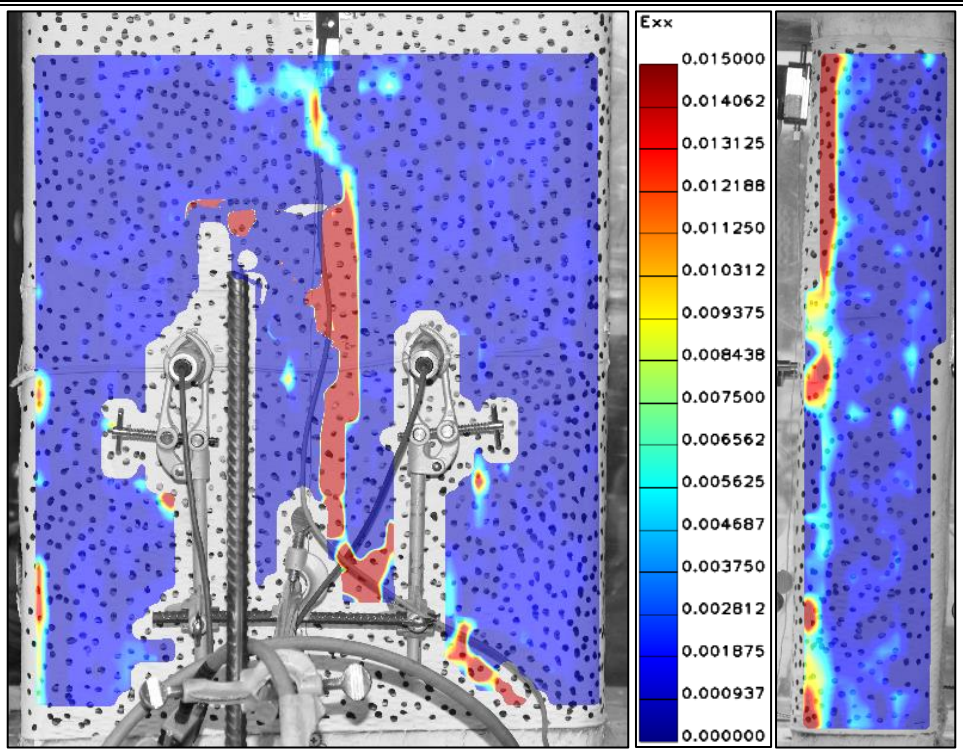

(a) Horizontal strains

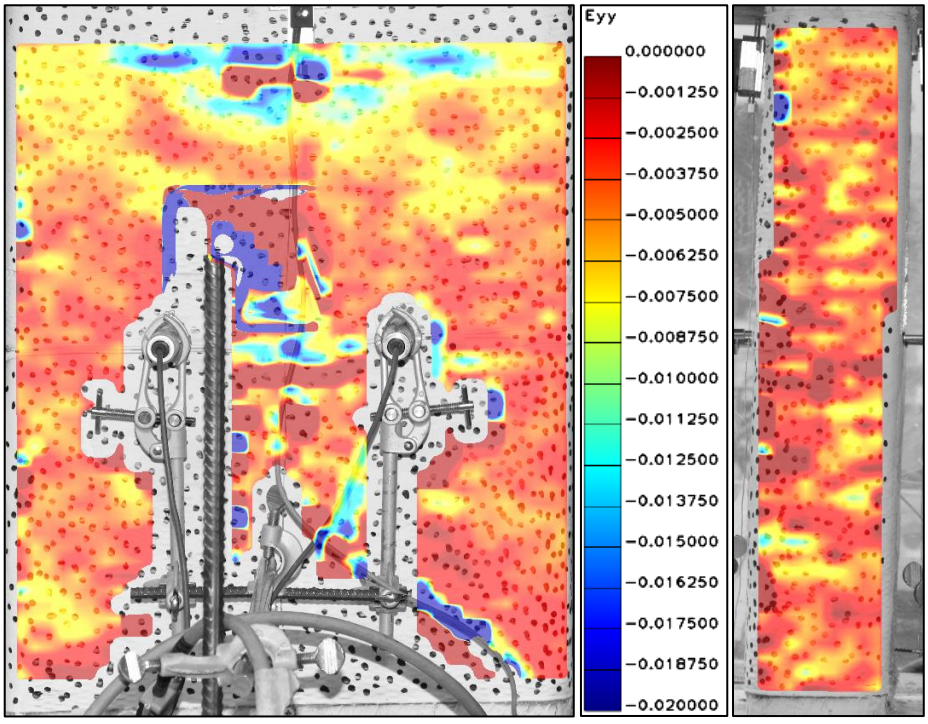

(b) Vertical strains

Figure 4.32: Strains immediately before failure captured by DIC. Specimen 225-10

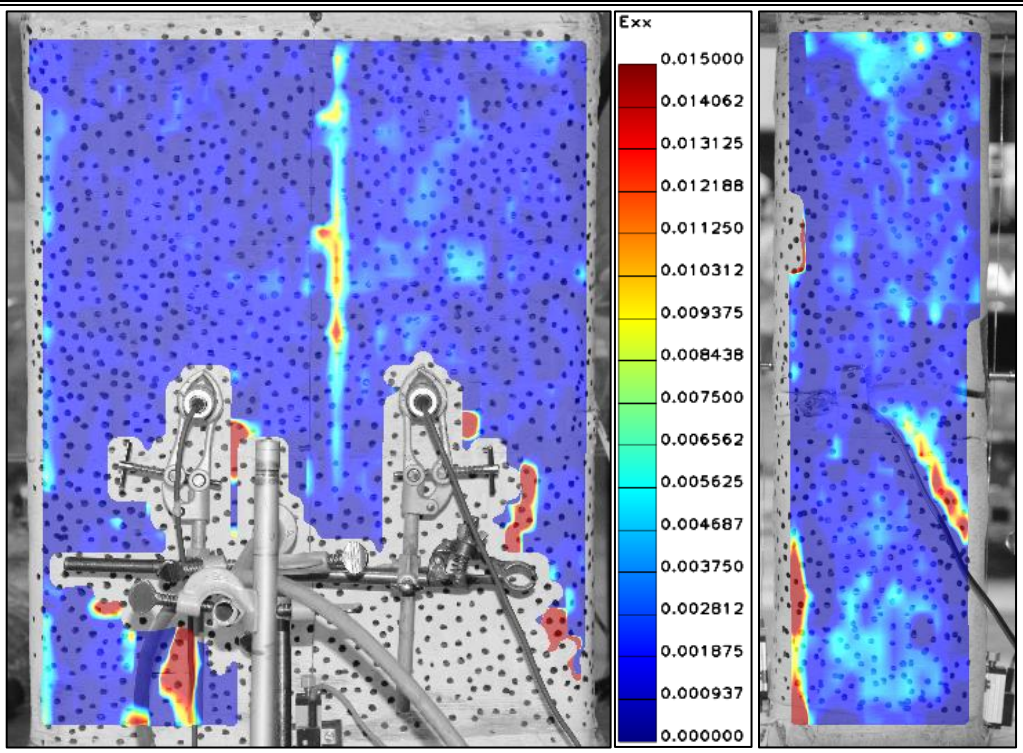

(a) Horizontal strains

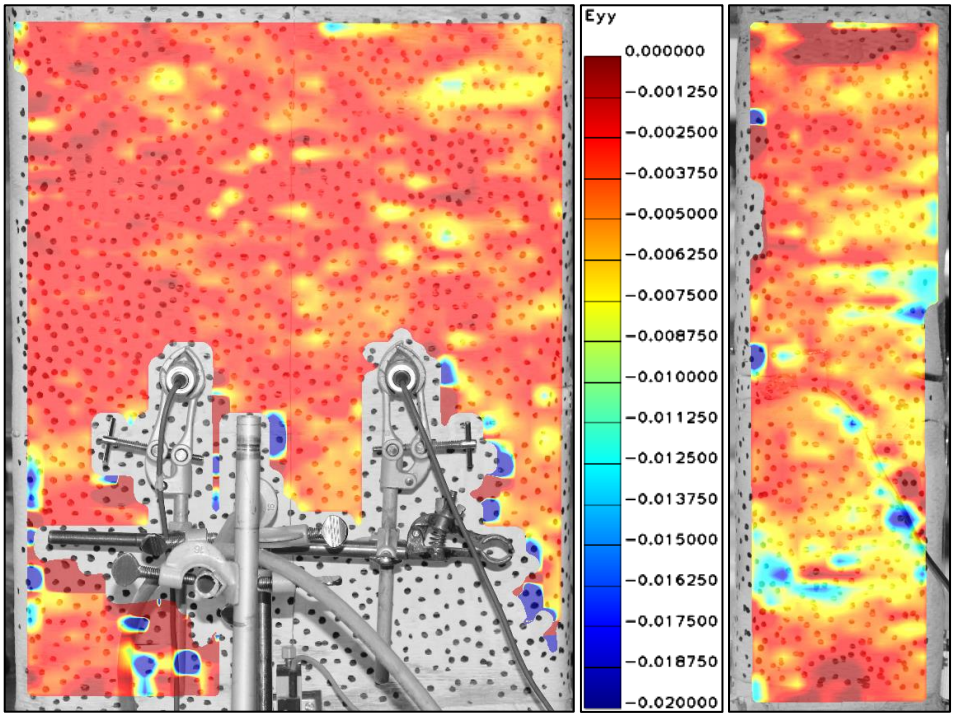

(b) Vertical strains

Figure 4.33: Strains immediately before failure captured by DIC. Specimen 225-15

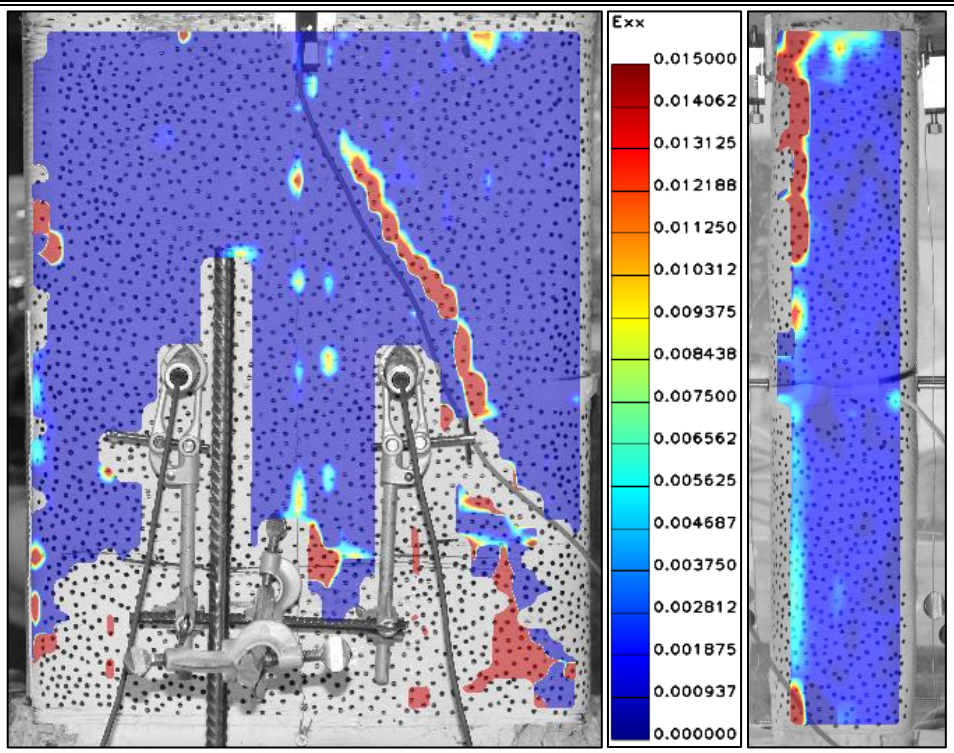

(a) Horizontal strains

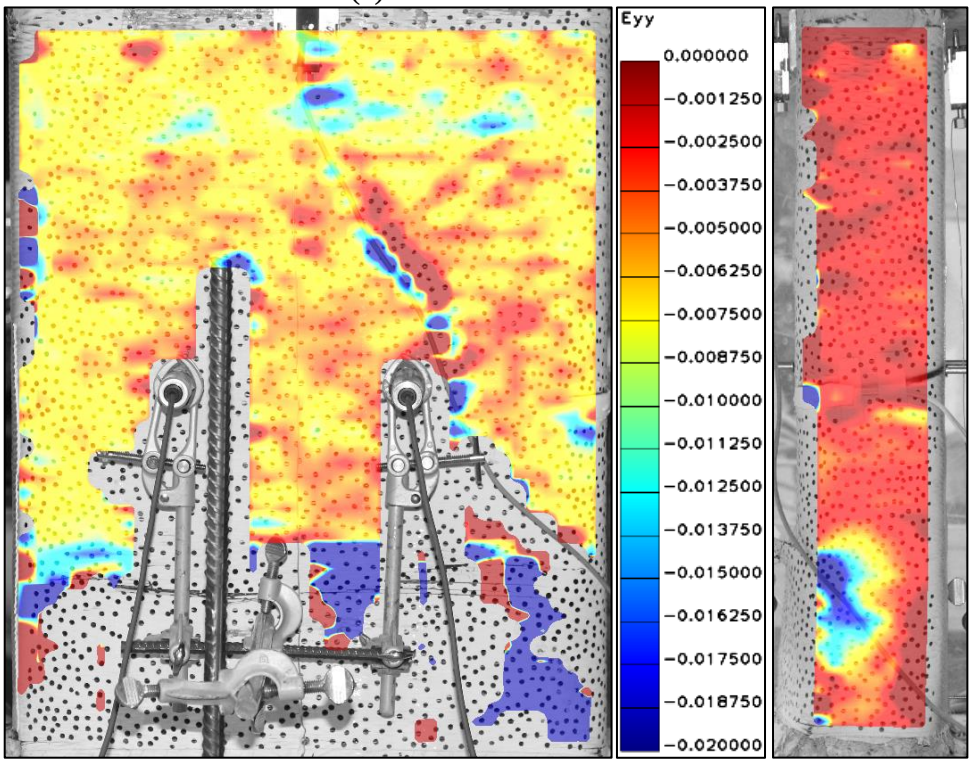

(b) Vertical strains

Figure 4.34: Strains immediately before failure captured by DIC. Specimen 235-10

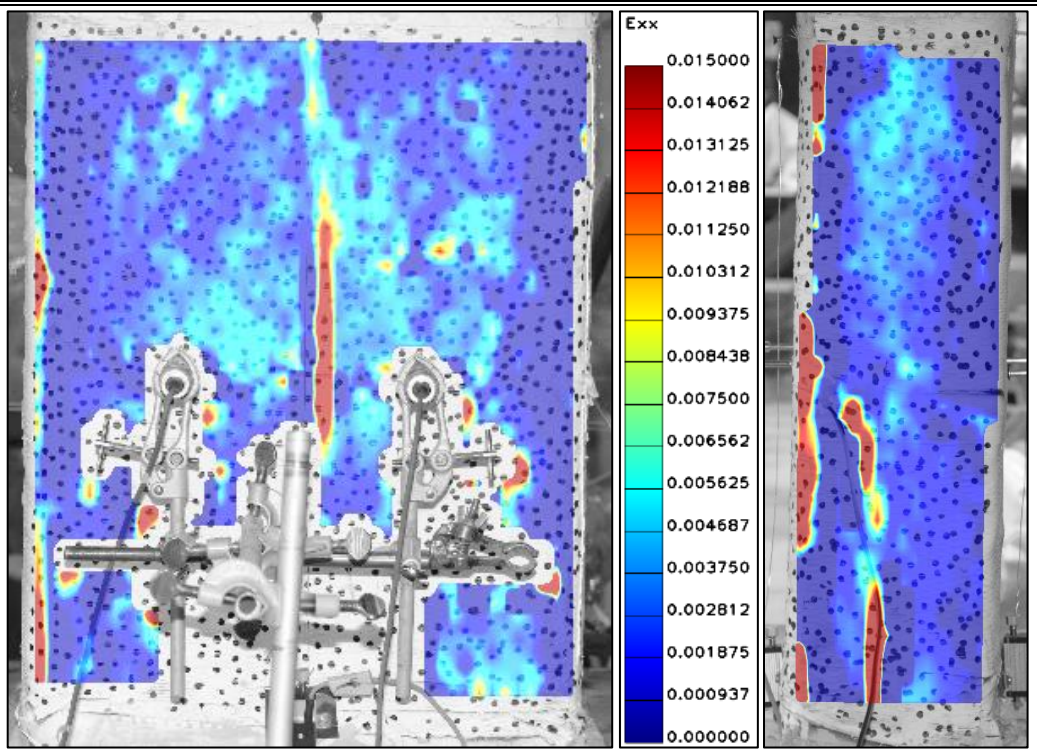

(a) Horizontal strains

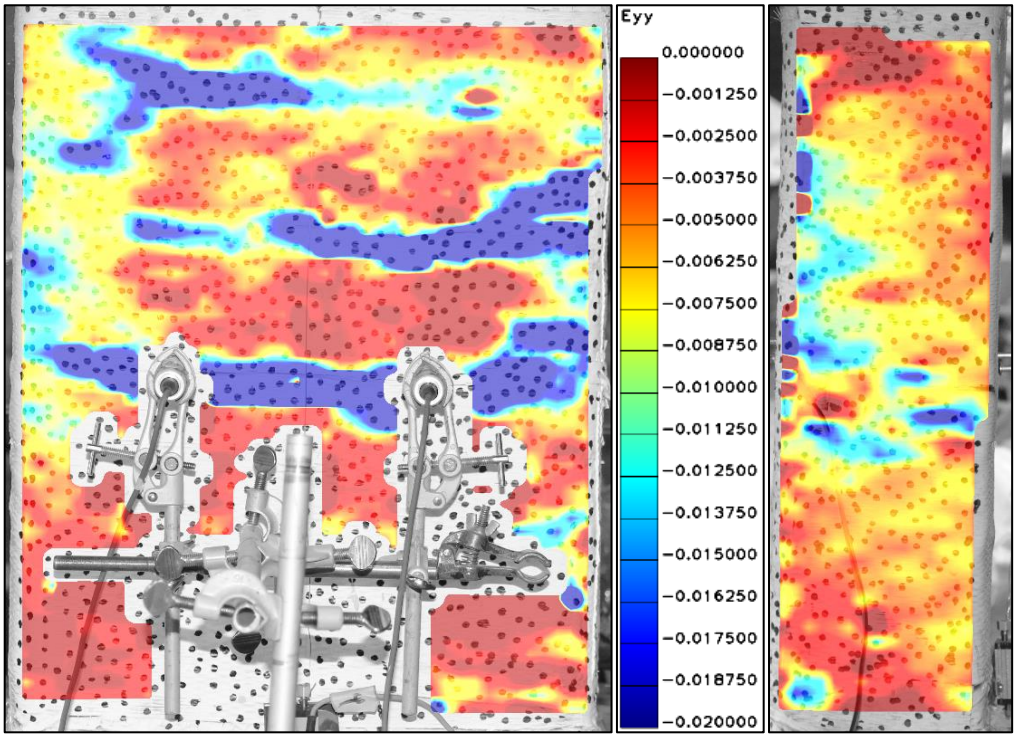

(b) Vertical strains

Figure 4.35: Strains immediately before failure captured by DIC. Specimen 235-15

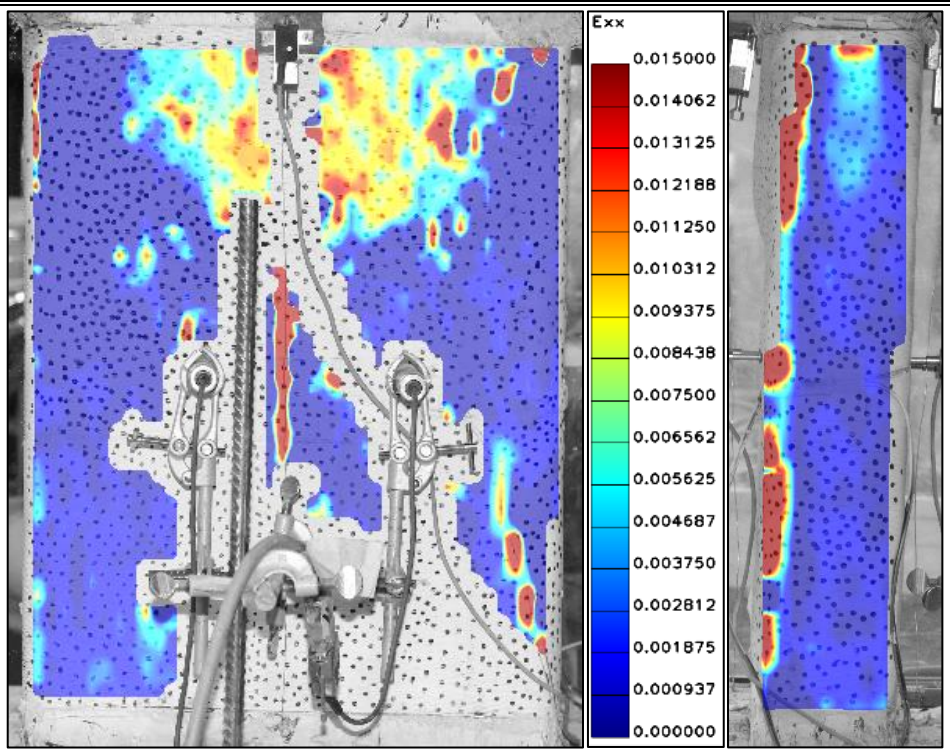

(a) Horizontal strains

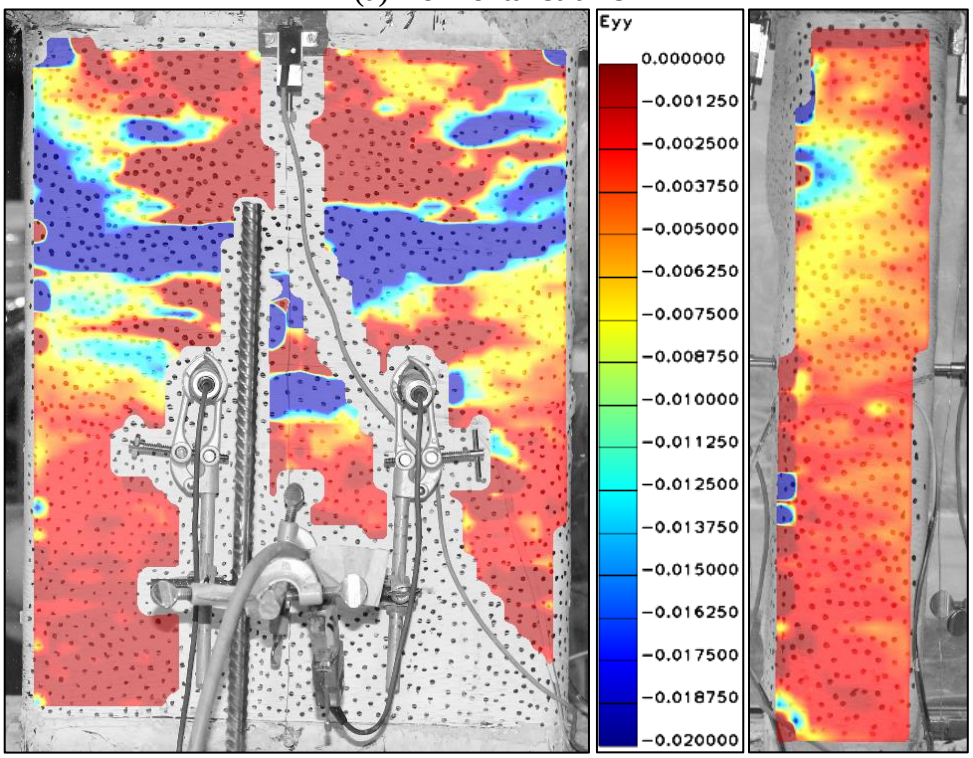

(b) Vertical strains

Figure 4.36: Strains immediately before failure captured by DIC. Specimen 325-10

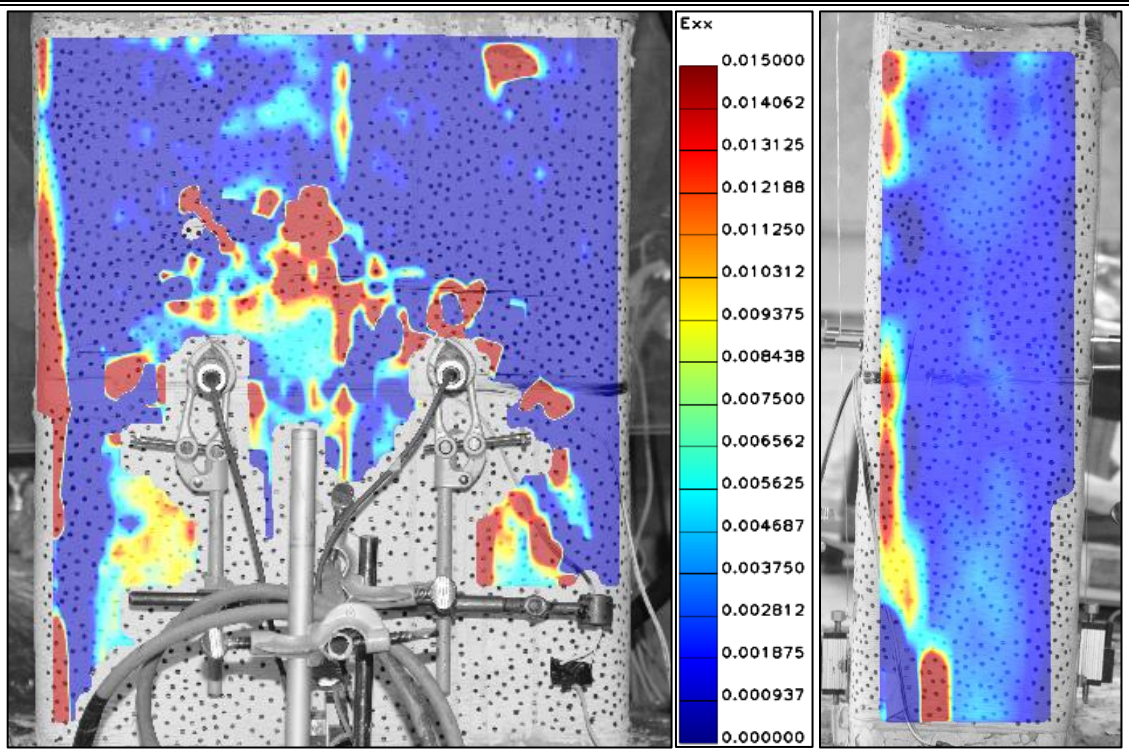

(a) Horizontal strains

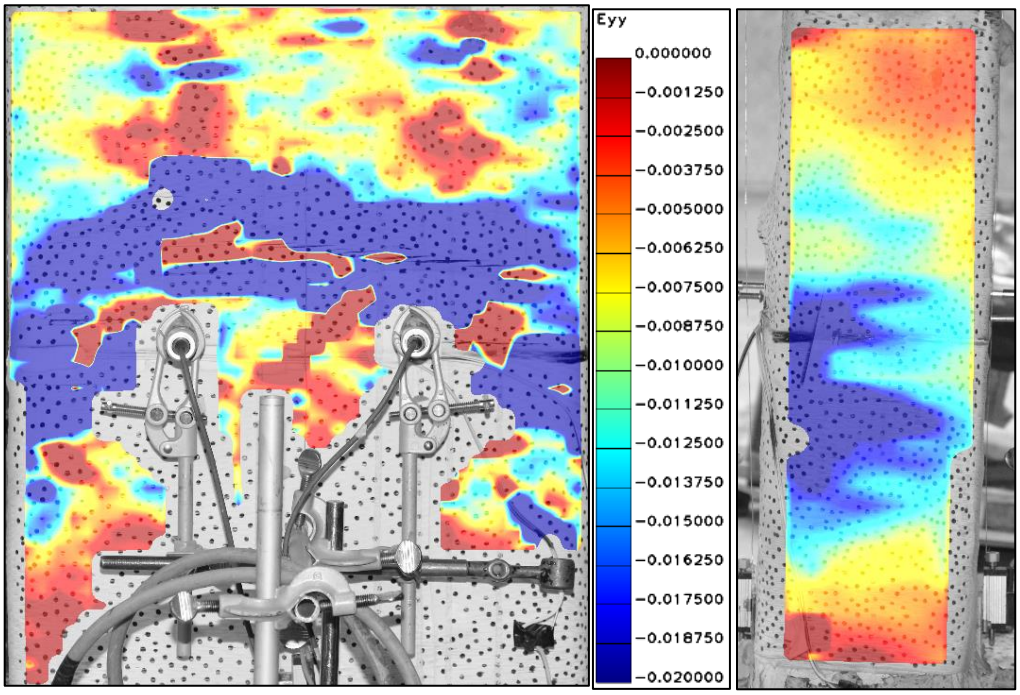

(b) Vertical strains

Figure 4.37: Strains immediately before failure captured by DIC. Specimen 325-15

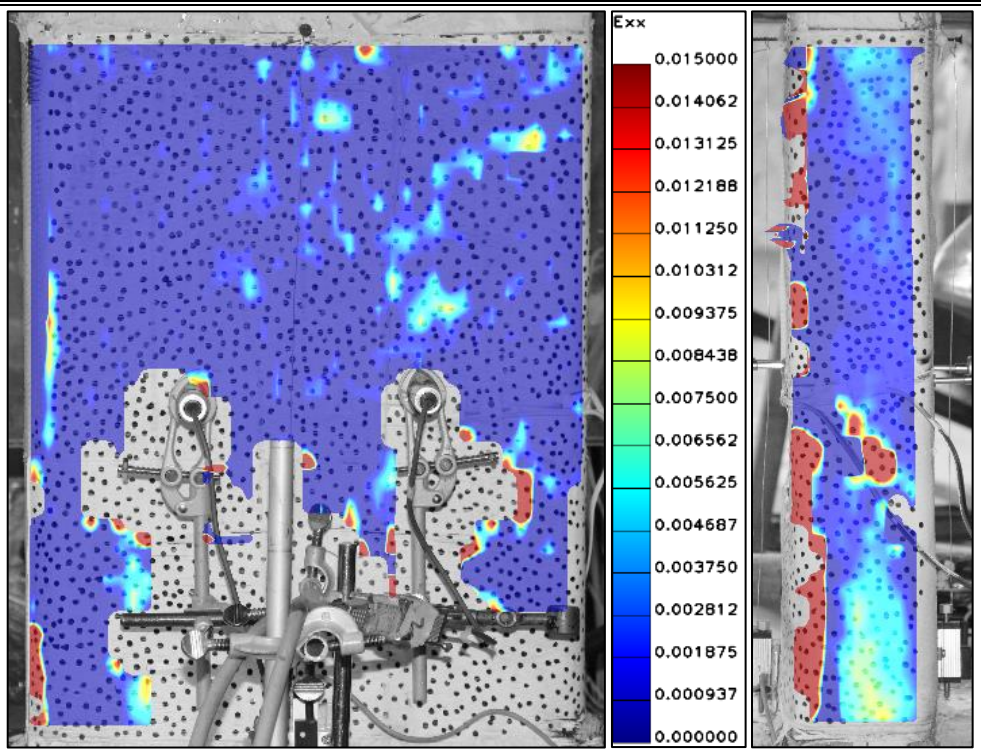

(a) Horizontal strains

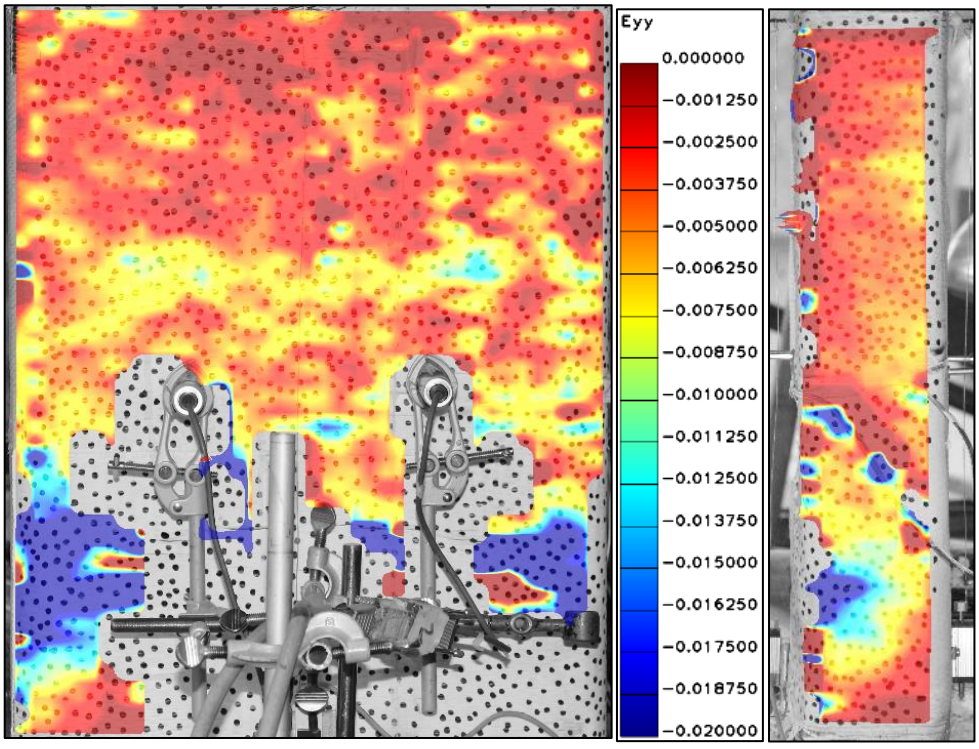

(b) Vertical strains

Figure 4.38: Strains immediately before failure captured by DIC. Specimen 335-10

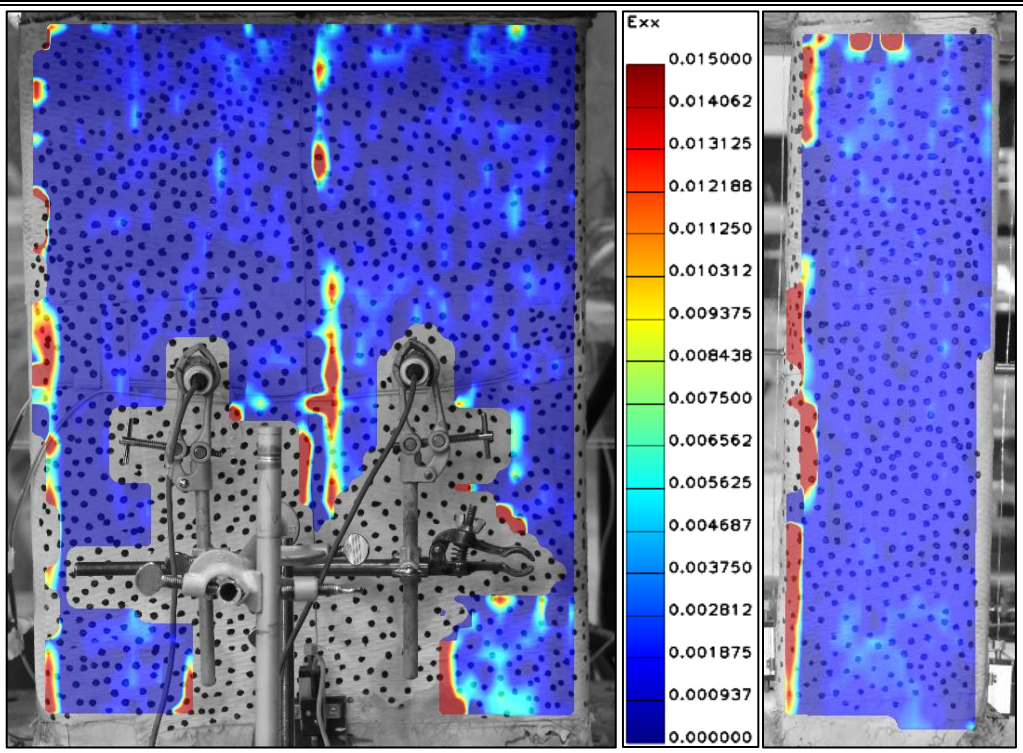

(a) Horizontal strains

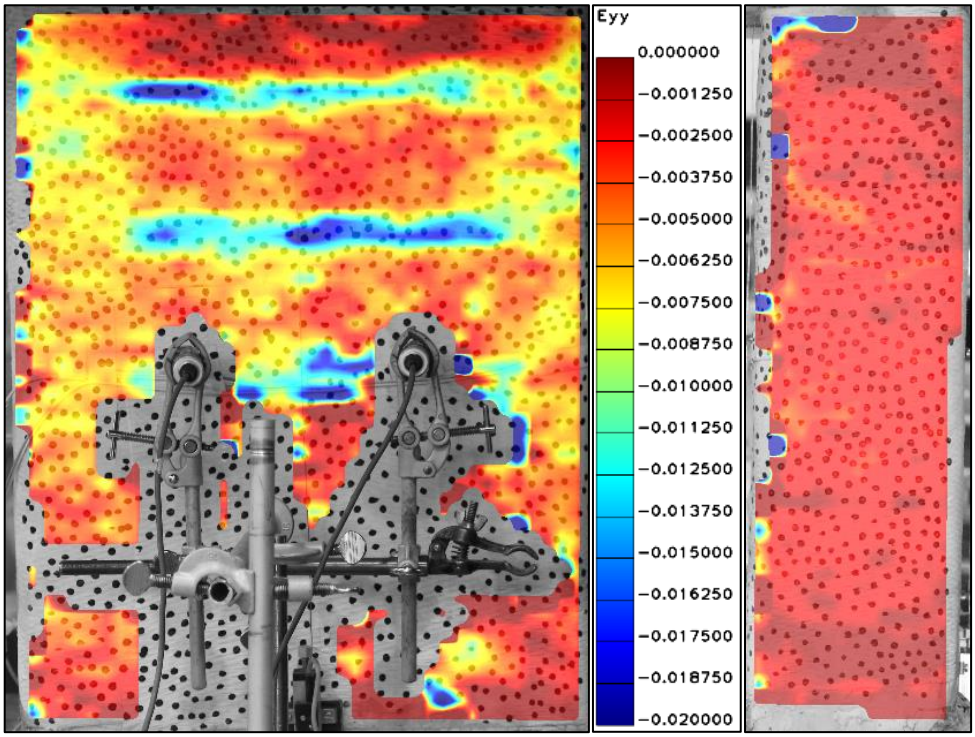

(b) Vertical strains

Figure 4.39: Strains immediately before failure captured by DIC. Specimen 335-15

According to the digital image correlation results the strains for both horizontal and vertical directions present a heterogeneous distribution.

In the horizontal direction, large strains tend to localize at corners and/or the middle of the large side of the column. Horizontal strains tend to reach values higher than 0.015 at localized zones but present very small strain at all other zones. This is consistent with the data captured with strain gages described at section 4.4, where it was observed that only the zones near the rupture tend to generate high strain while the rest of the fiber tend to present small strains.

In the vertical direction, strains tend to be uniform inside each transverse cross section, but tend to vary at different heights. Vertical strains tend to vary between 0.005 to values higher than 0.02. This also reflects that localized zones tend to present higher vertical deformations while other zones present smaller values. The axial strains captured with the LVDTs, described in section 4.3, capture an average axial strain of the complete column, while the strains captured by the DIC technique capture strains between dots. The localization of vertical strains possibly occurs because concrete near the failure zone continues to vertically compress while other zones decompress at the final loading stage.

4.6 Other measurements

In addition to the measurements presented in previous sections, one last parameter obtained during the tests was the widening of the column. This parameter was captured by 4 horizontal LVDTs placed on both sides of the specimen at mid-height as is explained in section 2.5.3. The graphics of these measurements are presented in the next chapter, where they are compared to the same information captured from the corresponding finite element models.

4.7 Summary

Twelve reinforced concrete columns (eight reinforced with CFRP wraps and anchors and four control specimens) were tested axially with the use of a forced controlled compression machine. The behavior of each columns was captured by a general description of failure mode, vertical LVDTs, horizontal LVDTs, strain gages on the outer layer of CFRP and digital image correlation techniques.

As was expected, a higher increase in concrete maximum stress and ultimate strain was obtained when a higher number of CFRP wraps and anchors was used. The initial secant concrete stiffness of CFRP confined columns tends to be on average 88% (ignoring specimen 235-15 because vertical LVDTs on this specimen could not capture the initial portion of the curve accurately) of the value captured in control specimen. This is mainly due to the presence of pre-cast holes that were not refilled after CFRP installation. Pre-cast holes were not refilled because of the introduction of epoxy into the cavities was blocked by the CFRP wraps. A more efficient CFRP installation technique needs to be developed to allow pre-cast holes refill.

In general, a higher value of maximum stress was obtained with the 3x5 CFRP anchor disposition than with the 2x5, except for the columns with 10-cm thickness and 2 layers of CFRP wraps and 1 layer of CFRP anchors. These columns were the exception mainly due to the smaller cross-section area which was more affected by the pre-cast holes which the fewer number of CFRP wraps could not compensate. The ultimate strain did not depend on the CFRP anchor disposition, columns 235-15 and 235-10 achieved a higher ultimate strain than their counterparts 225-15 and 225-10, but columns 335-15 and 335-10 achieved a similar ultima strain than their counterparts 325-15 and 325-10.

Strain gage reading showed that CFRP strain distribution is highly heterogenous, with a localized zone of fiber with strains high enough to generate CFRP rupture and other zones pressing fibers with smaller strains than the failure zone. Also, most of the CFRP confinement system presents very small strain until the maximum concrete stresses is reached, after this point strain in the CFRP wraps increase exponentially.

Digital image correlation can detect high strains in at the failure zone; however, the strain detected tend to be overestimated. Values as high or higher than 0.01 were captured by Optecal, this cannot be possible since the manufacturer specified 0.01 as the ultimate CFRP strain on a tension test. Ultimate strain of installed CFRP should be a fraction of this number. Optecal's overestimation is might be explained by the rate the photographs were taken (1 photographs every 5 seconds) and re-accommodation of CFRP wraps. Cameras with a higher shot speed are required to obtain more accurate strain data. Since it is possible some air bubbles were trapped between CFRP layers, a portion of the displacement captured with the photographs could have been translation of the fiber after expulsion of the air and not strain related to a stress state. Vertical bar buckling was prevented with CFRP confinement until the failure of the CFRP was reached. Even when CFRP failure was reached, vertical bar buckling was localized at the failure zone and not distributed across the complete section as occurred on specimen without CFRP confinement. Transverse steel stirrups opening was completely prevented by CFRP wraps even after CFRP failure was achieved. As excepted, none of the columns experienced a global buckling mode.

5. FINITE ELEMENT MODELS

5.1 Overview

In this section, the results obtained from finite element models are presented. The models were developed using the software ANSYS R15.0 (ANSYS, 2009) in the platform ANSYS Workbench.

The models are divided in two groups: complete specimen models and subsection models. Complete specimen models are made to represent the behavior of experimental tests. Subsection models are made to illustrate how the behavior of a complete column can be captured by analyzing independent sub columns.

5.2 Description of models

The first group of models represents 14 tested specimens. All models include transverse steel stirrups of 6 mm in diameter and spaced at 10 cm, as explained in section 3.3.1. Since the columns present two axes of symmetry, only 1/4 of the real column is modeled and internal borders are blocked from any horizontal displacement, as is explained in Figure 5.1. Below is a summary of the characteristics of each specimen modeled:

- O1-000-10-A: 10 cm in thickness, without rounded corners, without predrilled holes and without CFRP reinforcement. The transverse cross-section of this model is showed in Figure 5.1 with the subsection marked as I.
- O1-000-10-B: 10 cm in thickness, with rounded corners and 10 predrilled holes located in a 2x5 disposition (as explained by Figure 3.1) and without CFRP reinforcement. The transverse cross-section of this model is showed n Figure 5.1 with the subsection marked as VI.

- O1-000-10-C: 10 cm in thickness, with rounded corners and 15 predrilled holes located in a 3x5 disposition (as explained by Figure 3.1) and without CFRP reinforcement. The transverse cross-section of this model is showed in Figure 5.1 with the subsection marked as V.
- O1-000-15-A: 15 cm in thickness, without rounded corners, without predrilled holes and without CFRP reinforcement. The transverse cross-section of this model is showed in Figure 5.1 with the subsection marked as II.
- O1-000-15-B: 15 cm in thickness, with rounded corners and 10 predrilled holes located in a 2x5 disposition (as explained by Figure 3.1) and without CFRP reinforcement. The transverse cross-section of this model is showed in Figure 5.1 with the subsection marked as IV.
- O1-000-15-C: 15 cm in thickness, with rounded corners and 15 predrilled holes located in a 3x5 disposition (as explained by Figure 3.1) and without CFRP reinforcement. The transverse cross-section of this model is showed in Figure 5.1 with the subsection marked as III.
- O1-225-10: 10 cm in thickness, with rounded corners and 10 predrilled holes located in a 2x5 disposition (as explained by Figure 3.1) and with CFRP reinforcement of 1 mm in thickness. The transverse cross-section of this model is showed in Figure 5.1 with the subsection marked as VI.
- O1-225-15: 15 cm in thickness, with rounded corners and 10 predrilled holes located in a 2x5 disposition (as explained by Figure 3.1) and with CFRP reinforcement of 1 mm in thickness. The transverse cross-section of this model is showed in Figure 5.1 with the subsection marked as IV.

- O1-235-10: 10 cm in thickness, with rounded corners and 15 predrilled holes located in a 3x5 disposition (as explained by Figure 3.1) and with CFRP reinforcement of 1 mm in thickness. The transverse cross-section of this model is showed in Figure 5.1 with the subsection marked as V.
- O1-235-15: 15 cm in thickness, with rounded corners and 15 predrilled holes located in a 3x5 disposition (as explained by Figure 3.1) and with CFRP reinforcement of 1 mm in thickness. The transverse cross-section of this model is showed in Figure 5.1 with the subsection marked as III.
- O1-325-10: 10 cm in thickness, with rounded corners and 10 predrilled holes located in a 2x5 disposition (as explained by Figure 3.1) and with CFRP reinforcement of 1.5 mm in thickness. The transverse cross-section of this model is showed in Figure 5.1 with the subsection marked as VI.
- O1-325-15: 15 cm in thickness, with rounded corners and 10 predrilled holes located in a 2x5 disposition (as explained by Figure 3.1) and with CFRP reinforcement of 1.5 mm in thickness. The transverse cross-section of this model is showed in Figure 5.1 with the subsection marked as IV.
- O1-335-10: 10 cm in thickness, with rounded corners and 15 predrilled holes located in a 3x5 disposition (as explained by Figure 3.1) and with CFRP reinforcement of 1.5 mm in thickness. The transverse cross-section of this model is showed in Figure 5.1 with the subsection marked as V.
- O1-335-15: 15 cm in thickness, with rounded corners and 15 predrilled holes located in a 3x5 disposition (as explained by Figure 3.1) and with CFRP

reinforcement of 1.5 mm in thickness. The transverse cross-section of this model is showed in Figure 5.1 with the subsection marked as III.

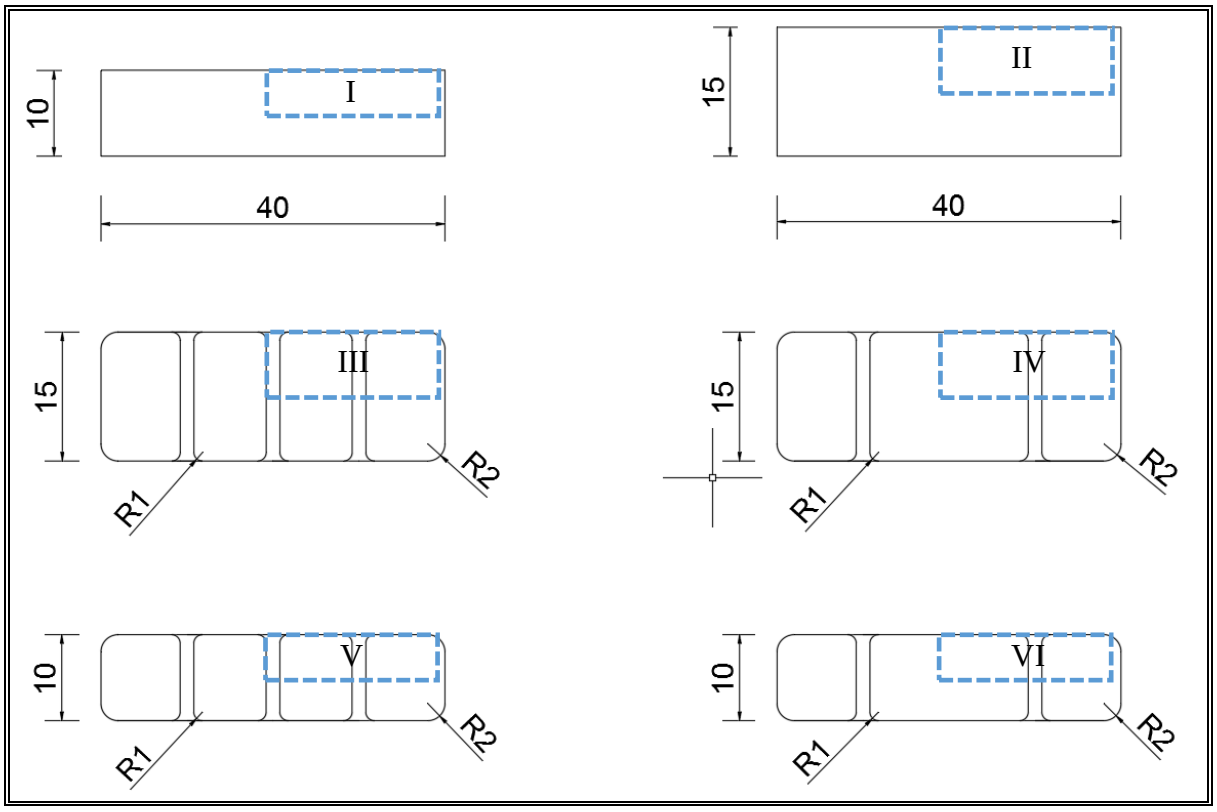

Figure 5.1: Transverse cross-section of group 1 models. Due to symmetry, only 1/4 of each column is modeled with internal borders blocked from horizontal displacement.

The second group of models represents 6 specimens. All of them present CFRP reinforcement of 1 mm in thickness. None of the models include steel reinforcement. Since these models represent a subsection of the complete column, the internal borders are blocked from any horizontal displacement, as explained in Figure 5.2. Below is a summary of characteristics of these models:

- O2-15-A: internal subsection with predrilled holes of a 3x5 disposition (as explained by Figure 3.1) and a 15-cm thickness. The transverse cross-section of this model is showed in Figure 5.2 with the subsection model marked as I.
- O2-15-B: internal subsection with predrilled holes of a 2x5 disposition (as explained by Figure 3.1) and a 15-cm thickness. The transverse cross-section of this model is showed in Figure 5.2 with the subsection model marked as II.
- O2-15-C: external subsection with predrilled holes of a 2x5 or 3x5 disposition (as explained by Figure 3.1) and a 15-cm thickness. The transverse cross-section of this model is showed in Figure 5.2 with the subsection model marked as III.
- O2-10-A: internal subsection with predrilled holes of a 3x5 disposition (as explained by Figure 3.1) and a 10-cm thickness. The transverse cross-section of this model is showed in Figure 5.2 with the subsection model marked as IV.
- O2-10-B: internal subsection with predrilled holes of a 2x5 disposition (as explained by Figure 3.1) and a 10-cm thickness. The transverse cross-section of this model is showed in Figure 5.2 with the subsection model marked as V.
- O2-10-C: external subsection with predrilled holes of a 2x5 or 3x5 disposition (as explained by Figure 3.1) and a 10-cm thickness. The transverse cross-section of this model is showed in Figure 5.2 with the subsection model marked as VI.

To increase computational efficiency, longitudinal bars are not considered in any of the models, either of group 1 or group 2. Initially models included longitudinal bars; however, computational time was significantly higher and experienced convergence problems. Therefore, longitudinal bars are removed and assumed to act as parallel columns to the specimen without buckling until failure, as was observed experimentally.

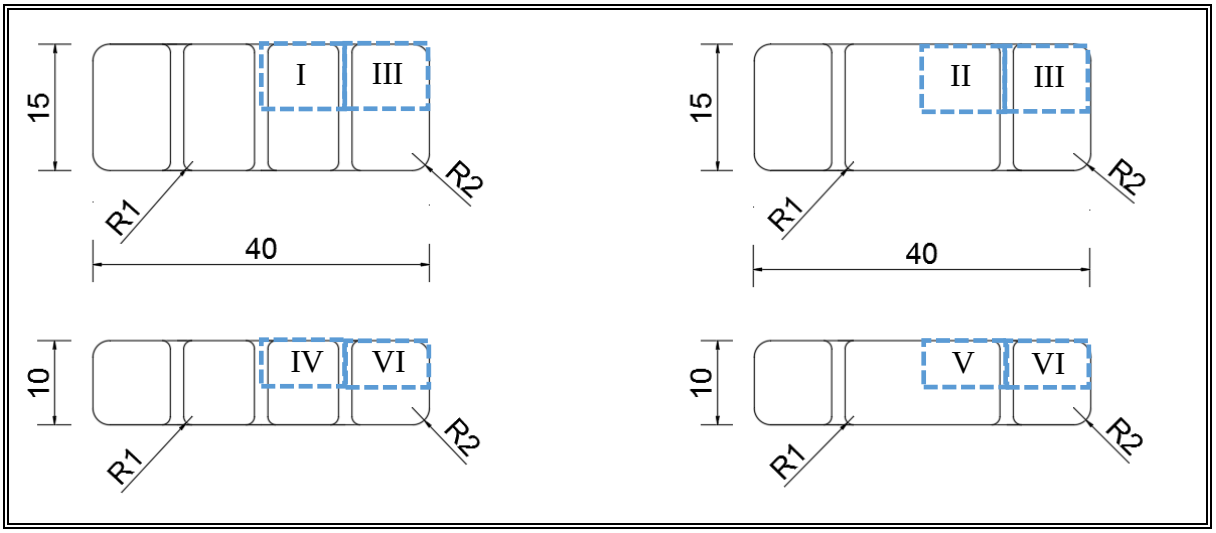

Figure 5.2: Transverse cross-section of group 2 models. Due to symmetry, only 1/2 of each subsection is modeled with internal borders blocked from horizontal displacement.

5.3 Materials

The finite element models are composed of three materials: concrete, steel reinforcement and CFRP reinforcement. In this section, the constitute models and element types that were used for each material are described.

5.3.1 Concrete

Concrete is modeled with the predefined ANSYS element SOLID65 (Figure 5.3). This element consists of a three-dimensional solid element capable of modeling concrete with or without rebar. The element is capable of modeling cracking in tension and crushing in compression. Cracking is permitted in three orthogonal directions at each integration point. If cracking occurs at an integration point, the cracking is modeled through an adjustment of material properties which effectively treats the cracking as a “smeared band” of cracks, rather than discrete cracks. The concrete material is assumed to be initially linear,

elastic and isotropic. In addition to cracking and crushing, the concrete may also undergo plasticity, with the Drucker-Prager failure surface being used. Plasticity is done before the cracking and crushing checks (SHARCNET, 2016; SHARCNET, 2015; STUBA, 1998).

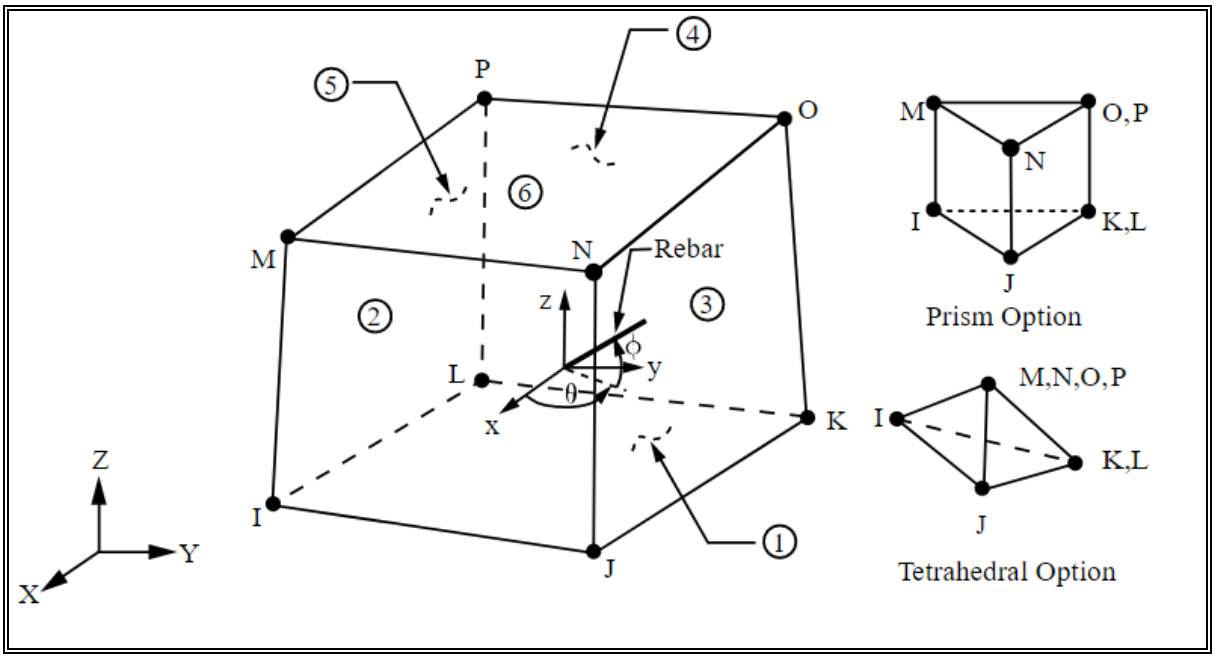

Figure 5.3: Geometry of ANSYS element SOLID65 (ref)

SOLID65 can be used in a hexahedral, prism or tetrahedral disposition (Figure 5.3). The hexahedral disposition is used for specimens without CFRP reinforcement, without predrilled holes and without rounded corners because of the simple geometry these columns present. The tetrahedral disposition is used for specimens with CFRP confinement because the predrill holes and curvature of corners generate a more complex geometry not easily represented with hexahedral elements.

The material parameters used to implement this element are:

- Modulus of elasticity: $E_c = 22180\ [MPa]$. The value is taken from tested unconfined concrete cylinders. The value is estimated at the day of testing, as explained in Appendix A.
- Unconfined concrete strength $f_c' = 37\ [MPa]$. The value is taken from tested unconfined concrete cylinders. The value is estimated at the day of testing, as explained in Appendix A.
- Poisson coefficient: $\nu_c = 0.2$. Nominal value frequently used for concrete modeling.
- Parameters required for Drucker Prager failure surface: the dilatation angle (ψ) is considered equal to 0, thereby neglecting any volumetric expansion (Mirmiran, Zagers, & Yuan, Nonlinear Finite Element Modeling Of Concrete Confined By Fiber Composites, 2000; Shahawy, Mirmiran, & Beitelman, 2000). The friction angle (ϕ) and the cohesion (c) are determined from the unconfined concrete strength (f_c') and experimental models available in the literature (Rochette & Labossiere, 1996).

$$\phi = \sin^{-1}\left(\frac{3}{1+1.592332*f_c'(ksi)}\right) = 18.335° \quad (4.1)$$

$$c = (f_c'(psi) - 1256\ [psi]) * \frac{3-\sin(\phi)}{6*\cos(\phi)} = 13.346\ [MPa] \quad (4.2)$$

The geometry of each column is introduced as a complete continuum which is later automatically meshed by ANSYS. The size of each element cannot be controlled individually, but the diameter of the sphere that circumscribes an average element is determined to be 5 mm.

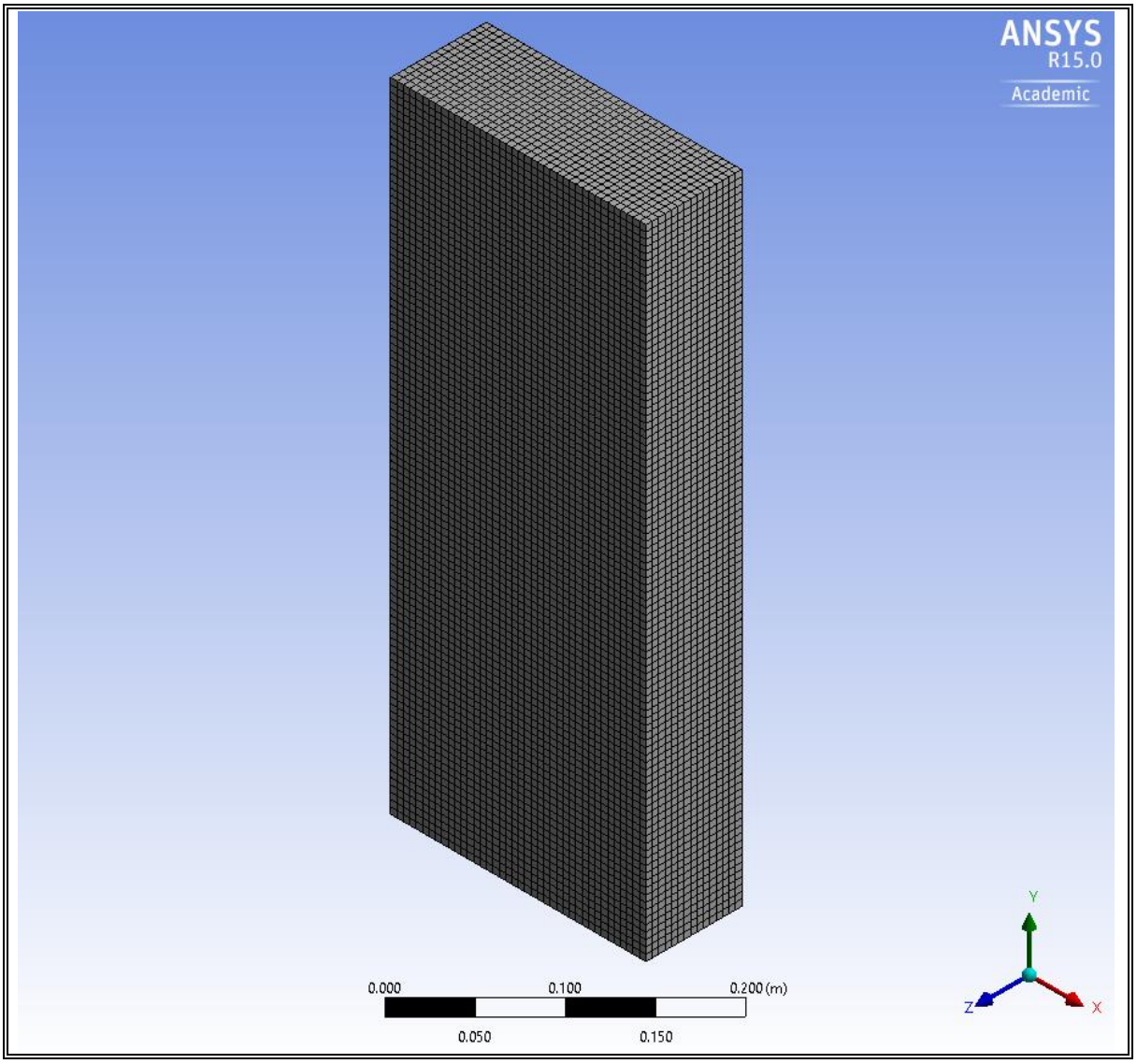

Figure 5.4: Geometry of concrete hexahedral elements. Specimen 000-15

Concrete is modeled in some cases without predrilled holes and straight corners (Figure 5.4) and in other cases with predrilled holes and round corners (Figure 5.5). Concrete in experimentally tested specimens contains predrilled holes when CFRP reinforcement is applied and do not contain predrilled holes when CFRP reinforcement is not applied. There are no experimentally tested specimens with predrilled holes and without CFRP reinforcement. However, finite element models of this last type are developed to

estimate the impact of the predrilled holes and rounded corners on the axial response of concrete.

As was mentioned in section 5.2, due to the symmetry only 1/4 of the column is modeled. For this reason, the areas intersecting with the axis of symmetry are block from any horizontal displacement, but are permitted to deform vertically. The height of all columns is 50 cm.

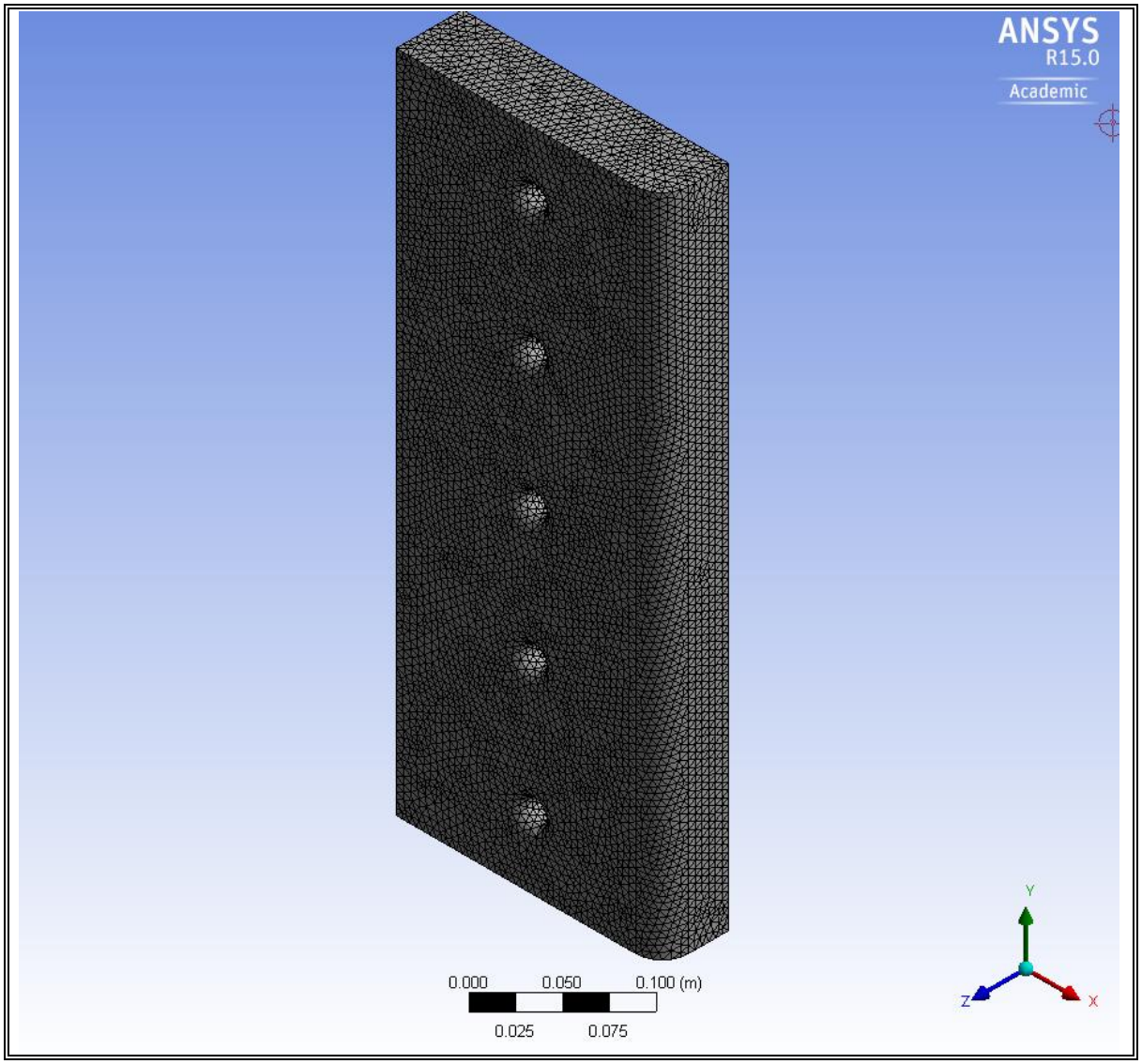

Figure 5.5: Geometry of concrete tetrahedral elements. Specimen 225-10

Although the full height of the experimentally tested specimens was 60 cm, the top and bottom 5 cm was omitted from the finite element models due to the complex distribution of stirrups and ties on these zones. The highly irregular distribution of stresses generated in this zone produced convergence problems during the analysis. Instead of modeling the exact geometry of the top and bottom 5 cm of each specimen, the top and bottom surfaces of each column are blocked from any horizontal displacements.

Finally, the external corners of all models with predrilled holes presents a radius of 2 cm and the internal corners near the predrilled holes present a radius of 1 cm.

5.3.2 Steel reinforcement

Steel reinforcement is modeled with the predefined ANSYS element BEAM188 (Figure 5.6). The element is based on Timoshenko beam theory; therefore, shear deformation effects are included. It uses three components of strain, one (axial) direct strain and two (transverse) shear strains. The degrees of freedom at each node include translations in x, y and z directions, and rotations about the x, y and z directions. The element is well-suited for linear, large rotation, and/or large strain nonlinear applications. (SHARCNET, 2015; SHARCNET, 2016; STUBA, 1998).

BEAM 188 elements are defined as linear elements with a defined cross section. These elements are used to model only transverse reinforcement. Longitudinal reinforcement is not considered in the models because their inclusion was observed to increase significantly the analysis time. Additionally, the inclusion of longitudinal bars was unnecessary since they are excepted to behave elastic perfectly plastic without buckling until failure. Transverse bars are unified with the concrete matrix by coupling degrees of freedom between coincident nodes within a tolerance of a 2-mm diameter. This was easily

achieved with the inbuilt ANSYS command *CPINTF*, which automatically couples coincident nodes of different elements. The constitutive curve of steel reinforcement is considered bilinear for both tension and compression, although the results show they only worked in tension.

The material parameters used to implement this element are:

- Modulus of elasticity: $E_s = 206010\,MPa$. Nominal value frequently used for structural steel modeling.
- Poisson coefficient: $\nu_s = 0.3$. Nominal value frequently used for steel modeling.
- Yield stress: $f_y = 420\,MPa$. Nominal value of the minimum yield stress determined by catalog of the used steel bars as explained in section 3.2.2.
- Tangent modulus: $E_{sh} = 2625\,MPa$. Calculated value of hardening stiffness considering the minimum elongation ultimate rupture of 8% and the minimum ultimate stress $f_u = 630\,MPa$ determined by catalog of the used steel bars as explained in section 3.2.2.

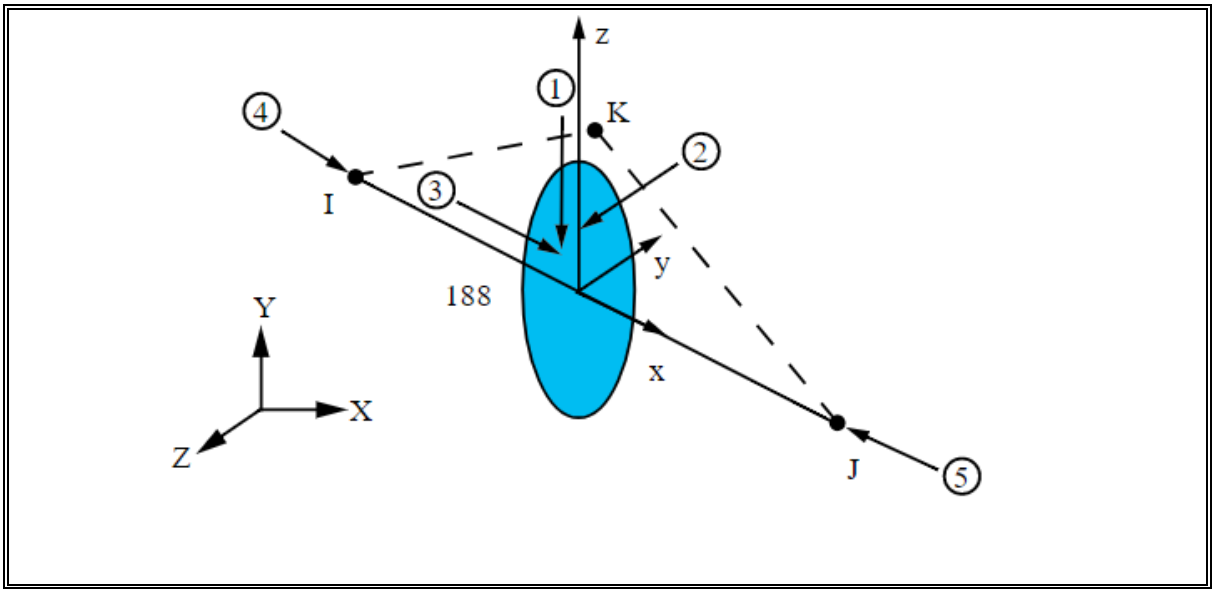

Figure 5.6: Geometry of ANSYS element BEAM188

The geometry of each transverse reinforcement is drawn as continuum line with a circular cross section with a diameter of 6 mm (nominal value determined by catalog of the used steel bars). ANSYS automatically meshed each bar into segments of 5 mm in length (Figure 5.7). All transverse steel reinforcements present a 1-cm radius around the bending corner.

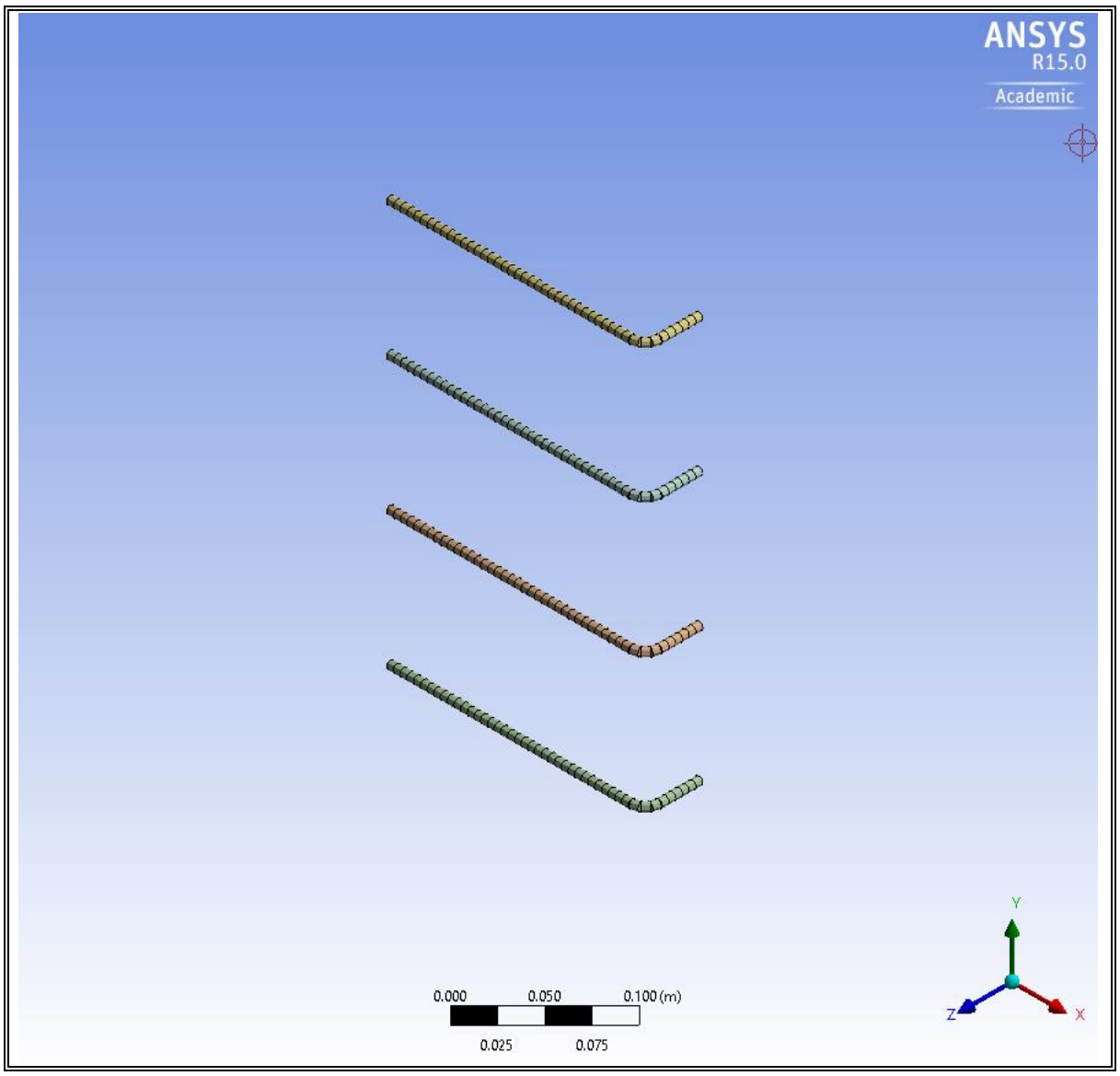

Figure 5.7: Geometry of transverse reinforcement

5.3.3 CFRP reinforcement

CFRP reinforcement is modeled with the predefined ANSYS element SHELL41 (Figure 5.8). The element is defined by nodes, thicknesses, a material direction angle and the material properties. This type of element does not have out-of-plane bending stiffness

This element has a nonlinear “cloth” option. This "cloth" option allows the element to wrinkle when it goes into compression. Wrinkling may be in one (or both) orthogonal directions. The “cloth” option is used to capture de anisotropic behavior of the CFRP reinforcement since carbon fibers are oriented in different directions around CFRP anchors. When the element is in tension its behavior is linear-elastic. (SHARCNET, 2015; SHARCNET, 2015; STUBA, 1998).

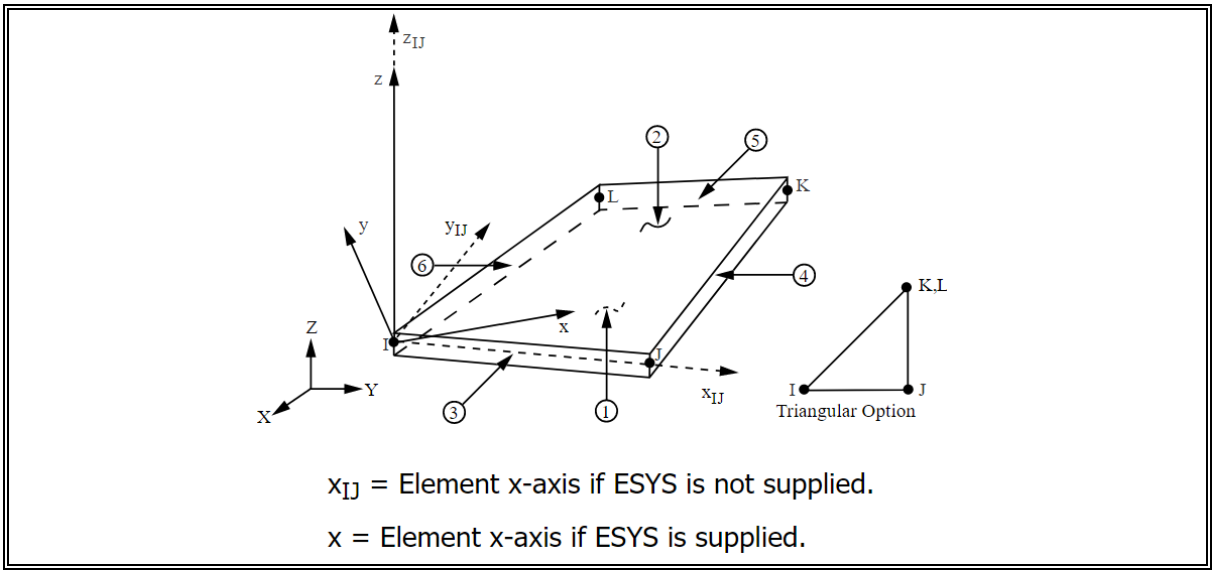

Figure 5.8: Geometry of ANSYS SHEEL41 element

SHELL41 elements can be used in a rectangular or triangular disposition (Figure 5.8). The triangular disposition was used to model CFRP reinforcement since its geometry is complex around CFRP anchors and corners and triangular elements can easily adapt such geometry. It is important to point out that the SHELL41 elements represent the cured composite composed of carbon fibers and epoxy resin. The carbon fibers are not modeled discretely because of the high geometric complexity this would introduce in the model. (Figure 5.9, 5.10).

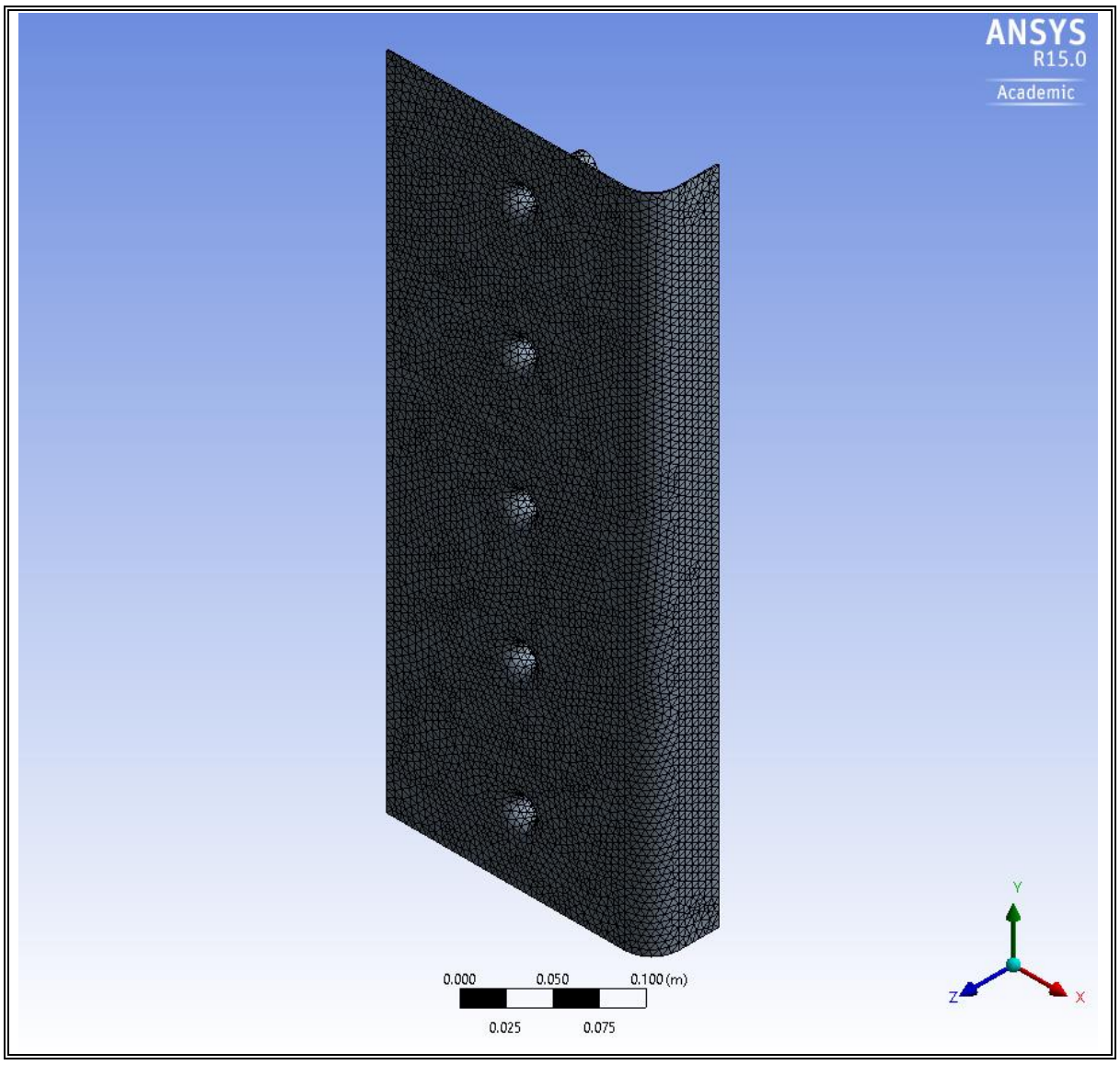

Figure 5.9: Geometry of CFRP elements, front view. Specimen 225-10

The material parameters used to implement this element are:

- Modulus of elasticity: $E_{CFRP} = 76000\ MPa$. Nominal value taken from the catalog of the manufacturer for the CFRP cured composite, as explained in section 3.2.3
- Poisson coefficient: $\nu_{CFRP} = 0.3$. Nominal value frequently used for CFRP

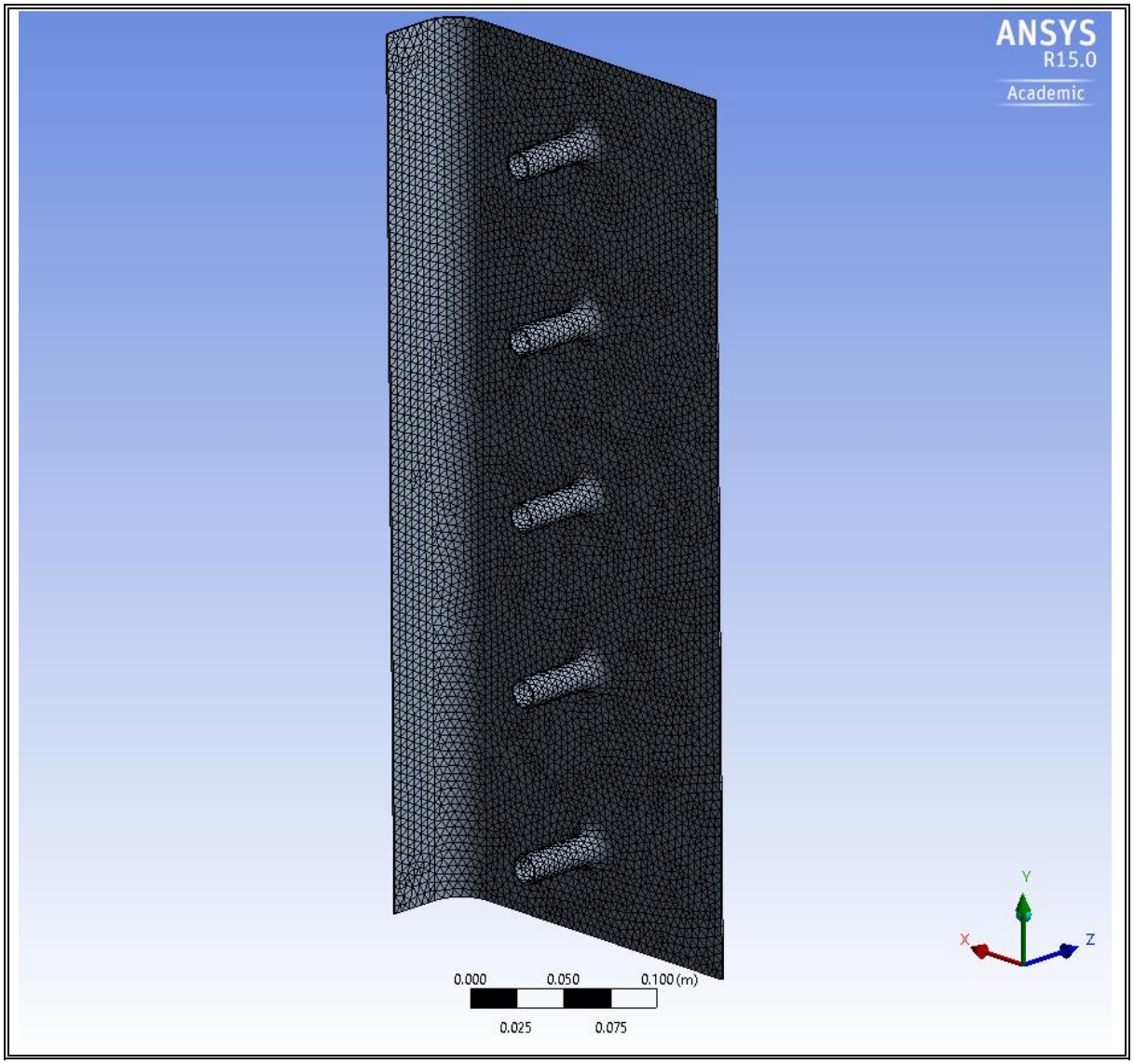

Figure 5.10: CFRP elements back view. Specimen 225-10

The geometry of the CFRP reinforcement is introduced to the model as a continuum surface. ANSYS automatically meshed the continuum surfaces in triangles with a size that could be circumscribed by a 5-mm diameter circumference. The manufactured specified a nominal thickness of the cured composite of 0.5 mm for each wrap, therefore, specimens with 2 wraps of CFRP (225-10, 225-15, 235-10 and 235-15) are assigned a 1 mm thickness

and specimens with 3 wraps of CFRP (325-10, 325-15, 335-10 and 335-15) are assigned a 1.5 mm thickness.

5.4 Loading method

All specimens are loaded by applying a uniform compression displacement on top of the column. This compression displacement is applied in steps of 0.25 mm, representing a displacement controlled testing machine.

ANSYS models are not capable of capturing a descending branch after the peak is reached in the axial load vs displacement curves, therefore all models present ascending curves. Also, ANSYS models are not capable of identifying the failure of the specimen, consequently, axial compression could be applied until unrealistic large strains without loss of convergence. For this reason, displacement is applied until a similar displacement to the one obtained in the experimental results is achieved.

For specimens reinforced with CFRP wraps, axial displacements are applied until a total displacement of 3 mm is achieved. Considering each displacement step consists of 0.25 mm, 12 displacement steps are applied. Also, considering all columns have a 500-mm height, specimens are compressed until a 0.006 average axial compression strain is obtained. This assumption is very conservative since that the maximum axial average strain of tested specimen was considerably influenced by the use of a force controlled machine. Similar studies have presented axial average strains as high as 0.02 using a displacement controlled machine (Hany, Hantouche, & Harajli, Generalized Axial Stress-Strain Response Of Rectangular Columns Confined Using CFRP Jackets And Anchors, 2016; Triantafillou, et al., 2016).

For specimen without CFRP reinforcement, axial displacements are applied until a total displacement of 1.75 mm is achieved. Considering each displacement step consists of 0.25 mm, 7 displacement steps are applied. Also, considering all columns have a 500-mm height, specimens are compressed until a 0.0035 average axial compression strain is obtained.

5.5 Group 1 models results

In this section, the results from the group 1 models are described. The main results obtained from these models are axial stress-strain curves, stress distributions of concrete, steel reinforcement and CFRP wraps and widening curves at a specific location. Because of the complex geometry of each specimen, stress distributions are presented graphically at a specific load step.

Due to the large number of developed models, stress distributions of only specimens O1-000-10-A, O1-000-10-C and O1-325-10 are presented. Although the results of only these specimens are described, all the observations obtained from specimens O1-000-10-A, O1-000-10-C and O1-325-10 also apply to the rest of the models. The stress distributions of all other models from group 1 are showed in Appendix C.

5.5.1 Specimens axial behavior

This section describes the axial behavior of each specimen and compares it with its corresponding experimental results. Conceptually all models present the same behavior, as a compressive displacement is applied on top of the column, concrete begins to widen transversally, this widening generates a passive confining effect from steel stirrups and

CFRP wraps which help the concrete reach higher stress values. The axial behavior is presented as average axial stress-strain curves.

The average strain is obtained as the displacement step applied to specimen divide by the original total height of the column (500 mm). As was explained in section 5.4, compression displacement is applied until an axial strain 0.0035 is reached in the case of columns without CFRP reinforcement and 0.006 for CFRP reinforced columns. The average concrete compression stress is obtained as the total axial reaction of the column's bottom support divided by the gross transverse cross section area. The transverse are of longitudinal steel bars is not subtracted from the gross area because those bars are not included in the ANSYS models.

The curves obtained in this section represent the average stress-strain response of the columns; however, due to the complex geometry of the specimens some localized zones present higher and lower values of stress and strain than the values presented in these curves, as is explained graphically in section 5.5.2.

Figure 5.11 shows the axial behavior of specimens without CFRP reinforcement and a 15-cm thickness from ANSYS and experimental models. Specimens 000-15a and 000-15b are identical experimental columns and do not contain predrilled holes nor rounded corner. Specimen 000-15-A is an ANSYS model similar to specimens 000-15a and 000-15b since it does not present predrilled holes nor rounded corners. Specimens 000-15-B and 000-15-C are ANSYS models with rounded corners and predrilled holes in a 2x5 and 3x5 disposition, respectively. Exactly the same description applies to Figure 5.12, where the axial behavior of specimens without CFRP reinforcement and a 10-cm thickness is described.

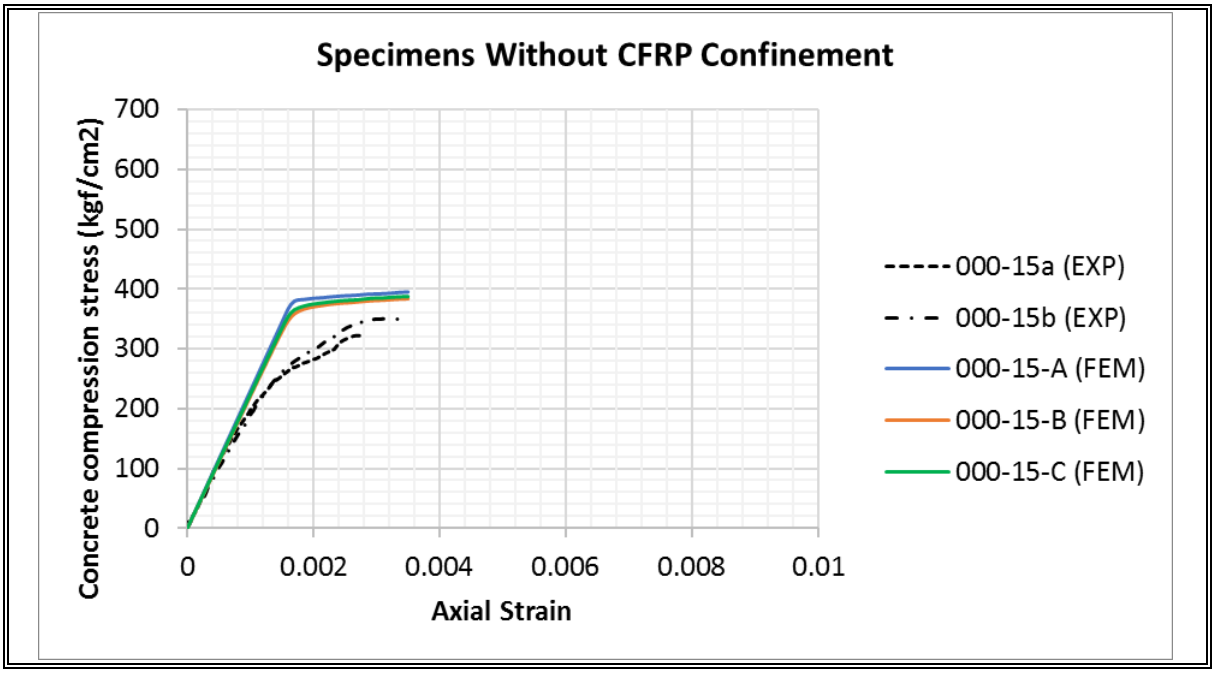

Figure 5.11: Comparison of axial behavior of experimental and ANSYS models without CFRP confinement and a 15-cm thickness

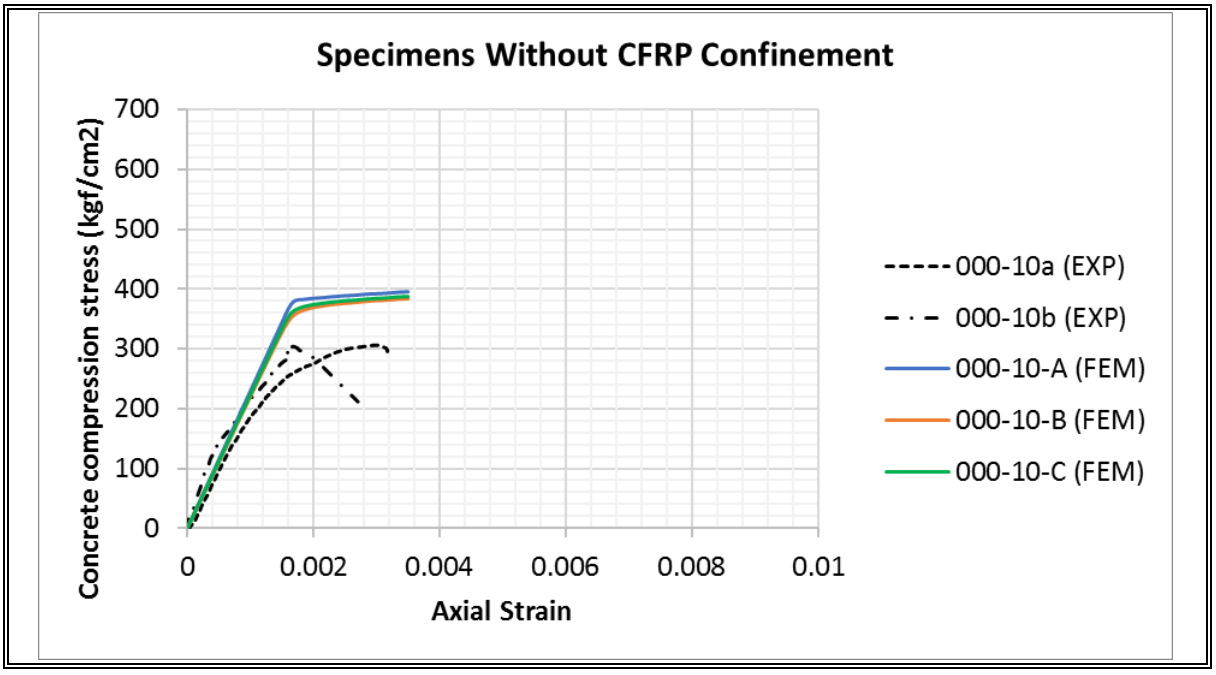

Figure 5.12: Comparison of axial behavior of experimental and ANSYS models without CFRP confinement and a 10-cm thickness

It can be seen from Figures 5.11 and 5.12 that ANSYS models overestimate the maximum stress capacity of experimentally tested columns. The FEM models are not able to represent a descending branch after a peak value is achieved. The FEM models with predrilled holes and rounded corners present a slightly lower curve than the FEM models without these elements; however, the difference is visually almost imperceptible and practically inexistent.

Figures 5.13, 5.14, 5.15 and 5.16 show the axial behavior of specimens 225-15, 235-15, 325-15, 335-15, 225-10, 235-10, 325-10 and 335-10. The curves are grouped according to the number of CFRP wraps and columns thickness.

It can be seen from these curves that the ANSYS models tend to overestimate the strength of columns with a 2x5 CFRP anchor disposition and underestimate the strength of columns with a 3x5 CFRP anchor disposition, independent from the number of CFRP wraps or column thickness. As is explained in section 5.5.2, these over and underestimation is mainly due to the compressive stresses generated in the columns. Specimens with a 3x5 CFRP anchor disposition tend to generate values of compressive axial stresses even lower than f'_{co} at the final axial strain and specimens with a 2x5 CFRP anchor disposition present compressive axial stresses much higher than f'_{co}.

The curves of specimens 225-15, 325-15, 225-10 and 325-10 are almost identical, although the thickness of the columns and CFRP thickness varies. The same is observed for columns 235-15, 335-15, 235-10 and 335-10. Although none of the curves approximates the experimental curves for high axial strains, the initial stiffness of all ANSYS specimens is close to the experimental initial stiffness.

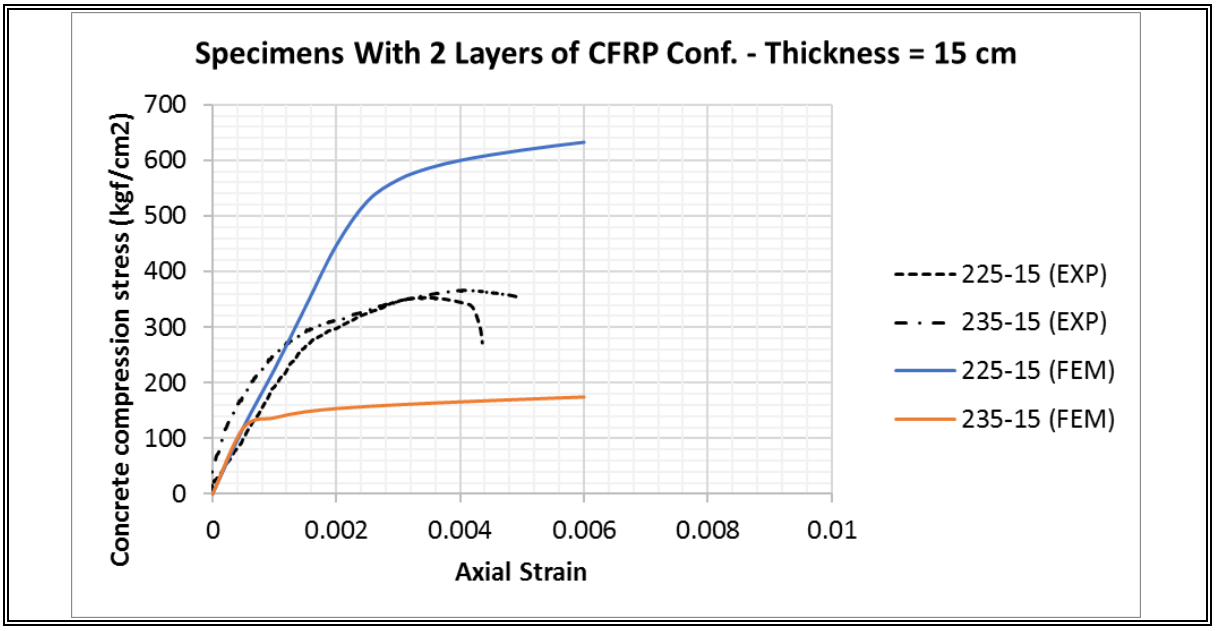

Figure 5.13: Comparison of axial behavior of experimental and ANSYS models of specimens 225-15 and 235-15

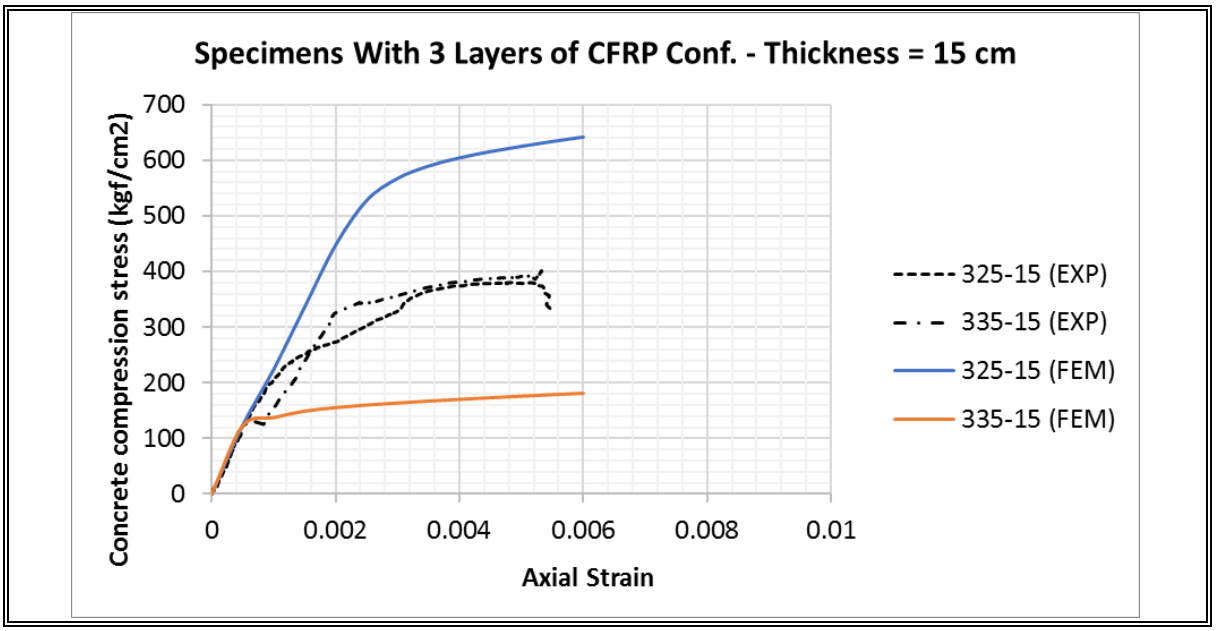

Figure 5.14: Comparison of axial behavior of experimental and ANSYS models of specimens 325-15 and 335-15

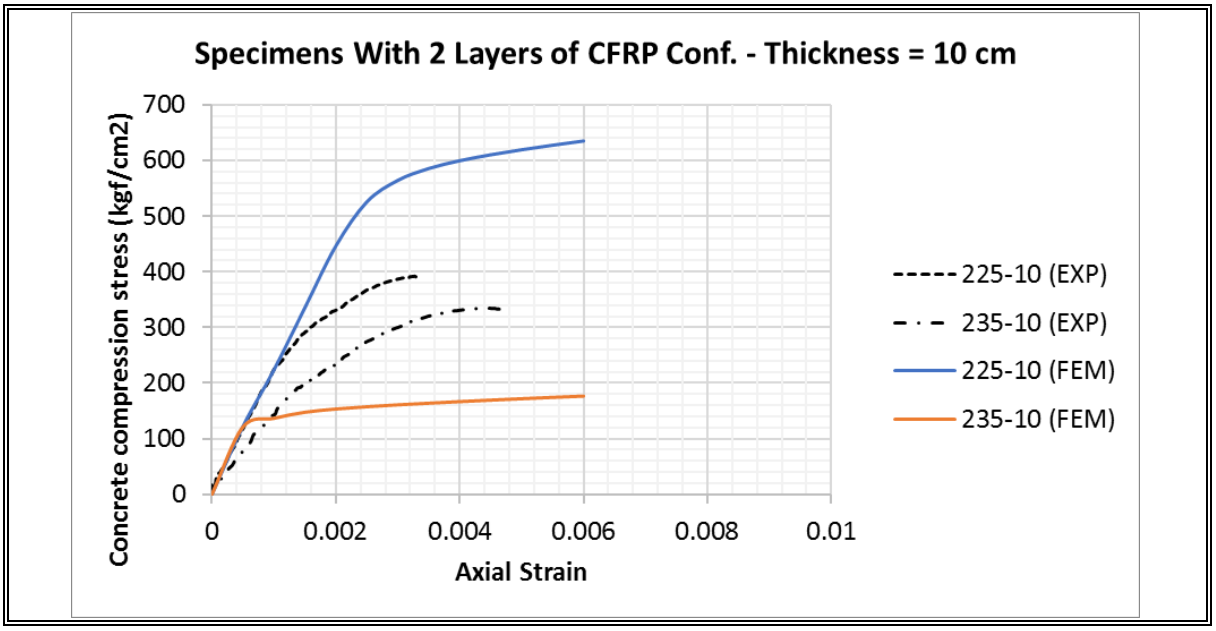

Figure 5.15: Comparison of axial behavior of experimental and ANSYS models of specimens 225-10 and 235-10

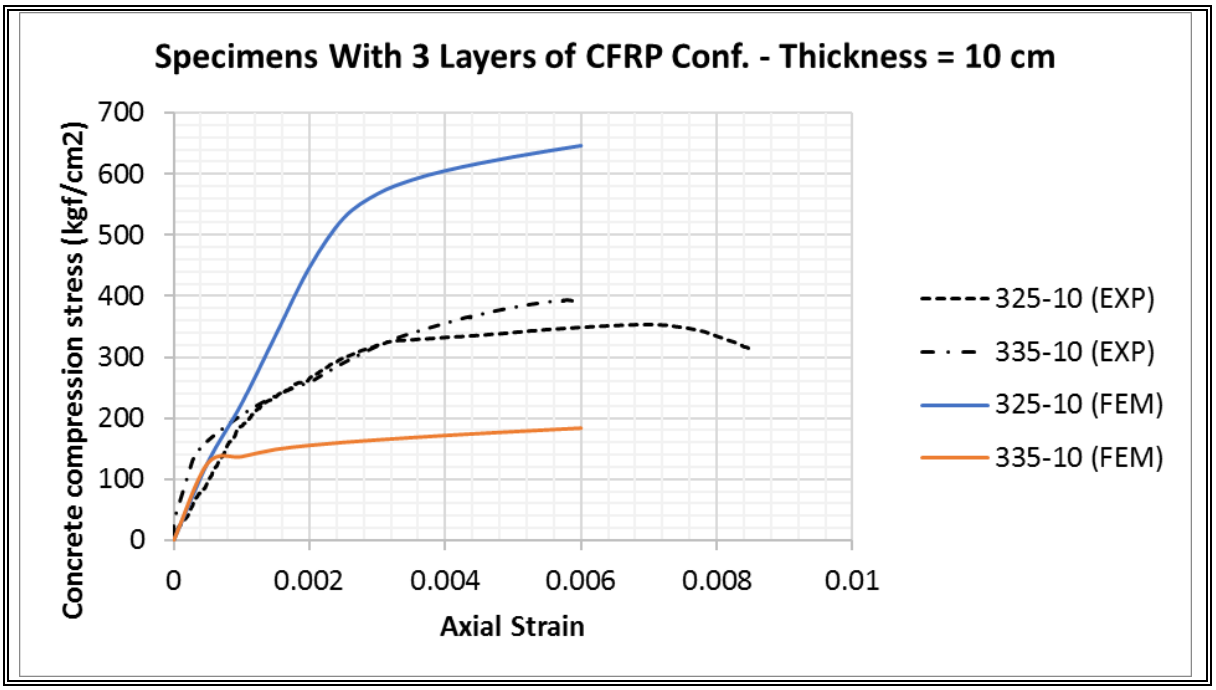

Figure 5.16: Comparison of axial behavior of experimental and ANSYS models of specimens 325-10 and 335-10

5.5.2 Concrete stress distribution

This section describes graphically the principal stresses generated in the concrete elements for specimens O1-000-10-A, O1-000-10-C and O1-325-10. As was explained in section 5.5, the graphics of all other specimens are showed in Appendix C and the observations of O1-000-10-A, O1-000-10-C and O1-325-10 are representative of all models.

Specimen O1-000-10-A represents a column without predrilled holes, without rounded corners and without CFRP reinforcement. Specimen O1-000-10-C represents a column with predrilled holes, with rounded corners and without CFRP reinforcement. Specimen O1-325-10 represents a column with predrilled holes, with rounded corners and with CFRP reinforcement. Each of these cases is described in its own subsection. All three specimens represent ¼ of a column with 10-cm thickness.

In all graphics, the distribution of principal stresses is presented. This is because it was observed that the orientation of the principal stresses is adequate to describe the stress state of confined concrete elements at the central zone of the columns, between predrilled holes (Figure 5.17).

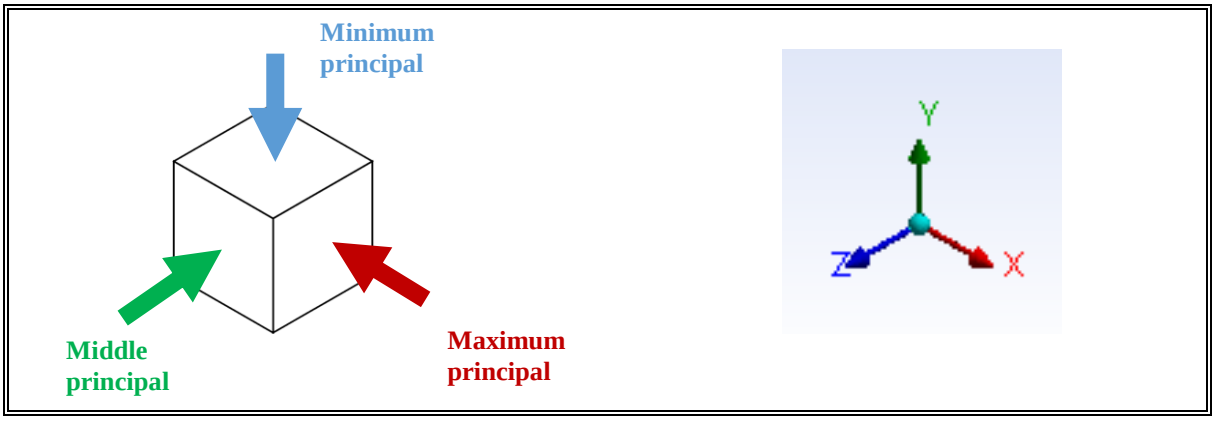

Figure 5.17: Direction of concrete principal stresses with respect of global coordinates. Y: axial direction, X and Z: horizontal directions.

At these zones, the principal minimum stress coincides with the vertical axis Y (longitudinal axis of the column). Since the specimens present a complex geometry, the middle and the maximum principal stresses do not coincide with the horizontal axis X and Z. However, since they are always orthogonal to the minimum principal stress, they are always present a direction contained in the transverse cross-section of the column

5.5.2.1 Specimens without CFRP wraps, without rounded corners or predrilled holes

Figure 5.18 shows the deformed configuration of specimen O1-000-10-A at the 7th displacement step (1.75 mm), the final displacement state. The deformation coincides with the expected behavior, with the largest widening occurring at the middle-height of the column and the top and bottom supports without any horizontal deformation. Although widening is concentrated at the center of the column, transverse cross sections do not deform in a significant manner under the application of an axial compression.

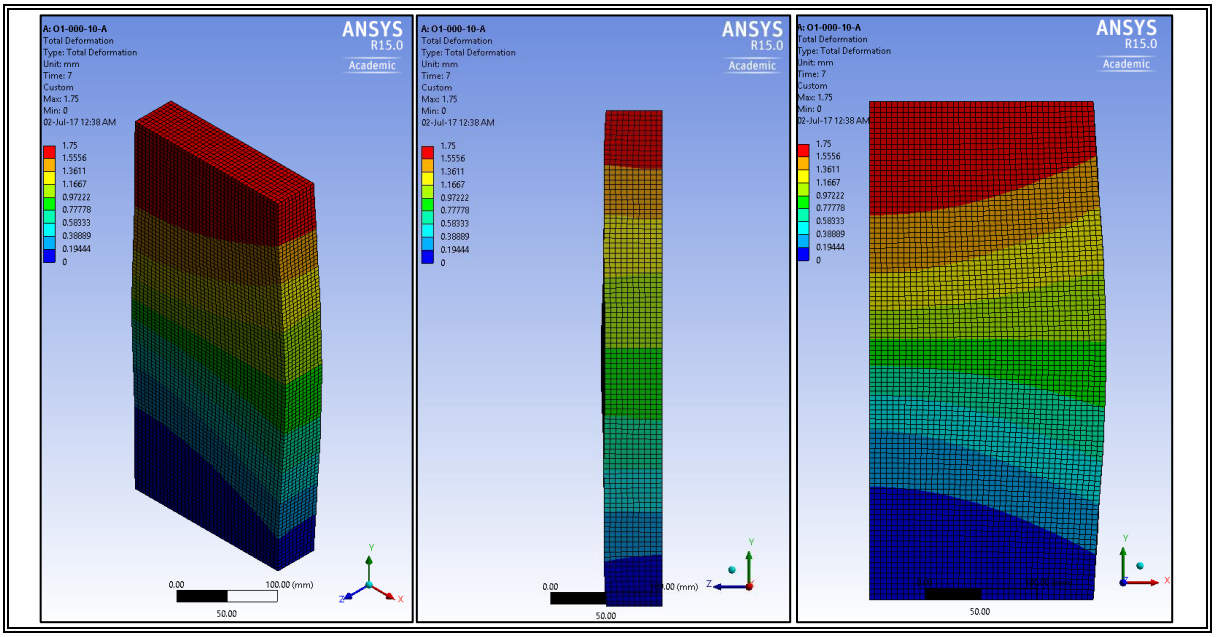

Figure 5.18: Total deformation of a column without predrilled holes, without rounded corners and without CFRP reinforcement. Scale amplified 31 times. Units: mm

Figure 5.19 shows the distribution of minimum principal stresses in specimen O1-000-10-A. The minimum principal stress coincides with the longitudinal direction of the column, and the middle and maximum principal stresses lie inside the transverse cross-section. The minimum principal stresses increase slightly near the stirrups corner, but the increase occurs at a very small zone. Most of the central cross section of the column presents an almost uniform axial stress of around 37 MPa. It is important to point out that f_c' is equal to 37 MPa, which reflects the minimum confinement provided by the stirrups.

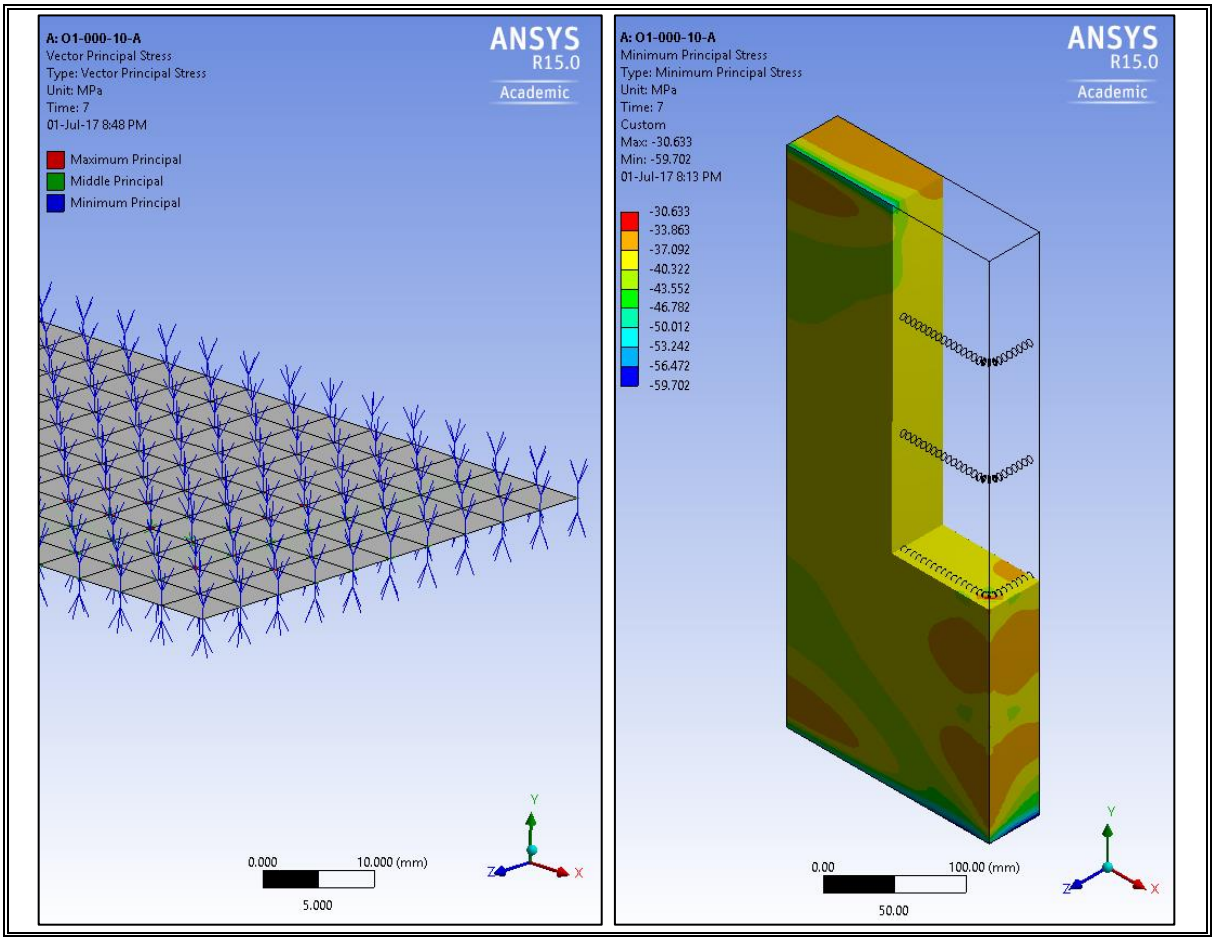

Figure 5.19: Principal stress orientation and minimum principal stresses. Specimen O1-000-10-A

Figure 5.20 shows the middle and maximum principal stresses. In both cases the stresses generated are very small, with a small increase near the corners of the stirrups. This show the poor confinement provided by the stirrups in any direction inside the transverse cross-section. The confining stresses near the mid height of the column are almost zero, with the highest confining stresses concentrated at the top and bottom supports of the column.

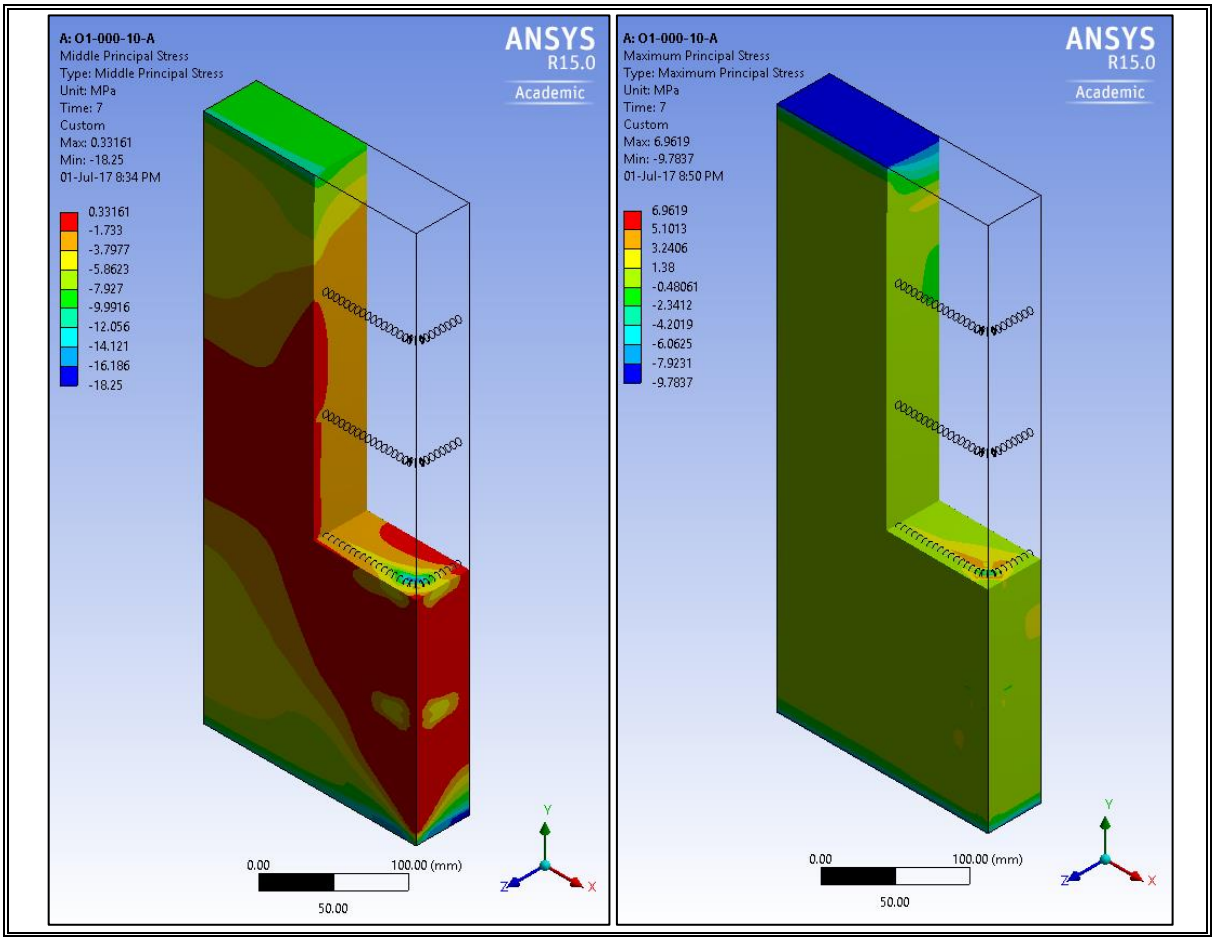

Figure 5.20: Middle and maximum principal stresses. Specimen O1-000-10-A

5.5.2.2 Specimens without CFRP wraps, with rounded corners and predrilled holes

Figure 5.21 shows the deformed configuration of specimen O1-000-10-C at the 7th displacement step (1.75 mm), the final displacement state. The deformation coincides with the expected behavior, with the largest widening occurring at the middle-height of the column and the top and bottom supports without any horizontal deformation. Although widening is concentrated at the center of the column, transverse cross sections do not deform in a significant manner under the application of an axial compression, at least

between predrilled holes. Predrilled holes tend to close as expected, but central holes seem to experience this with more severity.

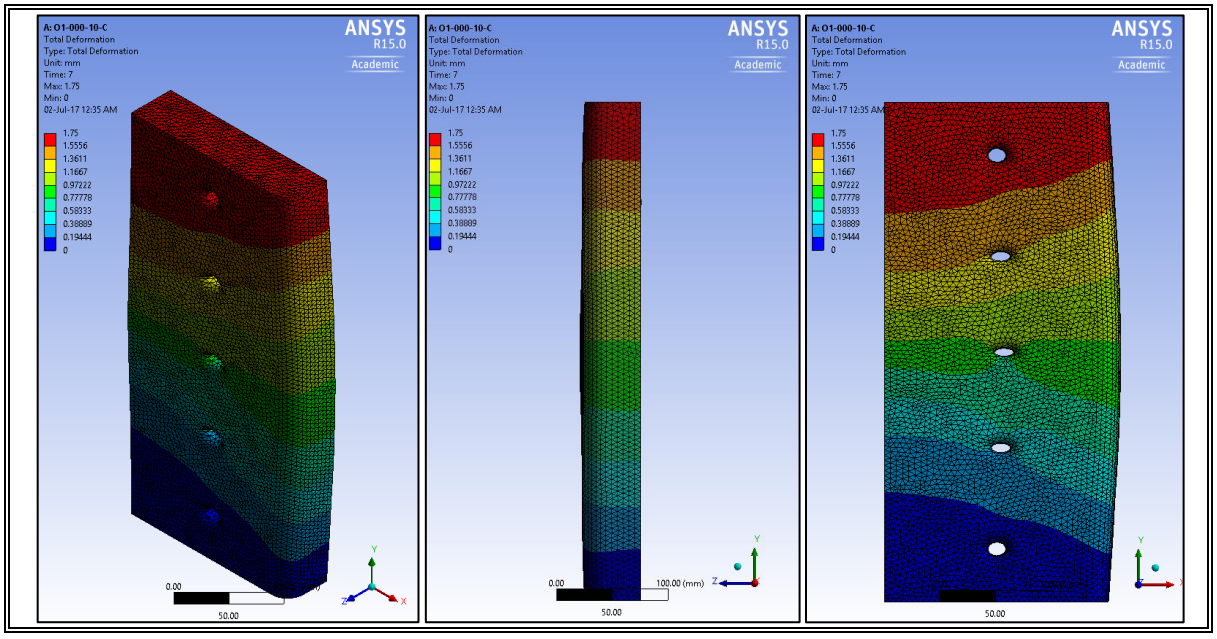

Figure 5.21: Total deformation of a column with predrilled holes, with rounded corners and without CFRP reinforcement. Scale amplified 31 times. Units: mm

Figure 5.22 shows the distribution of minimum principal stresses in specimen O1-000-10-C. The minimum principal stress coincides with the longitudinal direction of the column, and the middle and maximum principal stresses lie inside the transverse cross-section. The minimum principal stresses increase slightly near the stirrups corner, but the increase occurs at a very small zone. Due to the geometry of the predrilled holes, an increase of minimum principal stress occurs on the sides of the hole and a reduction occurs over and under the holes. The presence of the predrilled holes increases the heterogeneous distributions of stresses but the variations are localized mainly at predrilled holes. These

variations are of small magnitude since most of the cross-section remains with a stress around 37 MPa (f_c').

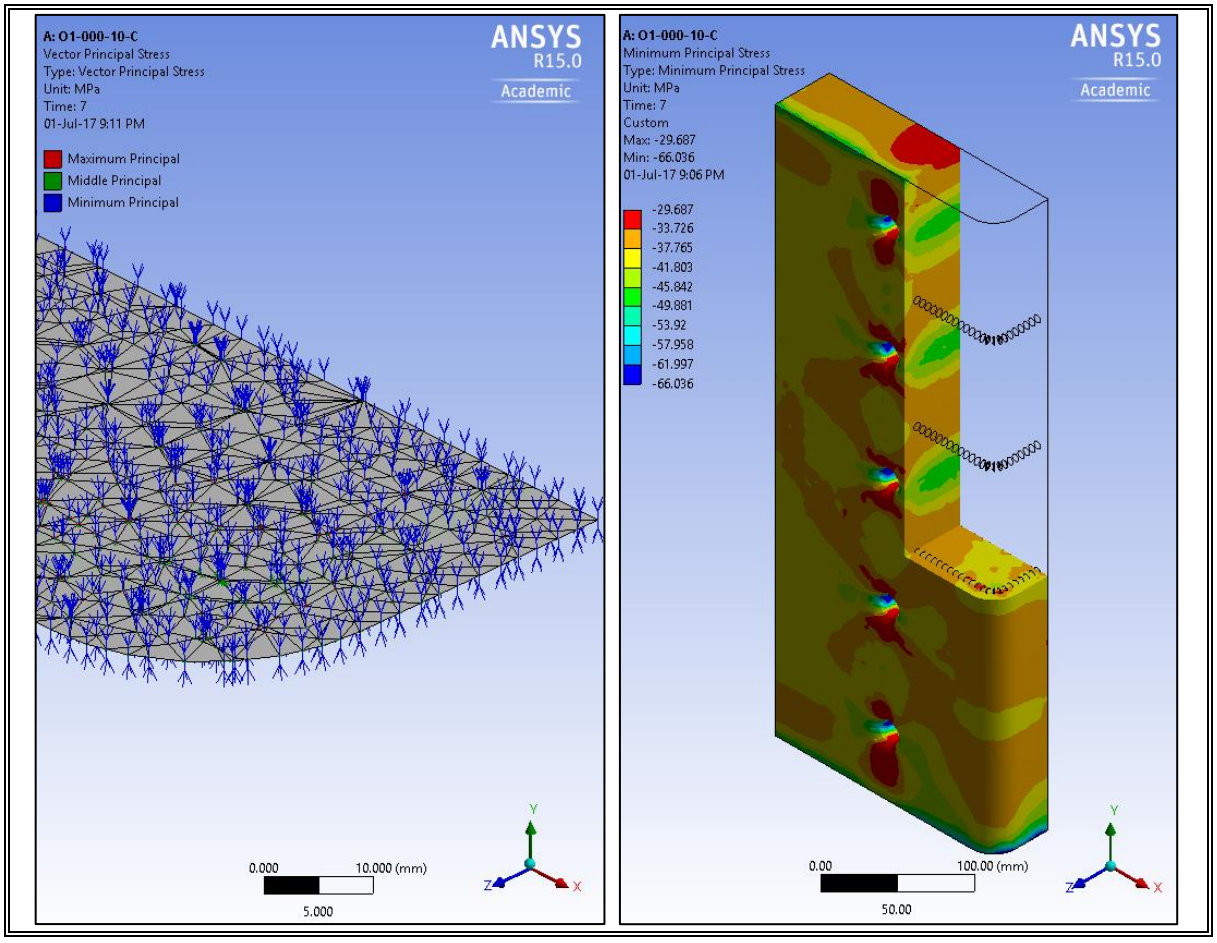

Figure 5.22: Principal stress orientation and minimum principal stresses. Specimen O1-000-10-C

Figure 5.23 shows the middle and maximum principal stresses that lay inside the transverse cross section. Due to the geometry of the rounded corner and predrilled holes, a heterogenous distribution of stresses generates; however, the values of this stresses remain very low. Only at the corners of the stirrups the values increase but in a much-reduced zone.

Some zones present positive stresses which represent tension mainly due to the presence of predrilled holes. The largest confinement comes from the top and bottom supports.

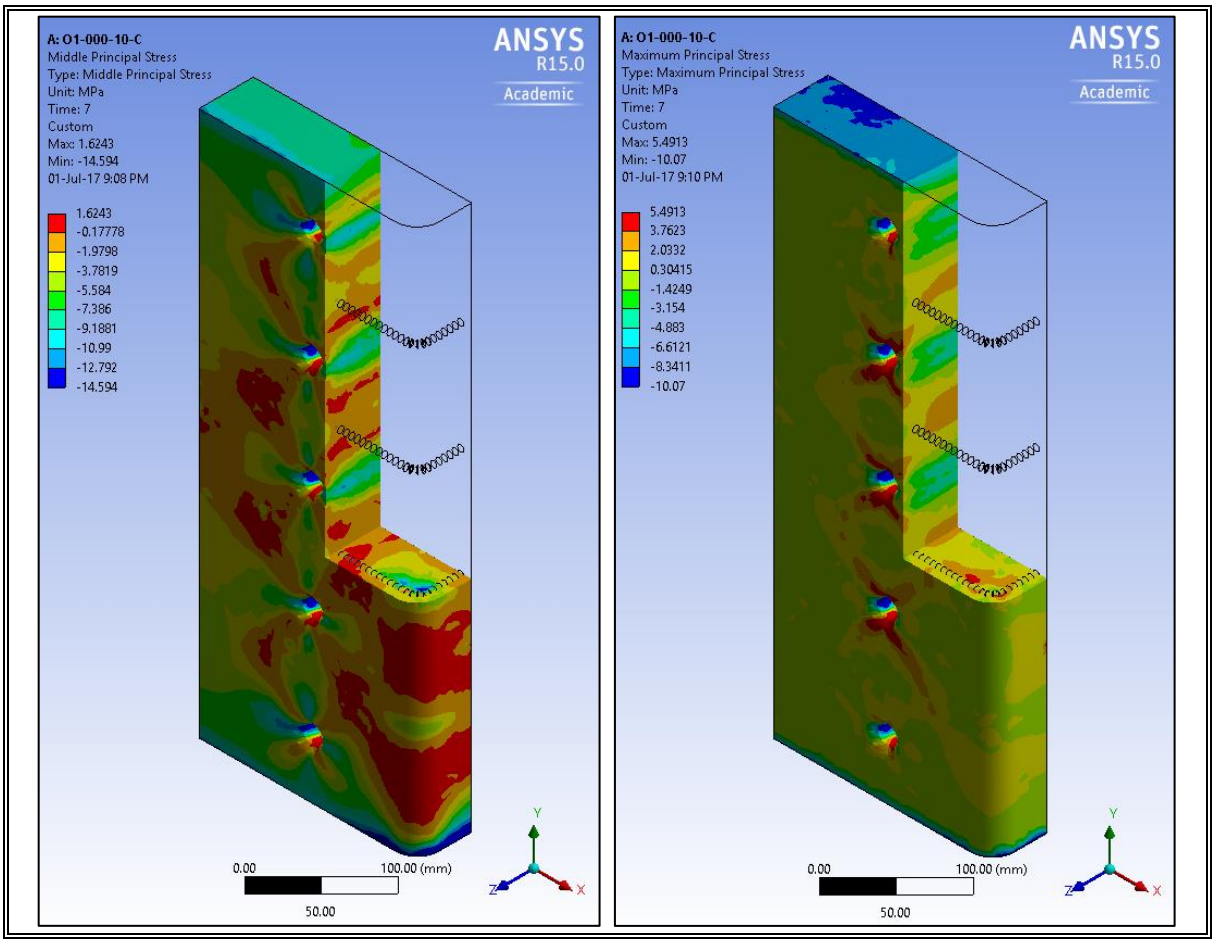

Figure 5.23: Middle and maximum principal stresses. Specimen O1-000-10-C

5.5.2.3 Specimens with CFRP confinement

Figure 5.24 shows the deformed configuration of specimen O1-325-10 at the 12th displacement step (3 mm), the final displacement state. The deformation coincides with the expected behavior, with the largest widening occurring at the middle-height of the column and the top and bottom supports without any horizontal deformation. Although widening is concentrated at the center of the column, transverse cross sections do not deform in a

significant manner under the application of an axial compression, at least between predrilled holes. Predrilled holes tend to close as expected, but central holes seem to experience this with more severity.

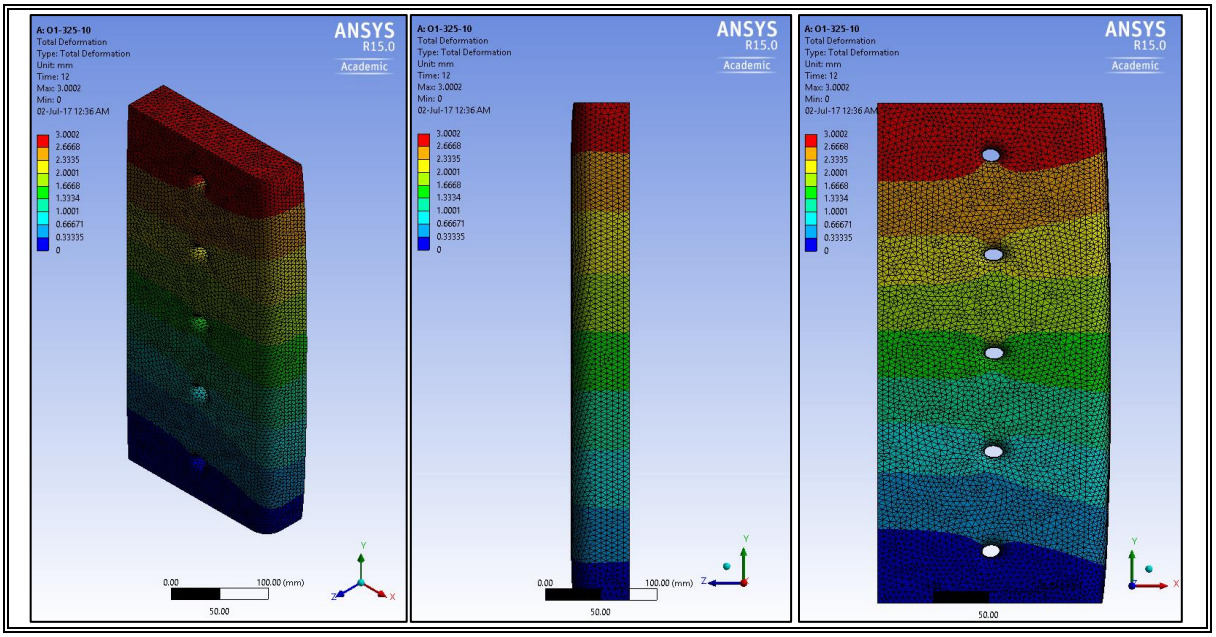

Figure 5.24: Total deformation of a column with predrilled holes, with rounded corners and with CFRP reinforcement. Scale amplified 18 times. Units: mm

Figure 5.25 shows the distribution of minimum principal stresses in specimen O1-325-10 at the 7th displacement step (1.75 mm), the final displacement state of specimens without CFRP wraps. The minimum principal stress coincides with the longitudinal direction of the column, and the middle and maximum principal stresses lie inside the transverse cross-section. The confinement provided by the stirrup is almost imperceptible. Due to the presence of CFRP confinement, the axial stresses in the column experience a significant change. Between predrilled holes vertically, the stress remains at 37 MPa ($f_c' =$ 37 MPa), but on the overall central cross-section the stress is around 53 MPa, due to the

confinement provided by CFRP reinforcement. The zone immediately next to the predrilled holes also present and increase in stress, mainly due to the CFRP anchors.

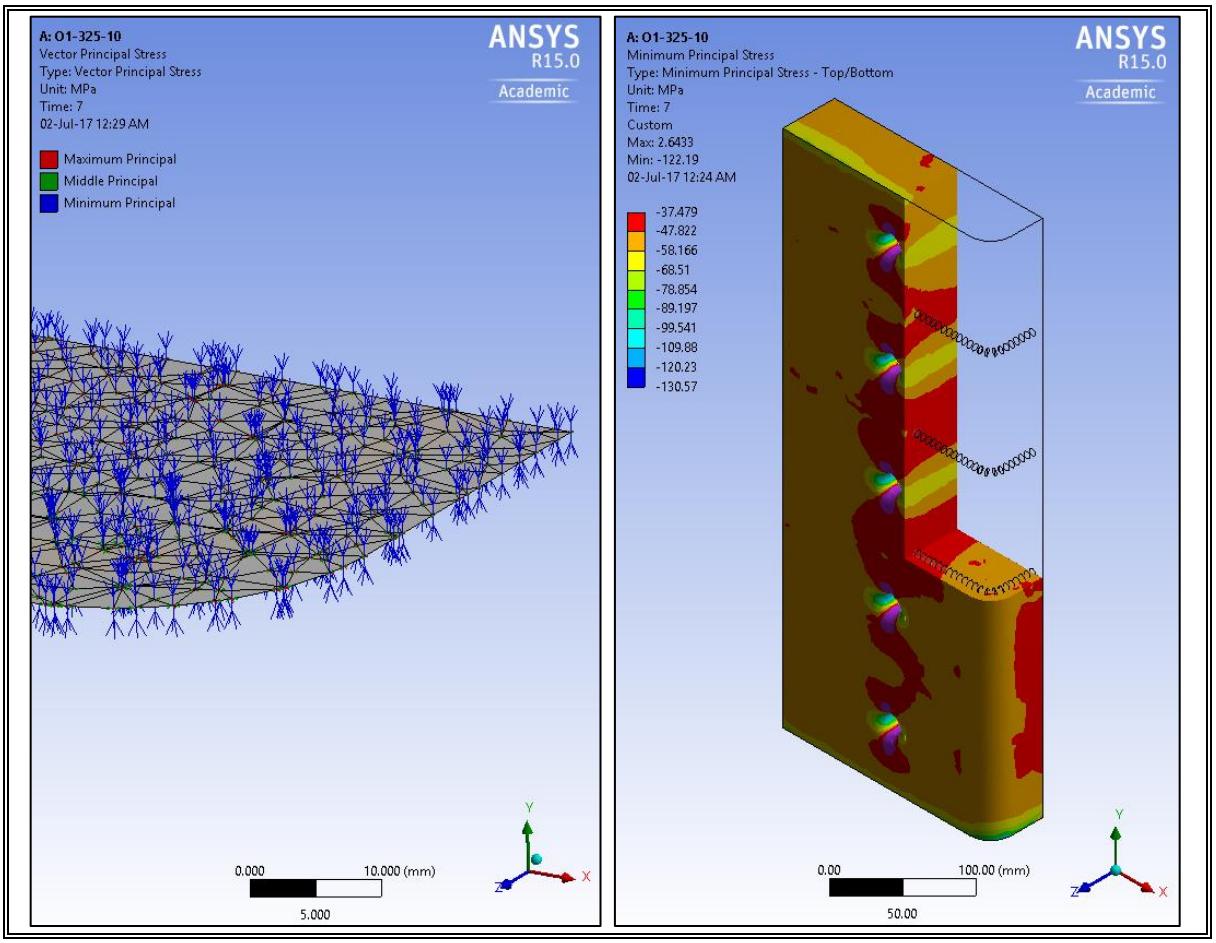

Figure 5.25: Principal stress orientation and minimum principal stresses. Specimen O1-325-10

Figure 5.26 shows the distribution of minimum principal stresses in specimen O1-325-10 at the 12th displacement step (3 mm), the final displacement state. Similar to the 7th step, the axial stresses in the column experience a significant increase. The zone of 37 MPa ($f_c' = 37$ MPa) reduces in size and most of the cross section shows a stress of around 53 MPa, mainly due to the CFRP anchor action. The zone near the corner of the specimen also

experiences an increase in stress, product of the CFRP wrap around the corner up to 68 MPa.

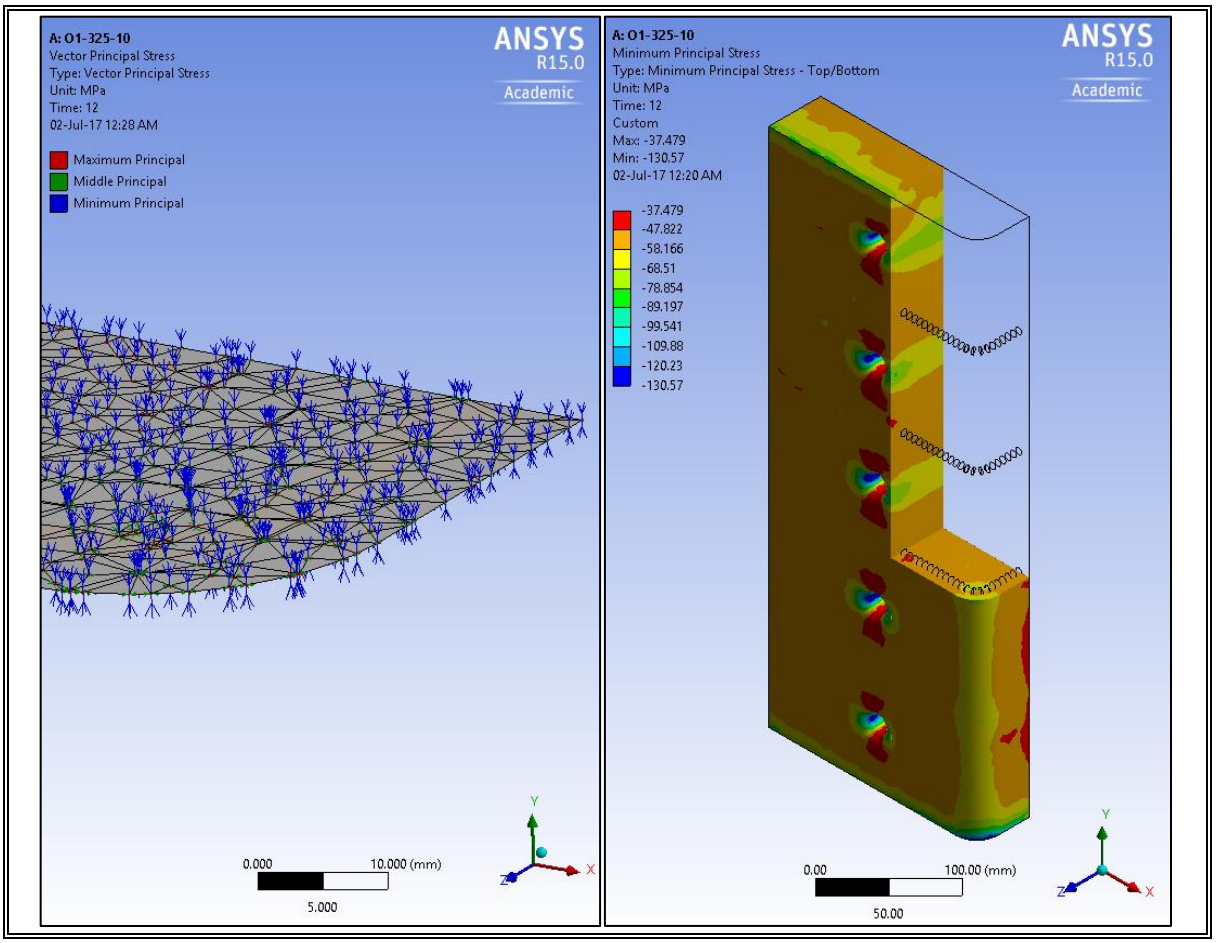

Figure 5.26: CFRP elements back view. Specimen 225-10

Figure 5.27 shows the middle and maximum principal stresses at the 7th displacement step (1.75 mm), the final displacement state of specimens without CFRP wraps. The values of confining stresses are significantly higher compared to the stresses in Figure 5.23, mainly due to the confining action of CFRP wraps. Confining stresses

concentrate near the CFRP anchors. A small increase in confining stresses is seen near stirrups corners.

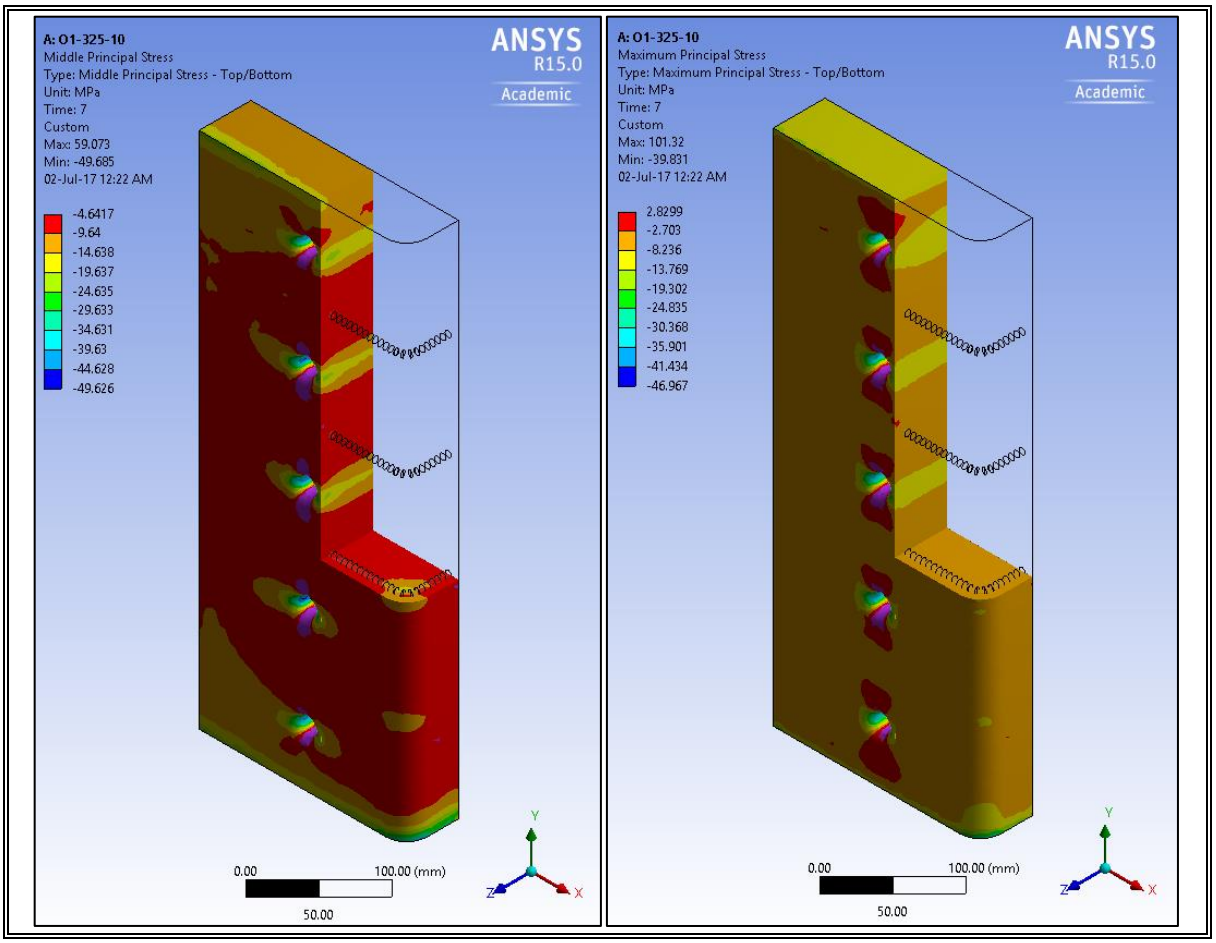

Figure 5.27: Middle and maximum principal stresses 7th step. Specimen O1-325-10

Figure 5.28 shows the middle and maximum principal stresses at the 12th displacement step (3 mm), the final displacement state. The confining stresses increased compared to Figure 5.27 and are even higher compared to Figure 5.23. High confining stresses are concentrated at CFRP anchors and at the column corner. Stirrups also generate an increase in confining stresses but is localized at a very reduced zone near the stirrups corners.

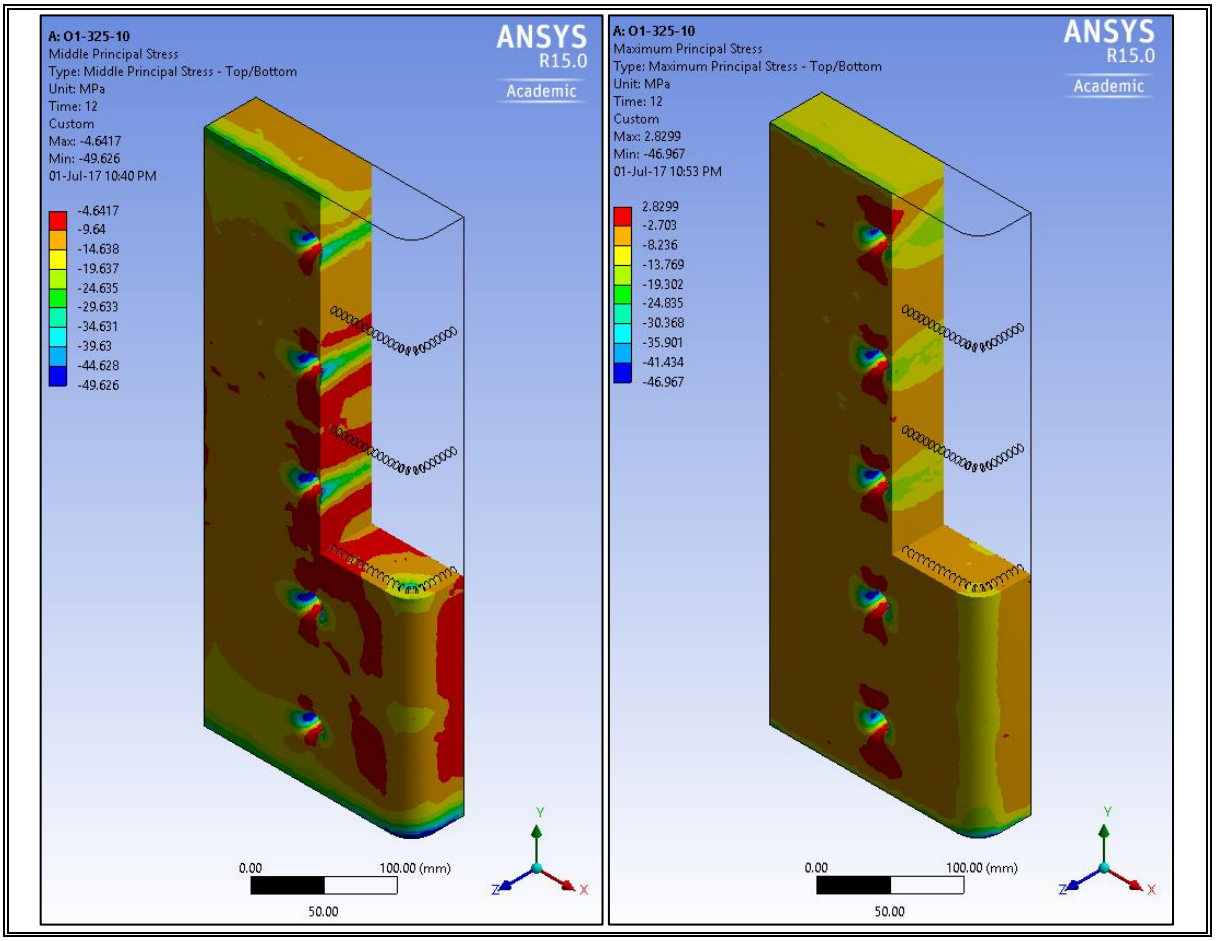

Figure 5.28: Middle and maximum principal stresses 12th step. Specimen O1-325-10

5.5.3 Steel stress distribution

This section describes graphically the axial stresses generated in the steel stirrups for specimens O1-000-10-A, O1-000-10-C and O1-325-10. As was explained in section 5.5, the graphics of all other specimens are showed in Appendix C and the observations of O1-000-10-A, O1-000-10-C and O1-325-10 are representative of all models. Figure 5.29 show the stresses in stirrups of specimens without CFRP wraps, without rounded corners or predrilled holes, Figure 5.30 show the stresses in stirrups of specimens without CFRP wraps, with

rounded corners and predrilled holes and Figure 5.31 show the stresses in stirrups of specimens with CFRP confinement.

Figures 5.29 and 5.30 show that by the final displacement step (7th step), specimens without CFRP wraps experience yielding in the stirrups near the center of the column. Yielding does not occur at the stirrups corners. Due to the confining action of the top and bottom supports the top and bottom stirrups do not experience yielding.

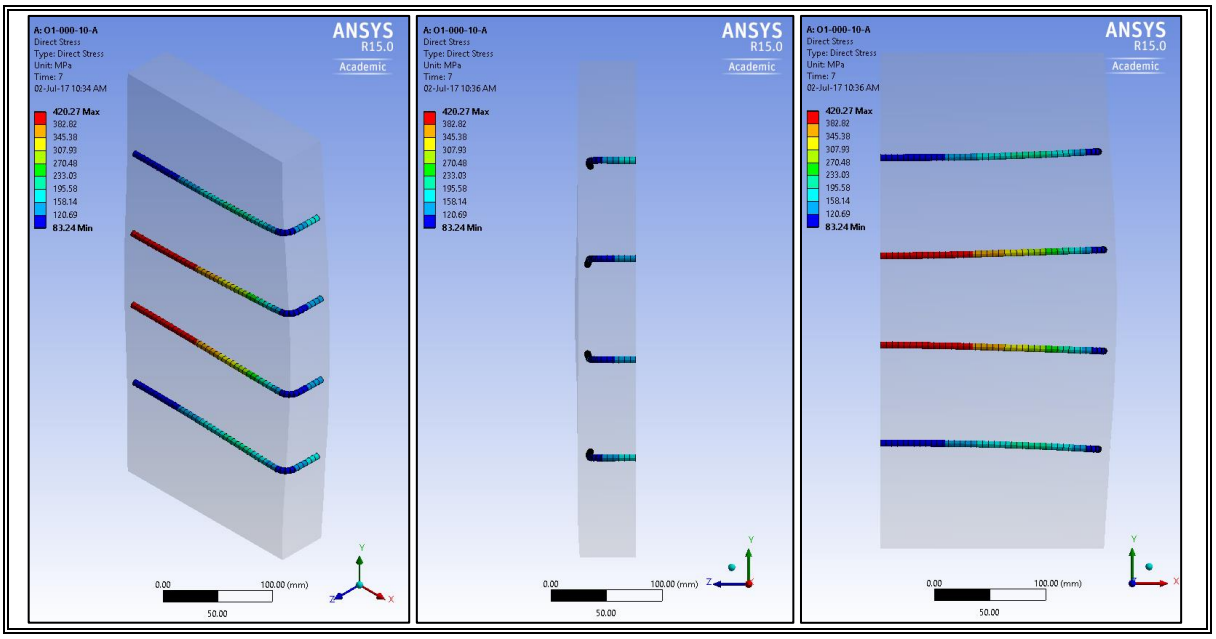

Figure 5.29: Steel stirrup axial stresses at final step (7th step). Specimen O1-000-10-A

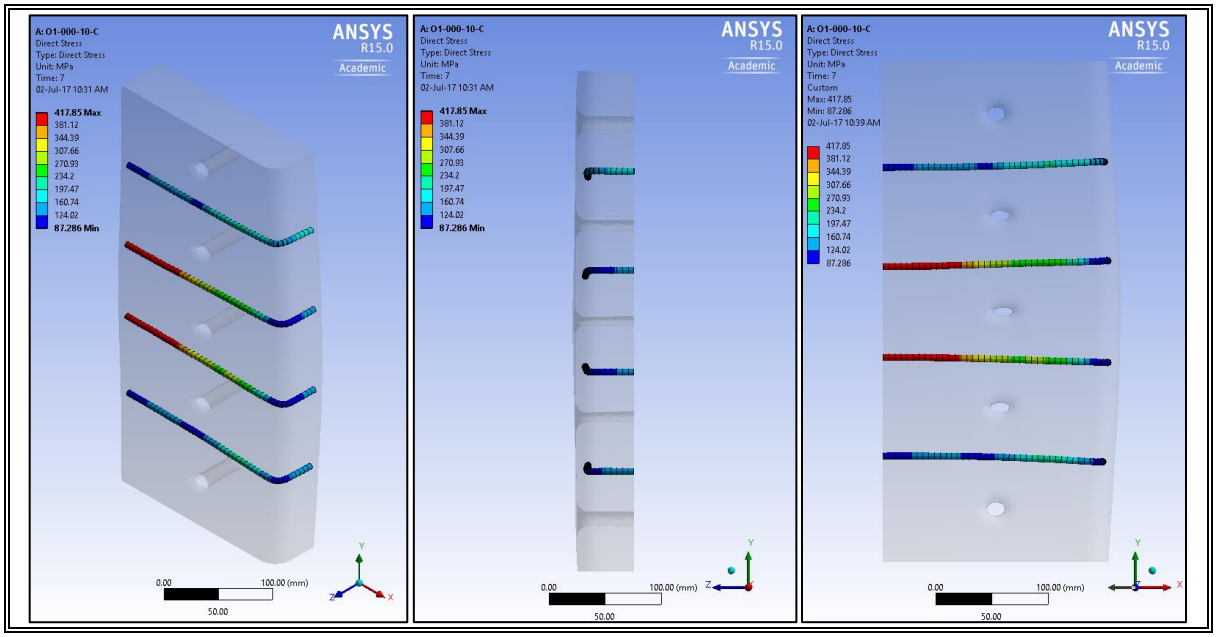

Figure 5.30: Steel stirrup axial stresses at final step (7th step). Specimen O1-000-10-C

Figure 5.31 show that the specimen with CFRP confinement, for the same displacement step as Figures 5.29 and 5.30 (7th step) do not present yielding of the stirrups.

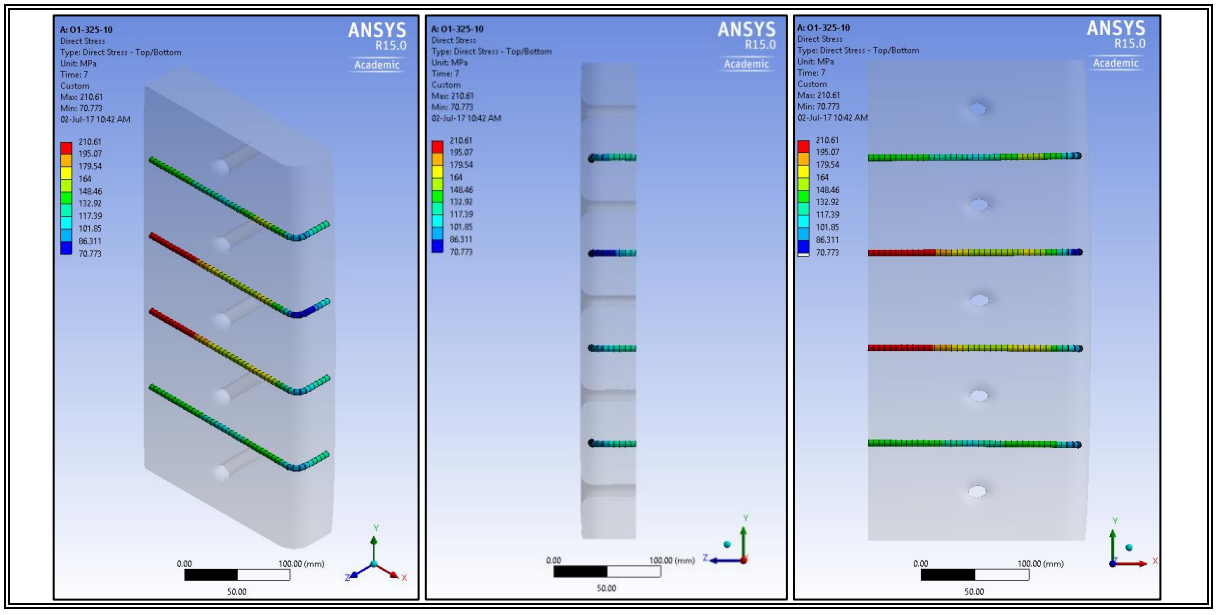

Figure 5.31: Steel stirrup axial stresses at 7th step. Specimen O1-325-10

Figure 5.32 show that the specimen with CFRP confinement presents yielding of the central stirrups for its final displacement step (12th step). The yielding is localized at the center of the column, no yielding is observed near the corners of the stirrups.

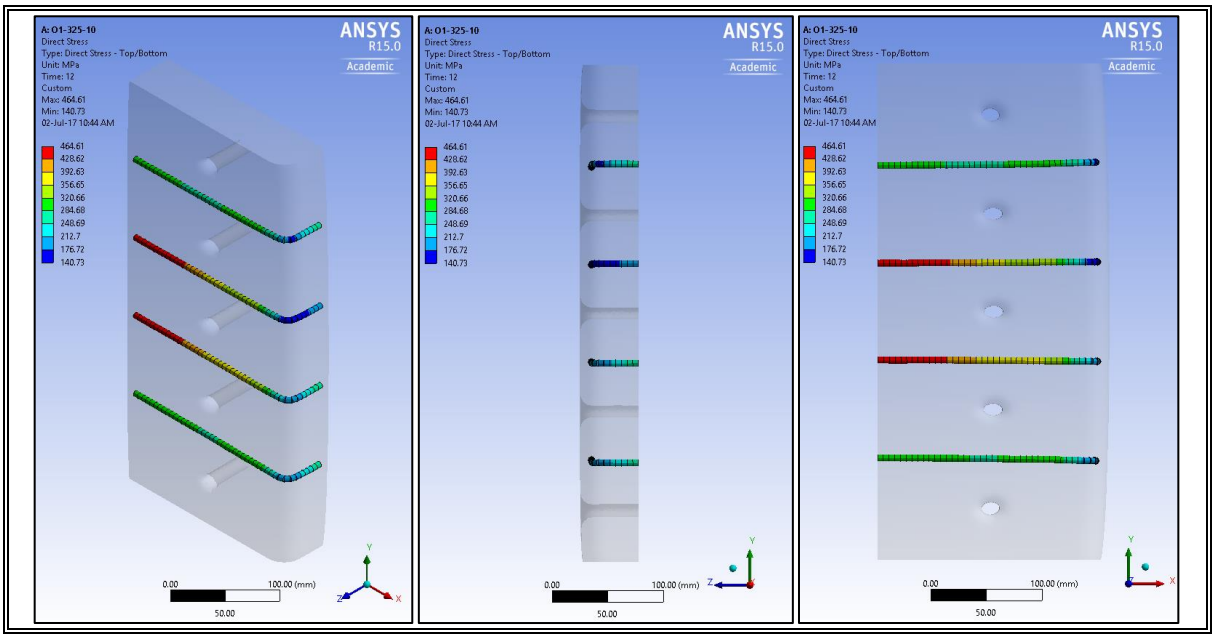

Figure 5.32: Steel stirrup axial stresses at final step (12th step). Specimen O1-325-10

5.5.4 CFRP ultimate stress

This section describes the stresses generated at the CFRP wraps. The principal stresses are displayed in following graphics because they represent appropriately the behavior of CFRP wraps. The orientation of the maximum principal stress changes with the orientation of the fiber (Figure 5.33). At most zones, the direction of the maximum principal stress is horizontal and tangent to the CFRP surface. At the zones of the CFRP anchors, the maximum principal stresses manage to change they orientation to accommodate the shape of the anchor. The maximum principal stress remains positive (in tension) in all the CFRP reinforcement.

Since the CFRP wraps are modeled with SHELL41 elements with the "cloth" option activated, no compressive stresses can be generated, therefore, the middle and minimum principal stresses cannot be negative.

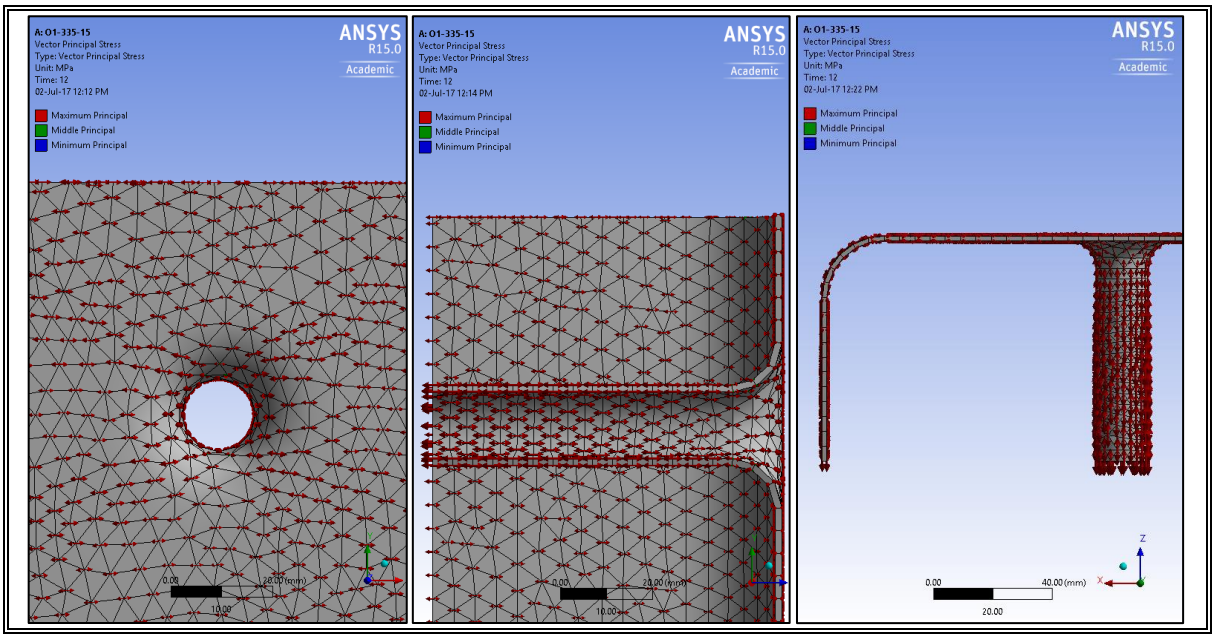

Figure 5.33: CFRP elements back view. Specimen 225-10

Table 5.1 presents a summary of the largest maximum principal stress for each specimen present at the final displacement step (12th step). As it is explained in Chapters 1 and 5, the hoop stress at which CFRP ruptures in CFRP confined concrete columns is a crucial parameter to determine the ultimate point of the stress-strain curve ($\varepsilon_c^{ult}, f_c^{ult}$). According to most design oriented models, the larger the failure hoop stress is, the larger ductility increase due to CFRP wrapping will be. In Table 5.1, the efficiency factor $\kappa_\varepsilon^{CFRP}$ is calculated based on CFRP stresses calculated with the ANSYS models for the ultimate axial applied strain.

Since most of the strain gages placed in the experimental models could not be located near the failure zone, and the digital imagine correlation could not capture with sufficient precision the strain during testing, the CFRP ultimate hoop stresses from the

ANSYS models are the most complete and coherent information available. The rupture tension of CFRP wraps specified by the manufacturer is 970 MPa. Although the CFRP strain experimental readings are considered not accurate enough, the axial behavior of the column captured experimentally is considered sufficiently accurate. Based on the experimental testing, most specimens failed at an average strain around 0.006. Therefore, the CFRP hoop failure tension is assumed to be the one that occurs at this axial strain.

Table 5.1: Summary CFRP failure hoop stresses according to ANSYS models.

Specimen	ε_c^{ult}	$f_{frp}^{ult,h}\ \left(\frac{kgf}{cm^2}\right)$	$\kappa_\varepsilon^{CFRP} = \frac{\frac{f_{frp}^{ult,h}}{E_{frp}}}{\frac{970\ MPa}{E_{frp}}}$	Location of maximum stress
225-10	0.006	2349	0.237	Around corner of predrilled hole (Figure 5.34a)
225-15	0.006	2463	0.249	Around corner of predrilled hole (Figure 5.34b)
235-10	0.006	2588	0.262	Middle of the CFRP anchor (Figure 5.35a)
235-15	0.006	2681	0.271	Middle of the CFRP anchor (Figure 5.35b)
325-10	0.006	2132	0.216	Around corner of predrilled hole (Figure 5.36a)
325-15	0.006	2266	0.229	Around corner of predrilled hole (Figure 5.36b)
335-10	0.006	2376	0.240	Middle of the CFRP anchor (Figure 5.37a)
335-15	0.006	2553	0.258	Middle of the CFRP anchor (Figure 5.37b)
Average			0.245	
Standard Deviation			0.018	
COV			13%	

As explained in section 5.5.1, the axial curves of the specimens modeled in ANSYS did not match the experimental curves. This occurred mainly due to early or later plasticity of concrete elements which generated too small or too big axial compressive stresses, respectively. Although concrete stress distribution presented much extensive variation within the ANSYS models, the horizontal expansion of the columns remained almost uniform. All ANSYS specimens presented similar expansions of the concrete elements due to the use of an angle of dilation of zero which prevents volumetric expansion during plasticity (Mirmiran, Zagers, & Yuan, Nonlinear Finite Element Modeling Of Concrete Confined By Fiber Composites, 2000; Shahawy, Mirmiran, & Beitelman, 2000). The lack of

expansion of concrete can be translated to a conservative CFRP stress generation. In short, by using CFRP failure hoop stresses obtained from the ANSYS models, one can be certain that the ductility increases due to CFRP wrapping will not be overestimated.

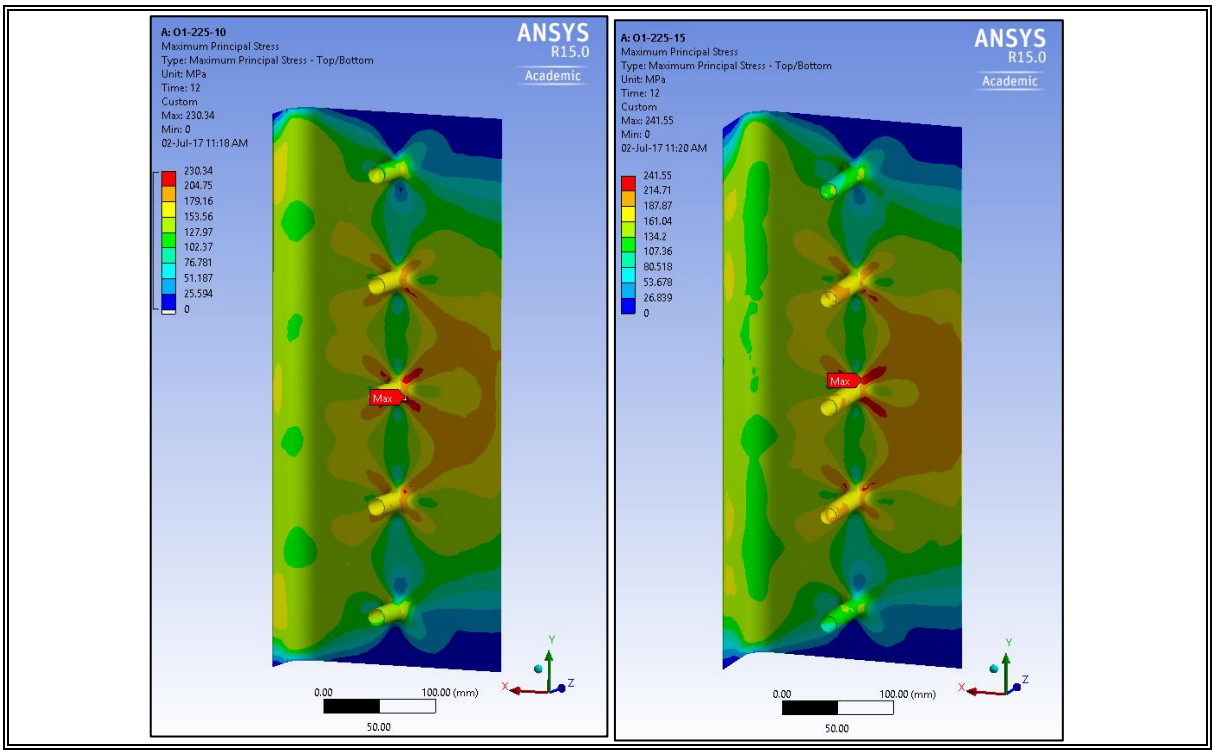

Figure 5.34: CFRP wraps maximum principal stresses. Specimens 225-10 and 225-15

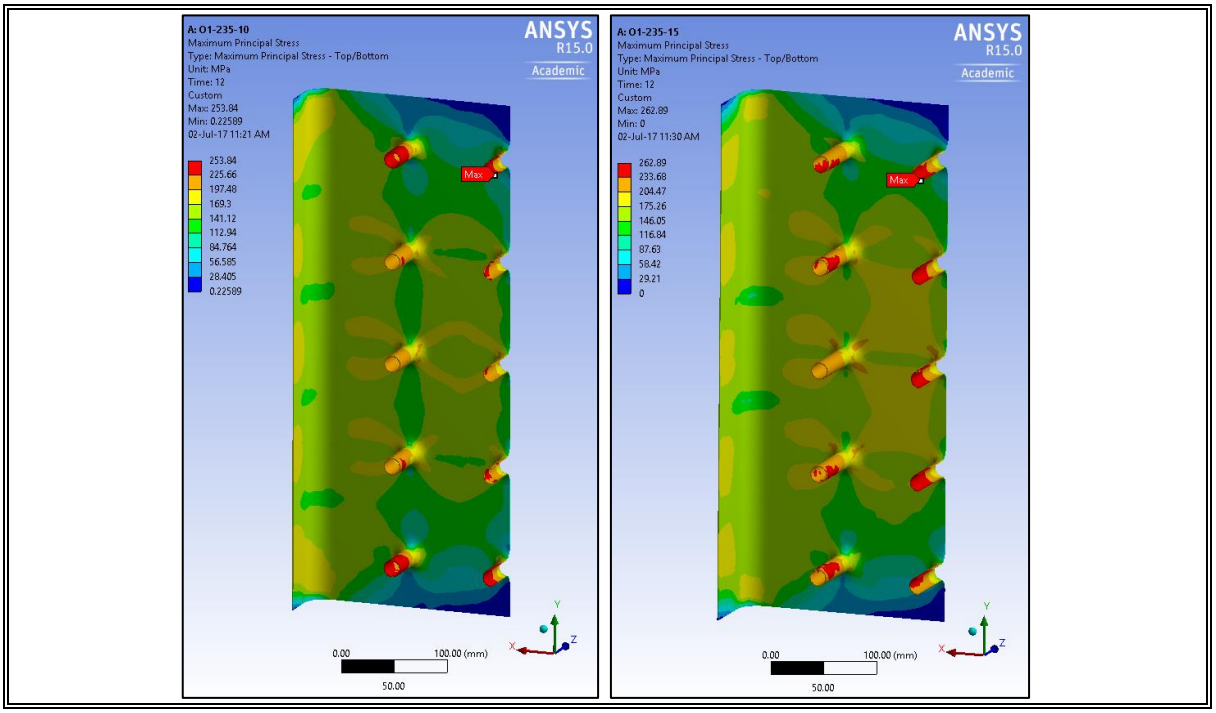

Figure 5.35: CFRP wraps maximum principal stresses. Specimens 235-10 and 235-15

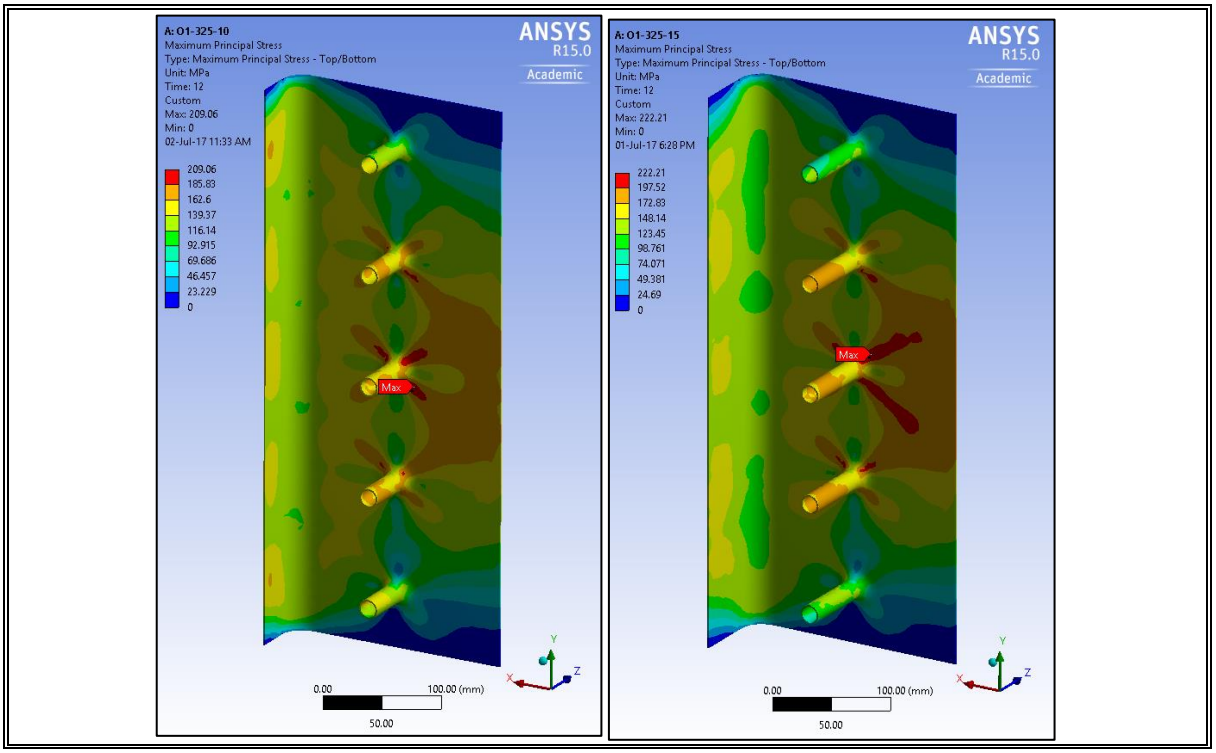

Figure 5.36: CFRP wraps maximum principal stresses. Specimens 325-10 and 325-15

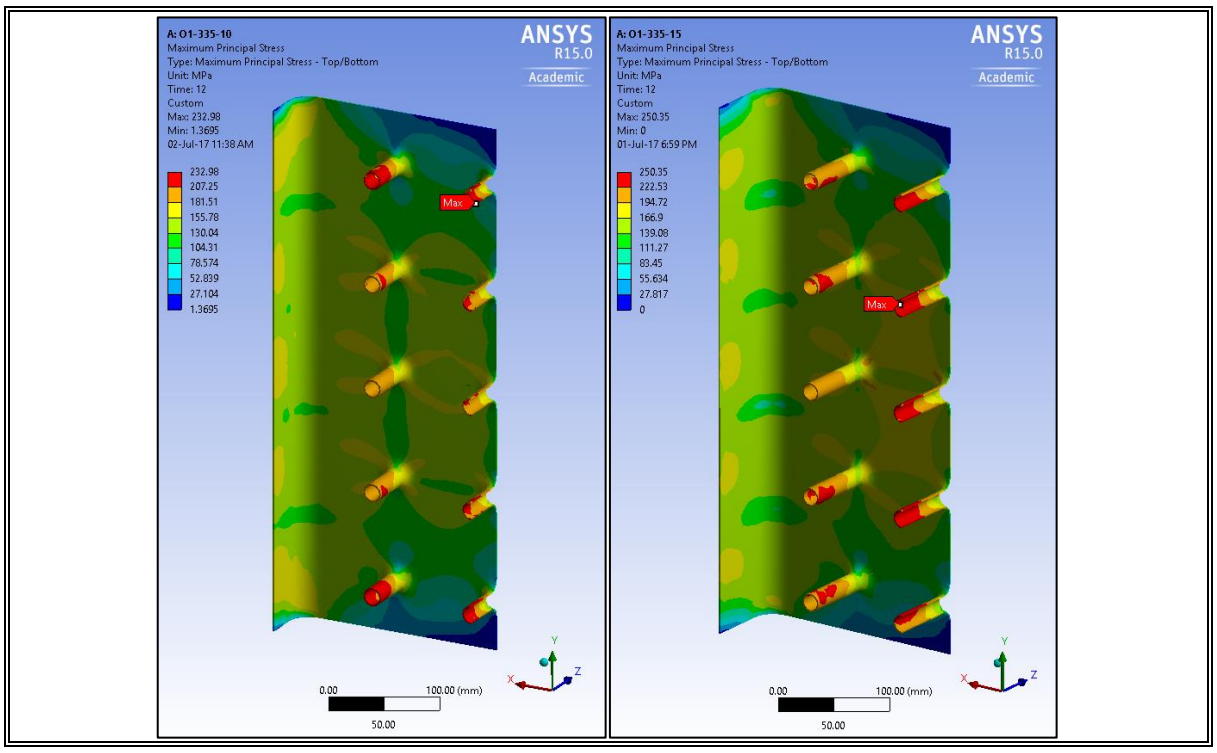

Figure 5.37: CFRP wraps maximum principal stresses. Specimens 335-10 and 335-15

5.5.5 Widening of specimens

This section compares the widening curves of experimentally tested columns with ANSYS models. As is explained in section 3.5.3, horizontal LVDTs were placed during tests to capture a horizontal widening of the column. At the same location, a deformation probe was placed in the ANSYS models to compare the obtained curves (Figure 5.38).

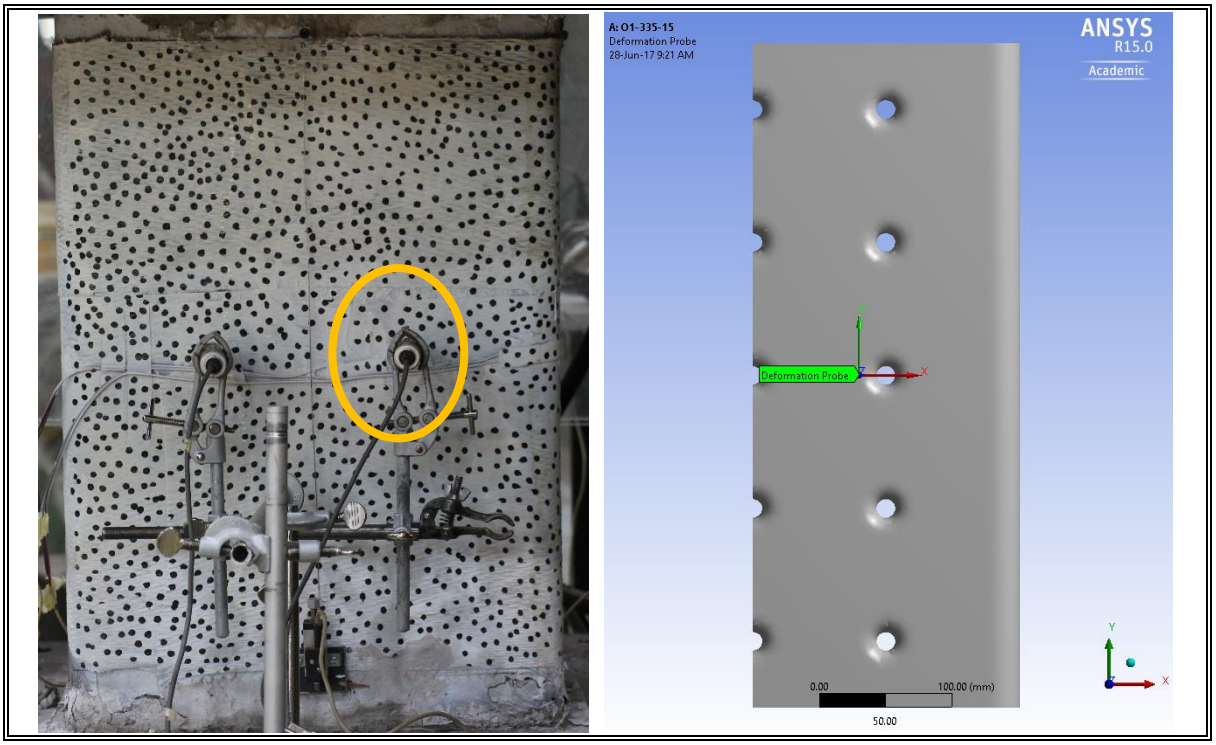

Figure 5.38: CFRP elements back view. Specimen 225-10

Figures 5.39 to 5.46 show the curves of the axial compression displacement vs the widening of the column at the measured point. These Figures show that in all specimens the widening experimentally captured is always bigger than the curve captured by ANSYS, showing that the expansion of the FEM models can be assumed to be conservative. It is important to notice that all curves present small widening at early stages of the test, but increase significantly at the last stages.

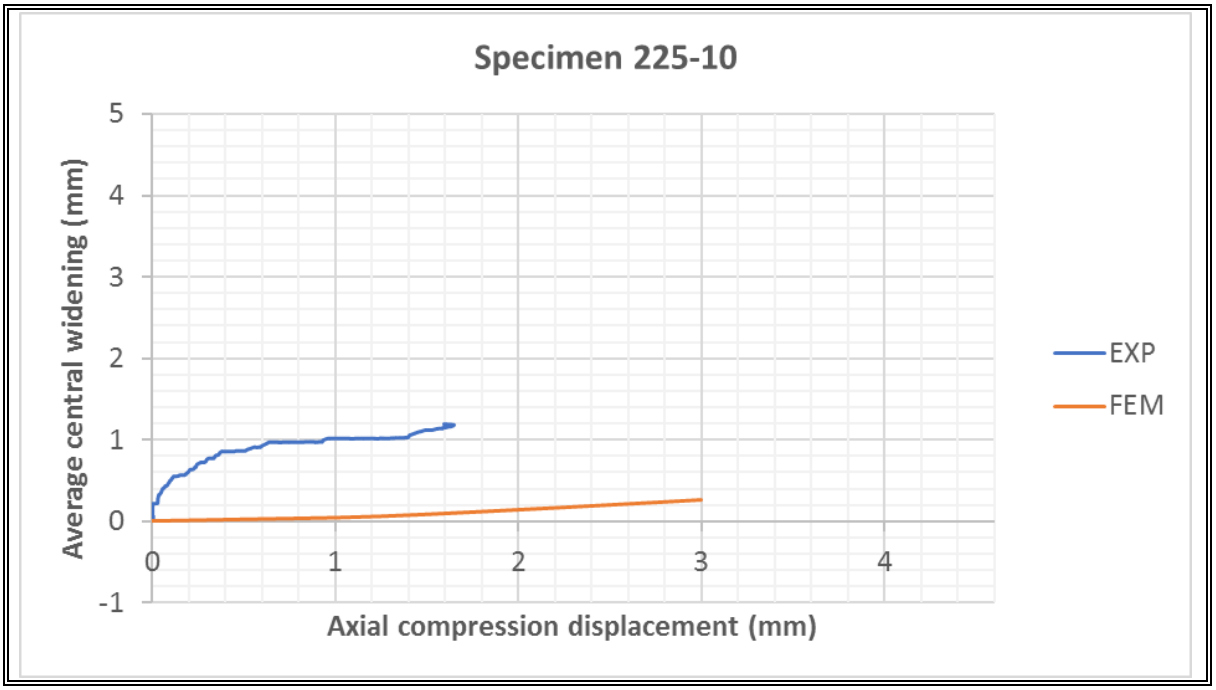

Figure 5.39: Experimental and ANSYS widening curves of Specimen 225-10

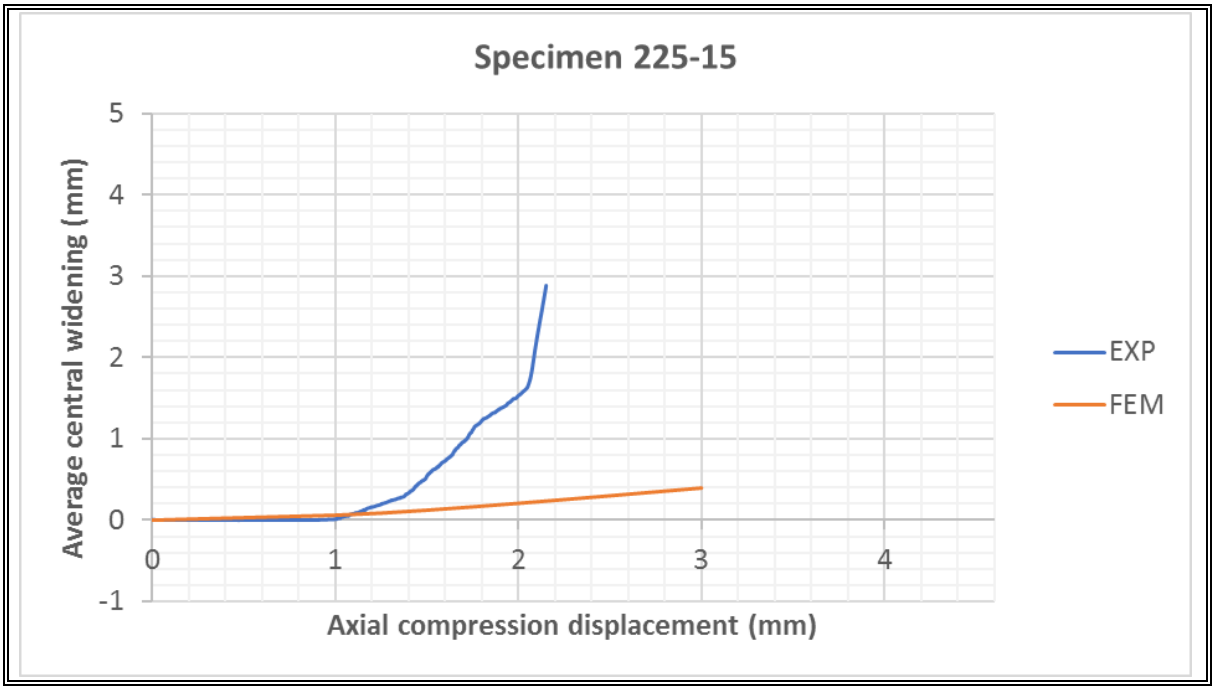

Figure 5.40: Experimental and ANSYS widening curves of Specimen 225-15

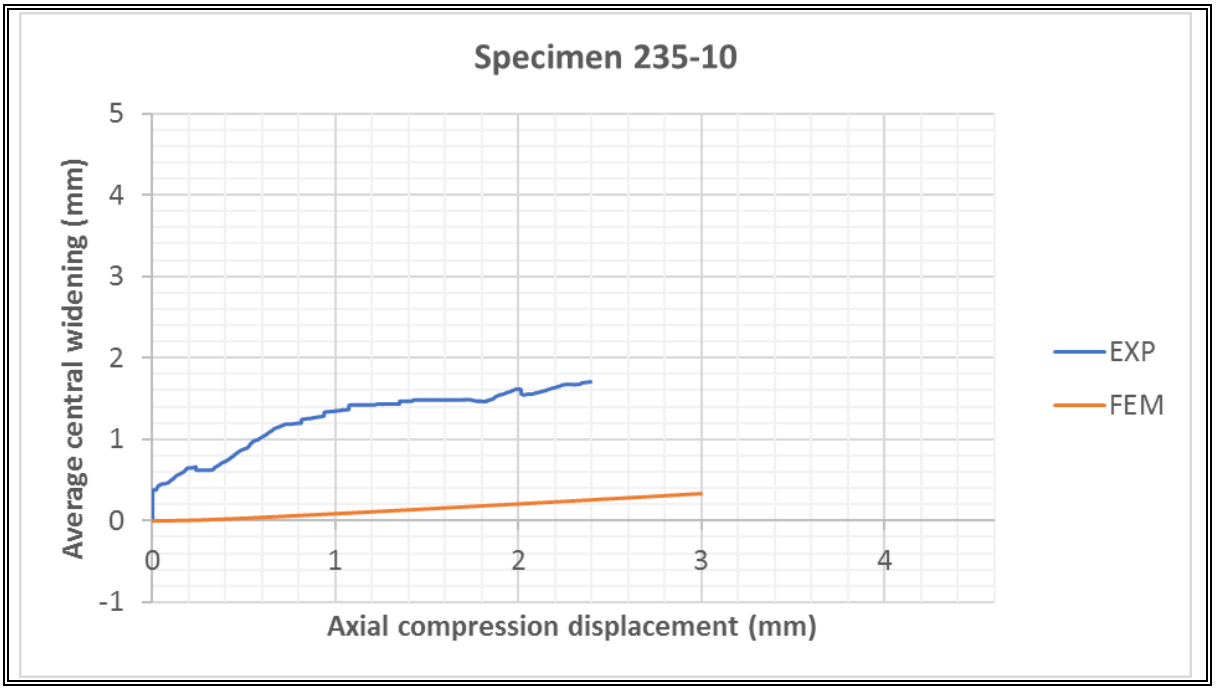

Figure 5.41: Experimental and ANSYS widening curves of Specimen 235-10

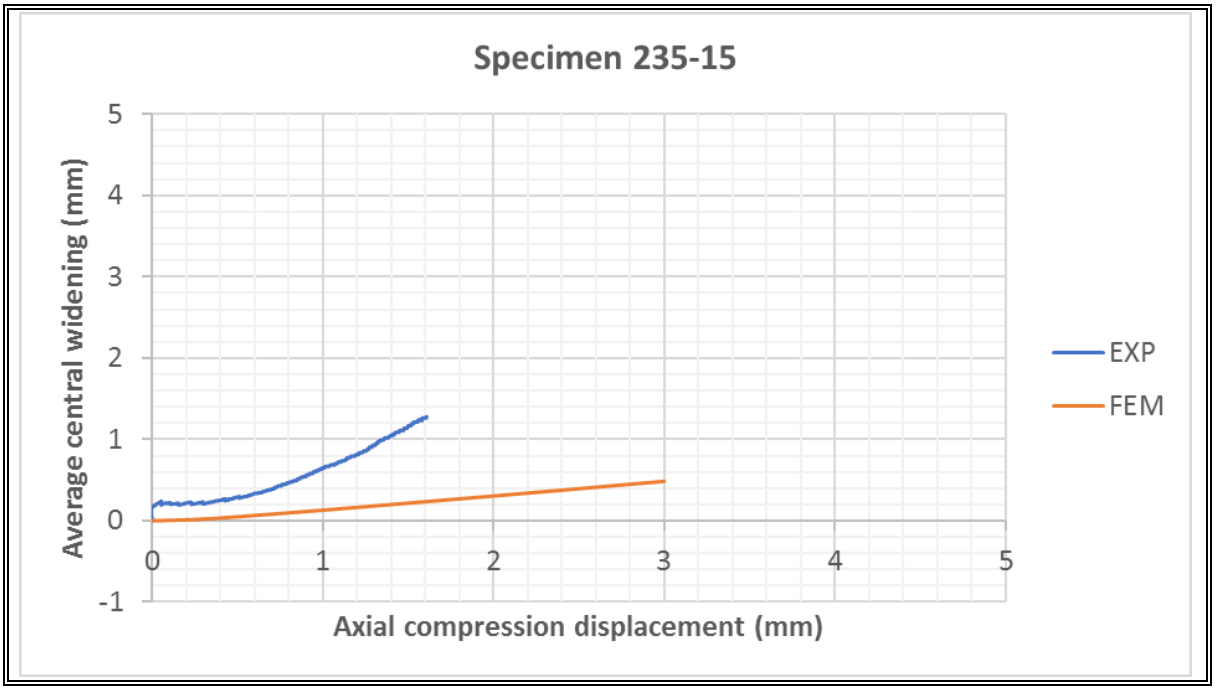

Figure 5.42: Experimental and ANSYS widening curves of Specimen 235-15

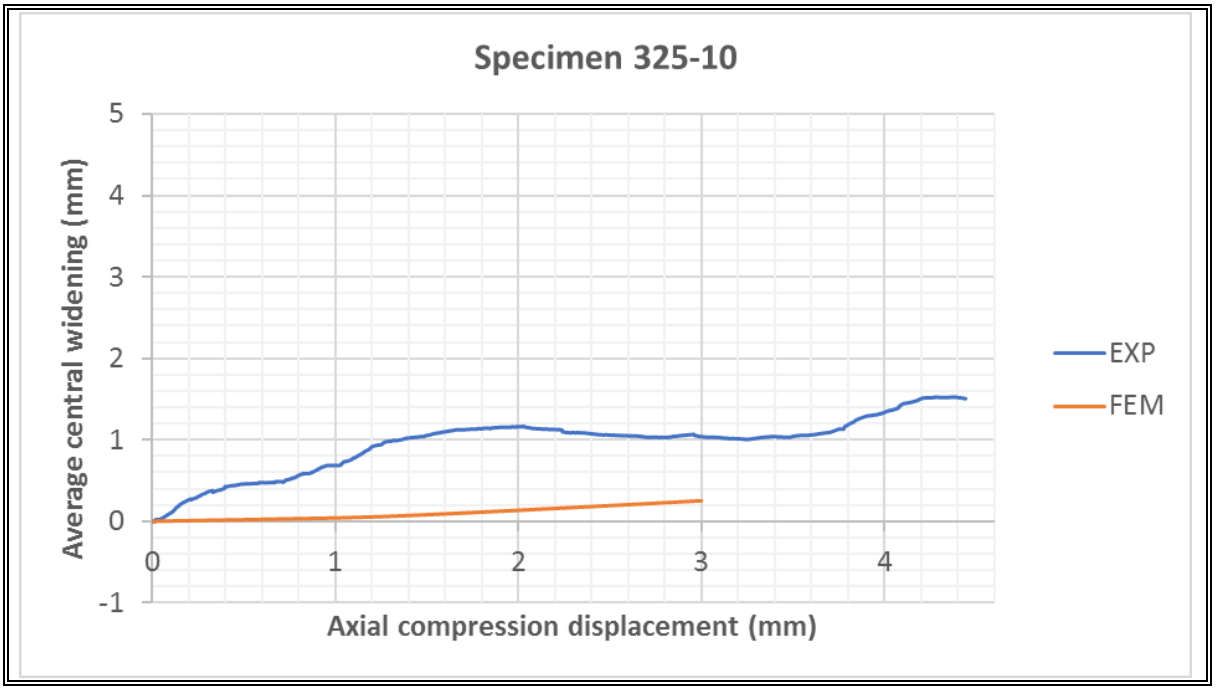

Figure 5.43: Experimental and ANSYS widening curves of Specimen 325-10

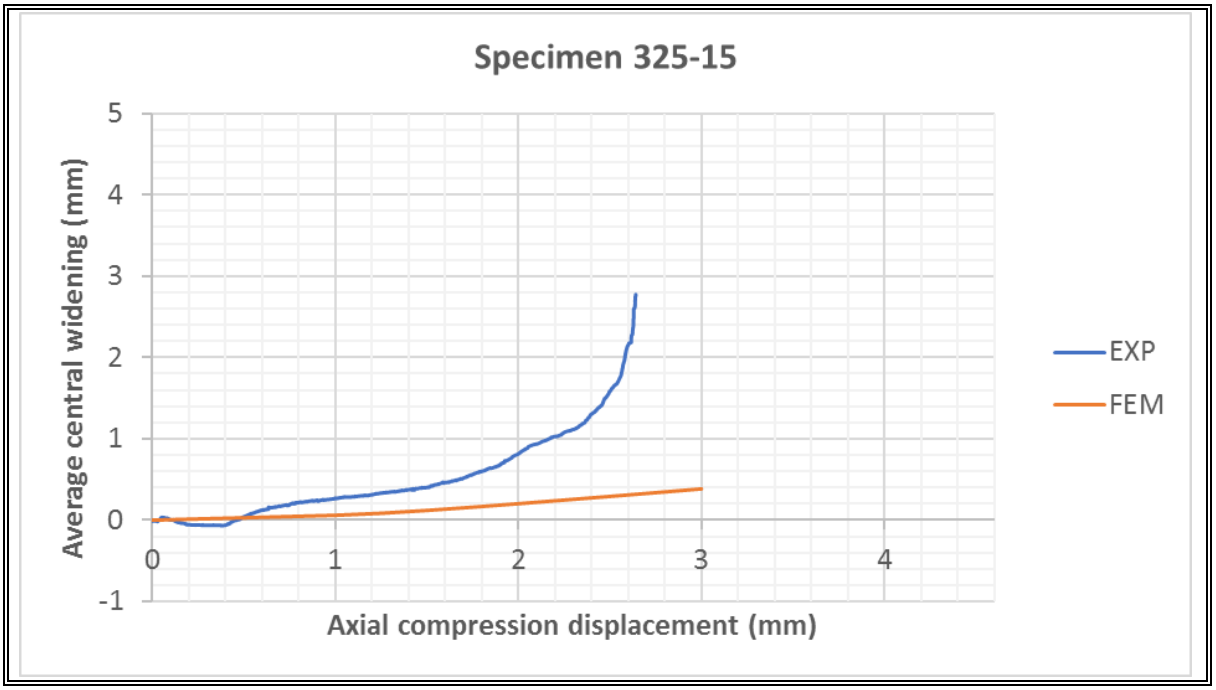

Figure 5.44: Experimental and ANSYS widening curves of Specimen 325-15

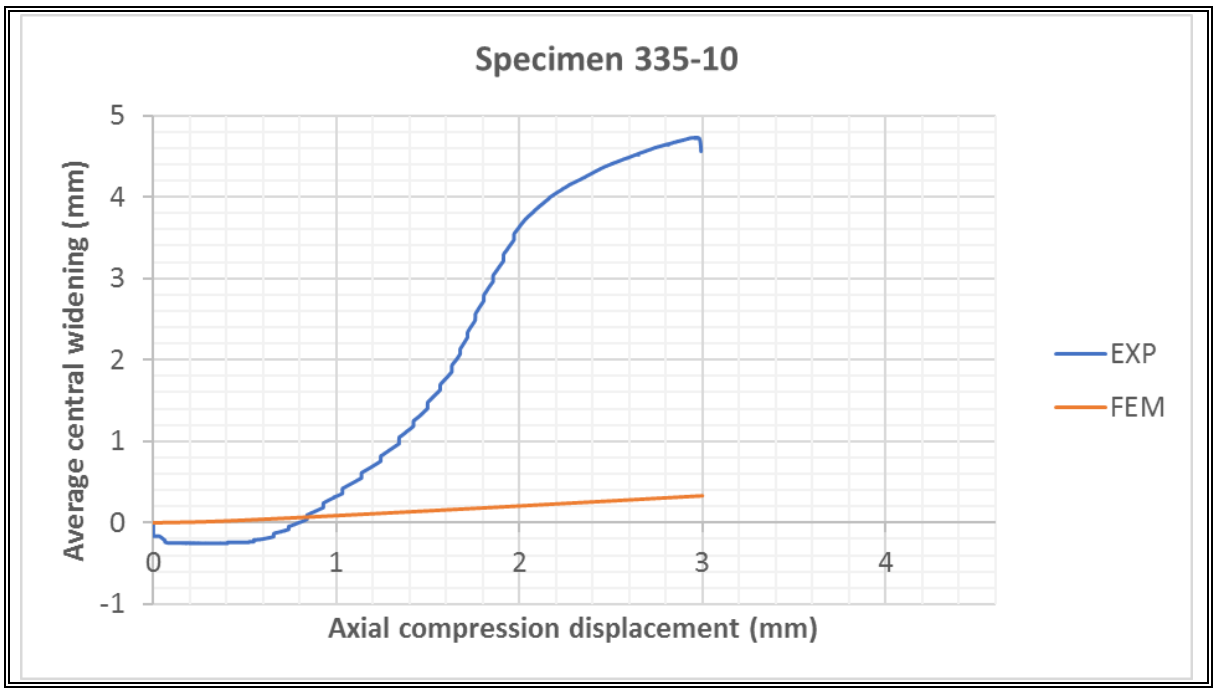

Figure 5.45: Experimental and ANSYS widening curves of Specimen 335-10

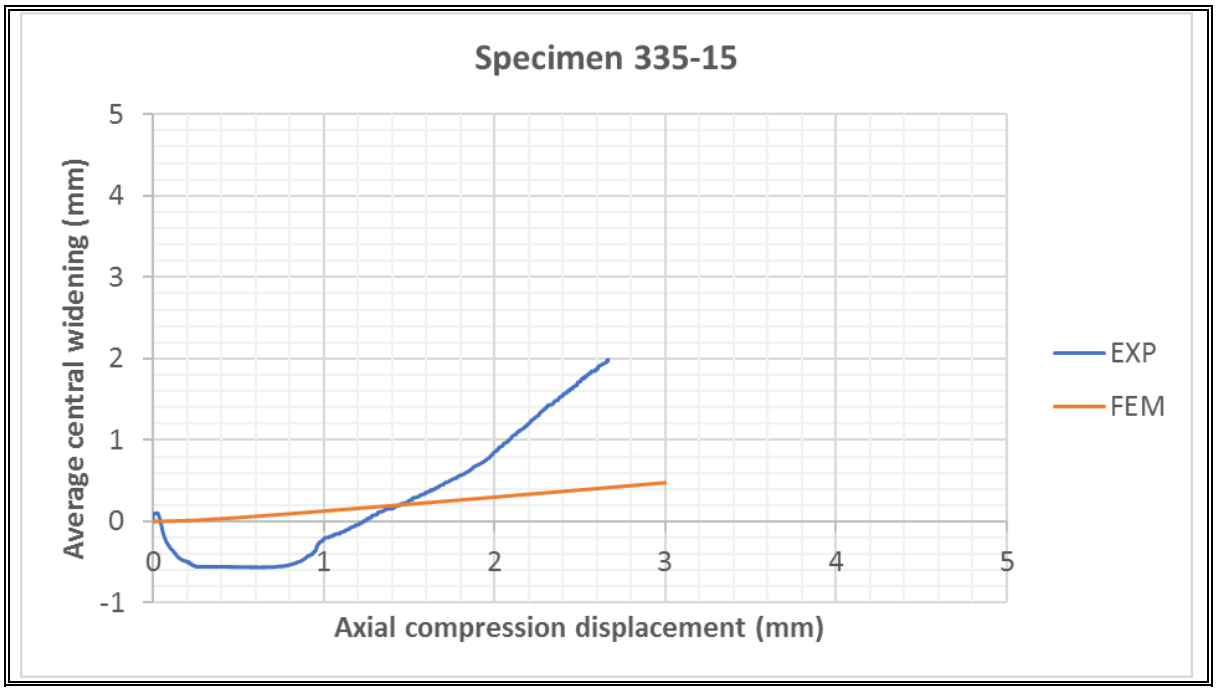

Figure 5.46: Experimental and ANSYS widening curves of Specimen 335-15

5.6 Group 2 models results

In this section, the results from the group 2 models are described. The main results obtained from these models are axial stress-strain curves, stress distributions of CFRP wraps and widening curves at a specific location. Because of the complex geometry of each specimen, stress distributions are presented graphically at a specific load step.

5.6.1 Specimens axial behavior

In this subsection, the axial stress-strain curves obtained from ANSYS models of group 1 and 2 are compared. The stress-strain curves of group 1 models are taken directly from section 5.5.1. The stress-strain curves of group 2 are obtained by adding the vertical reaction at the bottom support of the subsections that compose each specimen and dividing it by the total gross area of the transverse cross-section. The average axial strain for group 2 models is calculated in the same manner as for group 1 models, as explained in section 5.5.1.

As can be seen in Figures 5.47 and 5.48, the curves of corresponding specimens of groups 1 and 2 do not match. In some cases, the group 2 curves overestimate the group 1 curves and in other cases underestimate. This is mainly due to the great variation of compressive stresses in concrete elements. It is difficult to capture the exact stress distribution of stresses inside concrete elements due to the high geometrical complexity.

Although the curves do not match at high axial strains, the initial stiffness of all curves from groups 1 and 2 matches perfectly. Since curves cannot capture a descending branch after a peak is reached nor they can capture failure, displacement is applied until an average strain of 0.006 is reached.

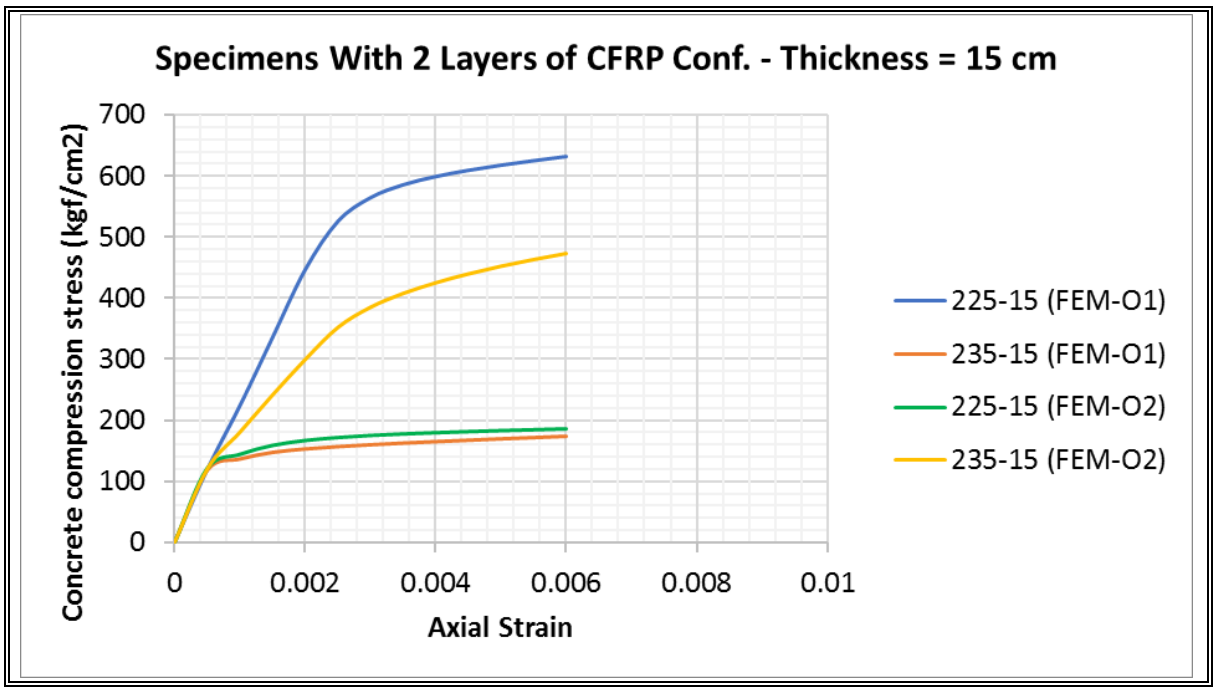

Figure 5.47: Comparison of axial behavior between Group 1 and 2 (15-cm thickness)

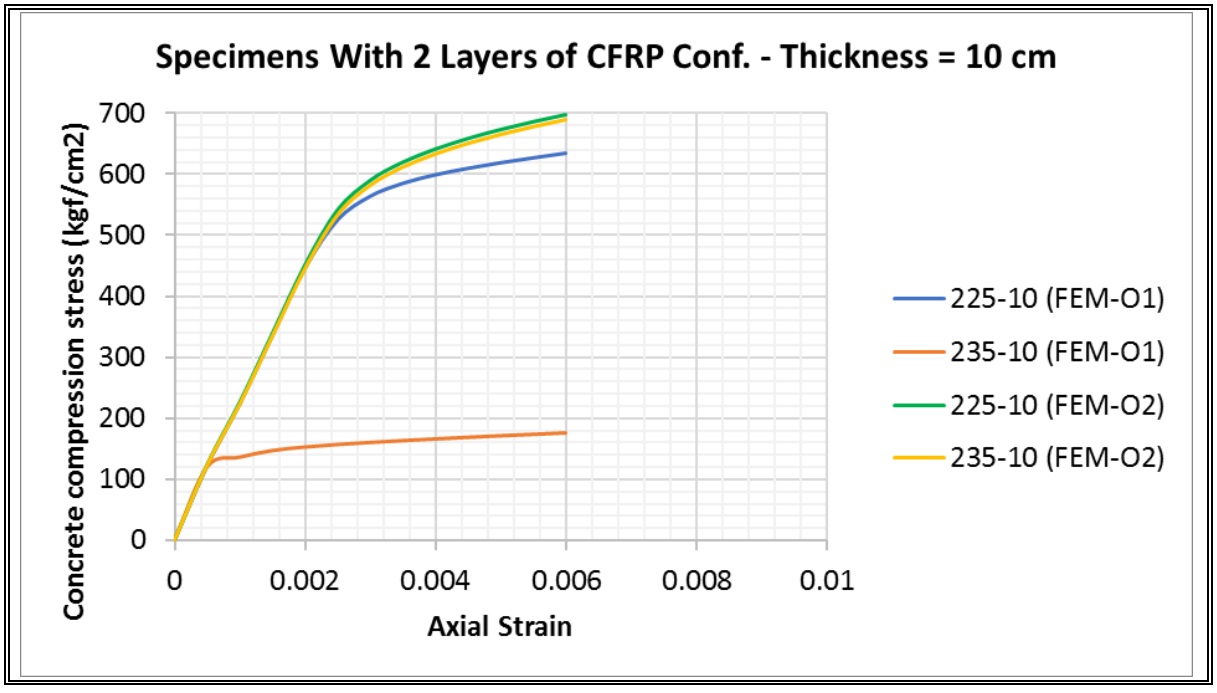

Figure 5.48: Comparison of axial behavior between Group 1 and 2 (10-cm thickness)

5.6.2 CFRP ultimate stress

Although the axial behavior of the specimens of group 2 do not match the behavior of group 1 models, the maximum CFRP principal stress of both groups closely match. This is mainly due to a similar expansion in concrete experienced in models of both groups, in spite of the very different concrete stresses generated.Same as in section 5.5.4, the maximum principal stress is used to display the stress distribution of CFRP wraps because its direction closely resembles the direction of the experimentally installed CFRP confinement.

Figures 5.49 to 5.56 show that not only the largest maximum principal CFRP stress is similar between groups 1 and 2 corresponding models, but also the shape of the distribution of principal stresses. Of course, the shape of distribution is not exactly similar because subsections in both groups present different boundary conditions. Subsections in group 2 models act as independent columns with internal border blocked from horizontal displacement, while subsections in group 1 model interact with each other. Despite this difference, the location of the biggest principal stress coincides between both group of models. If group 1 models predict that the biggest principal stress is located at the external surface of the CFRP wraps or at the internal CFRP anchor, group 2 models predict the same.

Specimen with CFRP wraps with 1.5 mm in thickness are not modeled in group 2 because it is considered unnecessary, since the objective of group 2 models is only to illustrate the resemblance with corresponding models of group 1. A variation of 0.5-mm in thickness will most likely illustrate the exact same phenomenon. It is important to notice that group 2 models do not present steel stirrup and that their absence did not generate any effect in CFRP principal stresses.

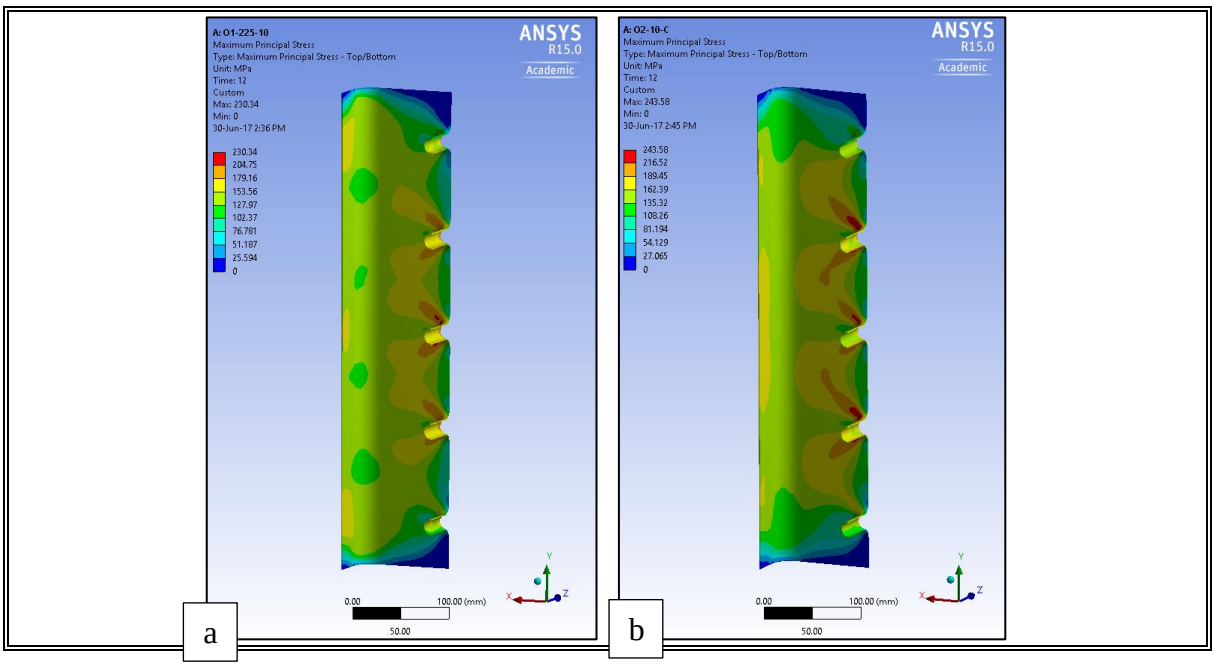

Figure 5.49: CFRP Maximum principal stresses. Specimen 225-10, subsection VI: (a) Group 1 model (b) Group 2 model

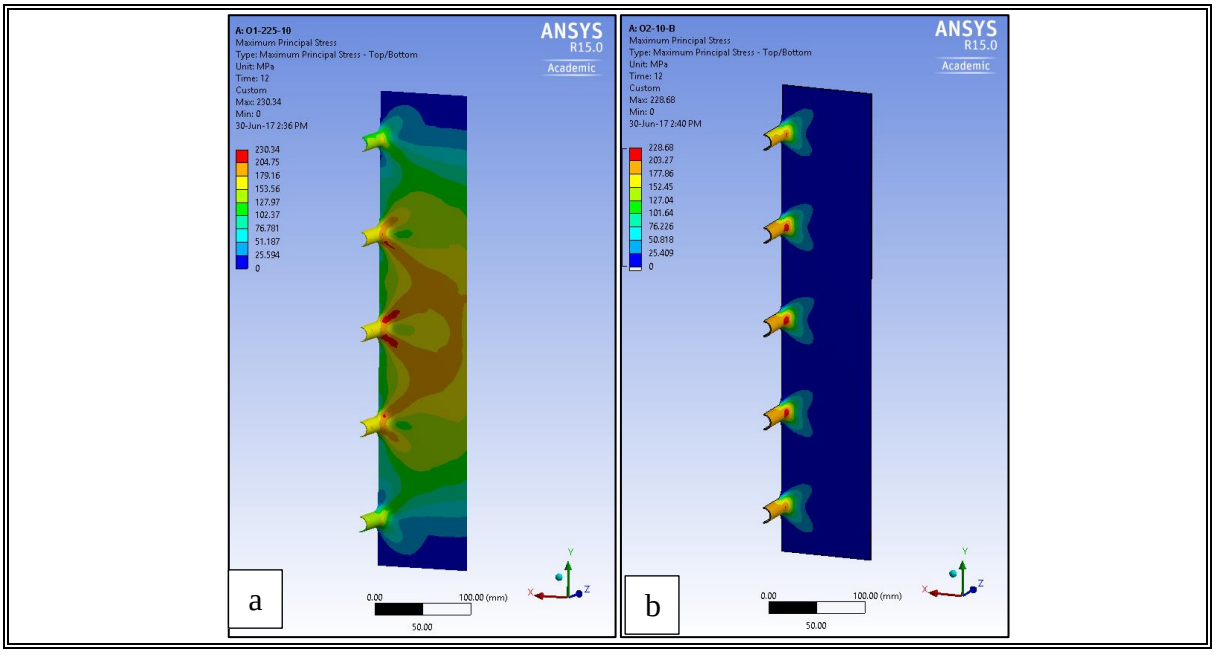

Figure 5.50: CFRP Maximum principal stresses. Specimen 225-10, subsection V: (a) Group 1 model (b) Group 2 model

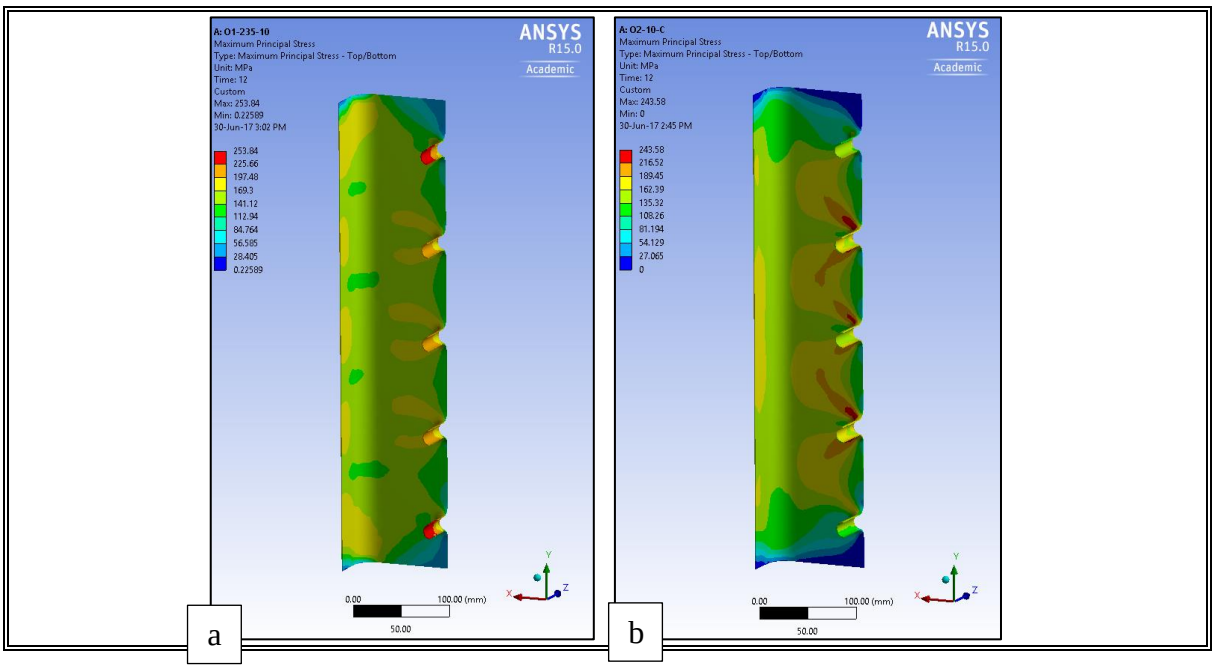

Figure 5.51: CFRP Maximum principal stresses. Specimen 235-10, subsection VI: (a) Group 1 model (b) Group 2 model

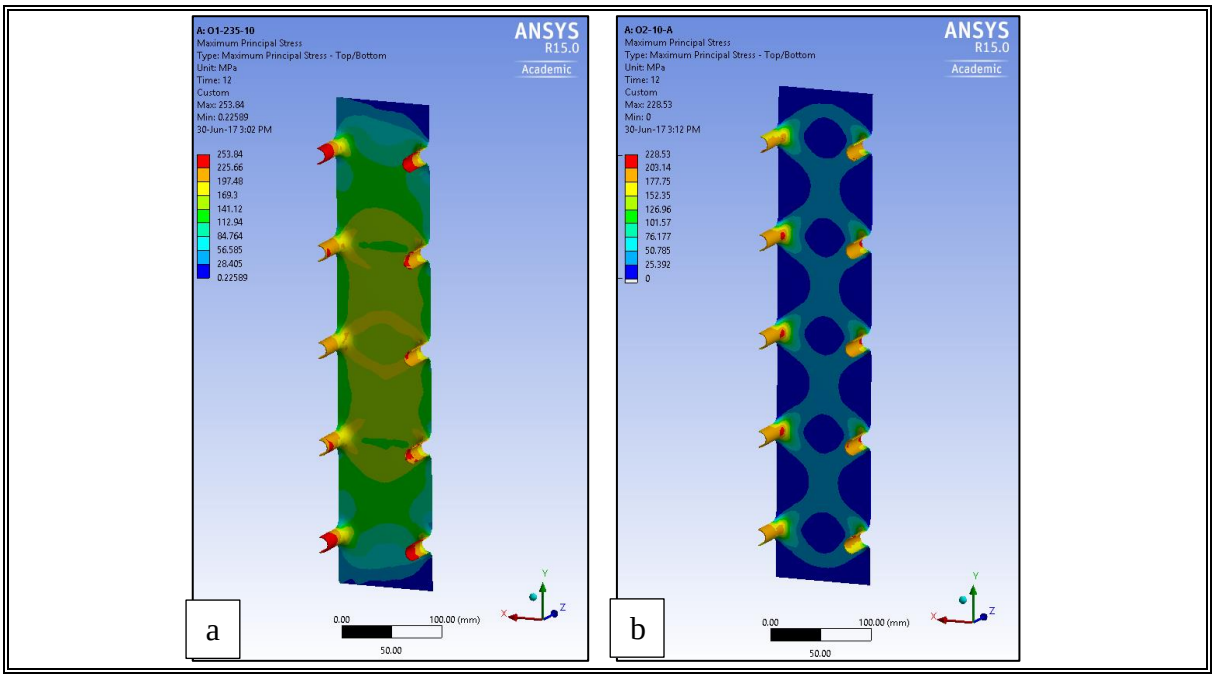

Figure 5.52: CFRP Maximum principal stresses. Specimen 235-10, subsection IV: (a) Group 1 model (b) Group 2 model

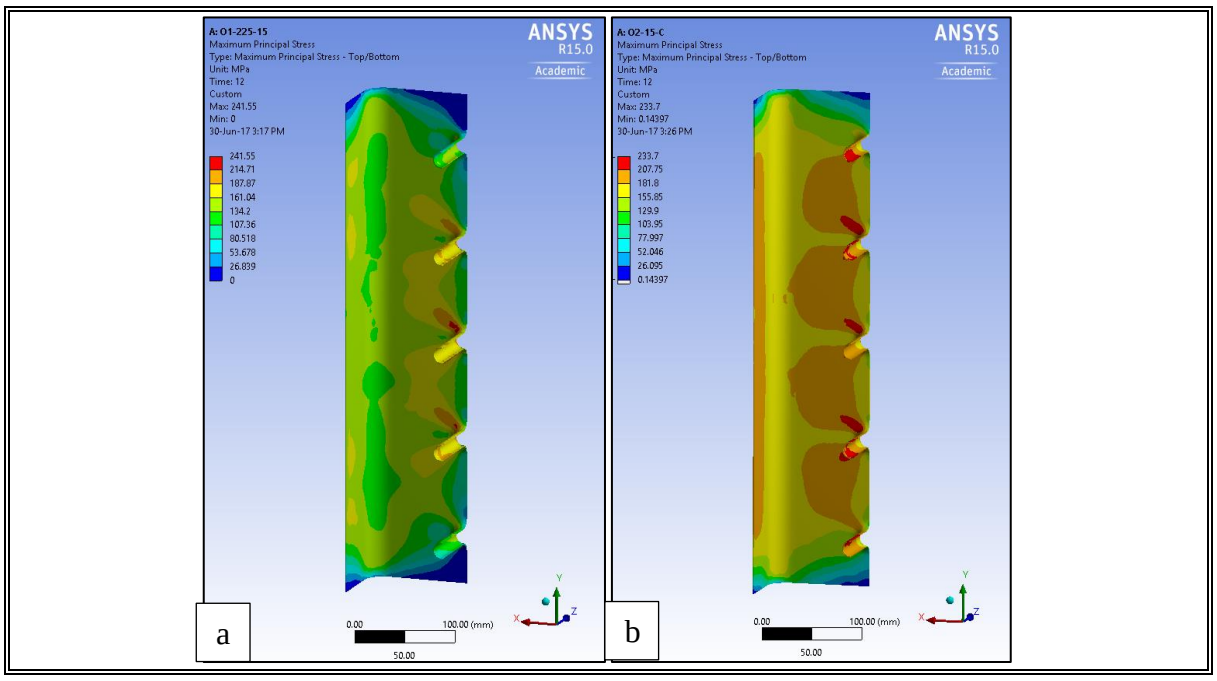

Figure 5.53: CFRP Maximum principal stresses. Specimen 225-15, subsection III: (a) Group 1 model (b) Group 2 model

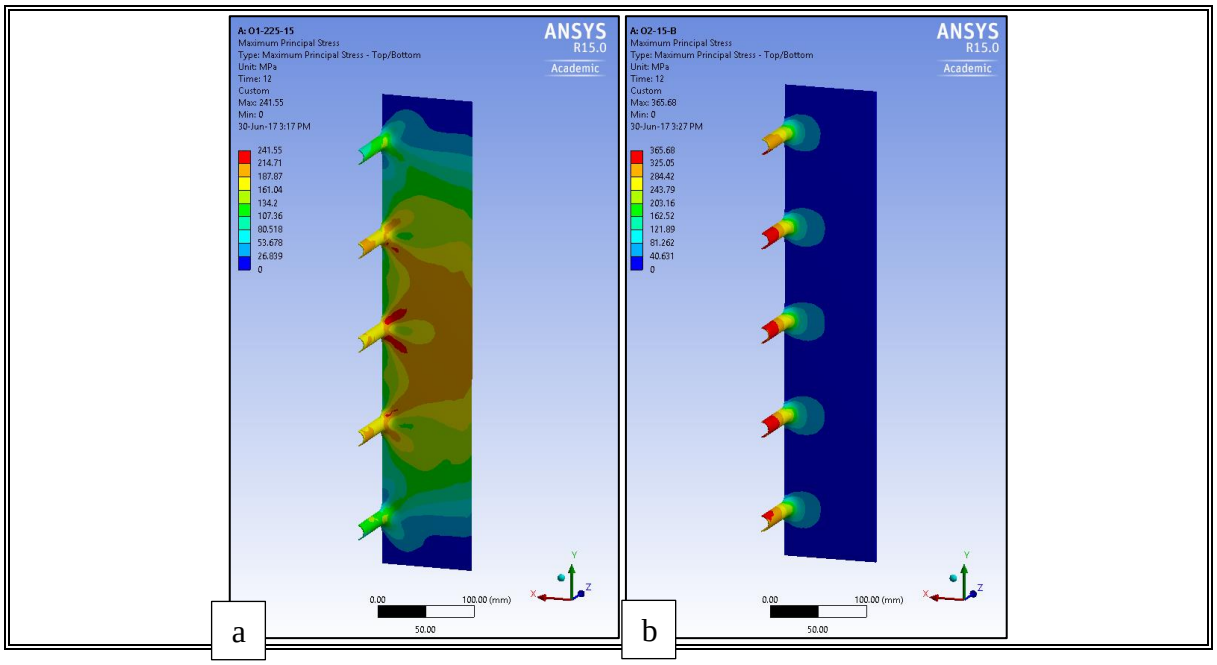

Figure 5.54: CFRP Maximum principal stresses. Specimen 225-15, subsection II: (a) Group 1 model (b) Group 2 model

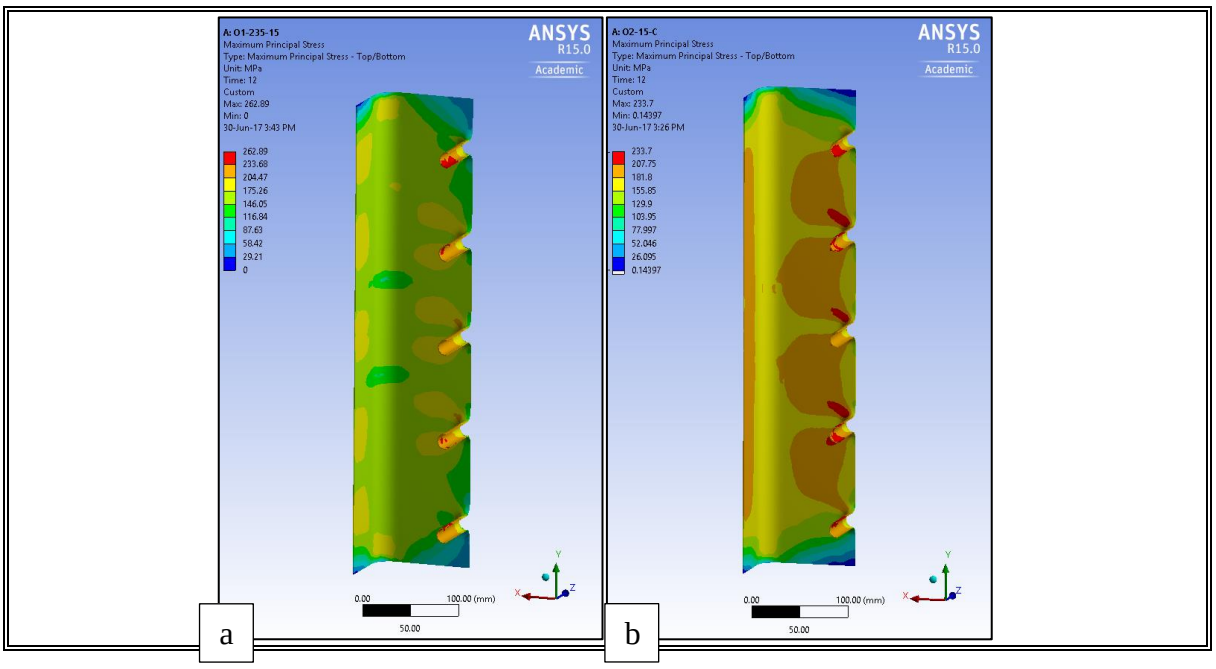

Figure 5.55: CFRP Maximum principal stresses. Specimen 235-15, subsection III: (a) Group 1 model (b) Group 2 model

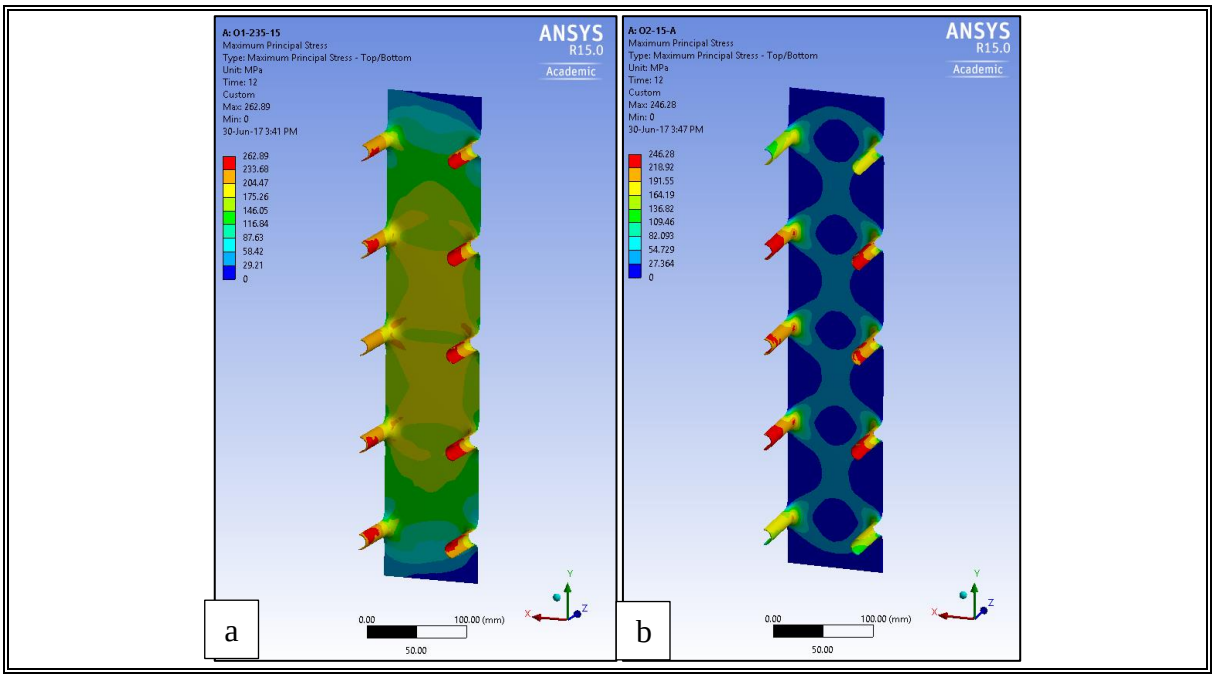

Figure 5.56: CFRP Maximum principal stresses. Specimen 235-15, subsection I: (a) Group 1 model (b) Group 2 model

5.6.3 Widening of specimens

In section 5.5.5, the widening of the tested specimens and models of group 1 at a specific location is compared. In this section, in addition to the curve presented in 5.5.5 the curves obtained from corresponding model from group 2 are added.

In all cases the ANSYS model from groups 1 and 2 closely resemble each other. Therefore, in all cases the curves obtained from ANSYS models present a smaller widening than the one captured experimentally. This shows that it is still conservative to consider the ANSYS estimations of CFRP stresses weather model from groups 1 or 2 are used.

It is important to notice that group 2 models do not present steel stirrup and that their absence did not generate any effect in the widening of the column.

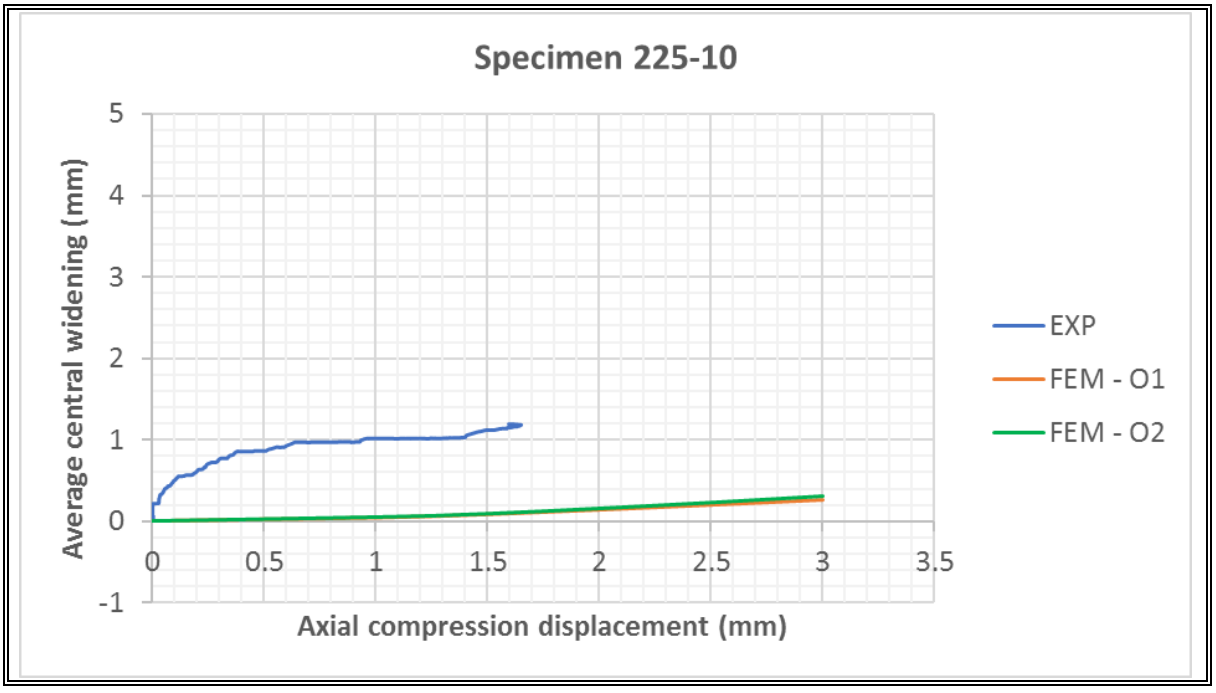

Figure 5.57: Widening curves comparison between Group 1 and 2 models (Spec. 225-10)

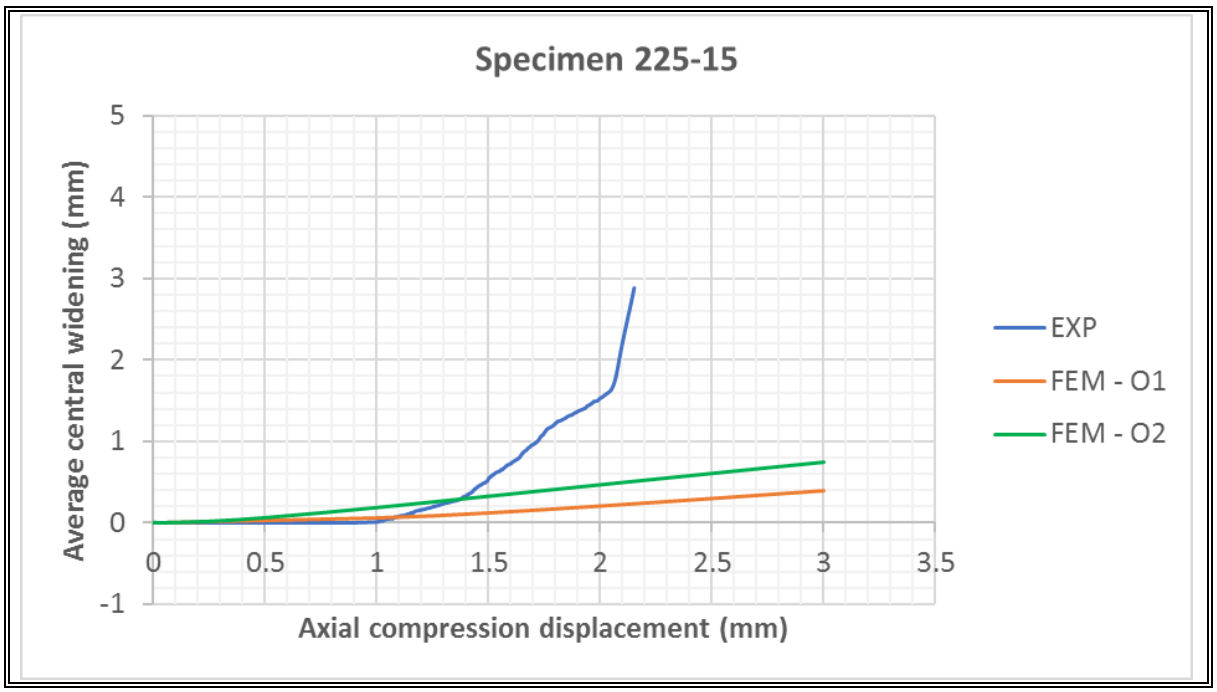

Figure 5.58: Widening curves comparison between Group 1 and 2 models (Spec. 225-15)

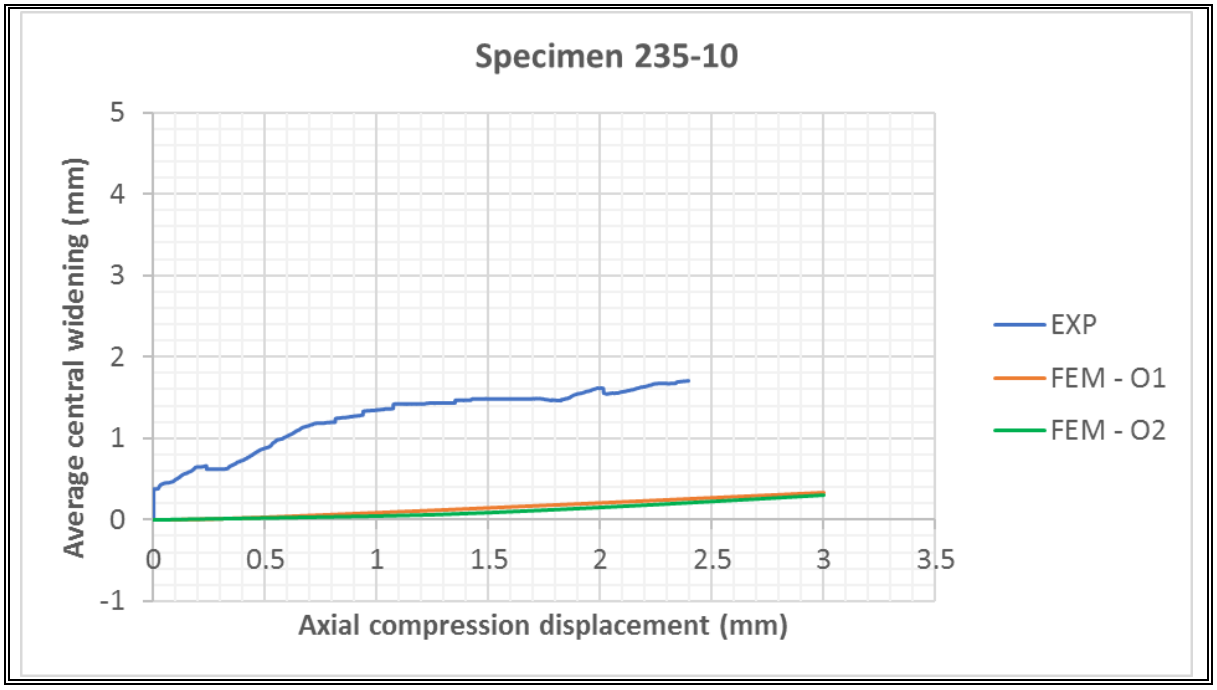

Figure 5.59: Widening curves comparison between Group 1 and 2 models (Spec. 235-10)

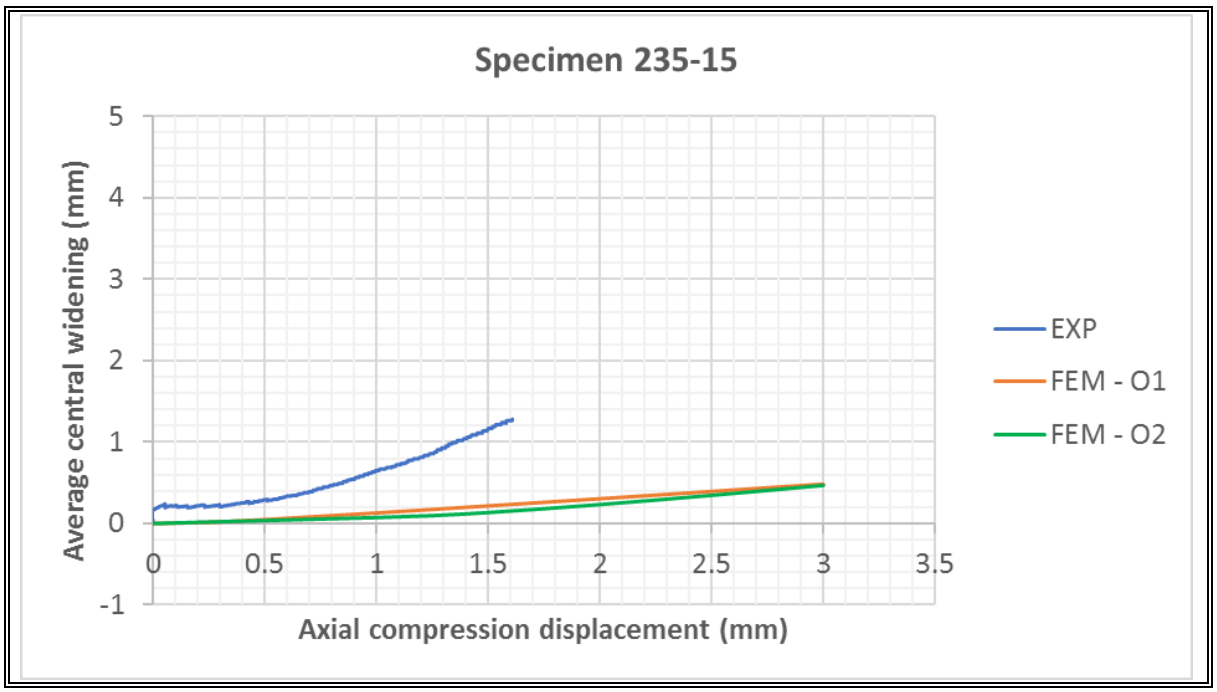

Figure 5.60: Widening curves comparison between Group 1 and 2 models (Spec. 235-15)

5.7 Summary

Two groups of nonlinear finite element models were developed: group 1 consisted of columns representing each of the experimentally tested specimens and group 2 consisted of sub columns illustrating how the behavior of a complete column can be approximated by independently analyzing subsections. All models were developed with the use of the platform ANSYS Workbench and were subject to a multi-step static analysis. FEM models were not capable to determine the failure of the column, but were able to show the distribution of stresses until a determined axial strain. In order to correlate the ANSYS results with the experimental model, specimens without CFRP confinement are compressed until an average axial strain of 0.0035 and specimens with CFRP confinement are compressed until an average axial strain of 0.006.

The models involved the use of three different materials: concrete, transverse steel reinforcement and CFRP reinforcement. Concrete material properties were taken from cylinder tests specified on Appendix A. Steel and CFRP reinforcement nominal material properties specified by the manufacturers were assumed.

The results of group 1 models focused on the axial stress-strain curves, concrete stresses, steel stresses, CFRP stresses and widening of the column at a specific location.

ANSYS axial stress-strain curves showed that control specimens (without CFRP confinement) with or without pre-cast holes presented a good proximity with experimental captured data. According to ANSYS models, the presence of holes does not generate a decrease in the initial stiffness. This is in contradiction with experimental observations where initial stiffness of columns with pre-cast holes tend to be on average 88% of the initial stiffness of columns without pre-cast holes.

ANSYS axial stress-strain curves of columns with CFRP reinforcement presented a similar initial stiffness to experimental curves, but the maximum stress differed considerably. While specimens with a 3x5 CFRP anchor disposition underestimated the maximum stress, specimen with 2x5 CFRP anchor disposition overestimated the maximum stress. These differences were reflected on both the average stress (calculated as the total bottom reaction divided by the gross cross-section area) and the principal stress distribution of concrete elements. This is possibly due to an early and late plastification of concrete elements generated by the complex geometry of the pre-cast holes.

Specimens without CFRP confinement presented yielding of the transverse steel stirrups at an average axial strain of 0.0035. On the contrary, specimens with CFRP do not presented yielding of the stirrup at an average axial strain of 0.0035, but they presented steel

yielding at a higher average axial strain of 0.006. This shows that CFRP confinement reduced the solicitation over steel stirrups, but did not prevent it for high axial deformations.

CFRP confinement was modeled by shells with a “cloth” option which means they cannot generate compression stress, only tension stress which behaves linear-elastic. Although the concrete stress distribution varied greatly between specimen with 2x5 and 3x5 anchor dispositions, the CFRP principal stresses do no present a high variability. Most of the maximum CFRP principal stresses captured at an average axial strain of 0.006 are around 25% of the ultimate tension stress of CFRP provided by the manufacturer. This means that the average efficiency factor for the proposed CFRP confinement is around 0.25 on average. This value is conservative because the expansion of the columns modeled in ANSYS was much lower than the expansion registered experimentally. Horizontal LVDTs captured, on experimental tests, widening at mid-height of the columns at least twice the value of the widening detected at the same point with the ANSYS models. This is mainly due to the use of dilation angle of 0, which neglects any volumetric expansion. Therefore, the CFRP maximum stress captured by the ANSYS models can be considered conservative. Since the complete field of principal stresses of the CFRP can be captured on the ANSYS models, the exact maximum value of CFRP principal stress and location can be easily determined, which makes the procedure easily replicable.

The results of group 2 models focused on the axial stress-strain curves, CFRP stresses and widening of the column at a specific location.

ANSYS axial stress-strain curves differ greatly from experimental tests and from ANSYS models group 1. This shows that a more sophisticated constative model of concrete elements is required to capture similar results between theoretical and experimental models.

Despite the great difference in stress-strain curves, the CFRP principal stresses captured in group 2 models coincide with the ones captured in group 1 models both in magnitude and distribution. This due to the conservative widening of the specimens captured in ANSYS models which is at most half the value detected experimentally with horizontal LVDTs located at mid-height of the columns. Group 2 models show that despite not considering steel reinforcement and considering sub columns between CFRP anchors as independent columns, similar CFRP stresses and widening reading were achieved.

6. DESIGN ORIENTED MODEL

6.1 Overview

In this section, a design oriented procedure is proposed to determine the increments in the axial stress-strain curve parameters of a rectangular reinforced concrete column, confined with CFRP wraps and anchors. The proposed procedure assembles the results from FEM models, existing design-oriented models and compares its results to values captured on experimental tests. Figure 6.1 shows a scheme of the methodology followed on the present investigation.

The proposed procedure assumes that the behavior of the complete cross section can be analyzed by studying the behavior of internal subsections between anchors. The procedure uses closed-form equations from 11 different authors derived originally for CFRP confined columns without CFRP anchors. The design-oriented procedure involves the use of closed-form equations available in literature. These formulas are faster to be computed than FEM models and require only the following parameters:

f_{co} = unconfined concrete compression strength at day of testing (377 $\frac{kgf}{cm^2}$).

E_{co} = unconfined concrete modulus of elasticity at day of testing (226189 $\frac{kgf}{cm^2}$).

ε_{co} = unconfined concrete strain at f_{co} (0.002) (Hognestad, 1951).

r = minimum radius of rounded corners.

b, d = nominal cross-section dimensions of subsections between anchors.

E_{frp} = nominal modulus of elasticity of CFRP reinforcement (76 GPa).

ε_{frp}^{ult} = nominal tensile ultimate strain of CFRP on coupon test (1%).

ρ_{frp} = volumetric ratio of CFRP reinforcement to concrete.

κ_s = shape reduction factor according to assumed arching action (Figures 6.2 to 6.5).

κ_ε = CFRP efficiency factor due to stress concentration (obtained from FEM models).

The theoretical increments obtained from the proposed procedure are compared to increments captured experimentally. The experimental results are assumed to be the closest to reality. The procedure is applied to the 8 experimentally tested columns with CFRP confinement of this investigation.

As in explained in Figure 6.1, the increments on each parameter are calculated with the experimental tests and with the theoretical model. In the experimental tests, the parameters of CFRP confined specimens tested experimentally are contrasted with parameters of control specimens tested experimentally. On the other hand, parameters calculated with the proposed procedure are contrasted with nominal unconfined concrete parameters that were used for the closed-form equations.

Finally, the theoretical and experimental increments, according to each approach, are compared. If the theoretical and experimental increments of a parameter are close to each other, then it reflects a better performance in the proposed procedure. All available design-oriented models fond in literature are evaluated according to their ability to predict increments in the 6 stress-strain curve parameters:

ε_c^{max} = concrete axial strain corresponding to the maximum compression stress

f_c^{max} = concrete axial maximum compression stress

E_c = concrete modulus of elasticity

ε_c^{ult} = concrete axial ultimate strain

f_c^{ult} = concrete axial ultimate stress

E_c^D = concrete descending slope after maximum compression stress

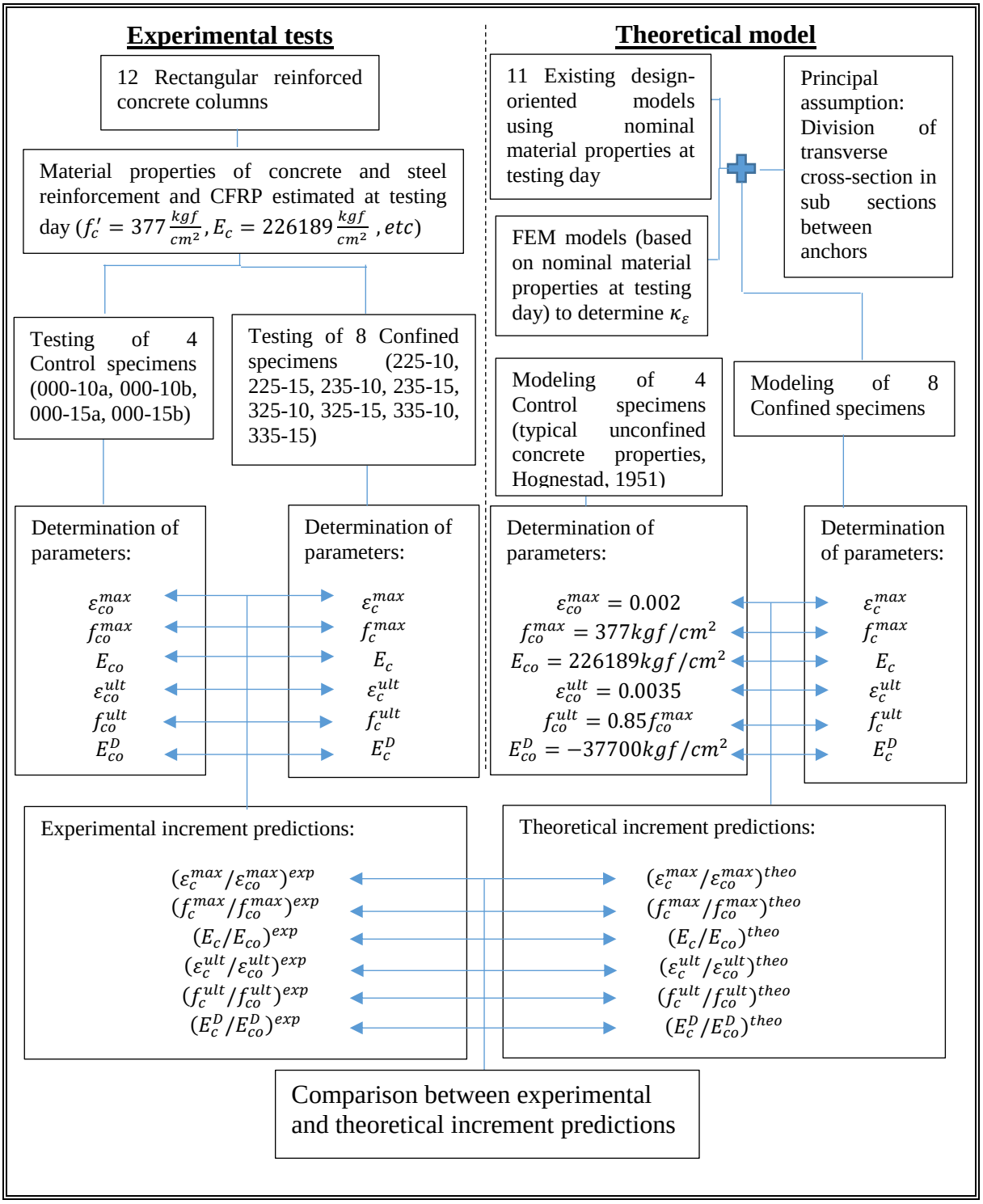

Figure 6.1: Investigation methodology scheme

6.2 Assumptions of proposed procedure

The principal assumption of the proposed procedure is that increments in axial stress-strain curve parameters can be predicted by applying closed-form models to sub columns located between CFRP anchors. Figures 6.2 to 6.5 show the sub column division for all 8 tested specimens. Each sub column is treated independent from the rest. The internal borders between sub columns are considered blocked from any horizontal displacement.

In this procedure, the original column is divided into individual sub columns confined with CFRP wraps but without CFRP anchors. Since design models found in literature are used for each sub column, then all the assumptions of these models are transferred to the proposed procedure. The assumptions of each of the 11 design models are explained in section 2.3. The results of the proposed procedure are compared to 2 closed-form models specifically designed for CFRP wrap and anchor confinement as explained in section 2.4.

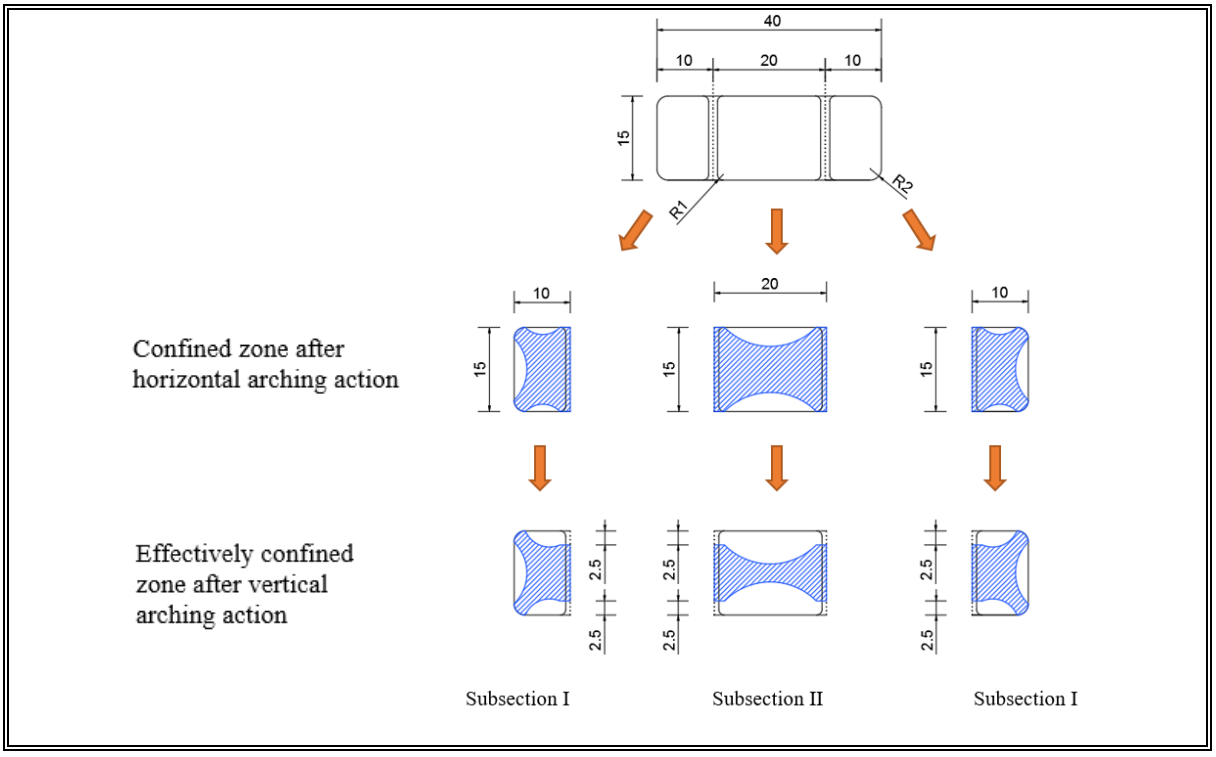

Figure 6.2: Sub columns of specimens 225-15 and 325-15 treated as independent columns

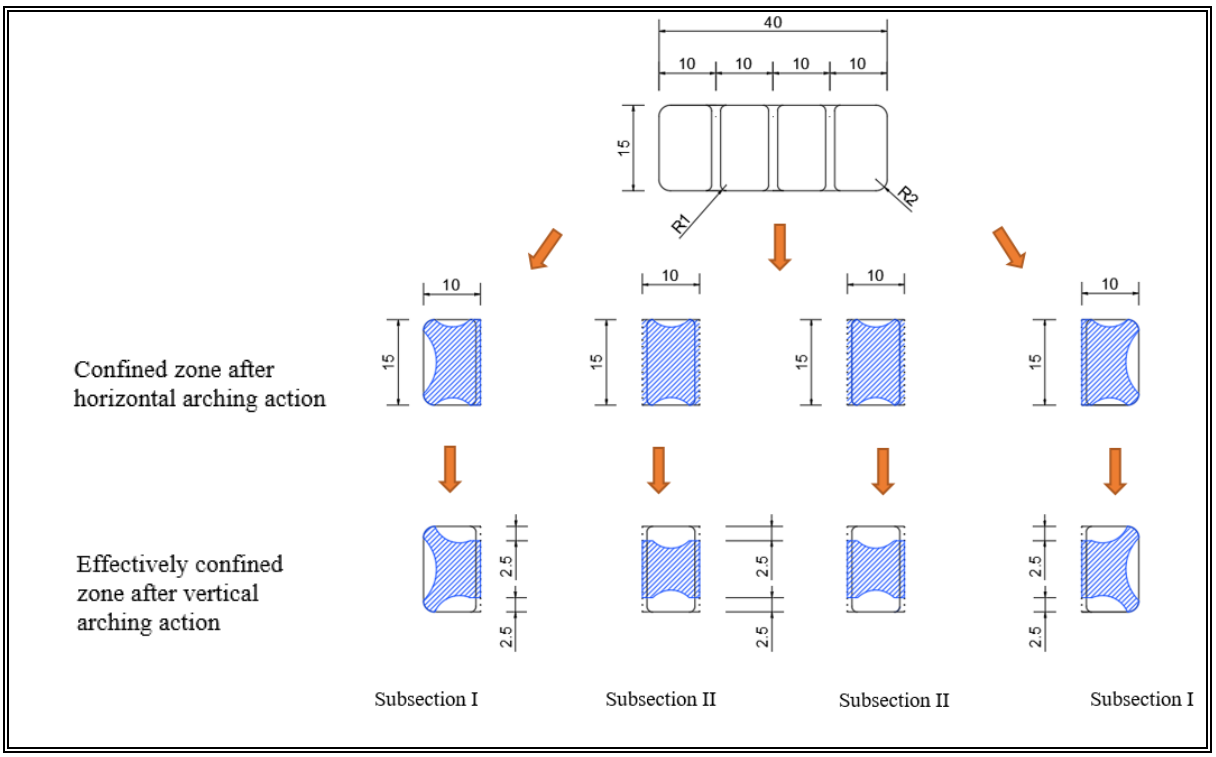

Figure 6.3: Sub columns of specimens 235-15 and 335-15 treated as independent columns

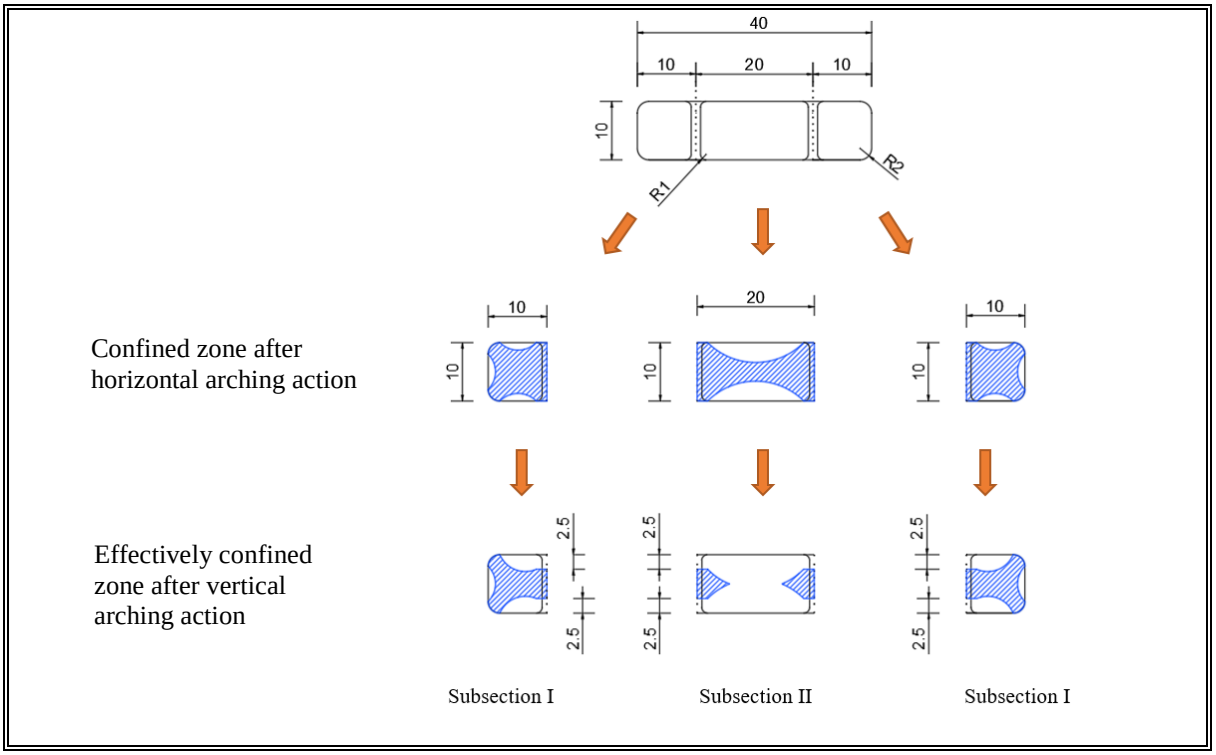

Figure 6.4: Sub columns of specimens 225-10 and 325-10 treated as independent columns

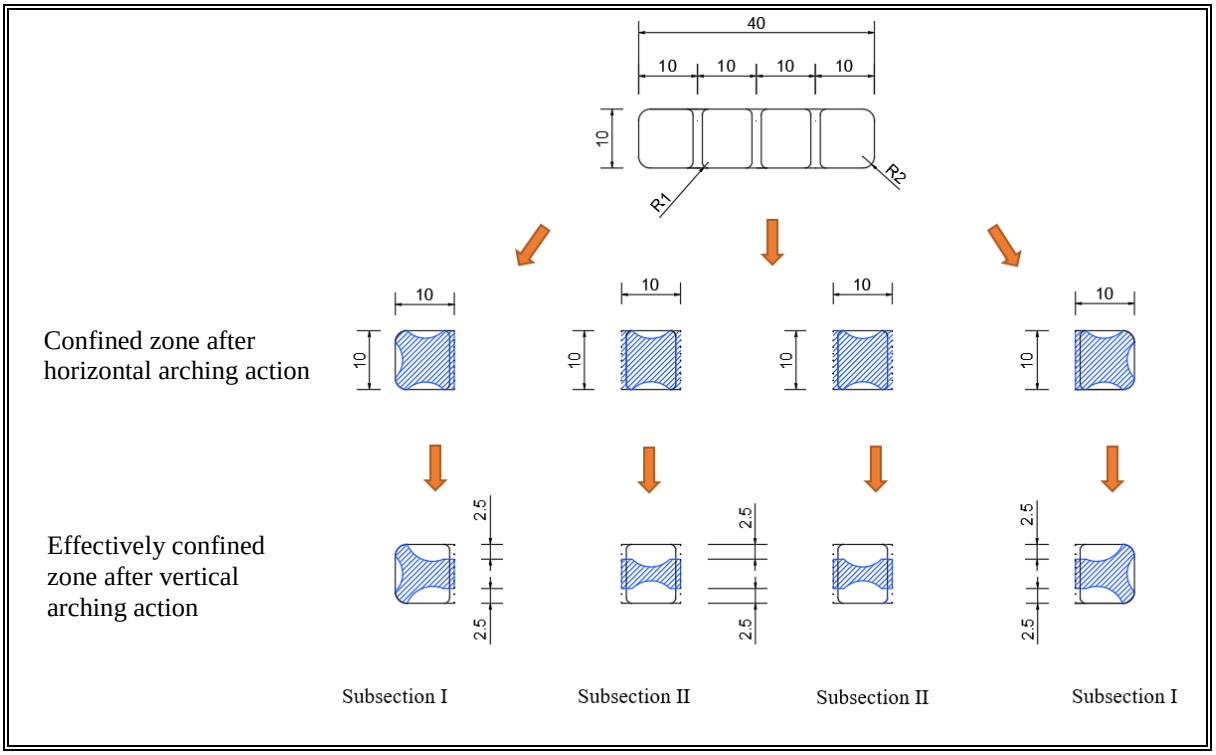

Figure 6.5: Sub columns of specimens 235-10 and 335-10 treated as independent columns

One of the most important parameters to calibrate design oriented models is the effective confining pressure. Each of the 11 closed-form models assume that the confining pressure due to the FRP jacket (f_l) of rectangular cross sections can be approximated by equation 6.1.

$$f_l = \frac{1}{2}\rho_{frp}E_{frp}\varepsilon_{frp}t_{frp} \tag{6.1}$$

where,

ρ_{frp} = volumetric ratio of the FRP, (FRP jacket volume divided by concrete volume).

E_{frp} = FRP modulus of elasticity obtained from flat coupon tensile tests.

ε_{frp} = FRP ultimate tensile strain obtained from flat coupon tensile tests.

t_{frp} = thickness of the FRP jacket.

Although Equation 5.1 is used for rectangular cross sections, this equation is based on transverse force equilibrium of circular columns (as is explained in Figure 2.8). Closed-form models for rectangular cross sections assume that Equation 5.1 can be adapted to rectangular cross section by multiplying it with correction factors. The two correction coefficients most commonly used are:

$\kappa_\varepsilon =$ efficiency factor that relates $\varepsilon_{frp,h}$ (actual hoop rupture strain of the FRP sheet installed on a confined column) to ε_{frp} (tensile rupture strain measured by the coupon test) as $\varepsilon_{frp,h} = \kappa_\varepsilon \varepsilon_{frp}$

$\kappa_s =$ shape factor that relates effectively confined area of the cross section to the gross cross section area.

With these correction factors, the effective confining pressure due to the FRP jacket (f_l^e) is obtained from Equation 6.1:

$$f_l^e = \frac{1}{2}\kappa_\varepsilon \kappa_s \rho_{frp} E_{frp} \varepsilon_{frp} t_{frp} \qquad (6.2)$$

Each of the 11-closed form models used in the proposed procedure contain their own equations and their own procedures, but the same correction factors (κ_ε and κ_s) and effective confining pressure (f_l^e) are used for all of them.

The shape factor (κ_s) is immediately obtained from the principal assumption of the proposed procedure and by applying second order parabolas with a 45-degree slope at the end of rounded corners (Mander, Priestley, & Park, Theoretical Stress - Strain Model For Confined Concrete, 1988a). Since internal borders are considered blocked from any horizontal displacement, arching action is not considered at them (Figures 6.2 to 6.5). Arching action is considered both on the transverse and vertical directions with a stablished procedure found in literature (Triantafillou, et al., 2016).

The efficiency factor (κ_ε) is difficult to obtain since the actual hoop rupture of the installed CFRP cannot be easily measured. In section 3.4, the measurements of strain gages installed on the surface of CFRP wraps are presented; however, most of the strain gages installed did not coincide with the failure zone and therefore underestimate the rupture stress. In section 4.5, the strain fields on the surface of the CFRP jacketing system captured by digital image correlation are presented; however, most of the images captured tend to overestimate the maximum strain presenting values as high as or higher than the maximum nominal tensile rupture strain measured with coupon test.

For these reasons, the most conservative values for the actual hoop rupture stress are taken from the ANSYS models. On tested specimens, the measured maximum axial average strain varied between 0.004 and 0.008; for this reason, the maximum principal stress calculated in the CFRP jacketing system was determined for each column for an ultimate axial strain of 0.006 on each column. The rupture of the CFRP system is assumed to coincide with the maximum principal stress of the CFRP shells when the column at an axial strain of 0.006. In Table 5.1, the maximum principal stress in the CFRP system for each column is detailed. For the proposed design procedure, an average of the maximum principal stresses presented in Table 5.1 is considered as the rupture stress of the CFRP system $\left(f_{frp}^{h} = 2426\,\frac{kgf}{cm^2} = 238\,MPa, \kappa_\varepsilon = \frac{238\,MPa}{970\,MPa} = 25\%\right)$.

6.3 Prediction of increments in the axial parameters

In this section, the results obtained from applying the proposed procedure to each specimen according to each one of the 11 design-oriented models for CFRP confinement without anchors found in literature (Hany, Hantouche, & Harajli, 2015; Wei & Wu, 2012; Wang, Wang, Smith, & Lu, CFRP-Confined Square RC Columns. Part II: Cyclic Axial

Compression Stress-Strain Model, 2012b; Pellegrino & Modena, 2010; Teng, Jiang, Lam, & Luo, 2009; Youssef, Feng, & Mosallam, Stress-Strain Model For Concrete Confined By FRP Composites, 2007; Wu, Wu, & Lu, 2007; Pantelides, Yan, & Reaveley, Shape Modification of Rectangular Columns Confined with FRP Composites, 2004; Hosotani, Kawashima, & Hoshikuma, 1998) and also to the 2 design-oriented models for CFRP confinement with anchors (Hany, Hantouche, & Harajli, 2016; Triantafillou, et al., 2016) are presented.

Tables 6.1 to 6.6 show the axial stress-strain parameters obtained with the proposed procedure for each specimen with each design model. In addition to theoretical models, the experimental results of each specimen with CFRP confinement and the corresponding unconfined specimen are also showed. The parameters are named according to Figure 2.10 in section 2.4. The unconfined concrete properties of Appendix A are used for the theoretical models and of the unconfined specimens for the experimental tests. The complete stress-strain curves of each specimen and each model are showed on Appendix D.

Table 6.1: Predictions for the parameter ε_c^{max} according to experimental and theoretical models

ec_max (mm/mm)	Experimental Tests		Theoretical Models												
	Confined	Unconfined	Hognestad, 1951	Hany et al, 2015	Wei & Wu, 2012	Wang et al, 2012	Pellegrino, 2010	Teng et al, 2009	Youssef et al, 2007	Wu et al, 2007 (Model I)	Wu et al, 2007 (Model II)	Wu et al, 2007 (Model III)	Pantelides et al, 2004	Hosotani et al, 1998	Hany et al, 2016
225-10	0.0032	0.0024	0.0020	0.0034	0.0031	0.0023	0.0035	0.0033	0.0025	0.0020	0.0020	0.0020	0.0094	0.0041	0.0032
225-15	0.0034	0.0030	0.0020	0.0034	0.0033	0.0023	0.0036	0.0042	0.0024	0.0020	0.0020	0.0020	0.0086	0.0036	0.0030
235-10	0.0044	0.0024	0.0020	0.0035	0.0034	0.0024	0.0046	0.0046	0.0026	0.0020	0.0020	0.0020	0.0086	0.0042	0.0035
235-15	0.0041	0.0030	0.0020	0.0034	0.0033	0.0023	0.0040	0.0041	0.0026	0.0020	0.0020	0.0020	0.0087	0.0037	0.0031
325-10	0.0070	0.0024	0.0020	0.0035	0.0034	0.0025	0.0040	0.0045	0.0026	0.0020	0.0020	0.0020	0.0084	0.0045	0.0034
325-15	0.0048	0.0030	0.0020	0.0035	0.0034	0.0025	0.0040	0.0045	0.0026	0.0020	0.0020	0.0020	0.0084	0.0045	0.0034
335-10	0.0058	0.0024	0.0020	0.0037	0.0035	0.0026	0.0052	0.0050	0.0029	0.0020	0.0020	0.0020	0.0074	0.0050	0.0042
335-15	0.0053	0.0030	0.0020	0.0035	0.0034	0.0025	0.0043	0.0044	0.0028	0.0020	0.0020	0.0020	0.0085	0.0049	0.0037

Table 6.2: Predictions for the parameter f_c^{max} according to experimental and theoretical models

fc_max (kgf/cm2)	Experimental Tests		Theoretical Models													
	Confined	Unconfined	Hognestad, 1951	Hany et al, 2015	Wei & Wu, 2012	Wang et al, 2012	Pellegrino, 2010	Teng et al, 2009	Youssef et al, 2007	Wu et al, 2007 (Model I)	Wu et al, 2007 (Model II)	Wu et al, 2007 (Model III)	Pantelides et al, 2004	Hosotani et al, 1998	Hany et al, 2016	Triantafillou et al, 2015
225-10	392	305	377	384	382	381	380	394	402	377	377	377	353	479	463	378
225-15	353	337	377	385	381	385	382	398	395	377	377	377	350	454	453	380
235-10	334	305	377	398	387	388	388	412	405	377	377	377	350	491	475	379
235-15	366	337	377	383	381	384	383	396	401	377	377	377	351	469	460	379
325-10	353	305	377	395	386	389	386	419	408	377	377	377	350	498	476	381
325-15	380	337	377	395	386	389	386	419	408	377	377	377	350	498	476	381
335-10	393	305	377	414	396	394	394	439	428	377	377	377	354	545	502	379
335-15	401	337	377	393	386	388	387	415	419	377	377	377	350	520	484	381

Table 6.3: Predictions for the parameter E_c according to experimental and theoretical models

Ec (kgf/cm2)	Experimental Tests		Theoretical Models												
	Confined	Unconfined	Hognestad, 1951	Hany et al, 2015	Wei & Wu, 2012	Wang et al, 2012	Pellegrino, 2010	Teng et al, 2009	Youssef et al, 2007	Wu et al, 2007 (Model I)	Wu et al, 2007 (Model II)	Wu et al, 2007 (Model III)	Pantelides et al, 2004	Hosotani et al, 1998	Hany et al, 2016
225-10	229693	222739	226189	172954	176389	229822	199543	174431	211657	292045	225809	292045	73843	182460	211432
225-15	199256	193278	226189	172993	172467	227407	199558	161323	215797	292077	225810	292077	79802	193956	215592
235-10	229693	142665	226189	171621	173322	222980	167077	156491	210693	292039	225808	292039	79800	181444	203876
235-15	199256	340588	226189	172814	172464	228063	186586	161052	212315	292059	225809	292059	78206	189119	212423
325-10	229693	191975	226189	171206	173160	218616	186667	157509	210659	292022	225808	292022	81438	175673	207225
325-15	199256	217056	226189	171206	173160	218616	186667	157509	210659	292022	225808	292022	81438	175673	207225
335-10	229693	221280	226189	170532	171247	214121	149886	153365	203198	291962	225805	291962	92863	168608	189827
335-15	199256	153208	226189	170920	173118	219561	173458	160233	206794	291994	225806	291994	79776	169383	199963

Table 6.4: Predictions for the parameter ε_c^{ult} according to experimental and theoretical models

ec_ult (mm/mm)	Experimental Tests		Theoretical Models												
	Confined	Unconfined	Hognestad, 1951	Hany et al, 2015	Wei & Wu, 2012	Wang et al, 2012	Pellegrino, 2010	Teng et al, 2009	Youssef et al, 2007	Wu et al, 2007 (Model I)	Wu et al, 2007 (Model II)	Wu et al, 2007 (Model III)	Pantelides et al, 2004	Hosotani et al, 1998	Hany et al, 2016
225-10	0.0030	0.0033	0.0035	0.0079	0.0036	0.0043	0.0041	0.0036	0.0043	0.0033	0.0033	0.0033	0.0162	0.0044	0.0096
225-15	0.0032	0.0044	0.0035	0.0085	0.0041	0.0060	0.0048	0.0042	0.0046	0.0036	0.0036	0.0036	0.0178	0.0042	0.0092
235-10	0.0030	0.0047	0.0035	0.0087	0.0046	0.0075	0.0054	0.0046	0.0047	0.0040	0.0040	0.0040	0.0165	0.0046	0.0103
235-15	0.0032	0.0050	0.0035	0.0084	0.0040	0.0057	0.0047	0.0041	0.0045	0.0036	0.0036	0.0036	0.0178	0.0044	0.0094
325-10	0.0030	0.0085	0.0035	0.0089	0.0044	0.0073	0.0053	0.0045	0.0047	0.0038	0.0038	0.0038	0.0134	0.0045	0.0100
325-15	0.0032	0.0055	0.0035	0.0089	0.0044	0.0073	0.0053	0.0045	0.0047	0.0038	0.0038	0.0038	0.0134	0.0045	0.0100
335-10	0.0030	0.0059	0.0035	0.0091	0.0049	0.0095	0.0061	0.0050	0.0050	0.0042	0.0042	0.0042	0.0123	0.0050	0.0115
335-15	0.0032	0.0000	0.0035	0.0088	0.0043	0.0068	0.0051	0.0044	0.0046	0.0037	0.0037	0.0037	0.0134	0.0049	0.0104

Table 6.5: Predictions for the parameter f_c^{ult} according to experimental and theoretical models

fc_ult (kgf/cm2)	Experimental Tests		Theoretical Models												
	Confined	Unconfined	Hognestad, 1951	Hany et al, 2015	Wei & Wu, 2012	Wang et al, 2012	Pellegrino, 2010	Teng et al, 2009	Youssef et al, 2007	Wu et al, 2007 (Model I)	Wu et al, 2007 (Model II)	Wu et al, 2007 (Model III)	Pantelides et al, 2004	Hosotani et al, 1998	Hany et al, 2016
225-10	254	390	320	324	304	299	357	384	269	284	150	209	347	479	274
225-15	333	272	320	315	280	244	340	398	262	260	105	181	337	453	279
235-10	254	332	320	349	282	258	362	412	281	230	67	194	339	491	276
235-15	333	353	320	313	289	251	357	396	265	260	105	184	338	468	281
325-10	254	310	320	339	286	273	344	419	290	245	84	191	344	498	287
325-15	333	334	320	339	286	273	344	419	290	245	84	191	344	498	287
335-10	254	380	320	385	304	309	369	439	299	217	54	211	345	545	281
335-15	333	0	320	335	289	266	362	415	292	252	94	202	344	520	289

Table 6.6: Predictions for the parameter E_D according to experimental and theoretical models

Ed (kgf/cm2)	Experimental Tests		Theoretical Models												
	Confined	Unconfined	Hognestad, 1951	Hany et al, 2015	Wei & Wu, 2012	Wang et al, 2012	Pellegrino, 2010	Teng et al, 2009	Youssef et al, 2007	Wu et al, 2007 (Model I)	Wu et al, 2007 (Model II)	Wu et al, 2007 (Model III)	Pantelides et al, 2004	Hosotani et al, 1998	Hany et al, 2016
225-10	-78567	-25698	-37700	-13517	-155677	-40917	-38650	-35462	-74237	-71282	-174982	-129250	-962	-1056	-29518
225-15	-20786	-89319	-37700	-13607	-126007	-38218	-35059	0	-60290	-73369	-169869	-122800	-1475	-1975	-28178
235-10	-78567	-8927	-37700	-9513	-87718	-25541	-32134	0	-59316	-73373	-155267	-91700	-1385	-588	-29342
235-15	-20786	-15206	-37700	-14011	-131442	-39342	-36646	0	-71243	-73333	-169768	-120549	-1428	-1386	-28433
325-10	-78567	-28031	-37700	-10431	-99804	-24104	-32150	0	-56608	-73582	-162910	-103578	-1169	0	-28638
325-15	-20786	-75119	-37700	-10431	-99804	-24104	-32150	0	-56608	-73582	-162910	-103578	-1169	0	-28638
335-10	-78567	-107958	-37700	-5298	-65443	-12320	-27688	0	-61531	-72610	-147016	-75691	-1804	0	-30287
335-15	-20786	0	-37700	-11043	-107436	-28298	-30679	0	-70788	-73448	-166287	-102720	-1131	0	-29123

Tables 6.7 to 6.12 show the increments of each of the axial stress-strain parameters according to the experimental tests and theoretical models. The increments represent the ratio of a CFRP confined parameter divided by the same parameter of unconfined concrete. The increments of the experimental specimens confined with CFRP are compared with their corresponding experimental specimens without CFRP confinement. The increments of the theoretical models confined with CFRP are compared with the properties of the unconfined concrete reported on Appendix A. The increments obtained from the experimental tests are assumed to be closer to reality, therefore the theoretical increments are evaluated according to their proximity to the experimental increments.

It is important to notice that all theoretical models (FEM models and design models) use the unconfined concrete properties of cylinders in their calculations, therefore, their increments should be compared with the unconfined concrete properties of cylinders (Appendix A). On the other hand, control specimens in experimental tests represent the results of actual columns without CFRP confinement constructed at the same time and with the same materials as the CFRP confined specimens. Therefore, experimental increments are compared with control columns to reflect the actual increment on each parameter.

This process represents a real-life situation where a shear wall is in need of boundary element retrofit with CFRP confinement. To predict accurately the increments expected from the CFRP confinement, the properties of the shear wall need to be determined. Since complete boundary elements cannot be removed and tested due to the impracticality of this procedure, the best way to approach this problem is to drill concrete cylinder probes and get the shear wall properties based on the probes. Then, the axial parameters increments are calculated with theoretical models calibrated with cylinder probe properties.

Table 6.7: Predictions for the increments in the ratio $\varepsilon_c^{max}/\varepsilon_{co}^{max}$ according to experimental and theoretical models

ec_max/eco_max	Experimental	Theoretical											
	Confined/Unconfined	Hany et al, 2015	Wei & Wu, 2012	Wang et al, 2012	Pellegrino, 2010	Teng et al, 2009	Youssef et al, 2007	Wu et al, 2007 (Model I)	Wu et al, 2007 (Model II)	Wu et al, 2007 (Model III)	Pantelides et al, 2004	Hosotani et al, 1998	Hany et al, 2016
225-10	1.33	1.70	1.55	1.15	1.75	1.65	1.25	1.00	1.00	1.00	4.70	2.05	1.60
225-15	1.13	1.70	1.65	1.15	1.80	2.10	1.20	1.00	1.00	1.00	4.30	1.80	1.50
235-10	1.83	1.75	1.70	1.20	2.30	2.30	1.30	1.00	1.00	1.00	4.30	2.10	1.75
235-15	1.37	1.70	1.65	1.15	2.00	2.05	1.30	1.00	1.00	1.00	4.35	1.85	1.55
325-10	2.92	1.75	1.70	1.25	2.00	2.25	1.30	1.00	1.00	1.00	4.20	2.25	1.70
325-15	1.60	1.75	1.70	1.25	2.00	2.25	1.30	1.00	1.00	1.00	4.20	2.25	1.70
335-10	2.42	1.85	1.75	1.30	2.60	2.50	1.45	1.00	1.00	1.00	3.70	2.50	2.10
335-15	1.77	1.75	1.70	1.25	2.15	2.20	1.40	1.00	1.00	1.00	4.25	2.45	1.85

Table 6.8: Predictions for the increments in the ratio f_c^{max}/f_{co}^{max} according to experimental and theoretical models

fc_max/fco_max	Experimental	Theoretical												
	Confined/Unconfined	Hany et al, 2015	Wei & Wu, 2012	Wang et al, 2012	Pellegrino, 2010	Teng et al, 2009	Youssef et al, 2007	Wu et al, 2007 (Model I)	Wu et al, 2007 (Model II)	Wu et al, 2007 (Model III)	Pantelides et al, 2004	Hosotani et al, 1998	Hany et al, 2016	Triantafillou et al, 2015
225-10	1.29	1.02	1.01	1.01	1.01	1.05	1.07	1.00	1.00	1.00	0.94	1.27	1.23	1.00
225-15	1.05	1.02	1.01	1.02	1.01	1.06	1.05	1.00	1.00	1.00	0.93	1.20	1.20	1.01
235-10	1.10	1.06	1.03	1.03	1.03	1.09	1.08	1.00	1.00	1.00	0.93	1.30	1.26	1.00
235-15	1.09	1.02	1.01	1.02	1.02	1.05	1.06	1.00	1.00	1.00	0.93	1.24	1.22	1.01
325-10	1.16	1.05	1.02	1.03	1.02	1.11	1.08	1.00	1.00	1.00	0.93	1.32	1.26	1.01
325-15	1.13	1.05	1.02	1.03	1.02	1.11	1.08	1.00	1.00	1.00	0.93	1.32	1.26	1.01
335-10	1.29	1.10	1.05	1.04	1.05	1.16	1.14	1.00	1.00	1.00	0.94	1.45	1.33	1.01
335-15	1.19	1.04	1.02	1.03	1.03	1.10	1.11	1.00	1.00	1.00	0.93	1.38	1.28	1.01

Table 6.9: Predictions for the increments in the ratio E_c/E_{co} according to experimental and theoretical models

Ec/Eco	Experimental	Theoretical											
	Confined/Unconfined	Hany et al, 2015	Wei & Wu, 2012	Wang et al, 2012	Pellegrino, 2010	Teng et al, 2009	Youssef et al, 2007	Wu et al, 2007 (Model I)	Wu et al, 2007 (Model II)	Wu et al, 2007 (Model III)	Pantelides et al, 2004	Hosotani et al, 1998	Hany et al, 2016
225-10	0.97	0.76	0.78	1.02	0.88	0.77	0.94	1.29	1.00	1.29	0.33	0.81	0.93
225-15	0.97	0.76	0.76	1.01	0.88	0.71	0.95	1.29	1.00	1.29	0.35	0.86	0.95
235-10	0.62	0.76	0.77	0.99	0.74	0.69	0.93	1.29	1.00	1.29	0.35	0.80	0.90
235-15	1.71	0.76	0.76	1.01	0.82	0.71	0.94	1.29	1.00	1.29	0.35	0.84	0.94
325-10	0.84	0.76	0.77	0.97	0.83	0.70	0.93	1.29	1.00	1.29	0.36	0.78	0.92
325-15	1.09	0.76	0.77	0.97	0.83	0.70	0.93	1.29	1.00	1.29	0.36	0.78	0.92
335-10	0.96	0.75	0.76	0.95	0.66	0.68	0.90	1.29	1.00	1.29	0.41	0.75	0.84
335-15	0.77	0.76	0.77	0.97	0.77	0.71	0.91	1.29	1.00	1.29	0.35	0.75	0.88

Table 6.10: Predictions for the increments in the ratio $\varepsilon_c^{ult}/\varepsilon_{co}^{ult}$ according to experimental and theoretical models

ec_ult/eco_ult	Experimental	Theoretical											
	Confined/Unconfined	Hany et al, 2015	Wei & Wu, 2012	Wang et al, 2012	Pellegrino, 2010	Teng et al, 2009	Youssef et al, 2007	Wu et al, 2007 (Model I)	Wu et al, 2007 (Model II)	Wu et al, 2007 (Model III)	Pantelides et al, 2004	Hosotani et al, 1998	Hany et al, 2016
225-10	1.10	2.26	1.03	1.23	1.17	1.03	1.23	0.94	0.94	0.94	4.63	1.26	2.74
225-15	1.38	2.43	1.17	1.71	1.37	1.20	1.31	1.03	1.03	1.03	5.09	1.20	2.63
235-10	1.57	2.49	1.31	2.14	1.54	1.31	1.34	1.14	1.14	1.14	4.71	1.31	2.94
235-15	1.56	2.40	1.14	1.63	1.34	1.17	1.29	1.03	1.03	1.03	5.09	1.26	2.69
325-10	2.83	2.54	1.26	2.09	1.51	1.29	1.34	1.09	1.09	1.09	3.83	1.29	2.86
325-15	1.72	2.54	1.26	2.09	1.51	1.29	1.34	1.09	1.09	1.09	3.83	1.29	2.86
335-10	1.97	2.60	1.40	2.71	1.74	1.43	1.43	1.20	1.20	1.20	3.51	1.43	3.29
335-15	0.00	2.51	1.23	1.94	1.46	1.26	1.31	1.06	1.06	1.06	3.83	1.40	2.97

Table 6.11: Predictions for the increments in the ratio f_c^{ult}/f_{co}^{ult} according to experimental and theoretical models

fc_ult/fco_max	Experimental	Theoretical											
	Confined/Unconfined	Hany et al, 2015	Wei & Wu, 2012	Wang et al, 2012	Pellegrino, 2010	Teng et al, 2009	Youssef et al, 2007	Wu et al, 2007 (Model I)	Wu et al, 2007 (Model II)	Wu et al, 2007 (Model III)	Pantelides et al, 2004	Hosotani et al, 1998	Hany et al, 2016
225-10	1.54	1.01	0.95	0.93	1.11	1.20	0.84	0.89	0.47	0.65	1.08	1.49	0.86
225-15	0.82	0.98	0.87	0.76	1.06	1.24	0.82	0.81	0.33	0.56	1.05	1.41	0.87
235-10	1.31	1.09	0.88	0.81	1.13	1.29	0.88	0.72	0.21	0.60	1.06	1.53	0.86
235-15	1.06	0.98	0.90	0.78	1.12	1.24	0.83	0.81	0.33	0.57	1.05	1.46	0.88
325-10	1.22	1.06	0.89	0.85	1.07	1.31	0.90	0.76	0.26	0.59	1.07	1.55	0.90
325-15	1.00	1.06	0.89	0.85	1.07	1.31	0.90	0.76	0.26	0.59	1.07	1.55	0.90
335-10	1.50	1.20	0.95	0.96	1.15	1.37	0.93	0.68	0.17	0.66	1.08	1.70	0.88
335-15	0.00	1.04	0.90	0.83	1.13	1.30	0.91	0.79	0.29	0.63	1.07	1.62	0.90

Table 6.12: Predictions for the increments in the ratio E_D/E_{Do} according to experimental and theoretical models

Ed/Edo	Experimental	Theoretical											
	Confined/Unconfined	Hany et al, 2015	Wei & Wu, 2012	Wang et al, 2012	Pellegrino, 2010	Teng et al, 2009	Youssef et al, 2007	Wu et al, 2007 (Model I)	Wu et al, 2007 (Model II)	Wu et al, 2007 (Model III)	Pantelides et al, 2004	Hosotani et al, 1998	Hany et al, 2016
225-10	0.33	0.36	4.13	1.09	1.03	0.94	1.97	1.89	4.64	3.43	0.03	0.03	0.78
225-15	4.30	0.36	3.34	1.01	0.93	0.00	1.60	1.95	4.51	3.26	0.04	0.05	0.75
235-10	0.11	0.25	2.33	0.68	0.85	0.00	1.57	1.95	4.12	2.43	0.04	0.02	0.78
235-15	0.73	0.37	3.49	1.04	0.97	0.00	1.89	1.95	4.50	3.20	0.04	0.04	0.75
325-10	0.36	0.28	2.65	0.64	0.85	0.00	1.50	1.95	4.32	2.75	0.03	0.00	0.76
325-15	3.61	0.28	2.65	0.64	0.85	0.00	1.50	1.95	4.32	2.75	0.03	0.00	0.76
335-10	1.37	0.14	1.74	0.33	0.73	0.00	1.63	1.93	3.90	2.01	0.05	0.00	0.80
335-15	0.00	0.29	2.85	0.75	0.81	0.00	1.88	1.95	4.41	2.72	0.03	0.00	0.77

In Tables 6.13 to 6.18, the increments of each parameter according to theoretical models are compared to the increments captured with the experimental tests. The increments on each parameter of each specimen according to the experimental models are assumed to be the closest approximation to the behavior of a real shear wall boundary element. Therefore, the increments predicted with the theoretical models are evaluated according to their approximation to the experimental values. If the theoretical models gave perfect predictions all ratios indicated in Tables 6.13 to 6.18 should be 1. If the theoretical model's predictions overestimate the experimentally observed increment, the ratio present is greater than 1. If the theoretical model's predictions underestimate the experimentally observed increment, the ratio present is less than 1.

The same data showed on Tables 6.13 to 6.18 is showed graphically on Figures 6.6 to 6.11. On these Figures, the data is also showed as statistical data for each specimen (average and standard deviation).

Table 6.13: Ratio of theoretical to experimental predictions of increment ratio $\varepsilon_c^{max}/\varepsilon_{co}^{max}$

		Hany et al, 2015	Wei & Wu, 2012	Wang et al, 2012	Pellegrino, 2010	Teng et al, 2009	Youssef et al, 2007	Wu et al, 2007 (Model I)	Wu et al, 2007 (Model II)	Wu et al, 2007 (Model III)	Pantelides et al, 2004	Hosotani et al, 1998	Hany et al, 2016
$\frac{\left(\frac{\varepsilon c_{max}}{\varepsilon co_{max}}\right)^{theo}}{\left(\frac{\varepsilon c_{max}}{\varepsilon co_{max}}\right)^{exp}}$	225-10	1.28	1.16	0.86	1.31	1.24	0.94	0.75	0.75	0.75	3.53	1.54	1.20
	225-15	1.50	1.46	1.01	1.59	1.85	1.06	0.88	0.88	0.88	3.79	1.59	1.32
	235-10	0.95	0.93	0.65	1.25	1.25	0.71	0.55	0.55	0.55	2.35	1.15	0.95
	235-15	1.24	1.21	0.84	1.46	1.50	0.95	0.73	0.73	0.73	3.18	1.35	1.13
	325-10	0.60	0.58	0.43	0.69	0.77	0.45	0.34	0.34	0.34	1.44	0.77	0.58
	325-15	1.09	1.06	0.78	1.25	1.41	0.81	0.63	0.63	0.63	2.63	1.41	1.06
	335-10	0.77	0.72	0.54	1.08	1.03	0.60	0.41	0.41	0.41	1.53	1.03	0.87
	335-15	0.99	0.96	0.71	1.22	1.25	0.79	0.57	0.57	0.57	2.41	1.39	1.05
	Average	1.05	1.01	0.73	1.23	1.29	0.79	0.61	0.61	0.61	2.61	1.28	1.02
	STD	0.29	0.28	0.19	0.27	0.32	0.20	0.18	0.18	0.18	0.86	0.28	0.23

Table 6.14: Ratio of theoretical to experimental predictions of increment ratio f_c^{max}/f_{co}^{max}

		Hany et al, 2015	Wei & Wu, 2012	Wang et al, 2012	Pellegrino, 2010	Teng et al, 2009	Youssef et al, 2007	Wu et al, 2007 (Model I)	Wu et al, 2007 (Model II)	Wu et al, 2007 (Model III)	Pantelides et al, 2004	Hosotani et al, 1998	Hany et al, 2016	Triantafillou et al, 2015
$\frac{\left(\frac{fc_{max}}{fco_{max}}\right)^{theo}}{\left(\frac{fc_{max}}{fco_{max}}\right)^{exp}}$	225-10	0.79	0.79	0.79	0.78	0.81	0.83	0.78	0.78	0.78	0.73	0.99	0.96	0.78
	225-15	0.97	0.96	0.97	0.97	1.01	1.00	0.95	0.95	0.95	0.89	1.15	1.15	0.96
	235-10	0.97	0.94	0.94	0.94	1.00	0.98	0.91	0.91	0.91	0.85	1.19	1.15	0.92
	235-15	0.94	0.93	0.94	0.94	0.97	0.98	0.92	0.92	0.92	0.86	1.14	1.12	0.93
	325-10	0.91	0.88	0.89	0.88	0.96	0.94	0.86	0.86	0.86	0.80	1.14	1.09	0.87
	325-15	0.93	0.91	0.92	0.91	0.99	0.96	0.89	0.89	0.89	0.82	1.17	1.12	0.90
	335-10	0.85	0.81	0.81	0.81	0.90	0.88	0.78	0.78	0.78	0.73	1.12	1.03	0.78
	335-15	0.88	0.86	0.86	0.86	0.93	0.93	0.84	0.84	0.84	0.78	1.16	1.08	0.85
	Average	0.90	0.89	0.89	0.89	0.95	0.94	0.87	0.87	0.87	0.81	1.13	1.09	0.87
	STD	0.06	0.06	0.07	0.06	0.06	0.06	0.07	0.07	0.07	0.06	0.06	0.07	0.07

Table 6.15: Ratio of theoretical to experimental predictions of increment ratio E_c/E_{co}

		Hany et al, 2015	Wei & Wu, 2012	Wang et al, 2012	Pellegrino, 2010	Teng et al, 2009	Youssef et al, 2007	Wu et al, 2007 (Model I)	Wu et al, 2007 (Model II)	Wu et al, 2007 (Model III)	Pantelides et al, 2004	Hosotani et al, 1998	Hany et al, 2016
$\frac{\left(\frac{Ec}{Eco}\right)^{theo}}{\left(\frac{Ec}{Eco}\right)^{exp}}$	225-10	0.79	0.80	1.05	0.91	0.80	0.96	1.33	1.03	1.33	0.34	0.83	0.96
	225-15	0.79	0.79	1.04	0.91	0.74	0.98	1.33	1.03	1.33	0.36	0.88	0.98
	235-10	1.22	1.23	1.59	1.19	1.11	1.50	2.08	1.61	2.08	0.57	1.29	1.45
	235-15	0.45	0.45	0.59	0.48	0.42	0.55	0.76	0.58	0.76	0.20	0.49	0.55
	325-10	0.91	0.92	1.16	0.99	0.83	1.11	1.54	1.19	1.54	0.43	0.93	1.10
	325-15	0.69	0.70	0.89	0.76	0.64	0.85	1.19	0.92	1.19	0.33	0.71	0.84
	335-10	0.78	0.79	0.98	0.69	0.70	0.93	1.34	1.04	1.34	0.43	0.77	0.87
	335-15	0.98	1.00	1.26	1.00	0.92	1.19	1.68	1.30	1.68	0.46	0.97	1.15
	Average	0.83	0.83	1.07	0.87	0.77	1.01	1.41	1.09	1.41	0.39	0.86	0.99
	STD	0.22	0.23	0.29	0.22	0.20	0.27	0.38	0.30	0.38	0.11	0.23	0.26

Table 6.16: Ratio of theoretical to experimental predictions of increment ratio $\varepsilon_c^{ult}/\varepsilon_{co}^{ult}$

		Hany et al, 2015	Wei & Wu, 2012	Wang et al, 2012	Pellegrino, 2010	Teng et al, 2009	Youssef et al, 2007	Wu et al, 2007 (Model I)	Wu et al, 2007 (Model II)	Wu et al, 2007 (Model III)	Pantelides et al, 2004	Hosotani et al, 1998	Hany et al, 2016
$\frac{\left(\frac{\varepsilon c_{ult}}{\varepsilon co_{ult}}\right)^{theo}}{\left(\frac{\varepsilon c_{ult}}{\varepsilon co_{ult}}\right)^{exp}}$	225-10	2.05	0.94	1.12	1.06	0.94	1.12	0.86	0.86	0.86	4.21	1.14	2.49
	225-15	1.77	0.85	1.25	1.00	0.87	0.96	0.75	0.75	0.75	3.70	0.87	1.91
	235-10	1.59	0.84	1.37	0.98	0.84	0.86	0.73	0.73	0.73	3.01	0.84	1.88
	235-15	1.54	0.73	1.04	0.86	0.75	0.82	0.66	0.66	0.66	3.25	0.80	1.72
	325-10	0.90	0.44	0.74	0.53	0.45	0.47	0.38	0.38	0.38	1.35	0.45	1.01
	325-15	1.48	0.73	1.21	0.88	0.75	0.78	0.63	0.63	0.63	2.23	0.75	1.66
	335-10	1.32	0.71	1.38	0.89	0.73	0.73	0.61	0.61	0.61	1.79	0.73	1.67
	Average	1.52	0.75	1.16	0.89	0.76	0.82	0.66	0.66	0.66	2.79	0.80	1.76
	STD	0.36	0.16	0.22	0.17	0.16	0.20	0.15	0.15	0.15	1.04	0.21	0.44

Table 6.17: Ratio of theoretical to experimental predictions of increment ratio f_c^{ult}/f_{co}^{ult}

		Hany et al, 2015	Wei & Wu, 2012	Wang et al, 2012	Pellegrino, 2010	Teng et al, 2009	Youssef et al, 2007	Wu et al, 2007 (Model I)	Wu et al, 2007 (Model II)	Wu et al, 2007 (Model III)	Pantelides et al, 2004	Hosotani et al, 1998	Hany et al, 2016
$\frac{\left(\frac{fc_{ult}}{fco_{ult}}\right)^{theo}}{\left(\frac{fc_{ult}}{fco_{ult}}\right)^{exp}}$	225-10	0.66	0.62	0.61	0.73	0.78	0.55	0.58	0.30	0.42	0.70	0.97	0.56
	225-15	1.20	1.07	0.93	1.30	1.52	1.00	0.99	0.40	0.69	1.29	1.73	1.06
	235-10	0.83	0.67	0.62	0.86	0.98	0.67	0.55	0.16	0.46	0.81	1.17	0.66
	235-15	0.92	0.85	0.74	1.05	1.17	0.78	0.76	0.31	0.54	0.99	1.38	0.83
	325-10	0.87	0.73	0.70	0.88	1.07	0.74	0.63	0.21	0.49	0.88	1.27	0.73
	325-15	1.06	0.89	0.85	1.07	1.30	0.90	0.76	0.26	0.59	1.07	1.55	0.89
	335-10	0.80	0.63	0.64	0.77	0.91	0.62	0.45	0.11	0.44	0.72	1.14	0.59
	Average	0.91	0.78	0.73	0.95	1.11	0.75	0.67	0.25	0.52	0.92	1.32	0.76
	STD	0.18	0.16	0.12	0.20	0.25	0.16	0.18	0.10	0.10	0.21	0.26	0.18

Table 6.18: Ratio of theoretical to experimental predictions of increment ratio E_D/E_{Do}

		Hany et al, 2015	Wei & Wu, 2012	Wang et al, 2012	Pellegrino, 2010	Teng et al, 2009	Youssef et al, 2007	Wu et al, 2007 (Model I)	Wu et al, 2007 (Model II)	Wu et al, 2007 (Model III)	Pantelides et al, 2004	Hosotani et al, 1998	Hany et al, 2016
$\frac{\left(\frac{E_D}{E_{Do}}\right)^{theo}}{\left(\frac{E_D}{E_{Do}}\right)^{exp}}$	225-10	1.10	12.62	3.32	3.13	2.88	6.02	5.78	14.19	10.48	0.08	0.09	2.39
	225-15	0.08	0.78	0.24	0.22	0.00	0.37	0.45	1.05	0.76	0.01	0.01	0.17
	235-10	2.22	20.48	5.96	7.50	0.00	13.85	17.13	36.25	21.41	0.32	0.14	6.85
	235-15	0.51	4.77	1.43	1.33	0.00	2.58	2.66	6.16	4.37	0.05	0.05	1.03
	325-10	0.78	7.42	1.79	2.39	0.00	4.21	5.47	12.11	7.70	0.09	0.00	2.13
	325-15	0.08	0.73	0.18	0.24	0.00	0.42	0.54	1.20	0.76	0.01	0.00	0.21
	335-10	0.10	1.26	0.24	0.53	0.00	1.19	1.40	2.84	1.46	0.03	0.00	0.58
	Average	0.69	6.87	1.88	2.19	0.41	4.09	4.78	10.54	6.71	0.08	0.04	1.91
	STD	0.78	7.41	2.13	2.59	1.09	4.78	5.87	12.47	7.47	0.11	0.05	2.35

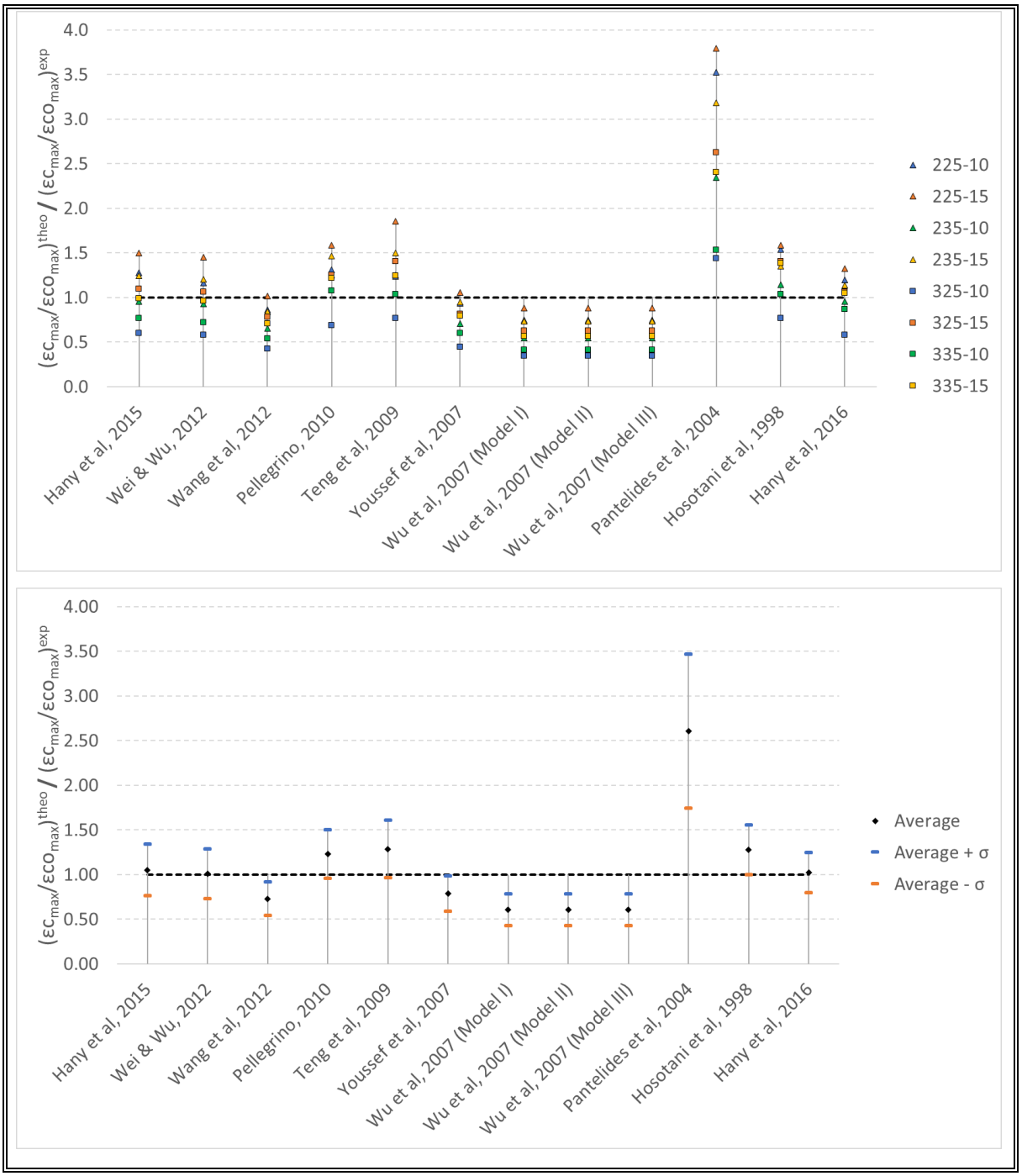

Figure 6.6: Theoretical increment compared with experimental increments for ec_{max}.

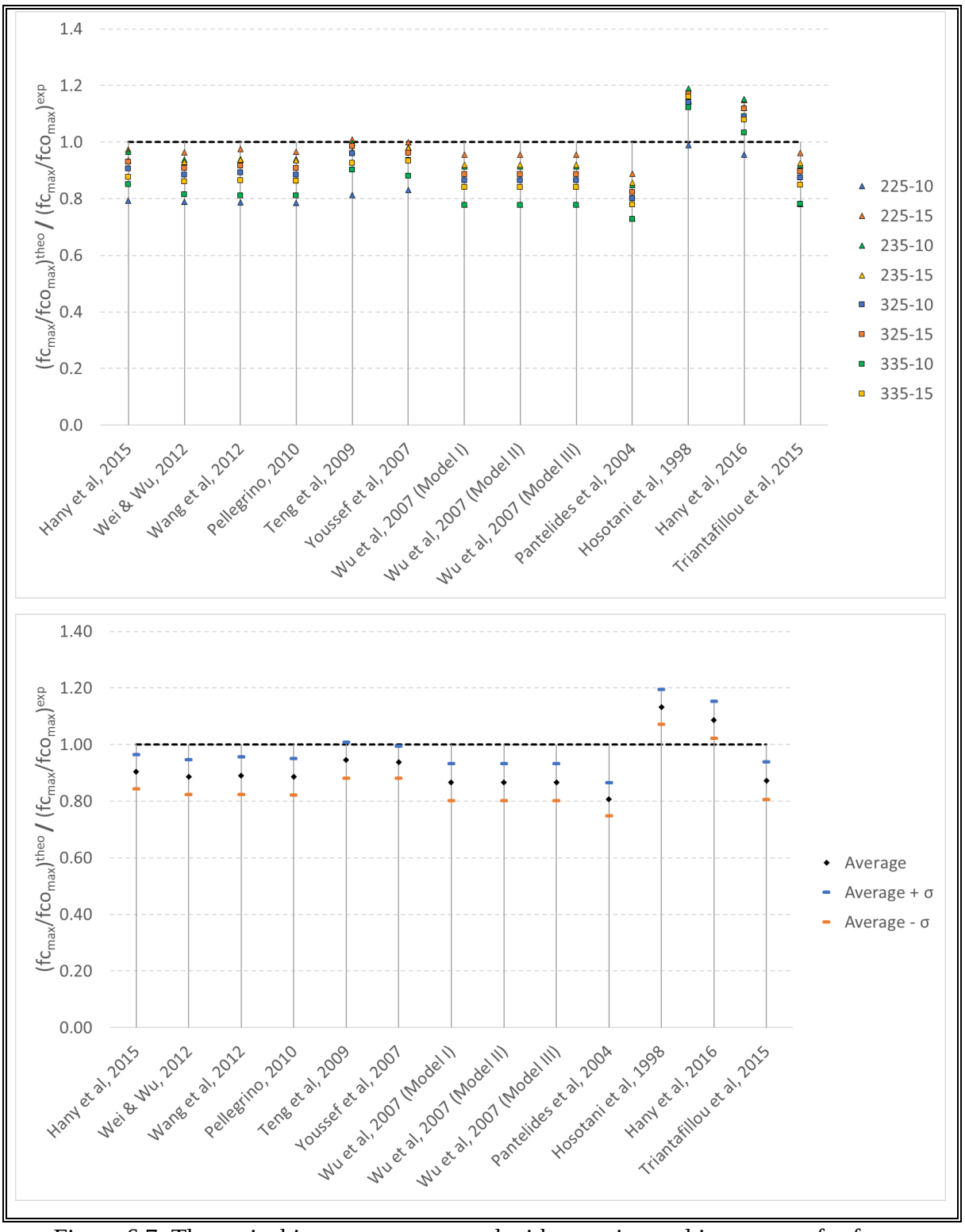

Figure 6.7: Theoretical increment compared with experimental increments for fc_{max}.

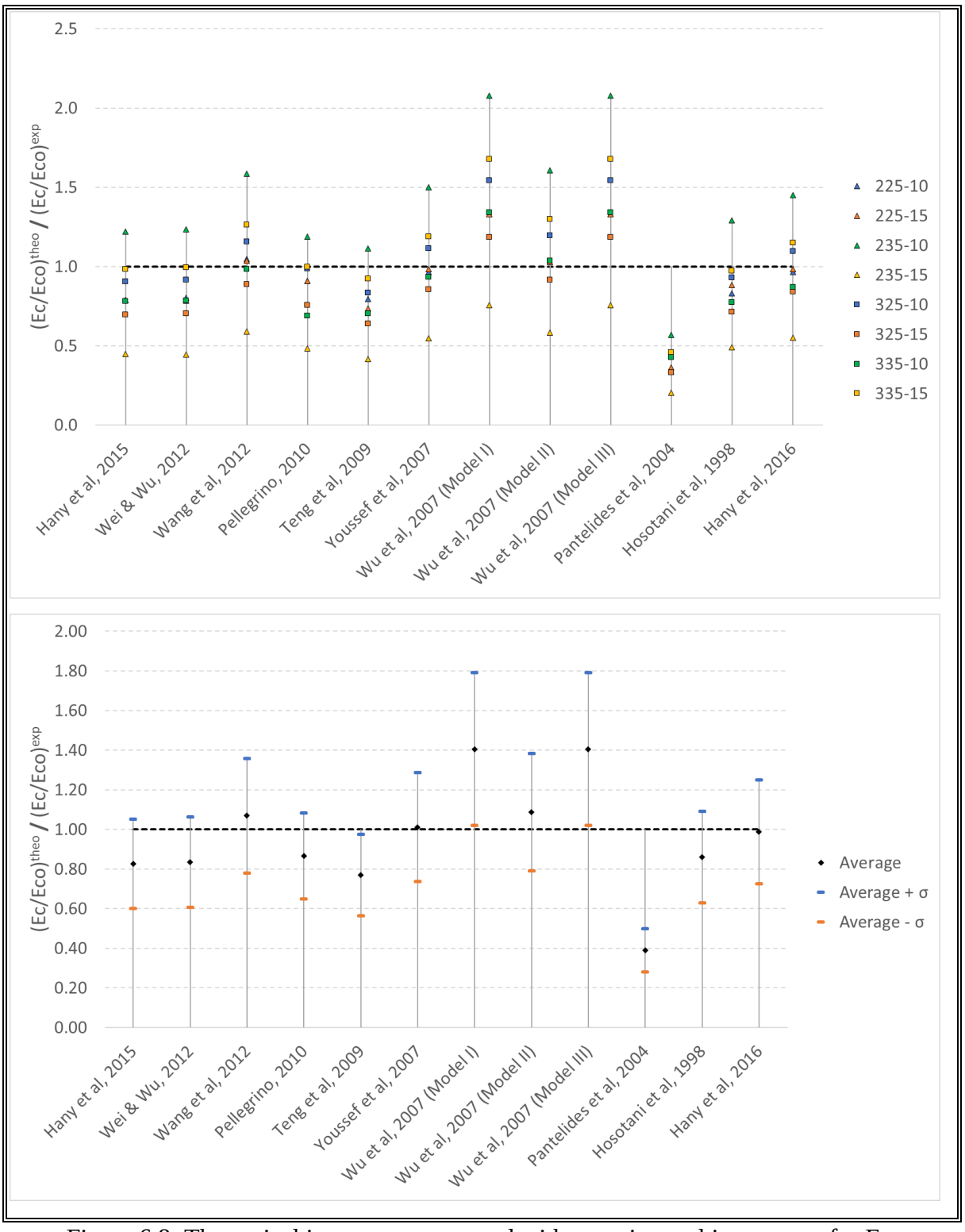

Figure 6.8: Theoretical increment compared with experimental increments for E_c.

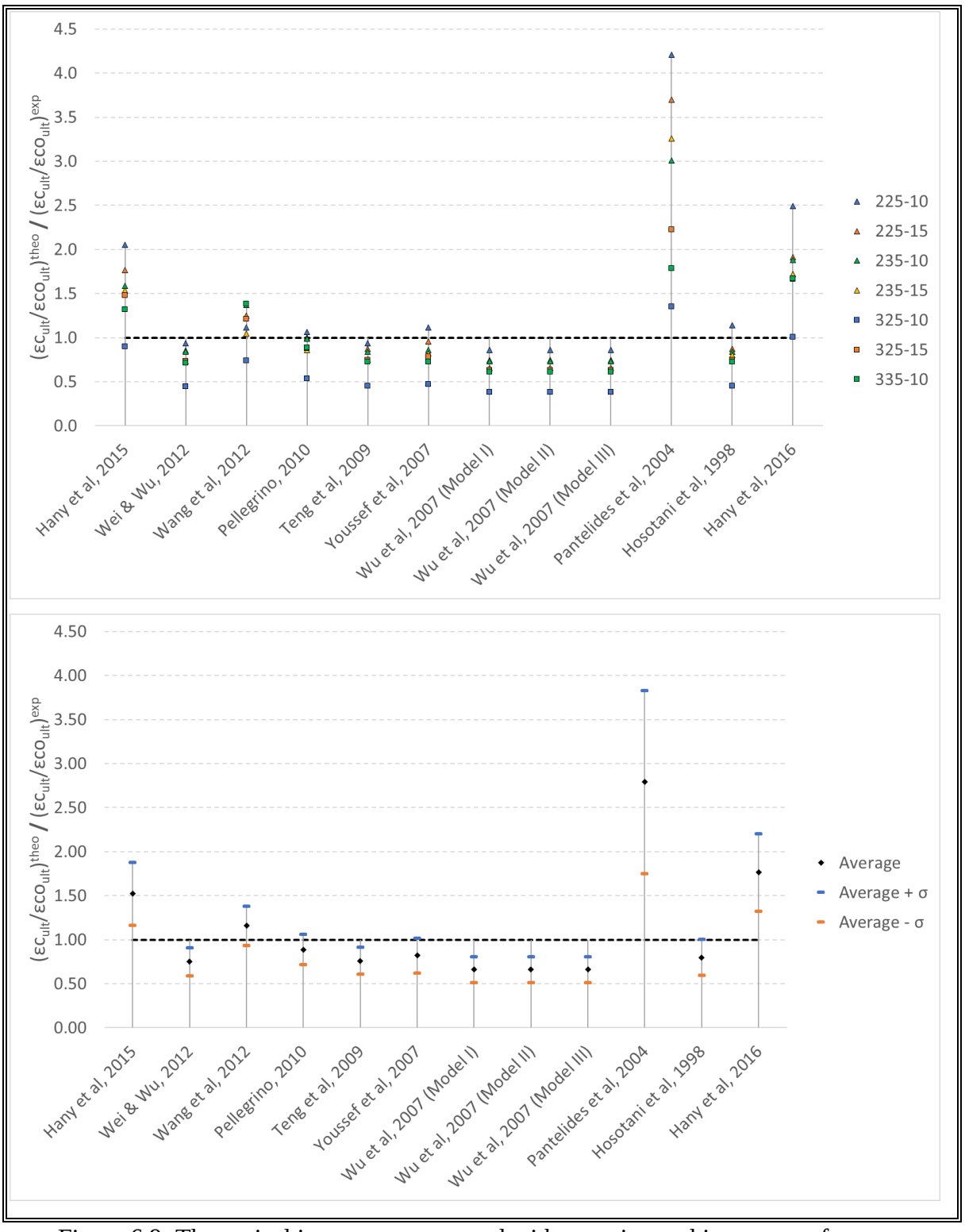

Figure 6.9: Theoretical increment compared with experimental increments for ec_{ult}.

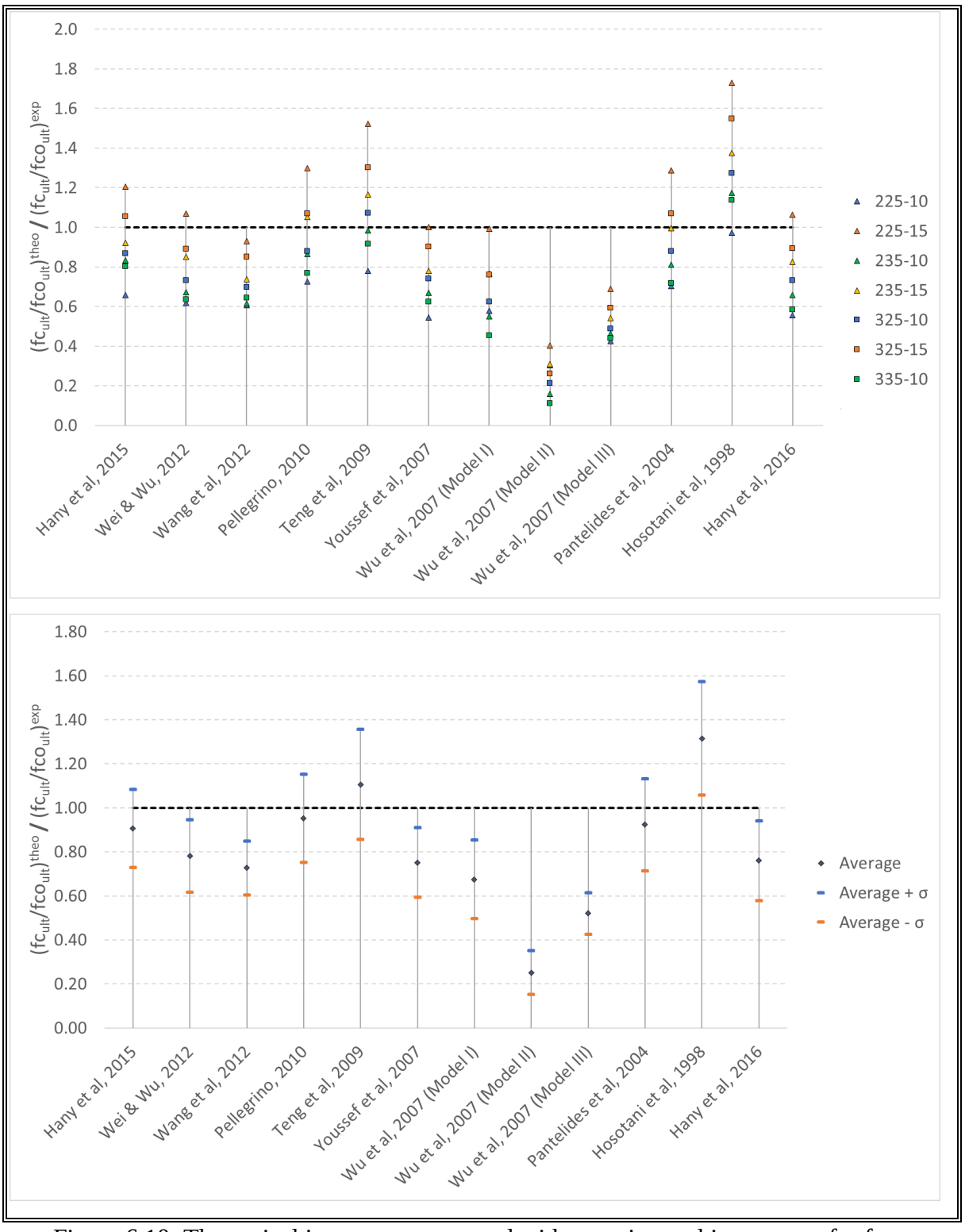

Figure 6.10: Theoretical increment compared with experimental increments for fc_{ult}.

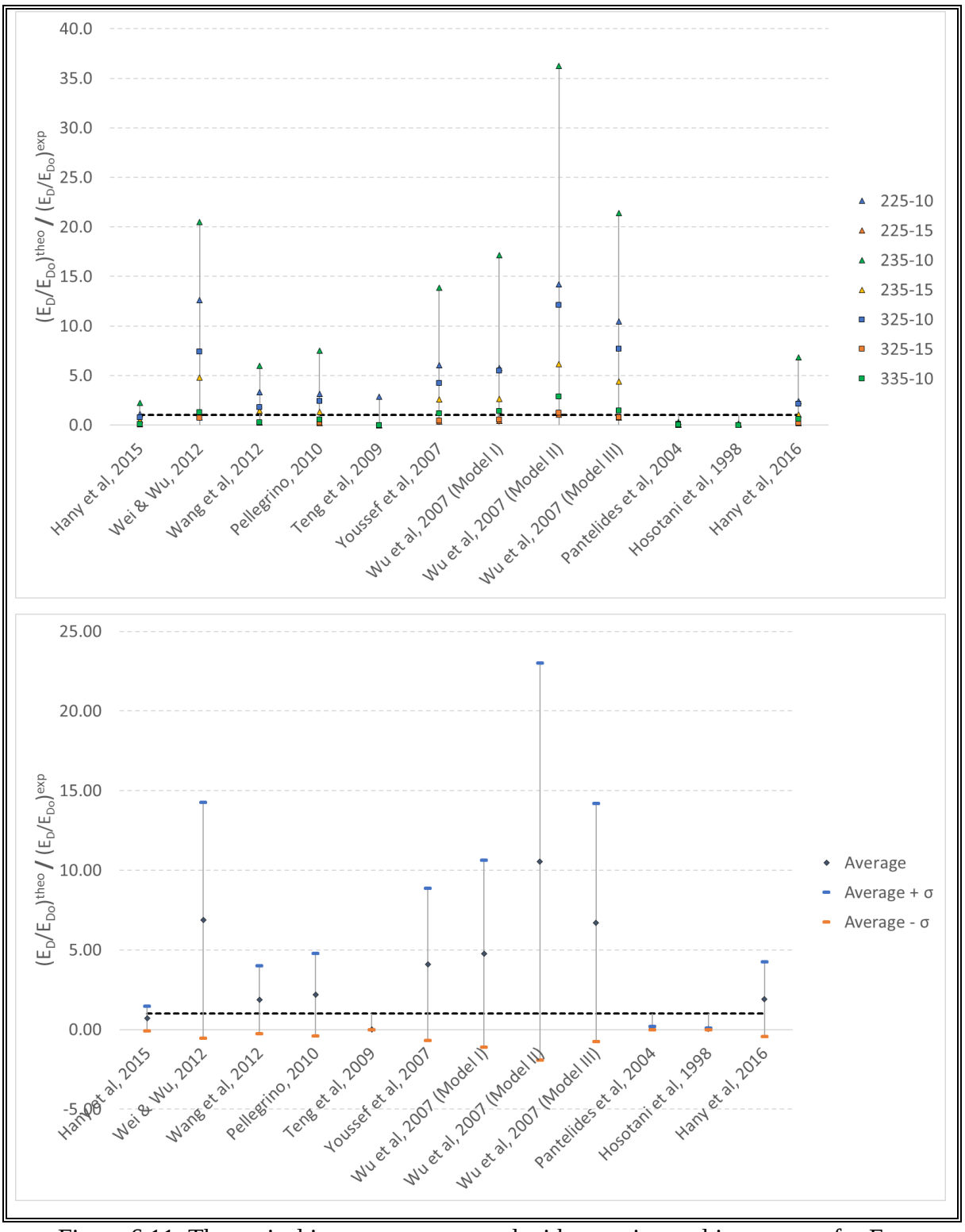

Figure 6.11: Theoretical increment compared with experimental increments for E_D.

In general, more accurate predictions are obtained from using newer design models of columns confined with CFRP wraps but no anchors. Additionally, the proposed procedure predictions tend to be as accurate as the ones obtained from design models specifically calibrated for columns confined with CFRP wraps and anchors (Hany, Hantouche, & Harajli, 2016; Triantafillou, et al., 2016). A description of the results obtained for each of the stress-strain curve parameters is detailed below.

The increments predicted for the strain corresponding to the maximum concrete stress (ε_c^{max}) present a good degree of accuracy. Most of the existing models predict increments close to the ones predicted on experimental tests. Older existing models present higher degree of dispersion (Pantelides, Yan, & Reaveley, Shape Modification of Rectangular Columns Confined with FRP Composites, 2004). The models from Wang, Wang, Smith, & Lu, 2012b, Youssef, Feng, & Mosallam, 2007 and Wu, Wu, & Lu, 2007 tend to predict more conservative increments. The model especifically calibrated for CFRP wraps and anchors, Hany, Hantouche, & Harajli, 2016, gives predictions as accurate and as dispersed as the ones obtained from the proposed porcedure.

The increments predicted for the maximum concrete stress (f_c^{max}) present a high degree of accuracy and mostly predict conservative increments. The oldest model, Hosotani, Kawashima, & Hoshikuma (1998), tends to overstimate the increment in concrete maximum stress. Also, the model especifically calibrated for CFRP wraps and anchor, Hany, Hantouche & Harajli (2016), tends to overestimate the incremente in this paramter. The other model especifically calibrated for CFRP wraps and anchor, Triantafillou et al. (2016), presents predictions as accurate and conservative as those of the propose procedure.

The increments predicted for the concrete secant modulus of elasticity (E_c) present a medium degree of accuracy and older models tend to present higher values of dispersion. The model especifically calibrated for CFRP wraps and anchor, Hany, Hantouche, & Harajli, 2016, present a level of accuracy and dispersion similar to the one by applying the proposed procedure with the lastest design models for columns confined with CFRP wraps but no anchors (Hany, Hantouche, & Harajli, 2015; Wang, Wang, Smith, & Lu, 2012b; Pellegrino & Modena, 2010; Teng, Jiang, Lam, & Luo, 2009). The increments predicted with the proposed procedure and the latest deisng models tend to give more conservative results than the model especifically calibrated for CFRP wraps and anchors.

The increments predicted for the ultimate strain (ε_c^{ult}) present a high degree of accuracy. When the proposed procedure is applied with the models Hany, Hantouche, & Harajli, 2015; Pellegrino & Modena, 2010; Hosotani, Kawashima, & Hoshikuma, 1998, the results tend to overestimate the increments predicted with the expeirmental models. The model especifically calibrated for CFRP wraps and anchor, Hany, Hantouche, & Harajli, 2016, also tends to overestimate the $_c^{ult}$ parameter. However, when the proposed procedure is applied with the remaining models, conservative and accurate predictions are obtained.

The increments predicted for the ultimate concrete stress (f_c^{ult}) present a medium degree of accuracy. The proposed procedure tends to underestimate the increments in this parameter with most models. There is a high degree of dispersion when applying the same procedure with different design models. The model especifically calibrated for CFRP wraps and anchor, Hany, Hantouche, & Harajli, 2016, presents a level of dispersion similar to the obtained by the proposed procedure with the lastest design models.

The increments predicted for the descending slope after the peak is reached (E_D) present a poor accuracy level. The proposed procedure applied to most of the design models predicts highly dispersed and highly overestimated results. The model especifically calibrated for CFRP wraps and anchors, Hany, Hantouche, & Harajli, 2016, also presents high dispersion and overestimation.

6.4 Summary

A design oriented procedure is proposed to capture the expected increments on each axial stress-strain curve parameters. The parameters studied are the concrete maximum stress (f_c^{max}), the corresponding axial strain (ε_c^{max}), the ultimate stress (f_c^{ult}), the ultimate strain (ε_c^{ult}), the secant modulus of elasticity (E_c) and the descending slope after the peak is reached (E_D).

The proposed procedure for rectangular columns confined with CFRP wraps and CFRP anchors consists of dividing each column into individual sub columns and analyze them separately with existing design models of columns confined with CFRP wraps but without CFRP anchors. The sub columns are located between CFRP anchors and between lateral edges and CFRP anchors (assuming a CFRP anchors are distributed in vertical columns). Each sub column is analyzed individually considering its internal boundaries blocked from any horizontal movement. The stress-strain curve of the complete specimen is obtained as an average of all the internal sub columns stress-strain curves and its ultimate point is obtained from the sub column that with the least value of ε_c^{ult}.

The procedure is designed to predict increments in stress-strain curve parameters of boundary elements with respect to the unconfined concrete properties tested with cylinder probes drilled from the existing boundary element. The experimental models represent more

accurately the behavior of a shear wall boundary element. Therefore, the theoretical predicted increments are compared to the increments obtained from experimental models. The increments predicted by the experimental models are obtained from the comparison of tested CFRP confined columns with control columns without CFRP confinement.

The confinement provided by the steel stirrups was neglected because experimental models showed that no ductility was provided by the steel reinforcement. Also, the theoretical model of Mander, Priestley, & Park, 1988a for steel confinement showed that due to the small quantity of steel reinforcement no increment in the stress-strain curve parameters due to steel confinement should be expected for these specific columns.

Since the proposed procedure is based on existing design-oriented models of columns confined with CFRP wraps but without CFRP anchors, the procedure is also design-oriented. That means that the input data required consists only of geometrical and material data and the results are obtained from closed equations. Additionally, based on conservative results of nonlinear finite element models developed on ANSYS, the efficiency factor κ_ε is assumed to be 0.25. The shape factor is obtained from the assumed arching action of confinement with the use of second degree parabolas with a 45-degree angle at the end of corners.

With the results obtained for each parameter it can be concluded that the parameters $\varepsilon_c^{max}, f_c^{max}$ and ε_c^{ult} can be predicted with good accuracy with the proposed procedure and the results obtained are as good as the ones obtained with the models especifically calibrated for CFRP wraps and anchors. No single design-oriente model available in literature gives more accurete predictions in all parameters, but in general the newer models tend to give better predictions. Since all the design models are calibrated on experimental tests, it is clear

that more testing of columns with CFRP wraps and anchors is required to determined a model than can be recommended for design guidelines

7. CONCLUSIONS

In this final chapter, the conclusions obtained from experimental tests, theoretical models and the comparison between them are presented at section 7.1 to 7.3. Additionally, recommendations for future research are also presented at section 7.4.

7.1 Experimental models

Twelve rectangular reinforced concrete columns were constructed to study the behavior of the proposed system of CFRP wraps and CFRP anchors. Eight of these columns are reinforced with the proposed system, while four are left without CFRP confinement to evaluate the impact on the axial stress-strain properties of the CFRP confinement. Following are the principal conclusions obtained from the construction and testing of these columns:

- The installation of the proposed CFRP jacketing system was more complex than the traditional CFRP installation on columns with circular or rectangular without anchors cross-sections. The time required to prepare each column with the work of two people was between one to two hours depending on the quantity of CFRP wraps. The installation of CFRP anchors sandwiched between CFRP wraps was the slowest part of the process since each anchor must be carefully extended.
- The sandwiched disposition of CFRP anchors between CFRP wraps demonstrated to generate a strong union between al the CFRP parts since none of the columns presented failures of deboning between CFRP components. All columns presented rupture at external corners of the column or at anchors near internal corners.

- Although the CFRP system was installed carefully, the presence of corners at precast holes and openings in the CFRP wraps to let the anchors pass generated the introduction of air bubbles inside the CFRP jacketing system. The presence of bubbles reduces the efficiency of the confining system since the portion of CFRP wrap over each bubble must first be extended before taking load. Despite of the few bubbles introduced the applied system generated increments the axial properties of the CFRO confined columns; however, an even greater increase could have been observed if a more efficient installation technique was explored.
- The columns confined with CFRP experienced higher maximum stress, ultimate stress and ultimate strain than their corresponding control columns. CFRP confined columns almost maintained the maximum stress while experiencing axial deformation, generating great energy dissipation and ductility. After the first CFRP fiber rupture, the load of the column dropped abruptly but the integrity of the columns remained throughout the complete loading. Buckling of vertical bars was observed only at failure zones and opening of stirrups was not observed.
- In the case of specimens without CFRP, failure of columns was characterized by concrete crushing throughout the complete cross section, buckling of vertical bars at all crushed concrete zones and opening of transverse stirrups.
- Since a force controlled testing machine was used only a few portion of the descending branch was obtained. Therefore, the increments captured could have been larger if a displacement testing machine was available.
- Strain gages installed on the CFRP outer layer present accurate results of the strain experienced by the CFRP confining system; however, most of the strain gages were

not located inside the failure zone. Due to the few strain gages available, it was unlikely to place a strain gage at the failure zone since due to the complex geometry of the column the location failure zone is difficult to predict.

- Strain gages located at or near the failure zone presented large strain values (higher than 0.01). This reflects the high level of stress these fibers were subject to. Strain gages outside the failure zone presented low values of strain (less than 0.005) showing that fibers outside the failure zone do not generate large stresses.
- Despite fibers outside the failure zone seem to take small loads, their presence is vital to maintain the integrity of the column. This is showed when comparing the failure mode of columns with and without CFRP confinement. Specimens with CFRP tend to generate localized failure zones while maintaining solid the rest of the column. Specimens without CFRP tend to generate a generalized failure, with complete crushing of concrete along the entire column.
- Digital image correlation (DIC) demonstrated its ability to determine the most stresses zones in the CFRP confinement system at its outer layer; however, the strain values predicted for the ultimate strain tend to be overestimated. The ultimate strain of a CFRP composite in a coupon axil test was given by the manufacturer as 0.01. The values of ultimate strain in the CFRP installed system should be a fraction of that value; however, DIC captured values close to 0.01 or even higher. This is mainly due to re accommodation of CFRP due to the presence of air bubbles beneath the outer layer, which generate a translation but not necessarily associated with stress. A much more reliable value for the ultimate

7.2 Finite element models

Nonlinear finite element models were developed for each of the columns tested experimentally. The models were divided in two categories:

- Group 1 models were developed to represent each of the tested columns with their complete transverse cross-section.
- Group 2 models were developed to illustrate how the behavior of a complete column can be approximated by modelling independent sub columns located between CFRP anchors.

The principal conclusion obtained from these models are presented next:

- Concrete elements modeled with a Drucker-Prager failure criterion captured the expected behavior of confined concrete. The principal stresses of each element were useful to illustrate the high heterogenous distribution of confinement inside the volume of the column. The horizontal and vertical arching action due to the CFRP confinement was observed in the principal stress distribution of the columns.
- Stresses reached on concrete elements tend to overestimate the axial average stress on columns with a 2x5 anchor disposition and tend to underestimate the axial average stress on columns with a 3x5 anchor disposition. This is mainly due to an early or late reach of the failure surface due to the highly complex geometry of the specimens.
- Although the axial average stress predicted by the FEM models varied greatly between columns with 2x5 and 3x5 anchor disposition, the widening of the columns reached very similar values. This mainly due to the use of a dilatancy angle of 0

degrees, which neglects volumetric expansion and generated a conservative and similar widening in all columns.

- Since widening of the FEM columns was smaller than widening captured on the experimental tests, stresses captured on the CFRP elements were considered conservative at rupture state. The rupture state was considered to occur at an axial strain of 0.006. FEM stress captured at rupture of CFRP fibers were used to determine a conservative value for efficiency factor (κ_ε) which is used in all design oriented models. Design model results are very sensitive the value of κ_ε. If a slightly overestimated value of κ_ε is used, design models generate greatly overestimated predictions. Therefore, it is adequate to use a conservative value for κ_ε.
- The use of shells with a "cloth" option for the CFRP wraps was highly useful since this provided a fast representation of the highly complex geometry of CFRP wraps and anchors. This "cloth" option consisted on shells that could not resist any compression load and acted linear and elastically in tension. The principal stresses on the CFRP wraps were especially useful to illustrate the direction of stresses around anchors and corners. The FEM models prove to be a conservative and coherent approach to determine the maximum strain of the CFRP wraps at the time of rupture.
- FEM models showed that CFRP confinement reduces the load experienced by steel transverse bars. Steel bars experimented yielding at an axial average strain of the column of 0.0035 on columns without CFRP confinement, while for columns with CFRP confinement yielding was postponed. However, FEM models predict that transverse bars could yield at the time of rupture of the CFRP wraps.

- Group 2 models showed that the behavior of concrete and CFRP elements is similar when modelled as a complete column or with individual sub columns. The shape of the principal stress distribution of concrete elements in group 2 models resembled the results obtained from group 1 models. The principal stresses on CFRP wraps on models of both group closely coincided not only in magnitude but in location.

7.3 Design-oriented models

The propose procedure for a design oriented model capable of predicting the behavior of rectangular columns confined with CFRP wraps and anchors uses existing design-oriented models originally design for rectangular columns confined with CFRP wraps but without anchors. The principal assumption made by the proposed procedure is that the complete cross-section of each column can be represented by analyzing independent sub columns. Next is a brief description of the procedure followed for the use of the proposed design oriented model.

- The objective of the proposed procedure is to predict the estimated increment in axial stress-strain curve parameters. In a real situation, the only information available from concrete of a shear wall in need of CFRP retrofit would be concrete properties taken from cylinder probes drilled from the existing wall. Therefore, the results from the proposed design oriented procedure are compared with the unconfined concrete properties of drilled probes presented in Appendix A. The ultimate strain of unconfined concrete is assumed 0.0035 and the ultimate stress is assumed $0.85f_c'$.
- The increments obtained from the proposed procedure are compared with the increments captured on the experimental testing. It would be very difficult to extract

complete boundary elements of existing shear wall to determine the expected increment in axial properties due to CFRP confinement. Therefore, the experimental data captured is very useful in evaluating the proposed design procedure.

- The design procedure compares the results of applying existing design models from 11 different authors. Additionally, the predictions of 2 models specifically designed for rectangular columns confined with CFRP wraps and anchors are also compared.
- The predicted axial stress-strain curve parameters are maximum stress (f_c^{max}), strain corresponding to the maximum stress (ε_c^{max}), ultimate stress (f_c^{ult}), ultimate strain (ε_c^{ult}), modulus of elasticity (E_c) and slope of the deciding branch (E_D).

The principal conclusions of the predicted increments are detailed next:

- Predicted increments depend greatly on which of the 11 existing design models is used. Existing design models developed recently tend to generate more accurate predictions. This is reasonable since all the design models are based on experimental calibrations and the more recent ones tend to have larger datasets of tests.
- Good increment predictions are obtained for f_c^{max}, ε_c^{max} and ε_c^{ult} with the proposed methodology. The increments predicted are as accurate as the ones predicted with models specifically calibrated for rectangular columns confined with CFRP wraps and anchors. Predictions for increments of f_c^{max} tend to be conservative being most of, while predictions of ε_c^{max} tend to depend more on the existing design model used. Prediction of increments of ε_c^{ult} tend to be conservative are in some cases closer to the experimentally captured increments than the predictions of models specifically calibrated for rectangular columns confined with CFRP wraps and anchors.

- Increment predictions for E_c and f_c^{ult} tend to be more dispersed than previous parameters. Newer models predict more conservative values while older models tend to overestimate. Although results are more dispersed than for f_c^{max}, ε_c^{max} and ε_c^{ult}, E_c and f_c^{ult} results from the proposed procedure are as good as the results from models specifically calibrated for rectangular columns confined with CFRP wraps and anchors.
- Increment predictions for E_D are too dispersed and generally overestimate the captured increments with experimental testing. Even with the use of models specifically calibrated for rectangular columns confined with CFRP wraps and anchors, the predictions for this parameter vary greatly between specimens.

7.4 Future research

The area of confinement of rectangular columns with CFRP wraps and CFRP anchors is at a very early stage with few experimental tests being developed. For circular columns with CFRP confinement hundreds of tests were used to calibrate reliable design oriented models; however, the tests for CFRP wraps and anchor confinement are still in the tens. This mainly due to the difficulty of construction of these specimens. Research is need in the development of a faster and more efficient procedure to apply CFRP confinement to rectangular columns with anchors. The wet lay-up procedure is highly used for circular columns; however, for regular columns with anchors a more appropriate procedure would be a precast CFRP shell which can be easily installed and sealed in terrain.

Design oriented models have proven to be a very efficient and reliable approach if there is a big database of tests. More tests are required before design recommendations

reach official design guidelines. Important information that cannot be easily captured with experimental tests can be acquired from finite element models such as the stress distribution of CFRP confinement and concrete stress states. More research is required in developing models that can more closely relate the results obtained from tests and from FEM models especially for the concrete elements.

Despite of the early stage of the research, it has been proven in this and at least two other investigations that it is possible to increment the axial stress-strain curve parameters by applying a CFRP confining system that includes the use of CFRP anchors.

REFERENCES

Abbasnia, R., & Holakoo, A. (2012). An Investigation Of Stress-Strain Behavior Of FRP Confined Concrete Under Cyclic Compressive Loading. *Int. J. Civil Eng., 10*(3), 201 - 209.

Abbasnia, R., & Ziaadiny, H. (2015). Experimental Investigation And Strength Modeling Of CFRP-Confined Concrete Rectangular Prisms Under Axial Monotonic Compression. *Mater. Struct., 48*(1), 485 - 500.

ACI Committee 105. (1933). Reinforced Concrete Column Investigation-Tentative Final Report of Committee 105. *ACI Journal Proceedings, 29*(5), 275 - 282.

ACI Committee 318. (1995). *Building Code Requirements For Structural Concrete: (ACI 318-14) ; And Commentary (ACI 318R-14).* Farmington Hills, MI: American Concrete Institute.

ACI Committee 318. (2008). *Building Code Requirements For Structural Concrete: (ACI 318-14) ; And Commentary (ACI 318R-14).* Farmington Hills, MI: American Concrete Institute.

ACI Committee 318. (2011). *Building Code Requirements For Structural Concrete: (ACI 318-14) ; And Commentary (ACI 318R-14).* Farmington Hills, MI: American Concrete Institute.

ACI Committee 318. (2014). *Building Code Requirements For Structural Concrete: (ACI 318-14) ; And Commentary (ACI 318R-14).* Farmington Hills, MI: American Concrete Institute.

ACI Committee 440. (2008). *Guide For The Design And Construction Of Externally Bonded FRP Systems For Strengthening Concrete Structures.* Farmington Hills, MI: American Concrete Institute.

Akgun, D., Demir, C., & Ilki, A. (2010). Axial Behavior Of FRP Jacketed Extended Rectangular Members Constructed With Low Strength Concrete. *CICE 2010 - The 5th International Conference On FRP Composites In Civil Engineering*, (pp. 622 - 625). Beijing, China.

Akiyama, M., Suzuki, M., & Frangopol, D. M. (2010). Stress-Averaged Strain Model For Confined High-Strength Concrete. *ACI Struct. J., 107*(2), 179 - 188.

Alarcon, C., Hube, M. A., & de la Llera, J. C. (2014). Effect Of Axial Loads In The Seismic Behavior Of Reinforced Concrete Walls With Unconfined Wall Boundaries. *Engineering Structures, 73*, 13 - 23.

Alarcon, C., Hube, M. A., Jünemann, R., & de la Llera, J. C. (2015). Characteristics And Displacement Capacity Of Reinforced Concrete Walls In Damaged Buildings During 2010 Chile Earthquake. *Bull. Earthquake Eng., 13*, 1119 - 1139.

Alcaino, P., Cinquia, A., Santa María, H., & Invernizzi, S. (2015). Confinement Of Reinforced Concrete Compression Members Using Bow-Tie CFRP Reinforcement. *XI Congreso Chileno De Sismología E Ingeniería Sísmica Achisina 2015.* Santiago, Chile.

ANSYS. (2009). Theory Reference For The Mechanical APDL And Mechanical Applications. Canonsburg, PA.

Arteta, C. A., & Moehle, J. P. (2010). A Study Of Seismic Response Of A Building Designed For Intermediate Seismic Hazard. *9th US National Conference on Earthquake Engineering.* Toronto, Canada.

Binici, B. (2005). An Analytical Model For Stress–Strain Behavior Of Confined Concrete. *Engineering Structures, 27*(7), 1040 - 1051.

CAN/CSA-S806. (2007). *Design And Construction Of Building Structures With Fibre-Reinforced Polymers.* Ontario, Canada: National Standard Of Canada.

Carpenter, L. D., Naeim, F., Lew, M., Youssef, N. F., Rojas, F., Saragoni, G. R., & Adaros, M. S. (2011). Performance Of Tall Buildings In Viña Del Mar In The 27 February 2010 Offshore Maule, Chile Earthquake. *Struct. Design Tall Spec. Build., 20*, 17 - 36.

CNR - DT 200. (2004). *Guide For The Design And Construction Of Externally Bonded FRP Systems For Strengthening Structures - Material, RC And PC Structures, Masonry Structures.* Rome, Italy: Advisory Committee On Technical Recommendations For Construction.

Comisión Provisoria Terremoto. (2010). *30 Propuestas Relativas al Terremoto*. Retrieved from http://www.sismo24.cl/500sismos/00imgsismos/600pdf/500estudioComisioterre.pdf

Comité Inmobiliario, Cámara Chilena de la Construcción (CChC). (2002). *Instituto Nacional De Estadistica*. Retrieved from http://www.ine.cl/

DS 60. (2010). *Requisitos De Diseño Y Cálculo Para El Hormigón Armado.* Santiago, Chile: Ministerio De Vivienda Y Urbanismo (MINVU).

Eckold, G. (1994). *Design And Manufacture Of Composites Structures.* Woodhead Publishing Series in Composites Science and Engineering Series.

EN 1992-1-1. (2004). *Eurocode 2: Design Of Concrete Structures - Part 1-1: General Rules And Rules For Buildings.* Brussels: European Committee for Standardization.

fib - Bulletin 35. (2006). *Retrofitting Of Concrete Structures By Externally Bonded FRPs With Emphasis On Seismic Applications.* Lausanne, Switzerland: International Federation for Structural Concrete (fib).

Hany, N. F., Hantouche, E. G., & Harajli, M. H. (2015). Axial Stress-Strain Model Of CFRP-Confined Concrete Under Monotonic And Cyclic Loading. *J. Compos. Constr., 19*(6).

Hany, N. F., Hantouche, E. G., & Harajli, M. H. (2016). Generalized Axial Stress-Strain Response Of Rectangular Columns Confined Using CFRP Jackets And Anchors. *J. Compos. Constr.*

HBM. (2017). *HBM Test And Meassurements*. Retrieved from https://www.hbm.com

Hognestad, E. (1951). *A Study Of Combined Bending And Axial Load In Reinforced Concrete Members.* Urbana, IL: University Of Illinois (Bulletin Series No. 399, Bulletin No. 1).

Hosotani, M., Kawashima, K., & Hoshikuma, J. (1998). A Stress-Strain Model For Concrete Cylinders Confined By Carbon Fiber Sheets. *J. Concr. Eng., 39*(592), 37 - 52.

Hube, M. A., Marihuén, A., de la Llera, J. C., & Stojadinovic, B. (2014). Seismic Behavior Of Slender Reinforced Concrete Walls. *Engineering Structures, 80*, 377 - 388.

Hurlbut, B. J. (1985). *Experimental And Computational Investigation Of Strainsoftening Softening In Concrete (Msc Thesis).* Boulder, CO: University Of Colorado At Boulder.

Ilki, A., Peker, O., Karamuk, E., Demir, C., & Kumbasar, N. (2008). FRP Retrofit Of Low And Medium Strength Circular And Rectangular Reinforced Concrete Columns. *J. Mater. Civ. Eng., 20*(2), 169 - 188.

Jansen, D. C., & Shah, S. P. (1997). Effect Of Length On Compressive Strain Softening Of Concrete. *J. Eng. Mech., 123*(1), 25 - 35.

Jünemann, R., de la Llera, J. C., Hube, M. A., Cifuentes, L. A., & Kausel, E. (2015). A Statistical Analysis Of Reinforced Concrete Wall Buildings Damaged During The 2010, Chile Earthquake. *Engineering Structures, 82*, 168 - 185.

Jünemann, R., Hube, M. A., de la Llera, J. C., & Kausel, E. (2012). Characteristics Of Reinforced Concrete Shear Wall Buildings Damaged During 2010 Chile Earthquake. *15 World Conference On Earthquake Engineering.* Lisboa, Portugal.

Kuang, J. S., & Ho, Y. B. (2009). Seismic Behavior And Ductility Of Squat Reinforced Concrete Shear Walls With Nonseismic Detailing. *ACI Structural Journal, 105*(2), 225 - 231.

Lam, L., & Teng, J. G. (2003a). Design-Oriented Stress-Strain Model For FRP - Confined Concrete. *Construction and Building Materials, 17*(1), 471 - 489.

Lam, L., & Teng, J. G. (2003b). Design-Oriented Stress–Strain Model For FRP-Confined Concrete In Rectangular Columns. *Journal Of Reinforced Plastics And Composites, 22*(13), 1149 - 1186.

Lam, L., & Teng, J. G. (2009). Stress-Strain Model For FRP-Confined Concrete Under Cyclic Axial Compression. *Eng. Struct., 31*(2), 308 - 321.

Lam, L., Teng, J. G., Cheung, C. H., & Xiao, Y. (2006). FRP-Confined Concrete Under Axial Cyclic Compression. *Cem. COncr. Res., 28*(10), 949 - 958.

Lertsrisakulrat, T., Watanabe, K., Matsuo, M., & Niwa, J. (2001). Experimental Study Of Localization Parameters In Concrete Subjected To Compression. *Proceedings of JSCE, 50*(669), 225 - 236.

Liu, Y., Zwingmann, B., & Schlaich, M. (2015). Carbon Fiber Reinforced Polymer For Cable Structures - A Review. *MDPI Polymers, 7*, 2078 - 2099.

Lüders, C., & Cruz, E. (1986). Comportamiento De Los Edificios Del Conjunto Habitacional Canal Beagle Durante El Sismo Del 3 De Marzo De 1985. *4th Chilean Conference of Seismology and Earthquake Engineering*, (pp. C218 - C-238). Santiago, Chile.

Mander, J. B., Priestley, M., & Park, R. (1988a). Theoretical Stress - Strain Model For Confined Concrete. *Journal Of Structural Engineering, 114*(8), 1804 - 1826.

Mander, J. B., Priestley, M., & Park, R. (1988b). Observed Stress-Strain Behavior Of Confined Concrete. *J. Struct. Eng., 114*(8), 1827 - 1849.

Markeset, G., & Hillerborg, A. (1995). Softening Of Concrete In Compression - Localization And Size Effects. *Cement Concrete Res., 25*(4), 702 - 708.

Massone, L. M., Bonelli, P., Lagos, R., Lüders, C., Moehle, J., & Wallace, J. W. (2012). Seismic Design And Construction Practices For Rc Structural Wall Buildings. *Earthquake Spectra, 28*(S1), S1 - S11.

Mirmiran, A., & Shahawy, M. (1997). Behavior Of Concrete Columns Confined By Fiber Composites. *J. Struct. Eng., 123*(5), 583 - 590.

Mirmiran, A., Zagers, K., & Yuan, W. (2000). Nonlinear Finite Element Modeling Of Concrete Confined By Fiber Composites. *Finite Elements in Analysis and Design, 35*, 79-96.

Moehle, J. P. (1992). Displacement - Based Design of RC Structures Subjected to Earthquakes. *Earthquake Spectra, 8*(3), 403 - 428.

Moehle, J. P., & Wallace, J. W. (1989). Ductility And Detailing Requirements Of Shear Wall Buildings. *5th Chilean Conference Of Seismology And Earthquake*, (pp. 131 - 149). Santiago, Chile.

Moehle, J. P., Ghodsi, T., Hooper, J. D., Fields, D. C., & Gedhada, R. (2011). *Seismic Design Of Cast-In-Place Concrete Special Structural Walls And Coupling Beams: A Guide For Practicing Engineers (Nehrp Seismic Design Technical Brief No. 6).* Gaithersburg, MD:

Produced by the NEHRP Consultants Joint Venture, a partnership of the Applied Technology Council and the Consortium of Universities for Research in Earthquake Engineering, for the National Institute of Standards and Technology, NIST GCR 11-917-11REV-1.

Monti, G., & Nuti, C. (1992). Nonlinear Cyclic Behavior Of Reinforcing Bars Including Buckling. *J. Struct. Eng., 118*, 3268 - 3284.

Moroni, M. O. (2011). *World Housing Encyclopedia*. Retrieved from http://www.world-housing.net/wp-content/uploads/2011/08/Type_RC_Wall.pdf

Music, J., & Ponce, M. (2014). Implicancia De Normas NCh 433 – Decreto 61 Y NCh 430 – Decreto 60 En El Diseño De Muros, En Edificio De Hormigón Armado. *Revista de Ingeniería Innova, 8*, 53 - 69.

Naeim, F., Lew, M., Carpenter, L. D., Youssef, N. F., Rojas, F., Saragoni, G. R., & Adaros, M. S. (2011). Performance Of Tall Buildings In Santiago, Chile During The 27 February 2010 Offshore Maule, Chile Earthquake. *Struct. Design Tall Spec. Build., 20*, 1 - 16.

Nakamura, H., & Higai, T. (2001). Compressive Fracture Energy and Fracture Zone Length of Concrete. *Modeling Of Inelastic Behavior Of Rc Structures Under Seismic Loads, ASCE*, 471 - 487.

NCh 204. (2006). *Acero - Barras Laminadas En Caliente Para Hormigón Armado.* Santiago, Chile: Instituto Nacional de Normalización (INN).

NCh 429. (1957). *Hormigón Armado Parte I.* Santiago, Chile: Instituto Nacional De Normalización (INN).

NCh 430. (1961). *Hormigón Armado Parte II.* Santiago, Chile: Instituto Nacional De Normalización (INN).

NCh 433. (1996 (Mod. 2009)). *Diseño Sísmico De Edificios.* Santiago, Chile: Instituto Nacional De Normalización (INN).

NCh 433. (1996). *Diseño Sísmico De Edificios.* Santiago, Chile: Instituto Nacional De Normalización (INN).

Optecal. (2016). *Optecal Digital Image Correlation Software*. Retrieved from http://www.optecal.com/

Pantazopoulou, S. J., & Mills, R. H. (1995). Microstructural Aspects Of The Mechanical Response Of Plain Concrete. *ACI Mater. J., 92*(1), 605 - 616.

Pantelides, C. P., & Yan, Z. (2007). Confinement Model Of Concrete with Externally Bonded FRP Jackets Or Posttensioned FRP Shells. *Journal of Structural Engineering, 133*(9), 1288 - 1296.

Pantelides, C. P., Yan, Z., & Reaveley, L. D. (2004). *Shape Modification of Rectangular Columns Confined with FRP Composites.* Salt Lake City, UT: University Of Utah (UT 84112-0561).

Parra, P., & Moehle, J. (2014). Lateral Buckling In Reinforced Concrete Walls. *10th U.S. National Conference On Earthquake Engineering.* Anchorage, Alaska.

Paulay, T., & Priestley, M. (1992). *Seismic Design Of Reinforced Concrete And Masonry Buildings.* John Wiley & Sons.

Pellegrino, C., & Modena, C. (2010). Analytical Model For FRP Confinement Of Concrete Columns With And Without Internal Steel Reinforcement. *J. Compos. Constr., 14*(6), 693 - 705.

Pivonka, P., Lackner, R., & Mang, H. (2000). Numerical Analyses Of Concrete Subjected To Triaxial Compressive Loading. *European Congress On Computation Methods In Applied Mechanics, ECCOMAS*, (p. 26). Barcelona, España.

Popovics, S. (1973). Numerical Approach To The Complete Stress-Strain Relation For Concrete. *Cem. Concr. Res., 3*(5), 583 - 599.

Richard, R. M., & Abbott, B. J. (1975). Versatile Elastic-Plastic Stress-Strain Formula. *J. Engrg. Mech. Div., 101*(4), 511 - 515.

Riddell, R., Wood, S. L., & de la Llera, J. C. (1987). *The 1985 Chile Earthquake: Structural Characteristics And Damage Statistics For The Building Inventory In Viña Del Mar*. Urbana, IL: Produced By The University Of Illinois At Urbana-Champaign For The National Science Foundation, Report No. UILU-ENG-8-2005.

Rocca, S. (2007). *Experimental And Analytical Evaluation Of FRP-Confined Large Size Reinforced Concrete Columns.* Rolla, MO: University Of Missouri, Rolla.

Rocca, S., Galati, N., & Nanni, A. (2008). Review Of Design Guidelines For FRP Confinement Of Reinforced Concrete Columns Of Noncircular Cross Sections. *Journal Of Composites For Construction, 12*(1), 80 - 92.

Rochette, P., & Labossiere, P. (1996). A Plasticity Approach For Concrete Columns Confined With Composite Materials. *Proceding of the Advanced Composite Materials in Bridges and Structures, CSCE,* (pp. 359 - 366). Montreal, Canada.

Rojas, F., Lew, M., & Naeim, F. (2010). An Overview Of Building Codes And Standards In Chile At The Time Of The 27 February 2010 Offshore Maule, Chile Earthquake. *Struct. Design Tall Spec. Build., 19,* 853 - 865.

Rojas, F., Naeim, F., Lew, M., Carpenter, L. D., Youssef, N. F., Saragoni, G. R., & Adaros, M. S. (2011). Performance Of Tall Buildings In Concepción During The 27 February 2010 Moment Magnitude 8.8 Offshore Maule, Chile Earthquake. *Struct. Design Tall Spec. Build., 20*, 37 - 64.

Rokugo, K., & Koyanagi, W. (1992). Role Of Compressive Fracture Energy Of Concrete On The Failure Behavior Of Reinforced Concrete Beams. *Applications Of Fracture Mechanics To Reinforced Concrete (ed. Carpinteri, A.), Elsevier Applied Science*, 437 - 464.

Saadatmanesh, H., Ehsani, M. R., & Li, M. W. (1994). Strength And Ductility Of Concrete Columns Externally Reinforced With Fiber Composite Straps. *ACI Structural Journal, 91*(4), 434 - 447.

Samaan, M., Mirmiran, A., & Shahawy, M. (1998). Model of Concrete Confined Fiber Composite. *J. Struct. Eng., 124*(9), 1025 - 1031.

Samani, A. K., & Attard, M. M. (2010). *A Stress - Strain Model For Uniaxial Compression And Triaxially Confined Plain Concrete Incorporating Size Effect.* Sydney, Australia: The University Of New South Wales (UNICIV Report No. R - 457).

Shah, S., & Sankar, R. (1987). Internal Cracking And Strain Softening Response Of Concrete Under Uniaxial Compression. *ACI Mater. J., 84*(3), 200 - 212.

Shahawy, M., Mirmiran, A., & Beitelman, T. (2000). Tests And Modeling Of Carbon-Wrapped Concrete Columns. *Composites: Part B, 31,* 471-480.

SHARCNET. (2015). *13.188. BEAM188 - 3-D 2-Node Beam*. Retrieved 06 26, 2017, from Shared Hierarchical Academic Research Computing Network: https://www.sharcnet.ca/Software/Ansys/16.2.3/en-us/help/ans_thry/thy_el188.html

SHARCNET. (2015). *13.41. SHELL41 - Membrane Shell*. Retrieved 06 26, 2017, from Shared Hierarchical Academic Research Computing Network: https://www.sharcnet.ca/Software/Ansys/16.2.3/en-us/help/ans_thry/thy_el41.html

SHARCNET. (2015). *SHELL41 Membrane Shell*. Retrieved 06 26, 2017, from Shared Hierarchical Academic Research Computing Network: https://www.sharcnet.ca/Software/Ansys/16.2.3/en-us/help/ans_elem/Hlp_E_SHELL41.html

SHARCNET. (2015). *SOLID65 3-D Reinforced Concrete Solid*. Retrieved 06 26, 2017, from Shared Hierarchical Academic Research Computing Network: https://www.sharcnet.ca/Software/Ansys/16.2.3/en-us/help/ans_elem/Hlp_E_SOLID65.html

SHARCNET. (2016). *13.65. SOLID65 - 3-D Reinforced Concrete Solid*. Retrieved 06 26, 2017, from Shared Hierarchical Academic Research Computing Network: https://www.sharcnet.ca/Software/Ansys/17.0/en-us/help/ans_thry/thy_el65.html

SHARCNET. (2016). *BEAM188 3-D 2-Node Beam*. Retrieved 06 26, 2017, from Shared Hierarchical Academic Research Computing Network: https://www.sharcnet.ca/Software/Ansys/17.0/en-us/help/ans_elem/Hlp_E_BEAM188.html

Sheik, S. A., & Uzumeri, S. M. (1982). Analytical Model For Concrete Confinement In Tied Columns. *J. Struct. Div., 108*(12), 2703 - 2722.

Sheikh, S. A., & Uzumeri, S. M. (1980). Strength And Ductility Of Tied Concrete Columns. *Journal Of The Structural Division, 106*(ST5), 1079 - 1102.

Smith, S. S., William, K. J., Gerstle, K. H., & Sture, S. (1989). Concrete Over The Top, Or: Is There Life After Peak? *ACI Materials Journal, 86*(5), 491 - 497.

Smith, S., William, K., Gerstle, K., & Sture, S. (1989). *Constitutive Driver For Triaxial Response Behavior Of Plain Concrete.* Boulder, CO: Department Of Civil Engeneering, University Of Colorado At Boulder.

Spoelstra, M. R., & Monti, G. (1999). FRP-Confined Concrete Model. *J. Compos. Constr., 3*(3), 143 - 150.

STUBA. (1998). *4.188 BEAM188 3-D Linear Finite Strain Beam*. Retrieved 06 26, 2017, from Slovak University of Technology in Bratislava: http://www.ansys.stuba.sk/html/elem_55/chapter4/ES4-188.htm

STUBA. (1998). *4.41 SHELL41 Membrane Shell*. Retrieved 06 26, 2017, from Slovak University of Technology in Bratislava: http://www.ansys.stuba.sk/html/elem_55/chapter4/ES4-41.htm

STUBA. (1998). *4.65 SOLID65 3-D Reinforced Concrete Solid*. Retrieved 06 26, 2017, from Slovak University of Technology in Bratislava: http://www.ansys.stuba.sk/html/elem_55/chapter4/ES4-65.htm

Takahashi, S., Yoshida, K., Ichinose, T., Sanada, Y., Matsumoto, K., Fukuyama, H., & Suwada, H. (2013). Flexural Drift Capacity Of Reinforced Concrete Wall With Limited Confinement. *ACI Structural Journal, 110*(1), 95 - 104.

Tan, K. H. (2002). Strength Enhancement Of Rectangular Reinforced Concrete Columns Using Fiber-Reinforced Polymer. *J. Compos. Constr., 6*(3), 175 - 183.

Teng, J. G., Chen, J. F., Smith, S. T., & Lam, L. (2002). *FRP - Strengthened RC Structures.* John Wiley & Sons, LTD.

Teng, J. G., Jiang, T., Lam, L., & Luo, Y. Z. (2009). Refinement Of A Design-Oriented StressStrain Model For FRP-Confined Concrete. *Journal Of Composites For Construction, 13*(4), 269 - 278.

Torrenti, J., Benaijia, E., & Boulay, C. (1993). Influence Of Boundary Conditions On Strain Softening In Concrete Compression Test. *Journal of Engineering Mechanics, 119*(12), 2369 - 2384.

Triantafillou, T. C., Choutopoulou, E., Fotaki, E., Skorda, M., Stathopoulou, M., & Karlos, K. (2016). FRP Confinement Of Wall-Like Reinforced Concrete Columns. *Materials And Structures, 49*(1), 651 - 664.

U.S. Geological Survey. (1986). *Seismic Site-Response Experiments Following The March 3, 1985 Cewtral Chile Earthquake (Topographical And Geological Effects).* USGS Open-File Report 86-90.

van Geel, E. (1998). *Concrete Behavior In Multiaxial Compression: Experimental Research (Doctoral Dissertation).* Eindhoven, The Netherlands: Eindhoven University of Technology.

van Mier, J. (2008). Framework For A Generalized Four-Stage Fracture Model Of Cement-Based Materials. *Engineering Fracture Mechanics, 75*(18), 5072 - 5086.

van Mier, J. G. (1984). *Strain-Softening Of Concrete Under Multiaxial Loading Conditions (Doctoral Dissertation).* Eindhoven, The Netherlands: Eindhoven University Of Technology.

Vonk, R. (1992). *Softening Of Concrete Loaded In Compression (Unpublished Doctoral Dissertation).* Eindhoven, The Netherlands: Eindhoven University Of Technology.

Wallace, J. W. (1995). Seismic Design Of RC Structural Walls. Part I: New Code Format. *Journal Of Structural Engineering, 121*(1), 75 - 87.

Wallace, J. W. (2011). February 27, 2010 Chile Earthquake: Preliminary Observations On Structural Performance And Implications For U.S. Building Codes And Standards. *2011 ASCE Structures Congress*, (pp. 1672 - 1685). Las Vegas, NV.

Wallace, J. W. (2012). Behavior, Design, And Modeling Of Structural Walls And Coupling Beams - Lessons From Recent Laboratory Tests And Earthquakes. *International Journal Of Concrete Structures And Materials, 6*(1), 3 - 18.

Wallace, J. W., & Orakcal, K. (2002). ACI 318-99 Provisions For Seismic Design Of Structural Walls. *ACI Structural Journal, 99*(4), 499 - 508.

Wallace, J. W., & Thomsen, J. H. (1995). Seismic Design Of RC Structural Walls. Part II: Applications. *Journal Of Structural Engineering, 121*(1), 88 - 101.

Wallace, J. W., Massone, L. M., Bonelli, P., Dragovich, J., Lagos, R., Lüders, C., & Moehle, J. (2012). Damage And Implications For Seismic Design Of RC Structural Wall Buildings. *Earthquake Spectra, 28*(S1), S281 - S299.

Wang, L. M., & Wu, Y. F. (2008). Effect Of Corner Radius On The Performance Of CFRP Confined Square Concrete Columns. *Eng. Struct., 30*(2), 493 - 505.

Wang, Z., Wang, D., Smith, S. T., & Lu, D. (2012a). CFRP-Confined Square RC Columns. Part I: Experimental Investigation. *Journal Of Composites For Construction, 16*(2), 150 - 160.

Wang, Z., Wang, D., Smith, S. T., & Lu, D. (2012b). CFRP-Confined Square RC Columns. Part II: Cyclic Axial Compression Stress-Strain Model. *Journal Of Composites For Construction, 16*(2), 161 - 170.

Watanabe, K., Niwa, J., Yokota, H., & Iwanami, M. (2004). Experimental Study On Stress-Strain Curve Of Concrete Considering Localized Failure In Compression. *Adv. Concr. Technol., 2*(3), 395 - 407.

Wei, Y.-Y., & Wu, Y.-F. (2012). Unified Stress-Strain Model Of Concrete For FRP Confined Columns. *Construction And Building Materials, 26*(1), 381 - 392.

Westenenk, B., de la Llera, J. C., Jünemann, R., Hube, M. A., Besa, J. J., Lüders, C., . . . Jordán, R. (2013). Analysis And Interpretation Of The Seismic Response Of RC Buildings In Concepción During The February 27, 2010, Chile Earthquake. *Bull. Earthquake. Eng., 11*, 69 - 91.

Wight, J. K., & MacGregor, J. G. (2012). *Reinforced Concrete: Mechanics and Design* (6th Edition ed.). Pearson.

William, K. J., & Warnke, E. P. (1975). Constitutive Model For The Triaxial Behavior Of Concrete. *Proc. Int. Assoc. for Bridge and Struct., 19*(1), 1 - 30.

Wood, S. L., Wight, J. K., & Moehle, J. P. (1987). *The 1985 Chile Earthquake: Observations On Earthquake - Resistant Construction In Viña Del Mar*. Urbana, IL: Produced By The University Of Illinois At Urbana-Champaign For The National Science Foundation, Report No. UILU-ENG-87-2002.

Wu, G., Wu, Z., & Lu, Z. T. (2007). Design-Oriented Stress-Strain Model For Concrete Prisms Confined With FRP Composites. *Construction And Building Materials, 21*(1), 1107 - 1121.

Wyllie, L. A., Abrahamson, N., Bolt, B., Castro, G., Durkin, M. E., Escalante, L., . . . Vallenas, J. (1986). The Chile Earthquake of March 3, 1985. *EERI, Earthquake Spectra, 2*(2), 513.

Xie, J., Elwi, A. E., & MacGregor, J. G. (1995). Mechanical Properties Of Three High-Strength Concretes Containing Silica Fume. *ACI Materials Journal, 92*(2), 135 - 145.

Yan, Z. (2005). *Shape Modification Of Rectangular Columns Confined With FRP Composites.* Salt Lake City, UT: University Of Utah.

Youssef, M. N. (2003). *Stress-Strain Model For Concrete Confined By FRP Composites (Doctoral Dissertation).* Irvine, CA: University Of California, Irvine.

Youssef, M. N., Feng, Q., & Mosallam, A. S. (2007). Stress-Strain Model For Concrete Confined By FRP Composites. *Composites Part B: Engineering, 38*(1), 614 - 628.

Zhao, T., & Xie, J. (2000). Experimental Study on Complete StressStrain Relation Curve of CFRP Confined Concrete. *Building Struct., 30*(7), 40 - 43.

APPENDICES

APPENDIX A: MEASURED AND ESTIMATED CONCRETE PROPERTIES

The measured material properties of concrete are reported in this appendix. Since specimen testing took place after more than a year of fabrication, concrete properties at the day of testing were estimated. The estimation process is also explained in this appendix.

The concrete unconfined compressive strength after 28 days of aging was determined testing 150 by 300-mm cylinders (Figure A.1). The 28th day of aging corresponded to the date 08-09-2015. The average of the measured results is shown in equation A.1.

Figure A.1: Concrete cylinders tested after 28 days of aging.

$$f'_{c\ 28\ days} = \frac{21.5\ [MPa]+24.7\ [MPa]}{2} = 23.1\ [MPa] = 235.47\ \left[\frac{kgf}{cm^2}\right] \quad \text{(A.1)}$$

The specimens were tested on different dates. Table A.1 shows the days of aging after the 28th day each specimen had at testing day.

Table A.1: Tested concrete properties 581 days after the 28th day of aging

Date of construction	**28th day of aging**	**Testing day**	**Days from 28th to Testing day**
08-09-15	06-10-15	15-11-16	406
08-09-15	06-10-15	15-11-16	406
08-09-15	06-10-15	11-11-16	402
08-09-15	06-10-15	11-11-16	402
08-09-15	06-10-15	13-12-16	434
08-09-15	06-10-15	11-01-17	463
08-09-15	06-10-15	13-12-16	434
08-09-15	06-10-15	06-02-17	489
08-09-15	06-10-15	13-12-16	434
08-09-15	06-10-15	03-01-17	455
08-09-15	06-10-15	03-01-17	455
08-09-15	06-10-15	11-01-17	463
		Average	437

After the testing day, six cylindrical probes were drilled from a remaining specimen. The drilled specimen had a 15-cm thickness and no CFRP reinforcement. The probes were approximately 100 mm in height and 55 mm in diameter (Figure A.2). The probes were removed with special attention to the location of steel reinforcement (Figure A.2a, A.2b) and with the use of a 55-mm drill (Figure A.2c, A.2d). The probes were tested in compression 581 days after the 28th day of aging (09-05-2017). Table A.2 shows the measured results for each probe and equations A.2 and A.3 show the average unconfined concrete strength and elastic modulus, respectively.

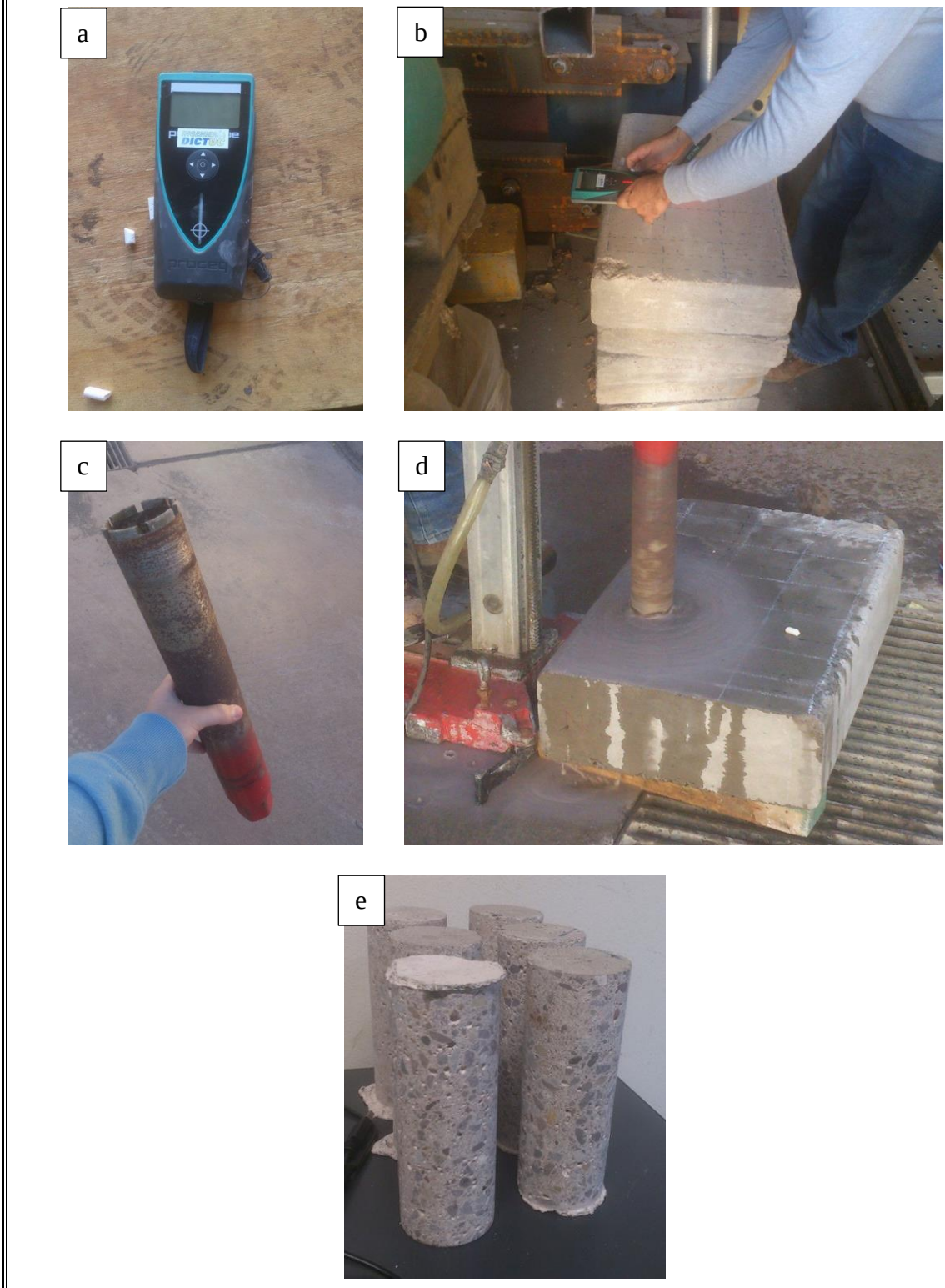

Figure A.2: Concrete probes tested 581 days after the 28th day of aging

Table A.2: Tested concrete properties 581 days after the 28th day of aging

Concrete Cylinder N°	Density (kg/m^3)	Failure Load (kN)	Failure stress (MPa)	Cylinder Strength With Slenderness Correction (MPa)	Estimated Cubic Strength (MPa)	Modulus of Elasticity (kgf/cm^2)
1	2260	90	37.9	37.3	42.3	-
2	2270	88	37.0	36.9	41.9	-
3	2240	87	36.6	36.5	41.5	-
4	2260	92	38.7	38.7	43.7	228220-230513
5	2270	89	37.5	37.4	42.4	217163-219289
6	2280	95	40.0	39.9	44.9	233019-237681
Average	2263	90.2	38.0	37.8	42.8	227647
Standard deviation	12	2.7	1.1	1.2	1.2	8690

$$f'_{c\,581\ days} = 37.8\ [MPa] = 385\ \left[\frac{kgf}{cm^2}\right] \quad \text{(A.2)}$$

$$E_{c_{581\ days}} = 22332.2\ [MPa] = 227647\ \left[\frac{kgf}{cm^2}\right] \quad \text{(A.3)}$$

Unconfined concrete properties at the time of testing were estimated based on the measured results showed in equations A.1, A.2 and A.3, the aging days of each specimen detailed in Table A.1 and time dependent expressions for concrete properties (EN 1992-1-1, 2004).

According to the European Code (EN 1992-1-1, 2004), the compressive strength of concrete at an age t depends on the type of cement, temperature and curing conditions. In this code, expression A.4 and A.5 are provided for a mean temperature of 20°C and curing conditions in accordance with EN 12390-3, 2009.

$$f'_c(t) = \beta_{cc}(t) * f'_{c\,28\ days} \quad \text{(A.4)}$$

$$\beta_{cc}(t) = e^{s*\left(1-\left(\frac{28}{t}\right)^{\frac{1}{2}}\right)} \quad \text{(A.5)}$$

where $s =$ is a coefficient which depends on the type of cement.

- 0,20 for cement of strength Class R (rapid early strength gain)
- 0,25 for cement of strength Class N (normal early strength gain)
- 0,38 for cement of strength Class S (slow early strength gain)

Since the actual temperature and curing conditions for the specimens were not recorded, it would not be appropriate to use any of the values of the s parameter suggested in the European Code.

Since the compressive strength is known for the 28th day of aging and 581 days after the 28th day of aging (after the testing day), the s parameter can be calibrated according to these measurements. Therefore, the concrete strength at the testing day can be estimated according the measured data and the shape of the function given in equation A.4 and A.5 (EN 1992-1-1, 2004). The calibrated value of the s parameter is presented in equation A.6

$$s_{calibrated} = 0.63 \tag{A.6}$$

According to the same European code (EN 1992-1-1, 2004), the modulus of elasticity of concrete can also be estimated based on the s parameter using equation A.7.

$$E_c(t) = \left(e^{s*\left(1-\left(\frac{28}{t}\right)^{\frac{1}{2}}\right)} \right)^{0.3} * E_{c\,28\,days} \tag{A.7}$$

Equation A.8 shows the estimated modulus of elasticity of concrete at the 28th day of aging using the calibrated s parameter.

$$E_{c\,28\,days} = 196416.4 \ \left[\frac{kgf}{cm^2}\right] \tag{A.8}$$

Figures A.1 and A.2 show the increase in compression strength and modulus of elasticity in time according to the calibrated s parameter.

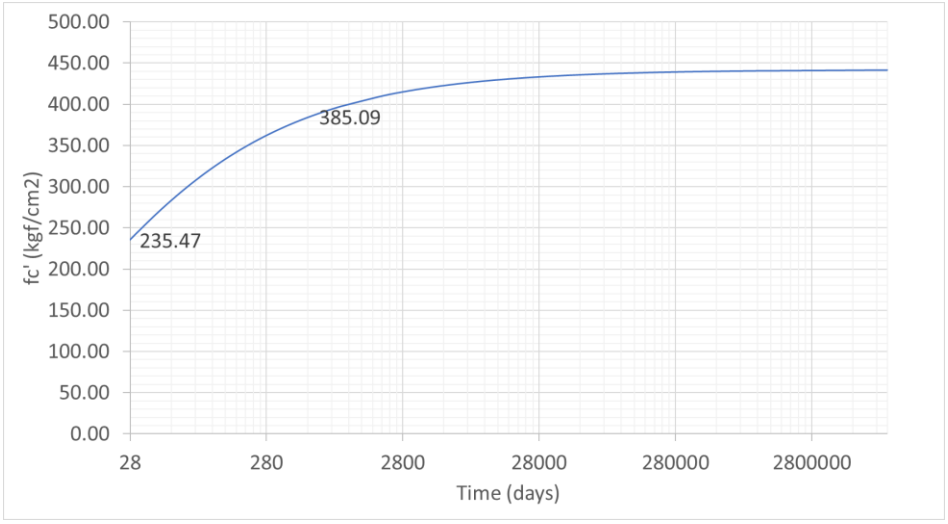

(a) Concrete compression strength in time

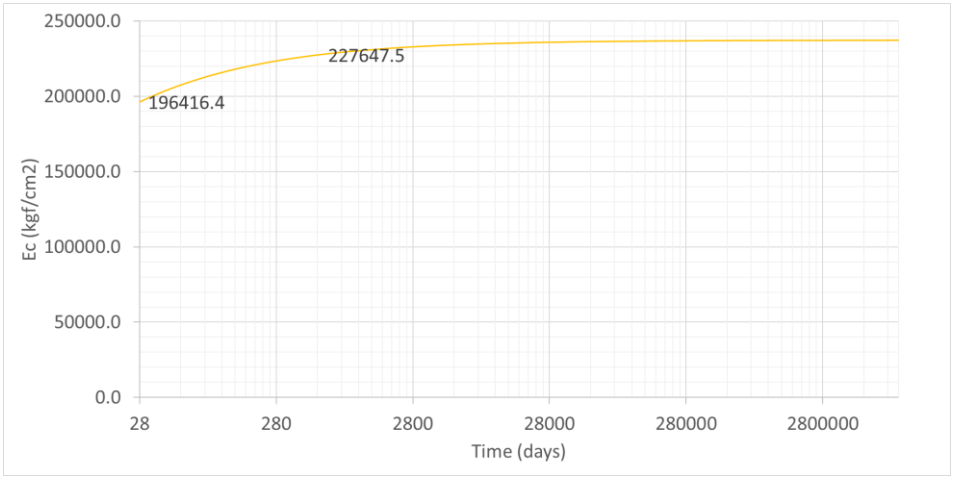

(b) Concrete modulus of elasticity in time

Figure A.3: Concrete properties in time with $s_{calibrated} = 0.63$

Considering the estimations of $f_c'(t)$ and $E_c(t)$, concrete properties are calculated for the testing day of each specimen and presented in Table A.3.

Table A.3: Estimated concrete properties at the day of testing

Date of construction	**28th day of aging**	**Testing day**	**Days from 28th to testing day**	**fc'(t) (kgf/cm^2)**	**Ec(t) (kgf/cm^2)**
08-09-15	06-10-15	15-11-16	406	375	225801
08-09-15	06-10-15	15-11-16	406	375	225801
08-09-15	06-10-15	11-11-16	402	374	225745
08-09-15	06-10-15	11-11-16	402	374	225745
08-09-15	06-10-15	13-12-16	434	377	226169
08-09-15	06-10-15	11-01-17	463	379	226515
08-09-15	06-10-15	13-12-16	434	377	226169
08-09-15	06-10-15	06-02-17	489	380	226799
08-09-15	06-10-15	13-12-16	434	377	226169
08-09-15	06-10-15	03-01-17	455	378	226422
08-09-15	06-10-15	03-01-17	455	378	226422
08-09-15	06-10-15	11-01-17	463	379	226515
			Average	377	226189
			Standard Deviation	2	335

Considering that all tests took place around the same date and that the estimation of concrete proprieties show little variation (Table A.3), average concrete properties at testing day are considered for modeling purposes (Equations A.9, A.10)

$$f_c' = 377 \ \left[\frac{kgf}{cm^2}\right] = 37 \ [MPa] \tag{A.9}$$

$$E_c = 226189 \ \left[\frac{kgf}{cm^2}\right] = 22180 \ [MPa] \tag{A.10}$$

APPENDIX B: STRAIN RATE OF LOADING IN CFRP-CONFINED TESTS

Figures B.1 to B.8 show all the readings of the vertical LVDTs placed on tested columns confined with CFRP jackets and CFRP anchors. At the left of all these Figures are shown the axial stress-strain curve according to each individual vertical LVDT. In all figures, the loading time vs strain reading is located to the right of the stress-strain curves. These curves show that until failure the strain rate applied by the testing machine was very low (1.42e-5 1/s on average). However, as the curves on the right of Figure B.1 to B.8 show, after the rupture of the CFRP is reached the rate of loading changes abruptly due to the forced controlled testing machine. For this reason, only the data captured before the abrupt change in loading rate is used for this study.

It is important to notice that if a displacement controlled testing machine was used to test the columns a much higher ultimate strain could have been captured. In the present study, the maximum ultimate strain captured was approximately 0.008, while other studies of rectangular columns confined with CFRP jackets and anchors reach values as high as 0.02 (Hany, Hantouche, & Harajli, Generalized Axial Stress-Strain Response Of Rectangular Columns Confined Using CFRP Jackets And Anchors, 2016; Triantafillou, et al., 2016)

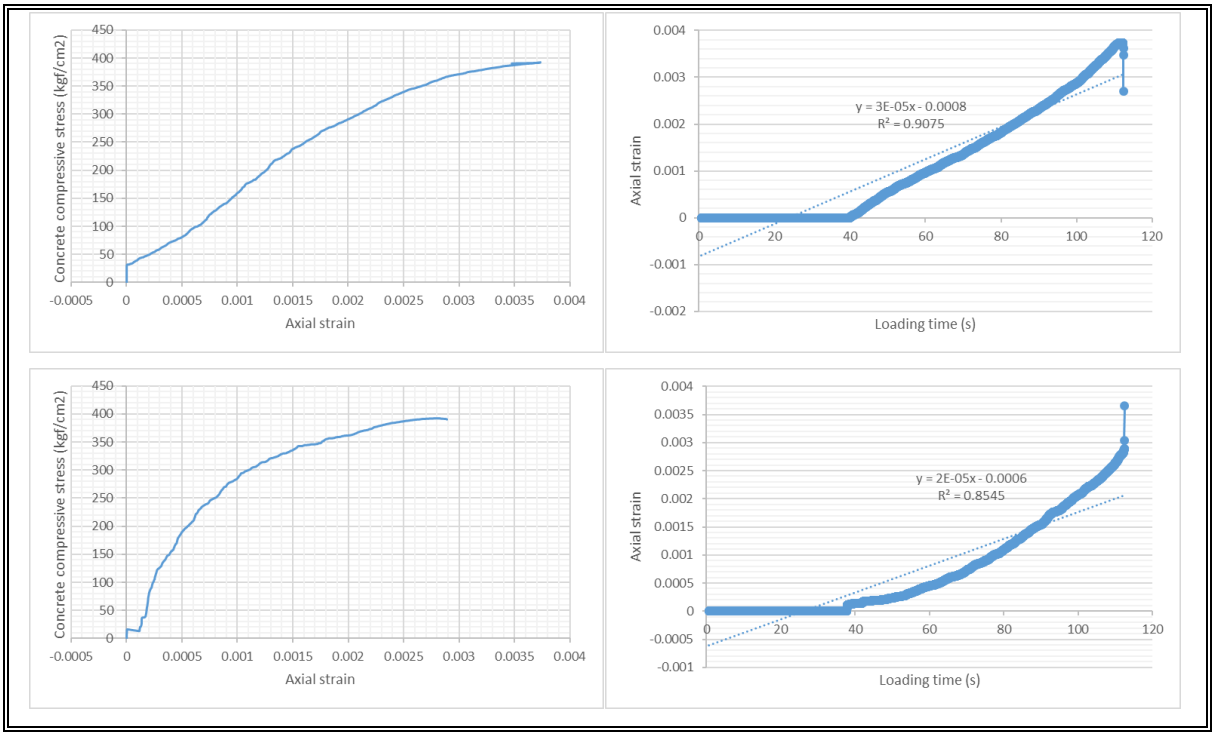

Figure B.1: Vertical LVDTs readings until change of displacement rate. Specimen 225-10

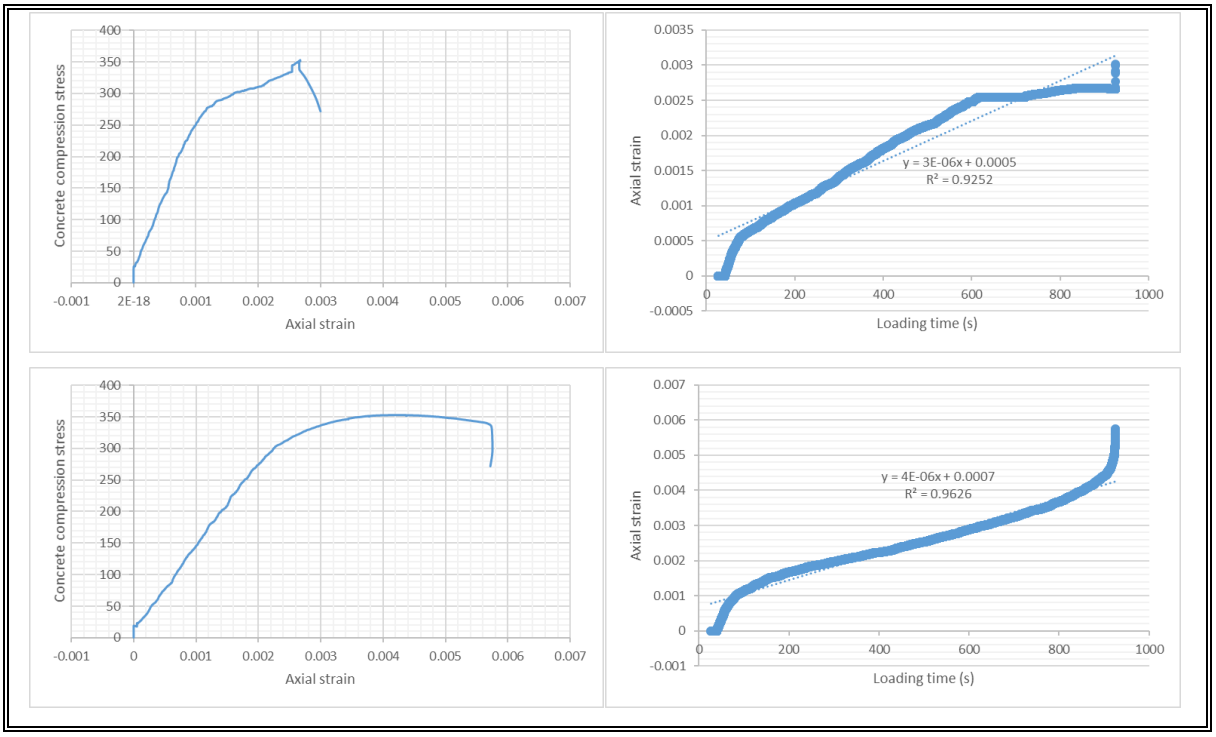

Figure B.2: Vertical LVDTs readings until change of displacement rate. Specimen 225-15

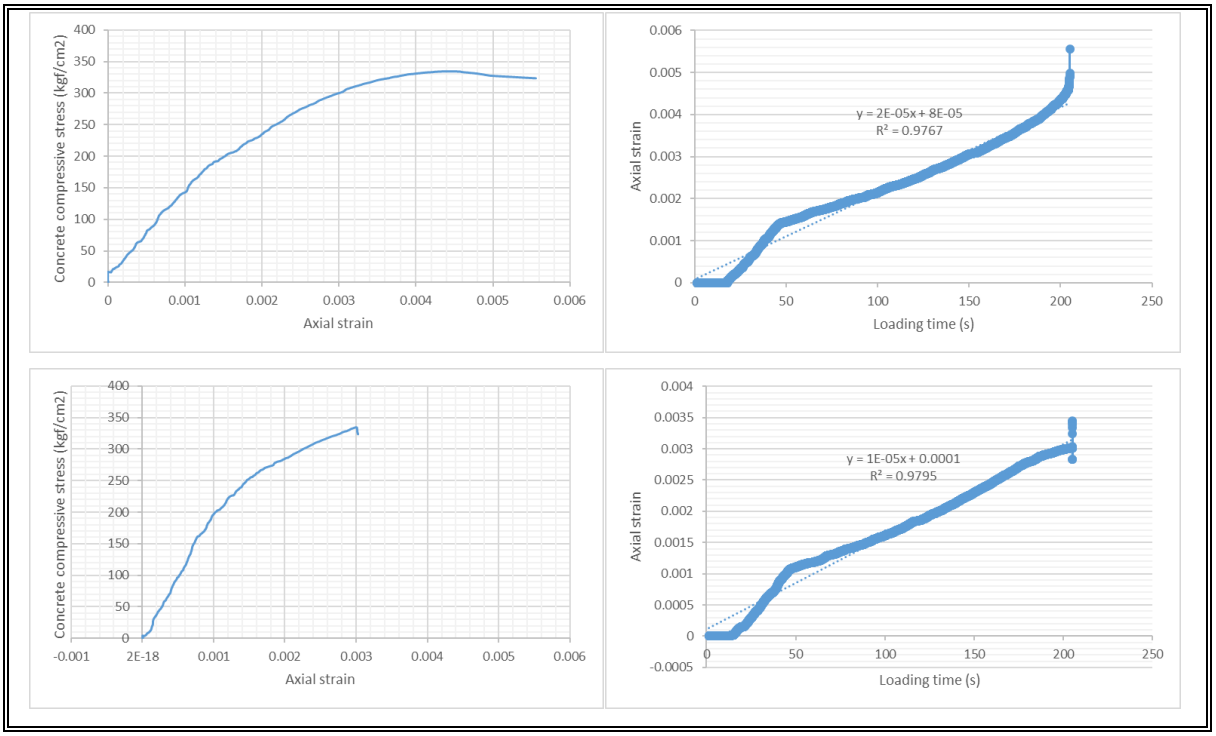

Figure B.3: Vertical LVDTs readings until change of displacement rate. Specimen 235-10

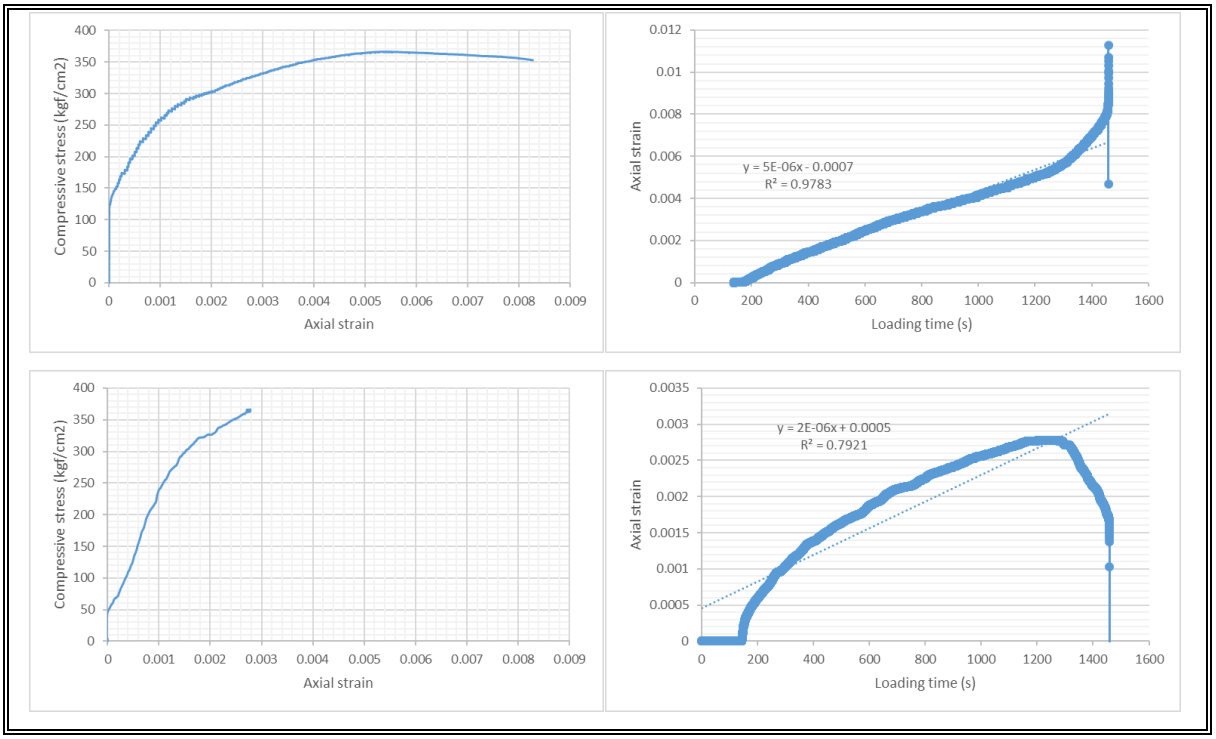

Figure B.4: Vertical LVDTs readings until change of displacement rate. Specimen 235-15

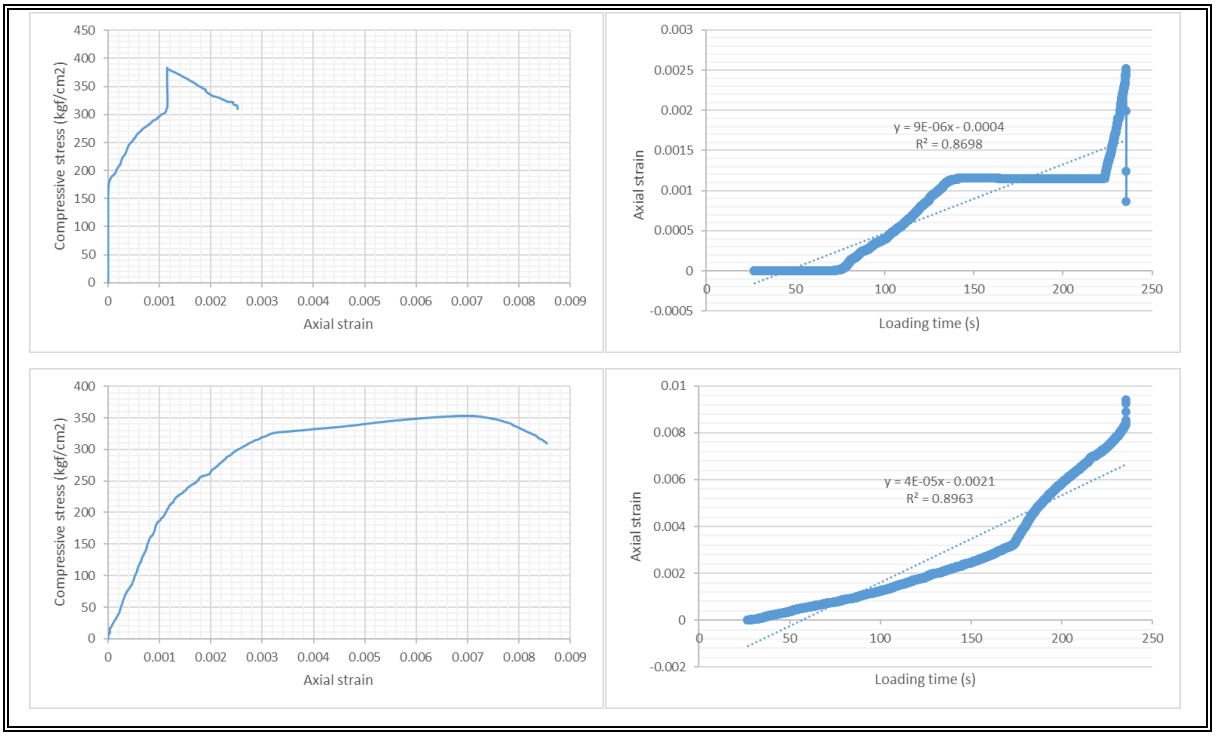

Figure B.5: Vertical LVDTs readings until change of displacement rate. Specimen 325-10

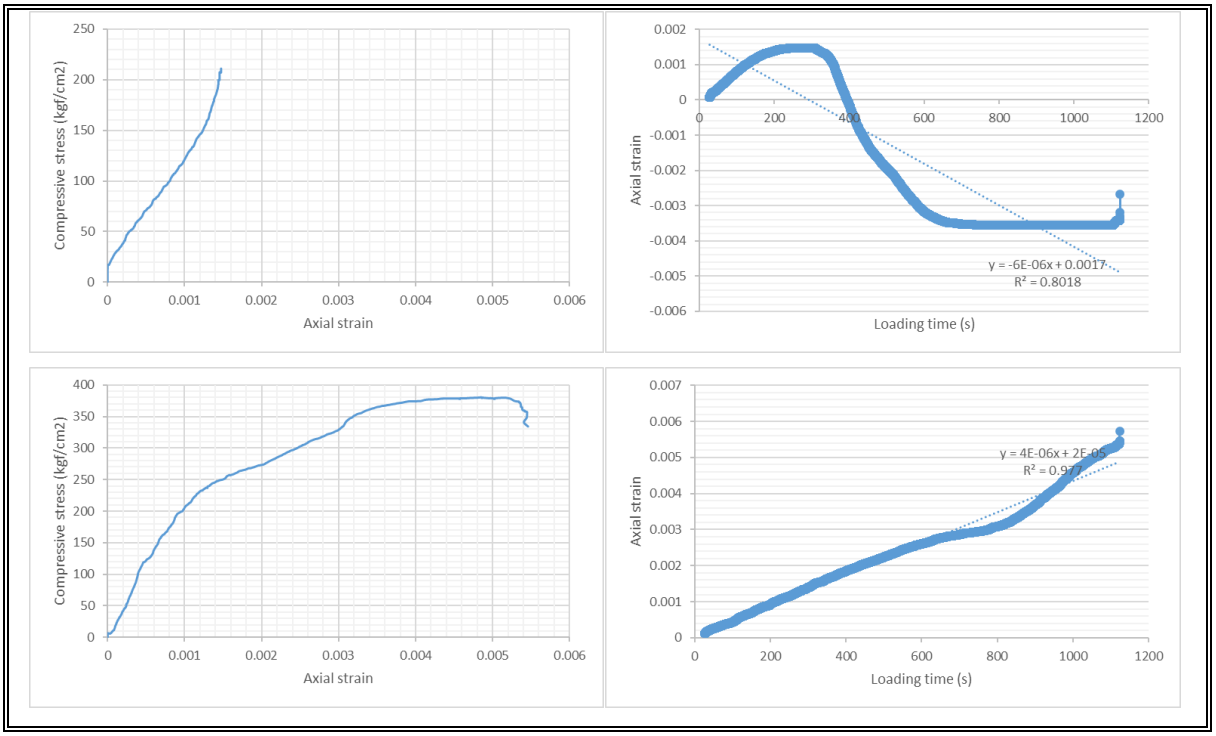

Figure B.6: Vertical LVDTs readings until change of displacement rate. Specimen 325-15

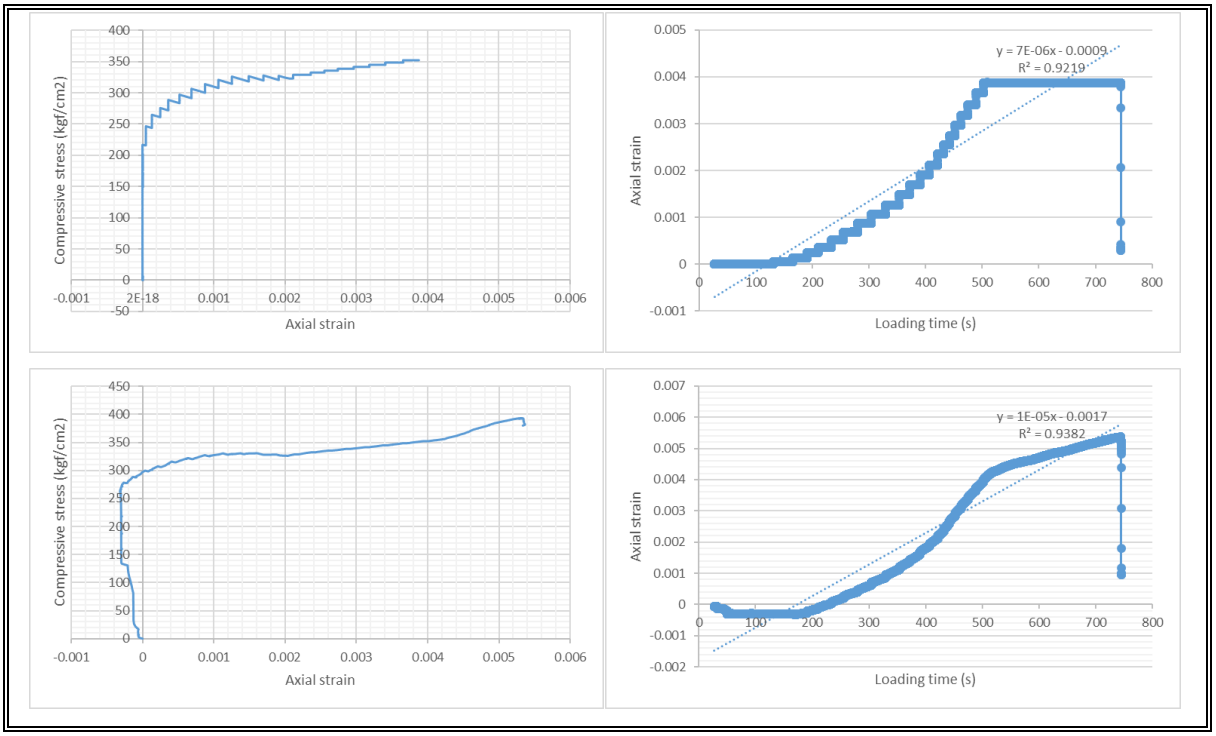

Figure B.7: Vertical LVDTs readings until change of displacement rate. Specimen 335-10

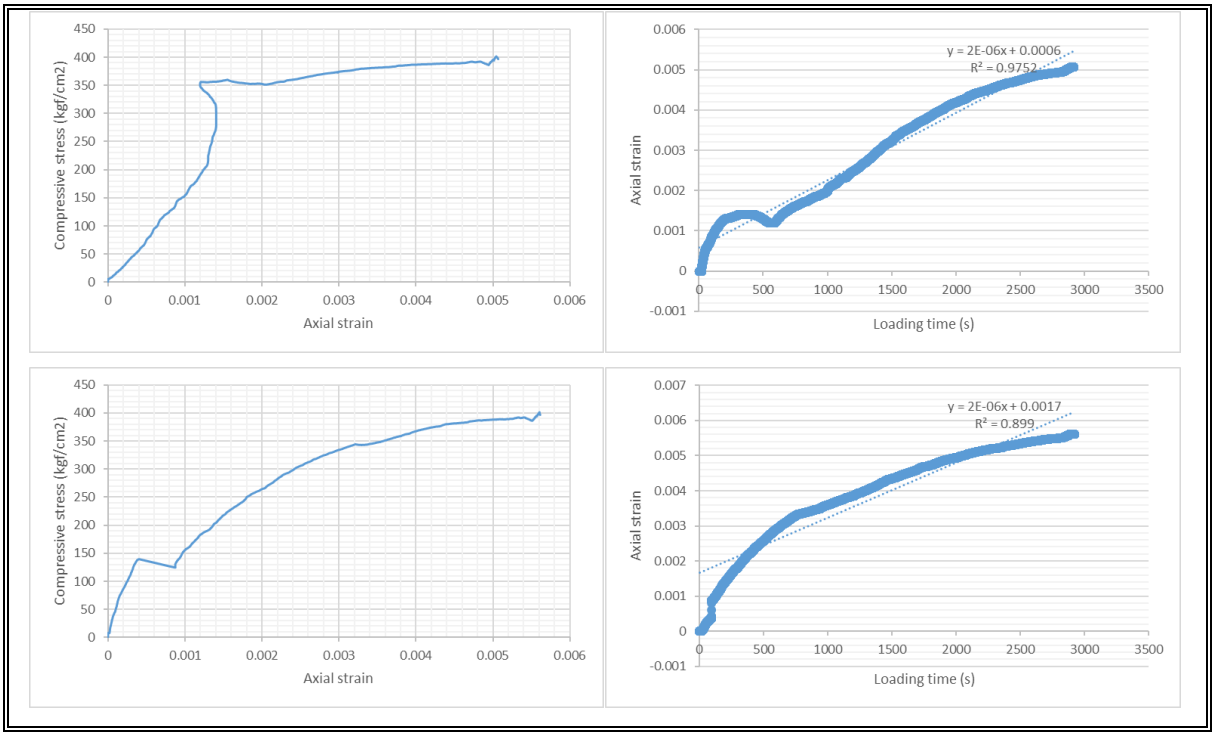

Figure B.8: Vertical LVDTs readings until change of displacement rate. Specimen 335-15

APPENDIX C: CONCRETE PRINCIPAL STRESSES AND STEEL AXIAL STRESS IN ANSYS MODELS OF TESTED SPECIMENS

Sections C.1 to C.8 contain the principal results of the ANSYS models developed for each of the tested columns with CFRP confinement. The results include the principal stress distribution inside concrete elements and transverse steel reinforcement axial stresses.

The principal stresses inside concrete elements are divided in minimum principal, middle principal and maximum principal. As explain in Figure 4.17, the principal stresses are a good representation of the axial and confining stresses on each element of concrete. The minimum principal stress presents an orientation parallel to the Y axis, namely the longitudinal axis of the column. The middle and maximum principal axis represents the confining stresses originated mainly from the CFRP confinement and in marginally from the transverse steel reinforcement. They are orthogonal to the minimum principal stress; therefore, they are contained inside the transverse cross-section of the column. Since the CFRP confinement presents a complex geometry including complete wrapping of the column and CFRP anchors, the confining stresses change their orientation depending on their location, but they are always parallel to the transverse cross section of the column (Figures 4.22 and 4.25). The concrete principal stresses are showed at an axial average strain of the complete column of 0.006.

The axial stress of the steel transverse reinforcement is show for two loading steps: load step number 7 (corresponding to an axial average strain of the complete column of 0.0035) and load step number 7 (corresponding to an axial average strain of the complete column of 0.006). The first step represents the maximum axial strain reached by the tested columns without CFRP confinement. The second step represents the maximum axial strain

reached by the tested columns with CFRP confinement. Since the steel bars present a nominal yield stress of 420 MPa, sections C.1 to C.8 show that for a 0.0035 axial strain the steel reinforcement does not experience yielding. As was explained in section 5.5.3, specimens without CFRP confinement present transverse steel yielding at an axial strain of 0.0035, therefore, CFRP confinement reduces considerably the solicitation on steel transverse reinforcement. However, for an axial average strain of 0.006, the steel bars present yielding. Therefore, at the moment of CFRP rupture steel bars presented yielding.

C.1 Specimen 225-10

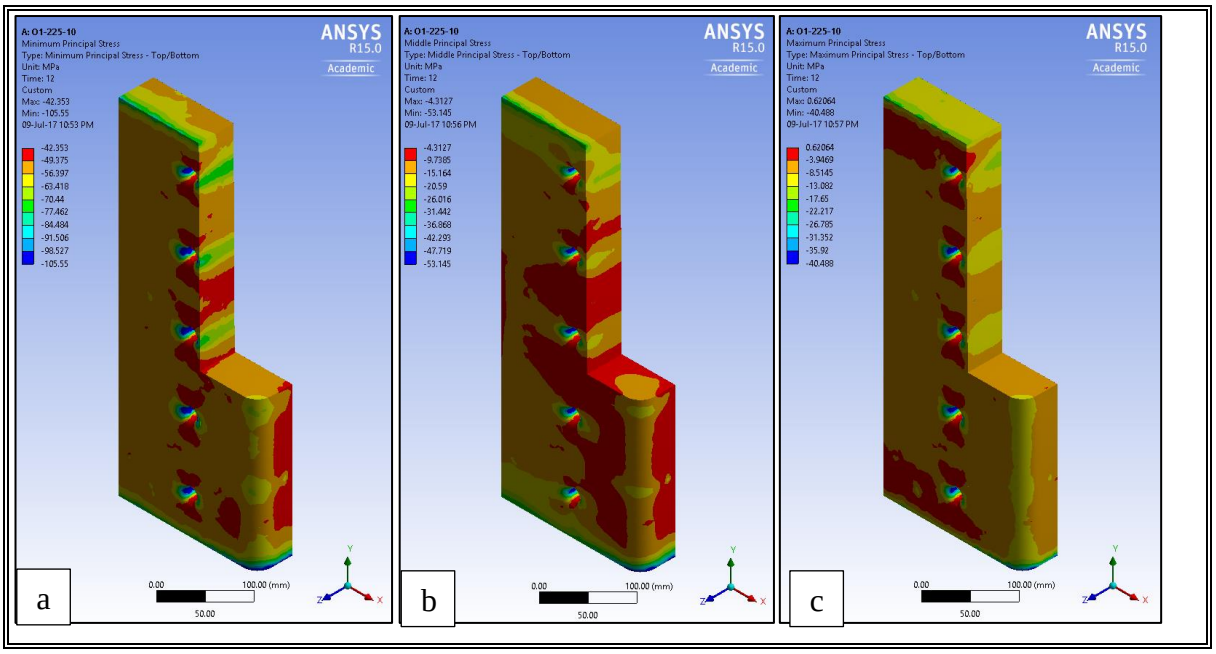

Figure C.1: Concrete (a) minimum, (b) middle and (c) maximum stress. Specimen 225-1

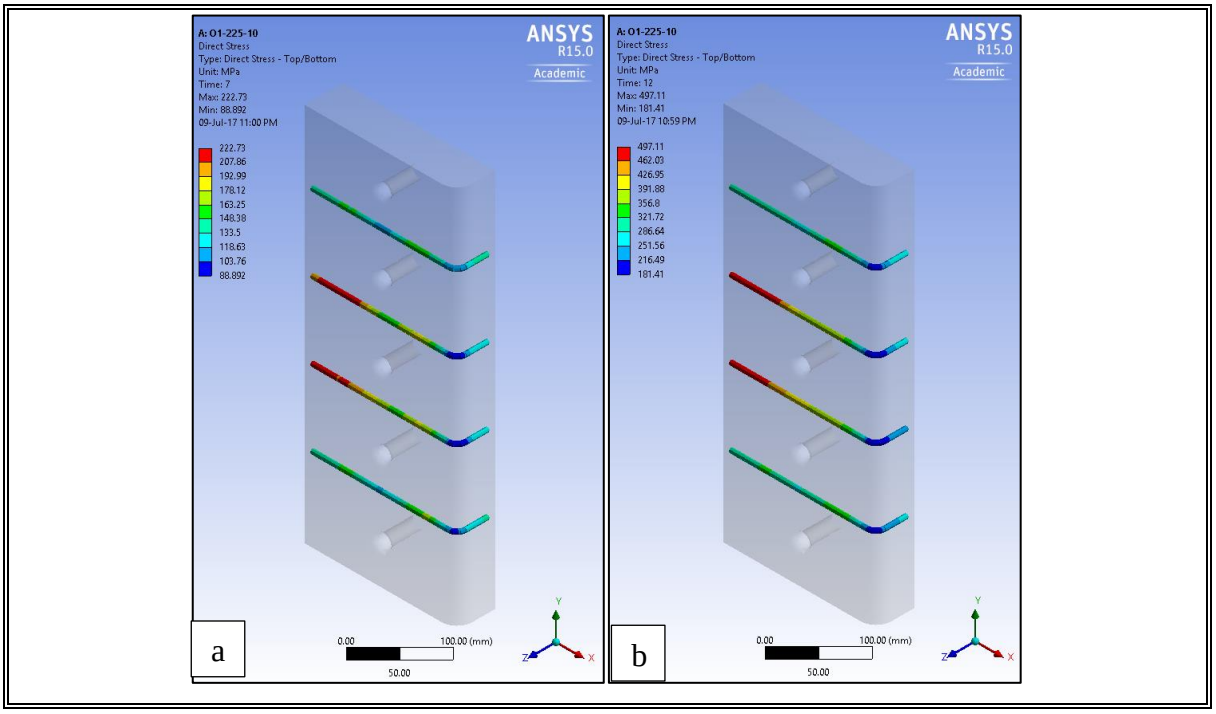

Figure C.2: Steel stress at an axial strain of: (a) 0.003 (b) 0.006. Specimen 225-10

C.2 Specimen 225-15

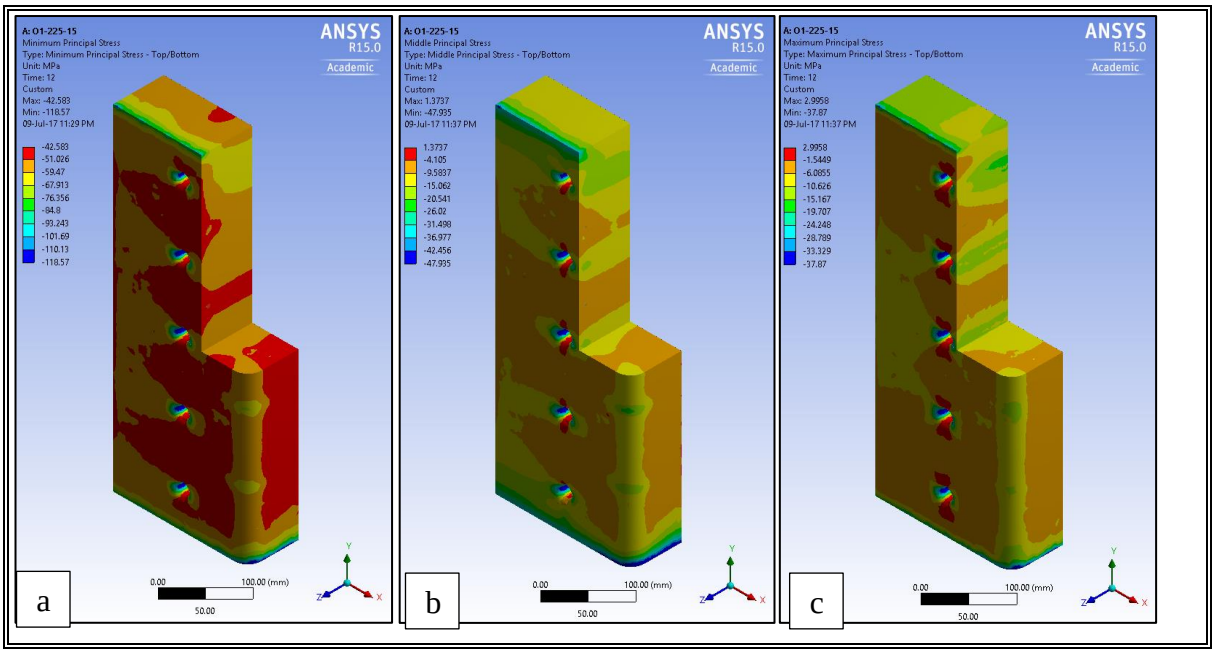

Figure C.3: Concrete (a) minimum, (b) middle and (c) maximum stress. Specimen 225-15

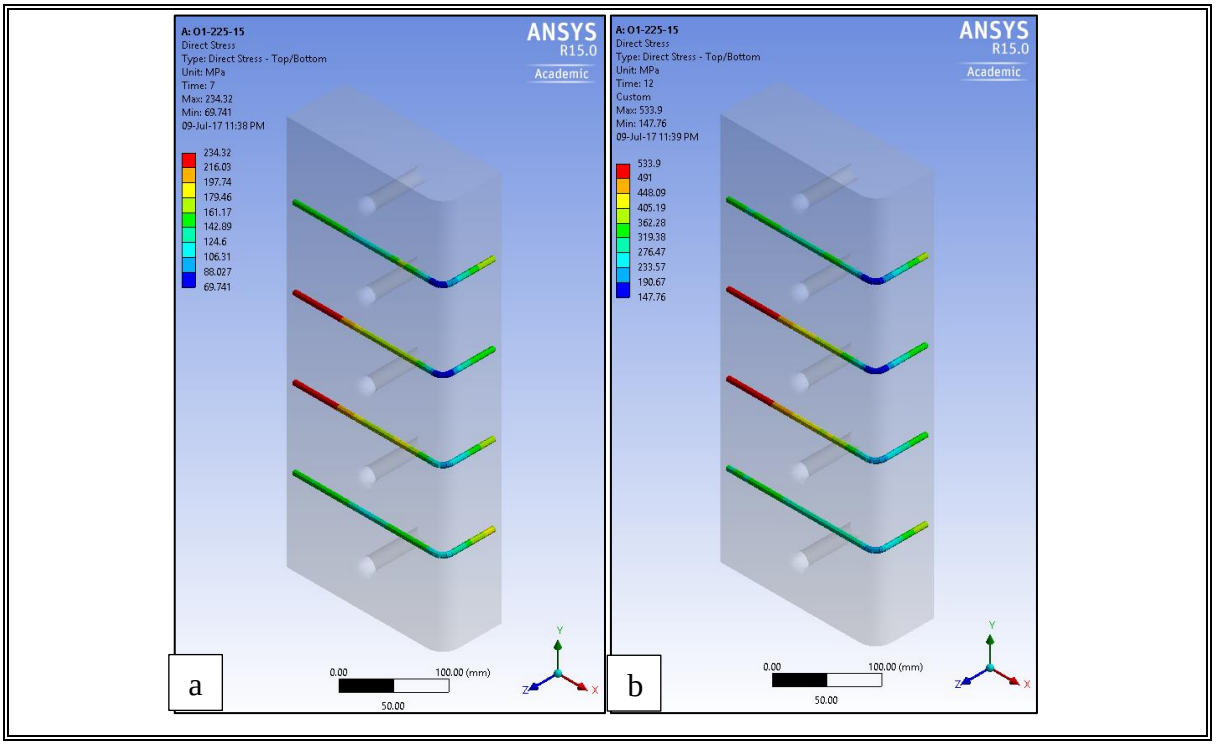

Figure C.4: Steel stress at an axial strain of: (a) 0.003 (b) 0.006. Specimen 225-15

C.3 Specimen 235-10

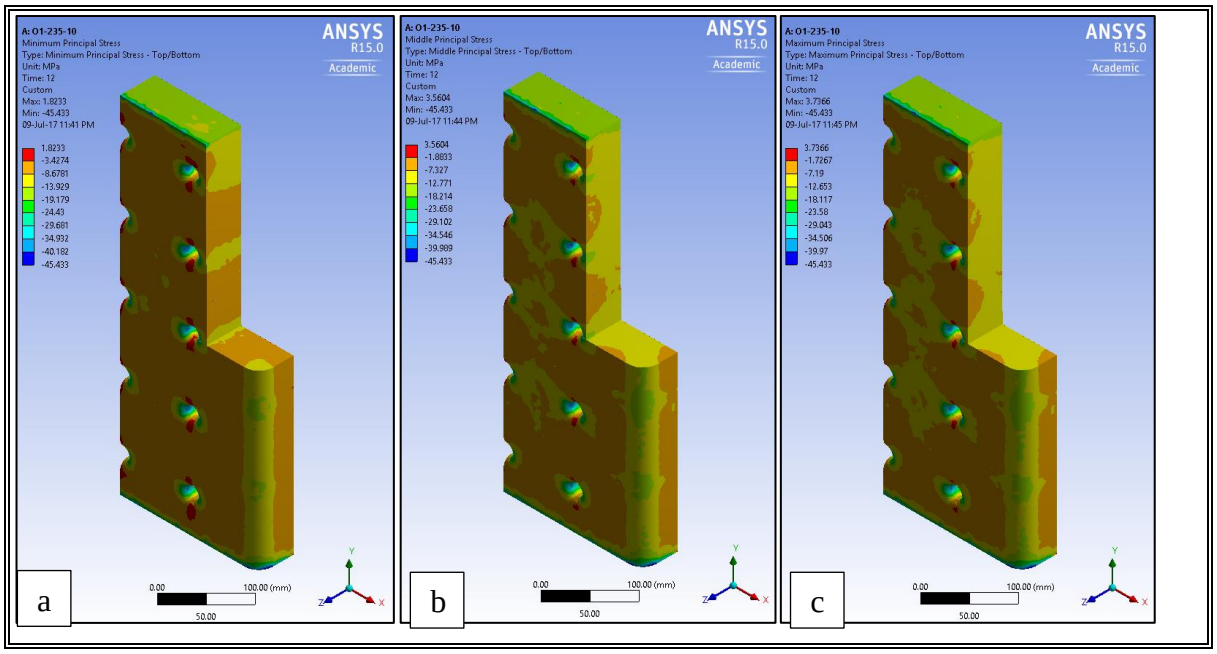

Figure C.5: Concrete (a) minimum, (b) middle and (c) maximum stress. Specimen 235-10

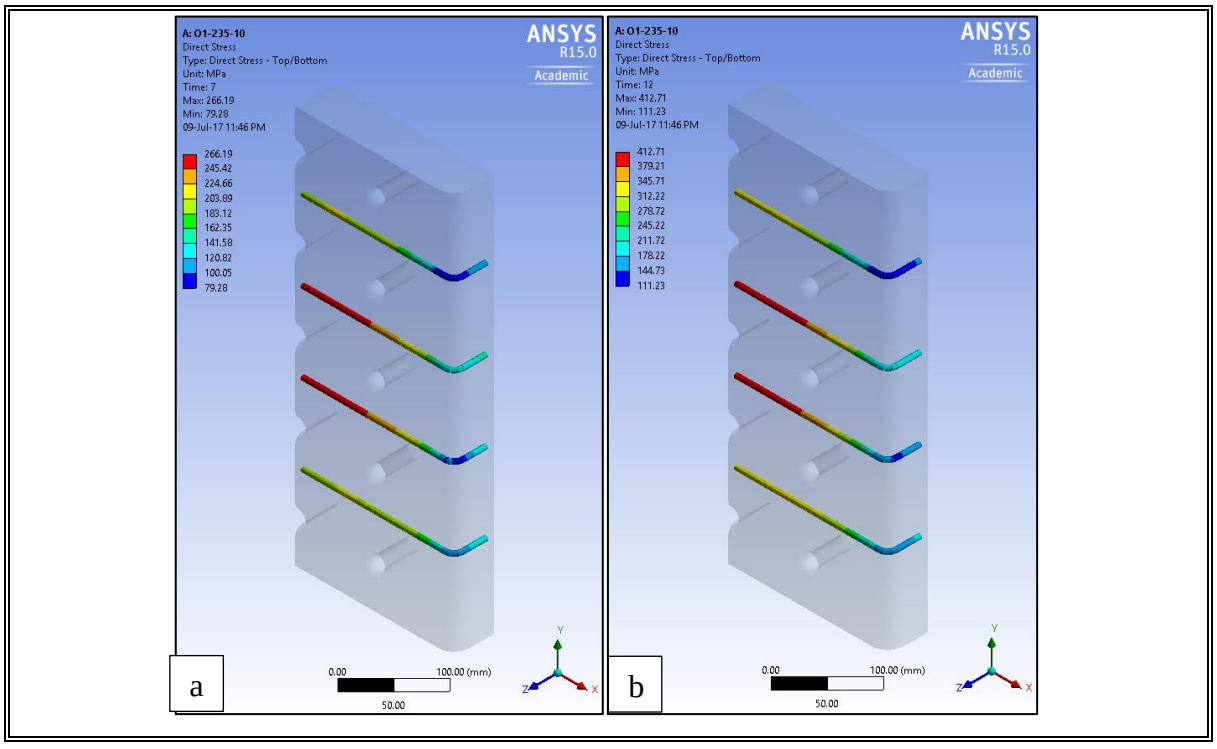

Figure C.6: Steel stress at an axial strain of: (a) 0.003 (b) 0.006. Specimen 235-10

C.4 Specimen 235-15

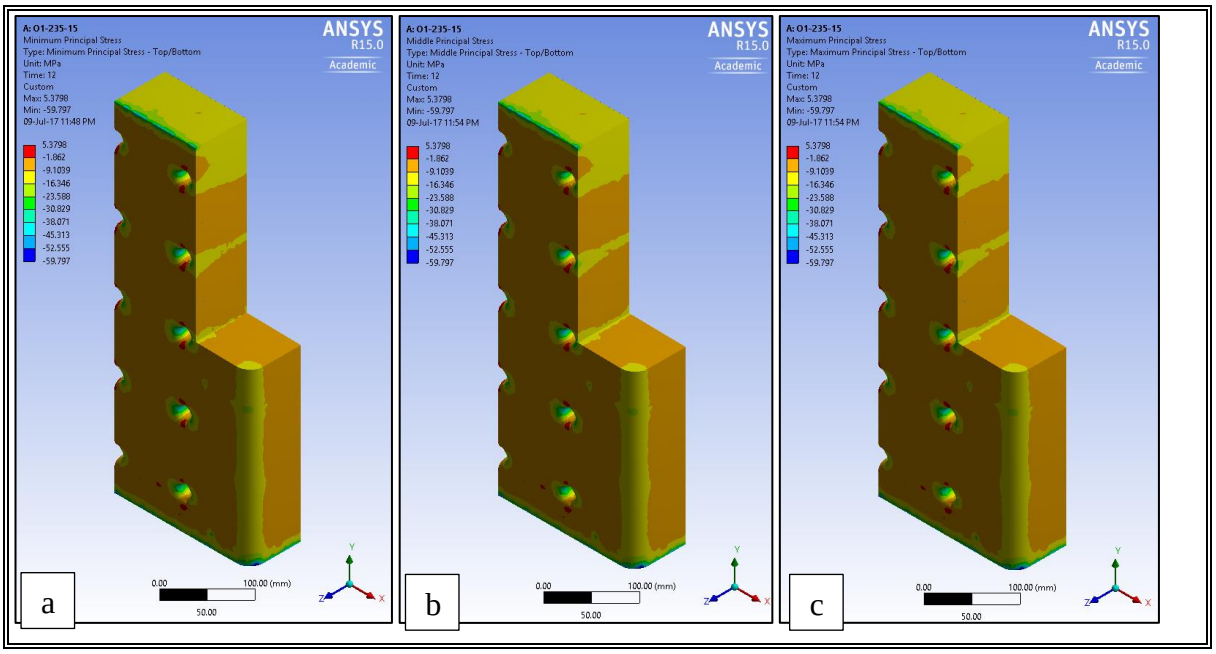

Figure C.7: Concrete (a) minimum, (b) middle and (c) maximum stress. Specimen 235-15

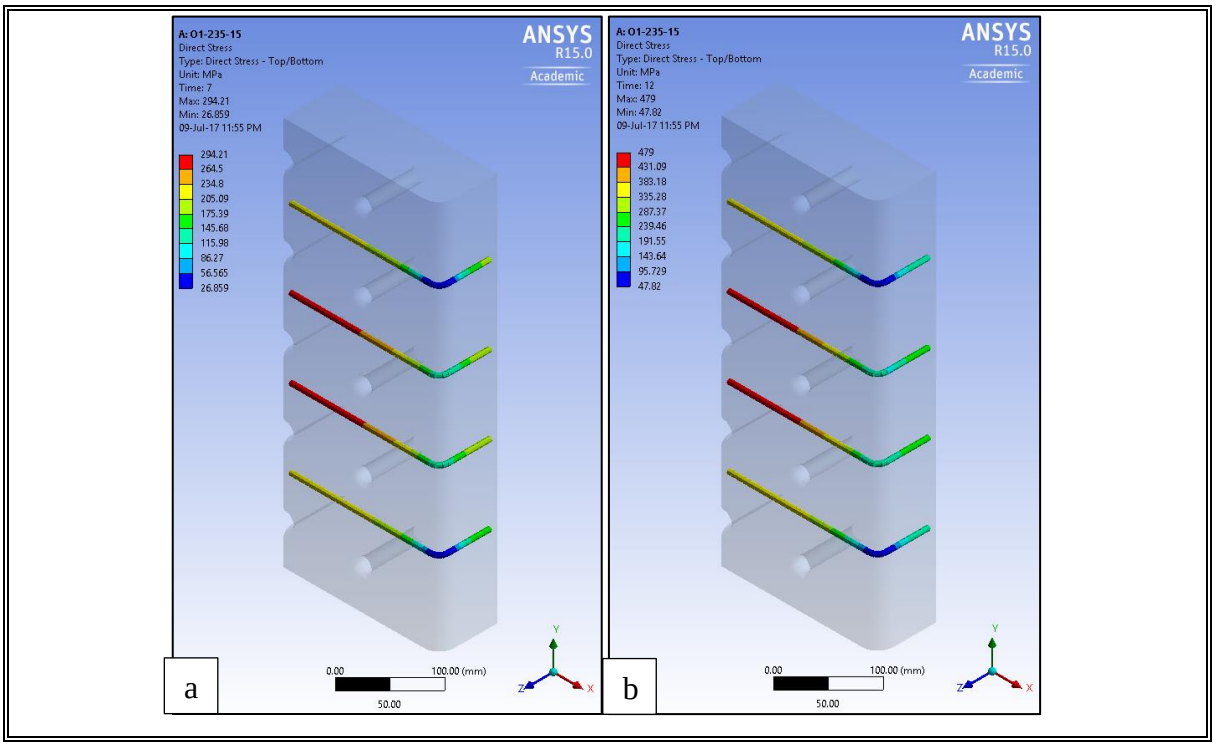

Figure C.8: Steel stress at an axial strain of: (a) 0.003 (b) 0.006. Specimen 235-15

C.5 Specimen 325-10

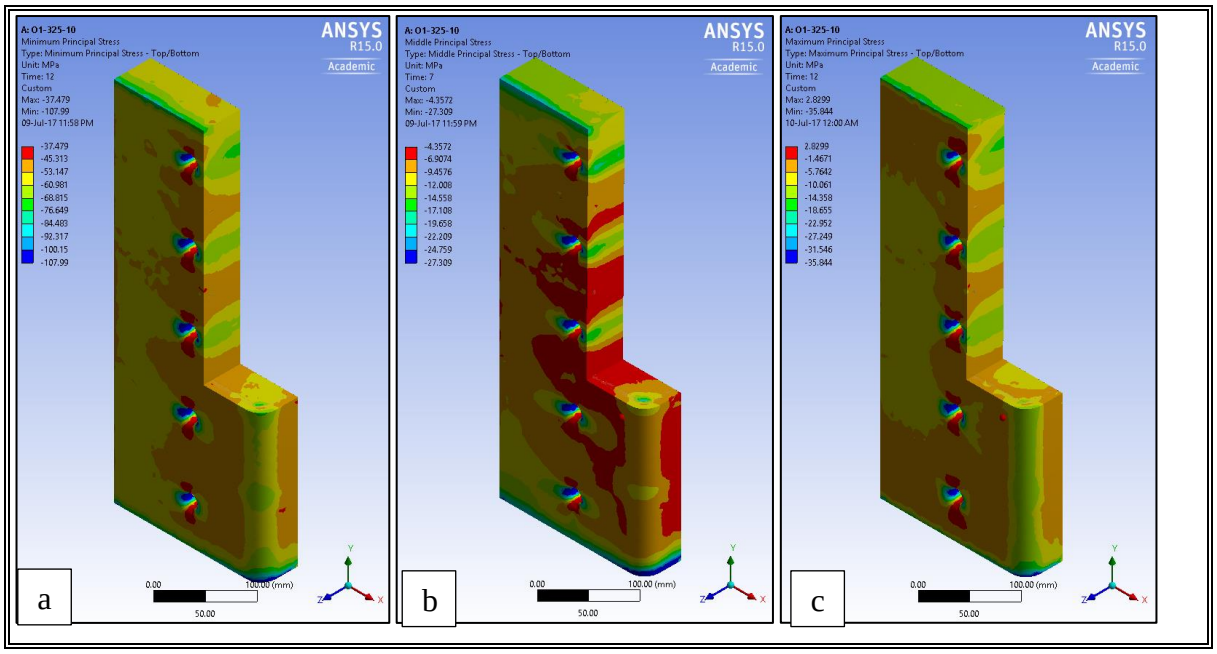

Figure C.9: Concrete (a) minimum, (b) middle and (c) maximum stress. Specimen 325-10

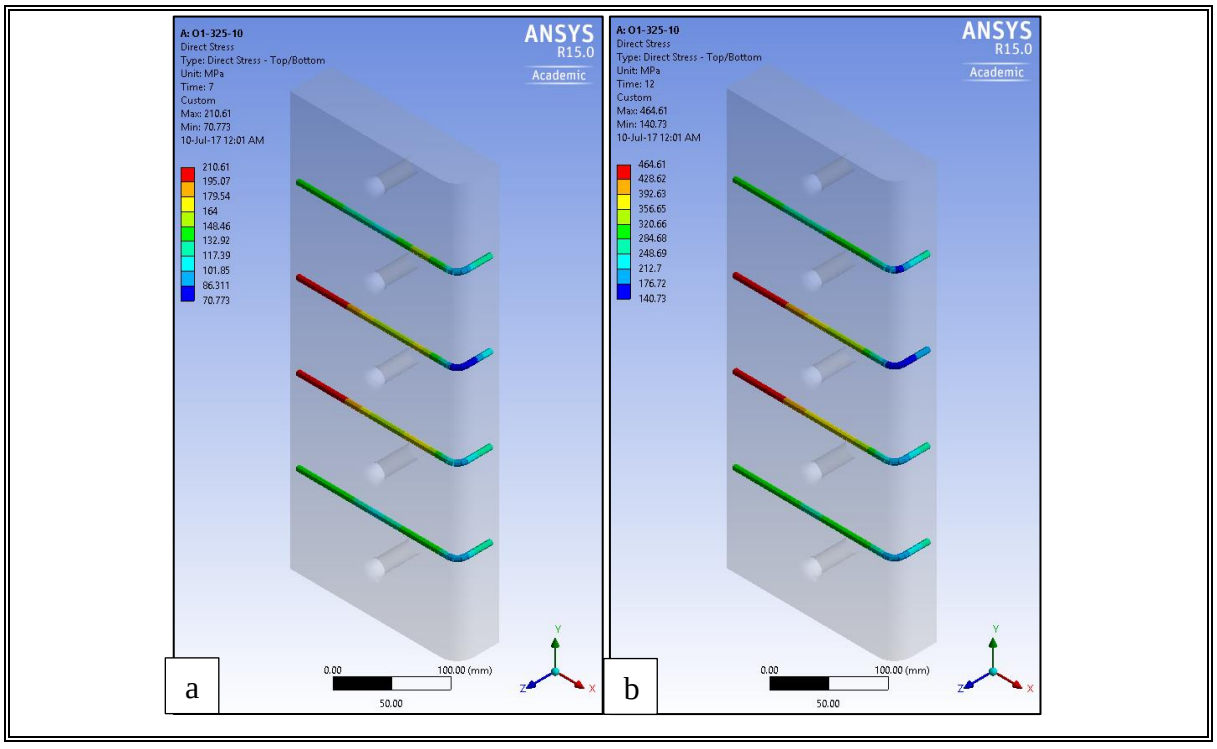

Figure C.10: Steel stress at an axial strain of: (a) 0.003 (b) 0.006. Specimen 325-10

C.6 Specimen 325-15

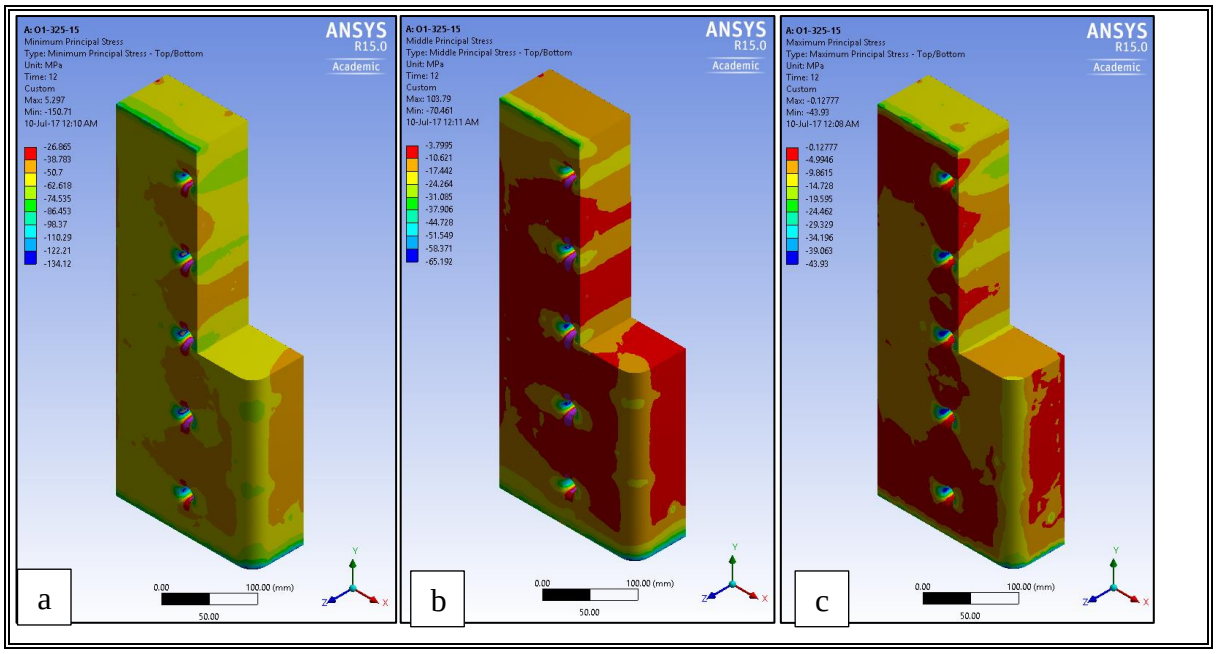

Figure C.11: Concrete (a) minimum, (b) middle and (c) maximum stress. Specimen 325-15

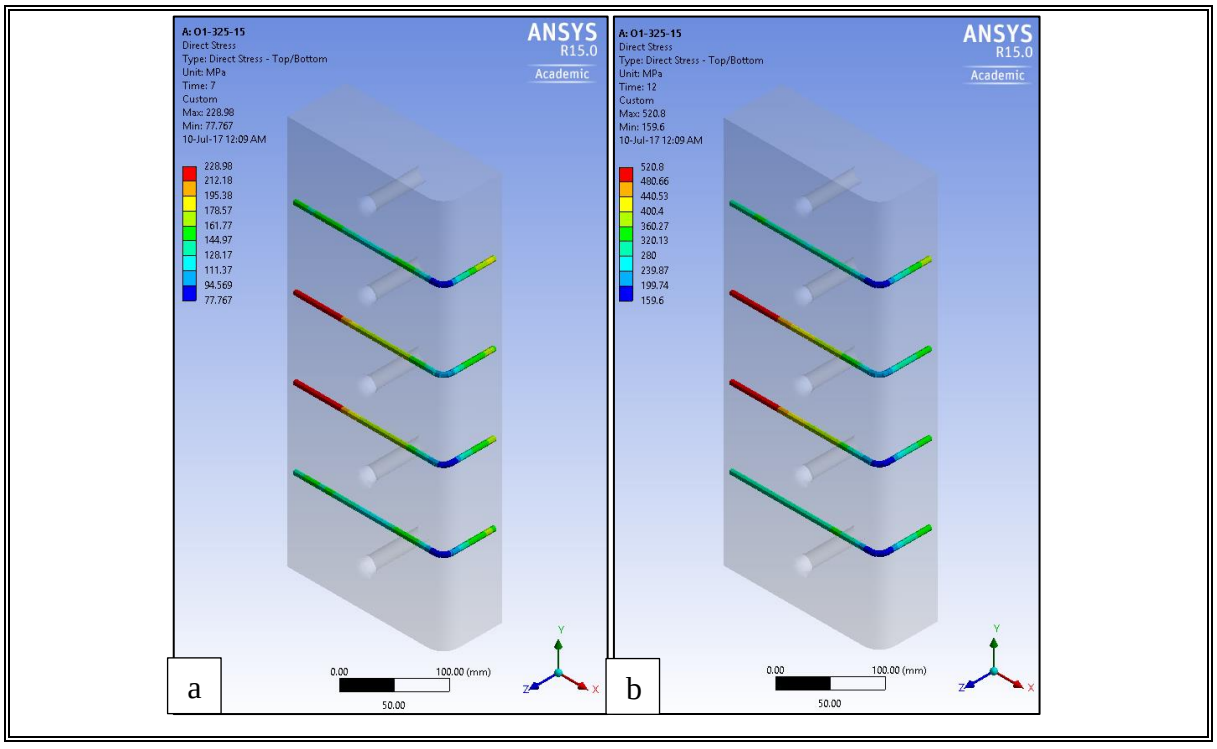

Figure C.12: Steel stress at an axial strain of: (a) 0.003 (b) 0.006. Specimen 325-15

C.7 Specimen 335-10

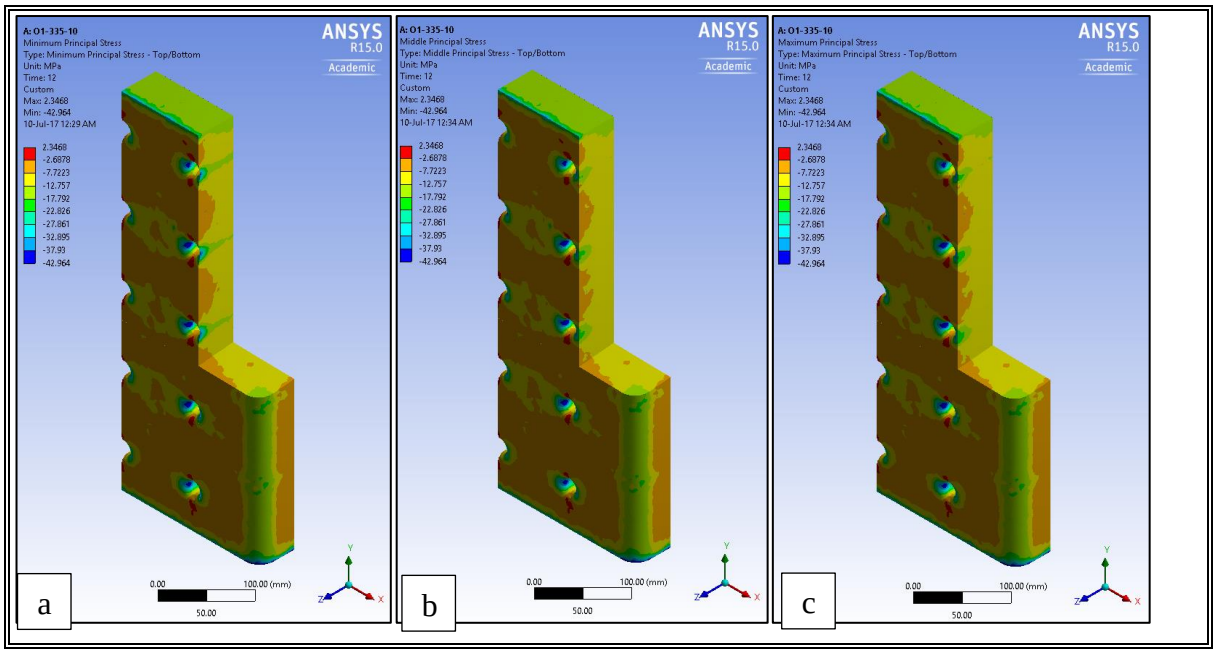

Figure C.13: Concrete (a) minimum, (b) middle and (c) maximum stress. Specimen 335-10

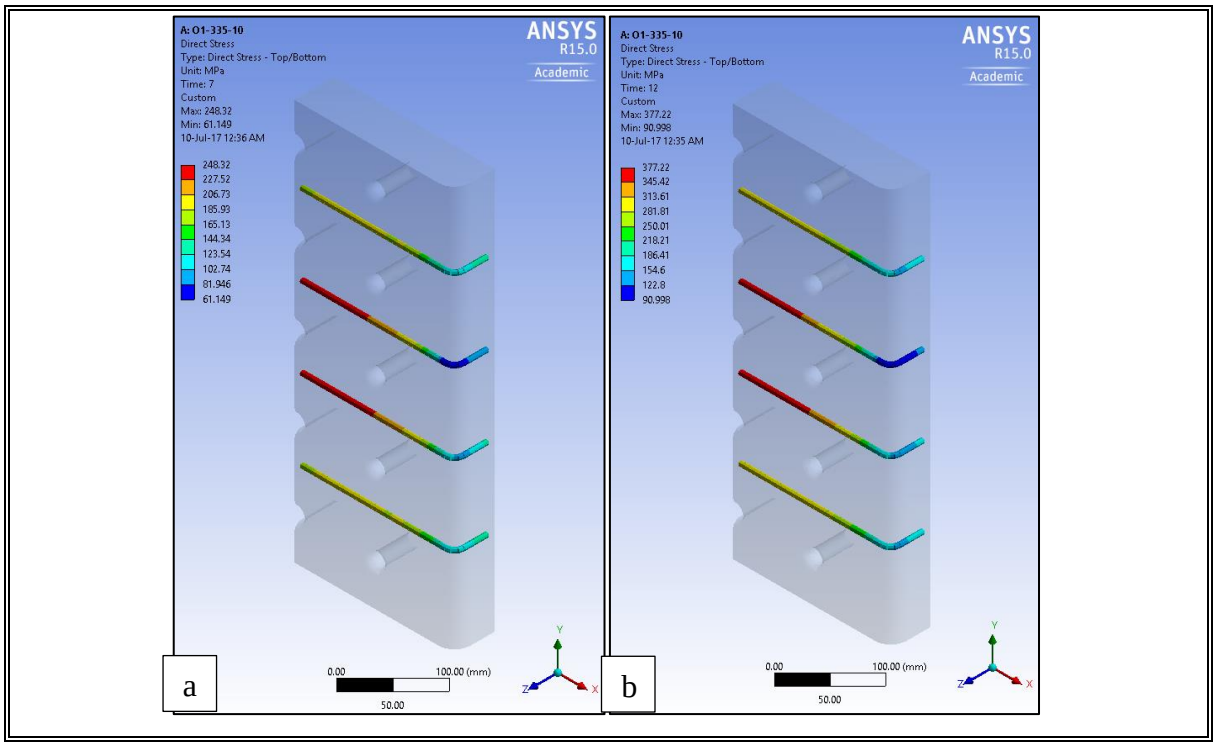

Figure C.14: Steel stress at an axial strain of: (a) 0.003 (b) 0.006. Specimen 335-10

C.8 Specimen 335-15

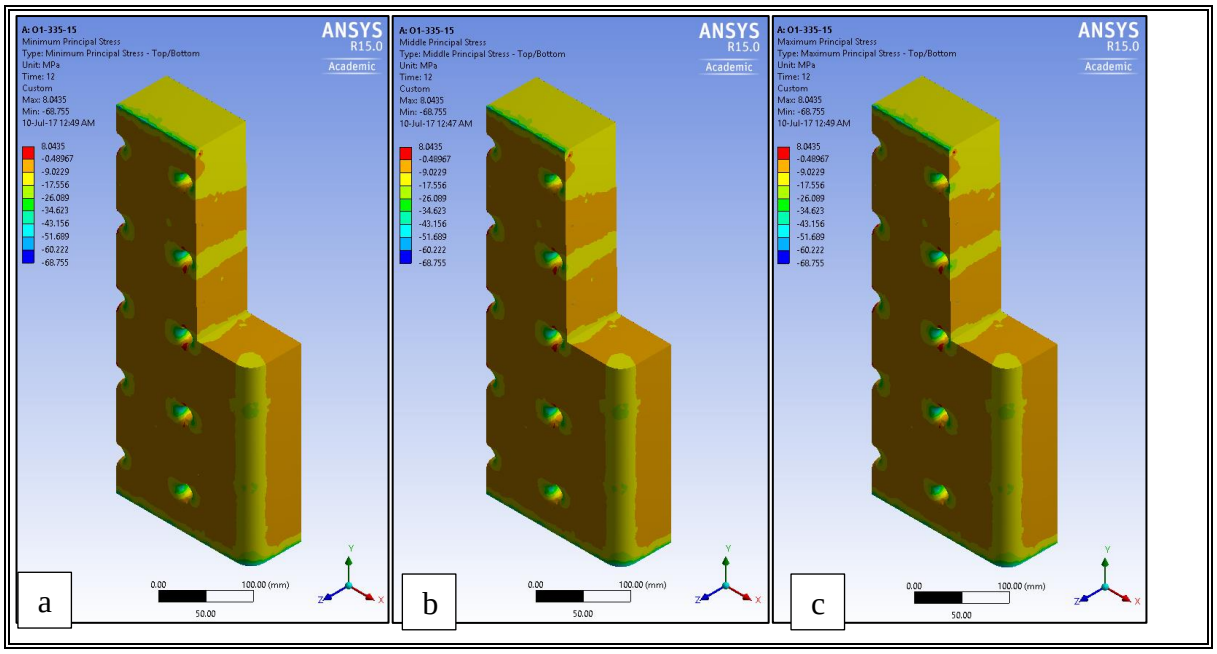

Figure C.15: Concrete (a) minimum, (b) middle and (c) maximum stress. Specimen 335-15

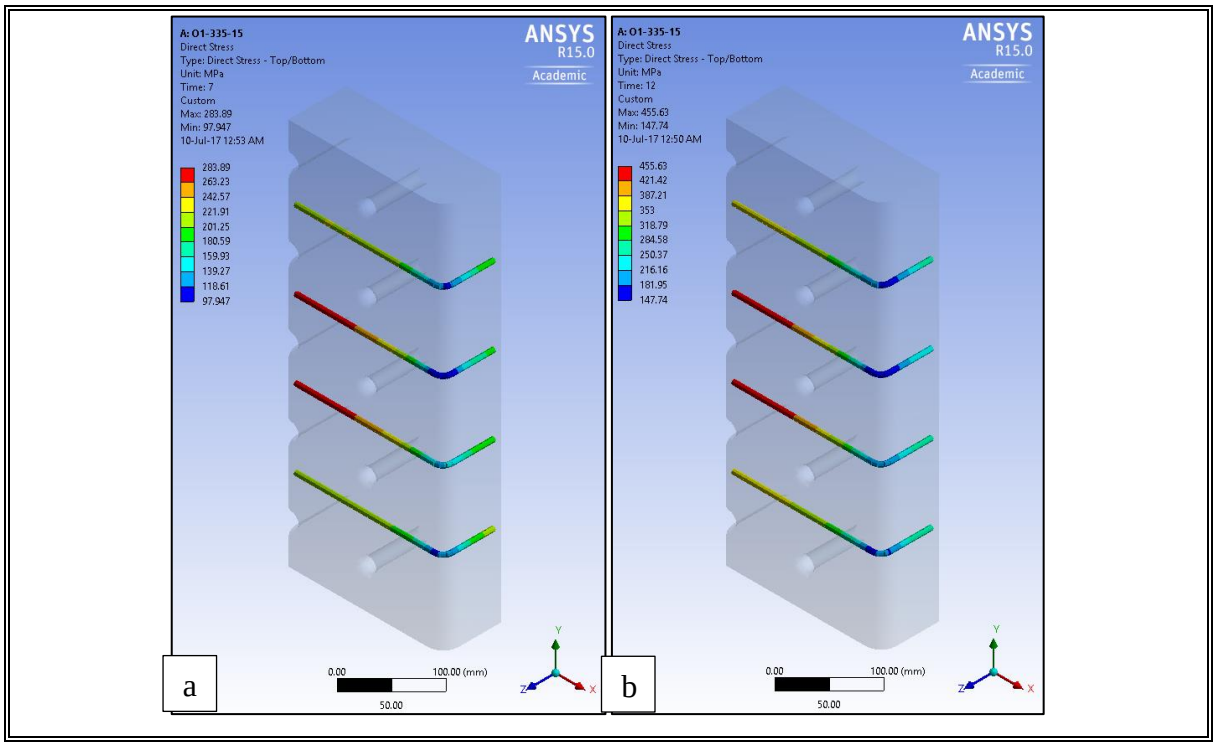

Figure C.16: Steel stress at an axial strain of: (a) 0.003 (b) 0.006. Specimen 335-15

APPENDIX D: AXIAL STRESS-STRAIN CURVES OF TESTED SPECIMENS USING DESIGN ORIENTED MODELS

Sections D.1 to D.8 show the axial stress-strain curves for each of the tested columns with CFRP confinement with the proposed procedure. As is explained in section 6.2, the proposed procedure uses existing CFRP design-oriented models. Figures D.1 to D.16 show curves resulting from applying each individual model to the proposed procedure.

In chapter 1, 11 different design-oriented models for columns confined with CFRP wraps but no CFRP anchors are explained. The curves resulting from using each of these 11 existing models are presented in Figures D.1 to D.16. in the curves marked as “a”, “b”, “c”, “d”, “e”, “f”, “g”, “h”, “i”, “j” and “k”. On each figure, the curves predicted for each individual sub column (as explain in section 6.2) are drawn with dotted lines. The curves corresponding to the complete cross-section is calculated as the weighted average of the subsection’s curves and their corresponding areas. The ultimate point of complete column curve is determined as the minimum strain of the sub columns ultimate strain.

Additionally, 2 design-oriented models specifically calibrated for columns confined with CFRP wraps and CFRP anchors (Hany, Hantouche, & Harajli, Generalized Axial Stress-Strain Response Of Rectangular Columns Confined Using CFRP Jackets And Anchors, 2016; Triantafillou, et al., 2016) are presented in the curves marked as “l”. The model corresponding to Hany, Hantouche, & Harajli, 2016 predicts the shape of the complete stress-strain curve. The model corresponding to Triantafillou, et al., 2016 predicts only the maximum stress, therefore, for this model only a horizontal line is drawn at the predicted maximum stress.

Additionally to the CFRP column curves, a Hognestad curve with the properties of the unconfined concrete taken from tested cylynders (Appendix A) are drawn to ilustrate the increment between curves. The Matlab code used to get all the curves is presented in D.9.

D.1 225-10

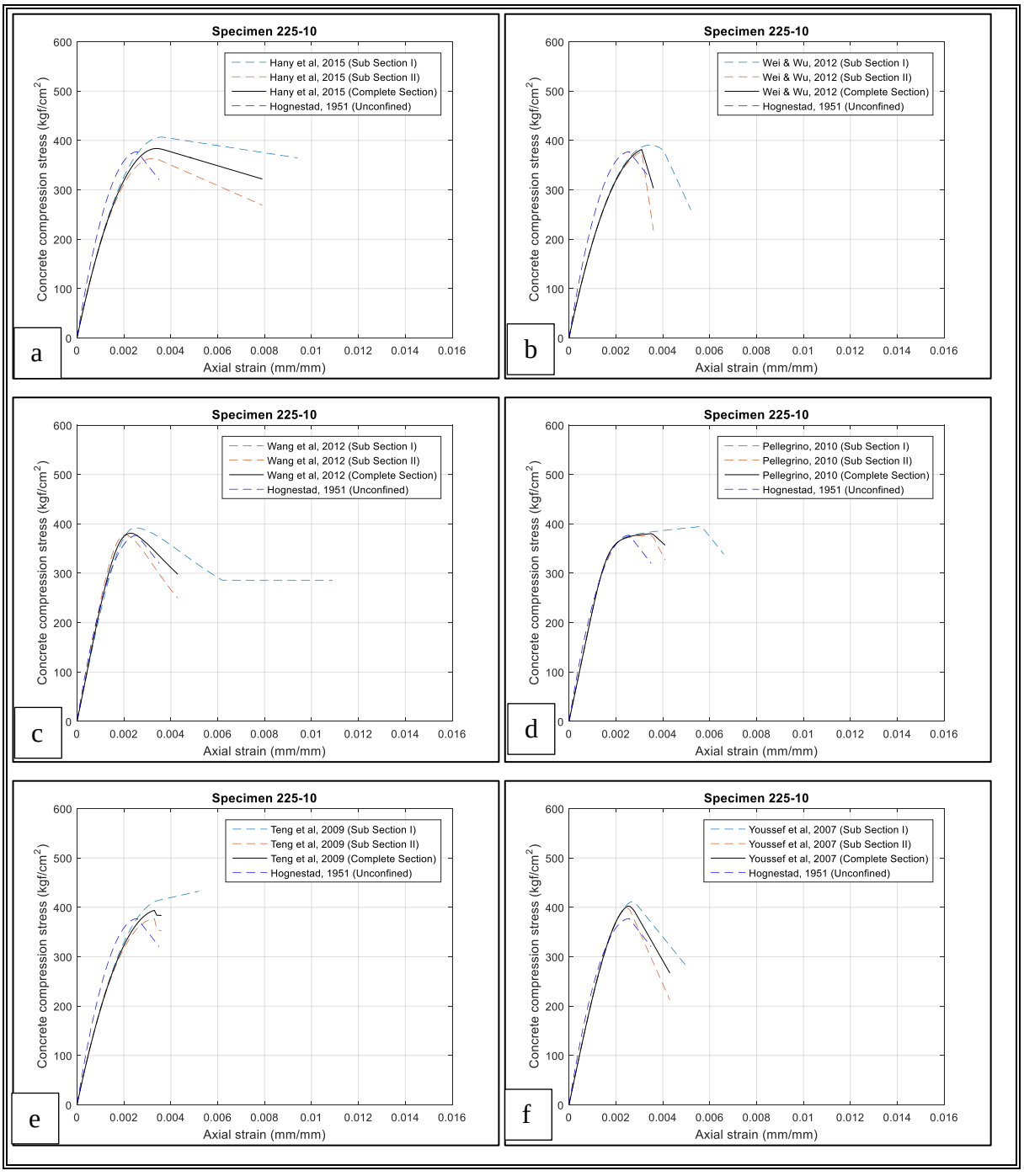

Figure D.1: Specimen 225-10 axial stress-strain curve prediction with design-oriented models according to the proposed methodology

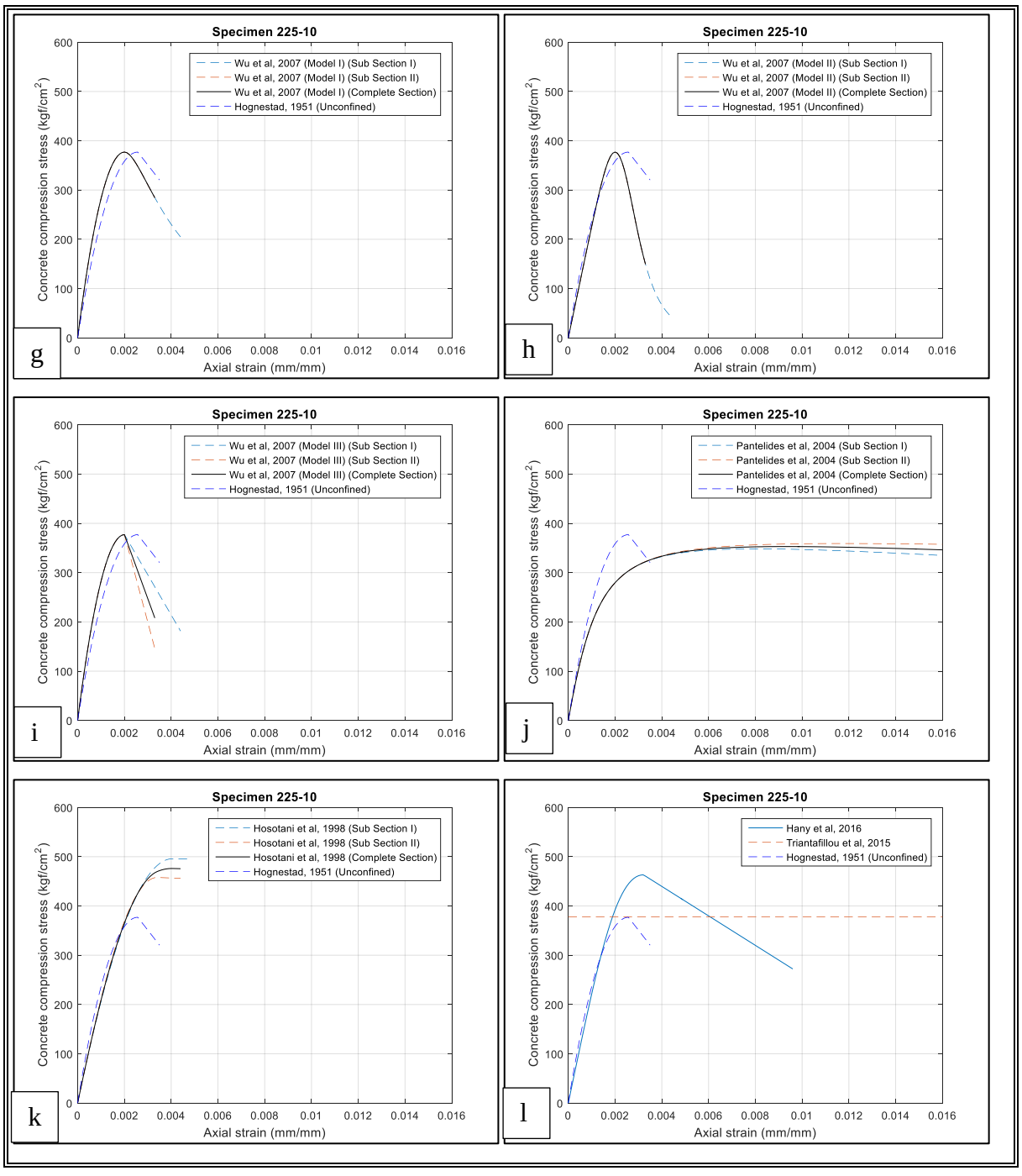

Figure D.2: Specimen 225-10 axial stress-strain curve prediction with design-oriented models according to the proposed methodology (continuation)

D.2 225-15

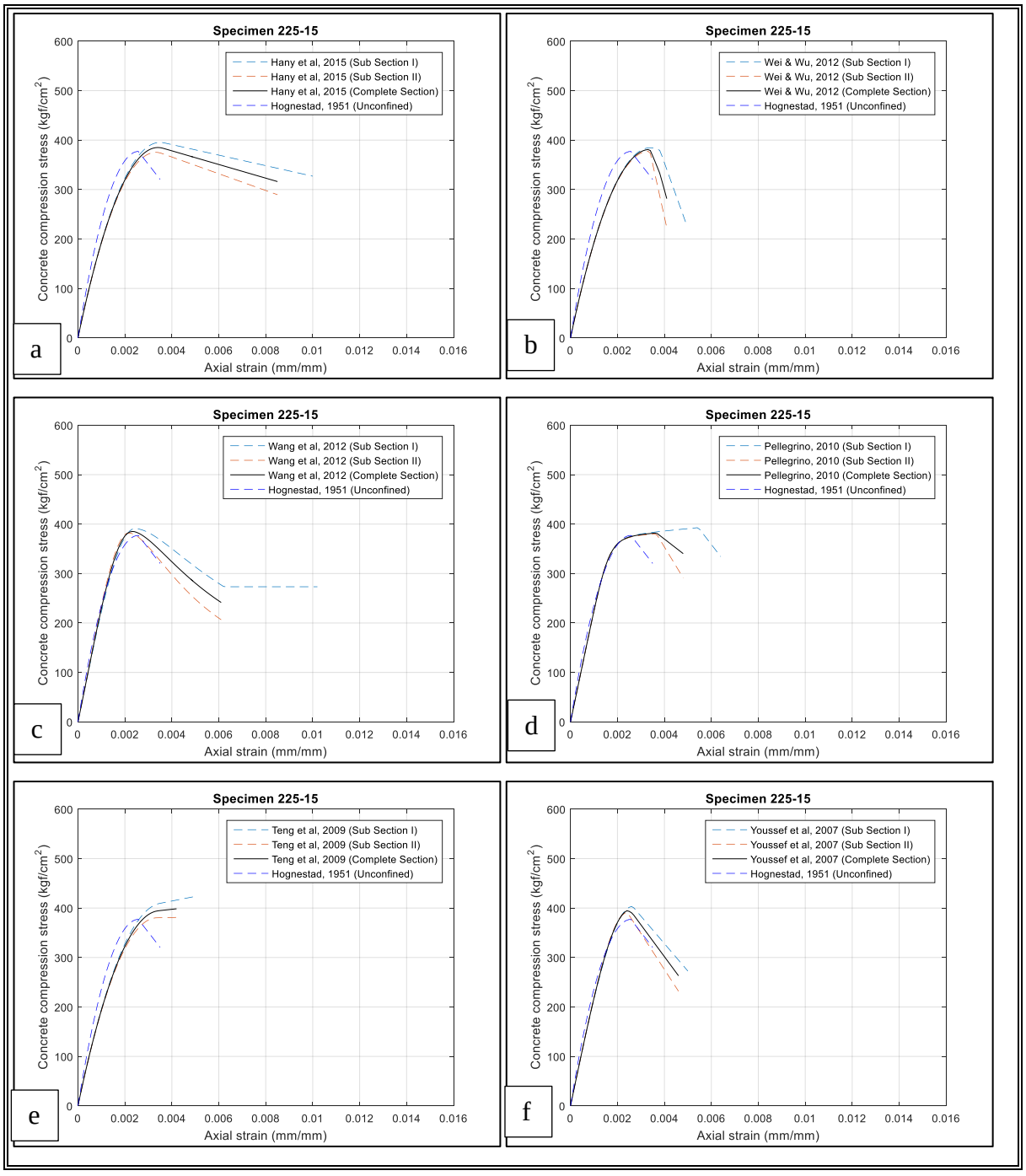

Figure D.3: Specimen 225-15 axial stress-strain curve prediction with design-oriented models according to the proposed methodology

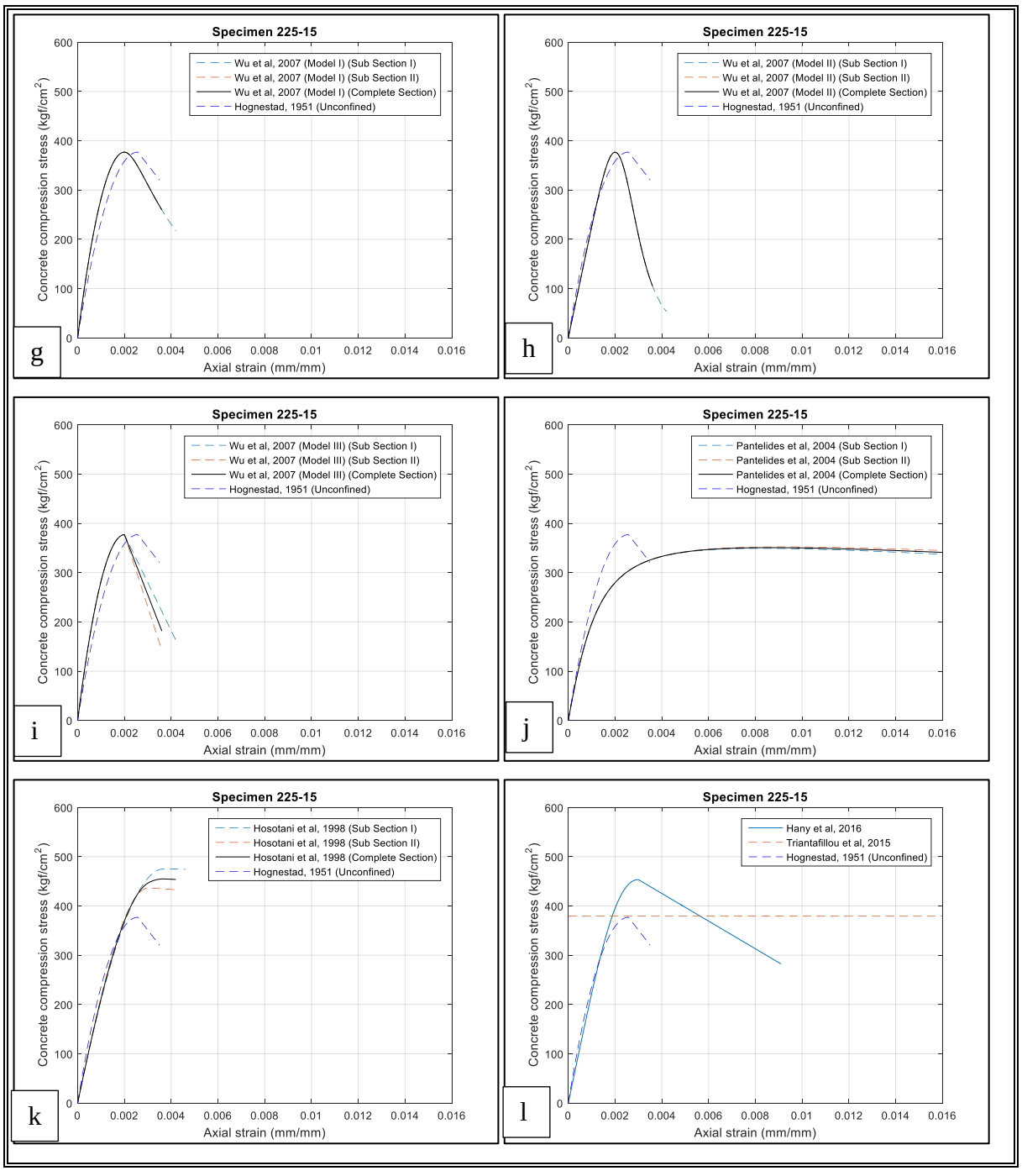

Figure D.4: Specimen 225-15 axial stress-strain curve prediction with design-oriented models according to the proposed methodology (continuation)

D.3 235-10

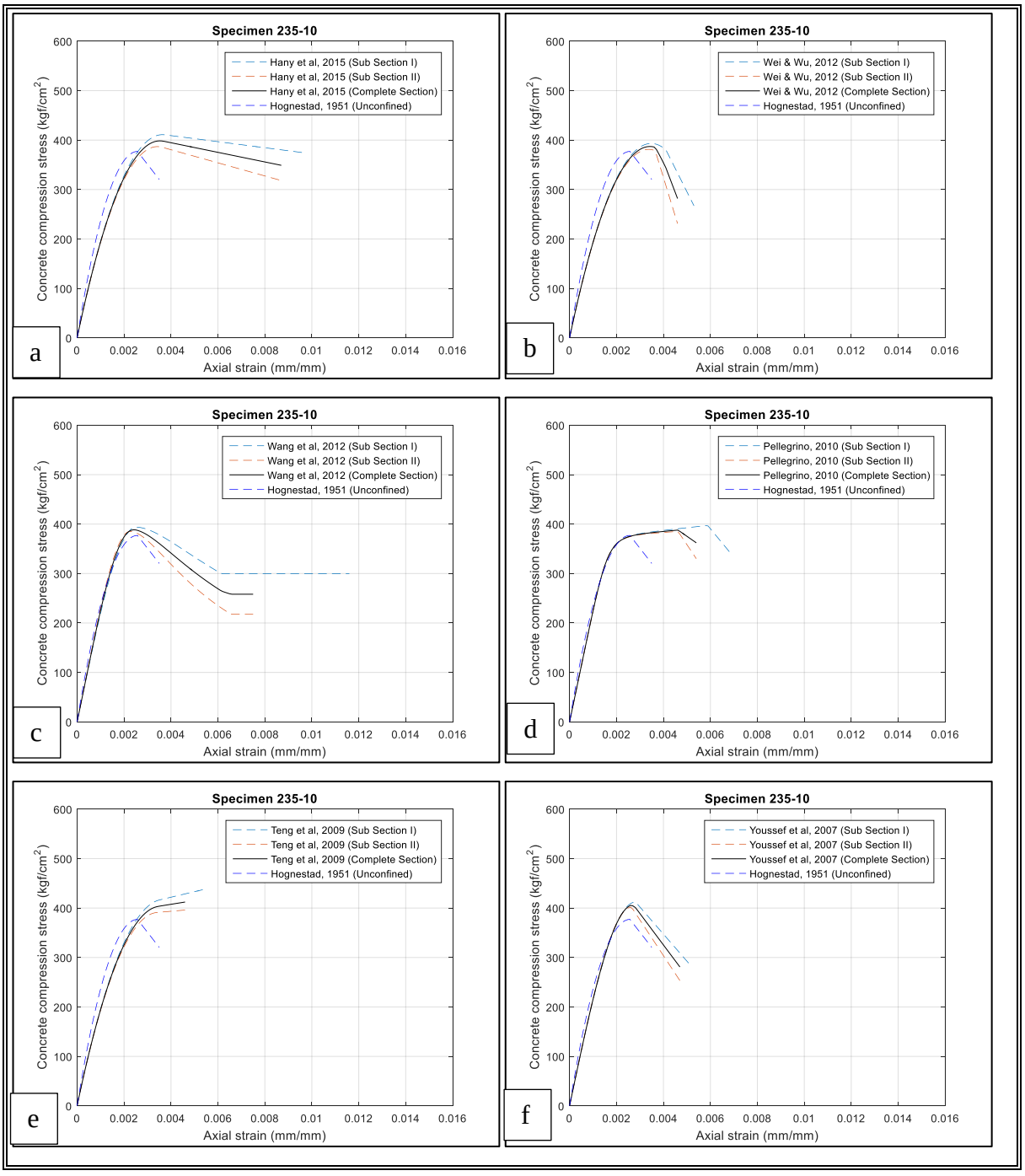

Figure D.5: Specimen 235-10 axial stress-strain curve prediction with design-oriented models according to the proposed methodology

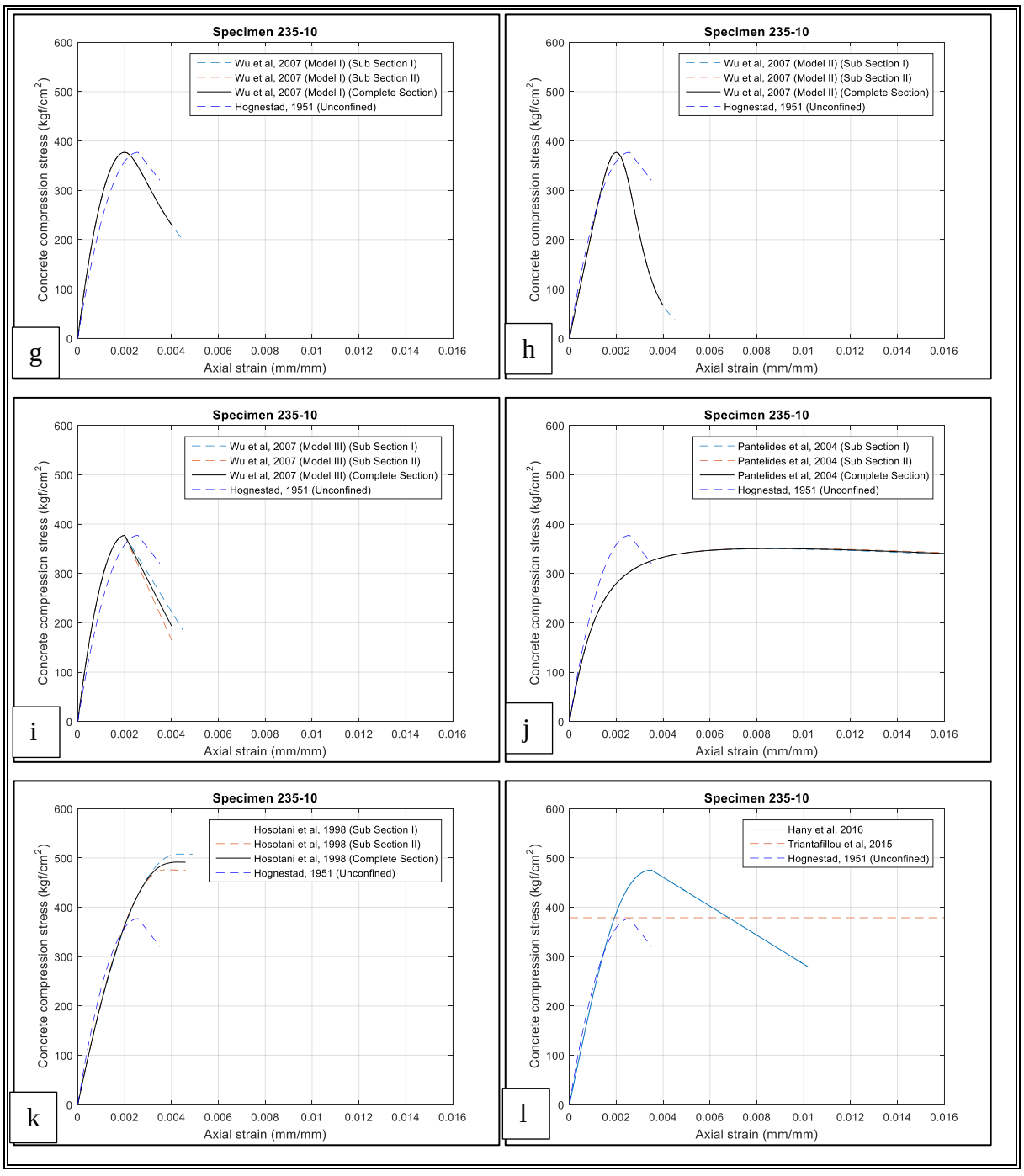

Figure D.6: Specimen 235-10 axial stress-strain curve prediction with design-oriented models according to the proposed methodology (continuation)

D.4 235-15

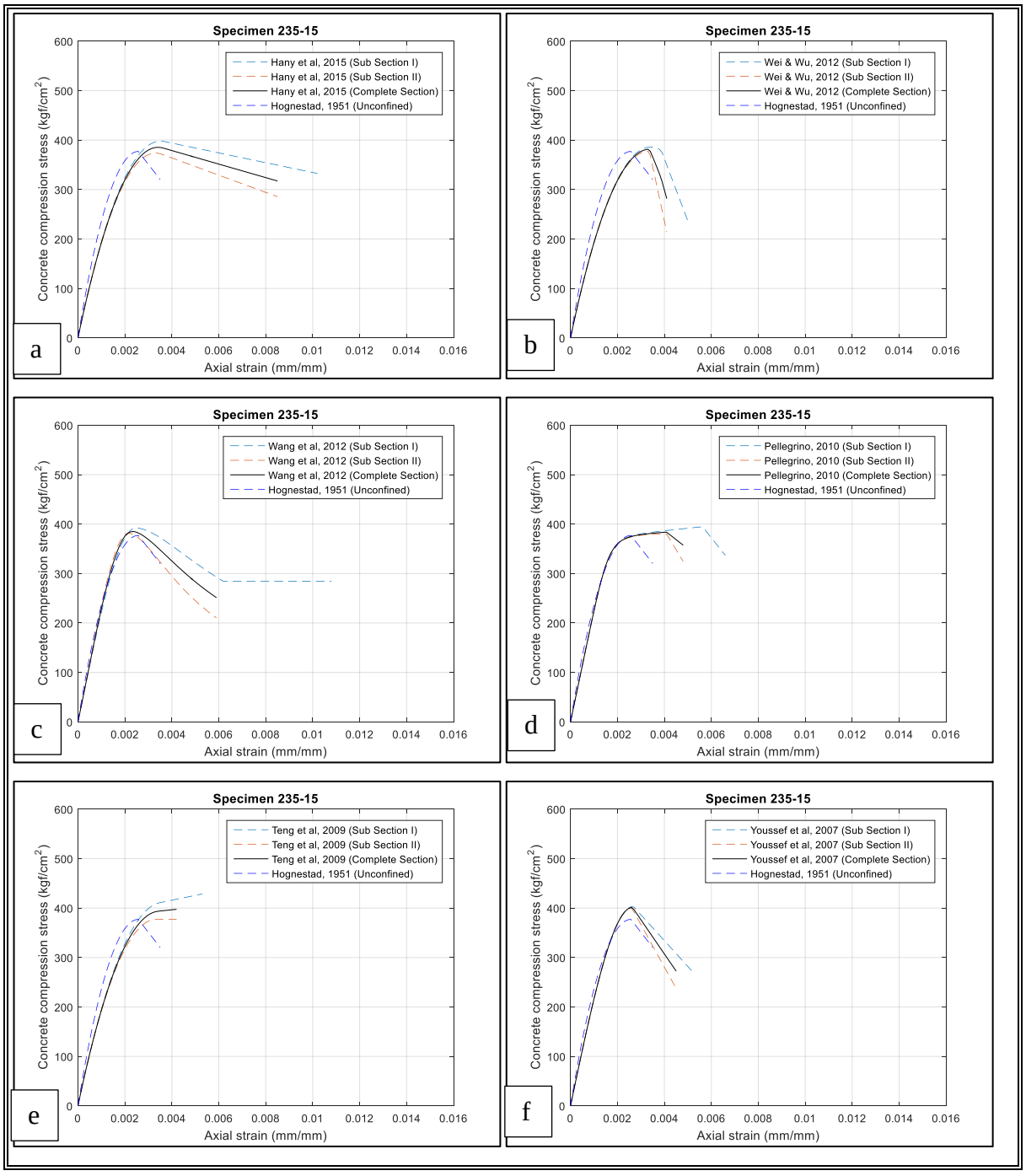

Figure D.7: Specimen 235-15 axial stress-strain curve prediction with design-oriented models according to the proposed methodology

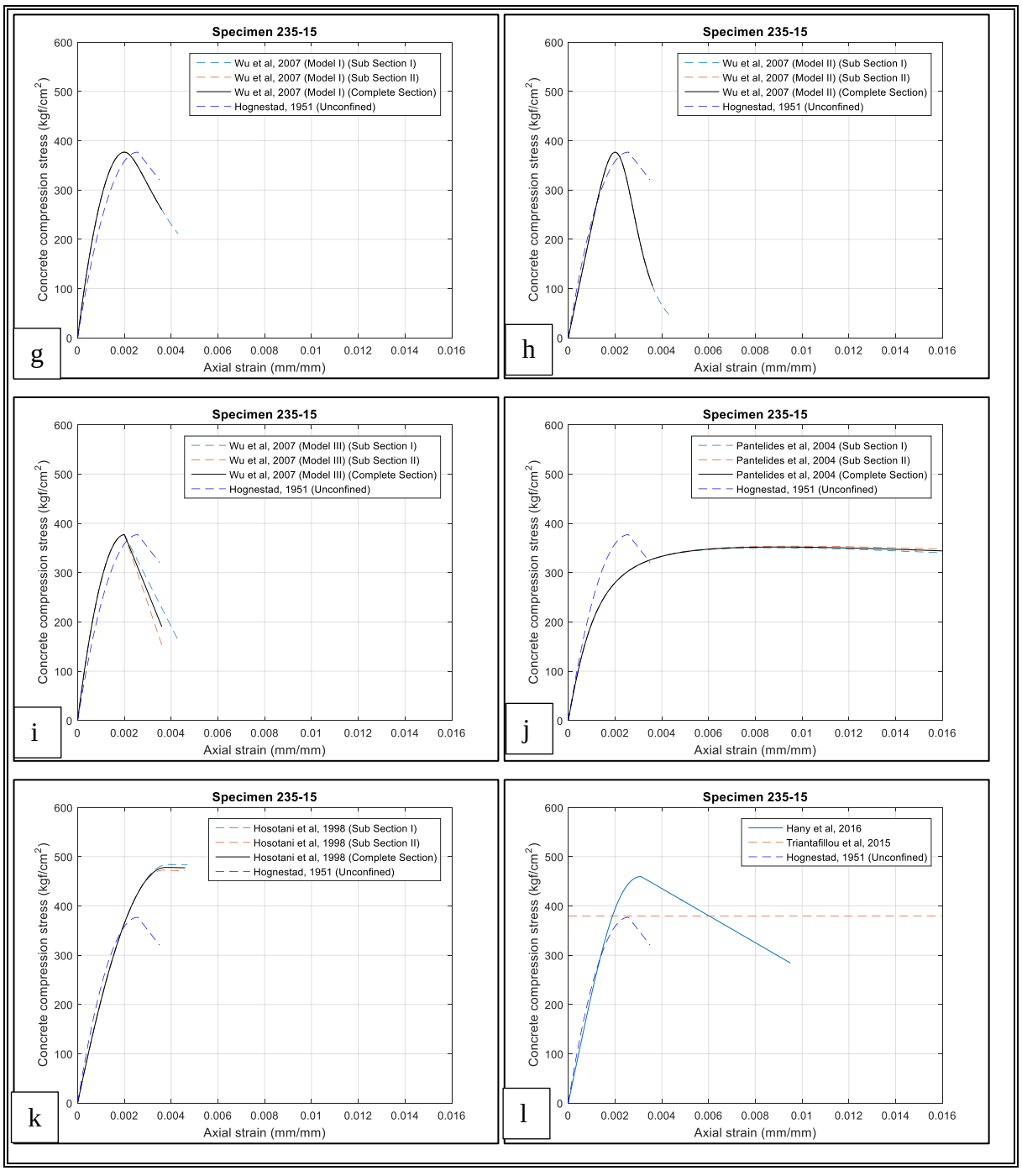

Figure D.8: Specimen 235-15 axial stress-strain curve prediction with design-oriented models according to the proposed methodology (continuation)

D.5 325-10

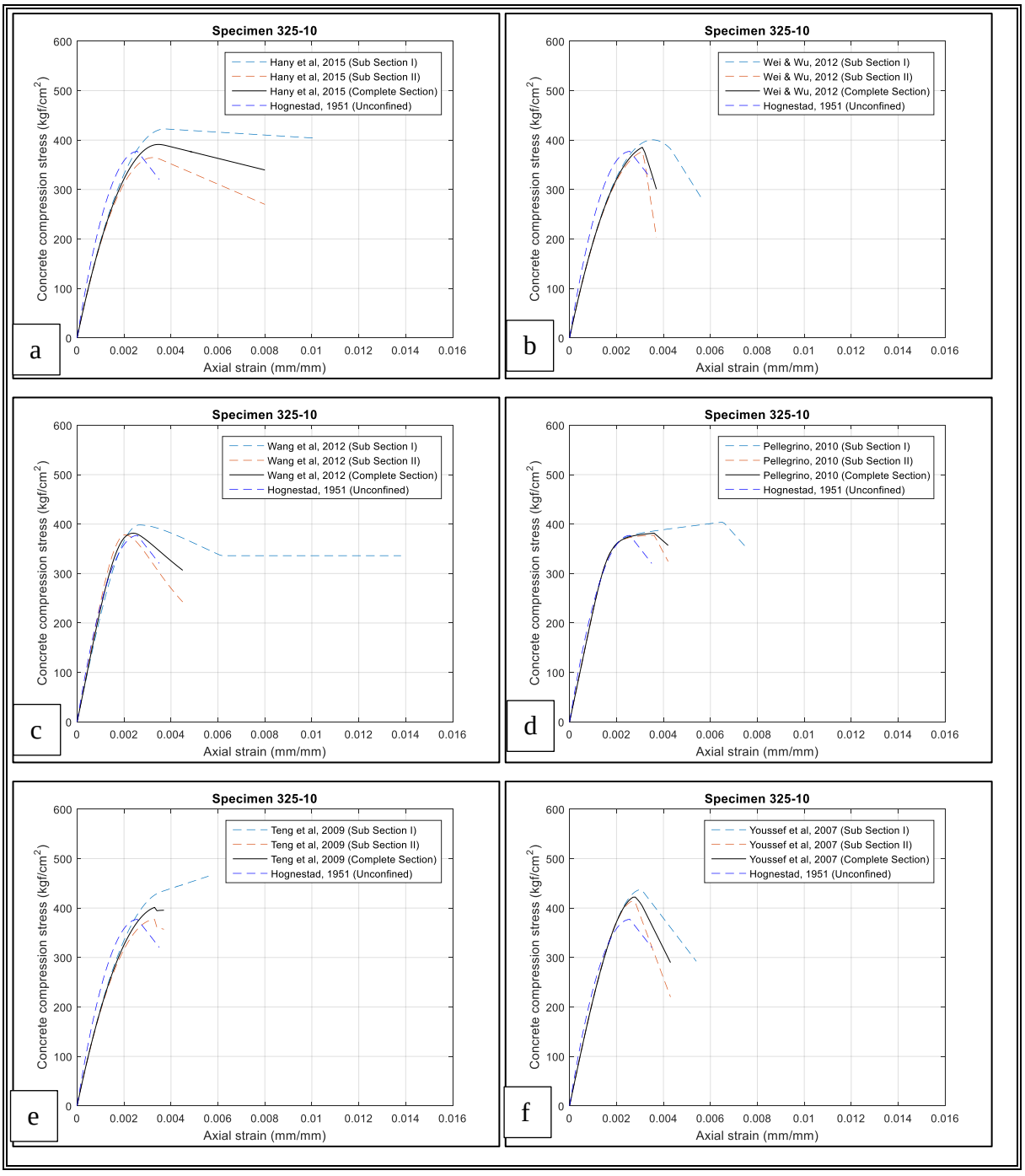

Figure D.9: Specimen 325-10 axial stress-strain curve prediction with design-oriented models according to the proposed methodology

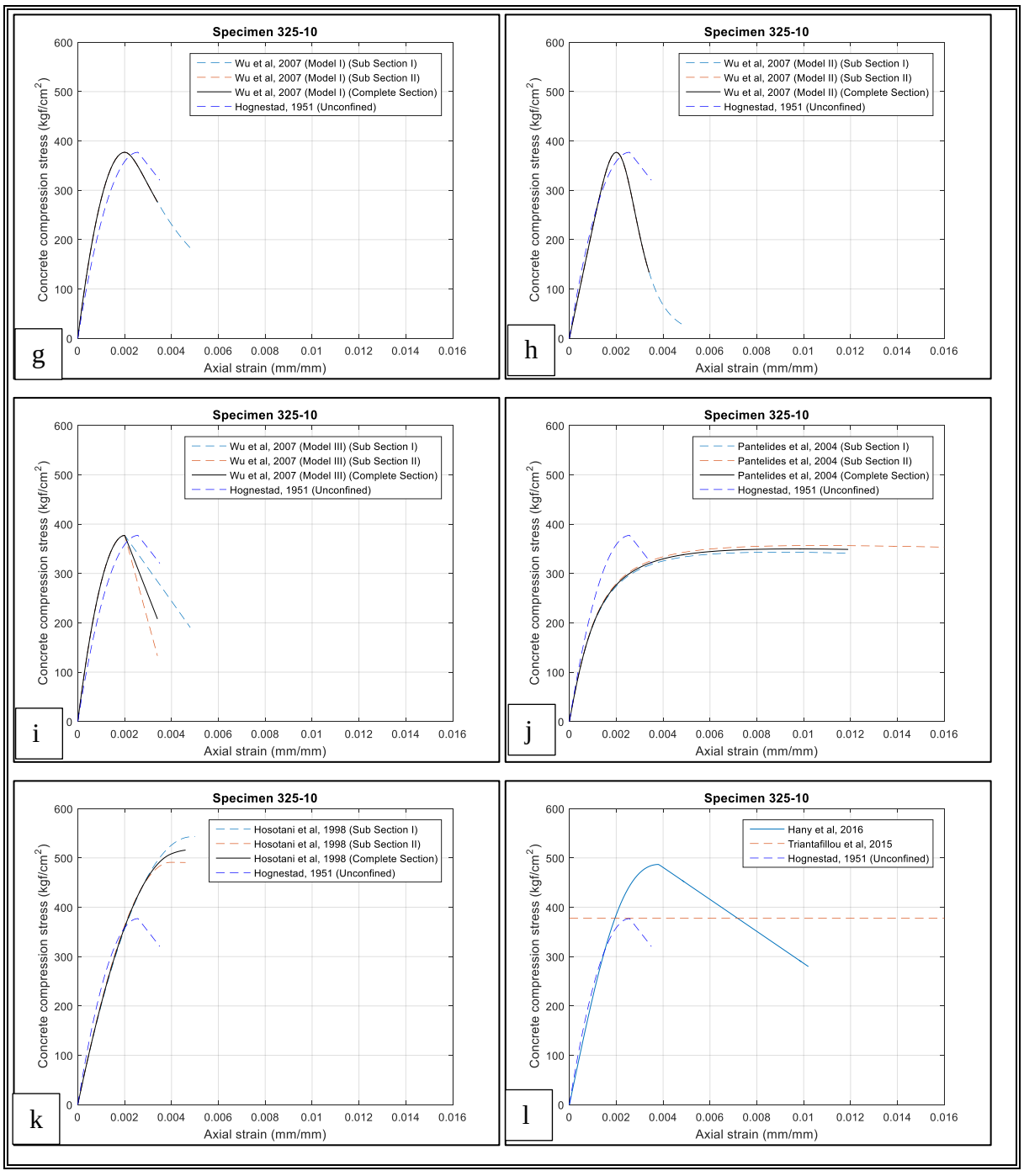

Figure D.10: Specimen 325-10 axial stress-strain curve prediction with design-oriented models according to the proposed methodology (continuation)

D.6 325-15

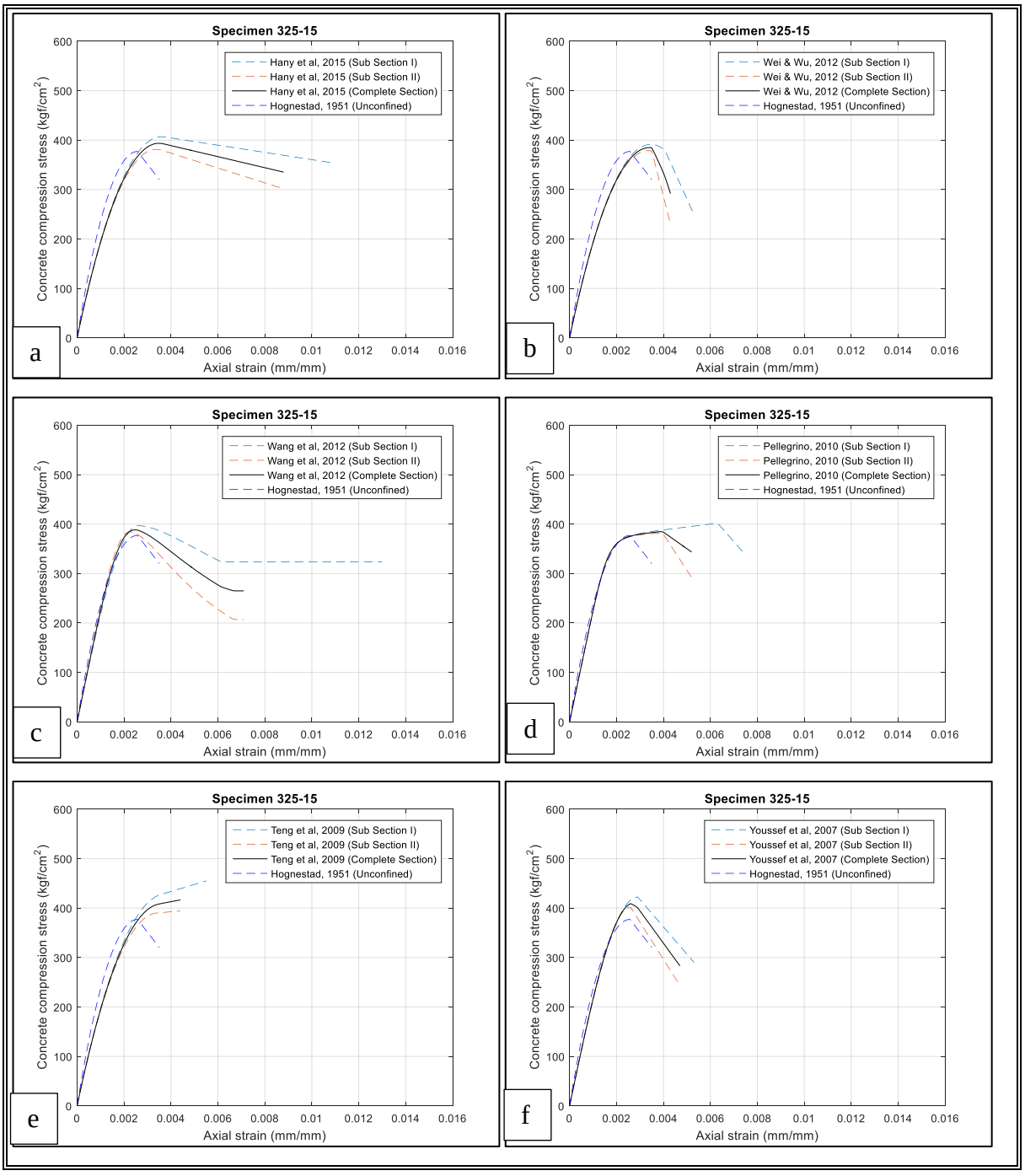

Figure D.11: Specimen 325-15 axial stress-strain curve prediction with design-oriented models according to the proposed methodology

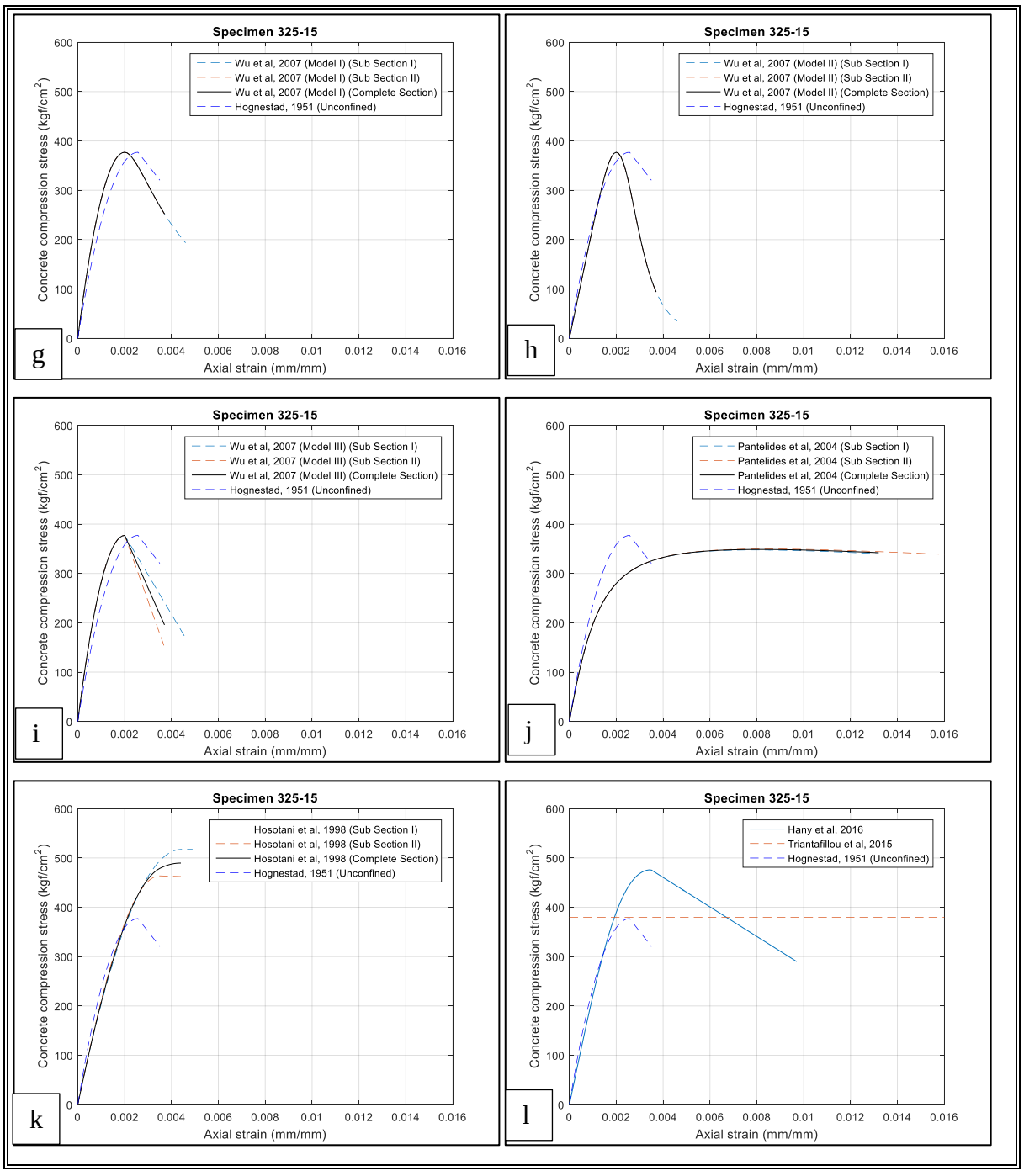

Figure D.12: Specimen 325-15 axial stress-strain curve prediction with design-oriented models according to the proposed methodology (continuation)

D.7 335-10

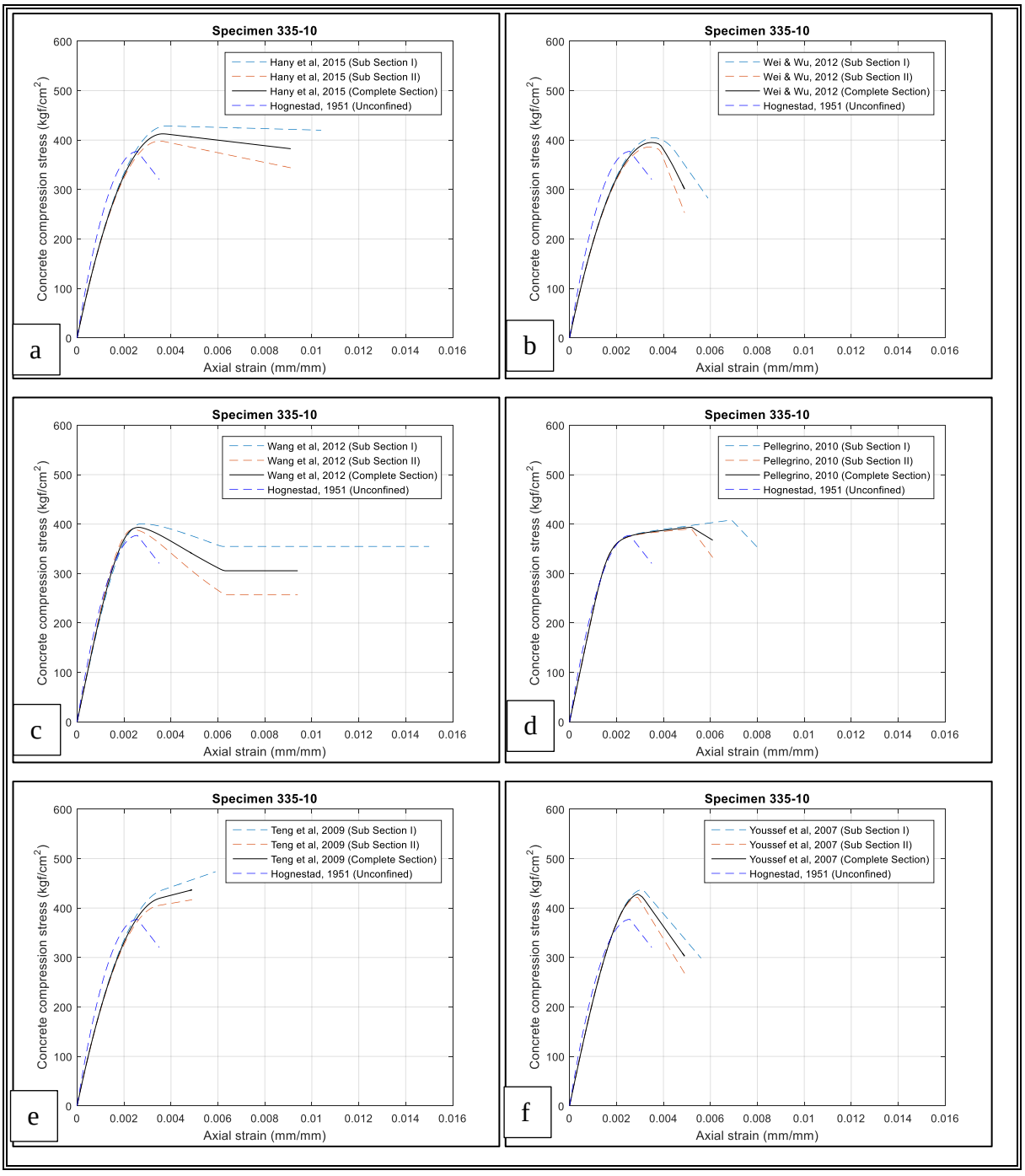

Figure D.13: Specimen 335-10 axial stress-strain curve prediction with design-oriented models according to the proposed methodology

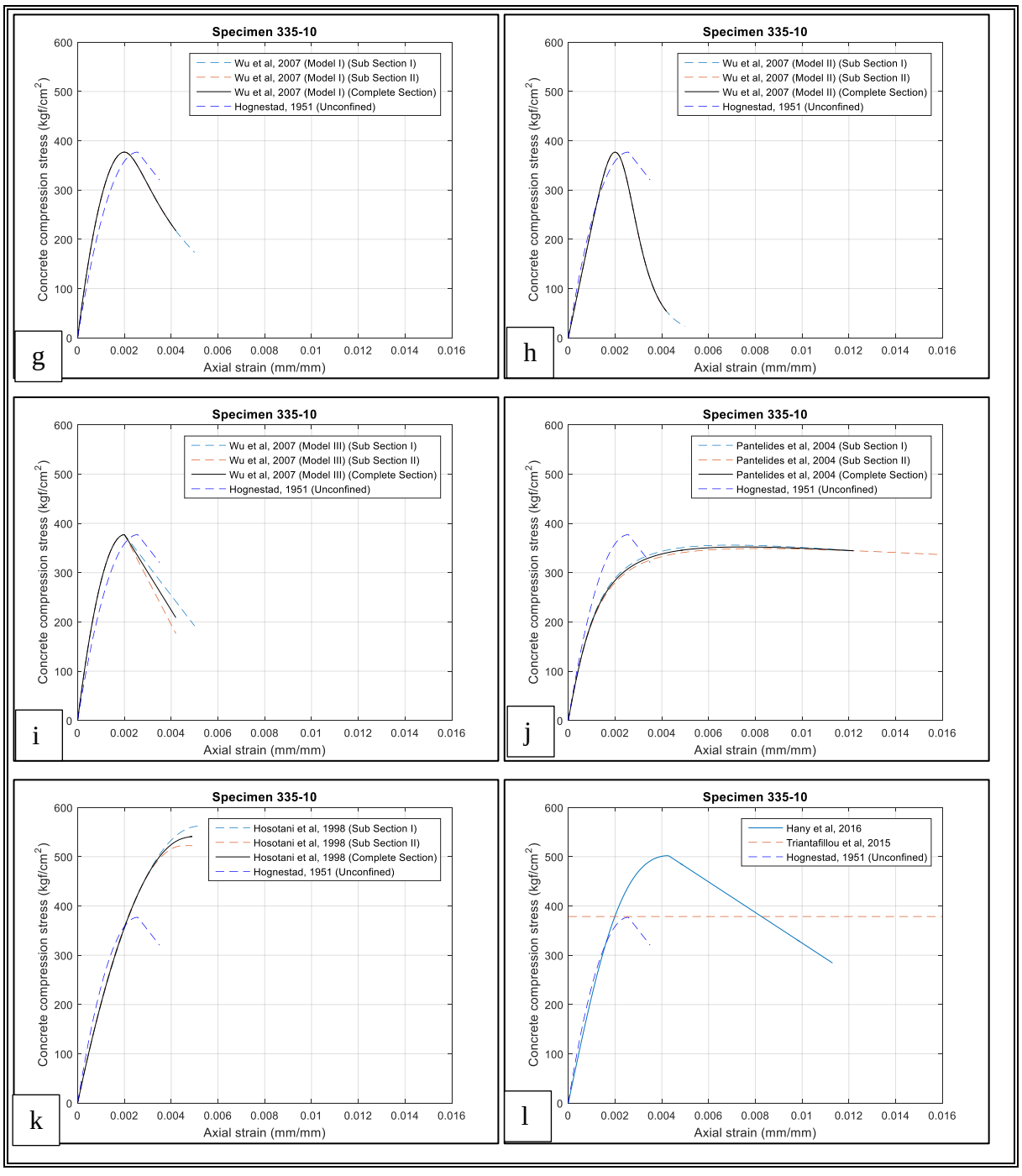

Figure D.14: Specimen 335-10 axial stress-strain curve prediction with design-oriented models according to the proposed methodology (continuation)

D.8 335-15

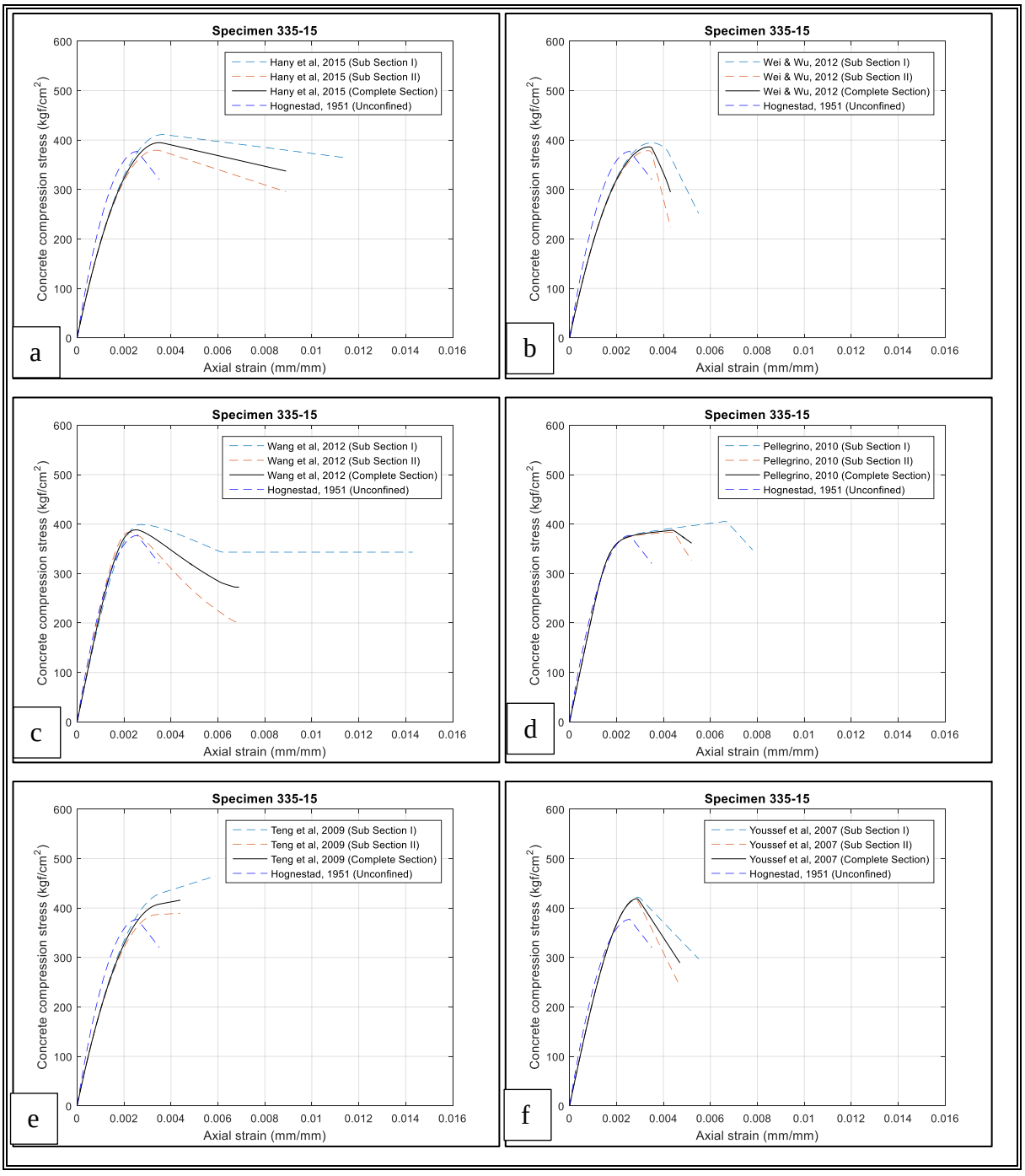

Figure D.15: Specimen 335-15 axial stress-strain curve prediction with design-oriented models according to the proposed methodology

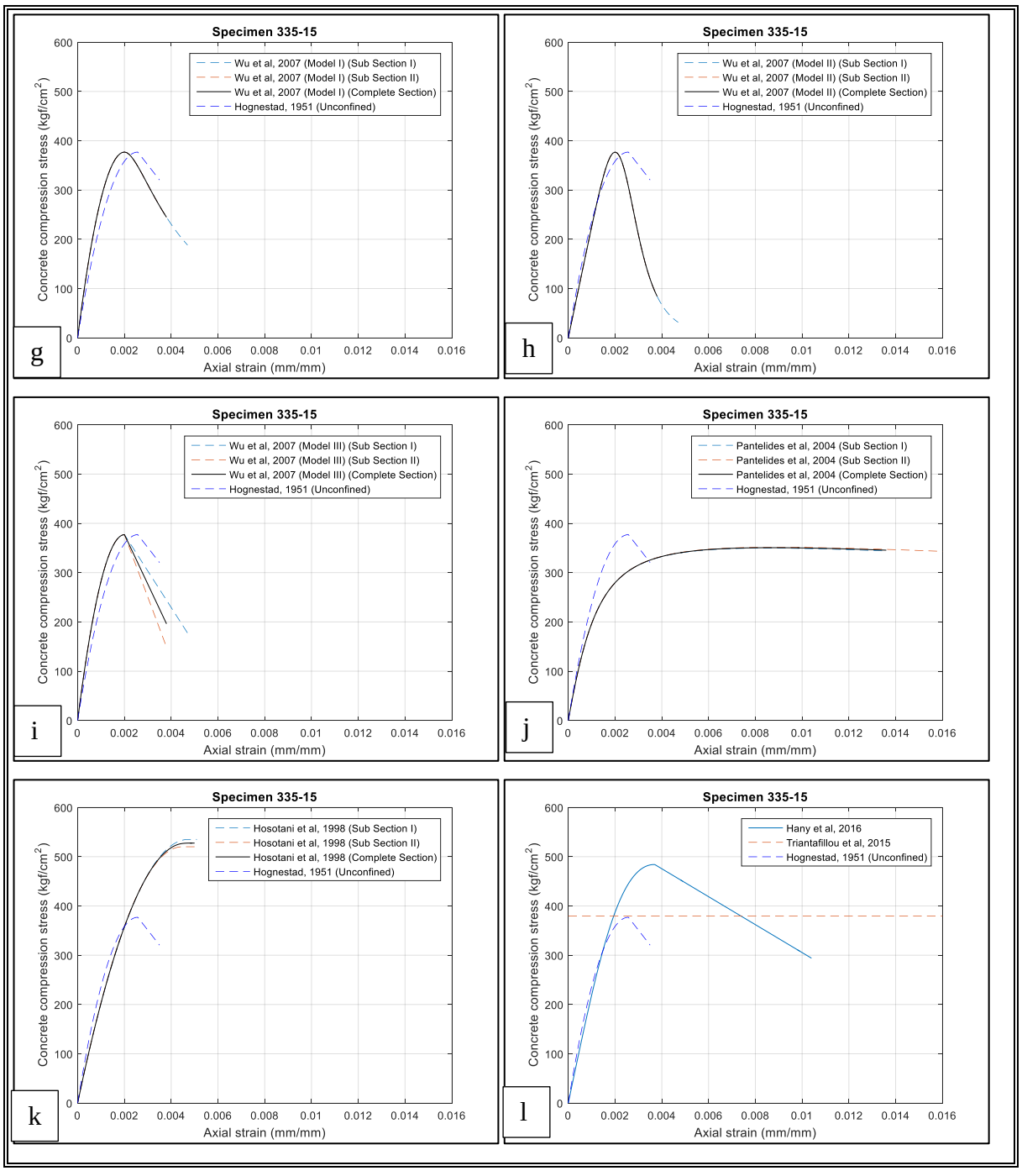

Figure D.16: Specimen 335-15 axial stress-strain curve prediction with design-oriented models according to the proposed methodology (continuation)

D.9 Matlab design-oriented closed models

```
function
[s_Hany,s_WeiWu,s_Wang,s_Pellegrino,s_Teng,s_Youssef,s_Wu_M1,s_Wu_M2,s_Wu_M3,s_Pantelides,s_Hosotani] =
ModeloDesignOriented(e,fco,Eco,eco,r,b,d,E_frp,eu_frp,rho_frp,k_s,k_e)
%% Todo en kgf-cm
%% Si se ponen los datos de frp nulos no necesariamente los modelos se convierten en hormigon no confinado
%% Datos de entrada
%{
e:      Deformacion para la cual se desea obtener la tension
fco:    Tension de resistencia maxima del hormigon no confinado en probeta cilindrica
Eco:    Modulo de elasticidad hormigon sin confinar
eco:    Deformacion correspondiente a fco
r:      Radio de giro de los bordes redondeados de las probetas
b:      Lado menor de la probeta rectangular
d:      Lado mayor de la probeta rectangular
E_frp:  Modulo elastico del frp medido en ensayo coupon
eu_frp: Deofmracion de ruptura del CFRP en ensayo de traccion pura
rho_frp:Razon volumen total de CFRP sobre volumne de columna
k_s:    Razon entre el area efectivamente confinada
k_e:    Razon entre la deforamcion de ruptura de CFRP instalado sobre la
        deforamcion de ruptura en ensayo de traccion
%}

%% Datos de Salida
%{
s_WeiWu:      Tension correspondiente a la deforamcion e, segun (Wei & Wu, 2012)
s_Wang:       Tension correspondiente a la deforamcion e, segun (Wang et al, 2012)
s_Pellegrino: Tension correspondiente a la deforamcion e, segun (Pellegrino et al, 2010)
s_Teng:       Tension correspondiente a la deforamcion e, segun (Teng et al, 2009)
s_Youssef:    Tension correspondiente a la deforamcion e, segun (Youssef et al, 2007)
s_Wu:         Tension correspondiente a la deforamcion e, segun (Wu, Wu & Lu, 2007)
s_Pantelides: Tension correspondiente a la deforamcion e, segun (Pantelides et al, 2004)
s_Hosotani:   Tension correspondiente a la deforamcion e, segun (Hosotani et al, 1998)
%}
%% Identificacion del lado corto y el lado largo
b_ = b;
d_ = d;
d = max(b_,d_);
b = min(b_,d_);

%% Tension lateral en el hormigon (sin ninguna reduccion)
fL = (1/2)*rho_frp*E_frp*eu_frp;           % Tension lateral, el GRAN supuesto de todos los Design Oriented
e_frp_h = k_e*eu_frp;                      % Deforamcion ultima del frp en la direccion de hoop

%% Tension efectiva lateral
fLe = k_s*k_e*fL;

%{
Sin importar lo que digan los distintos papers, esta es la tension que
utilizare en todos ellos. Esto por que ninguno de los papers esta hecho
para rectangulares con bandas de frp y que logran capturar softening y no
estan inspirados en modelos de acero
%}
%% Hany et al, 2015
fcu = fco*(0.7 + 4.62*(fLe/fco)*(b/d)^0.92);
ecu = eco*(3.89 + 14.76*(fLe/fco)*(d/b)^0.94);
E2 = (fcu - 1.15*fco)/ecu;
ft = 1.15*fco;
et = 2.3*fco/(Eco-E2);
if e < 0
    s_Hany = 0;
elseif e < et
    s_Hany = Eco*e - (Eco - E2)^2*e^2/(4.6*fco);
elseif e < ecu
    s_Hany = ft + E2*e;
else
    s_Hany = 0;
end
%% Wei & Wu, 2012
f30 = 300;                                 % Resistencia hormigon C30 (en EEUU) 30MPa en kgf/cm2 (probeta cilindrica)
% Punto ultimo
fcu = fco*(0.5 + 2.7*((2*r/b)^0.4)*((fLe/fco)^0.73)*((d/b)^(-1)));
ecu = eco*(1.75 + 12*((fLe/fco)^(0.75))*((f30/fco)^(0.62))*(0.36*2*r/b + 0.64)*((d/b)^(-0.3)));
% Punto de transicion
ft = fco*(1 + 0.43*((2*r/b)^(0.68))*((d/b)^(-1))*(fLe/fco));
if (ft + fcu + Eco*ecu)^2 - 8*ft*Eco*ecu < 0
    et = (ft + fcu + Eco*ecu)/(2*Eco);  % Modificacion que no esta en el orignal pero sin esto salen numero imaginario
else
    et = (ft + fcu + Eco*ecu - sqrt((ft + fcu + Eco*ecu)^2 - 8*ft*Eco*ecu))/(2*Eco);
end
% Pendiente de segundo tramo
E2 = (fcu - ft)/(ecu - et);
% Curva
if e < 0
    s_WeiWu = 0;
elseif e > ecu
    s_WeiWu = 0;
elseif e < et
    s_WeiWu = Eco*e + (ft - Eco*et)/(et^2)*e^2;
else
    s_WeiWu = ft + E2*(e - et);
end
% Comentarios
%{
Al parecer no hace ninguna reduccion a fL, no toca el tema de arcos de
confinamiento ni el tema de que la tension en el frp al momento de ruptura
no es la misma que la del ensayo coupon. No habla de como calculo las
tensiones en base a las curvas Carga-Deformacion que salen de los ensayos
Tiene el problema del sqrt((ft + fcu + Ec*ecu)^2 - 8*ft*Ec*ecu)
se vuelve imaginario, lo mejor es que seria trancarlo, eso voy a hacer
%}
%% Wang et al, 2012
```

```
% los lambdas
lambda_f = k_s*rho_frp*E_frp*e_frp_h/fco;
% Punto transicion
ft = fco*(1 + 0.35*lambda_f);
et = eco*(1 + 2.0*lambda_f);
% Punto ultimo
fcu = fco*(0.2 + 3.47*(fLe/fco)^0.64);
ecu = eco*(2 + 73.31*(fLe/fco)^1.07);
% Curvas
alfa = 1 - (fcu/ft)^1.66;
E2 = (fcu - ft)/(ecu - et);
Ep = ft/et;
A = Eco/Ep;
X = e/et;
fdt = fcu;
if e < 0
    s_Wang = 0;
elseif e > ecu
    s_Wang = 0;
else
    if E2 < 0 % softening
        if X <= 1 % al principio
            s_Wang = ft*(A*X + (3 - 2*A)*X^2 +
(A - 2)*X^3);
        else % al final
            s1 = ft*(X/(alfa*(X - 1)^2 + X));
            s2 = fdt;
            if s1 < fdt;
                s_Wang = s2;
            else
                s_Wang = s1;
            end
        end
    else % hardening
        if X <= 1 % al principio
            s_Wang = ft*(A*X + (3 - 2*A)*X^2 +
(A - 2)*X^3);
        else % al final
            s_Wang = ft*(1 + E2/Ep*(X - 1));
        end
    end
end
% Comentarios
%{
Trata de incluir los efectos de usar estribos y
frp al mismo tiempo, para
mis fines no creo que sea necesario hacerlo pues
la idea es ignorar el
confinamiento que proveen los estribos pues por
definicion tendria que ser
deficiente. Todo lo que tenga que ver son acero
es nulo para mis fines.
El paper esta pensado para columnas CUADRADAS
El paper usa fL con k_s y k_e pero define un k_s
para cuadradas envueltas
completas, yo usare el k_s real de mis
columnitas y el k_e lo elegire
%}
%% Pellegrino et al, 2010
% Datos de tablas para rectangulares sin
estribos
A = 2.25;
alfa = -0.25;
B = 23;
% Este es el jugo de sus regresiones
k_A = A*(fLe/fco)^(-alfa);
% Punto de trnasicion
et = eco;
ft = fco;
if 2*r/b <= 0.3 % softening
    k_R = 1 - 2.5*(0.3 - 2*r/b);
    % Punto de compresion maxima
    fcc = fco*(1 + k_A*k_R*fLe/fco);
    % Punto ultimo
    ecu = eco*(2 + B*(fLe/fco));
    % Punto de compresion max
    ecc = ecu*(0.55 + 1.5*(2*r/b));
    % Punto ultimo
    fcu = fcc*(0.55 + 1.5*(2*r/b));
    % Curva
    E1 = (fcc - ft)/(ecc - et);
    E2 = (fcu - fcc)/(ecu - ecc);
    Ecoo = fco/eco;
    fi1 = fcc - E1*ecc;
    fi2 = (ecu*fcc - ecc*fcu)/(ecu - ecc);
    n = 1 + 1/(Eco/Ecoo - 1);
    if e < 0
        s_Pellegrino = 0;
    elseif e > ecu
        s_Pellegrino = 0;
    elseif e < ecc
        s_Pellegrino = e*(Eco - E1)/(1 + (e*(Eco
- E1)/fi1)^n)^(1/n) + E1*e;
    else
        s_Pellegrino = E2*e + fi2;
    end
else % Hardening behavior
    k_R = 1;
    % Punto ultimo
    fcu = fco*(1 + k_A*k_R*fLe/fco);
    ecu = eco*(2 + B*(fLe/fco));
    % Curva
    E1 = (fcu - ft)/(ecu - et);
    Eco = fco/eco;
    fi1 = fcu - E1*ecu;
    n = 1 + 1/(Eco/Eco - 1);
    if e < 0
        s_Pellegrino = 0;
    elseif e > ecu
        s_Pellegrino = 0;
    else
        s_Pellegrino = e*(Eco - E1)/(1 + (e*(Eco
- E1)/fi1)^n)^(1/n) + E1*e;
    end
end
% Comentarios
%{
usa k_e
usa k_s
el modelo esta pensado para cuadradas y
rectangulares,
el modelo trata de capturar el tema de estribos
de acero pero yo lo ignoro
Hace un modelo para ver si es softening o
hardening, es mas desordenado que
los otros pero bueno
%}
%% Teng et al, 2009
rho_e = k_e*eu_frp/eco;
rho_K = fLe/fco/rho_e;
    if rho_K >= 0.01
    fcc = fco*(1 + 3.5*(rho_K - 0.01)*rho_e);
else
    fcc = fco;
end
% Punto ultimo
fcu = fco*(1 + rho_e*(3.2*rho_K^0.9 - 0.06));
ecu = eco*(1.75 + 6.5*rho_K^0.8*rho_e^1.45);
if fcu < 0.85*fco
    fcu = 0.85*fco;
end
if rho_K == 0
    fcu = 0.85*fco;
end
% Punto transicion
E2 = (fcc - fco)/ecu;
et = 2*fco/(Eco - E2);

% Curva
if e < 0
    s_Teng = 0;
elseif e > ecu
    s_Teng = 0;
elseif e < et
    s_Teng = Eco*e - (Eco - E2)^2/(4*fco)*e^2;
else
    if rho_K >= 0.01
        s_Teng = fco + E2*e;
    else
```

```
        s_Teng = fco - (fco - fcu)/(ecu -
eco)*(e - eco);
    end
end
% Comentarios
%{
lo enreda un poco con sus rho's pero al final es
lo mismo
Teng esta hecho para cilindros, su unica gracia
es que puede capturar
curva hacia abajo luego no sugiera nada para
rectagulos, luego hay que
tomar una desicion.
Los rhos igual salen del 1/2Efrp*ffrp
%}
%% Youssef et al, 2007
e_frp_t = 0.002; % uso la recomendacion del
mismo (Youssef et al, 2007), el mismo la da, def
en el frp en el punto de transicion
% Punto de transicion
ft = fco*(1 +
1.1350*(rho_frp*E_frp*e_frp_t/fco)^(5/4));
et = 0.002 +
0.0775*((rho_frp*E_frp*e_frp_t/fco)^(6/7))*((E_f
rp*e_frp_h/E_frp)^(1/2));

% Punto ultimo
fcu = fco*(0.5 + 1.225*(fLe/fco)^(3/5));
ecu = 0.004325 +
0.2625*(fLe/fco)*(E_frp*e_frp_h/E_frp)^(1/2);

% Curva tension deformacion
E2 = (fcu - ft)/(ecu - et);
if e < 0
    s_Youssef = 0;
elseif e > ecu
    s_Youssef = 0;
else
    if E2 < 0 % softening
        n = Eco*et/(Eco*et - ft);
        if e < et
            s_Youssef = Eco*e*(1 -
1/n*(e/et)^(n-1));
        else
            s_Youssef = ft + E2*(e - et);
        end
    else % hardeing
        n = (Eco - E2)*et/(Eco*et - ft);
        if e < et
            s_Youssef = Eco*e*(1 - 1/n*(1 -
E2/Eco)*(e/et)^(n-1));
        else
            s_Youssef = ft + E2*(e - et);
        end
    end
end
% Comentarios
%{
Este esta hecho para circulares y cuadradas.
Usa un e_frp_t que el mismo lo recomienda, ese
nadie mas lo usa
%}
%% Wu, Wu & Lu, 2007 ;-;
% todo entra en kgf-cm, pero algunas cosas estan
calibradas en GPa entonces
% dentro la funcion se las convierte
f30 = 300;                                      %
Resistencia hormigon C30 (en EEUU) 30MPa en
kgf/cm2 (probeta cilindrica)
alfa = f30/fco;
E_frp_GPa = E_frp*9.81*10000/1000000000;
f_c_MPa = fco*9.81*10000/1000000;
if E_frp_GPa < 250
    k_1 = 1;
    k_2 = 1;
    k_3 = (2 - alfa)*r/d + 0.5*alfa;
else
    k_1 = sqrt(E_frp_GPa/250);
    k_2 = E_frp_GPa/250;
    k_3 = (2 - alfa*sqrt(E_frp_GPa/250))*r/d +
0.5*alfa*sqrt(E_frp_GPa/250);
end
lamda = rho_frp*E_frp_GPa/sqrt(f_c_MPa);
if lamda < 0.13
    if E_frp_GPa < 250
        k_4 = (2 - 1.6*alfa)*r/d + 0.8*alfa;
    else
        k_4 = (2 -
1.6*alfa*sqrt(E_frp_GPa/250))*r/d +
0.8*alfa*sqrt(E_frp_GPa/250);
    end
else
    k_4 = (2 - 1.6*alfa)*r/d + 0.8*alfa;
end
% supongo que eu_frp del papaer era el del test
coupon pues no lo
% especifica
nu_frp = 0.56*(fLe/fco)^(-0.66);
% Punto de Transicion
ft = fco*(1 + 0.0008*alfa*k_1*lamda);
et = eco*(1 + 0.0034*alfa*k_2*lamda);
% Punto ultimo
if fLe/fco < 0.13
    fcu = fco*(k_3*(0.75 + 2.5*fLe/fco));
    ecu = k_4*0.0038*(1.3 + 6.3*fLe/fco);
else
    fcu = fco*(k_3*(0.739 + 3.418*fLe/fco -
1.215*(fLe/fco)^2));
    ecu = eu_frp/nu_frp;
end
% Curva Modelo 1
if e < 0
    s_Wu_M1 = 0;
elseif e > ecu
    s_Wu_M1 = 0;
else
    X = e/et;
    ft_MPa = ft*9.81*10000/1000000;
    B = ft_MPa/(10^6*et);
    A = -5130*B^2 + 44*B - 0.778;
    if X<=1
        s_Wu_M1 = ft*(2*X - X^2);
    else
        s_Wu_M1 = ft*(X^A)*exp(1 - X^A);
    end
end
% Curva Modelo 2
if e < 0
    s_Wu_M2 = 0;
elseif e > ecu
    s_Wu_M2 = 0;
else
    if fcu > ft
        X1 = e/ecu;
        Esec1 = fcu/ecu;
        n1 = Eco/(Eco - Esec1);
        s_Wu_M2 = fcu*X1*n1/(n1 - 1 + X1^n1);
    else
        X2 = e/et;
        Esec2 = ft/et;
        n2 = Eco/(Eco - Esec2);
        s_Wu_M2 = ft*X2*n2/(n2 - 1 + X2^n2);
    end
end
% Curva Modelo 3
if e < 0
    s_Wu_M3 = 0;
elseif e > ecu
    s_Wu_M3 = 0;
else
    if e <= et
        s_Wu_M3 = ft*(2*e/et - (e/et)^2);
    else
        s_Wu_M3 = ft + (fcu - ft)*(e - et)/(ecu
- et);
    end
end
% Comentarios
%{
```

```
Define 3 curvas, basadas en los mismo puntos lo
que pareceria innecesario,
pero lo hace. La primera solo produce softening
y las otras 2 podrian
producirlo.
%}
%% Pantelides et al, 2004
f_c_MPa = fco*9.81*10000/1000000;
E_0_MPa = 1.15*Eco*9.81*10000/1000000;
%5500*sqrt(f_c_MPa);
E_0 = E_0_MPa*1000000/9.81/10000;  % de vuelta
en kgf/cm2
beta = 190*(fLe/fco)^(-0.8);

if fLe/fco < 0.2 % con softening
    % Punto de transcicion
    if fLe/fco < 0.08
        ft = fco;
    else
        ft = fco*(4.721*sqrt(1 + 4.193*fLe/fco)
- 2*fLe/fco - 4.322);
    end
    et = 0.004; % hay un problema entre
(Pantelides, 2004) y (Pantelides, 2007),
(Pantelides, 2004) es mas razonable el otro da
cualquier cosa

    % Punto ultimo
    fcu = fco*(0.0768*log(fLe/fco) + 1.122);
    ecu = fcu*(1 + 2*beta*e_frp_h)/E_0;
else
    % Punto de transcicion
    et = 0.004;
    ft = E_0*et/(1 + beta*et);

    % Punto ultimo
    fcu = fco*(4.721*sqrt(1 + 4.193*fLe/fco) -
2*fLe/fco - 4.322);
    ecu = fcu*(1 + beta*e_frp_h)/E_0;
end

% Curva
Ep = (fcu - ft)/(ecu - et);
fi = fcu - Ep*ecu;
Ec0 = ft/et;
n = 1 + 1/(E_0/Ec0 - 1);

if e < 0
    s_Pantelides = 0;
elseif e > ecu
    s_Pantelides = 0;
else
    s_Pantelides = Ep*e + e*(E_0 - Ep)/(1 +
(e*(E_0 - Ep)/fi)^n)^(1/n);
end
% Comentarios
%{
Este viene de 1 papare y 1 reporte tecnico, en
el reporte tecnico esta
mejor explicado y de hecho en el paper hay un
error
%}
%% Hosotani et al, 1998
% Punto de transcicion
ft = fco*(1 + 1.53*rho_frp*E_frp*e_frp_h/fco);
%et = 0.00330 +
0.00995*(rho_frp*E_frp*e_frp_h/fc);
et = 0.002 +
0.00995*(rho_frp*E_frp*e_frp_h/fco);

% Punto ultimo
ecu = 0.00340 +
0.0802*((rho_frp*E_frp*e_frp_h/fco)^(3/4))*((E_f
rp*e_frp_h/E_frp)^(1/2));
Eg = -1.198*(fco^2)/(rho_frp*E_frp*e_frp_h) +
0.012*sqrt(rho_frp)*E_frp;

% Curva tension deformacion
if e < 0
    s_Hosotani = 0;
elseif e > ecu
    s_Hosotani = 0;
elseif e < et
    n = Eco*et/(Eco*et - ft);
    s_Hosotani = Eco*e*(1 - 1/n*(e/et)^(n-1));
else
    s_Hosotani = ft + Eg*(e - et);
end
% Comentarios
%{
El mas viejo de todos los modelos, Solo estaba
Este es el modelo completo mas antiguo que
encontre de frp en
rectangulares y de paso esta en japones. Cuando
este modelo fue creado
los supuestos para D nisiquiera existian.
%}
%% Tension promedio entre los distintos modelos
%s_Promedio =
mean([s_WeiWu,s_Wang,s_Pellegrino,s_Teng,s_Youss
ef,s_Wu_M1,s_Wu_M2,s_Wu_M3]);
%{
Estos modelos no me gustan por que salen muy
desfazados por eso no los
incluyo en el promedio:
s_Pantelides
s_Hosotani
%}
end


function [s_Hany,s_Triantafilliou] =
ModeloDesignOriented2(e,fco,Eco,eco,r,b,d,E_frp,
eu_frp,rho_frp,t_frp,k_s_Hany,k_s_Tria,k_e)
%% Todo en kgf-cm
%% Si se ponen los datos de frp nulos no
necesariamente los modelos se convierten en
hormigon no confinado
%% Datos de entrada
%{
e:      Deformacion para la cual se desdea
obtener la tension
fco:    Tension de resistencia maxima del
hormigon no confinado en probeta cilindrica
Eco:    Modulo de elasticidad hormigon sin
confinar
eco:    Deformacion correspondiente a fco
r:      Radio de giro de los bordes redondeados
de las probetas
b:      Lado menor de la probeta rectangular
d:      Lado mayor de la probeta rectangular
E_frp:  Modulo elastico del frp medido en ensayo
coupon
eu_frp: Deofmracion de ruptura del CFRP en
ensayo de traccion pura
rho_frp:Razon volumen total de CFRP sobre
volumne de columna
t_frp:  Espesor de las sistema de frp
k_s_Hany:    Razon entre el area efectivamente
confinada segun metodologia (Hany et al, 2016)
k_s_Tria:    Razon entre el area efectivamente
confinada segun metodologia (Triantafilliou et
al, 2015)
k_e:    Razon entre la deforamcion de ruptura de
CFRP instalado sobre la
        deforamcion de ruptura en ensayo de
traccion
%}

%% Datos de Salida
%{
s_Hanyetal:   Tension correspondiente a la
deforamcion e, segun (Hany et al, 2016)
s_WeiWu:      Tension correspondiente a la
deforamcion e, segun (Wei & Wu, 2012)
s_Wang:       Tension correspondiente a la
deforamcion e, segun (Wang et al, 2012)
```

```
s_Pellegrino: Tension correspondiente a la
deforamcion e, segun (Pellegrino et al, 2010)
s_Teng:       Tension correspondiente a la
deforamcion e, segun (Teng et al, 2009)
s_Youssef:    Tension correspondiente a la
deforamcion e, segun (Youssef et al, 2007)
s_Wu:         Tension correspondiente a la
deforamcion e, segun (Wu, Wu & Lu, 2007)
s_Pantelides: Tension correspondiente a la
deforamcion e, segun (Pantelides et al, 2004)
s_Hosotani:   Tension correspondiente a la
deforamcion e, segun (Hosotani et al, 1998)
%}
%% Identificacion del lado corto y el lado largo
b_ = b;
h_ = d;
d = max(b_,h_);
b = min(b_,h_);

%% Tension lateral en el hormigon (con la
reduccion del area efectivamente confinada)
KL = rho_frp*E_frp/2*k_s_Hany;
fL = KL*eu_frp;           % Tension lateral, el
GRAN supuesto de todos los Design Oriented

%% Datos utiles para la mayoria de los modelos
f30 = 300;                                      %
Resistencia hormigon C30 (en EEUU) 30MPa en
kgf/cm2 (probeta cilindrica)
%Eco = 15100*sqrt(fco);
% Modulo de elasticidad del hormigon no
confinado (ACI,2014), kgf/cm2 in - kgf/cm2 out
%eco = 0.000937*(fco*9.81*10000/1000000)^(1/4);
% Deformacion correspondiente a fc para hormigon
no confinado (Popovics, 1973), kgf/cm2 in - []
out
%eu = 1.75*eco;                                  %
Deformacion ultima del hormigon no confinado. Lo
tipico de las normas de diseno,
                                                %
otra opcion es usar hognestad 0.0038, o
0.0035=1.75*0.002
% Factor de eficiencia que relaciona e_frp_h =
k_e*eu_frp, varios autores
% sugieren varios tipos de k_e, lo mejor tomar
una desicion en alguno pero
% usarlo para todos
% k_e = 0.586;                                  %
Para CFRP en circulares (Lam and Teng, 2003a)
% k_e = 0.788;                                  %
Para CFRP high modulus en circulares (Lam and
Teng, 2003a)
% k_e = 0.851;                                  %
Para AFRP en circulares (Lam and Teng, 2003a)
% k_e = 0.624;                                  %
Para GFRP en circulares (Lam and Teng, 2003a)
% k_e = 0.5;                                    %
Para cuadradas y rectangulares (Pantelides &
Yan, 2007)
% k_e = 0.4;                                    %
Para cuadradas con b > 300mm (Wang et al, 2012a)
% k_e = 0.6;                                    %
Para cuadradas con 150mm < b < 300mm (Wang et
al, 2012a)
% k_e = 0.31 + 1.42*(r/b);                      %
Para cuadradas (Pantelides et al, 2004)
%k_e = 0.31 + 0.71*(r/b + r/d);                 %
Para rectangulares (Pantelides et al, 2004)
% Factor de forma que algunos paper usan es para
completamente envuelto, lo
% correcto para mi caso seria el de parcialmente
envuelto, claro solo
% cuando los paper lo pidan. De donde sale esa
ecuacion gigante esta en el
% word
e_frp_h = k_e*eu_frp;                           %
Deforamcion ultima del frp en la direccion de
hoop
%% Tension efectiva lateral
fLe = k_e*fL;
%k_s = KL*2/(rho_frp*E_frp);                     %
k_s ya deberia estar incluido en KL, luego lo
podemos sacar de ahi
% Esta correccion no la propone nadie, pero no
puede haber tension lateral
% negativa por definicion
if fLe < 0
    fLe = 0;
end
%{
Sin importar lo que digan los distintos papers,
esta es la tension que
utilizare en todos ellos. Esto por que ninguno
de los papers esta hecho
para rectangulares con bandas de frp y que
logran capturar softening y no
estan inspirados en modelos de acero
%}
%% Hany et al, 2016
% Punto de transicion
ft = fco*(0.88+0.12*(d/b)^0.3*(KL/fco)^0.38);
et = eco*(1.06+0.03*(d/b)^0.86*(KL/fco));
% Punto ultimo
fcu =
fco*(0.7+4.62*(b/d)^0.92*(KL/fco)*e_frp_h);
ecu =
eco*(3.89+14.76*(d/b)^0.94*(KL/fco)*e_frp_h);
% Curva
if e < 0
    s_Hany = 0;
elseif e > ecu
    s_Hany = 0;
elseif e < et
    x = e/et;
    Esec = ft/et;
    R = Eco/(Eco - Esec);
    s_Hany = ft*x*R/(R-1+x^R);
else
    s_Hany = (e - ecu)*(fcu - ft)/(ecu - et) +
fcu;
end

%% Triantafilliou et al, 2015
if r < 6
    k_R = r*10/60*(2-r*10/60);
else
    k_R = 1;
end
Dd = 2*b*d/(b+d);
f_frp_h = k_R*E_frp*eu_frp*k_e;
alfa_f = k_s_Tria;
s_Triantafilliou = fco*(1 +
3.3*(b/d)^2*alfa_f*(2*t_frp/Dd)*(f_frp_h/fco));
%2*t_frp/Dd
```